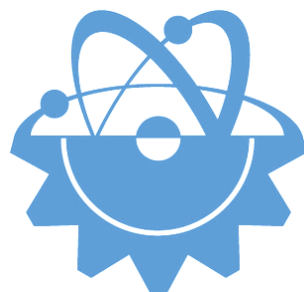


ISSN-Printed: 2536-5010
ISSN-Online: 2536-5134

Volume 11, No 2, 2021

EJT

EUROPEAN JOURNAL OF TECHNIC



Copyright © 2017

International Engineering, Science & Education Group

Email (for orders and customer services enquiries): info@ineseg.org, ejt@ineseg.org

Visit our home page on www.ineseg.org

All Rights Reserved. No part of this publication may be reproduced, stored in a retrieval system or transmitted in any form or by any means, electronic, mechanical, photocopying, recording, scanning or otherwise, except under the terms of the Copyright, under the terms of a license issued by the Copyright International Engineering, Science & Education Group (INESEG), without the permission in writing of the Publisher. Requests to the Publisher should be addressed to the Permissions Department, International Engineering, Science & Education Group (INESEG), or emailed to info@ineseg.org

Designations used by companies to distinguish their products are often claimed as trademarks. All brand names and product names used in this journal are trade names, service marks, trademarks or registered trademarks of their respective owners. The Publisher is not associated with any product or vendor mentioned in this journal.

This publication is designed to provide accurate and authoritative information in regard to the subject matter covered. It is sold on the understanding that the Publisher is not engaged in rendering professional services. If professional advice or other expert assistance is required, the services of a competent professional should be sought.



EUROPEAN JOURNAL OF TECHNIQUE (EJT)

ISSN-Printed: 2536-5010

ISSN-Online: 2536-5134

Scope: European Journal of Technique (EJT) established in 2010. It is a peer –reviewed international journal to be of interest and use to all those concerned with research in various fields of, or closely related to, Engineering disciplines. European Journal of Technique (EJT) aims to provide a highly readable and valuable addition to the literature which will serve as an indispensable reference tool for years to come. The coverage of the journal includes all new theoretical and experimental findings in the fields of Engineering or any closely related fields. The journal also encourages the submission of critical review articles covering advances in recent research of such fields as well as technical notes.

The scopes include:

- Mechanical Engineering
- Textile Engineering
- Electrical-Electronics Engineering
- Computer and Informatics Engineering
- Civil and Architecture Engineering
- Mining Engineering
- Chemical Engineering
- Metallurgical and Materials Engineering
- Environmental Engineering
- Food Engineering
- Geological Engineering
- Industrial Engineering
- Renewable Energy

EDITORIAL BOARD MEMBERS

Editor-in-Chief

- Musa YILMAZ

Publisher Of Journal

- Heybet KILIÇ

ETHICS and POLICIES

European Journal of Technique (EJT) is committed to following the Code of Conduct and Best Practice Guidelines of COPE (Committee on Publication Ethics). It is a duty of our editors to follow Cope Guidance for Editors and our peer-reviewers must follow COPE Ethical Guidelines for Peer Reviewers. We expect all prospective authors to read and understand our Ethics Policy before submitting any manuscripts to our journals.

Please note that submitted manuscripts may be subject to checks using the iThenticate service, in conjunction with CrossCheck, in order to detect instances of overlapping and similar text.

The [iThenticate](#) software checks submissions against millions of published research papers, documents on the web, and other relevant sources. If plagiarism or misconduct is found, consequences are detailed in the policy.

The chief goal of our policy is threefold: to provide advice for our authors, to maintain the scholarly integrity of our journals and their content, and to detail the ethical responsibilities of EJT, our editors and authors.

We expect all authors to read and understand our ethics policy before submitting to any of our journals. This is in accordance with our commitment to the prevention of ethical misconduct, which we recognise to be a growing problem in academic and professional publications. It is important to note that most incidents of plagiarism, redundant publication, copyright infringement or similar occur because of a lack of understanding, and not through fraudulent intent. Our policy is one of prevention and not persecution.

If you have any questions, please contact the relevant editorial office, or European Journal of Technique (EJT)' ethics representative: ejtineseg@gmail.com

Download a PDF version of the Ethics and Policies [PDF,392KB].

Authors' Responsibilities

Authors should:

- Ensure that all researched work submitted is original, fully referenced and that all authors are represented accurately. The submission must be exclusive and not under consideration elsewhere.
- Provide accurate contact details for a designated corresponding author, who shall be deemed by the publisher and editor as fully responsible for the authorship of the paper and all communications concerning the ethical status and originality of the paper. This includes any queries or investigations that may arise, pre- or post publication.
- Openly disclose the source of all data and third party material, including previously unpublished work by the authors themselves. Anything that could compromise the originality of the submission should be expressly avoided and/or discussed with the editorial office in the first instance.
- Identify any third party material that they intend to include in their article, and obtain written permission for re-use in each instance from the relevant copyright holders. Such permissions should be submitted once the manuscript is accepted, or requires small changes to be accepted. For further guidance on seeking permission to use 3rd party material please see the Rights and Permissions section.
- Openly disclose any conflict of interest - for example, if publication were to benefit a company or services in which the author(s) has a vested interest.

- Expect to formally agree publication terms which defines the author and the publishers rights for the work. Visit our website for further information.
- Expect the editor to scan submissions using plagiarism detection software at [iThenticate](#) to check a paper's originality before sending out for review.
- Fully correspond and comply with the editor and publisher in any requests for source data, proof of authorship or originality in a timely manner, providing reasonable explanation for discrepancies or failures to disclose vital information.
- Fully co-operate with any consequent investigations if the editor and/or publisher are dissatisfied with the evidence available or the explanations provided.
- Expect transparency, efficiency and respect from the publisher and the editor during the submissions process.
- Remain in good communication with both the publisher and the editor.
- When necessary, submit corrigenda in a timely and responsible fashion.
- Co-operate fully with the publication of errata and with the retraction of articles found to be unethical, misleading or damaging.
- Remain in good communication with the editor(s), the publisher and any co-authors.

Editors' Responsibilities

Editors should:

- Read and understand COPE guidelines as well as EJT's ethics policy, and follow them during all editorial processes.
- Protect the reputation of their journal(s) and published work by only publishing content of the highest quality and relevance in a timely and responsible manner.
- Carry out thorough, objective and confidential peer review for original article submissions that pass the initial quality check and editorial assessment, in adherence with COPE guidelines and EJT' ethics policy.
- Detail and justify any article types which will not be peer reviewed (e.g. editorials, opinion pieces etc.).
- Provide a transparent review and publication process as far as is possible, with full respect and care paid to the author(s).
- Provide advice and give reasonable explanation and updates to authors during the submissions process and once a decision has been made.
- Allow authors the right to appeal any editorial decision.
- Only accept papers based on the original merit, quality and relevance of their content.
- Support authors in queries concerning the originality of their submissions and request the support of EJT if necessary.
- Advise the publisher of any third party material which has been included for which they do not believe sufficient permission has been cleared.

- Be ready and prepared to publish corrections, corrigenda, errata when necessary, as well as retract articles that (the editor and EJT) deem unethical, misleading or damaging.
- Remain in good communication with both the publisher and the author(s).

Reviewers' Responsibilities

Reviewers should:

- Adhere to EJT's policy of confidential peer review of their journals. This includes, but is not restricted to, keeping their identity hidden from authors and not externally distributing any work that is passed to them for their eyes only.
- Only accept invitations to review work that is relevant to their own expertise and speciality.
- Review submitted work in a responsible, impartial and timely manner.
- Report any suspected ethical misconduct as part of a thorough and honest review of the work.
- Avoid the use of unnecessarily inflammatory or offensive language in their appraisal of the work.
- Accept the commitment to review future versions of the work and provide 'follow up' advice to the editor(s), if requested.
- Seek advice from the editor if anything is unclear at the time of invitation.
- Remain in good communication with both the publisher and the editor.

EJT's Responsibilities

EJT will:

- Protect the reputation of our journals and published work by only publishing content of the highest quality and relevance in a timely and responsible manner.
- Provide detailed information concerning both our understanding of publication ethics and our implementation of the same. Emphasise a desire for prevention, not eventual detection, of ethical misconduct.
- Uphold our COPE membership (or of such similar organisations) and keep our editorial offices, publishing staff and society partners up-to-date with their guidelines and policies, adapting our own where appropriate (and publicising any update).
- When necessary, request proof of originality/accuracy from the corresponding author of any work submitted to any of our journals.
- Use plagiarism detection software when necessary for any submission to any journal at any stage of the submissions and publication process.
- Provide a transparent submissions and publication process, with full respect and care paid to the author. This includes detailed and dedicated instructions to authors for each journal, outlining referencing style, accepted article types and submission processes.
- Investigate thoroughly any suggestion of ethical misconduct detected during any stage of the submissions process. This can include, but is not restricted to, the following: plagiarism, redundant publication, fabrication or misuse of data and authorial disputes.

- When necessary, retract articles that we deem to be unethical, misleading or damaging.
- When necessary, publish errata, corrigenda and retractions in a timely and responsible fashion, detailing the decision online in an open access format and publishing in print as soon as possible.
- Remain in good communication with editors, authors, reviewers and society partners (where applicable).

Further reading

- Authorship of the paper: Authorship should be limited to those who have made a significant contribution to the conception, design, execution, or interpretation of the reported study.
- Originality and plagiarism: The authors should ensure that they have written entirely original works, and if the authors have used the work and/or words of others that this has been appropriately cited or quoted.
- Data access and retention: Authors may be asked to provide the raw data in connection with a paper for editorial review, and should be prepared to provide public access to such data.
- Multiple, redundant or concurrent publication: An author should not in general publish manuscripts describing essentially the same research in more than one journal or primary publication. EJT do not view the following uses of a work as prior publication: publication in the form of an abstract; publication as an academic thesis; publication as an electronic preprint. Information on prior publication is included within each EJT and its journal Guideline for Authors.
- Acknowledgement of sources: Proper acknowledgment.
- Disclosure and conflicts of interest: All submissions must include disclosure of all relationships that could be viewed as presenting a potential conflict of interest.
- Fundamental errors in published works: When an author discovers a significant error or inaccuracy in his/her own published work, it is the author's obligation to promptly notify the journal editor or publisher and cooperate with the editor to retract or correct the paper.
- Reporting standards: Authors of reports of original research should present an accurate account of the work performed as well as an objective discussion of its significance.
- Hazards and human or animal subjects: Statements of compliance are required if the work involves chemicals, procedures or equipment that have any unusual hazards inherent in their use, or if it involves the use of animal or human subjects.
- Use of patient images or case details: Studies on patients or volunteers require ethics committee approval and informed consent, which should be documented in the paper.

EJT has also accessed and learned from the existing policies of other publishers and leading experts as well as open access articles that detail and define ethical misconduct.

- 'Plagiarism and the law', Joss Saunders, Learned Publishing, 23:279-202: <http://www.ingentaconnect.com/content/alpsp/lp/2010/00000023/00000004/art00002>
- iThenticate Plagiarism Resources: <http://www.ithenticate.com/resources/6-consequences-of-plagiarism>

Editor-in-Chief

Musa Yilmaz, Batman University, Turkey

Vice Editor

Furkan Emre Sahin, Maxim Integrated, San Jose, CA, US

International Editorial Board

Aayush Shrivastava	University of Petroleum and Energy Studies, Dehradun, India
Adelino Pereira	Engineering Institute of Coimbra, Portugal
Ahmad Fakharian	Islamic Azad University, Qazvin, Iran
Ahmed Saber	Cairo University, Egypt
Arvind Kumar Jain	Rustam Ji Institute of Technology, India
Aydogan Ozdemir	Istanbul Technical University, Turkey
Baseem Khan	Hawassa University, Hawassa, Ethiopia
Behnam Khakhi	University of California Los Angeles, US
Behnam Mohammadi-ivatloo	University of Tabriz, Tabriz, Iran
Bharti Dwivedi	Institute of Engineering & Technology, Lucknow, UP, India
Carlos A. Castro	University of Campinas – UNICAMP, Brasil
Cafer Budak	Dicle University, Turkey
Deepak Kumar	University of Petroleum & Energy Studies (UPES), India
Ernesto Vazquez	University of Nuevo Leon, Mexico
Faisal Khan	COMSATS Institute of Information Technology, Pakistan
Farhad Shahnia	Murdoch University, Perth, Australia
Farrokh Aminifar	University of Tehran, Iran
Fatih Kocyigit	Dicle University, Turkey
Fiaz Ahmad	National University of Computer and Emerging Sciences, Pakistan
Gouthamkumar Nadakuditi	V R Siddhartha Engineering College, India
Hafiz Ahmed	School of Mechanical, Coventry University, UK
Hamed Pourgharibshahi	Lamar University, US
Hassan Bevrani	University of Kurdistan, Iran
Hayri Yildirim	Dicle University, Turkey
Hemant Kumar Gianey	Thapar University, Patiala, Punjab, India
Hessam Golmohamadi	Semnan University, Semnan, Iran
Heybet Kilic	Dicle University, Turkey
Hilmy Awad	Helwan University, Cairo, Egypt
Hüseyin Acar	Dicle University, Turkey
Idris Candan	Kocaeli University, Turkey
Jamshed Ahmed Ansari	Sukkur IBA University, Pakistan
José A. Domínguez-Navarro	University of Zaragoza, Spain
Kalpana Chauhan	Galgotias College of Engineering and Technology, India
Khaled Ellithy	Qatar University, Doha, Qatar
Kim-Doang Nguyen	South Dakota State University, US
Kundan Kumar	KIIT University, India
Lalit Kumar	GBPIET Pauri, India
Leila Mokhnache	University of Batna 2, Algeria
Linquan Bai	ABB Inc., US
Mehmet Emin Asker	Dicle University, Turkey
Md Shafiullah	King Fahd University of Petroleum & Minerals, Saudi Arabia
Mohamed Shaaban	Universiti Malaysia Sarawak, Malaysia

Mohammed Albadi	Sultan Qaboos University, Oman
Mohd Tariq	Aligarh Muslim University, India
Mousa Marzband	Northumbria University, Newcastle upon Tyne, United Kingdom
Neeraj Kanwar	Manipal University Jaipur, India
Nishant Kumar	Indian Institute of Technology Delhi, India
Nitin Kumar Saxena	Wolaita Sodo University, Ethiopia
Nouar Tabet	University of Sharjah, UAE
Omar Hafez	Umm Al-Qura University, Makkah, Saudi Arabia
Omveer Singh	Gautam Buddha University, India
Payam Teimourzadeh Baboli	University of Mazandaran (UMZ), Iran
Payman Dehghanian	George Washington University, US
Ragab A. El Sehiemy	Faculty of Engineering, Kafrelsheikh Univrsity, Egypt
Rajeev Kumar Chauhan	Galgotias College of Engineering and Technology, India
Rajiv Singh	G.B. Pant University of Agriculture & Technology, India
Reza Sharifi	Amir Kabir university Tehran, Iran
Rudranarayan Senapati	Kalinga Institute of Industrial Technology, India
Saleh Y. AbuJarad	Universiti Teknologi Malaysia, Malaysia
Sanjay Dambhare	College of Engineering, Pune, India
Saptarshi Roy	NIT Warangal, India
Shailendra Kumar	Indian Institute of Technology Delhi, India
Shariq Riaz	The University of Sydney, Australia
Shengen Chen	University of Maine, US
Syafaruddin	Universitas Hasanuddin, Indonesia
T. Sudhakar Babu	VIT University, Vellore, India
Thamer Alquthami	King Abdulaziz University, Saudi Arabia
Theofilos Papadopoulos	Democritus University of Thrace, Greece
Uday P. Mhaskar	CSA Group, US
Vedat Veli Cay	Dicle University, Turkey
Yogesh Rohilla	K LakshmiPat University, Jaipur, India
Yunfeng Wen	School of Electrical Engineering, Chongqing University, China
Zbigniew M. Leonowicz	Wroclaw University of Science and Technology, Poland

Publisher of Journal

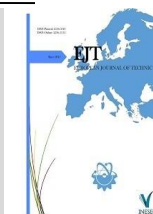
Heybey Kilic

Dicle University, Turkey / TU Delft, Netherland



CONTENTS

Design and Implementation of EOG Signal Based Wireless System to Control Smart Devices Nazmi EKREN, Abdalrahman SKHETA	107 - 114
Investigation of Leakage and Stability Analysis in Rock Filling Dams: The Example of Kolludere Pond Hayrullah AKYILDIZ	115 - 119
EEG Channel Selection using Differential Evolution Algorithm and Particle Swarm Optimization for Classification of Odorant-Stimulated Records Mesut ŞEKER, Mehmet Sıraç ÖZERDEM	120 - 125
While Covid-19 Outbreak Affects Economies and Societies; Exploring The Energy Demand in Turkey Hasan Huseyin COBAN	126 - 135
Measurement of the Number of Photoelectrons per MeV for Neutron Detectors Emre İREN, Ferhat ÖZOK, Mustafa Nizametin ERDURAN	136 - 139
Application of Choline Chloride as Natural Deep Eutectic Solvents for the Green Extraction of Phenolic Compounds from Rheum Ribes Leaves Fatih BİLDİK	140 - 143
Submodule Based MPPT with Synchronous Buck Converter Under Dynamic Partial Shading Conditions Mustafa Engin BAŞOĞLU	144 - 152
Comparative Analysis of Lighting Elements' Effects on Electric System Sait DURSUN, Ümit TERZİ, Onur AKAR, Temel SÖNMEZOCAK	153 - 164
A Novel Local Feature Generation Technique Based Sound Classification Method for Covid-19 Detection using Lung Breathing Sound Türker TUNCER, Erhan AKBAL, Emrah AYDEMİR, Samir Brahim BELHAOUARI, Sengul DOGAN	165 - 174
Investigation of the Effects of Use of GNP and GNP Reinforced Nano-Fibers with Epoxy Adhesive on Tension Tests Edip ÇETKİN	175 - 181
Investigation the Physical and Rheological Properties of Bitumen Modified with Warm Mix Asphalt Additive İslam GOKALP	182 - 189
Model of Combined IPT and NNLVQ for Classification of Healthy and Sick Broilers In Terms of Avian Influenza Ahmet KAYABAŞI	190 - 194
A New Joining Algorithm for Multi-hop Non-mobile Wireless Sensor Networks Musa ÇIBUK, Davut ARI, Fikri AĞGÜN	195 - 199
Investigation of Power Consumption Effect of Various Memristor Emulators on a Logic Gate Sevgi GÜRSUL, Serdar Ethem HAMAMCI	200 - 208
Medium and Large Vector-Based SVPWM Technique for Five-Phase Two-Level Inverter Erkan DENİZ	209 - 216
An Investigation on Mechanical and Microstructural Properties of Porous Nickel-Based Alloy Fabricated by Investment Casting as an Implant Materials Yusuf ER	217 - 221
Investigation of Failure Mechanism of a DCI Engine Connecting Rod Mustafa Güven GÖK, Ömer CİHAN	222 - 228
Design and Development of a Helmholtz Pair System for Production of a Low-Magnetic Field of up to 7.5 mT Yenal GÖKPEK, Özgün Boray YURDAKOŞ, Özkan DOĞANAY	229 - 233
Comparative Analysis of Six Phase Induction Motor İsmail SARIGÜL, Mehmet ÖZDEMİR	234 - 238
Demand-Side Energy Management in Smart Buildings: A Case Study Nazlı HASANOVA, Seçil VARBAK NEŞE	239 - 247
Detection of Covid-19 from X-ray Images via Ensemble of Features Extraction Methods Employing Randomized Neural Networks Ömer Faruk ERTUĞRUL, Emrullah ACAR, Abdulkemir ÖZTEKİN, Erdoğan ALDEMİR	248 - 254
Evaluation of Machine Learning Hyperparameters Performance for Mice Protein Expression Data in Different Situations Cafer Tayyar BATI, Gazel SER	255 - 263
Investigation of Mechanical And Tribological Properties of Boric Acid Reinforced Composite Plates Taner AYDIN, Kadir TURAN, Nejat Yıldırım SARI	264 - 269



Design and Implementation of EOG Signal Based Wireless System to Control Smart Devices

Abdulahman SKHETA^{1*} , Nazmi EKREN² 

¹Marmara University, Electrical and Electronic Engineering Department, 34854, Istanbul, Turkey. (e-mail:eng.abdulahman.sk@gmail.com).

²Marmara University, Electrical and Electronic Engineering Department, 34854, Istanbul, Turkey. (nazmiekre@marmara.edu.tr).

ARTICLE INFO

Received: Sep., 15. 2021
Revised: Oct., 21. 2021
Accepted: November, 01. 2021

Keywords:
EOG
ALS
Vital-Signals

Corresponding author: A. Skheta

ISSN: 2536-5010 / e-ISSN: 2536-5134

DOI: <https://doi.org/10.36222/ejt.996015>

ABSTRACT

Vital signals like Electroencephalogram (EEG), Electrooculography (EOG), and Electroretinogram (ERG) have been used in many areas due to their effectiveness and accuracy. Electrodes can obtain the signals, and then they can be amplified and processed. This study helps people with reduced mobility like paralysis and Amyotrophic Lateral Sclerosis (ALS) using EOG signals. EOG signal is effective in this case because these people can use their eyes without any obstacles. EOG aid system can enable them to rely on themselves in the use of smart devices. This is one of the first studies to present a detailed analysis of the signal acquisition and processing and the results were promising with a result that scored 95% rate.

1. INTRODUCTION

Helping people with disabilities is one of the most important and humane jobs. Supporting disabled people can help transient them from an inactive status in the community to active individuals who can perform daily activities independently and eventually contribute to society's building. Vital signals like (EEG), (EOG), and (ERG) have been used in many domains for medical treatment, for instance, the analysis of brain signals and capturing it for disease identification, and discovering muscle disorders. It is proved to be a promising solution for people with special needs, as these signals can be easily obtained using electrodes that can capture these signals, and then apply a set of techniques to amplify them and process them. The experiment on people with reduced mobility like paralysis and (ALS) using EOG signals is effective in this case because these people can use their eyes without any obstacles, which allows them to extend their physical capabilities with the help of technology. Such as giving commands to a computer through a mouse cursor without having direct physical contact with it. There have been useful case studies in this field that discussed various methodologies and applications, for instance, the article written by Manuel Merino (2010) [1], included developing an EOG signal processing algorithm method to detect the direction of eye movements. Another article written by Octavio Rivera, et al. (2013) [2], used an algorithm that

captures the EOG signal and converts this vital signal into a mechanical one [3], which helped study and design a motorized wheelchair with EOG control for disabled people. Nese Ozkan, et al. (2017) [4], studied the design and acquisition of EOG based interactive communications for patients with ALS by applying the EOG signal to them. In the article written by Lawrence Y. Deng Chun Liang Hsu (2002) [5], an EOG-based Human-Computer interface system was developed. The article written by Lawrence R. Barea, et al. (2012) [6], discussed codification of captured EOG signals from eye movement was used for human-computer. In the article written by Cristian-Cezar Postelnicu (2012) [7], a method to develop an EOG-based visual navigation interface by using HCI interface was studied. In the article written by A. Schlögl, C.Keinrath (2007) [8], Merging EEG signal with EOG signal to improve the quality of EOG signal was studied. In a thesis written by Ramis Ileri (2010) at Erciyes University, the determination of the most appropriate writing characters for educating children with dyslexia by using EOG signal was studied [9]. In a thesis written by Ahmet Coşkun (2017) at Selcuk University, sleep staging with (EOG) signals by 36 features was studied [10]. The advantage of this study is the ability to obtain the EOG vertical and horizontal signal simultaneously. The system is wireless; hence it can provide more convenience to the user. Vertical and horizontal eye movement is processed by a dedicated microprocessor device, and another customized

processor is responsible for operating the connected smart device. In this way, the system is efficient as it can operate in a fast and smooth manner

2. METHOD AND MATERIAL

As all smart devices have the same control method, one case was studied, which is controlling the mouse cursors of a computer. The system consists of two parts (two electric circuits): the main circuit that the user places in his pocket and a second circuit placed in the smart device. The main circuit includes an effective EOG signal acquisition section. The most important components of this circuit are the instrument amplifier, second-order low pass filter, adder amplifier, ATMEGA-328 microprocessor, and HC-05 Bluetooth module. The analog EOG signal is converted into a digital signal by the microprocessor. The digital EOG signal is processed to identify the location and movement of the eye. Then the main circuit sends the data (eye location) to the second circuit via (HC-05) Bluetooth module. Where the second circuit receives the data and moves the mouse cursor of the device (computer). The second circuit includes an Arduino Leonardo and HC-05 Bluetooth module. Arduino Leonardo has a feature that can be used as a USB mouse or keyboard. Using the five electrodes placed on the head, the user can control the cursor that appears on the screen just by looking at the exact location where the user wants to move the cursor.

2.1. The structure of the eye

The eye is the main organ of the visual process. It is responsible for grasping events happening outside the body. Figure 1 shows major eye departments. The eye can be compared to a camera in general. Both have a lens on the front. It is responsible for projecting images onto sensitive areas at back. While a camera contains photosensitive photographic film, there is a layer called the retina in an eye. Images falling on the retina are taken by millions of nerves endings here, transmitted to the center of vision in the brain, and the image is perceived [11].

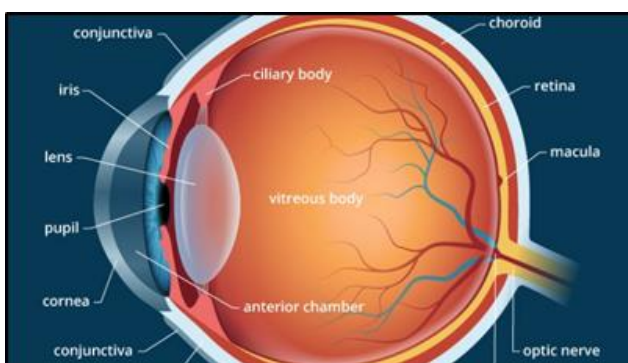


Figure 1. The Major Eye Departments [12]

2.2. Amyotrophic lateral sclerosis (ALS)

Diseases such as paralysis and ALS cause people to lose some basic motor skills, especially in their hands or feet. ALS, also known as motor neuron disease, is caused by the loss of motor nerve cells (neurons) in the central nervous system, spinal cord, and brainstem area. With the loss of these cells, muscle weakness and melting (atrophy) begin. On the other hand, paralysis is a clinical problem caused by brain damage caused by the cessation of flow in blood vessels feeding the brain due

to a clot. The limb (s) where this brain damage occurs can no longer be controlled. Figure 2 shows the difference between an average person and a person with ALS.

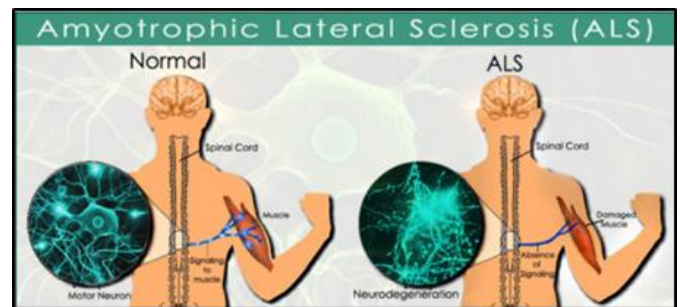


Figure 2. The Difference Between an Average Person and a Person with ALS [13]

2.3. The origin of eye vital signals

To understand these signals, it is necessary to know eye anatomy. The eye is not a perfect sphere. It is a fused two-part unit. It consists of the anterior segment and posterior segment. The anterior segment consists of the cornea, iris, and lens. The larger posterior segment consists of the vitreous, retina, choroid, and outer white shell called the sclera. There is a permanent electrical potential difference between the anterior segment and the posterior segment. This potential arises from the retinal pigment epithelial layer. Two different vital signals can be extracted from this potential difference: ERG signal and EOG signal.

2.3.1. ERG signal

To measure the electrical responses of various cell types in the retina, ERG can be used. Figure 3 shows the electrical response of eye cells according to cell type. The signal is too small and normally measured in microvolts or nano-volts.

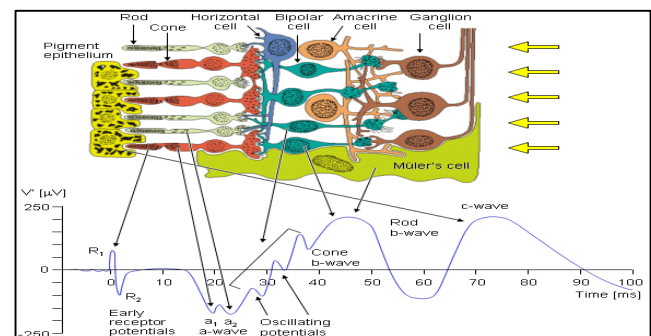


Figure 3. Review of Electrical Signals (ERG) [14]

2.3.2. EOG signal

The eye can be compared to an electrical dipole, where the positive pole is a cornea and the negative pole is the retina. The difference is thought to be due to the high metabolic rate in the retina. EOG is the process of recording the potential difference between the front and back of the eye, this potential difference is obtained with special electrodes that are placed appropriately around the eye [15]. Figure 4 shows EOG's electrical response as a function of time when looking left and right.

The range of the EOG signal is between 0.4 and 1.0 millivolts (without amplification). When recording a signal, it is difficult to determine the degree of eye accurately, so the achieved

accuracy is up to ± 2 degrees, sensitivity is between 5&20 microvolts per degree.

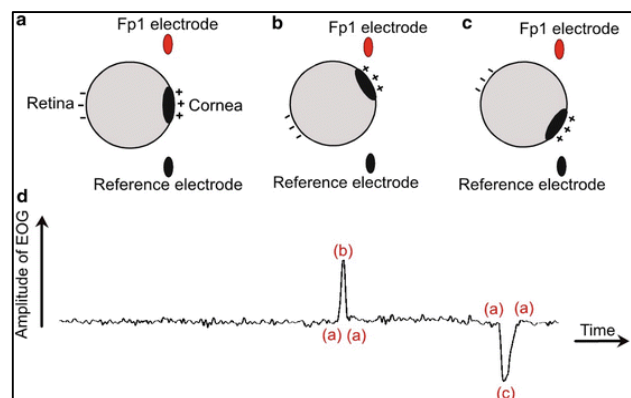


Figure 4. EOG Signals as biometrics when looking left and right [16]

The recorded EOG signal is represented as a function of time and is caused by the eye moving to a certain degree over a period of time. The difference between EOG and ERG is shown in table 1.

TABLE II
THE DIFFERENCE BETWEEN EOG AND ERG

Signal	ERG	EOG
The range of the signal	-125>>200 uV	0.4>>1.0 mV
Type of electrode used	Fiber electrodes	Silver-silver chloride electrodes
Uses	Measure the electrical response of optical eye cells	Determine the location of the eye

2.4. Obtaining EOG signal

EOG signal is obtained by special electrodes. Because the received signal is very low, it must be processed to become a signal that can be used. Figure 5 shows simply how the signal is obtained and amplified using an amplifier. The steps will be explained in more detail in the following paragraphs.

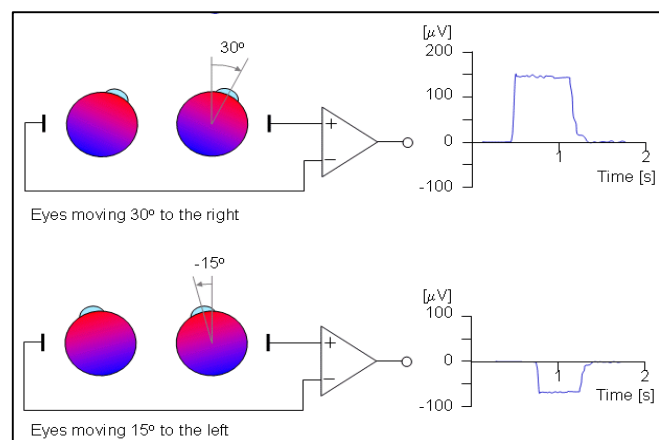


Figure 5. EOG signal Obtaining [17]

2.5. Places where electrodes must be placed to obtain EOG

To obtain the vertical and horizontal signals, four electrodes must be used. To reduce overlapping signal noise, a reference electrode must be placed on the forehead. Two electrodes are placed to right and left of the eye to record the horizontal signal in the eye, and two electrodes are placed below and above the eye to record the vertical signal. Figure 6 shows electrode fixation positions to determine horizontal and vertical eye movement.

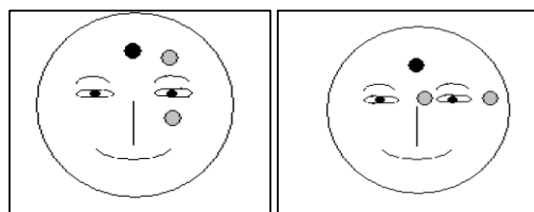


Figure 6. Electrodes placement [18]

2.6. Difficulties while measuring EOG and the procedures must followed

The main difficulty is that person applying electrodes should avoid moving the muscles of the head or face as this will interfere with the signal. While using this signal to control smart devices, it is difficult to keep up the stability of these muscles during prolonged use of the signal. Filtration circuits are usually used to solve this problem. The most important steps considered to increase the accuracy of measurement:

- A- Use appropriate electrodes to improve the signal.
- B- Adding gel to increase conductivity of electrodes.
- C- Before applying electrodes, the skin should be thoroughly cleaned.
- D- Suitable insulated cables must be used to prevent electrical signals from overlapping.

2.7. Amplifying the EOG signal

The special operational amplifiers which is used to process vital signals from the human body is called instrument amplifiers [19]. Important signals acquired from the human body often have small amplitudes. It is challenging to obtain necessary information from small values, so the signal must be amplified and filtered. The instrument amplifier is the best combination to achieve amplification of the vital signal. It depends on the amplification of the difference between two signals in inverting and non-inverting inputs. Figure 7 shows the internal structure of the instrument amplifier.

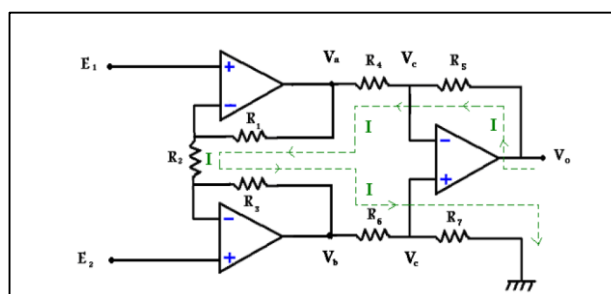


Figure 7. Internal structure of instrument amplifier [19]

The gain of this amplifier can be controlled by changing the resistance value of R2 (External resistance) according to the following equation:

$$\text{Gain} = 1 + \left(\frac{50000}{R2} \right) \quad (1)$$

To amplify signal 126 times, 400Ω resistance must be used.

2.8. EOG signal filtering

After amplifying the vital signal, it must be filtered from the interfering signals. Filters are electronic circuits used to prevent certain frequencies from passing through; these frequencies are noise superimposed on the frequency of the useful signal. To eliminate these frequencies, the properties of capacitors and coils were used to obtain passive filters [20]. Amplifiers are used to obtain effective filters.

2.8.1. Effective low-pass filter

The second-order effective low-pass filter can be used to get a better response, second-order low-pass filter is widely used as it's easy to design and operate [21]. Figure 8 shows the electric circuit of a second-order low-pass filter. Different values for R1, R2, C1, and C2 were tried until a cutoff frequency of 7 Hz was obtained. (When experimenting, it was observed that the best value of cut-off frequency is 7 Hz). To obtain a cutoff frequency of 7 Hz, the following values were selected; R3 = R4 = 220 kΩ., C1 = C2 = 10 nf.

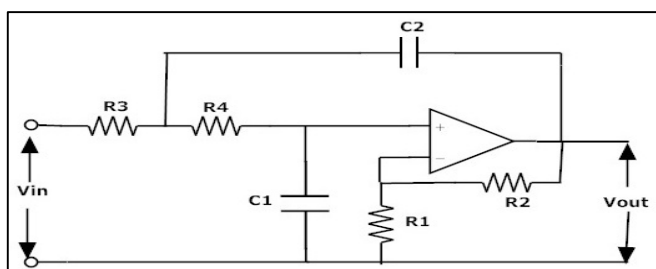


Figure 8. Effective low pass filter [22]

2.9. Adder amplifier

After filtering the signal, it must be converted into a digital signal, the microprocessor can be used to convert an analog signal into digital. But analog EOG signal ranges between positive and negative values. Since the microprocessor can't read negative values, another amplifier must be used to raise the negative portion of the signal and make it a positive value [23]. The best solution to increase the negative portion is using an adder amplifier. Figure 9 shows the adder amplifier circuit. This circuit is similar to an inverting operational amplifier circuit except that it has multiple inputs instead of a single input.

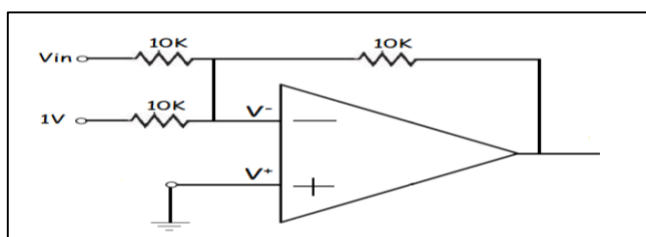


Figure 9. Adder amplifier [24]

When applying 1V to V⁻ in-circuit showed in Figure 9, and applying an analog signal to V_{in} (±2). The output signal must be V_{in}+1. Figure 10 shows V_{in} signal. Figure 11 shows the output signal. Likewise, the negative part of EOG signal can be amplified. The EOG signal is applied to V_{in}. On other input, to control value it must be added to EOG signal to increase it from negative part, a voltage divider must be used.

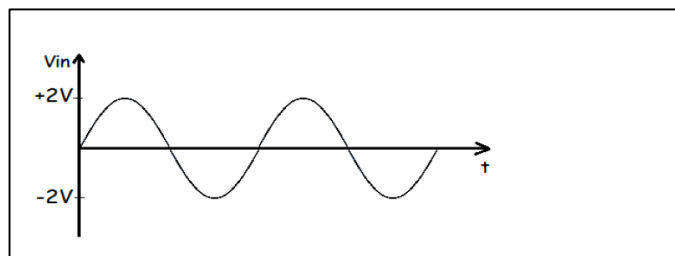


Figure 10. Adder amplifier input [24]

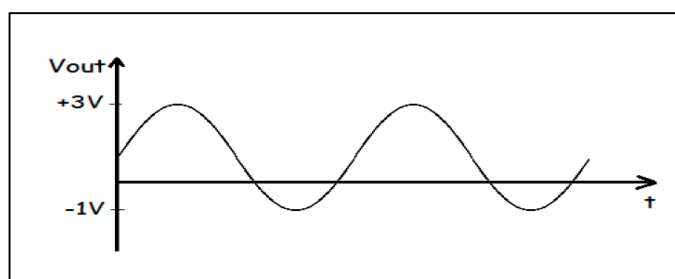


Figure 11. Adder amplifier output [24]

2.10. Circuit Installation and components

To amplify the vital signal, INA118 instrument amplifier was used. Then the signal is filtered with an effective low-pass filter. Next, the signal value is raised via an adder amplifier. A TL082 IC is used to filter and increase signal, where TL082 IC contains two amplifiers inside it. After obtaining the signal and filtering it, it was converted into a digital signal via AT-MEGA-328p microprocessor [25]. The task of the processor in this circuit is to convert an analog signal into a digital signal and process signal to determine horizontal and vertical eye position, then send data to HC-05 Bluetooth module via UART serial port [26]. The Bluetooth module converts data into wireless signals and sends it to the second circuit. The second circuit contains a Bluetooth module and Arduino Leonardo. Bluetooth module decodes received wireless signal to obtain data, then sends data to Arduino Leonardo via serial port UART, Arduino moves mouse cursor according to received data. The Arduino Leonardo is used for this task because it has a USB connection feature and it can be programmed easily to be used as a mouse. The mission of the Arduino Leonardo is limited to converting data format from UART to USB. Two batteries were used to power the circuit (negative and positive voltages are required for the operational amplifier). It is preferable to use a battery in those circuits to reduce noise resulting from alternating current.

2.10.1. Block diagram

The block diagram shows the stages of signal acquisition, amplification, filtering, processing, and converting it to digital, then sending it via Bluetooth to the second circuit. The second circuit moves the mouse cursor according to data coming from the main circuit, where the circuit is fed with continuous ±12 volts through two batteries. Figure 12 shows the block diagram.

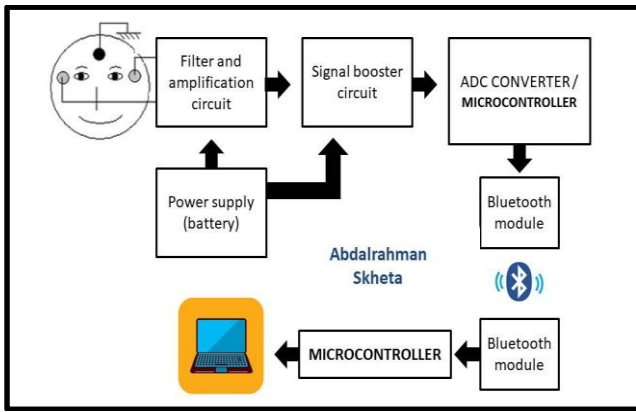


Figure 12. Block diagram

2.10.2. Electrodes

AG/AG-CL electrodes were used. The AG/ AG-CL electrode is one of the most widely used electrodes to obtain the EOG signal. Figure 13 shows one of the electrodes that were used to obtain the signal. Where silver used must be 99.99% pure.



Figure 13. AG / AG-CL electrode

2.10.3. Connecting cables

To reduce noise ECG device cable was used. Figure 14 shows the used cable



Figure 14. ECG cable

2.10.4. PCB

A PCB for the main circuit has been designed. The circuit is made of two layers with 7.5x8.5 cm dimensions. The circuit consists of three main sections: horizontal EOG signal processing section, vertical EOG signal processing section, and third section.

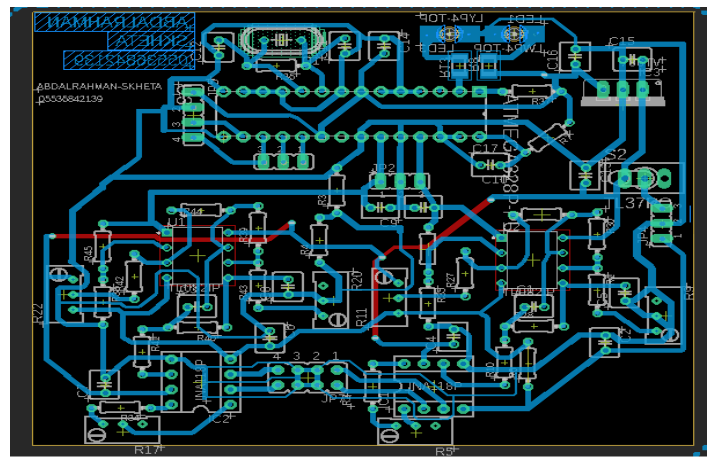


Figure 15. The board after drawing it

The third section contains the AT-MEGA328 microprocessor and HC-05 Bluetooth module. It also has a voltage regulator to feed the processor and Bluetooth module at a voltage of 5V. Horizontal & vertical EOG signal processing sections are identical, both contain INA118 amplifier and TL082 amplifier, in addition to passive components such as capacitors and resistors. The circuit is drawn using EAGLE program [27]. Figure 15 shows PCB after drawing it. Figure 16 shows front and back of PCB after it has been printed.

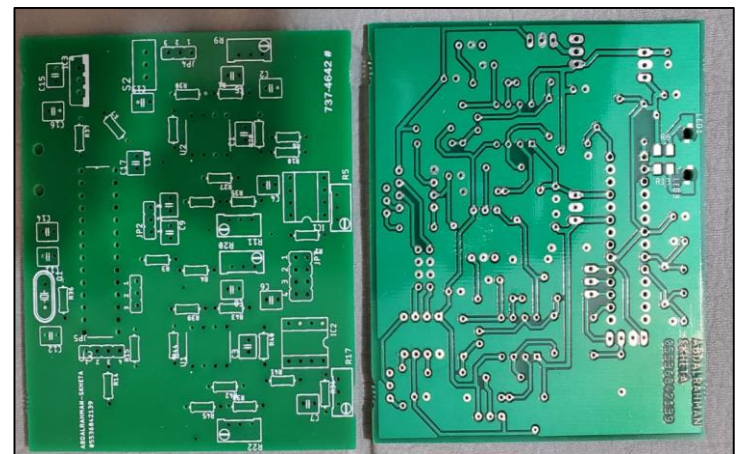


Figure 16. PCB, after being printed

2.11. Code flowchart

The flowchart shows how code works. After obtaining horizontal and vertical analog signals, they are converted into a digital signal and stored in two variables: (Xreading) for vertical signal and (Yreading) for horizontal signal. Looking ahead saved as a center point and stored in a variable called (center). To ensure that there is no interference (interfering signals) such as eyelid movement and noise signals from surrounding muscles, a constant so-called (threshold) was used. Threshold subtracts from the value of the obtained signal.

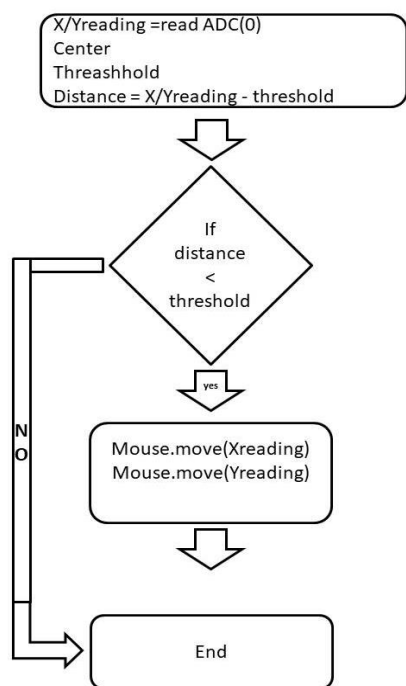


Figure 17. Code flowchart

The microcontroller determines the location of the eye according to the final value, then gives orders to move the mouse cursor accordingly. Figure 17 shows the Code flowchart.

3. RESULTS

After electronic elements were placed on the circuit, electrodes were attached to the eye area and fed to the circuit, then signals obtained at each stage were examined (after amplification, after filtering, and after raising signal value). As explained previously, the circuit contains three main sections. Two of them are similar: the horizontal EOG acquisition circuit and the vertical EOG acquisition circuit. As results will be the same in the second section, EOG signal in the first section was studied. Since the circuit is complex and contains many elements, the first section in a simplified way was drawn, where passive components such as resistor and capacitor were removed.

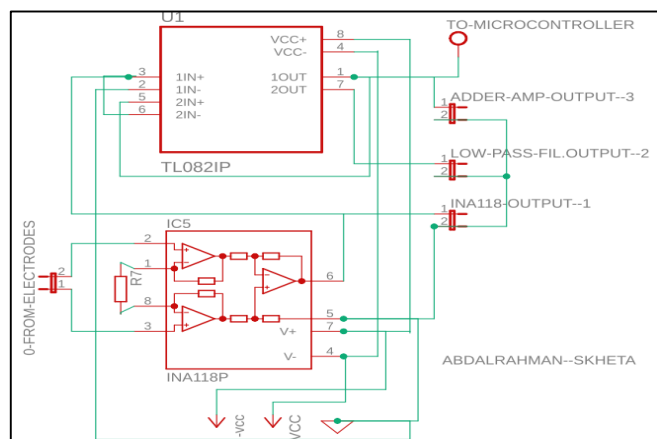


Figure 18. Simple diagram of the signal acquisition section

Figure 18 shows a simplified diagram of the signal acquisition section. Number 0 jumper is the input of INA118 [28] (where electrodes are connected). Number 1 jumper shows the output

of INA118. Number 2 jumper shows the output of TL082 [29] (low pass filter) where the output of this amplifier will be the input of adder amplifier. Number 3 jumper shows the output of the adder amplifier and it is the final signal that will be converted into a digital signal, so it is connected to the microcontroller.

The oscilloscope probe was connected to jumper number 1 and the person who uses the device began to look left and right. The result is observed to be good, but the noise is still high. The obtained signal is shown in Figure 19.

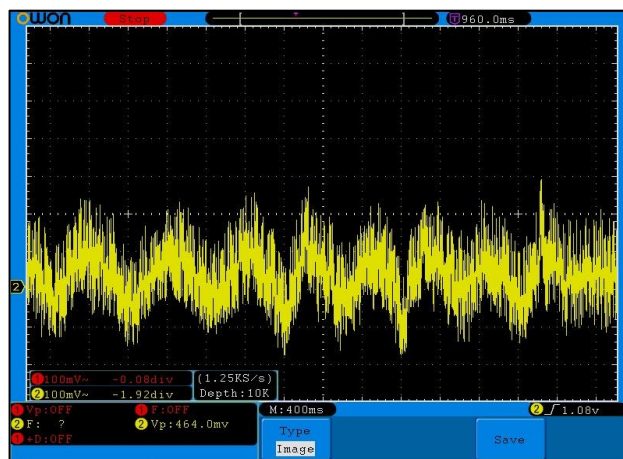


Figure 19. INA118 output

Afterward, the oscilloscope probe was connected to jumper number 2 (low pass filter output) and the person who uses the device started to look left and right. In this case, the noise level was reduced by 95%, the signal was low noise and clear. Figure 20 shows the state of the signal after filtering.

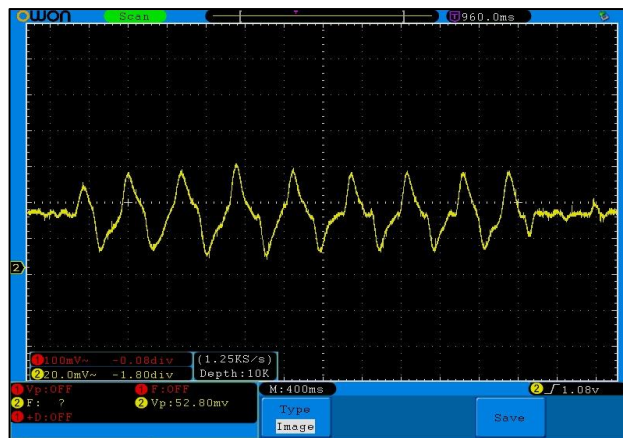


Figure 20. The output after it has been filtered

Then the person looked to the far-right for a second, and then looked ahead. A positive pulse with low noise is displayed on the oscilloscope screen. Figure 21 shows a positive pulse.

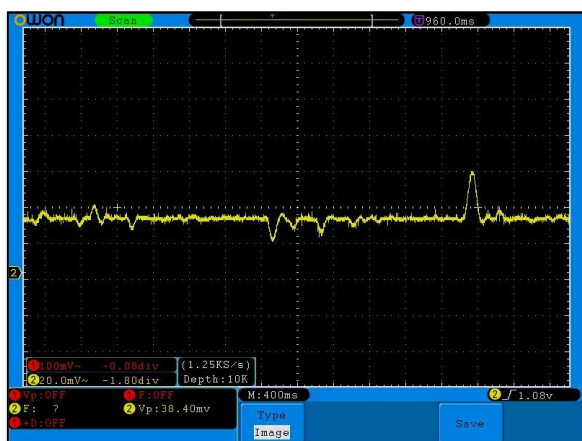


Figure 21. The output when looking right

Next, the person wearing the electrode looked far left for one second, then forward. A low-noise negative pulse is displayed on the oscilloscope screen. Figure 22 shows a negative pulse. In this way, a clear signal that can be used was obtained. Then the negative side of the signal was raised to a positive value by the adder amplifier. After increasing the value of the signal, it was converted into a digital signal.

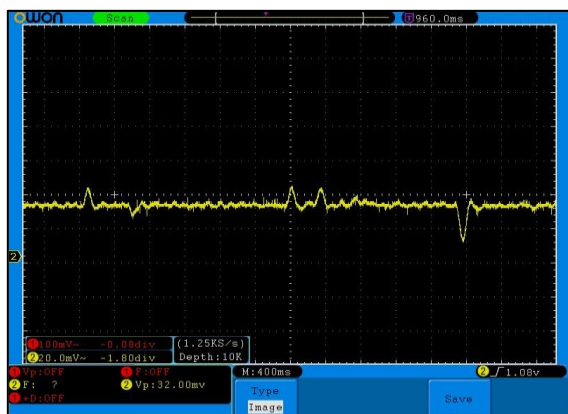


Figure 22. The output when looking left

The EOG signal value must be positive. The second amplifier in TL082 circuit was used to raise the negative portion of the signal from negative to positive. The value of primitive potential (Electric potential when looking forward) was calibrated at 2.5V by changing the value of variable resistance that connected to the amplifier. Figure 23 shows the output of the adder amplifier when looking forward.

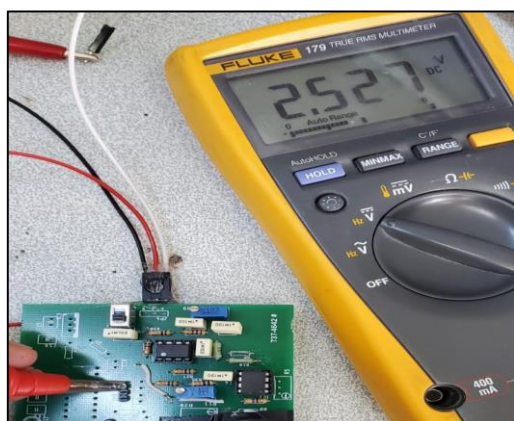


Figure 23. Adjust output at 2.5V when looking straight

TABLE II
THE OUTPUT CHANGES ACCORDING TO EYE MOVEMENT

Eye direction	Output(Volt)
Forward	2.5
Right (25 degrees)	2.7
Far-Right	2.9
Left (25 degrees)	2.3
Far-Left	2.1

The final results show that the circuit output is positive in all cases. This means that the resulting EOG signal can be processed by the processor.

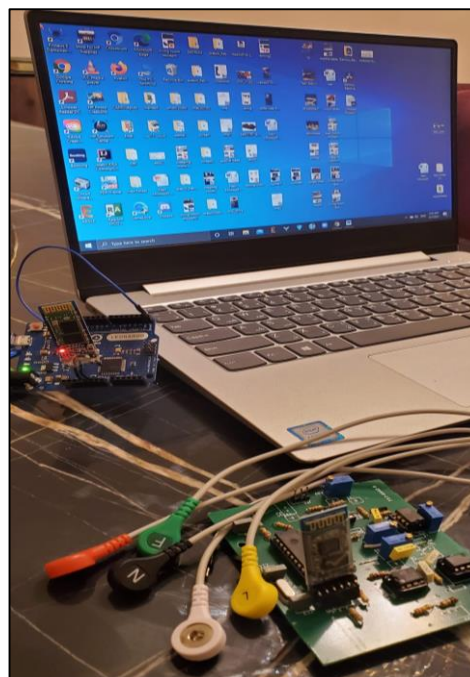


Figure 24. The final shape of the system

Since the output value is in the range of (0-5) volts, the processor can convert this signal to a digital signal. In this way, a positive and pure EOG signal is obtained. The final signal is effective and usable. Figure 24 shows final shape of the system when connected to a computer. After calibrating the adder amplifier at 2.5V when looking forward, the output voltage was measured when looking right with a small degree, far right, left with a small degree, and far left. The circuit output is shown in Table 2.

4. CONCLUSION

Medical assistance systems can be used in many cases and diseases such as visual impairment, mobility disability, paralysis, deafness. Creating an assistive system using vital signals for people with special needs can provide many benefits and advantages. In recent years, the use and dependence of vital signals have increased due to their effectiveness and easy acquisition. The designed system has many advantages over systems designed for the same purpose. The main advantages of the system:

- The system is wireless, this provides more convenience to the user. Since there is no cable connecting the patient to the computer, the patient can use the computer more comfortably.

• Two processors are used in the system. The first processor is for processing the EOG signal, the second processor is for controlling the computer. Using two processors ensures the speed of the system. In this way, the user can control the computer smoothly and effectively.

Several steps were taken to obtain an effective signal:

- A special PCB is designed to separately process the horizontal and vertical EOG signal.
- The circuit is powered by a DC current to reduce noise.
- Special cables were used to effectively acquire the EOG signal and reduce signal loss during transmission from the patient's body to the electrical circuit.
- The negative part of the EOG signal was shifted to a positive value and the signal was filtered with active filters.

ACKNOWLEDGEMENT

This study has been produced from the Master's degree dissertation of Abdalrahman SKHETA.

REFERENCES

- [1] M.Merino & O. Rivera & I. Gómez & A. Molina. A Method of EOG Signal Processing to Detect the Direction of Eye Movements. First international conference on sensor device .2010.
- [2] A. Naga Rajesh, S. Chandralingam, T. Anjaneyulu, K. Satyanarayana. EOG Controlled Motorized Wheelchair for Disabled Persons, vol. 115 ,pp. 965-970, 2014.
- [3] B.Narayanan. Micro controller based EOG guided wheelchair-January 33(2), 3398-3401, 2013.
- [4] N. ÖZKAN , A.İŞİK , U. FİDAN. Design and Acquisition of EOG Based Interactive Communications for ALS Patients, Electronics And Computers Special Issue, 2017.
- [5] L. Y., Hsu, C.-L., Lin, T.-C., Tuan, J.-S., & Chang, S.-M. EOG-based Human-Computer Interface system development. Expert Systems with Applications37(4), 3337-3343, 2010.
- [6] Barea, R., Boquete, L., Ortega, S., López, E., & Rodríguez-Ascariz, J. M. (2012). EOG-based eye movements codification for human computer interaction, 39(12), pp. 2677-2683, 2012.
- [7] Postelnicu, C.-C., Girbacia, F., & Talaba, D. (2012). EOG-based visual navigation interface development. 39(3), 2677-2683.
- [8] Schlögl, A., Keinrath, C., Zimmermann, D., Scherer, R., Leeb, R., & Pfurtscheller, G. (2007). A fully automated correction method of EOG artifacts in EEG recordings. DOI:10.1016/j.clinph.2006.09.003.
- [9] RAMİS İLERİ: Determination of the most appropriate writing characters for the education of children with dyslexia by using EOG signals- UlusalTezMerkezi - 2020.
- [10] AHMET COŞKUN:Sleep staging with electrooculography (EOG) signals, 22-35, 2017.
- [11] Eye anatomy, parts of the eye and how we see, 2021. <https://www.aao.org/eye-health/anatomy/parts-of-eye>
- [12] Eye anatomy: close look at the parts of the eye. 2021. <https://www.allaboutvision.com/resources/anatomy.htm>
- [13] M.C Kiernan, S. Vucic, B. C. Cheah, M. R. Turner, A., Orla, J. R Burrell, M.C Zoing. Amyotrophic lateral sclerosis 7, 2011. DOI:10.1016.
- [14] Berthoz A, Melvill Jones G Büttner.Ennever JA. The Electric Signals Originating in the Eye.
- [15] Estrany, B., Fuster, P., Garcia, A., & Luo, Y. (2009). EOG signal processing and analysis for controlling computer by eye movements. DOI:10.1145/1579114.1579132.
- [16] Abo-Zahhad, M., Ahmed, S. M., & Abbas, S. N. (2015). A New EEG Acquisition Protocol for Biometric Identification Using Eye Blinking Signals, 2015.06.05.
- [17] Mala Sundaram Feature selection in activity recognition using eye movements: Filter based approach Jan 2015.
- [18] Ma, J., Zhang, Y., Cichocki, A., & Matsuno, F. (2015). A Novel EOG/EEG Hybrid Human-Machine Interface Adopting Eye Movements and ERPs: Application to Robot Control. tme.2014.2369483.
- [19] Ivailo Milanov Pandiev-Analysis and Design of Instrumentation Amplifiers-June 2013. DOI: 10.1125
- [20] T. Dear, J. Chang, W. Chow, D. Wai, J. Wang-Filters -Summer 2012.
- [21] A. Goen.Analysis and Design of Low Pass Filter by Using DGS for WLAN Application-January 2007 DOI:10.15662.
- [22] W. Hendra Gunawan STT Migas. Low Pass Filter Design With Artificial Ground Structure-November 2017:10.32487.
- [23] R. Reddy R. PERFORMANCE ANALYSIS OF ADDER CIRCUITS USING FINFET'S. January 2017 DOI:10.26634.
- [24] James M. Fiore. Operational Amplifiers & Linear Integrated Circuits: Theory and Application-Version 3.2.5, 15 December 2020.
- [25] ATmega328P 8-bit AVR Microcontroller with 32K Bytes In-System Programmable Flash. <https://datasheetspdf.com/datasheet/ATmega328P.html>
- [26] HC-05 -Bluetooth to Serial Port Module. <http://www.electronic60norte.com/mwfls/pdf/newBluetooth.pdf>
- [27] autodesk.com/products/eagle/overview.
- [28] INA118 Precision, Low-Power Instrumentation Amplifier-Datasheet - production data. https://www.ti.com/lit/ds/symlink/ina118.pdf?ts=1636968472131&ref_url=https%253A%252F%252Fwww.google.ru%252F
- [29] tl082- General purpose JFET dual operation amplifiers -Datasheet - production data. <https://www.ti.com/lit/ds/symlink/tl082-n.pdf>

BIOGRAPHIES

Abdalrahman SKHETA received his bachelor's degree in medical electronics engineering from Aleppo University, Syria in 2017. After obtaining a C1 certificate in Turkish, he began studying for a master's degree at Marmara University in 2019. In 2020 Participated in the 9th International Conference on Advanced Technologies With an article entitled: Study and Design of Power Supply Based on Pettier to Charge the EV Auxiliary Battery. The article was published in the IJEAT journal.

Nazmi EKREN received the B.S. degree from the Electrical Engineering Department, Yildiz Technical University (YTU), Istanbul, Turkey, in 1987, and the M.S. degrees from the Marmara University in 1989 and PhD degrees from the Istanbul University in 1996. He is currently an associate professor at the Marmara University. His research interests PV systems, fabrication at Nano level and lighting. He works on tissue engineering applications, 3D-bioprinting, electrospinning.

Investigation of Leakage and Stability Analysis in Rock Filling Dams: The Example of Kolludere Pond

Mehmet Hayrullah Akyildiz  , İbrahim Halil Oral 

^{1,2}University of Dicle Engineering Department, Civil Engineering, Diyarbakır, Turkey (e-mail: hayrullah.akyildiz@dicle.edu.tr).

ARTICLE INFO

Received: May., 24. 2020

Revised: Jan., 07. 2021

Accepted: Dec, 18. 2021

Keywords:

Rockfill Dams,
Pore Water Pressure,
Ground,
Stability,
Seepage

Corresponding author: *M. H. Akyildiz*

ISSN: 2536-5010 / e-ISSN: 2536-5134

DOI: <https://doi.org/10.36222/ejt.684428>

ABSTRACT

Dams and ponds as engineering structures pose various risks during design, construction and operation. Deformation in dams, slope stability problems or excessive pore pressure can cause serious damage that cannot be prevented. It is critical to position these areas correctly and to evaluate the potential damage quantitatively. In rockfill dams, serious work needs to be done during the planning and project phase, especially on infiltration and slope safety. Otherwise, serious damages that cannot be prevented may occur in the dams. In this article, an example of rockfill dam type, infiltration and body stability analyzes of the 34 m high Kolludere Pond were calculated using the finite element method. The Geostudio program developed by the Geo-Slope company was used in the calculation of this analysis. For the analysis, the parameter values included in the field studies carried out with DSI were used. The dam body was modelled using parameter values and laboratory experiments. As a result of the modelling, whether the body of the pond remained in slope safety and the infiltration analysis results were evaluated.

1. INTRODUCTION

renewable energy types, has a large-scale distribution potential [1]. In the last thirty years, concrete faced rockfill dams have been widely used in large-scale hydroelectric projects due to their advantages such as low material cost, good adaptation to geological conditions and better performance under seismic loading conditions [2]. Hydroelectric energy reduces fossil fuel use, protects the environment and helps flood control [3]. A rockfill dam with a concrete face is an example of the dam type applicable for high dam design [4]. Concrete surface slab is the main component of the leak control system. Deformation, slope stability problems or excessive pore water pressure that may occur in dams can cause serious damage. This situation gives priority to dam safety in dam design [5]. Dynamic and static conditions should be considered together in the design and necessary safety precautions should be taken. The slope can be generally defined as "the horizontal mass that makes a certain angle with the existing land surface". The type, shape and land features of the body materials in the existing dams in our country differ. For this reason, there are differences in deformation, pore pressure and stability of each dam structure whose construction is completed. It is necessary to provide the necessary precautions by planning and project processes to be made before the construction phase of the dams against these problems that may occur during the operation process. The material parameters to be included in the dam structure

should be analyzed by finding the required parameters as a result of the experimental applications. The basis of the parameters used in the numerical analysis method is based on the triaxial pressure test. The triaxial pressure test was performed only for the clay core. The clay core is modeled using an elastic-plastic model.

Another important analysis made in Embankment Dams is the seepage analysis. Infiltration is one of the important problems in dams. Seepage may cause internal erosion and tubing or dam collapse may occur as a result of slope stability shifts due to seepage pressures. The collapse rate that occurred as a result of the piping formed in the body of large embankment dams until 1986 was 32.5% [6]. This ratio increases more when taking into account the piping collapses in the foundation floor.

In the study, the Kolludere Pond, which is located within the borders of Bağlar district of Diyarbakır province, about 15 km west of the province, on the Kodi stream, was modeled with the finite element method. Some of the parameters in the modeling were taken from the experiments made during the study phase. Determination of shear strength parameters of cylindrical rock exposed to triaxial compression is done with code. For some parameters, DSI embankment dams are modeled based on the design guide [7].

Dam Location and Characteristics

The Kolludere Pond is on the Kodi Stream, approximately 2250 m west of the Koldere Village. Kodi Stream's precipitation area in the pond area is 41.81 km² and the average elevation of the precipitation area is 1085 m. The irrigation area of the pond is 800 ha gross. Kolludere Pond was built in clay core rock fill type and for irrigation purposes. The height of the pond is 25 m from the thalweg, 34 m from the foundation, the body crest length is 2225.60 m, and the crest width is 8 m [8]. The reservoir volume of the dam has been determined as 1240593 m³ and the lake as 1708 km² (Fig. 1).

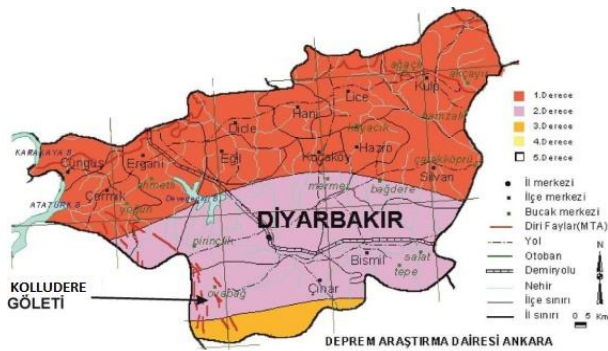


Figure 1. Project Area on Earthquake Zones Map of Diyarbakir Province

Generally shallow and medium-depth earthquakes occur around the dam site. Region; Ministry of Public Works Disaster Affairs General Directorate, issued in 1996, and the Council of Ministers 18.04.1996 dated and 96/8109 decree in accordance with enacted "Turkey Earthquake Regions map" is located in the 2nd degree earthquake zone, according to the (Fig. 2).

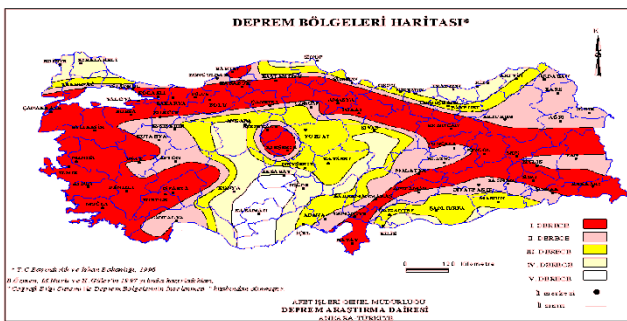


Figure 2. Turkey Earthquake Zones Map

2. MAIN TEXT

In this context, the effective ground acceleration coefficient is suggested to be between $A_0 = 0.40-0.30$ g. However, according to the Kolludere Pond Seismic Hazard Analysis Report within the scope of the work, in the works carried out for "Diyarbakir-Central Kolludere Pond and Irrigation Project"; The maximum horizontal ground acceleration (PGA) found as a result of deterministic calculations was calculated as 0.065g. The OBE is calculated as 0.082g for the expected maximum horizontal ground motion acceleration (144-year return period) with the probability of exceeding 50% within the 100-year economic life calculated by probabilistic calculation [9]. It is recommended to take $MDE = MCE = 0.141g$ and seismic design coefficient (k) = 0.10 for the expected maximum horizontal ground acceleration (475 years return period) with

a probability of exceeding 10% within 50 years of the structure. (DSI, 2015) New maps, AFAD National Earthquake Research Program (UDAP) supported by Turkey "Updating the Seismic Hazard Maps" has been prepared under the project entitled Public and University Cooperation. (Fig. 3).



Figure 3. Turkey Earthquake Hazard Map (AFAD, 2019)

The new map was created with much more detailed data, taking into account the most up-to-date earthquake source parameters, earthquake catalogs and new generation mathematical models. In the new map, unlike the previous map, the highest ground acceleration values are shown instead of earthquake risk zones and the concept of "earthquake risk zone" has been eliminated. The earthquake hazard map is not a risk map. In order to be a risk map, it is necessary to know the effects of the buildings and the population during an earthquake, to determine the economic losses, to calculate the damages that the earthquake will cause to the environment and to create a map showing the consequences of these damages and losses [10]. According to this new map, the maximum ground acceleration of the Kolludere Pond area and its surroundings should be around 0.1 g (Fig. 4).

Each 16-dimension vector formed with four quads and this is where the quad processing unit name comes from. QPUs are arranged into groups of slices which share instruction cache, a special function unit, texture and memory lookup units and interpolation units. The QPUs are scheduled automatically by the VideoCore hardware with QPU scheduler. Raspberry Pi-3 contains 12 QPUs in its graphic engine. Each QPU has following key features:

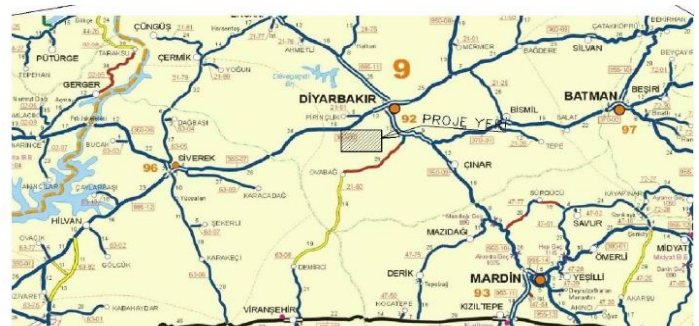


Figure 4. Kolludere Pond and Its Surroundings

In 2014, Broadcom Inc. announced to release of documentation for VideoCore IV and sources files for linux drivers under BSD license so that we were able to use the Video Core GPU as a very powerful parallel accelerator in our work.

3. EXPERIMENTS

Two methods are commonly used in the stability analysis made by the finite element method. In the first method, gravity enhancement method, the gravity acceleration is increased until the slope collapses and the static state deteriorates [11]. In the second method, in the strength reduction method, c and ϕ are reduced until the slope migrates and the static situation deteriorates [12]. In this method, elasto-plastic analysis was made by taking different shear strength values obtained by dividing the shear strength parameters by a number of safety numbers. For the Mohr Coulomb material model, the shear strength reduced by the safety number (F_s) can be determined using Equation (1).

This relation

$$\frac{\tau}{F_s} = \frac{c}{F_s} + \frac{\tan\phi}{F_s} \quad (1)$$

$$\frac{\tau}{F_s} = C^* + \tan\phi^* \quad (2)$$

It can also be written as. In this case,

$$C^* = \frac{c}{F_s} \text{ ve } \phi^* = \arctan\left[\frac{\tan\phi}{F_s}\right] \quad (3)$$

Shown in the figure. Here, c and ϕ are the shear strength parameters and c^* , ϕ^* are the reduced shear strength parameters.

Before designing dams and ponds, seepage and slope stability analyzes are the main issues that need to be studied. Before the hull slope analysis, some materials taken from the field are subjected to various tests in the laboratory environment. Especially in the field, the necessary parameters were determined by making a triaxial pressure test on the clay core material, and 7 boreholes (SK-1, SK-2, SK-3, SK-4, SK-5, SK-6, DSK-1) was opened and the properties and parameters of the ground were determined. It was investigated whether the bearing capacity of the soil was carried out by the Uniaxial Compressive Strength test, and whether the leakage of the dam floor where the body is located was within the intervals stipulated by DSI (Table 1).

Table 1. Boring Well Bst and Uniaxial Compressive Strength Test Results Taken at the Armdere Pond Construction Sites

Well No	Well Level (m)	Single Axis Pressure (kgf/cm ²)	Bst (Lugeon)
SK-1	824.5	756	2.48
SK-2	820.5	719	2.58
SK-3	816	641	2.7
SK-4	801	714	2.55
SK-5	815	717	2.02
SK-6	824.5	689	3.18
DSK-1	798.4	769	2.53

Since the Kolludere Pond is built in the Rock Fill Dam type, the rock material to be used for the filling material will be provided from Karcadağ basalts, which are abundant in the Karacadağ Region. Rock Fill Dams mainly cut the direct contact of the water in the reservoir area of the dam or pond with the clay core, but adds more stability to the pond compared to earthfill dams. (Fig. 5.).

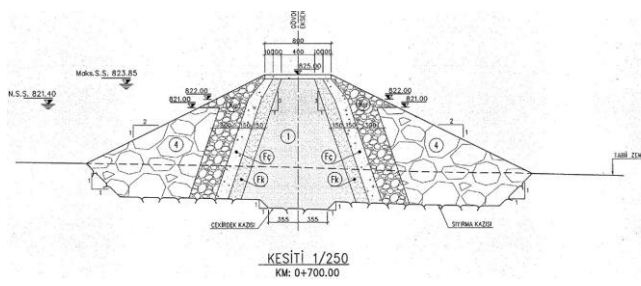


Figure 5. Kolludere Pond Body Cross Section

Analysis of slope stability according to the Kolludere pond project data will be made for 2 states. The situation was examined for the OBE and MDE earthquake situations before the impoundment, and the second case was examined for the OBE and MDE earthquake situations in the operational state where the impoundment of the dam was completed. According to the data in the project, the calculations and designs of the Kolludere Pond, which has not been completed yet, were made and it was investigated whether the slope status remained in the safe zone (Table 2.)

Table 2. Zone 1, Zone 2 and Filter Material Model and Final (average) Material Parameters (DSİ, 2015)

Malzeme	Permeability (K) m/s	Unit Volume Ağırlık (KN/m ³)	Cohesion (C) Kpa	Internal Friction Angle (Φ)
Zone No.1	3,4 x 10 ⁻⁷	18	15	25
Zone No.2	1,0 x 10 ⁻⁵	25	0	45
Bedrock	2 x 10 ⁻⁵	26	500.00	55.00
Filter Gravel	0.005	19	0	35
Filter Sand	0.005	19	0	35
Rocky	0,005	23	0	40

While performing slope analysis, Mohr-Coulomb shear circles method was used. Upstream and downstream slopes were evaluated and it was investigated whether the dam structure is located in the safe zone [13]. Another analysis of the Kolludere Pond is infiltration analysis. Seepage is a common problem, especially in rockfill dams. Concrete is manufactured on the front face of the rock fill in most projects to prevent leakage problem in rockfill dams. However, in the design of the Koldere Pond in question, the front face of the concrete was not designed. The infiltration event appears as a serious problem frequently encountered in dams and ponds, especially in operation. During the survey and field stage, it is necessary to obtain results with devices calibrated in the laboratory environment, especially for the materials taken in the field, and a good design should be created with the data obtained. Otherwise, the clay core, which provides pond impermeability, and the pond floor will cause serious problems, which we call piping. Due to the decrease in the amount of water pressure sent to irrigation in the reservoir area, which decreased as a result of the infiltration, the expected irrigation amount in the irrigation area foreseen as gross 800 ha may not be realized. Tubing causes increased pore water pressure inside the body, and has a negative effect on the stability of the body over time, affecting the body of the pond until it collapses. In short, the Infiltration and Slope

Stability Analysis is a situation that should be studied together.

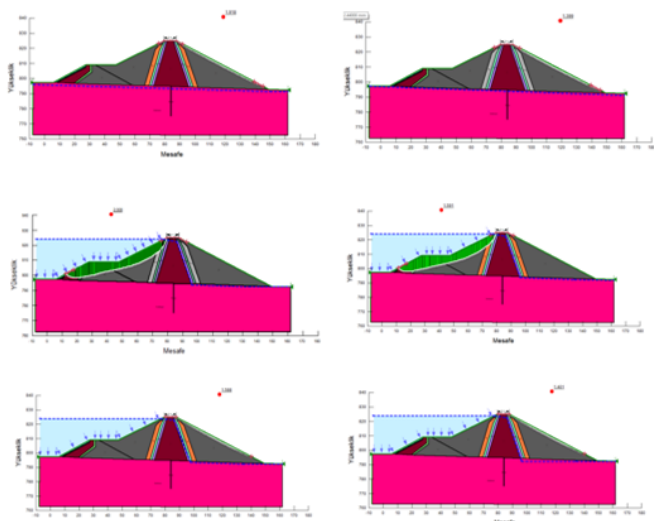


Figure 6. End of construction; Seismic and Earthquake, Operation Upstream OBE Earthquake and MDE Seismic, Operation Downstream OBE Seismic and MDE Seismic Slope Security Status

4. DISCUSSION

Before the hull slope (stability) analysis, some materials taken from the field were subjected to various tests in the laboratory environment. Especially in the field, the necessary parameters were determined by making a triaxial pressure test on the clay core material, and 7 boreholes (SK-1, SK-2, SK-3, SK-4, SK-5, SK-6, DSK-1) was opened and the properties and parameters of the ground were determined. With the Single Axis Compressive Strength test, it was investigated whether the bearing strength of the soil and the Pressurized Water test value the leakage of the dam floor where the body is located is within the intervals prescribed by DSI. In the researches, it has been determined that the values measured by experiments are within the desired ranges.

Table 3. Kolludere Pond Safety Coefficients, Recommended Loading Conditions and Safety Coefficients (DSİ, 2012)

Status	Loading State	Safety Coefficient	Kolludere Pond Safety Coefficient
End of Construction	Unusual	1.3	1.92
End of construction Earthquake (OBE)	Extreme	>1.0	1.59
Operational	Usual	1.5	1.92
Operation Earthquake (OBE)	Unusual	1.2	1.59
Operation Earthquake (MDE)	Extreme	>1.0	1.40
Sudden Discharge	Unusual	1.2	2.59

The hull stability analysis was carried out to ensure that the upstream and downstream slopes are in the safe zone. As a result of the analysis, the said slope slopes and material parameters were evaluated together and the analysis was

concluded. When the slope security situations in the table above are examined; End of construction downstream slope security status without earthquake 1,918, End of construction MDE earthquake downstream slope security number 1,399, post-construction OBE earthquake upstream slope security number 2,006, Operation MDE earthquake upstream slope security number 1,591, Operation MDE earthquake In the case of downstream OBE slope safety, the security number was 1.588, and in the case of Operation MDE earthquake downstream slope safety, the security number was 1.401 (Table 3.).

It has been observed that the stability values of the dam remain in the safe zone in each of the aforementioned cases. It has been concluded that the dam body will remain stable even in case of OBE (Operating Basis Earthquake) and MDE (Maximum Design Earthquake) seismic earthquakes (Fig. 6).

Seep analysis was carried out on the pond body. In this way, water flow lines, amount of leaking water per unit meter, equipotential curves and water pressure height values were determined. In the examination, it was determined that the water pressure heights in the body decreased from upstream to downstream (Fig. 7.).

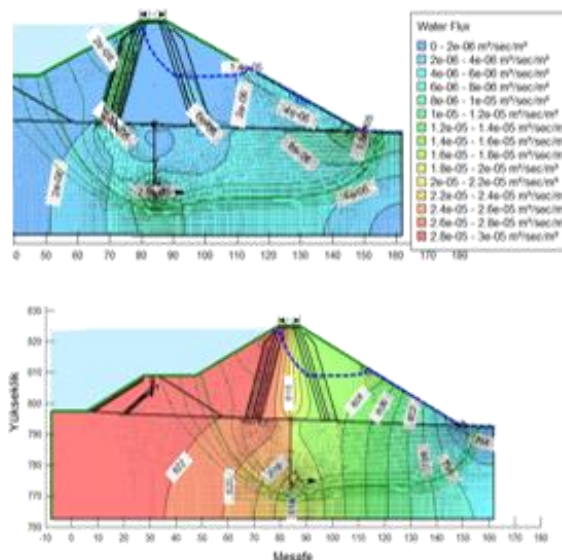


Figure 7. Leakage Analysis in Operational Status Amounts of Water Leaking per Unit Meter, Leakage Analysis Equipotential Curves and Water Pressure Head Distribution

In this way, it has been determined that the energy of the water pressure is broken while moving through the body of the pond. Another study is the analysis of the amount of water leaking per unit meter through the pond body of the rockfill-type Kolludere pond. The energy breaking of the water on the upstream side while passing through the body and the vertical water flow by increasing its speed while passing through the filter materials was directed towards the pond foundation and gathered around the injection curtain. Therefore, as a result of the analysis, the maximum leaking water amount per unit meter was determined as $2 \times 10^{-5} \text{ m}^3 / \text{s}$ just below the pond injection curtain. It has been determined that the maximum amount of water leaking per unit after the injection curtain passes through the filter materials on the upstream side and the parts located in the downstream heel of the pond body at $1.6 \cdot 10^{-5} \text{ m}^3 / \text{s}$ per second.

Symbols

Fs: Security Numberc: Kohezyon (KN/m²)

ϕ : Internal Friction Angle (°)

c*: Reduced Cohesion (KN/m²)

ϕ^* : Reduced Internal Friction Angle (°)

E: Elasticity Module

REFERENCES

- [1] Qu Y., Zou D. Seismic cracking evolution for anti-seepage face slabs in concrete faced rockfill dams based on cohesive zone model in explicit SBFEM-FEM frame. *Soil Dynamics and Earthquake Engineering* 2020; 133(1):106106
- [2] Chen Y., Hu R., Modeling coupled processes of non-steady seepage flow and non-linear deformation for a concrete-faced rockfill dam. *Computures and Structures* 2011 pp 1333-1351 <https://doi.org/10.1016/j.compstruc.2011.03.012>
- [3] Zarfl C, Lumsdon AE, Berlekamp J, et al. A global boom in hydropower dam construction. *Aquat Sci* 2015;77(1):161–70.
- [4] Qu Y, et al. Seismic damage performance of the steel fiber reinforced face slab in the concrete-faced rockfill dam. *Soil Dynam Earthq Eng* 2019;119:320–30.
- [5] Cernica J.N *Geotechnical Engineering: Soil Mechanics*, John Wiley and Sons Inc., Canada 1995.
- [6] Sağlıca, 2013 *Leakage Analysis of Embankment Dam Bodies*, Master's Thesis, University Gazi, Ankara, 85 p.
- [7] Ministry of Forestry and Water Affairs, General Directorate of State Hydraulic Works, 1st Dams Congress, *Embankment Dams Design Guide* October, 2012 Ankara p, 1-151
- [8] Devlet Su işleri, DSİ, 2015 *Kolludere Pond, Planning Report*
- [9] Devlet Su işleri, DSİ, 2015 *Kolludere Pond, Geotechnical Report*
- [10] AFAD, 2019, [https://depem.afad.gov.tr/ earthquake-hazard-map](https://depem.afad.gov.tr/earthquake-hazard-map) Internet Resource
- [11] Chen, W. F. ve Mizuno, E., *Nonlinear Analyses in Soil Mechanics: Theory and Implementation*, Elsevier, Amsterdam, 1990.
- [12] Zienkiewicz, O.C. ve Taylor, R. L., *The Element Method*, Vol. 1, 4thEdition, Mc Hill, New York, 1989.
- [13] Zorluer ve ark. 2018 *Investigation of Dam Leakage and Slope Stability Analysis: The Case of Kızık Dam*, 5th International Dam Safety Symposium, 27 October-1 November 2018, İstanbul

BIOGRAPHIES

Mehmet Hayrullah AKYILDIZ obtained his BSc degree in civil engineering from Near East University in 1997. He received the BSc., and MSc. diploma in Civil Engineering from the Sakarya University in 2004 and PhD degrees from the same university in 2011. His research areas geosynthetics, ground improvement methods, ground reinforcement techniques. Continues to work in the University of Dicle Department of the Civil Engineering.

Halil İbrahim ORAL obtained his BSc degree in civil engineering from Dicle University in 2012. He received the BSc., and MSc. diploma in Civil Engineering from the Dicle University in 2016. Continues to work in the DSI 10. Regional Directorate Dams and HES Office



EEG Channel Selection using Differential Evolution Algorithm and Particle Swarm Optimization for Classification of Odorant-Stimulated Records

Mesut Şeker^{1*} , Mehmet Sıraç Özerdem² 

^{1*}Dicle University, Electrical-Electronics Engineering Department, Diyarbakir, Turkey. (e-mail: mesut.seker@dicle.edu.tr).

²Dicle University, Electrical-Electronics Engineering Department, Diyarbakir, Turkey. (e-mail: sozerdem@dicle.edu.tr).

ARTICLE INFO

Received: Feb. 02. 2021

Revised: Dec. 14. 2021

Accepted: Dec. 21. 2021

Keywords:

DEA

EEG Channel Selection

Evolutionary computing

PSO

Swarm intelligence

Corresponding author: Mesut Şeker

ISSN: 2536-5010 / e-ISSN: 2536-5134

DOI: <https://doi.org/10.36222/ejt.873351>

ABSTRACT

A significant advancement has been made in the evolutionary computing and swarm intelligence methods in past decades. These methods have been commonly used to calculate well optimized solutions. Methods select the best elements or cases among set of alternatives. In EEG signal processing applications, efficient channel selection algorithms are required to reduce high dimensionality and remove redundant features. To do this, we examined optimal 5 electrodes out of 14 using Particle Swarm Optimization (PSO) and Differential Evolution Algorithm (DEA). The proposed work is related with pleasant-unpleasant EEG odors classification problem. Classification error rates were calculated by Linear Discriminant Analysis (LDA), k-NN (k Nearest Neighbour), Naive Bayes (NB), Regression Tree (RegTree) classifiers and used as fitness function for optimization algorithms. The results showed that PSO with selected 5 channels gave lowest error rates compared with DEA for all runs. RegTree classifier generated optimal fitness function value among other classifiers. PSO algorithm can effectively support channel selection problem to identify the best channels to maximize classification performance.

1. INTRODUCTION

EEG signals have commonly used in many applications such as motor imagery, mental task, and sleep stage classifications in addition to emotion recognition, seizure detection and drug effects diagnosis. EEG records are required multiple electrodes to achieve good performance but some of electrodes may include irrelevant, redundant, and noisy features. Efficient channel selection algorithms are required to remove redundant contents from EEG signals. The purposes of channel selection are reducing computational complexity of any processing task with EEG signals and selecting the relevant channels. [1-2].

Various channel selection algorithms have been proposed in literature. Time domain analysis, wavelet transform, and power spectral estimation can be considered as signal processing tools for feature extraction and channel selection algorithms [2]. Population based search procedures such as Particle Swarm Optimization (PSO) and Differential Evolution Algorithm (DEA) have been in demand for researchers in past decades [3]. These algorithms look for the best subset of channels by individually assessing the usefulness of each channel with the help of search engine and fitness function.

Many numbers of research have been carried out in the area of odor stimulation-based EEG pattern classification and

recognition. Schriever et al. (2017) used time-frequency analysis of olfactory-induced EEG in respect to power change. They distinguished olfactory impairment from healthy individuals with sensitivity of 75% and specificity of 89% [4]. Vanarse et al. (2020) demonstrated the classification capabilities of 3D-spiking neural network using Java-based Neucube network by achieving overall accuracy of 94.5% to identify 20 different odor compounds [5]. Kim et al. (2019) investigates EEG activity in response to odors produced by different chemicals. They proved that structure of chemicals, odor types, and sensitivity of olfactory receptors may produce different EEG activity [6]. Aydemir (2017) extracted continuous wavelet transform based features to classify EEG records stimulated from valerian, lotus flower, cheese, and rosewater. He achieved 85.50% classification accuracy using k-NN. He also investigates that gamma EEG sub-band is highly associated with olfaction stimulation [7]. Zhang et al. (2019) presented that channel-frequency convolutional neural network yields best accuracy of 68.79% in gamma band using power spectrum density and differential entropy features using 13 odor stimuli [8]. Laha et al. (2018) evaluated concentration of odors using general type-2 fuzzy set for odor classification. According to their work, higher density of odor yields higher classification performance [9]. Becerra et al. (2018) proposed and odor identification system within 5 sub-bands. of EEG, and

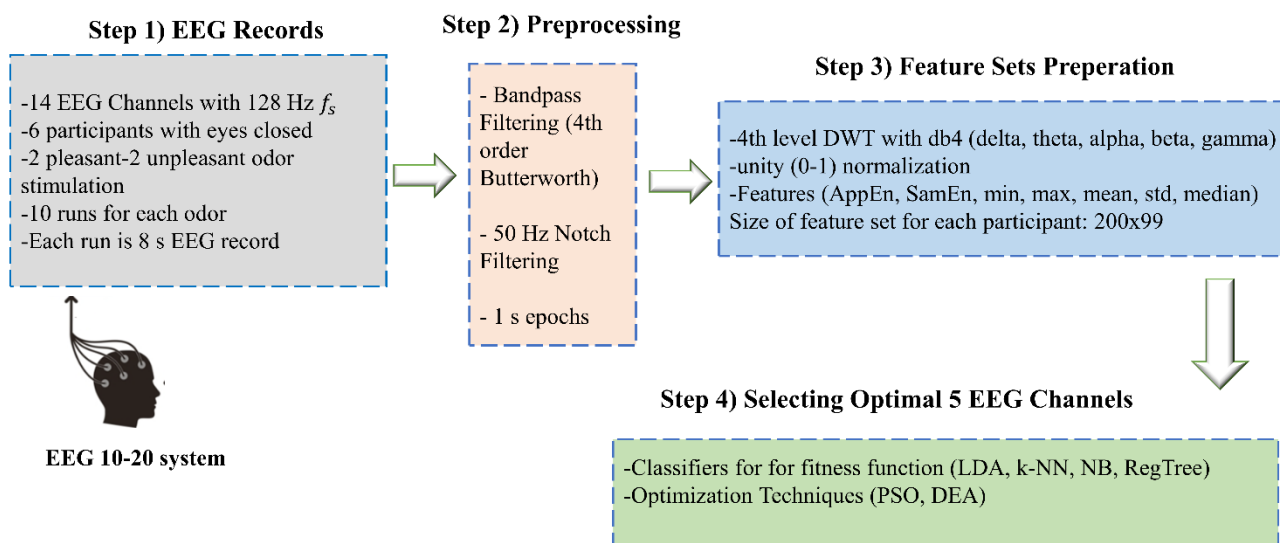


Figure 1. The followed methods in proposed study

statistical features using SVM classifier. They achieved 99.9% classification performance and alpha and beta sub-bands are stated more relevant for odor pleasantness classification task [10]. Zhang et al. (2021) proposed wavelet-spatial domain feature to classify 2 different EEG datasets. They achieved 100% and 94.47% average accuracy for eyes open and closed, respectively using SVM classifier [11]. Finally Hou et al. (2020) used different odors to develop an emotion recognition system based on average frequency band division of EEG signals using SVM. They found 98.9% accuracy for 2 (pleasure and disgust) and 88.5% accuracy for 5 degrees of pleasantness [12].

Some researchers paid attention to apply optimization algorithms to achieve more efficient signal processing system in BCI systems. Li et al. (2020) recommended improved Particle Swarm Optimization (PSO) for feature selection to enhance BCI-based emotion recognition. They achieved 76.67% accuracy for 4-class emotion recognition [13]. Moreover, Qi et al. (2020) showed that channel and feature selection scheme can accelerate the speed of convergence and global optimum and reduce training time in motor imagery based BCI system within PSO [14].

The proposed study stands on the intersection avenue of previous studies. The main purpose of this study to develop a practical EEG channel selection method using population-based methods, namely Particle Swarm Optimization (PSO) and Differential Evolution Algorithm (DEA). We used odorant-stimulated EEG records to classify pleasant and unpleasant odors. We obtained EEG sub-bands and extracted

statistical features in line with the previous studies. Error rates obtained from classification algorithms are used for fitness function in optimization problem. We obtained 5 subset of EEG channels that work together perfectly. According to our knowledge, there is no study to carry out similar EEG channel selection task and it strengthens the novelty of the paper.

The rest of this paper is organized as follows: Section 2 describes the population-based channel selection methods. Section 3 introduces experimental dataset, preprocessing steps and feature extraction techniques. Section 4 illustrates practical results of PSO and DEA with selected channels. Finally, proposed work is concluded in Section 5.

2. POPULATION-BASED METHODS FOR CHANNEL SELECTION

2.1. Particle Swarm Optimization

PSO was developed by Kennedy and Eberhart (1995) as a meta-heuristic algorithm based on the social behavior exhibited by birds when struggling to reach a destination. The scenario can be assumed as follows: group of birds are randomly looking for food in an area and they don't know where to food is. Effective strategy to find food is following the bird that is known to be nearest to the food [15].

Position and velocity of particles are randomly initialized in search space. Firstly, fitness values of particles are calculated. The best position among all particles is the global best position. The velocity and position of each particle are updated to produce new solutions. Then, the fitness values of the updated particles are recalculated, and best positions are updated.

Finally, velocities and positions of new particles are generated. When the termination criteria are met, algorithm ends its iterations [15-16].

The velocity of the j_{th} particle (V_j) represented by N dimensional optimization problem $1 \times N$ array is as follow:

$$V_j = (V_{j,1} + V_{j,2} + \dots + V_{j,i} + V_{j,N}) \quad (1)$$

where $j = 1, 2, \dots, M$. $V_{j,i}$ is the velocity of the j_{th} particle in the i_{th} dimension calculated as follow:

$$V_j = (V_{j,1} + V_{j,2} + \dots + V_{j,i} + V_{j,N}) \quad (2)$$

where $j = 1, 2, \dots, M$. $V_{j,i}$ is the velocity of the j_{th} particle in the i_{th} dimension calculated as follow:

$$V_{j,i}^{(new)} = \omega * V_{j,i} + c_1 * \text{Rand} * (p_{j,i} - x_{j,i}) + c_2 * \text{Rand} * (g_i - x_{j,i}) \quad (3)$$

where $V_{j,i}^{(new)}$ is the new velocity, $V_{j,i}$ is previous velocity, ω is inertia weight parameter, Rand is a random value in $[0,1]$, c_1 is cognitive parameter and c_2 is social parameter.

Particles move from old position to new position and this movement is based on the velocities. Particle's position is updated as follows:

$$x'_{j,i} = x_{j,i} + V_{j,i}^{(new)} \quad (4)$$

where $x'_{j,i}$ is new value of i_{th} variable of j_{th} new solution.

2.2. Differential Evolution Algorithm

DEA was developed by Storn and Price (1997). Algorithm was designed mainly for continuous optimization problems. Method compares each trial solution with the best solution previously obtained, and the result of the comparison determines the next trial solution. Population of candidate solutions in algorithm are called agents. These agents are moved in the decision space by using crossover and mutation operators that change their position. If the new position of an agent is an improvement, it is accepted and it replaces the old solutions. This is accepted as success and trial agent is added to population of solutions [15].

In proposed work, the algorithm in [17] was implemented as DEA. This algorithm is simply form of Genetic Algorithm (GA). It looks for the combinational channels that works the best together. For both PSO and DEA, methods are simplest versions of these algorithms.

2. EXPERIMENTAL DATASET, PRE-PROCESSING, AND FEATURE EXTRACTION TECHNIQUES

3.1. EEG Dataset

EEG records are collection of 14 channel, 128 Hz f_s data from 6 male, non-smoker, right-handed undergraduate students between 22-26 ages using the EMOTIV headset while their eyes were closed. Channel labels are AF3, F7, F3, FC5, T7, P7, O1, O2, P8, T8, FC6, F4, F8 and AF4. Related channels can be seen in Table 1. 10-20 international positioning of scalp electrodes is given in Figure 2. 2 pleasant (rosewater, vanilla) and 2 unpleasant (onion-garlic) odors were used in this study. Odors were selected based on other studies [7]. Rosewater and vanilla are expected to include same patterns since both odors give relaxation and pleasantness to subjects, so two odors were taken into one class. Onion and garlic are unpleasant odor substances and allocated for another class. Subjects were asked to breathe normally while sitting on comfortable chair in a ventilated room. The experiment consists of 10 runs. In each run, experimenter was randomly selecting glass tube of odor and kept it under subject's nose for 8 seconds. The reason for

choosing short stimuli duration is to prevent unwanted adaptations. The time interval between successive odors is 20 seconds and this break is not included in EEG recordings. After completed 10 trial, same steps were repeated for another odor until 4 odors were used.

TABLE I

CHANNEL NUMBERS AND LABELS	
Channel #	Labels
1	AF3 (Left frontmost)
2	F7 (Leftmost frontal)
3	F3 (Left frontal)
4	FC5 (Left frontal-central)
5	T7 (Left temporal)
6	P7 (Left parietal)
7	O1 (Left occipital)
8	O2 (Right occipital)
9	P8 (Right parietal)
10	T8 (Right temporal)
11	FC6 (Right frontal-central)
12	F4 (Right frontal)
13	F8 (Rightmost frontal)
14	AF4 (Right frontmost)

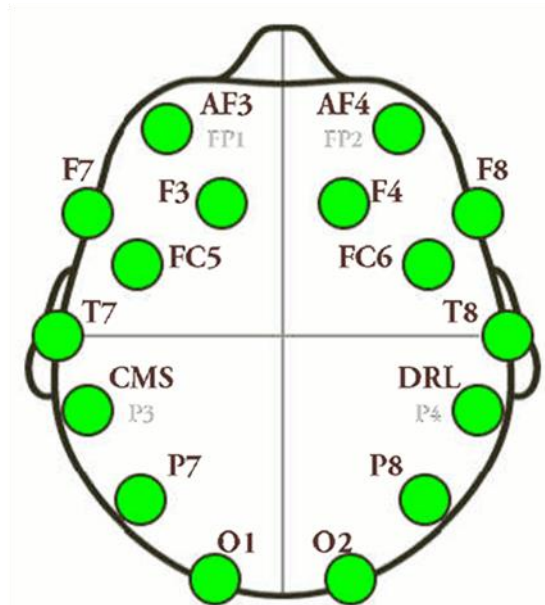


Figure 2. 10-20 International Electrode Positioning of 14 scalp electrodes

3.2. Pre-processing and Feature Extraction techniques

Received EEG records have 0.2-45 Hz signal bandwidth and 50 Hz notch filtered. 3rd order Butterworth band-pass filter was applied to EEG records to extract 0.5-42 Hz band frequency. 8s EEG records were divided into 1 second epochs. Discrete Wavelet Transform (DWT) with db4 was implemented to each epochs using 4th decomposition levels. DWT coefficients were averaged for 8 epochs. 10 trials were combined for each odor. Delta (0.5-4Hz), theta (4-8 Hz), alpha (8-14 Hz)- beta (14-30 Hz) and gamma (30-100 Hz) EEG subbands were obtained. Before feature extraction step, data was normalized between 0-1. Normalization method was processed as follows:

$$z_i = (x_i - \min(x)) / (\max(x) - \min(x)) \quad (5)$$

where $x = (x_1, \dots, x_n)$ and z_i is i^{th} normalized data. 7 statistical feature extraction methods were used to reduce the dimension of EEG sub-bands to a smaller set of features. The present features are Approximate and Sample Entropy, minimum and maximum of absolute values, mean value, standard deviation and median.

Besides general known statistical features, Approximate and Sample Entropy need to be explained. Approximate Entropy (*ApEn*) quantifies regularity in short, noisy neural time series by pattern length (m) and similarity coefficient (r). *ApEn* is defined by

$$ApEn = \ln \left(\frac{C_m(r)}{C_{m+1}(r)} \right) \quad (6)$$

in which $C_m(r)$ refers to pattern mean of length m . *ApEn* depends on pattern length. Sample Entropy (*SamEn*) also gives the regularity of signal, and it is independent of pattern length. *SamEn* is calculated as:

$$SamEn = -\ln \left(\frac{A^m(r)}{B^m(r)} \right) \quad (7)$$

where $B^m(r)$ refers to probability of 2 sequences match for m points and $A^m(r)$ does for $m+1$ points. In this work, m is chosen as 2 and r is chosen as 0.2 times standard deviation of time series [19].

Feature vectors were arranged as illustrated in Figure 3. Each odor has 10 trials, and each trial has 14 active channels. 7 features were extracted from each channel. We totally have size of $(10 \times (14 \times 7)) = 10 \times 98$ vectors. This size just belongs to one odor and one sub-band. If we take 4 odors into consideration, overall size reaches 40×98 . Labels (0-1) were given to last column of vectors for unpleasant and pleasant classes accordingly. Finally, 200×99 feature matrix for each subject was created within combination of EEG sub-bands. Feature vectors were randomized and the 60% of them was considered as training and the rest was for validation.

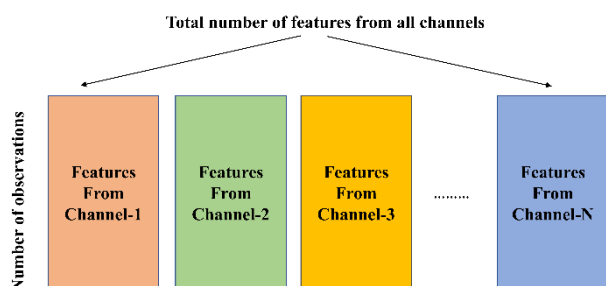


Figure 3. Arranging extracted features in order of channels

3. PRACTICAL RESULTS

Same initial population was defined for both PSO and DEA. Population size was chosen as 100. Number of iterations are limited with 100 and both algorithms stop when iteration number exceeds 100. 5 optimal channels were selected between 14 channels and performance evolution of both optimization algorithms were analyzed. Experiment was repeated for 25 times and classification results were averaged for both algorithms. This study doesn't select optimal number of channels but presents which channel combinations are best for classification. Classification error rates are defined by classifiers and error rates are for fitness functions. In this work, 4 different classifiers were selected which are Linear Discriminant Analysis (LDA) quadratic classifier, k Nearest Neighbor (k-NN) classifier, Naïve Bayes (NB) classifier and

Regression Tress (RegTree) classifier. LDA assumes both classes have normal distribution and same covariance matrices. The purpose of LDA is to solve following problem:

$$y = w^T x + w_0 \quad (8)$$

When the distance between two classes maximizes and variance minimizes, the separating hyper plane is obtained and vector of w and w_0 are determined. x refers to feature vector in (7). k-NN uses Euclidean distances with $k=3$ closest samples. The unlabeled test values are labeled according to closest distance from class samples. NB is a ordinary probabilistic algorithm which uses Bayes' theory. When we consider a group of training trials which includes m discrete features and a class named C , NB can estimate the class of unknown trials using probability to calculate highly probable output. Decision Trees have root of the tree which refers to problem statement and branches of tree which represents set of solutions and consequences. Classification Trees and Regression Trees are types of Decision Trees. Classification Tree is used for categorical target variable and Regression Tree is utilized when Decision Tree has continuous target variable. Root represents population sample, leaves are terminal nodes and child node occurs when nodes are divided into sub-branches. Each step in RegTree can be visualized to help users to make logical decisions. If one criteria is more important than other, RegTree gives priority this criteria and brings it on top of tree. Thus, redundant data is filtered out after each step [20].

4.1. Experiments with PSO

Dimension of the problem equals to number of desired EEG channels. Coefficients c_1 and c_2 were selected as 2. ω was chosen as 0.9 [21]. Optimal 5 channels were determined by the lowest error rates after all runs. Optimal classification error rates for PSO were averaged among 6 subjects and results can be shown in Figure 4. Average optimal error rate in LDA is 11.42%, in k-NN is 5.825, in NB is 12.775 and in RegTree is 0.55% for PSO. Success of selecting optimal sub-channels increases when error rates converge to zero. RegTree classifier gave lowest classification error rate, and it seems to be best algorithm as a fitness function to select optimum 5 EEG channels. NB classifier showed highest classification error rate and it seems to be not a preferable method to select optimum subsets of EEG channels when using PSO.

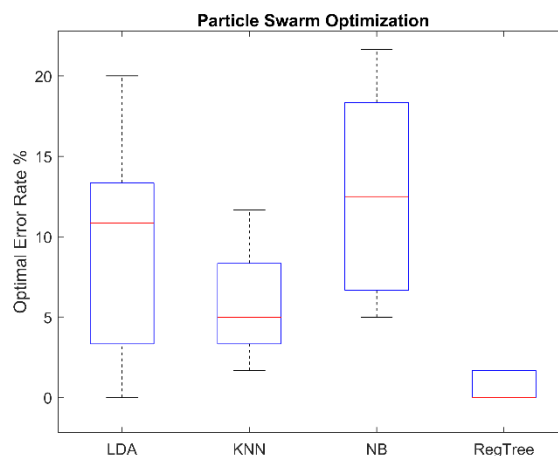


Figure 4. Optimal error rates taken in PSO

4.2. Experiments with DEA

DEA to select optimal subset of channels works as follows: Algorithm selects the first channel, then the second-best

channel that works the best with first selected, then the third channel that works the best with the first two selected channels, and these steps continue until selecting last channel. 5 separate channels may perform so weak individually, but when best channels are combined together, they easily outperform. DEA looks for best combination of individual channels. Optimal classification error rates for DEA were averaged among 6 subjects and results can be shown in Figure 5.

Average optimal error rate in LDA is 14.16%, in k-NN is 9.99%, in NB is 18.61 and in RegTree is 4.16 for DEA. RegTree classification algorithm gave also lowest error rate, and it seems to be appropriate algorithm as a fitness function for selecting 5 subsets of channels. The rankings to produce successful fitness values are same as in PSO.

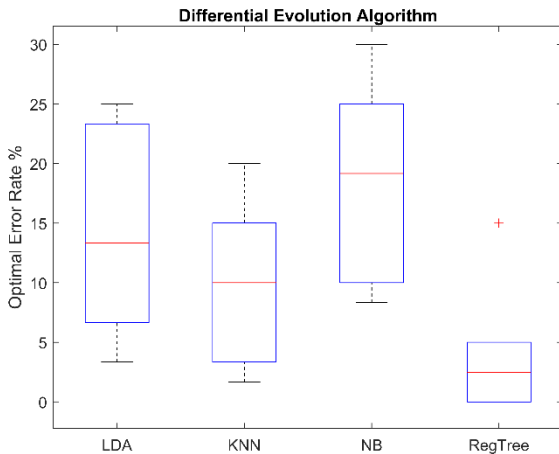


Figure 5. Optimal error rates taken in DEA

In Fig. 4-5, only lowest error rates belong to 6 subjects were taken and averaged. In Fig. 6, average classification results of the selected 5 channels are shown.

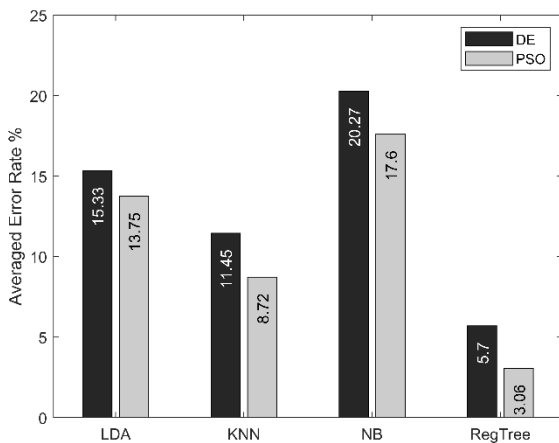


Figure 6. Average error rates of PSO and DEA

Average error rates belong to PSO is nearly 2% lower than DEA. It was noticed that PSO showed better performance than DEA regardless of selected classifiers. Best choice of 5 EEG channel selection is achieved by PSO with RegTree classifier. Selected channels for each subjects using PSO and DEA with RegTree classifier is given in Tab. 2 and 3 respectively.

TABLE II
SELECTED CHANNELS USING PSO WITH REGTREE

Subjects	Optimized Channels	Error Rate(%)
A	AF3 – F7 – T7 – O1 – AF4	1.66
B	F7 – T7 – P7 – F8 – AF4	0
C	F3 – FC5 – T7 – P7 – F8	0
D	F3 – O1 – O2 – P8 – F4	1.66
E	FC5 – T7 – P7 – FC6 – AF4	0
F	F7 – P7 – O1 – FC6 – AF4	0

TABLE III
SELECTED CHANNELS USING DEA WITH REGTREE

Subjects	Optimized Channels	Error Rate(%)
A	AF3-FC5-T7-O1-F8	3.33
B	F3-T7-P7-O1-T8	0
C	F7-F3-P7-O2-F8	15
D	F7-O2-P8-T8-FC6	5
E	F3-T7-P8-FC6-F8	1.66
F	P7-O1-O2-F4-F8	0

The combinations of channels differ from each other for both PSO and DEA even in each iteration, so specific brain regions that are more sensitive with odors cannot be deduced. Table II-III only gives combinations of 5 superior EEG channels that have lowest fitness function values and highest classification accuracies. High error rate gained from subject C using DEA was improved applying PSO.

4. SUMMARY AND FUTURE WORK

In the present study, pleasant and unpleasant odors were applied to 6 subjects to record EEG signals. Filtering process was implemented using band pass filter. DWT was applied to 1 s epochs of signals and wavelet coefficients were calculated. EEG sub-bands were gained using these coefficients. Sub-bands were normalized in range of 0-1. 7 statistical features were extracted to decrease feature space. All EEG sub-bands were combined and totally 200x99 feature matrix were gained. %60 of this features were used for training and rest were for validation.

Population based PSO and DEA optimization techniques were used to select optimal 5 EEG channels and performance of these methods were evaluated. LDA, KNN, NB and RegTree classifiers defined classification error rates to estimate fitness function values. RegTree gave minimum error rates for both PSO and DEA. NB failed to give minimum error rates among other classifiers, but results obtained from NB were still satisfactory. PSO showed better performance than DEA for EEG channel selection in all cases. In current work, 5 optimal out of 14 channels are selected to classify pleasant and unpleasant odor EEG records. The EEG electrode settlement including a greater number of EEG channel may be more convenient to investigate brain regions sensitively. We may also analyze not only 5 but more optimal channels for another study. Selecting different classifiers may be another goal to decrease the classification error rate converging to zero. Including more participants from different gender can strength the generalization of proposed method. In the future work, more population-based algorithms with different fitness function methods may be applied to odor EEG records. Statistical features can be evolved to get higher accuracies. In this sense, selection of EEG subset channels might be in more optimized form.

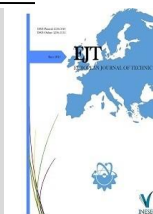
REFERENCES

- [1] S. M. Park, J. Y. Kim, and K. B. Sim, "EEG electrode selection method based on BPSO with channel impact factor for acquisition of significant brain signal," *Optik (Stuttg.)*, vol. 155, pp. 89–96, 2018.
- [2] T. Alotaiby, F. E. A. El-Samie, S. A. Alshebeili, and I. Ahmad, "A review of channel selection algorithms for EEG signal processing," *EURASIP J. Adv. Signal Process.*, vol. 2015, no. 1, p. 66, 2015.
- [3] S. Das, A. Abraham, and A. Konar, "Particle swarm optimization and differential evolution algorithms: Technical analysis, applications and hybridization perspectives," *Stud. Comput. Intell.*, vol. 116, no. 2008, pp. 1–38, 2008.
- [4] V. A. Schriever, P. Han, S. Weise, F. Hösel, R. Pellegrino, and T. Hummel, "Time frequency analysis of olfactory induced EEG-power change," *PLoS ONE*, vol. 12, no. 10, 2017.
- [5] A. Vanarse, J. I. Espinosa-Ramos, A. Osseiran, A. Rassau, and N. Kasabov, "Application of a Brain-Inspired Spiking Neural Network Architecture to Odor Data Classification," *Sensors*, vol. 20, no. 10, 2020.
- [6] M. Kim, J. Song, K. Nishi, K. Sowndhararajan, and S. Kim, "Changes in the Electroencephalographic Activity in Response to Odors Produced by Organic Compounds," *J. Psychophysiol.*, vol. 34, no. 1, pp. 35–49, 2020.
- [7] O. Aydemir, "Olfactory Recognition Based on EEG Gamma-Band Activity," *Neural Comput.*, vol. 29, no. 6, pp. 1667–1680, 2017.
- [8] X. Zhang, H. Hou, and Q. Meng, "EEG-based odor recognition using channel-frequency convolutional neural network," *Chinese Control Conf. CCC*, vol. 2019-July, pp. 7763–7767, 2019.
- [9] M. Laha, L. Ghosh, S. Parui, S. Ghosh, and A. Konar, "Evaluation of Density Based Odor Classification by General Type-2 Fuzzy Set Induced Pattern Classifier," *2018 Int. Conf. Wirel. Commun. Signal Process. Networking, WiSPNET 2018*, no. February 2019, pp. 1–6, 2018.
- [10] M. A. Becerra et al., "Odor pleasantness classification from electroencephalographic signals and emotional states," *Commun. Comput. Inf. Sci.*, vol. 885, no. August, pp. 128–138, 2018.
- [11] X.-N. Zhang, Q.-H. Meng, M. Zeng, and H.-R. Hou, "Decoding olfactory EEG signals for different odor stimuli identification using wavelet-spatial domain feature," *J. Neurosci. Methods*, vol. 363, p. 109355, 2021.
- [12] H.-R. Hou, X.-N. Zhang, and Q.-H. Meng, "Odor-induced emotion recognition based on average frequency band division of EEG signals," *J. Neurosci. Methods*, vol. 334, p. 108599, 2020.
- [13] Z. Li et al., "Enhancing BCI-Based Emotion Recognition Using an Improved Particle Swarm Optimization for Feature Selection," *Sensors*, vol. 20, no. 11, 2020.
- [14] Y. Qi, F. Ding, F. Xu, and J. Yang, "Channel and Feature Selection for a Motor Imagery-Based BCI System Using Multilevel Particle Swarm Optimization," *Comput. Intell. Neurosci.*, vol. 2020, p. 8890477, 2020.
- [15] O. Bozorg-Haddad, M. Solgi, and H. A. Loaiciga, *Meta-Heuristic and Evolutionary Algorithms for Engineering Optimization*, First. New Jersey, USA: John Wiley & Sons, Inc., 2017.
- [16] S. K. Satapathy, S. Dehuri, and A. K. Jagadev, "EEG signal classification using PSO trained RBF neural network for epilepsy identification," *Informatics Med. Unlocked*, vol. 6, no. November 2016, pp. 1–11, 2017.
- [17] R. N. Khushaba, A. Al-Ani, and A. Al-Jumaily, "Feature subset selection using differential evolution and a statistical repair mechanism," *Expert Syst. Appl.*, vol. 38, no. 9, pp. 11515–11526, 2011.
- [18] E. Kroupi, A. Yazdani, J.-M. Vesin, and T. Ebrahimi, "EEG Correlates of Pleasant and Unpleasant Odor Perception," *ACM Trans. Multimed. Comput. Commun. Appl.*, vol. 11, no. 1s, pp. 1–17, 2014.
- [19] [U. R. Acharya, H. Fujita, V. K. Sudarshan, S. Bhat, and J. E. W. Koh, "Application of entropies for automated diagnosis of epilepsy using EEG signals: A review," *Knowledge-Based Syst.*, vol. 88, pp. 85–96, 2015.
- [20] O. Aydemir and T. Kayikcioglu, "Comparing common machine learning classifiers in low-dimensional feature vectors for brain computer interface applications," *Int. J. Innov. Comput. Inf. Control*, vol. 9, no. 3, pp. 1145–1157, 2013.
- [21] A. Gonzalez, I. Nambu, H. Hokari, and Y. Wada, "EEG Channel Selection Using Particle Swarm Optimization for the Classification of Auditory Event-Related Potentials," *Sci. World J.*, vol. 2014, p. 350270, 2014.

BIOGRAPHIES

Mesut Şeker received the B.Sc. degree in 2014 from Zirve University, Gaziantep, Turkey. He received his M.Sc degree in Electrical-Electronics Engineering in 2017 from Dicle University and he is currently studying for Ph.D in Electrical-Electronics Engineering at Dicle University. He is also Research Assistant in the same department. His research interest include neural time series analysis, EEG signal processing, neuroscience, pattern recognition and machine learning.

Mehmet Sıraç Özerdem received the B.Sc. degree in Electrical-Electronics Engineering in 1994 from Eastern Mediterranean University in Northern Cyprus. He received his M.Sc degree in Electrical Engineering in 1998 from Yıldız Technical University. He received the Ph.D. degree in Computer Engineering in 2003 from Istanbul Technical University. Currently, he works as Professor and researcher at Dicle University, Diyarbakır, Turkey. His research focuses on machine learning, biomedical signal processing, bioinformatics and embedded system design.



While Covid-19 Outbreak Affects Economies and Societies; Exploring The Energy Demand in Turkey

Hasan Huseyin Coban

Ardahan University, Electrical-Electronics Engineering Department, 75002, Ardahan, Turkey. (e-mail: huseyincoban@ardahan.edu.tr).

ARTICLE INFO

Received: Mar., 10. 2021

Revised: Sep., 05. 2021

Accepted: Dec, 17. 2021

Keywords:

COVID-19

ANN

Regression

Energy demand

ARDL model

Corresponding author: *H.H. Coban*

ISSN: 2536-5010 / e-ISSN: 2536-5134

DOI: <https://doi.org/10.36222/ejt.894463>

ABSTRACT

The fear and panic environment created by the Coronavirus infectious disease 2019 (COVID-19), which affects the whole world, deeply affects the market mechanisms and causes energy supply and demand shocks. The common point of the predictions is that 2021 will pass with negative growth and increasing unemployment problem all over the world, with the economic reflections of the epidemic being felt seriously. In this study, Turkey in particular; a neural network and comparative regression model has been developed to analyze the effects on electricity and oil demand as part of COVID-19 economic measures. The purpose of this article is to contribute to the determination of Turkey's demand for electricity and oil during the epidemic and future by collecting information about direct and indirect factors, the events in the internal and external environments, and their relationships of the pandemic. As a consequence, the elasticity of electricity and petroleum demand toward the population of the infected people is -0.323% and -0.397% respectively. The impact of COVID-19 on energy demand will be many times greater than the impact of the 2008 financial crisis on global energy demand. The mentioned findings show that the crisis deeply affected not only human health but also the global economy, clearly showed how the energy sector interacts with other factors of the economic structure.

1. INTRODUCTION

The Coronavirus infectious disease 2019 (COVID-19) has affected our societies, also it has impacted the energy sector worldwide [1]. Although the full impact of the energy sector is very difficult to predict precisely, because the market is fluctuating, decreased energy consumption and energy prices, as well as a sharp decline in oil prices, are already observed. Due to the supply chain and the logistical risks to companies across the different energy transition sub-sectors the current situation also represents the main uncertainty as to whether the pandemic will speed up or slow down the energy transition. Many researchers [2-4] and companies [5,6] discuss the implications of COVID-19 on the energy transition towards a sustainable future. The authors [7,8] share their research consequences faced by the renewable electricity generation sector and possible reactions of energy regulators. For many experts and researchers, it is difficult to assess the whole impact we are still only at the start; but some of the first effects can be seen at least the short-term effects [9, 10]. The first step and also what it meant for energy regulators was that is seen a lot of emergency decisions taken by governments across all Europe [11] and in Turkey [12]. It implied immediately some measures for the day-to-day work of National Regulatory Authorities, energy market actors and operators and etc.

Across the country as well as most of the operators are starting to say that weekdays now look like weekends. Because people are staying at home and using more electricity in the residential side versus the commercial side that had a change of energy demand, drop in demands [13]. This has resulted in a wide variety of effects on the grid such as decreased electricity prices. Besides that, it implied that regulators could not have the usual contracts. The operators quite rapidly applied emergency plans successfully; on the other hand, the security of supply stability of the grid provided, and what was most important of course was that they re-organized the staff and the workers in the control center [14].

Also, it is needed to reduce global CO₂ emissions by 70% by 2050 perhaps even more to be in line with the Paris agreement and to reach an energy transformation [15]. The energy transformation needs to be based on renewables, needs to be based on energy efficiency, and it needs to be based on electrification of entuses. These three strategies are really critical and it can be concluded that such a transition is technically and economically feasible. The investment needs significant between 110 and 130 trillion dollars, but it's not so much higher than a reference case it's around 95 trillion dollars between now and 2050 [15].

With the effect of the COVID-19 epidemic the energy demand is down; CO₂ emissions are down 7% on an annual basis [16]. It is also seen that the impact on fossil fuels is much more

significant than the impact on renewables in terms of consumption, generation and pricing [17]. The European electricity market and compare that the May 2020 numbers with the same numbers from the last year; it has been reported that electricity production and electricity demand decreased by about 10% [18]. But if you look at the generation side in more detail then you see a significant drop in call against based power generation 20 to 30 % drop. But renewables generation increased by about 8 % [18]. The reason is that because first of all last year it is added significant new renewable generation capacity that starts to produce this year. Secondly, the solar and wind have virtually zero operating costs. That makes the renewables generation share has increased very significantly; as of January 2021, 48% of all power generated in Europe was renewable. That is a very remarkable number thanks to the good work of the power plant and grid operators and regulators. As a result of this, fossil fuel prices have been significantly decreased. As the natural gas prices in Europe; so, the enterprises for imported gas and the gas prices in the Turkish system are about \$2 per meter of €2 per division so that's a very low price not seen before [19]. But it's not completely attributable to the crisis because if you look at the import prices it has been declining already for some time.

There are also other things going on in the system; it's not only the demand effect but also important supply effects. The gas prices this year half, the oil prices have nearly half the coal price went down from \$70 to \$55 [20]. The change in prices has also affected the relative competitiveness of gas versus coal-based power generation. That access baits the impacts on coal-based generation and that's why it is seen that coal-based generation has dropped faster than a gas-based generation.

Another important cost component in the power market is the CO₂ permit prices, and it has been fairly stable over this year; which is at around slightly above 20 euros per ton of CO₂. It translates into an incremental cost of about 2 cents per kilowatt-hour of coal-based generation or a cent per kilowatt hour of gas-based generation [21]. That is also still a very important cost component that also affects the competitiveness of renewables versus oil, especially in coal.

Due to this epidemic that affected the world, the expected growth in electricity demand could not be achieved in Turkey due to the following reasons; (i) It is one of the main countries suffering from COVID-19 [22,23], (ii) it is the seventeenth largest economy in the world, (iii) It has the one of the highest energy consumption in Europe and the largest growth in wind, solar and hydro installation respectively [24].

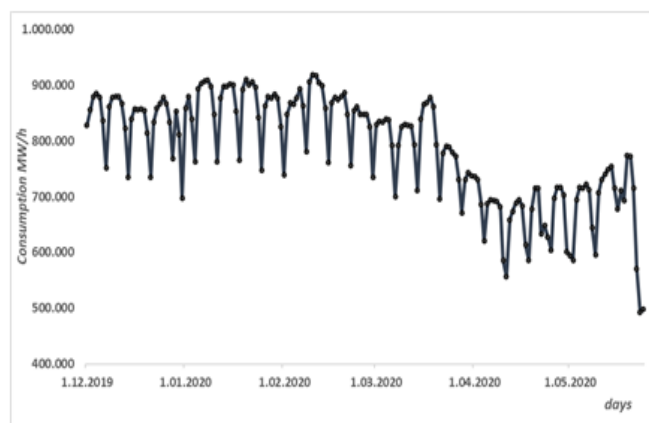


Figure 1. Daily electricity consumption in Turkey (December 1st 2019 – May 30th 2020)

As the daily electricity consumption seen in Figure 1, the developments in the months of January and February can be observed very easily. Demand increased by 2.45% in January and decreased by 4.02% in February [25]. However, from the first positive case on March 11, the measures taken by the companies in the process from the first positive case to the precautions, for example, from the first day the case was seen, people started to work directly at home; and it still continues that way.

The recovery in electricity demand in the short and medium-term will likewise depend on economic growth. For this reason, both domestic consumption and export dynamics of the country should be closely monitored. The correlation between Gross domestic product (GDP) growth rates and electricity demand growth rates between 2001 and 2020 is remarkable [25,26]. Figure 2 shows the relationship between the growth of Gross Domestic Product and electricity demand. As seen from Figure there was a sharp decline in Gross Domestic Product in 2009. Despite a nearly 5% decrease, electricity demand fell by 2.1%. On average, Turkey's economy grew by only 1.8% in 2020 due to the effects of COVID-19. With this shrinkage, according to estimates, it decreases between 2% and 4% compared to the previous year in different scenarios. In the IMF January 2021 report [27]; Turkey's economy shrinks by 5% in 2020, while next year it estimates will grow by 6%. In case of a single outbreak of the study looking at slightly different in the OECD predicted to fall by 4.8% of Turkey's economy. It estimates the growth as 4.3% in 2021. If there is a third wave of the epidemic; according to OECD analysis the things go wrong in Turkey and in the world, also predicts that there will be an 8.1% contraction in the economy and a growth of 2% next year.

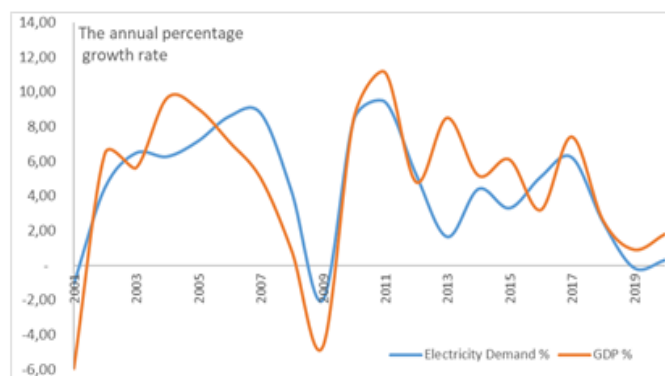


Figure 2. Comparison annual growth rate of GDP and electrical energy demand since 2001 up to 2020

As renewable energy for the first time in 2019, the total electricity production was increased from solar energy 3% and up to 7% in wind. The total production of other renewable resources was 4%. There was a wetland on the hydroelectric side, it broke the record for many years; there was a 34.1% share of hydroelectric production in 2019. The share of renewable energy in total has reached 44% [28]. In fact, for the first time since 1996, the capacity utilization rate of natural gas in electricity generation fell below 20%. On 24 May 2020, the total renewable energy reached 90% on the feast day and on a day of curfew [29].

It is very difficult to make predictions during the pandemic. One reason for the difficulty is that we are dealing with an ongoing crisis. However, how much the pandemic will shake the global economy, the change in consumption and production levels from COVID-19 in the energy and

electricity systems, and perhaps more importantly, changes in usage patterns are not yet fully known. Travel bans imposed due to COVID-19 caused domestic and international flights to be disrupted to a great extent. When the measures are taken to prevent the spread of the epidemic slow down the economy and significantly reduce the demand for energy; Oil prices were the first to be affected by this lack of demand [1]. Then there were decreases in the prices of natural gas and other energy resources. The most important question for the global economy is whether the economies thousands of kilometers from where the virus originated will come to a standstill. Such approaches will clearly inform about energy policies in the post-COVID-19 era.

As the impact of the coronavirus pandemic continues to be explored, this article aims to conduct quantitative analysis through a neural network-based modeling and sensitivity analysis of energy inputs to determine the importance and fragility of different economic sectors, with a special focus on electricity and oil demand.

2. ENERGY DEMAND AND NEURAL NETWORKS

The increase in the world population and the developments in technology increase the energy demands and fluctuations. It is the main input of all kinds of sectors such as energy production, agriculture, transportation. Energy runs the economy so it has deep implications for the nature of work and economic growth in the coming years. Therefore, energy forecasting and modeling is becoming increasingly important. Many different estimation techniques and tools are used in the literature for energy demand forecasting. For example; time series [30-32], gray prediction [33], regression model [34], particle swarm optimization [35-37], genetic algorithm [38], fuzzy logic [39], artificial neural networks [40,41] and so on. Energy demands are estimated using forecasting techniques. To reach broader energy demand forecasting models, Suganthi and Samuel's [42] study can be examined.

One of the most frequently used estimation tools in the field of energy demand estimation is ANN. Dumitru and colleagues [43] Romania's wind power forecasting, Galvan et al [44] Oklahoma's daily solar energy, Jasinski [45] Slovakia's electricity consumption, Alanis [46] electric energy price prediction, Akarslan et al [47] Afyon Kocatepe University's total electricity demand, Gajowniczek and friends [48] detect Poland's peak load in the electricity system, Codur and colleagues [49] estimate the energy demand in the transportation sector and Tumbaz and Ipek [50] have used the ANN to estimate Turkey's primary energy consumption. Oil and electricity consumption today is non-linear and variable, subject to a wide variety of exogenous variables such as weather conditions, calendar effect, demographic and economic variables, and general randomness in individual use. How to successfully integrate various factors and sources into the prediction model and obtain accurate load predicts are always a challenge toward the modern energy systems. For modeling such extraordinariness, the advantage of using neural networks is that when the functional structure of the data set cannot be determined exactly, it can successfully model the functional structure in many different forms based on the data. Artificial neural networks (ANN), also known as general function approximations, do not require any presumptions on the data set, unlike statistical methods.

There are many studies in the literature regarding the comparison of artificial neural networks and traditional

methods [51-54]. Estimation accuracy has a significant impact on the planning of electrical energy generation, transmission and distribution systems investments, power system studies, and daily system operation. Overestimating the demand causes unnecessary use of spare reserves or the activation of too many power units. On the other hand, low demand forecasts may cause the electricity energy demand to be insufficient and the supply reserve to be insufficient and prevent the efficient operation of the system.

In recent times and after the COVID-19 outbreak started, ANN attracted the attention of many researchers. In this context neural networks have been carried out on many studies to forecast the prevalence of outbreak in Egypt [55] in Saudi Arabia [56], river flow forecasting [57], the wind power curve forecasting [58], the impact of the pandemic on GDP of major economies [59], liver cancer risk [60], water quality [61] fluid properties of kerosene [62], predict the number of COVID-19 cases [63]. In an article published in 2020, energy consumption for a residential building was estimated by 2050 through an ANN forecast model [64]. According to the results obtained by the author; ANN is better suited to estimating the energy consumption of residential buildings because other models perform better compared to traditional statistical methods, namely linear regression analysis. Another study [65] used a multiple nonlinear regression model for cooling systems in public buildings to accurately estimate short-term cooling loads.

Due to the variables affecting energy carrier demand variable over the time series period nonlinear stochastic methods are used to provide higher accuracy and lower run for energy consumption. In this study, to ensure Turkey's oil and electricity consumption patterns; forecasting models were created using time series analysis and feed-forward neural networks, and short-term estimation results were obtained using daily, weekly, and monthly data.

3. THE PRESENT STUDY AND METHODOLOGY

The purpose of this study is to analyze the impact of COVID -19, the first global epidemic in the 21st century, on electricity and oil consumption. The novelty of this article is that the IMF, world health organization, stock market, GDP indicators are used for variables in the analysis of the model that is comprehensively linked to the new COVID-19 pandemic. In order to compare the period before and after the COVID-19 outbreak, data from 2019, the year just before the beginning of the outbreak, is needed. However, in order to reduce the impact of possible shocks on the macroeconomic and public finance indicators of the country in 2019, the last three years, 2017, 2018 and 2019, were included in the analysis as the period before COVID-19. In this context, for the period before COVID-19, the daily and monthly values of the macroeconomic and public finance data of 2017, 2018 and 2019 were taken for three years. Since only the data for the years 2020 and 2021 for the post-COVID-19 period are included, the analysis is limited to the years 2017-2021. The main aim of this study contribute to decision-makers to have higher accuracy prediction the responses of the demand and supply side of the energy markets, the possible consequences of the impacts of economic stagnation during and post COVID-19.

The subject of this study is to investigate the relationship between the consumption of petroleum and electrical energy and the basic parameters of the economy in the epidemic

period. The experimental results obtained by the author also revealed that the Regression model generally performed better in predicting linear time series, while ANN performed better in predicting nonlinear time series [66]. This study proposes a nonlinear ANN method to investigate the current novel coronavirus epidemic that occurred in early 2020, instead of the classical method available in the literature [67, 26].

The most important problem to be addressed after the method selection is the research period. The economic and social changes caused by the outbreak make the existing models developed using the historical data worthless and incorrect. The model was trained with daily and monthly data between January 2019 and January 2020, as long-term analysis would reduce the model's inaccuracy and overcome the lack of data problem. The methodology of this paper is shown in Figure 3 which uses the regression and ANN method to develop a stable framework to interpret the impact of the COVID-19 epidemic on the Turkish economy.

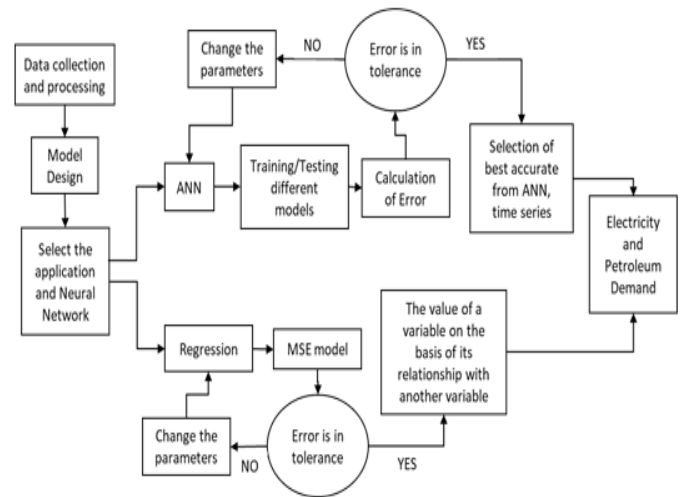


Figure 3. The schematics diagram of the methodology to understand the impact of COVID-19 epidemic on the Turkish economy

The variables used to model the impact of COVID-19 on the economic situation and energy demand are summarized in Table 1. Table 2 presents the descriptive statistics for each data.

TABLE I
DEFINITIONS AND SUMMARY OF INDEPENDENT VARIABLES USED IN THE MODEL

Variable	Unit	Reference	Definition
GDP Growth	%	tradingeconomics [68]	The Turkish gross domestic product (GDP) growth
Oil Demand	Ton Barrel	EPDK [25]	The monthly oil demand for Turkey
Electricity Demand	MWh	teias [22]	The daily electricity demand for Turkey
Epidemic status	-	WHO [23]	The daily death cases
Infected people	People	ourworldindata [69]	The number of infected people in Turkey.
Manufacturing PMI	-	tradingeconomics [70]	The manufacturing productivity in Turkey.
Export Income	USD Million	tradingeconomics [71]	The monthly export income of Turkey.
Foreign Direct Investment	USD Million	tradingeconomics [72]	The monthly foreign direct investments into Turkey
Industrial Productivity	-	tradingeconomics [73]	Turkey's monthly industrial production
Stocks Value	-	investing.com [74]	The Turkey Istanbul Stock Market Index.

TABLE II
THE SUMMARY STATISTICS OF THE VARIABLES

	Min	Max	Skew	Mean	Median	Std. D.	Var.
Petroleum demand	730,00	1338,00	0,25	1038,64	1014,50	171,08	29269,96
EI	0,00	0,98	1,43	0,20	0,00	0,35	0,12
IP	0,00	320070,0	1,47	60344,68	0,00	102853,37	10578815137,94
IP	-31,30	10,60	-1,68	-0,43	-0,35	9,67	93,51
Diesel	775200,0	1423000	0,43	1032993,18	1016620,0	198177,69	39274398594,42
Gasoline	389500,0	470000,0	-0,21	430970,45	432100,00	22952,36	526810831,61
Stocks	888,65	1192,43	0,05	1031,18	1031,02	85,79	7359,26
PMI	33,00	56,00	-1,27	48,48	48,50	4,94	24,43
FDI	170,00	1223,00	1,19	474,64	395,50	259,76	67472,96
Exports	8971,15	17308,72	-1,11	14037,39	14526,22	1947,59	3793089,95
Electricity	670193,0	986254,0	0,18	817757,64	830542,50	98919,17	9785002694,78
GDP growth	-9,72	5,99	-1,12	0,17	0,17	3,86	14,94

3.1. Regressive model and ANN

In the present paper, the NARX neural network model and cointegration analysis were used to estimate Turkey's electricity and energy demand pattern at the time of COVID-19 or actual epidemic situations. The Autoregressive Distributed Lag Model (ARDL) procedure employs a single equation to estimate the long-term relationships between the variables. So, the ARDL model consists of time series for the functional specification of long-run relationship between energy and COVID-19. In the next step, if there is an evidence of long-run cointegration between variables, the form of

Equations (1) and (2) to use this approach efficiently, are estimated using the following selected ARDL models:

$$LnDemand_{electricity} = B_1GDP + B_2LnDemand_{oil} + B_3LnEpidemic + B_4LnPopulation_{infected} + B_5LnPMI + B_6LnExports + B_7LnFDI + B_8LnStocks + B_9LnP_{industry} \quad (1)$$

$$LnDemand_{oil} = B_1GDP + B_2LnDemand_{electricity} + B_3LnEpidemic + B_4LnPopulation_{infected} + B_5LnPMI + B_6LnExports + B_7LnFDI + B_8LnStocks + B_9LnP_{industry} \quad (2)$$

In the study, an estimation equation given in Equation (1, 2) is created. Calculations are made by taking the natural logarithms of the variables in the estimation equation. After determining the existence of a long-term equilibrium relationship between the variables, the parameters reflecting the long-term relationship should be estimated. The specifications of the selected ANN for the ARDL model are 10 neurons and 0.5 momentum coefficient.

The ARDL test developed by Pesaran, Shin, and Smith, which can be used in samples with a limited number of observations and allows variables to be analyzed without the need for integration as in the Johansen-Juselius and Engle-Granger cointegration tests, is an effective method to predict short- and long-term relationships. In other words, with this method, a variable at the level of variables, the first aware or a variable level can be included in the analysis as the first awareness constant [75].

ANN is the system that learn the relationship between the given events and make decisions based on the information they learned about the situations they have never seen. There are a wide variety of network structures and models in artificial neural networks. An ANN consists of a series of neural cells connected by forward-driven and feedback-linking forms. Today, many neural network models suitable for specific purposes and use in different fields have been developed. Among these network structures, multi-layer feed-forward neural networks are the most widely used and used in our study. The feed-forward network consists of an input layer, an output layer, multiple hidden layers, and several successive neuron layers. Neurons are linked together using weight vectors.

Theoretically, the main purpose of an ANN is to learn the structure in the sample data set and make generalizations to fulfill the expected task [76]. In order to do this, the network is trained with the examples of the relevant event and gained the ability to make generalizations. The learning of ANN is done by changing the weights of the process elements with the selected training algorithms. Multi-Layer Perceptron is a learning algorithm based on error. It performs the two basic functions of learning and decision-making through weighting, activation function and bias. Weight is the coefficient by which each input is multiplied before going to the next stage. All entries are added up by multiplying them by their respective weights. Then, the response resulting from sending this value to the activation function becomes the decision of the system. Bias, on the other hand, is a parameter added by the user, which can vary from user to user, the way the mechanism works or its purpose. In order to be used in the time series estimation of MLP networks, the structure of the network must be determined. When determining the ANN structure, it is necessary to determine the values such as how many layers the network will consist of, how many operations these layers will perform, how many different layers and how much weight it will be attached to. The number of output neurons is determined depending on how many periods the estimation will be made. Determining the number of neurons to be used in input is not as easy as determining the number of output neurons, because determining how many observations values the series' value at time t is affected by is a critical question and the answer to this question shows how many input processing elements will be.

In artificial neural networks, there is no certain rule of numbers such as how many hidden layers the structure will consist of or how many neurons it will combine with. These

numbers are determined by the trial-and-error way. The number of the hidden layer neurons was adjusted considering the complexity of the data and in a practical way, and the number of neurons was optimized (increases or decreases in numbers) according to the feedback of the network environment. The number of nodes in the input layer is 9 and the hidden layers/neurons are 10; as the structure of the selected ANN is illustrated in Figure 4.

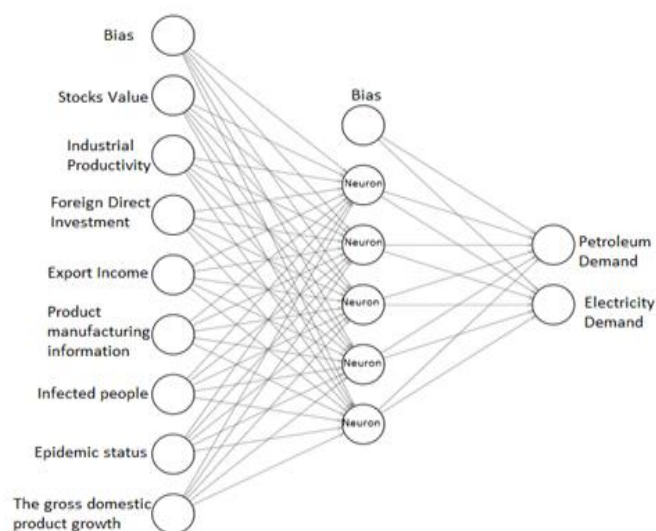


Figure 4. The selected neural network structure

4. RESULTS

Considering that energy consumption and economy have a complicated relationship, after determining the cointegration relationship between the series and there was a relationship between the variables in the short and long term. Since a single linear approach cannot model by that much data, especially during periods of trend change, a correlated regression model is used to investigate all of the direct and indirect relationships between the main parameters that derive the system.

Correlation analysis is a statistical method that reveals the direction, rate, and importance of the relationship between variables [77]. By using the Pearson coefficient, the coefficient indicates the direction and rate of the relationship is called the correlation coefficient, denoted by r . The correlation coefficient takes values ranging from -1 to $+1$ ($-1 \leq r \leq +1$), and the sign of the correlation coefficient determines the direction of the relationship. If the value of r takes values close to -1 , it is determined that there is a negative relationship between the variables, and a positive relationship if it takes values close to $+1$. If the value of r takes values close to zero, it is concluded that there is no relationship between the two variables.

The epidemic resulting in disease and death deeply affected the supply and demand leg of the economy. This process includes the real aspect of the economy, the goods, wage and factor markets; in its financial aspect, the monetary policy authority has transformed the economic relations network in another direction by influencing the preferences and precautionary policies of institutions such as banking, especially the Central Banks. As in the whole world in Turkey as well the physical and social isolation and non-contact life have resulted in the contraction of the supply of agriculture, industry and especially the service sector by affecting the labor supply through the production pillar.

Table 3 presents the flexibility of each economic parameter against the pandemic and shows that PMI, stock market and GDP growth are more severely damaged by COVID-19. Although all other parameters such as production efficiency, and foreign direct investment are also affected by the epidemic, they are less important. These in turn affect the

energy demand and supply side directly or indirectly. The Foreign Direct Investment is not directly affected by the COVID-19's outbreak, it is considerably affected by the decrease in petroleum demand and export income, therefore being indirectly affected by COVID-19.

TABLE III
CORRELATION MATRIX OF VARIOUS PARAMETERS

	GDP growth	Infected People	Petroleum demand	FDI	Stocks	Exports	PMI	Industrial Productivity	Epidemic
GDP growth	1	.410	-.025	.034	.169	.232	.282	-.617	-.390
Infected People	.410	1	.042	.014	-.068	.099	.377	-.360	-.986
Petroleum demand	-.025	.042	1	-.386	.377	-.514	-.375	.289	-.021
FDI	.034	.014	-.386	1	-.334	.508	.360	-.399	.012
Stocks	.169	-.068	.377	-.334	1	-.183	-.328	.020	.051
Exports	.232	.099	-.514	.508	-.183	1	.565	-.736	-.124
PMI	.282	.377	-.375	.360	-.328	.565	1	-.828	-.446
Industrial Productivity	-.617	-.360	.289	-.399	.020	-.736	-.828	1	.396
Epidemic	-.390	-.986	-.021	.012	.051	-.124	-.446	.396	1

According to the results obtained, the flexibility of each target parameter to coronavirus is calculated and shown in Table 4. This demonstrates that the COVID-19 has a significant influence on the financial system and electricity/petroleum demand status of Turkey.

TABLE IV
FLEXIBILITY OF EACH PARAMETER TO THE SEVERITY OF THE CORONAVIRUS OUTBREAK AND THE INFECTED POPULATION.

		Elasticity Value	t-parameter	Sigma
Petroleum Analysis	Industrial	-0.257	-4.152	0.0082
Electricity Analysis	Productivity	-0.089	2.047	0.00963
Petroleum Analysis	Stocks	-0.407	-2.281	0.0224
Electricity Analysis		-0.018	-2.049	0.00962
Petroleum Analysis	GDP growth	0.028	5.062	0.00952
Electricity Analysis		0.025	5.051	0.00960
Electricity demand		-0.323	2.328	0.0209
Petroleum demand		-0.397	4.328	0.00209

The findings indicate that Industrial Productivity has decreased due to pandemic, but the more important effect is due to the severity, as a 1% increase in the severity index causes a 1.465% decrease in the petroleum demand index. Also, for export income and Manufacturing PMI decreasing by 0.62% and 0.743% respectively when the electricity demand decreases by 1%. GDP growth is also being hit by the population of the infected people, which a 1% increase experiences a 0.394% decrease in the GDP growth rate. At the same time, the electricity demand is one of the most sensitive to the severity index, when a 1% increase in the severeness index causes a 0.89% decrease in demand. Foreign direct investments are less affected than other parameters by the epidemic, as the imposition of restrictions on economic activities to prevent the spread of the epidemic slows down existing investment projects. When the activities of some workplaces are stopped, the production of the sectors that provide raw materials to these workplaces will naturally decrease [78]. For this reason, there will be

shrinkage and loss of employment not only in the sectors that are suspended, but also in the sectors that provide input. In addition, unpaid leave and dismissal practices will be experienced in shrinking sectors, and the income of employees in these sectors will decrease. As a result, consumption demand will decrease and the production of consumer goods sectors will decrease. All these effects result from the direct or indirect effects of crisis on energy demand and supply side. Some parameters are directly affected by the COVID-19 outbreak, while others are indirectly affected.

Equation 3 is used to determine how different values of an independent variable affect a particular dependent variable under a given set of assumptions. The F is the Dickey-Fuller Statista which shows the correctness of regression the hypothesis and the sigma (ω) is the probabilistic dual of F. The test is used to determine whether the unit root exists (the series is not stationary) in the observed series. Efficiency is stated by calculating the ratio of output changes to each input. The main factor affecting the accuracy of the research is the inability to choose well the independent variables that may affect the dependent variable to be examined. [77]

$$S_{\omega}^F = \frac{\partial F / F}{\partial \omega / \omega} \quad (3)$$

Table 5 shows the elasticity of each parameter to the coronavirus outbreak index and the infected individuals to investigate the structural model of Figure 5-6 which shows the effect value of each parameter of different behavioral attitudes on the other parameters. The coefficients represent the elasticity of each parameter to the other parameters, and Figures 5a and 5b clearly show the impact of the COVID-19 pandemic on petroleum and electricity consumption respectively in Turkey. Initially, through performing sensitivity analysis on different variables, the amount of the impact and how it affects the change in the output of the model are investigated. Secondly, the amount of electricity and oil demand of Turkey will be predicted for the coming days and months.

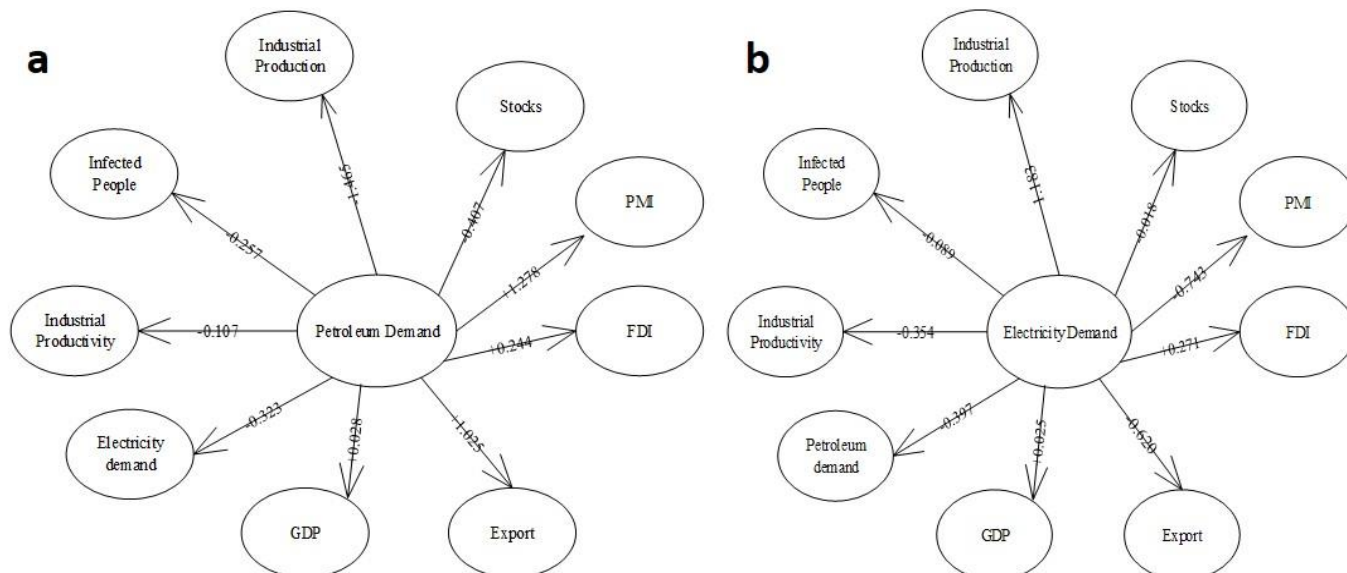


Figure 5. (a) The relation of each parameter of the petroleum model on the other parameters, (b) The relation of each parameter of the electricity model on the other parameters.

TABLE IV
THE RATIO OF ELASTICITY VALUES

Variable	The ratio of the output changes	
	For petroleum	For electricity
Infected People	-1,465	1,183
GDP growth	0,028	0,025
Petroleum demand	-	-0,397
Electricity demand	-0,323	-
Foreign Direct Investment	0,244	0,271
Stocks Value	-0,407	-0,018
Export Income	1,025	-0,62
Manufacturing PMI	1,278	-0,743
Industrial Productivity	-0,257	-0,089
Epidemic status	-0,107	-0,354

Different models were created in ANN models and the effective parameters on prediction were examined. The number of neurons is found by trial and error. The number

of neurons has an effect on the prediction. The number of hidden layers; It is effective on estimates and is also related to the number of neurons to be selected. Excessive training data increases forecast performance.

While creating the analysis prediction model, the data with low correlation and high correlation relationship were used together and the data with low correlation values were removed from giving accurate results. The results have shown that the established ANN model and forecasting process was performed very successfully. High regression and low error values in the training, testing, and verification stages also supported results. This confirms that artificial neural networks give positive results especially in solving nonlinear problems.

Figure 6 shows the graphical representation of the estimation made with ANN and the values realized with 3-year data. As can be seen from the graph, the actual values tested and the predicted values were very close to each other. Figure 7 shows the prediction error by percentage.

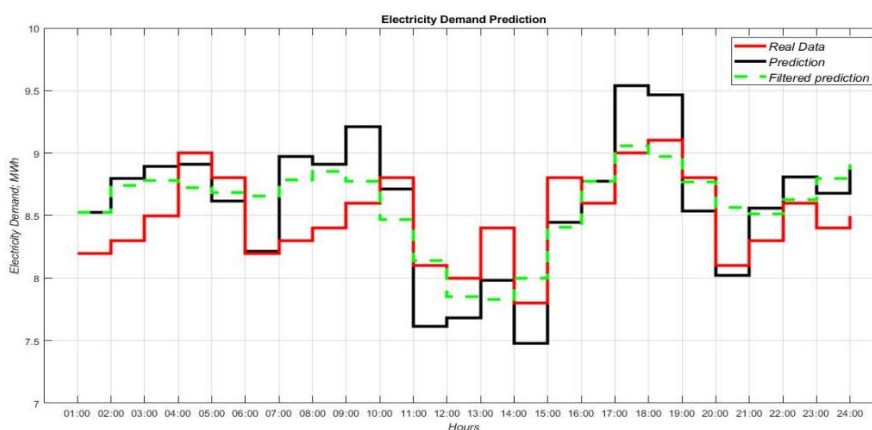


Figure 6. Electricity demand prediction.

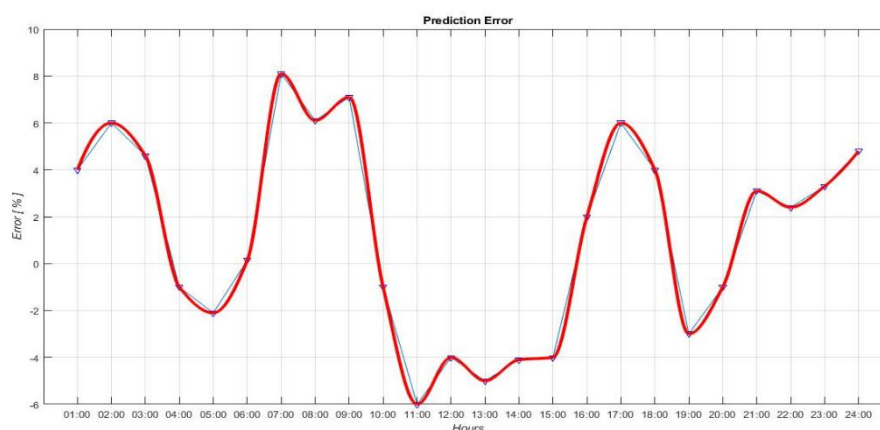


Figure 7. Electricity demand prediction error.

5. CONCLUSION

With the COVID-19 pandemic, all countries of the world have faced a very serious challenge that they have not experienced before. The world economy has witnessed some major economic crises that have had a global impact since the twentieth century. After the Ebola epidemic in Guinea, Liberia and Sierra Leone, the 2008 financial crisis caused by the USA changed the economic balances. While faced with an economic picture shaped by low growth rates after the last crisis, the COVID-19 epidemic, which emerged in China in December 2019 and spread to the world, leaves social, social and economic effects that are still ongoing and likely to continue. The rapid spread of the COVID-19 virus has caused countries to implement protective measures. However, the measures taken by countries against this epidemic bring unprecedented collapse to the economy.

Among the energy types, electricity and petroleum were the most affected during the COVID-19 outbreak. Because the first and most effective measure taken against the epidemic was to stop international/domestic flights and restrict travel to work or elsewhere, this hit air, land, and sea transportation the most. Due to the measures taken, electricity has seen significant declines in consumption in Turkey; As a result, decreases in peak loads are observed. The decrease in peak load means that this is to the advantage of the renewable energy sector. Because renewable energy sources with zero fuel cost in price competition after demand decrease while supply is constant will be able to dominate the market compared to fossil fuels.

When we look at Turkey's daily petroleum and electricity consumption in 2020 shows that major changes occurred prior to and after COVID-19 measures. Turkey, a country largely dependent on foreign energy sources; it is very important to correctly predict the demand for electricity and petroleum. In current predictions, it is essential to take into account epidemic status and infected people for the near future. As a consequence, the elasticity of electricity and petroleum demand toward the population of the infected people is -0.323% and -0.397% respectively. The actual values tested and the predicted values were very close to each other.

Currently, the new Coronavirus outbreak is still ongoing, preventing a thorough investigation of its full effect. As a future work; the impact of the energy demand and economic consequences of the epidemic on emissions and production should be investigated.

ACKNOWLEDGEMENT

I would like to express my very great appreciation to Nima Norouzi from the Amirkabir University of Technology for professional guidance, valuable support, and useful and constructive recommendations on this paper.

REFERENCES

- [1] Mofijur, M., et al. "Impact of COVID-19 on the social, economic, environmental and energy domains: Lessons learnt from a global pandemic." *Sustainable production and consumption* (2020).
- [2] Steffen, Bjarne, et al. "Navigating the clean energy transition in the COVID-19 crisis." *Joule* 4.6 (2020): 1137-1141.
- [3] Rosenbloom, Daniel, and Jochen Markard. "A COVID-19 recovery for climate." (2020): 447-447.
- [4] Hosseini, Seyed Ehsan. "An outlook on the global development of renewable and sustainable energy at the time of COVID-19." *Energy Research & Social Science* 68 (2020): 101633.
- [5] Rapaccini, Mario, et al. "Navigating disruptive crises through service-led growth: The impact of COVID-19 on Italian manufacturing firms." *Industrial Marketing Management* 88 (2020): 225-237.
- [6] Donthu, Naveen, and Anders Gustafsson. "Effects of COVID-19 on business and research." (2020): 284-289.
- [7] Elavarasan, Rajvikram Madurai, et al. "COVID-19: Impact analysis and recommendations for power sector operation." *Applied energy* 279 (2020): 115739.
- [8] Sovacool, Benjamin K., Dylan Furszyfer Del Rio, and Steve Griffiths. "Contextualizing the Covid-19 pandemic for a carbon-constrained world: Insights for sustainability transitions, energy justice, and research methodology." *Energy Research & Social Science* 68 (2020): 101701.
- [9] Polemis, Michael, and Symeon Soursou. "Assessing the Impact of the COVID-19 Pandemic on the Greek Energy Firms-An Event Study Analysis." *Energy Research Letters* (2021).
- [10] Akrofi, Mark McCarthy, and Sarpong Hammond Antwi. "COVID-19 energy sector responses in Africa: A review of preliminary government interventions." *Energy Research & Social Science* 68 (2020): 101681.
- [11] Wolff, Sarah, and Stella Ladi. "European Union Responses to the Covid-19 Pandemic: adaptability in times of permanent emergency." *Journal of European Integration* 42.8 (2020): 1025-1040.
- [12] Demirbilek, Yasemin, et al. "COVID-19 outbreak control, example of ministry of health of Turkey." *Turkish journal of medical sciences* 50.SI-1 (2020): 489-494.
- [13] Abu-Rayash, Azzam, and Ibrahim Dincer. "Analysis of the electricity demand trends amidst the COVID-19 coronavirus pandemic." *Energy Research & Social Science* 68 (2020): 101682.
- [14] Werth, Annette, Pietro Gravino, and Giulio Prevedello. "Impact analysis of COVID-19 responses on energy grid dynamics in Europe." *Applied energy* 281 (2021): 116045.
- [15] Outlook, IRENA Global Renewables. "Energy transformation 2050." IRENA: Abu Dhabi, Page:15, 34, UAE (2020)
- [16] Oxford Analytica. "Climate change demands drastic action internationally." *Emerald Expert Briefings* oxan-es.

- [17] Selmi, Refk, et al. "The energy transition, Trump energy agenda and COVID-19." *International Economics* 165 (2021): 140-153.
- [18] Wärtsilä Corporation, Press release 17 April 2020
- [19] Fulwood, Mike. "\$2 gas in Europe is here: who will blink first." OIES, March (2020).
- [20] Nab Minerals and Energy Outlook, June 2020
- [21] Ember, Daily EU ETS carbon market price (Euros) , <https://ember-climate.org/data/carbon-price-viewer/>
- [22] Ybts information page, https://ytbsbilgi.teias.gov.tr/ytbsbilgi/frm_istatistikler.jsf
- [23] World health organization, <https://covid19.who.int/region/euro/country/tr>
- [24] Yilmaz, Musa, Kilic, Heybet, "Smart grid road map and challenges for Turkey" IET Digital Library, Microgrids for Rural Areas, page:389-420, (2020), ISBN:9781785619991
- [25] Epdk, <https://www.epdk.gov.tr/Detay/Icerik/3-0-104/aylik-sektor-raporu>
- [26] Yilmaz, Musa, "Real Measure of a Transmission Line Data with Load Fore-cast Model for The Future". *Balkan Journal of Electrical and Computer Engineering* 6 / 2 (April 2018): 141-145.
- [27] International Monetary Fund, <https://www.imf.org/en/Publications/WEO/Issues/2021/01/26/2021-world-economic-outlook-update>
- [28] TSKB Enerji Gorunumu Report, 2020.
- [29] Intelligent living, <https://www.intelligentliving.co/turkey-new-record-renewable-energy/>
- [30] Di Piazza, Annalisa, et al. "An artificial neural network-based forecasting model of energy-related time series for electrical grid management." *Mathematics and Computers in Simulation* 184 (2021): 294-305.
- [31] Deb, Chirag, et al. "A review on time series forecasting techniques for building energy consumption." *Renewable and Sustainable Energy Reviews* 74 (2017): 902-924.
- [32] Ghofrani, Mahmoud, and Anthony Suherli. "Time series and renewable energy forecasting." *Time Ser. Anal. Appl* 2017 (2017): 77-92.
- [33] Berthou, Thomas, et al. "Development and validation of a gray box model to predict thermal behavior of occupied office buildings." *Energy and Buildings* 74 (2014): 91-100.
- [34] Hong, Tao, et al. "Probabilistic energy forecasting: Global energy forecasting competition 2014 and beyond." (2016): 896-913.
- [35] Rahmani, Rasoul, et al. "Hybrid technique of ant colony and particle swarm optimization for short term wind energy forecasting." *Journal of Wind Engineering and Industrial Aerodynamics* 123 (2013): 163-170.
- [36] Kıran, Mustafa Servet, et al. "A novel hybrid approach based on particle swarm optimization and ant colony algorithm to forecast energy demand of Turkey." *Energy conversion and management* 53.1 (2012): 75-83.
- [37] AlRashidi, M. R., and K. M. El-Naggar. "Long term electric load forecasting based on particle swarm optimization." *Applied Energy* 87.1 (2010): 320-326.
- [38] Azadeh, Ali, et al. "Integration of artificial neural networks and genetic algorithm to predict electrical energy consumption." *Applied Mathematics and Computation* 186.2 (2007): 1731-1741.
- [39] Viswavandya, Meera, et al. "Fuzzy Logic and ANFIS based Short Term Solar Energy Forecasting." *International Journal on Future Revolution in Computer Science & Communication Engineering* 4.4 (2018): 631-636.
- [40] Runge, Jason, and Radu Zmeureanu. "Forecasting energy use in buildings using artificial neural networks: A review." *Energies* 12.17 (2019): 3254.
- [41] Tonyali, O., Bayram, D. (2021). Forecast for Market Clearing Price with Artificial Neural Networks in Day Ahead Market. *Balkan Journal of Electrical and Computer Engineering*, 9(4), 398-403.
- [42] Suganthi, L., and Anand A. Samuel. "Energy models for demand forecasting—A review." *Renewable and sustainable energy reviews* 16.2 (2012): 1223-1240.
- [43] Dumitru, Cristian-Dragos, and Adrian Gligor. "Daily average wind energy forecasting using artificial neural networks." *Procedia Engineering* 181 (2017): 829-836.
- [44] Galván, Inés M., et al. "Multi-objective evolutionary optimization of prediction intervals for solar energy forecasting with neural networks." *Information Sciences* 418 (2017): 363-382.
- [45] Jasiński, Tomasz. "Modeling electricity consumption using nighttime light images and artificial neural networks." *Energy* 179 (2019): 831-842.
- [46] Alanis, Alma Y. "Electricity prices forecasting using artificial neural networks." *IEEE Latin America Transactions* 16.1 (2018): 105-111.
- [47] Akarslan, Emre, and Fatih Onur Hocaoglu. "Electricity demand forecasting of a micro grid using ANN." 2018 9th International Renewable Energy Congress (IREC). IEEE, 2018.
- [48] Gajowniczek, Krzysztof, Rafik Nafkha, and Tomasz Ząbkowski. "Electricity peak demand classification with artificial neural networks." 2017 Federated Conference on Computer Science and Information Systems (FedCSIS). IEEE, 2017.
- [49] Yasin Çodur, Muhammed, and Ahmet Ünal. "An estimation of transport energy demand in Turkey via artificial neural networks." *Promet-Traffic&Transportation* 31.2 (2019): 151-161.
- [50] Tumbaz, MN Morgül, and M. Ipek. "Energy Demand Forecasting: Avoiding Multi-collinearity." *Arabian Journal for Science and Engineering* 46.2 (2021): 1663-1675.
- [51] Han, Te, et al. "Comparison of random forest, artificial neural networks and support vector machine for intelligent diagnosis of rotating machinery." *Transactions of the Institute of Measurement and Control* 40.8 (2018): 2681-2693.
- [52] Metaxiotis, K., et al. "Artificial intelligence in short term electric load forecasting: a state-of-the-art survey for the researcher." *Energy conversion and Management* 44.9 (2003): 1525-1534.
- [53] Hippert, Henrique Steinherz, Carlos Eduardo Pedreira, and Reinaldo Castro Souza. "Neural networks for short-term load forecasting: A review and evaluation." *IEEE Transactions on power systems* 16.1 (2001): 44-55.
- [54] Jamei, Mehdi, et al. "Predicting all-cause risk of 30-day hospital readmission using artificial neural networks." *PLoS one* 12.7 (2017): e0181173.
- [55] Saba, Amal I., and Ammar H. Elsheikh. "Forecasting the prevalence of COVID-19 outbreak in Egypt using nonlinear autoregressive artificial neural networks." *Process safety and environmental protection* 141 (2020): 1-8.
- [56] Hamadneh, Nawaf N., et al. "Artificial neural networks for prediction of covid-19 in Saudi Arabia." *Computers, Materials and Continua* 66.3 (2021).
- [57] Sahoo, Abinash, et al. "Estimation of Flood in a River Basin Through Neural Networks: A Case Study." *Communication Software and Networks*. Springer, Singapore, 2021. 755-763.
- [58] Pillai, Swaroop Ramaswamy, Apurv Yadav, and Vineet Kumar Vashishtha. "Prediction of Wind Power Curve Based on Wind Speed and Direction Utilizing Artificial Neural Network." *Recent Advances in Mechanical Engineering*. Springer, Singapore, 2021. 515-522.
- [59] Jena, Pradyot Ranjan, et al. "Impact of COVID-19 on GDP of major economies: Application of the artificial neural network forecaster." *Economic Analysis and Policy* 69 (2021): 324-339.
- [60] Ataei, Afrouz, et al. "Liver Cancer Risk Quantification through Artificial Neural Network." *Bulletin of the American Physical Society* (2021).
- [61] Noori, Navideh, Latif Kalin, and Sabahattin Isik. "Water quality prediction using SWAT-ANN coupled approach." *Journal of Hydrology* 590 (2020): 125220.
- [62] Li, Bo, et al. "Development and application of ANN model for property prediction of supercritical kerosene." *Computers & Fluids* 209 (2020): 104665.
- [63] Kaya, C. B., Ebubekir, K. A. Y. A. (2021). A Novel Approach Based to Neural Network and Flower Pollination Algorithm to Predict Number of COVID-19 Cases. *Balkan Journal of Electrical and Computer Engineering*, 9(4), 327-336.
- [64] Verma, Anurag, Surya Prakash, and Anuj Kumar. "ANN-based energy consumption prediction model up to 2050 for a residential building: Towards sustainable decision making." *Environmental Progress & Sustainable Energy* 40.3 (2021): e13544.
- [65] Fan, Chengliang, and Yunfei Ding. "Cooling load prediction and optimal operation of HVAC systems using a multiple nonlinear regression model." *Energy and Buildings* 197 (2019): 7-17.
- [66] Prybutok, Victor R., Junsun Yi, and David Mitchell. "Comparison of neural network models with ARIMA and regression models for prediction of Houston's daily maximum ozone concentrations." *European Journal of Operational Research* 122.1 (2000): 31-40.
- [67] Goldthorpe, John H., and Official Fellow John H. Goldthorpe. *On sociology: Numbers, narratives, and the integration of research and theory*. Oxford University Press on Demand, 2000.
- [68] Tradingeconomics, <https://tradingeconomics.com/turkey/gdp-growth-annual>

- [69] Our world in data page, Turkey: Coronavirus Pandemic Country Profile, <https://ourworldindata.org/coronavirus/country/turkey?country=~TUR>
- [70] Tradingeconomics, Turkey Manufacturing PMI, <https://tradingeconomics.com/turkey/manufacturing-pmi>
- [71] Tradingeconomics, <https://tradingeconomics.com/turkey/exports>
- [72] Tradingeconomics, <https://tradingeconomics.com/turkey/foreign-direct-investment>
- [73] Tradingeconomics <https://tradingeconomics.com/turkey/industrial-production>
- [74] Fusion Media, <https://tr.investing.com/indices/ise-100-historical-data>
- [75] Satrovic, Elma. "Financial development and human capital in Turkey: ARDL approach." *Kapadokya Akademik Bakış* 1.2 (2017): 1-15.
- [76] Cetinkaya, Zeynep, and Erdal Erdal. "Daily food demand forecast with artificial neural networks: Kırıkkale University case." 2019 4th International Conference on Computer Science and Engineering (UBMK). IEEE, 2019.
- [77] Norouzi, Nima, et al. "When pandemics impact economies and climate change: exploring the impacts of COVID-19 on oil and electricity demand in China." *Energy Research & Social Science* 68 (2020): 101654.
- [78] Bartik, Alexander W., et al. What jobs are being done at home during the COVID-19 crisis? Evidence from firm-level surveys. No. w27422. National Bureau of Economic Research, 2020.

BIOGRAPHIES

Hasan Huseyin Coban obtained his BSc degree in electronics engineering from Vilnius Gediminas Technical University (VGTU) in 2008. He received the MSc. diploma in Electrical Engineering from Klaipeda University in 2010, and PhD degrees in Riga Technical University in 2016. He worked as a project engineer in the industry between 2010 and 2018. His research interests are Sustainable Energy Technologies, Renewables energy systems, Energy Policy, Energy Access, ANN. Since Feb. 2018, he is an Assistant Professor at Ardahan University Electrical & Electronics Engineering department. He teaches Power Systems, Energy Systems, and Optimization for Engineers courses.

Measurement of the Number of Photoelectrons per MeV for Neutron Detectors

Emre Iren^{1*} , Ferhat Özok² , M. Nizamettin Erduran³ 

¹Mimar Sinan Fine Arts University, Physics Department, Istanbul, Turkey. (e-mail: emre.iren@msgsu.edu.tr).

²Mimar Sinan Fine Arts University, Physics Department, Istanbul, Turkey. (e-mail: ferhat.ozok@msgsu.edu.tr).

³Istanbul Sabahattin Zaim University, Faculty of Engineering And Natural Sciences Department of Computer Engineering, Istanbul, Turkey. (nizamettin.erduran@izu.edu.tr).

ARTICLE INFO

Received: Jun., 11.2021

Revised: Jul., 02.2021

Accepted: Dec, 17.2021

Keywords:

Photomultiplier Tube
Single Photoelectron
Liquid Scintillator
Photoelectron Yield
Neutron Detection

Corresponding author: *Emre Iren*

ISSN:2536-5010 | e-ISSN: 2536-5134

DOI: <https://doi.org/10.36222/ejt.950944>

ABSTRACT

The light gains of a detector system (photomultiplier tube and scintillator) is characterized by the number of photoelectrons produced per unit of energy (usually MeV). In this study, the results of light gain tests for 10 Hamamatsu R11833 model photomultiplier tubes are shown. Various radioactive sources were used in conjunction with the EJ309 liquid scintillator to determine the light gain. The number of photoelectrons produced per unit energy was determined by comparing the size of the signal generated by the photons produced by photomultiplier tube during the scintillation process using radioactive sources and the size of the signal generated when a single photoelectron was produced by the photomultiplier tube. The test results show that the performances of the photomultiplier tubes are sufficient for neutron detector arrays used in experiments with radioactive ion beams. The supply voltage of the photomultiplier tubes must be changed to achieve similar light gains.

1. INTRODUCTION

Neutrons by their nature do not interact with the electrons of atoms and do not cause ionization or excitation. Therefore, they cannot be measured directly. In order to detect neutrons, it is necessary to make them to interact with atomic nuclei. Proton recoils resulting from neutron interaction are measured with liquid scintillator based neutron detectors. These detectors are generally designed for use in experiments with radioactive ion beams. An example of this is the Neutron Detector Array (NEDA) project [1]. These detectors are also designed to work with radioactive beam generating systems under construction, such as SPIRAL2 at GANIL [2], SPES at LNL [3], ISOLDE at CERN [4] and FAIR at Darmstadt [5]. Neutron detector arrays consist of a large number of detectors covering a large solid angle of about 2π . It's also possible to use very large gamma ray detector arrays as an auxiliary detector system, such as AGATA [6], EXOGAM2 [7], GALILEO [8] and PARIS [9] spectrometers that use both with the test set up established in the Centre for Nuclear detectors and the Robotic Application and Research (NAR).

2. EXPERIMENTAL SETUP

To characterize photomultiplier tubes (PMTs), a 2"x2" cylindrical shaped liquid scintillator (EJ309) was used [10].

The light yield of EJ309 was about 12300 photons/MeV [11]. Since the PMTs's windows size are 5", the scintillator is solidly positioned in the center of the PMTs using a black plastic ring. The ring is made of plastic material with a 2" radius hole to hold the scintillator cell in the center of the PMT during each individual measurement. Before each measurement, the scintillator was attached to the PMT with a thin layer of silicone grease, and the system was placed in a housing prepared to seal off external light (Figure 1).

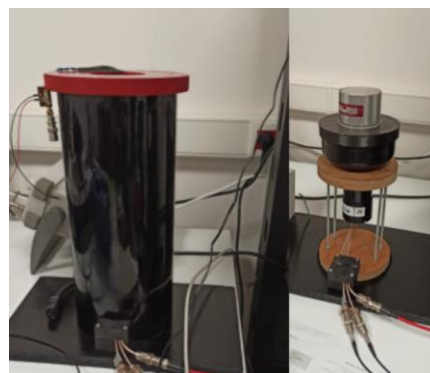


Figure 1. Neutron detector and housing designed using EJ309 liquid scintillator and Hamamatsu R11833 PMT

Data acquisition systems combining both NIM and VME based devices were used. The schematically representation of the data acquisition system is shown in Figure 2.

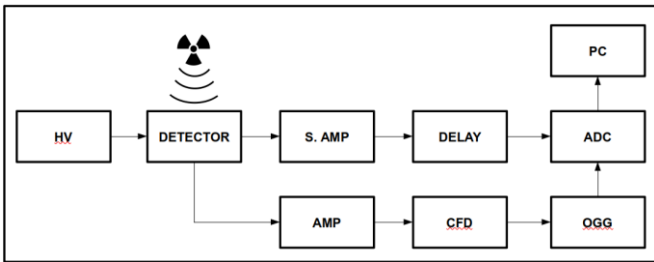


Figure 2. Schematic representation of the experimental setup

^{137}Cs and ^{22}Na radioactive sources were used in the measurements. The anode pulse output of the PMT was connected to a Shaping Amplifier (S.AMP) and then the signal shape was corrected and sent to the Analogue to Digital Converter (ADC) after a certain delay was applied. After the cathode output signal was first amplified via AMP, the gate signal was obtained using the Constant Fraction Discriminator (CFD) and the Octal Gate Generator (OGG) NIM modules and then this signal was sent to the ADC.

The supply voltage of PMTs has been determined between the negative 1100 - 1400 V range, considering the values used in the final test sheet provided by the manufacturer (Table 1).

TABLE 1

FINAL TEST SHEET SENT BY THE MANUFACTURER COMPANY (SUPPLY VOLTAGE IS 1250V FOR ALL PMTS)

PMT	Cathode Luminous Sens. $\mu\text{A}/1\text{m}$	Cathode Luminous Sens. $\mu\text{A}/1\text{m}$	Anode Dark Current nA	Cathode Blue Sens. Index
CA0137	129.0	31.9	2.9	14.7
CA0143	156.0	207.0	14.0	15.2
CA0146	140.0	31.6	7.6	14.8
CA0148	152.0	125.0	2.3	15.6
CA0150	160.0	131.0	4.3	16.0
CA0151	147.0	228.0	3.1	15.6
CA0153	155.0	149.0	5.2	16.1
CA0156	144.0	121.0	6.5	14.8
CA0157	126.0	166.0	5.3	13.4
CA0158	124.0	82.3	2.3	14.1

The signals digitized in the VME ADC module were sent to the PC and filled into histograms. The configuration information of the modules used in the experimental setup is shown in Table 2.

TABLE 2

CONFIGURATION OF THE MODULES USED IN THE EXPERIMENTAL SETUP SHOWN IN FIGURE 2 IN MEASUREMENTS MADE WITH SINGLE PHOTOELECTRON (SPE) AND RADIOACTIVE SOURCES FOR EACH PMT

PMT	Source	HV Value (V)	CFD Thre shold (mV)	AMP Gain	S. AMP Gain	S. AMP S. Time	OGG Width
CA0151	Na	-1100	-10	x30	x5	2 μs	6 μs
	Cs	-1100	-10	x30	x5	2 μs	6 μs
	SPE	-1100	-10	x100	x2k	2 μs	6 μs
CA0143	Na	-1100	-10	x30	x5	2 μs	6 μs
	Cs	-1100	-10	x30	x5	2 μs	6 μs
	SPE	-1100	-10	x100	x2k	2 μs	6 μs
CA0150	Na	-1100	-10	x30	x5	2 μs	6 μs
	Cs	-1100	-10	x30	x5	2 μs	6 μs
	SPE	-1100	-10	x100	x2k	2 μs	6 μs
CA0148	Na	-1100	-10	x30	x5	2 μs	6 μs
	Cs	-1100	-10	x30	x5	2 μs	6 μs
	SPE	-1100	-10	x100	x2k	2 μs	6 μs

CA0157	SPE	-1100	-10	x100	x2k	2 μs	6 μs
	Na	-1100	-10	x30	x5	2 μs	6 μs
	Cs	-1100	-10	x30	x5	2 μs	6 μs
CA0153	SPE	-1100	-10	x100	x2k	2 μs	6 μs
	Na	-1100	-10	x30	x5	2 μs	6 μs
	Cs	-1100	-10	x30	x5	2 μs	6 μs
CA0156	SPE	-1100	-10	x100	x2k	2 μs	6 μs
	Na	-1100	-10	x30	x5	2 μs	6 μs
	Cs	-1100	-10	x30	x5	2 μs	6 μs
CA0158	SPE	-1200	-10	x100	x2k	2 μs	6 μs
	Na	-1200	-10	x30	x5	2 μs	6 μs
	Cs	-1200	-10	x30	x5	2 μs	6 μs
CA0137	SPE	-1400	-10	x100	x2k	2 μs	6 μs
	Na	-1400	-10	x30	x5	2 μs	6 μs
	Cs	-1400	-10	x30	x5	2 μs	6 μs
CA0146	SPE	-1400	-10	x100	x2k	2 μs	6 μs
	Na	-1400	-10	x30	x5	2 μs	6 μs
	Cs	-1400	-10	x30	x5	2 μs	6 μs

3. MEASUREMENT

The light yield of a detector system (PMT and scintillator) is usually characterized by the number of photoelectrons (N_{phe}) produced per unit energy (usually MeV). N_{phe} is an important parameter that determines the performance of PMT. During the scintillation process, a γ -ray from a radioactive source interacts with the scintillator to create photons (usually in the visible lightspectrum). This value is around 12300 photons/MeV for the EJ309 liquid scintillator. These scintillation photons formed in the scintillator strike the photocathode on the PMT and eject electrons from photocathode. The ejected electrons are then multiplied at the dynodes in the PMT, creating an output signal of a certain amplitude and shape. If a single electron is ejected from the photocathode, the amplitude of the signal to be generated is lower. N_{phe} is usually determined by comparing these two signal sizes.

When the 661.6 keV γ -rays emitted from ^{137}Cs radioactive source interact with the EJ309 liquid scintillator, it forms a Compton distribution with a Compton edge of 0.48 MeV energy. Similarly, when the 511 keV and 1274.5 keV γ -rays emitted from the ^{22}Na radioactive source interact with the EJ309 liquid scintillator, they form a Compton distribution with a Compton edge at 0.36 MeV and 1.06 MeV, respectively. The energy of the Compton edge is used to measure N_{phe} . The expression that gives the value of N_{phe} is as follows:

$$N_{\text{phe}} = \frac{P_{\text{SPE}} - P_{z0}}{P_{\text{C.E.}} - P_{z0}} \cdot \frac{G_{\text{SPE}}}{G_{\text{SRC}}} \cdot \frac{1}{E_{\text{C.E.}}} \quad (1)$$

where $P_{\text{C.E.}}$ and P_{SPE} respectively are the positions of the Compton Edge peak and the single photoelectron peak. P_{z0} is the zero offset of the data acquisition system, G_{SRC} and G_{SPE} respectively are the gains of the amplifier used for the measurements with the source and single photoelectron. $E_{\text{C.E.}}$ is the Compton Edge energy [12-13].

3.1. Determination of P_{SPE}

The setup shown in Figure 2 was used to determine the single photoelectron spectrum. After applying the appropriate voltage value to each PMTs, the PMT's anode output signal was passed through S.AMP, the shaping time was adjusted to 2 μs and the unipolar output was connected to the ADC. The gain of the amplifier is set to the maximum level. This value

will be used as the G_{SPE} value in the calculation of N_{phe} . After making sure that there was no radioactive source around the detector, data collection was performed until a uniform spectrum was obtained (Figure 3). Here, a Gaussian fit is applied to the top of the SPE and the mean value (channel number) will be used as the P_{SPE} value in calculating the N_{phe} .

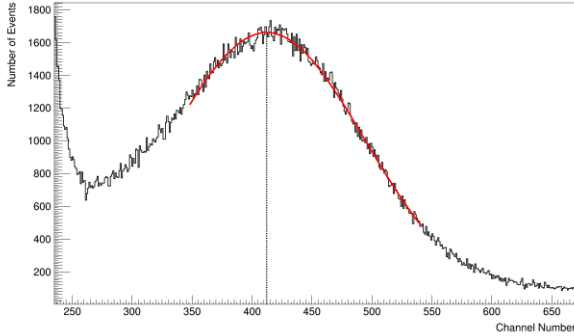


Figure 3. Single photoelectron spectrum obtained with the experimental setup

3.2. Determination of $P_{C.E.}$

The setup shown in Figure 2 was used to determine the Compton edge. After applying the appropriate voltage value to each PMT, the PMT's anode output signal was passed through S.AMP, the shaping time was adjusted to 2 μ s and the unipolar output was connected to the ADC. The gain of the amplifier was set to the minimum level. This value will be used as the G_{SRC} value in the calculation of N_{phe} . ^{137}Cs and ^{22}Na sources were placed over the separate semi-detector housing at a distance of 15 cm for ^{22}Na and 2 cm for ^{137}Cs and data collection was carried out until a uniform spectrum was obtained (Figure 4).

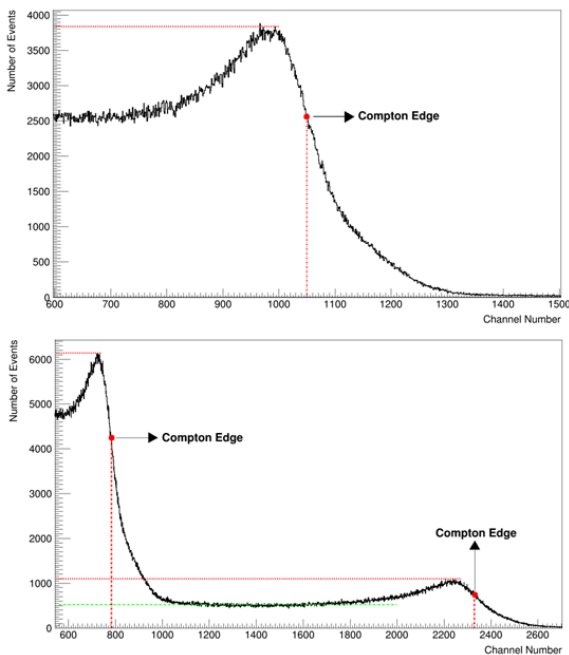


Figure 4. ^{137}Cs spectrum and (top) ^{22}Na spectrum (bottom) obtained with the experimental setup. The Compton edges are indicated by a solid dot.

3.3. Determination of P_{z0}

If there is no offset in the system, the P_{z0} value should be taken as 0. However, in some cases DC offsets based on AMP or/and ADC may occur [14]. In this case, if the necessary corrections are not made, the obtained N_{phe} values will be incorrect. In order to determine whether there is DC offset in the system energy calibration was performed with different radioactive sources with well-known values (Figure 5). The offset value was determined using energy calibration curve plotted in Figure 5. the offset value was determined. This value will be used as P_{z0} value in the calculation of N_{phe} .

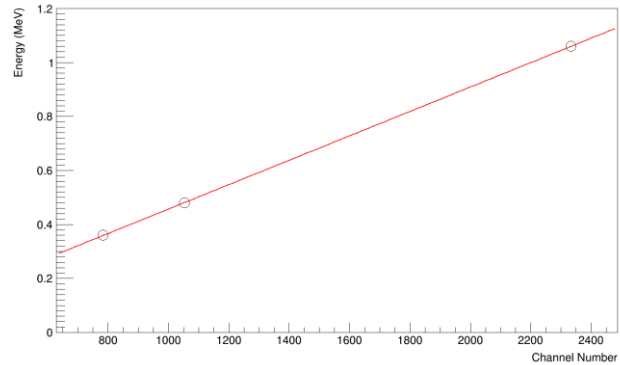


Figure 5. Energy calibration with different radioactive source

4. RESULTS

Measurement results of detector using EJ309 liquid scintillator and Hamamatsu R11833 model PMT are shown in Table 3. N_{phe} determined for both ^{137}Cs and ^{22}Na are consistent with each other. The difference in N_{phe} obtained for each PMT is an expected result due to the structural differences of PMTs shown in Table 1.

TABLE 3
YIELD OF PHOTOELECTRONS (N_{PHE} [MeV^{-1}]) FOR THE PMTs MEASURED WITH EJ309 LIQUID SCINTILLATORS IN THREE DIFFERENT ENERGY RANGES.

PMT	$N_{phe}[\text{MeV}^{-1}]$		
	^{22}Na (0.36 MeV)	^{137}Cs (0.48 MeV)	^{22}Na (1.06 MeV)
CA0137	1792	1770	1781
CA0143	1817	1807	1812
CA0146	2009	1985	1997
CA0148	1690	1632	1661
CA0150	1846	1815	1831
CA0151	2066	2076	2071
CA0153	1836	1782	1810
CA0156	2002	1983	1993
CA0157	1697	1664	1681
CA0158	1704	1650	1677

ACKNOWLEDGEMENT

This study is supported by the Scientific and Technological Research Council of Turkey (TUBITAK Project No: 117F114).

REFERENCES

- [1] ***, NEutron Detector Array (GANIL), <http://pro.ganil-spiral2.eu/spiral2/instrumentation/neda>
- [2] ***, SPIRAL2, <http://pro.ganil-spiral2.eu/spiral2/what-is-spiral2/description-of-spiral2>
- [3] ***, SPES, <http://web.infn.it/spes/>
- [4] ***, ISOLDE(CERN), <http://isolde.web.cern.ch/ISOLDE/>
- [5] ***, FAIR (Darmstadt), <http://www.gsi.de/en/research/fair.htm>
- [6] ***, AGATA, <http://www-w2k.gsi.de/agata/>
- [7] ***, EXOGAM2, <http://pro.ganil-spiral2.eu/spiral2/instrumentation/exogam2>
- [8] ***, GALILEO, http://www.inl.infn.it/~annrep/read_ar/2013/contributions/pdfs/074_C_118_C113.pdf
- [9] ***, PARIS, <http://paris.ifj.edu.pl/index.php?lng=en>
- [10] ***, HamamatsuR11833 model Photomultiplier Tubes, <https://www.hamamatsu.com/eu/en/product/type/R11833-100-03/index.html>
- [11] ***, EJ309 liquid scintillator, <https://eljentechnology.com/products/liquid-scintillators/ej-301-ej-309>
- [12] Johan Nyberg, HOWTO measure the number of photoelectrons per MeV for the detectors of the Neutron Wall, <https://nsg.physics.uu.se/sites/default/files/howto-nphe-v02.pdf>
- [13] D. Guarrera , G. Jaworski , B. Saygı , PMTs of NEDA - Measurement of Photoelectrons Yield and Quantum Efficiency, http://www.inl.infn.it/~annrep/read_ar/2016/contributions/pdfs/092_C_96_C091.pdf
- [14] E. İnce and M. Türk , "COMPARATIVE STUDY OF 0.18MM LINEARIZED CMOS LOW NOISE AMPLIFIER", *European Journal of Technique (EJT)*, c. 7, sayı. 2, ss. 219-228, Ara. 2017

BIOGRAPHIES

Emre İREN Fatih, İstanbul, born in 1987. He received the B.S. in Physics from İstanbul University in 2012. He received the M.S. in Physics from Mimar Sinan Fine Arts University in 2017. From 2017 to 2019, he was a Teaching Assitant in İstanbul Arel University. Currently He is a PhD student in Mimar Sinan Fine Arts University Physics Department. Since 2019, he has been a Research Assistant with the Physics Department, Mimar Sinan Fine Art University.

Ferhat ÖZOK Kadıköy, İstanbul, born in 1979. He received the B.S. and M.S. degrees in Physics from the İstanbul University, in 2001,2004 respectively and the Ph.D. degree in Physics from İstanbul University, in 2011. From 2002 to 20011, he was a Research Assistant with the High Energy and Plasma Physics Department, Istanbul University. Since 2011, he has been an Assistant Professor with the Physics Department, Mimar Sinan Fine Arts University. His research interests include Instrumentation in Particle and Nuclear Physics, Detector R&D and its applications.

M. Nizamettin ERDURAN Kadirga, Istanbul, born in 1951. He received the B.Sc. degree in physics in Istanbul University in 1975 and M.Sc. degree in the University of Edinburgh in physics and nuclear instrumentation in 1978, the Ph.D. degree in physics also from the University of Edinburgh, UK, in 1984. From 1985 to 1998, he was a Researcher with the Cekmece Nuclear Research Centre, Physics Laboratory. From 1998 to 2010, he was professor of nuclear physics with the Istanbul University, he has been a Professor with the Computer Engineering Department, Istanbul Sabahattin Zaim University since 2011. He is the author of more than 50 articles. His research interests include fast neutron physics, nuclear structure physics and applied nuclear physics.

Application of Choline Chloride as Natural Deep Eutectic Solvents for the Green Extraction of Phenolic Compounds from Rheum Ribes Leaves

Fatih Bildik 

¹Istanbul Technical University, Food Engineering Department, 34280, Maslak, Istanbul, Turkey. (e-mail: bildikfatih@itu.edu.tr).

ARTICLE INFO

Received: Jun., 30. 2021

Revised: Dec., 01. 2021

Accepted: Dec, 17. 2021

Keywords:

Deep eutectic solvents(DESs)

Rheum ribes L.leaves

Green extraction

Phenolic compounds

Corresponding author: *Fatih Bildik*

ISSN: 2536-5010 / e-ISSN: 2536-5134

DOI: <https://doi.org/10.36222/ejt.960412>

ABSTRACT

Deep eutectic solvents are applied as a new type of sustainable solvents. The new generation of green solvents are considerable utilize to extraction of bioactive compounds due to their physicochemical properties and structure. In this study, the extraction process of phenolic compounds from rhubarb roots using of ultrasound-assisted extraction (UAE) method was investigated. Totally 8 different types of choline chloride- and L-proline-based deep eutectic solvents containing various H-bond donors/acceptors were synthesized. The extraction conditions for phenolic acids such as effect of different DESs, extraction temperature, water content in nades, ratio of solid to liquid and extraction time were studied. The optimal parameters were found to be extraction time of 30 min, temperature of 313.15 K, DES 30 wt % water and solid/liquid ratio of 1:20 led to significantly effect on the extraction of phenolic contents from plant material. The quantification and characterization of two bioactive flavonoids in the extracts was analyzed via ultra-high pressure liquid chromatography (UPLC) with photodiode detection. Compared with conventional extraction system, deep eutectic solvents (DESs) showed high extraction efficiency for both polar and less polar compounds.

This study reveals, the developed DESs have significant as alternative new green dissolving agents in the extraction of phenolic compounds from plant resource due to their high solubilization ability and low toxicity.

1. INTRODUCTION

Environmentally friendly (or green) solvents have a new type of fluids known as deep eutectic solvents (DES). DESs were discovered in 2003 by Abbott et al. [1]. DESs and DES-based material are alternatives to traditional solvents which are often toxic, environmentally unfriendly, volatile, poorly biodegradable and flammable [2]. The new generation of liquids show many attractive physicochemical properties: low melting point, high solubility, biodegradable, nonvolatility, thermal stability and easy synthesized which can be composed of natural substances (e.g., salts, amino acids, organic acids and sugar, etc.) [3-6]. These solvents consist of two or more salts that are melting point of eutectic mixtures; salts are much lower than its starting substances. However, green deep eutectic solvents have been widely utilized for isolation and extraction of a variety of active compounds from medical plants [7]. The extraction method is also play important role. Ultrasonic assisted extraction method (UAE) has many advantages such as lower cost, higher yield and shorter extraction time, compared to the current extraction techniques [8]. There is capable strong electrostatic interaction between DES and phenolic

compounds. Thus, eutectic solvents show great potential to extract phenolic substances. We mainly studied on the DES combination of natural compounds such as alcohols, sugar, amine, organic acid and choline chloride. The main feature of choline chloride is that unique component properties such as high solubility, non-toxic, biodegradable quaternary ammonium salt [9]. In a previous study the capability of various ChCl, lactic acid and oxalic acid based DES assisted by microwave were evaluated for extraction of different phenolic compounds from *Lonicera japonica* Flos such as chlorogenic acid, caffeic acid, 3,4-dicaffeoylquinic acid, and 4,5-dicaffeoylquinic acid [10]. In another similar research, the combination of DES and methanol-water was used to extract the phenolic acids from *Herba artemisiae scopariae* among different 12 DES, tetramethylammonium chloride/urea (1:4 mole ratio) was the best mixture for extraction Park and co-workers [11].

Moreover, phenolic acids were extracted using betaine-, L-proline-, or ChCl-based DES. Totally, for the extraction of different bioactive compounds including phenolic acids from five Chinese herbal medicines different DES combinations were tested [12]. Quercetin, kaempferol, and isorhamnetin also were extracted from *Flos sophorae* using different ratios

of HBA (ChCl, L-proline and citric acid) and HBD (glycerol, xylitol, glucose, adonitol, or malic acid) [13].

Rhubarb (*Rheum ribes L.*) is a plant native to found mostly in eastern Turkey, Lubnanon, India and Iran. Rheum species are medicinal value herbs due to its source of one of anthroquinone. In Turkey, *R.ribesis* is locally called "ısgın, usgun". Its roots and leaves have been commonly consumed as raw or cooked. *R.ribesis* roots are used as pharmaceutical raw material in the middle east [14,15].

Roots (and leaves) of this plant species are used against variety of diseases such as diabetes [16], obesity [16], hypertension [16], diarrhoea [17] and psychological disorder. The roots of this species has been mainly comprised of antioxidant molecules such as quercetin, 5-desoxyquercetin, quercetin 3-O-galactoside, kaempferol-3-O-rhamnoside and quercetin 3-O-rutinoside [18].

In this study, ultrasonic assisted extraction method was utilized and other extraction-conditions including temperature, time and water content in DES were examined. This green method for extraction of two bioactive components in the *R.ribes* were used. The determination of flavonoid contents (quercetin and kaempferol) in this plant species was carried out utilizing high performance liquid chromatography-photodiode detection.

2. MATERIAL AND METHODS

2.1. Chemicals and Materials

The *R.ribes* flowers were from Elazığ, in eastern Turkey. The samples were dried and stored in the dark to use. Citric acid monohydrate, choline-chloride (99.0%), D(+)-glucose (98.0%), D-(+)-sucrose (99.0%), urea (98.0%), L-(+)-lactic acid (98.0%) and L-proline (98.0%) were supplied by Sigma-Aldrich. All others materials were used analytical grade.

2.2. Instrumentation

The quantify and identify the individual phenolic compounds were determined using HPLC analysis. The separation was carried out on Agilent (1100) UPLC chromatography equipped with a photodiode, an automatic column temperature oven, an autosampler, a quaternary pump and a Phenomenex C18 column (5 μ m, 4.6 x 150 mm.). The mobile phase was water with 0.05% trifluoroacetic acid (A) and acetonitrile (B). The elution performed was set as follow: 0–10 minute, 10% B; 10–20 minute, 30% B; 20–35 minute, 40% B; 35–50 minute, 10% B. The UV spectrum of kaempferol and quercetin were monitored at $\lambda = 280$ nm. The constant flow rate was 1.0 mL/min. The standards and samples were filtered utilizing Millipore 0.20 μ m filter. The calibration curves were depicted using different concentrations (10-50 ppm) of all compounds by dissolving them in solvent.

2.3. Ultrasound-assisted extraction (UAE)

UAE was performed using an ultrasonic equipment (Hielscher Ultrasonics, Teltow, Germany). The DES-based ultrasonic-assisted extraction process was performed as follows: Temperature was ranged from 30 to 65 °C, water content used in DES was between 5 to 50 %, liquid-solid ratio was ranged from 5 to 40 mLg⁻¹, extraction was

performed 30-65 minutes and ultrasonic power was applied as 100 W and 30 kHz.

2.4. Synthesis of deep eutectic solvents

In the present study, 8 kinds of eutectic mixtures were prepared according to known studies [3,19]. Eight different DESs included pure choline chloride-glycerol (ChGly), pure choline chloride-lactic acid (ChLac), pure choline chloride-D(+) glucose (ChGlu), pure choline chloride-urea (ChUr), pure choline chloride-citric acid (ChCA), pure choline chloride-D(+) glucose-citric acid (ChGluCA), pure choline chloride-urea-glycerol (ChUrGly), L-proline-lactic acid (ProLac).

Component mixture were prepared in deionized water and stirred at 60 °C till a transparent liquid obtained. After this time, natural deep eutectic solvents (NADESs) components were shaken again by a vortex for 1 min, and then they were kept in a desiccator [20]. Abbreviations, appearances and molar ratios of the NADESs were displayed in Table 1. Ratios selected as 1:1 as described by Sylwia and Jakup, 2018 [7].

TABLE 1
LIST OF TESTED DESs FOR EXTRACTION

Type	Name	Combination	Molar ratio
DES-1	ChLac	Choline chloride:lactic acid	1:1
DES-2	ChGly	Choline chloride:glycerol	1:1
DES-3	ChGlu	Choline chloride:glucose	1:1
DES-4	ChUr	Choline chloride:urea	1:1
DES-5	ChCA	Choline chloride: citric acid	1:1
DES-6	ChCAGlu	Choline chloride: citric acid: glucose	1:1:1
DES-7	ChUrGly	Choline chloride: urea: glycerol	1:1:1
DES-8	ProLac	L-proline:lactic acid	1:1

3. RESULTS AND DISCUSSION

3.1. Extraction effect of different DESs

In this research, we use L-Cholineproline and choline chloride as the various types of H-bond donors and HBAs to prepare green solvents. Then, the extraction efficiency of eight analytes perform were compared. Based on comparison among all NADESs, ChCl-Lac based DES provided highest solubility (510 mg/mL).

The yields of polar and non-polar analytes continued as follows ChLac > ChGly > ChUrGly \approx MeOH > ChUr > ProLac > ChCAGlu > ChGlu > ChCA.

ChLac (359.8 \pm 0.02 mg/mL) and ChGly (340.1 \pm 0.01 mg/mL) showed the best extraction efficiency quercetin due to good ability of quercetin to form hydrogen bonds with DES. The solubility quercetin in methanol was 362.9 \pm 0.01 mg/mL, 196.7 \pm 0.01 mg/mL in ethanol. ProLac, ChCAGlu and ChCA showed lower capacity to dissolve target compounds.

These results are accordance with similar to previous reports [21,22]. The special structure of DES is critical for extracting analytes and is based on physicochemical interactions, other factors such as intrinsic properties and stability of the analytes should also be considered. However, there is a large number of hydrogen bonds allowing to be extraction efficiency increased which cause a positive effect the interactions between active compounds and NADES [20]. Figure 1 show that the extraction effect of different DESs solvents.

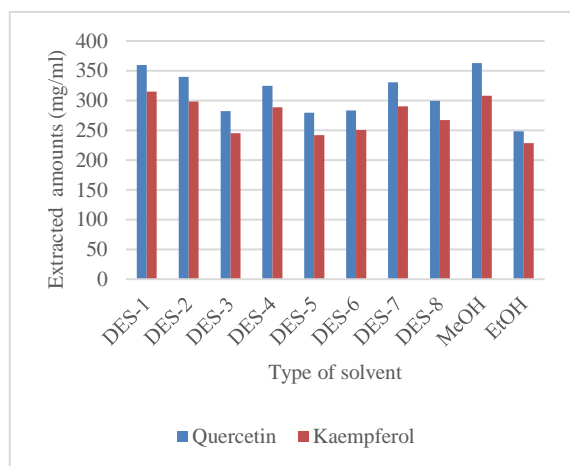


Figure 1. The extraction effect of different DESs solvents

3.2. Effect of extraction time

Time is an important operational parameter in the completeness of the extraction yield. The sonication time has close related with extraction performed. The effect of extraction time between 15 and 60 min on the target compounds was examined. Figure 2 shows that the bioactive components completely extracted before up to 30 min. and thus, this extraction time was optimum. When the sonication time was increased with above 30 min, extraction performed was decreased. A long extraction time potentially causes solvent polarity to change and also flavonoid contents interaction with ChCl-based DES to form polymer chain structure [23,24].

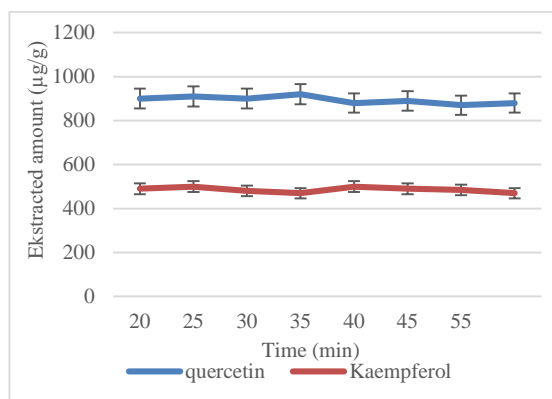


Figure 2. The extraction effect of sonication time

3.3. Effect of the extraction temperature

Temperature also affects extraction. The extraction temperature was examined between 30°C and 65 °C [25]. When the working temperature was higher than 40 °C, the yields were decrease in the amount of all extracted phenol. This is likely because the enhance the solvent viscosity, decrease the mass transfer, which affect the stabilization of the extraction capacity [26].

Although the ultrasonic power performed was achieved. when temperature was increased from 56 to 65 °C. The targeted compounds significantly decomposed, as shown in Figure 3. These results showed a close relationship between extraction efficiency and extraction temperature.

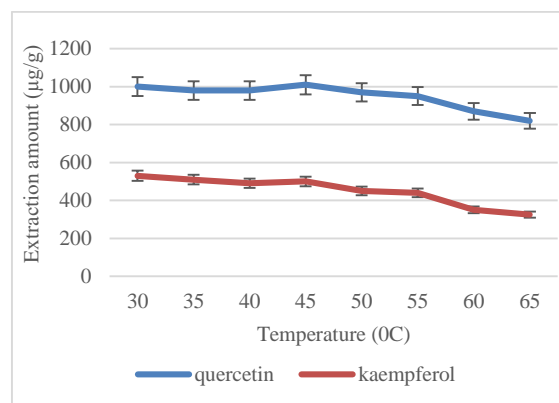


Figure 3. The extraction effect of temperature

3.4. Effect of water content

The effect of water amount in NADES on the extractability of target compounds was also examined. The addition of water in extraction system can impact on the extraction efficiency [16]. The addition of different percentage water could eminently decrease the viscosity and could provide to a positive effect on polar components. With dilutions ranging between %5 and 50% of water content in NADES the extractability of target bioactive flavonoid was examined. As shown in figure 4, the extraction efficiencies of phenolic compounds reduced when the water content to more than 30% increased which cause a negatively impacts interactions between DES and analytes. The excessive high water content would result in the loss of occurring, H-bonds and as a result, interaction between the molecules gradually disappear. Results showed that, a concentration of 30% (v/v) water in NADES could contributed to perform better effects extraction system.

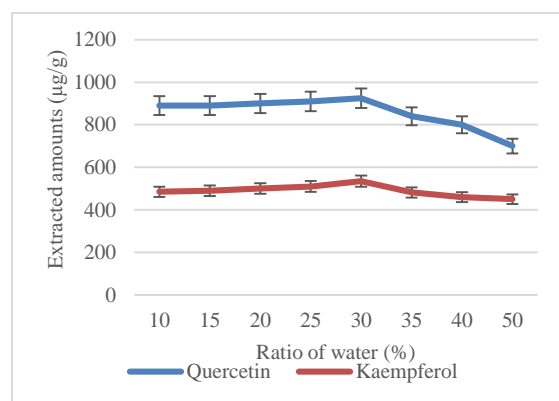


Figure 4. The extraction effect of water content

4. CONCLUSION

In the experiment, deep eutectic solvents (DESs) was utilized as more effective solvents for the dissolution of compounds, which could be associated with their hydrogen bonding interactions between the medium and components.

The biorenewable eutectic mixtures was established for extraction of quercetin and kaempferol from Rhubarb (*Rheum ribes L.*) roots in high yields. Overall, The parameters of different extraction conditions (i.e solid/liquid ratio, solvent concentration, temperature and time) were provide higher performance extraction for phenolic compounds.

The qualitative identification of individual active components were confirmed by high pressure liquid

chromatography-photodiode. UPLC results showed that better compound separation was observed compared to HPLC methods. Quercetin and kaempferol were the most abundant phenolic acids identified in extract.

The deep eutectic solvents as new green solvents showed a high extraction capacity and efficiently extract bioactive compounds of diverse polarity.

5. ACKNOWLEDGEMENT

This study was carried out in the Food Engineering Department of Istanbul Technical University, Food Processing Laboratories.

REFERENCES

- [1] A.P.Abbott, G. Capper, D.L. Davies, R.K. Rasheed, V. Tambyrajah, "Novel solvent properties of choline chloride/urea mixtures", *Chem. Commun.*, pp. 70–71, 2003.
- [2] H. Wang, Y. Jia, X. Wang, "Physical–chemical properties of nickel analogs ionic liquid based on choline chloride", *J. Therm. Anal. Cal.*, vol. 115, pp. 1779–1785, 2014.
- [3] Y. Dai, J. Van Spronsen, G.J. Witkamp, R. Verpoorte, Y.H. Choi, "Natural deep eutectic solvents as new potential media for green technology", *Anal. Chim. Acta*, vol. 766, pp. 61–68, 2013a.
- [4] Y. Dai, G.J. Witkamp, R. Verpoorte, Y.H. Choi, "Natural deep eutectic solvents as new extraction media for phenolic metabolites in safflower", *Anal. Chem.*, vol. 85(13), pp. 6272–6278, 2013b.
- [5] A.P.Abbott, G. Capper, D.L. Davies, R.K. Rasheed, V. Tambyrajah, "Novel solvent properties of choline chloride/urea mixtures", *Chem. Commun.*, pp. 70–71, 2003.
- [6] R.P. Xin, S.J. Qi, C.X. Zeng, F.I. Khan, B. Yang, Y.H. Wang, "A functional natural deep eutectic solvent based on trehalose: structural and physicochemical properties", *Food Chem.*, vol. 217, pp. 560–567, 2017.
- [7] B. Sylwia, A. Jakup, "Development of a method based on natural deep eutectic solvents for extraction of flavonoids from food samples", *Food Anal. Methods*, vol. 11, pp. 1330–1344, 2018i
- [8] X. Zhang, G.Teng, J. Tang, "Deep eutectic solvents aqueous two-phase system based ultrasonically assisted extraction of ursolic acid (UA) from *Cynomorium songaricum* Rupr.", *Chemical Engineering Communications.*, vol. 206, pp. 419–431, 2018-
- [9] P. Xiao, D. Ming-Hui, Y. Xiao-Hui, Z. Chun-Jian, Z. Yuan-Gang, F. Yu-Jie, "Green extraction of five target phenolic acids from *Lonicerae japonicae* Flos with deep eutectic solvent", *Sep. Pur. Tech.*, vol. 157, pp. 249–257, 2016.
- [10] X. Peng, M.H. Duan, Zhang Y.H, C.J. Zhao, Y.G Zu, Y.J.Fu, "Green extraction of five target phenolic acids from *Lonicerae japonicae* Flos with deep eutectic solvent", vol. 157, pp. 249–257, 2016, 157.
- [11] H.E. Park, B.Tang, K.H. Row, "Application of deep eutectic solvents a additives in ultrasonic extraction of two phenolic acids from *Herba artemisiae scopariae*", *Anal. Lett.*, vol. 47 (9), pp.1476–1484, 2014.
- [12] L. Duan, L.L. Dou, L. Guo, P. Li, E.H. Liu, "Comprehensive evaluation of deep eutectic solvent in extraction of bioactive natural products", *ACS Sustainable Chem. Eng.*, vol. 4(4), pp. 2405–2411, 2016.
- [13] M.W. Nam, J. Zhao, M.S. Lee, J.H. Jeong J. Lee, "Enhanced extraction of bioactive natural products using tailor-made deep eutectic solvent: application to flavonoid extraction from *Flos sophorae*", *Green Chem.*, vol. 17 (3), pp. 1718–1727, 2015.
- [14] K. Yoshiki, N. Gen-Ichiro, N. Itsuo, Y. Takashi, "Galloyl and hydroxy cinnamoyl glucoses from rhubarb", *Phytochemistry*, vol. 27(5), pp. 1473–1477, 1988.
- [15] A. Shokravi, K. Agha Nasiri, "Synthesis of 1,2,3,4,5,6,7,8-Octahydro-9-ethoxy-10-hydroxy-1-anthracenone (OEHA)", *Iranian J. Chem. and Chem. Eng.*, vol.16, pp. 10–15, 1997.
- [16] B.E. Abu-Irmaileh, F.U. Afifi, "Herbal medicine in Jordan with special emphasis on commonly used herbs", *J.Ethnopharmacology*, vol. 89, pp. 193–197, 2003.
- [17] M. Tabata, E. Sezik, G. Honda, E. Yesilada, H. Fuki, K. Goto, "Traditional medicine in Turkey III. Folk Medicine in East Anatolica, Van and Bitlis provinces", *Int. J. Pharmacognosy*, vol. pp. 32,3–12, 1994.
- [18] F. Tosun, C. Akyuz-Kızılay, "Anthraquinones and flavonoids from *Rheum ribes*", *J. Faculty of Pharmacy, Ankara*, vol. 32, pp. 31–35, 2003.
- [19] S. Bajkacz, J. Adamek, "Evaluation of new natural deep eutectic solvents for the extraction of isoflavones from soy products", *Talanta*, vol. 168, pp. 329–335, 2017.
- [20] M. Zhaorui, Z. Jing, H.D. Hongxia, G. Yuanyuan, Z. Longshan, "Green and efficient extraction of four bioactive flavonoids from *PollenTyphae* by ultrasound-assisted deep eutectic solvents extraction", *J. Pharmaceutical and Biomedical Analysis*, vol. 161, pp. 246–253, 2018.
- [21] E.M. Sánchez-Salcedo, P. Mena, C. García-Viguera, F. Hernández, J.J. Martínez, "(Poly)phenolic compounds and antioxidant activity of white (*Morus alba*) and black (*Morus nigra*) mulberry leaves: their potential for new products rich in phytochemicals", *J. Funct. Foods*, vol.18, pp.1039–1046, 2015.
- [22] Y. Zou, S. Liao, W. Shen, F. Liu, C. Tang, C.Y.O. Chen, Y. Sun, "Phenolics and antioxidant activity of mulberry leaves depend on cultivar and harvest month in southern China", *Int. J. Mol. Sci.*, vol. 13, pp. 16544–16553, 2012.
- [23] Z. Pengfei, W. Xuping, L. Pengzhan, H. Jing, W. Chen, P. Mushui, "Enhanced phenolic compounds extraction from *Morus alba* L. leaves by deep eutectic solvents combined with ultrasonic-assisted extraction", *Industrial Crops & Products*, vol. 120, pp. 47–154, 2018.
- [24] M. Wang, J. Wang, Y. Zhou, M. Zhang, Q. Xia, W. Bi, D.D.Y. Chen, "Ecofriendly mechanochemical extraction of bioactive compounds from plants with deep eutectic solvents", *ACS Sustain. Chem. Eng.*, vol. 5, pp. 6297–6303, 2017.
- [25] L. Duan, L.L. Dou, L. Guo, P. Li, E.H. Liu, "Comprehensive evaluation of deep eutectic solvents in extraction of bioactive natural products", *ACS Sustain. Chem. Eng.*, vol. 4, pp. 2405–2411, 2016.
- [26] Y. Dai, R. Verpoorte, Y.H. Choi, "Natural deep eutectic solvents providing enhanced stability of natural colorants from safflower (*Carthamus tinctorius*)", *Food Chem.*, vol. 159, pp.116–121, 2014.

BIOGRAPHIES

Fatih Bildik obtained his BSc degree in Chemistry Department from Istanbul University (ITU) in 2002. He received the MSc., and PhD. diploma in Chemistry Department from Istanbul Technical University (ITU) in 2006 and 2016 respectively, and PhD degrees in Graduate Faculty of Science and Letters, Department of Chemistry of the same university in 2016.

His research interests are polymer technologies, especially the synthesis and electrical properties of liquid crystal polymer. He has recently focused on food chemistry. In 2007 he joined the Engineering Faculty, İstanbul Technical University as a research assistant. He is active in teaching and research in instrumental systems.



Submodule Based MPPT with Synchronous Buck Converter Under Dynamic Partial Shading Conditions

Mustafa Engin Başoğlu^{1*}

^{1*}Gümüşhane University, Electrical and Electronics Engineering Department, 29100, Gümüşhane, Turkey. (e-mail: menginbasoglu@gumushane.edu.tr).

ARTICLE INFO

Received: Apr., 18. 2021

Revised: Dec., 12. 2021

Accepted: Dec, 27. 2021

Keywords:

Photovoltaic

MPPT

Submodule

Synchronous buck

Perturb & Observe

Corresponding author: *M. E. Başoğlu*

ISSN: 2536-5010 / e-ISSN: 2536-5134

DOI: <https://doi.org/10.36222/ejt.919346>

ABSTRACT

In order to obtain more power from photovoltaic (PV) modules under mismatching operating conditions, the submodule-based MPPT technique is an important solution. In this technique, since the power-voltage (P-V) curve of a submodule cannot be multi-peaked, the maximum power point (MPP) tracking (MPPT) is easily achieved through a DC-DC converter connected to each submodule. Since the P-V curve cannot be in a multi-peaked form, the maximum power can be obtained with a simple MPPT algorithm. For this reason, perturb & observe (P&O) algorithm can be chosen. In this study, the behaviour of a submodule-based MPPT with synchronous buck converter (SBC) is investigated for dynamic shading conditions. In addition, submodule-based MPPT and module-based MPPT technique were compared and the comparison was confirmed by simulation studies that submodule-based MPPT performed better. In this context, simulation studies were carried out for different shading conditions. According to the simulation results, the submodule-based MPPT approach achieves greater efficiencies to the module-based MPPT. In some simulations, when the module-based MPPT technique is used, the operation at the local MPP has been realized. In such cases, more advanced algorithms are needed. However, a simple algorithm is sufficient in submodule-based MPPT. The only disadvantage of this MPPT is the high hardware cost. However, the increase in efficiency obtained is at a level that can easily tolerate this cost.

1. INTRODUCTION

The desire to utilize renewable energy sources is one of the biggest motivations of the 21st century. Energy sources such as wind, water flow, rain, bio fuel, geothermal wave, tide offered by nature are based on the great energy power promised by the sun. Due to its potential, the sun has the capacity to meet the energy needs of the whole world. Despite this, the percentage of utilization from solar energy, in other words, the share of electricity generation from solar energy is at the level of 3% as of the end of 2019 [1].

Electricity generation from the sun is carried out by PV cells. Since PV cells have p-n junction structure, the current equations of PV cells are exponential. Consequently, the P-V and current-voltage (I-V) characteristics are in nonlinear form. Since PV cells are semiconductor materials with a voltage of approximately 0.6V and producing a maximum of 5W power, their applications are very limited. For this reason, cells are connected in series to form submodules, submodules connected in series to form PV modules. On the other hand, PV cells can generate maximum power for only one current and voltage value. For this reason, the current and voltage values of the PV cells are continuously controlled, and the maximum possible power is generated.

Commercial PV modules are generally equipped with at least three bypass diodes. In order to avoid hot-spot problems in PV modules, these diodes are connected in reverse parallel to the submodules in the junction box in order to bypass the shadowed submodule and increase the possible maximum power to a certain extent [2].

Synchronous buck is a converter used in low voltage applications. In [3], zero voltage transition SBC has been investigated for small voltages. Switching losses are considerably reduced and efficiency increased compared to conventional buck converter. Performance of a SBC with MPPT controller has been evaluated in [4]. It is shown that an increase of around 12-13% was obtained in the output voltage and output current of the SBC. Submodule integrated MPPT has been realized in [5]. SBC with high efficiency and high energy density has been realized. It has been shown that with the sub-module-based approach, 20% more energy is obtained compared to the module-based MPPT. In another study [6], a SBC was compared to the classical buck converter and the isolated buck converter. The SBC is recommended for UPS application [7]. It was determined that conduction losses decreased and efficiency increased by at least 5% thanks to the MOSFET element used instead of diode in the SBC. A SBC is used in a study [8] where the advantages of distributed

MPPT are presented. In this study, module level MPPT is proposed in systems where large power PV modules are used, and string level MPPT is proposed in systems using small power PV modules. Thanks to high frequency SBCs, the size has been reduced and submodule-based MPPT has been realized. In this way, a power increase of 27.55% was achieved. In another study [9], a distributed MPPT system using a common LC filter SBC whose outputs are serially connected is proposed. The optimum flow control-tracking algorithm has been implemented at the submodule level and small-scale incompatibility problems have been resolved. The performance of the SBC in a standalone system has been experimentally evaluated [10]. The efficiency change of the converter operated at different frequencies has been examined and it has been observed that the frequency has a serious effect on the efficiency. In [11], a new robust observer nonlinear control is proposed.

SBC is a circuit used for MPPT purposes in PV systems in order to obtain high efficiency in low voltage applications. For this purpose, in this study, the performance of the SBC in submodule and module-based MPPT applications has been investigated since the voltage level is generally small in the submodule-based MPPT approach. The following details are mentioned in the rest of the study. In the second section, the mathematical model and equivalent circuit of the classical buck converter are given and the working principle is explained. In addition, the advantages obtained with the use of a SBC are mentioned. In the following section, the MPPT algorithm used in the study is briefly explained. Then, the results of the simulation studies made to compare module-based MPPT and submodule-based MPPT techniques are presented in the fourth section. In addition, comparative analyzes are made in this section. Finally, the results of the study are mentioned.

2. BUCK CONVERTER UNDER STEADY STATE CONDITIONS

Buck converter circuit is used in many areas such as LED drivers, telemetry systems, automotive industry, smart phones, battery charging, solar charging and motor control, which may require lower voltage than input voltage. As with other DC-DC converters, buck converters consist of at least one active switch, a diode, an inductance and a capacitor. Buck converters work on the principle of energy transfer of inductance. The circuit diagram of the buck converter is given in Figure 1. As seen in Figure 2, if a second active switch is used instead of a diode in the buck converter, a synchronous converter is obtained. In this case, the synchronous buck will have two active switches in the converter.

The working principle of buck converters depends on the principle of energy transfer in the inductance element. First, the energy stored in the inductance at a time interval of the period is transferred to the output in the remaining time of the period. Value of the inductance current can be continuous or discontinuous. If continuous mode of operation is taken as reference, because the inductance current is constantly changing, voltage is induced in the inductance according to the induction principle.

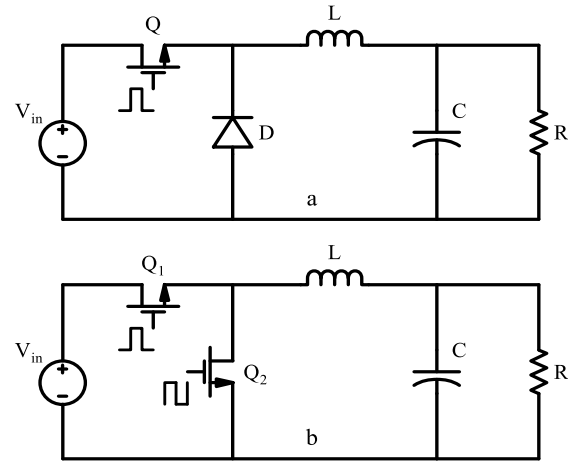


Figure 1. The circuit diagram of a buck converter a) classical b) Synchronous

2.1. Synchronous Buck Converter

In the SBC, the Q_1 and Q_2 switches are turned on sequentially. PWM applied to Q_1 is applied to Q_2 by passing through the not logic gate. The important thing here is to ensure that the Q_1 and Q_2 switches are not turned on at the same time. If Q_1 and Q_2 are turned on at the same time, the input voltage source will be short-circuited. Therefore, a dead time is left for the Q_2 switch to not transmit before the Q_1 switch is turned off. When Q_1 is turned on, there is a voltage equal to difference of input voltage and output voltage on the inductance element as presented in Fig. 2. Since this voltage is greater than zero, the current and energy of the inductance increase between $t=0$ and $t=t_{on}$. The time of t_{on} is the conduction time of Q_1 switch. Voltage and current change on inductance are defined as in Eq. (1) and Eq. (2), respectively.

$$v_L = V_{in} - V_o \quad (1)$$

$$v_L = L \frac{di_L}{dt} = L \frac{\Delta i_L}{\Delta t} \rightarrow \Delta i_L = \frac{(V_{in} - V_o)DT_P}{L} \quad (2)$$

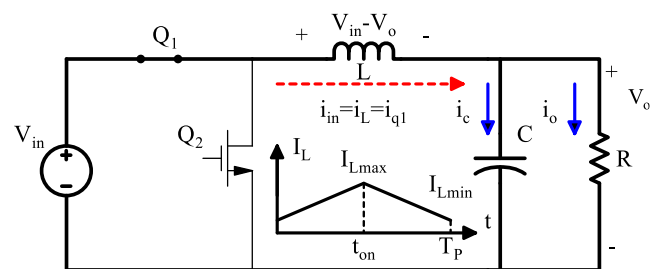


Figure 2. Equivalent circuit when Q_1 turned on (Q_2 turned off)

V_L is the voltage of inductance, V_{in} is the input voltage, V_o is the output voltage of the SBC, D is the duty ratio, f is the switching frequency, L is the value of inductance and T_p is the period of the PWM in Eq. (1) and Eq. (2). When Q_1 is turned off, Q_2 switches on after a very small dead time. When Q_2 is turned on, as it can be understood from Figure 3, the connection between the source and the output is disconnected. During this period, there is a voltage of $-V_o$ on the inductance and the energy of the inductance decreases between $t=t_{on}$ and $t=T_p$. At the end of a period, the principle of transferring energy on inductance has been realized. In steady state, the net energy on the inductance is expected to be zero. The voltage, current and energy changes on the inductance are defined as given in Eq. (3), Eq. (4) and Eq. (5), respectively.

$$v_L = -V_o \quad (3)$$

$$v_L = L \frac{di_L}{dt} = L \frac{\Delta i_L}{\Delta t} \rightarrow \Delta i_L = \frac{-V_o D}{Lf} \quad (4)$$

$$W_{L,on} = \frac{1}{2} L (I_{L,max}^2 - I_{L,min}^2) = |W_{L,off}| \quad (5)$$

$W_{L,on}$ and $W_{L,off}$ are the energy values of the inductance at certain times of the period. $I_{L,min}$ and $I_{L,max}$ are the minimum and maximum values of the inductance current, respectively.

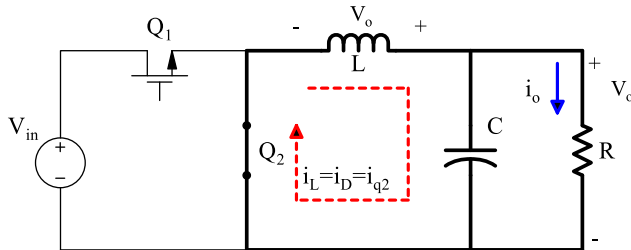


Figure 3. Equivalent circuit when Q_2 turned on (Q_1 turned off)

2.2. Design Procedure

In this section, the design procedure for the design of the SBC power stage is given. Duty ratio of a buck converter is calculated as in Eq. (6).

$$D = \frac{V_o + V_{low}}{V_{in} + V_{high}} \quad (6)$$

In Eq. (6), V_{low} and V_{high} low side and high side are MOSFET voltage drops, respectively. Inductance is selected for continuous current mode. For this purpose, the current fluctuation percentage can be chosen between 15% and 30%. In this framework, inductance is calculated as follows.

$$L = \frac{(V_{in} - V_{high} - V_o)DT_P}{\Delta I_L} \quad (7)$$

The other element of the LC filter is the capacitor. Capacitor value calculation is defined in Eq. (8).

$$C = \frac{\Delta I_L}{8f\Delta V_o} \quad (8)$$

3. SIMULATION STUDIES

Many approaches, methods or techniques have been proposed for MPPT in PV systems [12-17]. Although some hardware-based studies are carried out, especially in incompatible working conditions such as partial shading, the number of algorithm-based studies is quite high. In algorithm-based studies, the need for sensors, microcontroller power, heavy mathematical operations required by the running algorithm, etc. stand out as the problems encountered. In this study, it has been focused on enhancing MPPT performance in hardware and for this purpose, SBCs have been used and

some determinations have been made for dynamic and rapidly changing shading conditions with a simple algorithm. The performances of module-based MPPT and submodule-based MPPT were compared for two different shading situations. The technical features of the PV module used are given in Table I, and main properties of the SBC are given in Table II.

TABLE I
MAIN SPECIFICATIONS OF THE PV MODULE [18]

Bosch PV Module c-Si M 48	Value
Short circuit current	8.5A
Open circuit voltage	28.9V
Maximum power voltage	23.4V
Maximum power current	7.9A
Maximum power	180W
Bypass diodes	3
Submodule - Bosch	Value
Maximum power voltage	7.8V
Maximum power current	7.9A
Maximum power	60W

TABLE II
MAIN SPECIFICATIONS OF THE SBC

Features	Value
Input / output capacitor	630 μ F / 63 μ F μ F
Inductance	0.5mH
Switching frequency	100kHz
MOSFET on resistance (R_{dson})	0.025 Ω
Initial value of duty ratio (D_{first})	0.4
Load resistance (R_{load})	1 Ω

Simulink model of submodule-based MPPT is given in Figure 4. As can be seen from this model, each submodule is connected to the SBC and three different MPPT operations are performed. An example of dynamic partial shading is given in Figure 5. As can be seen from this figure, there are five different irradiation conditions. PV module consists of three submodules and these submodules consist of 32 serial cells (one square = two cells). These submodules are defined as SPV-1, SPV-2 and SPV-3. A bypass diode is not required for submodule MPPT. In the first simulation study, the irradiation values applied to the submodules change in 0.1 seconds periods. This means that the radiation on the PV module changes dynamically. The change of the irradiation on the submodules within a certain period means the change of the MPP.

As can be seen in Fig. 5, an example of a PV module is exposed to five different irradiation profiles at 0.1 seconds intervals. In this example, the irradiation changes of each submodule are given in Irradiation SPV-1, Irradiation SPV-2 and Irradiation SPV-3, respectively in the Figure 6. In the submodule-based MPPT approach, there is a single MPP P-V curve for each submodule. P-V curves of the submodules are given in Figure 7 for five different radiation conditions. In this way, MPPT operation can be achieved with a simple Hill Climbing (HC) algorithm. The results of the submodule-based MPPT simulation for the dynamic shading condition are given in Figure 6. As can be seen from the results, the irradiation showed a rapid change in 0.1 seconds intervals. However, since there is only one MPP in the P-V curve of each submodule, the submodules operate at the MPP after a while. In this study, although different tracking efficiency and convergence times were obtained for submodules, global MPPT (GMPPT) was provided at steady state. The efficiency values obtained in 0.5 seconds are given in Table III.

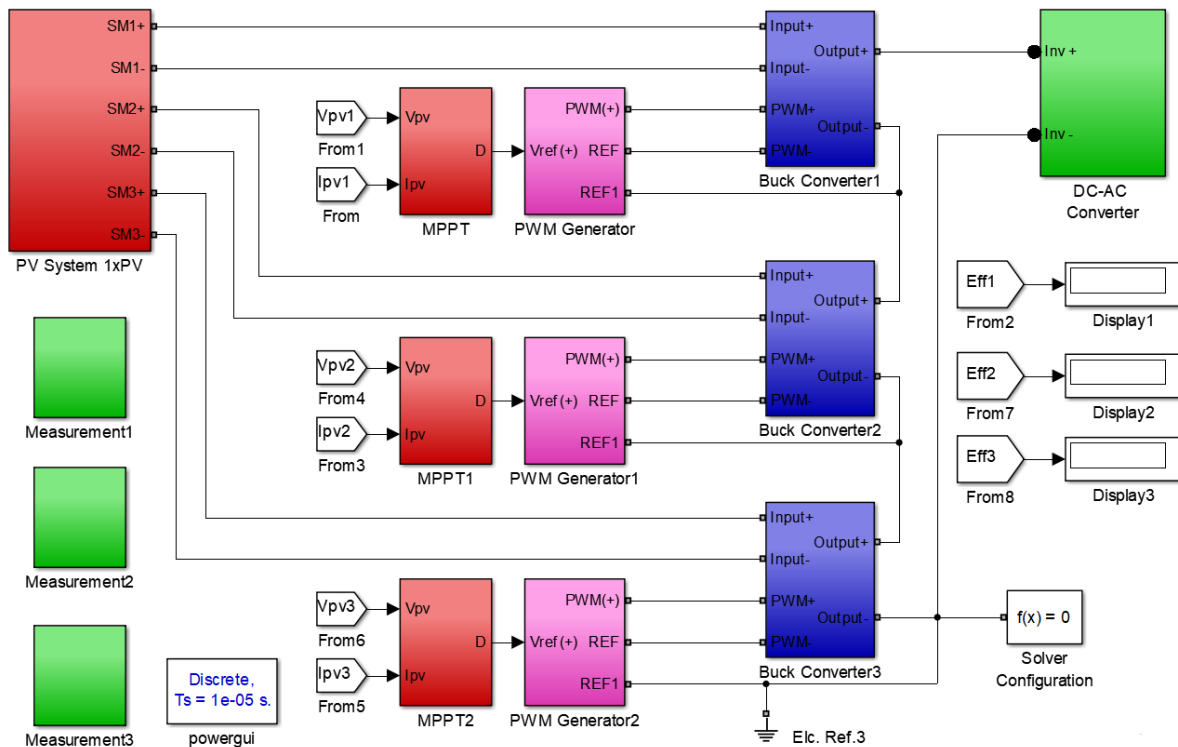


Figure 4. Simulink model of the submodule MPPT approach

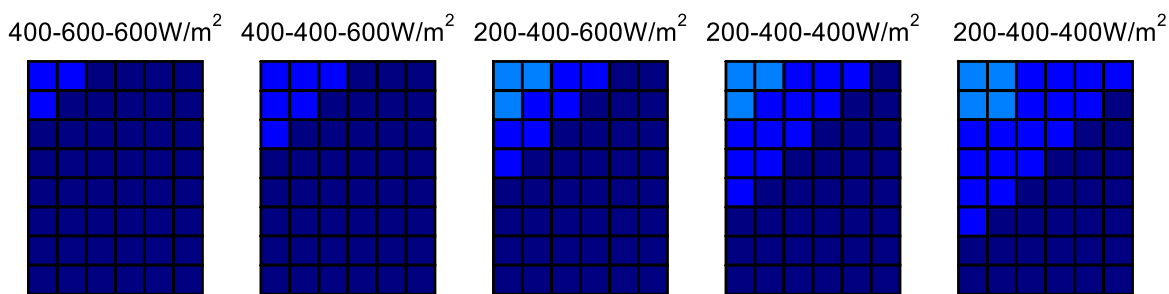


Figure 5. Dynamic partial shading scenario-1

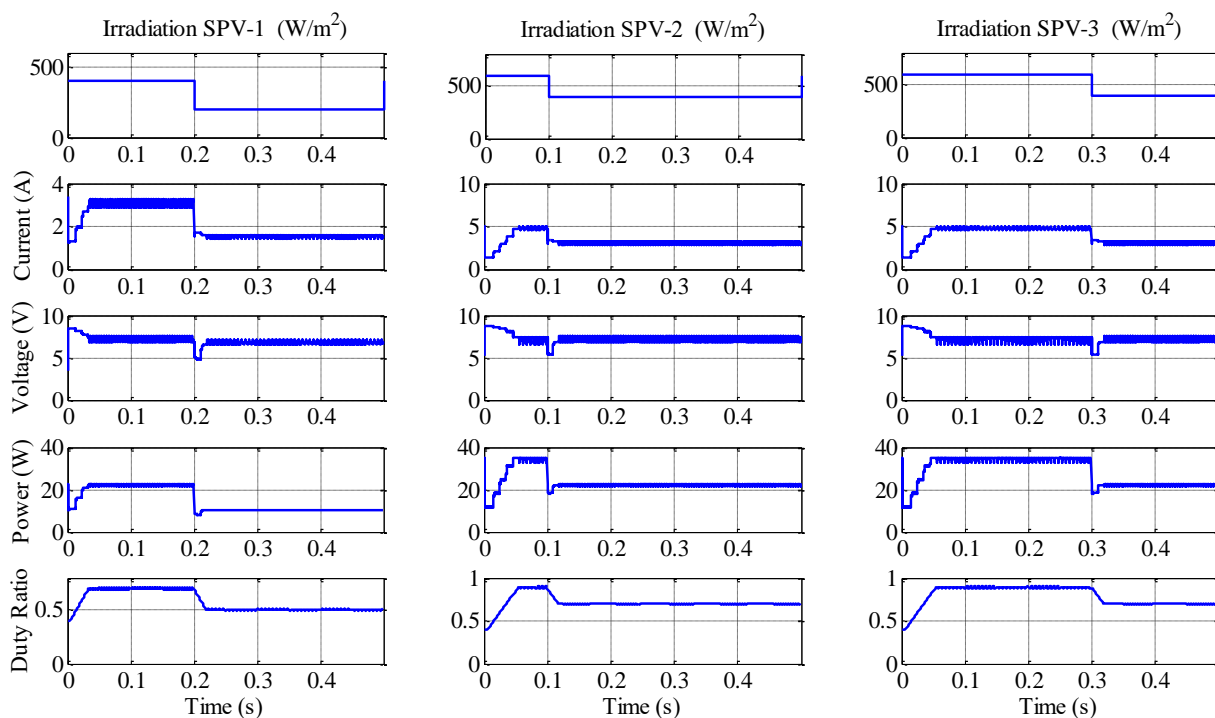


Figure 6. Simulation results of submodule-based MPPT for PSC-1

TABLE III
SIMULATION RESULTS FOR DYNAMIC SHADING SCENARIO-1

Irradiation Profile (W/m ²)			Power (W)			Tracking Efficiency Submodule-based MPPT		
SPV-1	SPV-2	SPV-3	P _{max-SPV1}	P _{max-SPV2}	P _{max-SPV3}	SPV-1	SPV-2	SPV-3
400	600	600	22.38	34.75	34.75	96.16	94.72	93.90
400	400	600	22.38	22.38	34.75			
200	400	600	10.53	22.38	34.75			
200	400	400	10.53	22.38	22.38			
200	400	400	10.53	22.38	22.38			
Irradiation Profile (W/m ²)			Power (W)			Tracking Efficiency (%)94.72		
SPV-1	SPV-2	SPV-3	P _{max}			Module-based MPPT		
400	600	600	76.51			96.79		
400	400	600	71.34					
200	400	600	48.92					
200	400	400	44.53					
200	400	400	44.53					

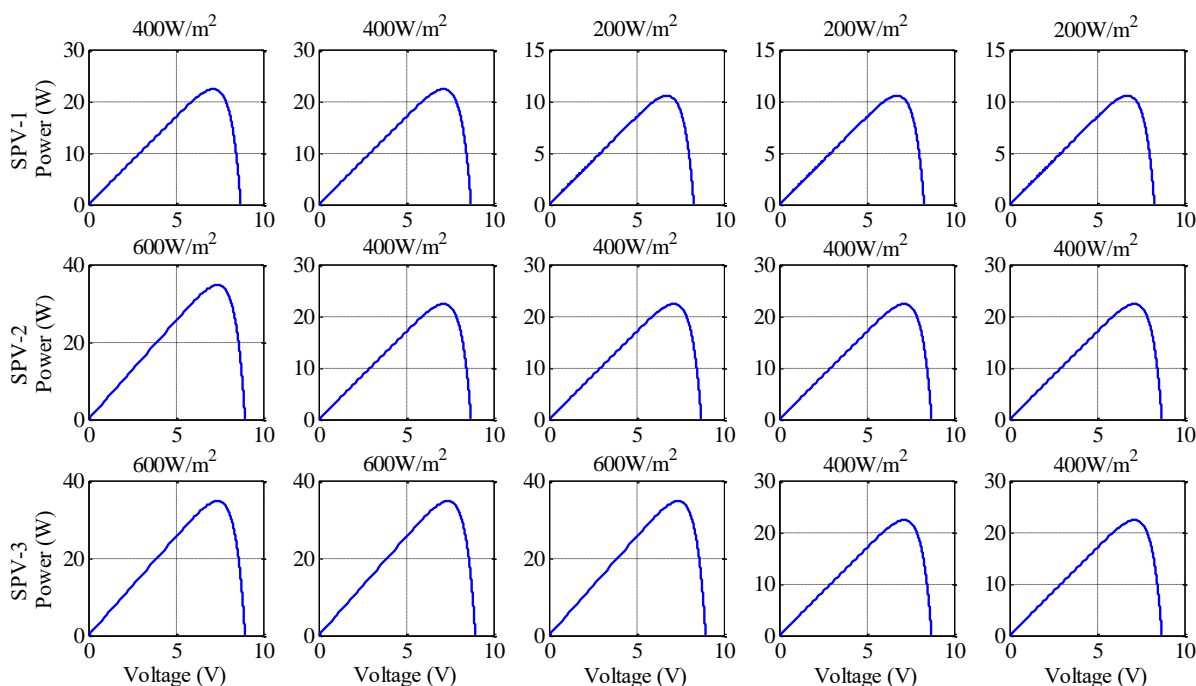


Figure 7. Dynamic P-V curves of the submodules for PSC-1

If module-based MPPT is applied with a typical HC algorithm for the same dynamic shading situation, it will be observed that the success of GMPPT depends heavily on the conditions at the starting point of the tracking. Because in a HC based MPPT, the algorithm is stuck at the first hill in the P-V curve. However, it is not known whether this point is global maximum power point (GMPP). In other words, GMPPT occurs depending on the initial value of the PWM applied to the MOSFET in the SBC. For dynamic shading scenario-1, module-based MPPT enabled operation at GMPP

as presented in Figure 8. Five different irradiation conditions indicated in Table III are applied at 0.1 seconds intervals and there are five different P-V curves for these five cases. These curves given in Figure 8 are different when compared to the P-V curves obtained for the submodule-based MPPT. In the module-based MPPT, diodes connected to submodules in reverse parallel have created multiple peaks in the P-V curves. Therefore, global maximum power values are smaller than submodule-based MPPT. Simulation results for module-based MPPT are presented in Figure 9.

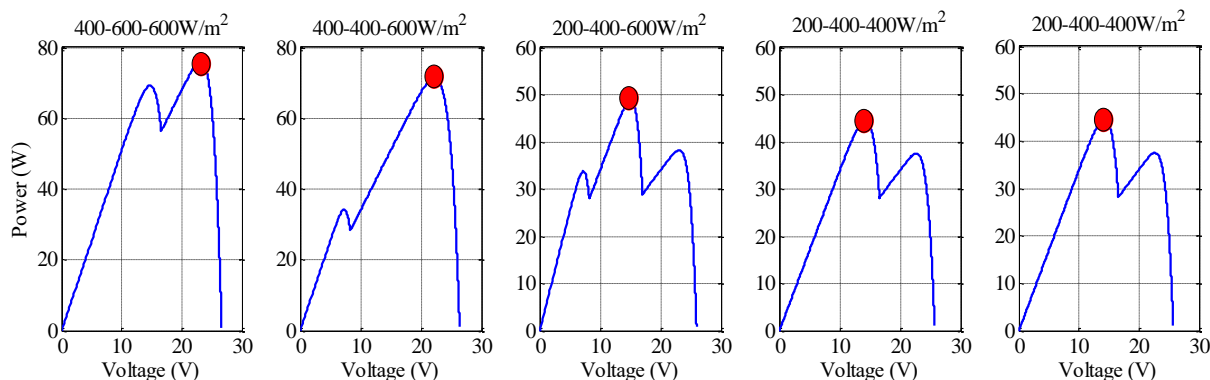


Figure 8. P-V curves of the PV module (when module-based MPPT is applied)

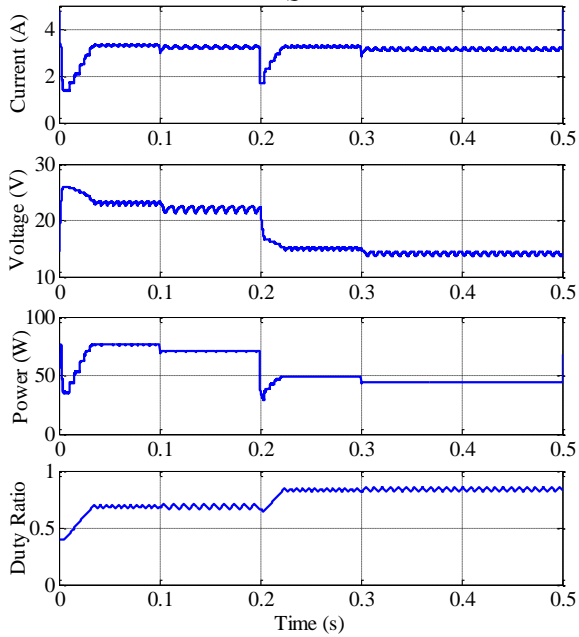


Figure 8. Simulation results of module based MPPT for PSC-1

Submodule-based MPPT and module-based MPPT simulations are performed for dynamic partial shading scenario-2. The panel view for this situation is given in Figure. 10. According to the simulation results, when there is a radiation change, it is seen that the P&O algorithm reaches its maximum power point in a short time. The power values that the submodules operate can be seen in Figure 11, and the maximum power values that the submodules can produce in

the MPP can be seen from the P-V curves in Figure 12. Tracking efficiencies for submodules are 94.48%, 93.12% and 91.41% in 0.5 seconds. Table IV lists the power values and tracking efficiencies for the submodules at the MPP.

MPPT operation performed at module level is expressed as GMPPT. Because in the P-V curve of a partially shaded PV module, the number of MPPs changes depending on the dynamic shading condition and the amount of bypass diode. In this case, the MPPT process becomes difficult. In the module level MPPT simulation, it is understood from the P-V curves given in Figure 13 that GMPPT cannot be performed for some shading conditions. From this figure, it can be concluded that the PV module sometimes works in local MPP and sometimes in GMPP. Tracking efficiency in PV module operating in local MPP for a certain period was calculated as 82.87%. For the same dynamic shading condition, the tracking efficiency in the submodule-based MPPT approach is given in Table IV, where it ranges between 91.41% and 94.48%. These efficiency values are given for 0.5 seconds, and it is possible to predict that the efficiency will reach values above 99% in submodule-based MPPT after a while. Because the PV module performs continuously in GMPP. On the other hand, in module-level MPPT, the P&O algorithm cannot prevent operation in local MPP. For this reason, achieving an efficiency level of 90% in module level MPPT is not possible with the current algorithm choice. Simulation results of module level MPPT are given in Figure 13. When the GMPP points are examined in the P-V curves given in Figure 12, it is seen that the PV module performs at local MPP when the irradiation is 200-200-400W/m² and 600-600-200W/m².

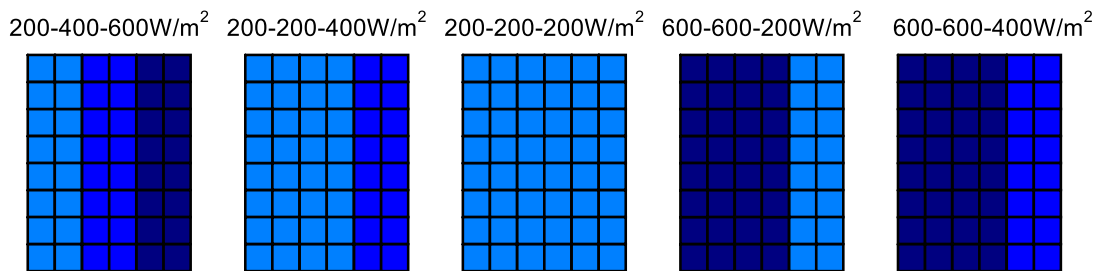


Figure 9. Dynamic partial shading scenario-2

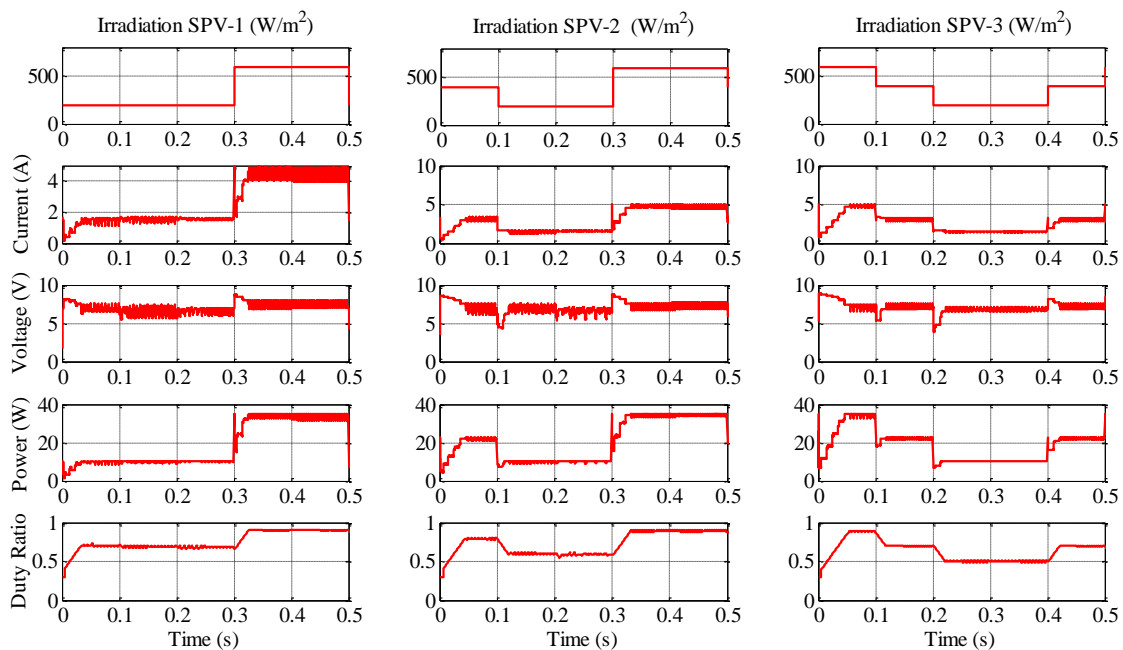


Figure 10. Simulation results of submodule-based MPPT for PSC-2

TABLE IV
SIMULATION RESULTS FOR DYNAMIC SHADING SCENARIO-2

Irradiation Profile (W/m ²)			Power (W)			Tracking Efficiency Submodule-based MPPT (%)		
SPV-1	SPV-2	SPV-3	P _{max-SPV1}	P _{max-SPV2}	P _{max-SPV3}	SPV-1	SPV-2	SPV-3
200	400	600	10.53	22.38	34.75	94.48	93.12	91.41
200	200	400	10.53	10.53	22.38			
200	200	200	10.53	10.53	10.53			
600	600	200	34.75	34.75	10.53			
600	600	400	34.75	34.75	22.38			
Irradiation Profile (W/m ²)			Power (W)			Tracking Efficiency (%)		
SPV-1	SPV-2	SPV-3	P _{max}			Module-based MPPT		
200	400	600	48.92			82.87		
200	200	400	34.25					
200	200	200	31.58					
600	600	200	68.81					
600	600	400	76.51					

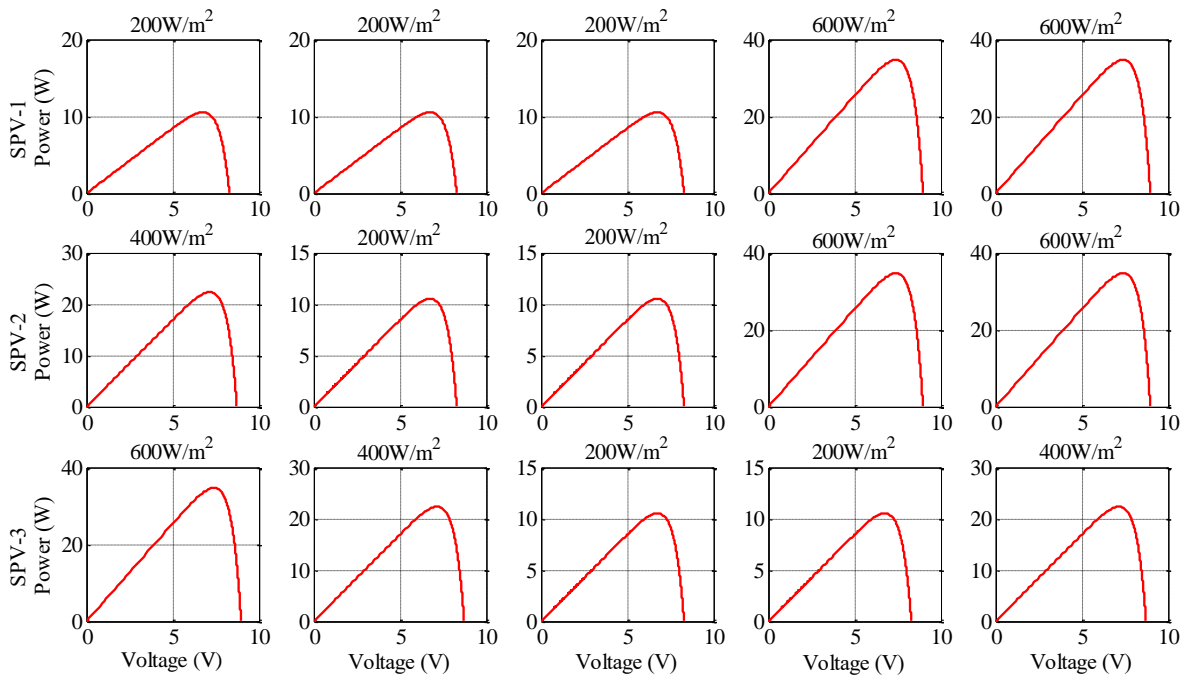


Figure 11. Dynamic P-V curves of the submodules for PSC-2

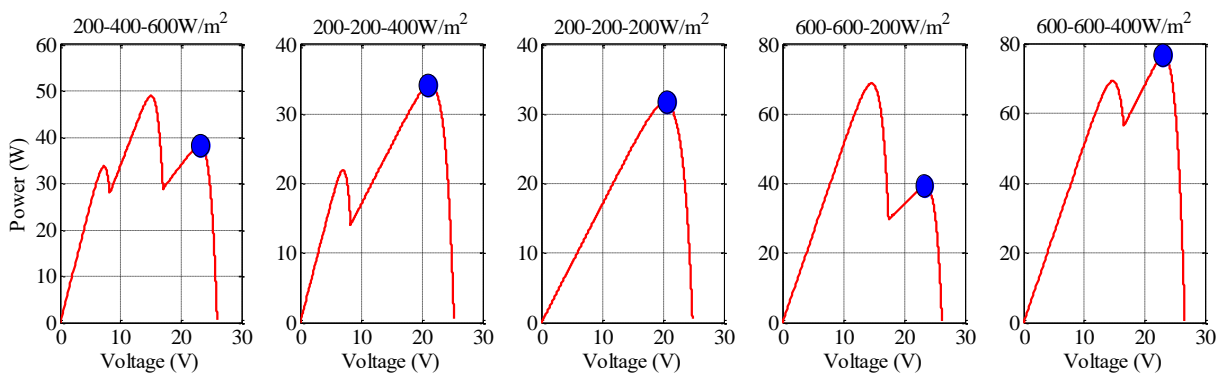


Figure 12. Simulation results of module based MPPT for PSC-2

4. DISCUSSIONS

In this section, the simulation results obtained between MPPT at the submodule level and the module level MPPT have been evaluated and compared. As stated in the previous sections, the maximum power that can be obtained in MPPT realized at the submodule level is the sum of the powers generated by all submodules under the current irradiation conditions. The theoretical maximum power is defined in Eq. (9).

$$P_{sbm} = P_{max_SPV1} + P_{max_SPV2} + P_{max_SPV3} \tag{9}$$

In Eq. (9), P_{sbm} is the sum of the power generated by the submodules, P_{max_SB1} , P_{max_SB2} and P_{max_SB3} are the theoretical maximum power values of the submodules, respectively. In Eq. (10), the formula defining the sum of the powers generated by the submodules at steady state is given.

$$P_{sbm,real} = P_{SPV1} + P_{SPV2} + P_{SPV3} \tag{10}$$

An index has been defined to determine the performance difference between submodule based MPPT and module based MPPT. This index is defined in Eq. (11).

$$\text{diff}(\%) = 100 \frac{P_{sbm,real} - P_{m,real}}{P_{sbm,real}} \quad (11)$$

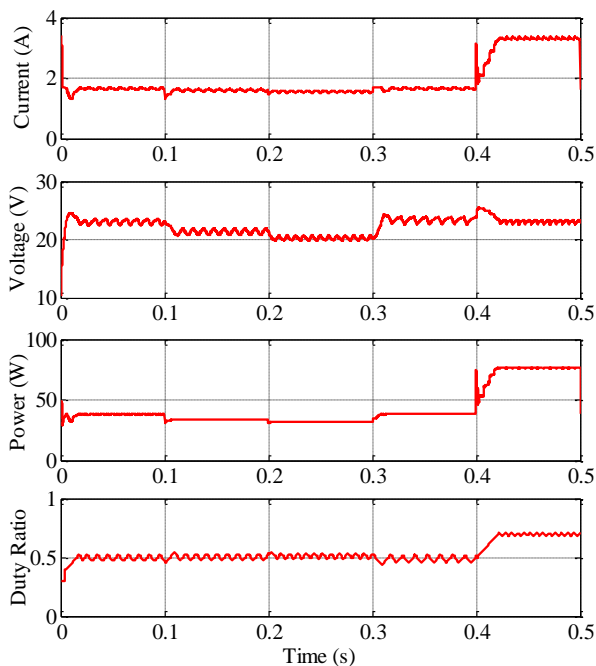


Figure 13. Simulation results of the module based MPPT for PSC-2

In this study, two different dynamic shading conditions are defined and two MPPT approaches are compared using SBC and P&O algorithm. The comparison is made on the power generated under the same conditions. In the submodule-based MPPT technique, MPPT was performed independently in each submodule and the total power to be generated theoretically

was defined as the maximum power as given in Table V. As can be seen in Table V, the theoretical maximum power has been generated under all irradiation conditions thanks to the flexibility of the submodule-based MPPT approach. In module-based MPPT, even if GMPPT is realized, since MPPT is not as flexible as submodule-based MPPT, the maximum possible power value can never be as much as in the submodule-based MPPT technique. According to the first simulation results, submodule-based MPPT produced around 27% more power than module based MPPT. The maximum power that each submodule can produce can be checked from Table III and Table IV, and if it is calculated according to Eq. (9), the values in Table V can be obtained. Similar analyzes can be made for the second simulation results. According to Table V, a power increase of up to 27% has been achieved in submodule based MPPT.

5. CONCLUSION

In this study, partial shading, which is one of the factors affecting the power to be generated in photovoltaic systems, is discussed. In order to avoid complexity, a simple system consisting of a single PV module has been considered and the performances of submodule based MPPT and module based MPPT under dynamic shading conditions have been investigated. In this context, since submodules have small voltage, a SBC was used and P&O was preferred as MPPT algorithm. According to the simulation studies carried out, the MPPT performed at the module level operates at lower efficiency than the MPPT performed at the submodule level. Although MPPT at submodule level is more complex and costly hardware, the GMPPT operation can be performed perfectly with a simpler algorithm. On the other hand, complex algorithms are needed for module-based MPPT to provide GMPPT perfectly. However, in any case there will be a lower power generation than the power obtained in the submodule level MPPT.

TABLE V
EVALUATIONS OF THE SIMULATION RESULTS

No	Irradiation Profile (W/m ²)		Power (W)		
	SPV-1/SPV-2/SPV-3	Max. Power	Submodule	Module	Diff. (%)
1	400-600-600	91.88	91.88	76.51	16.72
	400-400-600	79.51	79.51	71.34	10.27
	200-400-600	67.66	67.66	48.92	27.69
	200-400-400	55.29	55.29	44.53	19.46
	200-400-400	55.29	55.29	44.53	19.46
2	Irradiation Profile (W/m ²)		Power (W)		
	SPV-1/SPV-2/SPV-3	Max. Power	Submodule	Module	Diff. (%)
	200-400-600	67.66	67.66	48.92	27.69
	200-200-400	43.44	43.44	34.25	21.15
	200-200-200	31.58	31.58	31.58	0
	600-600-200	80.53	80.53	68.81	14.55
600-600-400	91.88	91.88	76.51	16.73	

REFERENCES

- [1] IEA Renewable Energy Market Update Outlook for 2020 and 2021, <https://www.iea.org/reports/solar-pv>, (accessed time: 06.04.2021)
- [2] M.E. Başoğlu and B. Çakır, "A novel voltage-current characteristic based global maximum power point tracking algorithm in photovoltaic systems", *Energy*, vol. 112, pp. 153-163, 2016.
- [3] A. K. Panda and K. Aroul, "A novel technique to reduce the switching losses in a synchronous buck converter", presented at the International Conference n.on Power Electronics, Drives and Energy Systems, New Delhi, India, 12-15 December, 2006.
- [4] N. Z. Yahaya and A. A. A. Zamir, "Performance evaluation of SRBC circuit using MPPT controller", presented at the IEEE Symposium on Industrial Electronics and Applications, Bandung, Indonesia, 23-26 September, 2012.
- [5] R. C. N. Pilawa-Podgurski and D. J. Perreault, "Submodule integrated distributed maximum power point tracking for solar photovoltaic applications", *IEEE Transactions on Power Electronics*, vol. 28, no. 6, pp. 2957-2967, 2013.
- [6] Z. Iqbal, U. Nasir, M. T. Rasheed and K. Munir, "A comparative analysis of synchronous buck, isolated buck and buck converter"

- presented at the 15th International Conference on Environment and Electrical Engineering, Rome, Italy, 10-13 June, 2015.
- [7] J. Sreedhar and B. Basavaraju, "Design and analysis of synchronous buck converter for UPS application", presented at the International Conference on Advances in Electrical, Electronics, Information, Communication and Bio-Informatics, Chennai, India, 27-28 February, 2016.
- [8] H. Luo, H. Wen, X. Li, L. Jiang and Y. Hu, "Synchronous buck converter based low-cost and high-efficiency sub-module DMPPT PV system under partial shading conditions", *Energy Conversion and Management*, vol. 126, pp. 473-487, 2016.
- [9] F. Wang, T. Zhu, F. Zhuo, H. Yi and S. Shi, "Submodule level distributed maximum power point tracking PV optimizer with integrated architecture", *Journal of Power Electronics*, vol. 17, no. 5, pp. 1308-1316, 2017.
- [10] K. Pal and M. Pattnaik, "Performance of a synchronous buck converter for a standalone PV system: an experimental study", presented at the 1st International Conference on Energy, Systems and Information Processing, Chennai, India, 4-6 July 2019.
- [11] S. Abdelmalek, A. Dali, A. Bakdi and M. Bettayeb, "Design and experimental implementation of a new robust observer-based nonlinear controller for DC-DC buck converters", *Energy*, vol. 213, Article Number: 118816, 2020.
- [12] M. E. Başoğlu and B. Çakır, "Experimental evaluations of global maximum power point tracking approaches in partial shading conditions", presented at the IEEE International Conference on Environment and Electrical Engineering, Milan, Italy, 6-9 June 2017.
- [13] M. E. Başoğlu and B. Çakır, "Hybrid global maximum power point tracking approach for photovoltaic power optimisers", *IET Renewable Power Generation*, vol. 12, no. 8, pp. 875-882, 2018.
- [14] M. E. Başoğlu, "An improved $0.8V_{oc}$ model based GMPPT technique for module level photovoltaic power optimizers", *IEEE Transactions on Industry Applications*, vol. 55, no.2, pp. 1913-1921, 2019.
- [15] M. E. Başoğlu, "Analyzes of flyback DC-DC converter for submodule level maximum power point tracking in off-grid photovoltaic systems", *Balkan Journal of Electrical & Computer Engineering*, vol. 7, no. 3, pp. 269-275, July 2019.
- [16] R. Çelikel, M. Yılmaz and A. Gündoğdu, "A voltage scanning-based MPPT method for PV power systems under complex partial shading conditions", *Renewable Energy*, vol. 184, pp. 361-373, 2022.
- [17] R. Çelikel and A. Gündoğdu, "Comparison of PO and INC MPPT methods using FPGA In-The-Loop under different radiation conditions", *Balkan Journal of Electrical and Computer Engineering*, vol. 9, no. 2, pp. 114-122, 2021.
- [18] Bosch Solar Services, <http://bosch-solarenergy.de/en/customer-service/product/kundendienst-2.html> (accessed: 25.03.2021)

BIOGRAPHIES

Mustafa Engin Başoğlu was born in 1988. He received the M.Sc. degree of Electrical Engineering at Kocaeli University, Turkey in 2013. He receives Ph.D. in 2017 with thesis "Development and implementation of a new maximum power point tracking method for photovoltaic systems". From 2012, he is research assistant in the department of Electrical Engineering in University Kocaeli. From 2020, he is associate professor in Electrical and Electronics Department of Gümüşhane University. His research interests include: photovoltaic systems, renewable energy, maximum power point tracking algorithms, power electronics, switch mode power supplies and control of electrical machines.



Comparative Analysis of Lighting Elements' Effects on Electric System

Sait Dursun¹, Umit Kemalettin Terzi², Onur Akar³, Temel Sonmezocak⁴

¹ Department of Electrical-Electronics Engineering, Marmara University, MSc Student, Istanbul, Turkey, (e-mail: saitdursun@marmara.edu.tr).

² Department of Electrical-Electronics Engineering, Marmara University, Istanbul, Turkey, (e-mail: terzi@marmara.edu.tr).

³ Department of Electrical and Energy, Istanbul Gedik University, Istanbul, Turkey, (e-mail: onur.akar@gedik.edu.tr).

⁴ Department of Electrical and Energy, Istanbul Haliç University, Istanbul, Turkey, (e-mail: temelsonmezocak@halic.edu.tr).

ARTICLE INFO

Received: Aug., 11, 2021

Revised: Sep., 15, 2021

Accepted: Oct., 17, 2021

Keywords:

Quality of power

Lighting elements

Harmonics

Crest factor

Inrush Current

Flicker effect

Corresponding author: *Onur AKAR*

ISSN: 2536-5010 / e-ISSN: 2536-5134

DOI: <https://doi.org/10.36222/ejt.981153>

ABSTRACT

Due to the increase of demand for energy requirement, and the decrease of energy sources day by day, it is being understood that it is required to efficiently use the energy sources in order to ensure the balance of demand for electric energy. The lighting elements use about 1/5 of the electric energy produced in our country. Especially while selecting the lamps with high energy efficiency, it is important to consider the circumstances which may create negativities such as harmonics, power factor, crest factor, inrush current, and flicker effect in terms of quality of power. Moreover, impurity which may occur in the network affects the other devices negatively. In this study, the quality of power of lighting elements of more than one type was examined in detail. In the experiments, technical analyses were performed by the use of 13 different lighting elements extensively used in our country at site, factory, and domestic environments, and they were evaluated in terms of their positive and negative effects on the network.

1. INTRODUCTION

Please The lighting elements have significant place in electricity production. The use of electricity for lighting is 40% in the field of industry, 20% at sales stores, and 40% at office buildings. As understood by the rates given, lighting has great share on energy consumption. Significant energy saving may be ensured by the efficiency of light sources used for lighting, and by the use of sources with the lowest damage on electricity system [1]. About 20-25% of the electrical energy is used in lighting sector in Turkey. It is expressed that 56% of the energy consumed for lighting is being used in the buildings. When considered from this point of view, the requirement for the effective and efficient use of lighting energy arises [2]. Today, 35% of the electrical energy is consumed at lodgings, and in service sector. This data is about 40% of the world average. 60% of the electrical energy is consumed at lodgings and in service sector for only lighting [3, 4].

The increase of requirement for lighting day by day causes its share to be high in energy consumption, and the increase of use of energy transmission lines. For this reason, in order to attain uninterrupted lighting, the efficient use of sources providing lighting should be considered. It is required to well separate the efficiency, and saving. Turning off one of the two

lighting lamps is saving, and the use of lighting elements which consume the energy more technologically and less is an example of efficiency [5, 6]. In order to provide quality electrical energy for the lighting system, it is required to consider some criteria such as the requirement of having the voltage and frequency steady, of having the power factor close to 1, of having the phase voltages balanced, and of having the amount of harmonics in voltage within specific limit values [7]. The harmonics arising in the networks to which lamps with glow filament are connected causes increase of voltage, and this causes the excessive heating of filaments. This condition decreases the lifetime of filaments by 50%. The main reason of this is the excessive temperature arising in the filaments connected to harmonics. And single layer harmonics significantly affect the fluorescent lamps. The components of harmonics arising from voltage cause loss of iron in the ballasts of fluorescent lamps along with noise. In case of a comparison between fluorescent with magnetic ballast, and fluorescent with electronic ballast, it is observed that fluorescents with electronic ballast add 2-3 times more harmonics on electric system. Moreover, they are significant 3rd sources of harmonics in lamps of discharge group, and the harmonics

being 3 and products of 3 complete their cycle from the neutral line. This circumstance causes the excessive heating of neutral line, and additionally the increase of voltage between neutral and ground. For this reason, it causes occurrence of failures in electronic devices connected to the system [8-10]. Another type of lamp is LED. The harmonic effects of LED lamps on electric system are less compared to fluorescent lamps, and more compared to other lamp groups. In terms of efficiency, it is observed that LED lamps are 80% more efficient compared to fluorescent lamps and lamps with glow filament, and that fluorescent lamps are 84% more efficient compared to lamps with glow filament. In addition, the drawing of high current by the LED lamps at initial run, and the formation of harmonic effect by them are their undesired features [11]. Another issue drawing attention in lighting is the flicker effect. Flicker effect arises in an electric system in which the number of lamps with glow filament and fluorescent lamps are high, and in which voltage fluctuations occur by the effect of harmonics. This condition also negatively affects the health of eyes [12].

2. MATERIAL AND METHOD

2.1. Quality of power relationship of lighting elements

The harmonics are significant components for the quality of power. For a clean and environment friendly energy, it is required to have voltage amplitude, voltage surges, and flicker effects, and to have the wave in sinus form, to preserve the frequency, and to have the phases balanced, and to preserve the voltage amplitude. But as the lighting elements draw non-linear current from the network, they generate harmonics, and this circumstance significantly affects the quality of power [13, 14]. Total Harmonic Distortion (THD) indicates the ratio between the RMS values of harmonics and main components of current and voltage. The total harmonic distortion of voltage is calculated as in Equation (1) [15].

$$THD_V = \frac{\sqrt{\sum_{n=2}^{\infty} V_n^2}}{V_1} = \frac{\sqrt{V_2^2 + V_3^2 + V_4^2 + \dots + V_n^2}}{V_1} \quad (1)$$

And the total harmonic distortion of current is calculated as in Equation (2).

$$THD_I = \frac{\sqrt{\sum_{n=2}^{\infty} I_n^2}}{I_1} = \frac{\sqrt{I_2^2 + I_3^2 + I_4^2 + \dots + I_n^2}}{I_1} \quad (2)$$

The ratio between the peak value (I_m , or U_m) and RMS value of non-sinusoidal current or voltage is called the crest factor. Thus, the crest factor (CF) if wave not covering harmonic components is $\sqrt{2}$ and it is indicated in Equation (3).

$$CF = \frac{\text{Peak Value of Wave}}{\text{Effective Value of Wave}} \quad (3)$$

2.2. The relationship between harmonics and lighting

The element with highest effect in the network is the 3rd harmonic with a frequency of 150 Hz. The 3rd harmonics generally arise from non-linear loads such as lighting elements and computer which are single phase loads. Under normal conditions, there is no current in the neutral conductor in networks where three phases are balanced. But in case of presence of 3rd harmonic component in the network, current is observed on the neutral line. The amount of harmonics occurring in the phase conductor of the network with lighting

element of discharge group is about 30% of the phase current. For instance, as seen in Figure 1, a current three times the amount of harmonics arising from a single phase current is able to pass on neutral line to which three phase currents are connected, and thus heating is able to occur on the neutral line [10, 16]. For this reason, as per the international EMC directive, the currents caused by the 3rd harmonic should be considered while making the cross-section calculation of neutral conductor at a project facility. If 3rd harmonic filter will be present on the system of project facility, the calculation of currents to be caused by the 3rd harmonic, and the design of neutral conductor at high values will not be required [9].

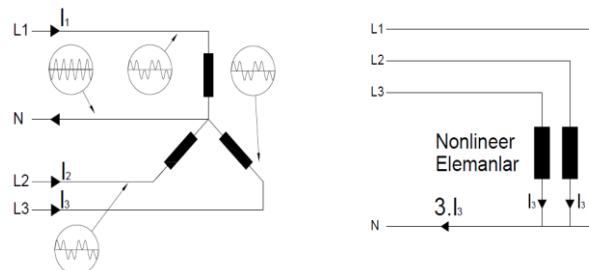


Figure 1. 3rd harmonic currents passing from neutral line

In cases when the 3rd harmonic currents arising at neutral pass from primary coils of the transformer, 3rd harmonic occurs on transformer coils. As seen in Figure 2, the passage of arising 3rd harmonic again to the network from the transformer may be prevented by making delta connection on transformer coils. But this condition causes the increase of losses at the transformer [16, 17].

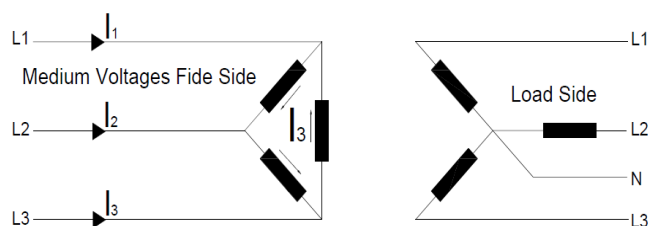


Figure 2. Prevention of harmonics on transformer coils

The increase of sources generating harmonics causes undesired circumstances on the electrical network. In order to prevent such circumstances, the standard institutions of various countries have required bringing in some limitations against the harmonics [18]. Such standards may be applied on electronic and electrical equipment whose input current is up to 16 A (including 16 A) per phase, and which are considered to be connected to low voltage networks. The equipment specified for lighting equipment cover the following.

- Lighting devices and lamps,
- Lighting part of multi-functional equipment that light as one of the primary functions,
- Independent ballasts, and independent glow lamp transformers for discharge lamps,
- Ultraviolet (UV), and infrared (IR) radiation equipment,
- Lit advertising sign boards,
- Attenuators used in lamps except glow lamps

The above are equipped in 4 different manners for limitation of harmonic current. They are categorized in 4 classes named in Classes A, B, C, and D given in Table 1.

TABLE I
CLASSIFICATION OF ELECTRIC DEVICES

CLASS	FEATURE
Class A	<ul style="list-style-type: none"> Balanced 3 phase devices Household appliances except Class D Devices except portable ones Dimmers of lamps with glow filament Audio devices All devices except Classes B, C, and D
Class B	<ul style="list-style-type: none"> Portable devices Non-professional arc devices
Class C	<ul style="list-style-type: none"> Lighting devices
Class D	<ul style="list-style-type: none"> Computers, and computer monitors Television receivers <p>Note: The devices' power level should be between 75 W and 600 W.</p>

According to TS EN 61000-3-2 device classification, the lighting devices are addressed in Class C. The limit values determined for Class C equipment are as follows:

a) Active input power ≥ 25 W

The currents for lighting equipment with an input power greater than 25 W are like the relative limit values specified in Table 2. They shouldn't exceed these limit values.

b) Filter Active Power ≤ 25 W

The lighting equipment with gas discharge, with an active input power equal to or smaller than 25 W, should conform to one of the following terms:

- Harmonic currents shouldn't exceed limit value relevant to power on Column 2 in Table 3.
- The 3rd harmonic current, expressed as a percentage of the main component current, shouldn't exceed 86%, and the 5th shouldn't exceed 61%. If the discharge lighting equipment has a light attenuator device, the measurement should only be performed in case of full load [19].

TABLE 2
HARMONIC LIMIT VALUES FOR CLASS C EQUIPMENT

Harmonic degree (h)	Largest harmonic current allowed expressed as the percentage of input current in basic frequency (%)
2	2
3	30XPower factor of circuit
5	10
7	7
9	5
11 <h>39</h>	3

TABLE 3
HARMONIC LIMIT VALUES FOR CLASS C EQUIPMENT

Harmonic degree (h)	P \leq 600W Largest harmonic current allowed per Watt (mA/W)	P \geq 600W Largest harmonic current allowed (A)
3	3.4	2.30
5	1.9	1.14
7	1.0	0.77
9	0.5	0.40
11	0.35	0.33
13	0.296	0.21
15 <h>39</h>	3.85/h	2.25/h

2.3. Quality of power relationship of lamps with glow filament

The lamps with glow filament don't draw reactive power for the network as ohmic load, and their power factor is equal to 1. For this reason, they don't generate harmonics, and their active and visible powers are equal. In a study performed, the total harmonic effect of lamp with glow filament was measured as 1.2%. This is much below the standards [14]. The lamps with glow filament are devices affected from network voltage fluctuations. The resistance of the lamp varies depending on the temperature. During initial run, the glow lamp may draw inrush current 20-30 times more than the nominal current due to coldness of its resistance. For this reason, it is required for the fuse, used for protection, to be delay action fuse [20].

2.4. Quality of power relationship of lamps of discharge group

They fluorescent, mercury, and sodium vapor lamps operating with discharge principle. They operate with the principle of discharge of gas being present in their tubes. These lamps operating with discharge principle have a non-linear current voltage form, and for this reason they are source of 3rd harmonics. The magnetic ballasts connected to discharge group lamps are also significant sources of harmonics. Recently, electronic type ballasts are being used instead of old type magnetic ballasts. It has become possible to prevent the harmonics by placing harmonic filter in such ballasts [15].

2.5. Quality of power relationship of LED lamps

As all types of lighting elements are sources of harmonics, it was determined that LED lamps, rapidly entering the electric market recently, have significant distorting effect on quality of power of electrical network. In a study performed, the Total Harmonic Distortion (TDH) of LED lamp group for the network was measured as 159%, and this is much above the standards. For this reason, it is obligatory to apply a filter on LED lighting groups [13, 21-23].

3. RESULTS AND DISCUSSION

In this section, analyses of quality of power and harmonics were performed by forming real-time experimental mechanism on 13 different lighting elements used in lighting sector. The effect of each lighting element on the network was examined, and their superiorities or negative aspects in terms of type of light source and actuator constructs were compared. The light sources, used in the experiment, consisted of lamps with glow filament, discharge group lamps, and LED lamps.

3.1. Quality of power relationship of LED lamps

In the experiment, voltage, current drawn from the system, power factor, changes in %THD, inrush currents, and crest factors were examined for lamp with glow filament. In Figure 3, the testing mechanism of this lamp is indicated

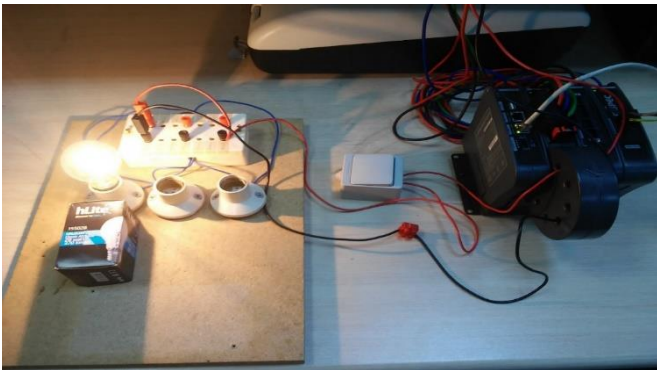


Figure 3. Experiment mechanism for lamp with glow filament

In Figure 4, when the graphs obtained from the analyzer for lamp with glow filament are examined, it is observed that it is steady ohmic load in terms of quality of power, and thus it consumes only active load from the network.

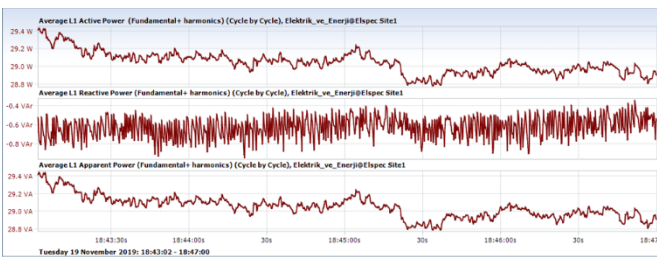


Figure 4. The lamp's active power (basic + harmonic), reactive power (basic + harmonic), visible power (basic + harmonic) values in the measurement process

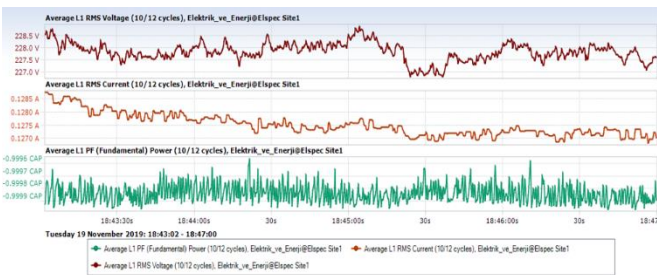


Figure 5. RMS voltage, RMS current, and replacement power coefficient (Cosφ) values in the measurement process

As observed in Figure 4, a lamp of 30 W consumed a reactive power below the value of 1 VAr thus, as observed in Figure 5, PF value was measured as 0.99. Moreover, significant variations in current and voltages based on time were observed for the lamp with glow filament. When we consider this lamp in terms of inrush currents during switching arising at start and stop, by the examination of test records obtained from the analyzer in a period of 30 sec., it was observed that it is drawing an instant current 10 times the approximate load current of the network. The results of experiment are shown in Figure 6.

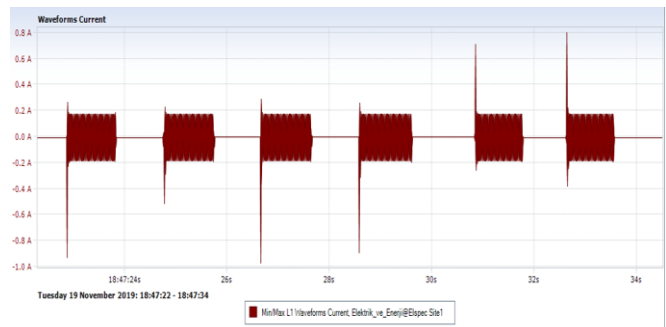


Figure 6. Inrush currents at six switching moments in the process of switching at 30 sec.

The crest factor value of glow lamps is having a value very close to $\sqrt{2}$. These values Vary between 1.440 Amperes and 1.480 Amperes as observed in Figure 7.

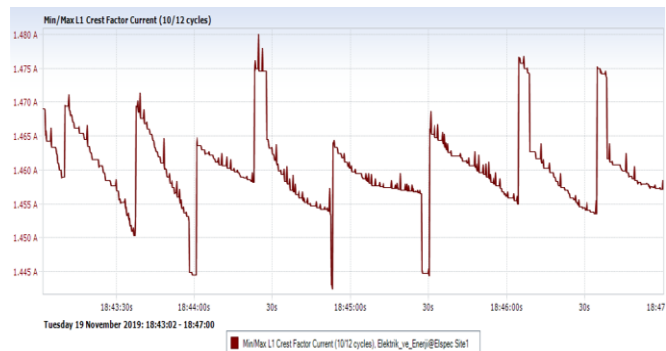


Figure 7. Crest factor of the current passing from the lamp during the measurement

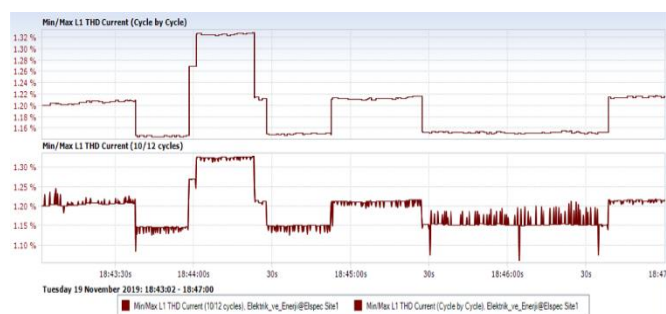
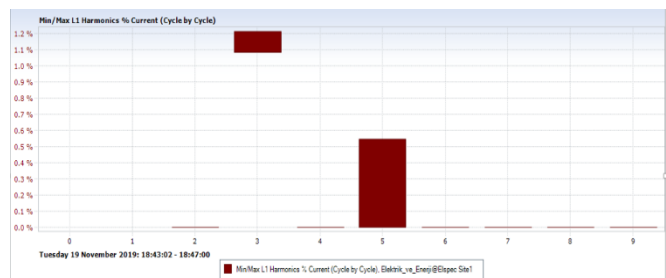


Figure 8. Current and voltage harmonics of glow lamps

When considered in terms of (%) THD, along with the harmonic values of voltage and current were at the level of 1% THD, it was understood by the examination of graphs in Figure 8 that they were very low, and that they were arising from 3rd harmonic. Because glow lamps are ohmic linear loads.

3.2. Results of network analysis obtained for discharge type lamps

They are fluorescent, mercury, and sodium vapor lamps operating with discharge principle. They operate with the principle of discharge of gas being present in their tubes. In this study, these lamps were examined under two groups as being low pressure and high pressure.

3.2.1. Low Pressure Fluorescent Type Lamps

In the experiment, the analyses of different types of fluorescent lamps frequently used at lodgings, factories and stores were performed. The testing mechanisms are indicated in Figure 9. In the experiment, voltage and current drawn from the system, power factor, changes in Total Harmonic Distortion (%THD), inrush currents, and crest factors were examined for these lamps.

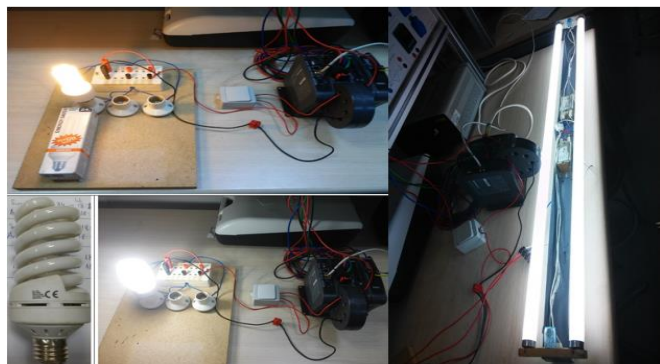


Figure 9. Testing mechanisms for fluorescent lamps

Fluorescent lamps also consume power reactively from the network. Reactive power amounts are different as per the igniter ballast mechanism used by the lamp. Thus, the lamp gets capacitive values above $\cos\phi=0.90$ in electronic type igniter systems, and its power factor (PF) = 0.6 is not being equal in terms of capacity. The main reason of this is that it grounds on other waves that actually exist while measuring the power factor value, in other words the harmonics arising in the system decrease the PF value of the system as reactive components, and the PF value draws away from the $\cos\phi$ value in the system. In Figure 10, this difference is specifically indicated.

As also shown in the above figure, even if the $\cos\phi$ value of electronic igniter compact fluorescent lamps is high, their PF values are actually low and have capacitive characteristics. The main reason of this is that this load exhibits a non-linear behavior, and that the wave form of current distorts in the system depending on the sinusoidal voltage applied, in other words current harmonics are present. The presence of harmonics is clearly indicated on graphs in Figures 11, 12, and 13.

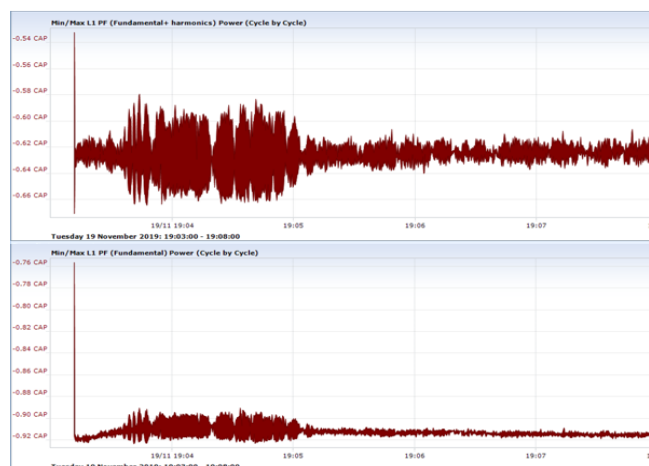


Figure 10. $\cos\phi$ and PF relationship of electronic igniter 32 W compact fluorescent lamp

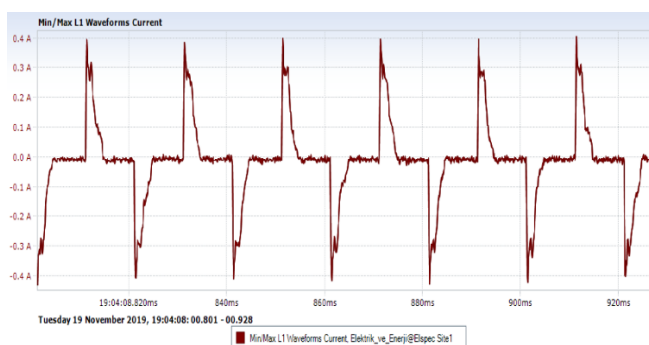
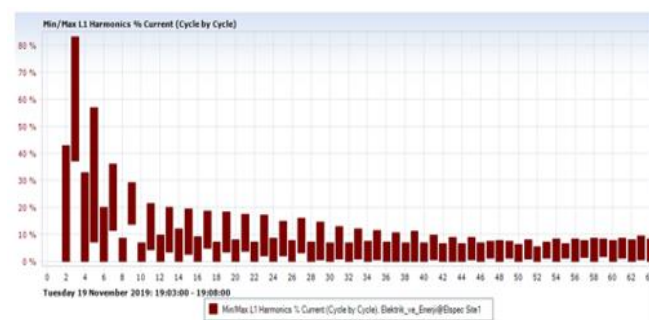


Figure 11. Waveform of current passing from the 32 W compact lamp



during the measurement

Figure 12. Harmonic current spectrum in L1 phase of electronic 32 W compact lamp (% rate)

As seen in Figure 12, it is observed that the 3rd harmonic component in this lamp is dominant as above 80%. In this type of lamps, respectively 5th and 7th harmonic components are also present at high rates following 3rd harmonic.

Total harmonic distortion of this lamp was measured as 100% in a time interval of 30 sec. as seen in Figure 13.

But this circumstance is different in fluorescent lamps with magnetic ballast. In this type of lamps, $\cos\phi$ and PF values are equal, and they indicate 0.45 inductive characteristic. Along with the reactive power component is high in the network, it lacks in harmonic values as the $\cos\phi$ and PF values are nearly the same.

In Figure 14, the current waveform obtained as the result of measurement of a T₅ type fluorescent lamp of 2x36 W. As observed in Figure 14, waveform of current is very close to sinusoidal form. In other words, the harmonic values of current are at low rates below 10%. This is also shown in Figure 15.

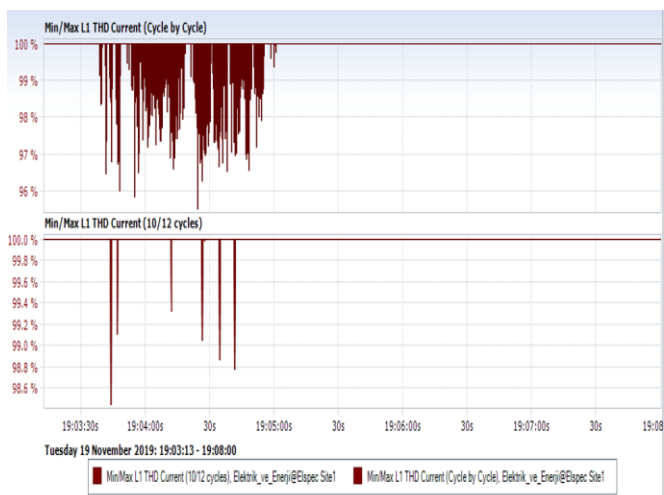


Figure 13. Change of THD (Total Harmonic Distortion) value of L₁ phase current during measurement of 31 W compact lamp

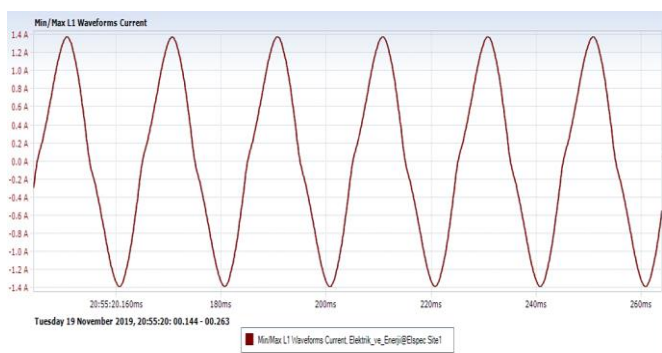


Figure 14. Waveform of current in T₅ type fluorescent lamp with magnetic ballast during measurement



Figure 15. Change of THD (Total Harmonic Distortion) value of L₁ phase current during 32 W measurement

In the above figure, the THD values reached peak values at instant temporary state behavior only during initial switching, and then decreases below the level of 10% at a constant rate in the permanent state.

In the examinations performed, it was found that the fluorescent type lamps with electronic ballast have non-linear load characteristic by containing electrostatic switching elements. Moreover, they contain harmonics in the network. In this sense, it was observed by the analyses that the values of crest factor and inrush current are high compared to lamps with magnetic ballast. This difference is clearly observed by graphs in Figures 16 and 17.

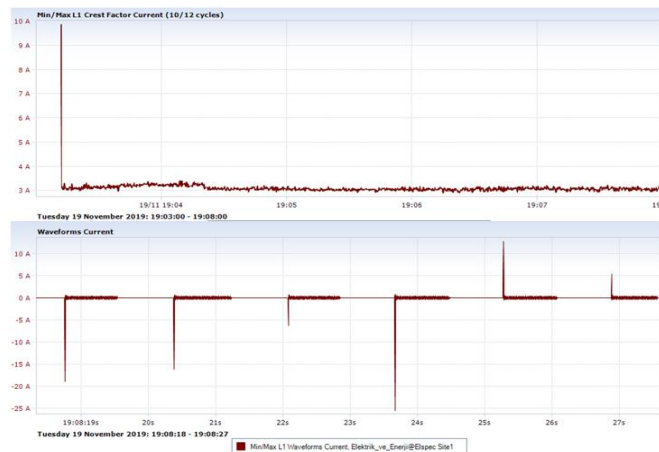


Figure 16. Change of inrush current and crest factor obtained for 2x36 W for fluorescent lamp with magnetic ballast



Figure 17. Change of inrush current and crest factor obtained for 2x36 W for fluorescent lamp with magnetic ballast

3.2.2. High pressure mercury and sodium vapor lamps

High pressure lamps are generally used at lighting sites, and for lighting streets and roads. These lamps have external ballast unit as in the low pressure fluorescent lamps. Thus, these lamps were examined as mercury and sodium vapor ones along with their control gears. Lamp control gears used in the experiments are shown in Figure 18.



Figure 18. Testing Mechanisms of High Pressure Sodium Vapor and Mercury Vapor Lamps

In the experiment, high pressure lamps of different powers, and different types were used. These lamps show same characteristics with each other. Especially the inrush currents of these lamps are at high levels compared to low pressure lamps. In Figures 19 and 20, the inrush current graphs of two different lamp types with the same power (150 W) obtained by performing on-off a specific intervals are indicated. As seen in these figures, the power and current values that these types of lamps demand from the system are high compared to other lamps. It is observed that the inrush currents also have high values. The inrush current values of both of these lamps were measured as the same as 75.5 A. These lamps have non-linear characteristics. In the experiments performed, it was observed that they form current harmonics in the connected network.

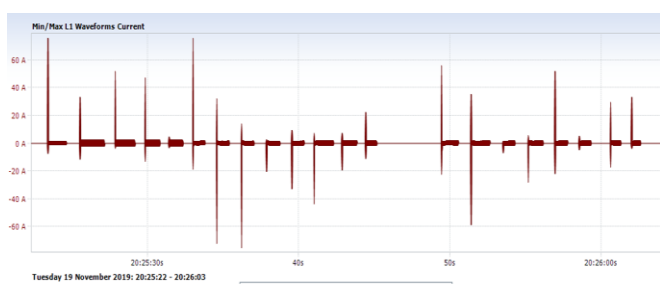


Figure 19. Temporal change of inrush currents obtained during one minute switching of 150 W mercury vapor lamp

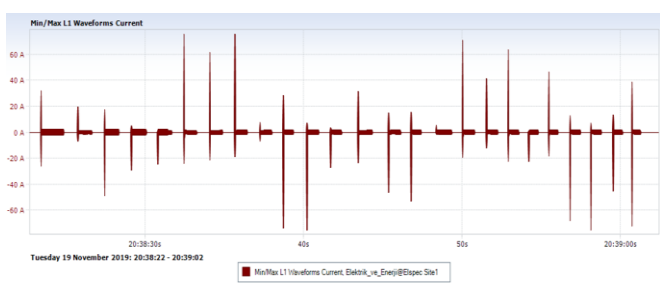


Figure 20. Temporal change of inrush currents obtained during one minute switching of 150 W sodium vapor lamp

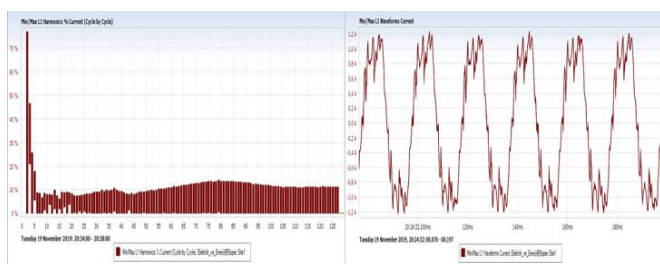


Figure 21. Current harmonics (% THD), and current waveform of 150 W mercury vapor lamp

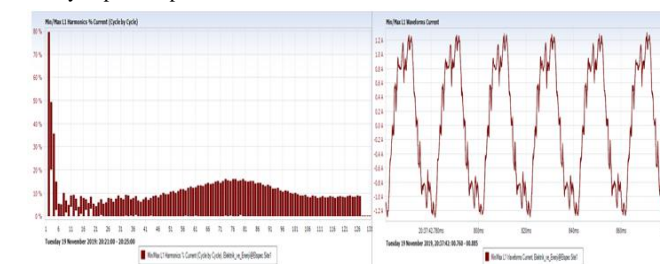


Figure 22. Current harmonics (% THD), and current waveform of 150 W sodium vapor lamp

By the above Figure 21 and 22, it is observed that the sodium and mercury vapor lamps are subjected to non-linear load in the current waveforms due to presence of non-linear load in the network, and especially due to the dominance of 3rd harmonics. This distortion is at the level of 20-30% THD. Current and voltage fluctuations were not observed on the network. But during heating of the lamp, the values of current and voltage are able to vary. PF value got inductive values up to 0.9 with an average of 0.56 along with heating as starting from a minimum value of 0.30. In Figure 23, the changes of current, voltage and PF are shown.

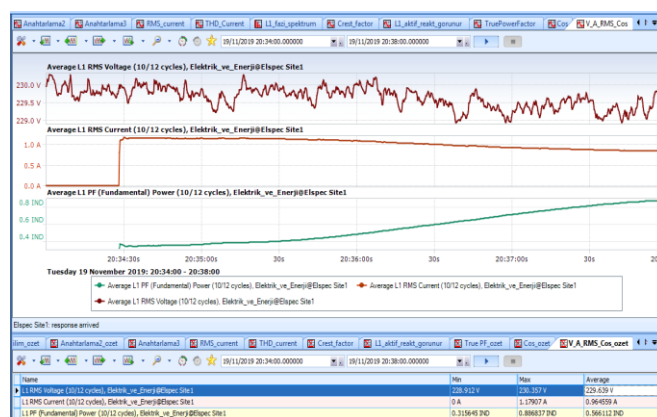


Figure 23. RMS voltage, RMS current, and replacement PF values during measurement

3.3. Results of network analysis obtained for LED lamps

In this study, experimental measurements were performed on 5 different LED loads, and the quality of power of each load was examined. These loads are ones that are becoming extensive today especially in industry, and at stores and lodgings. Considering the features of actuators used in the design of each LED system, they have difference in terms of quality of power. In this sense, in the study experimental LED loads for LED bulbs, LED projectors, downlights, and panel type LED systems were used. The testing mechanisms of the LED loads used are shown in Figure 24.



Figure 24. Testing mechanisms for LED lamps

In the experiments performed, it was observed that the LED lamps didn't cause voltage and current waves in the network they were connected. But considering that the actuators used were non-linear, significant differences in the PF values and harmonic values of the network were in subject.

If we examine the LED loads respectively, values of current, voltage and PF measured on the network in terms of quality of

power for different LED loads are indicated in Figures 25, 26, and 27.

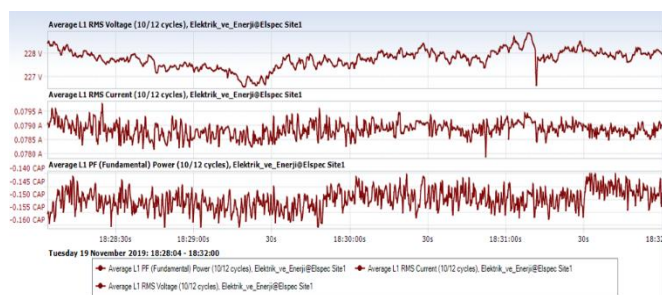


Figure 25. Values of RMS voltage, RMS current, and replacement PF of LED bulb (4 W) during measurement

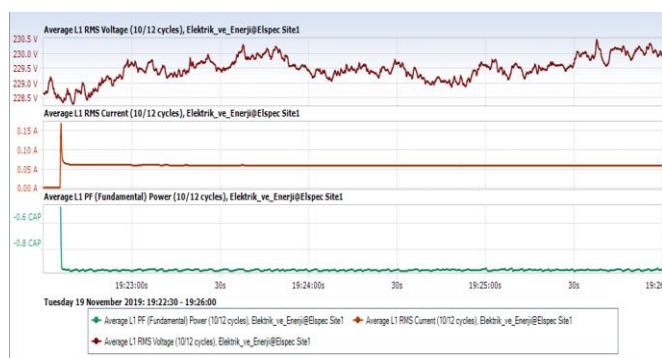


Figure 26. Values of RMS voltage, RMS current, and replacement PF of LED Slim Panel (6 W) Luminaire during measurement

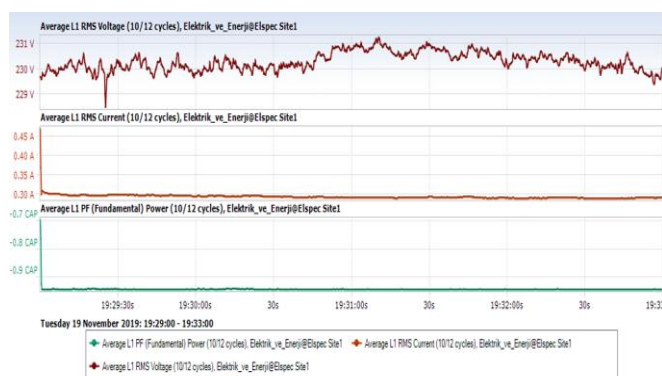


Figure 27. Values of RMS voltage, RMS current, and replacement PF of LED Projector (50 W) Luminaire during measurement

As observed in the above figures, the LED systems cause a non-linear capacitive load state, and the PF values rise much above the value of 1 despite lack of formation of current and voltage fluctuations on the network. Moreover, distortions in the current waveforms of these systems were in subject, and in terms of % THD, current harmonics were observed in the environment.

As clearly observed on graphs in Figures 28, 29, and 30, even if the LED loads are being preferred as efficient light sources today, they are able to highly distort the quality of power due to their non-linear characteristics, and they are harmonic light sources which can reach to 100% THD values.

These systems don't form current waves on the network, and the value of crest factor is able to a bit higher than $\sqrt{2}$. In Figure 31, graphs of different loads are present.

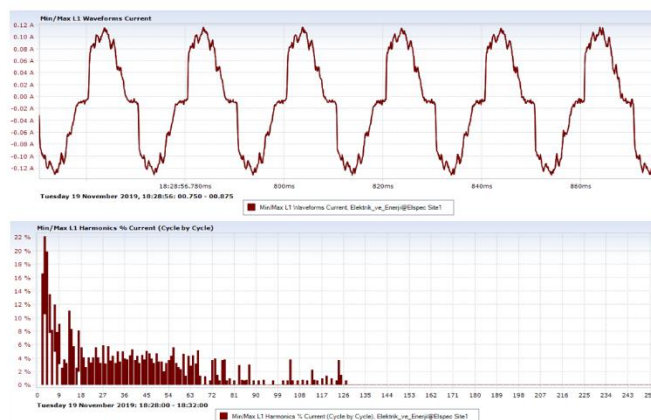


Figure 28. Current harmonics (% THD), and current waveform for a LED bulb (4 W)

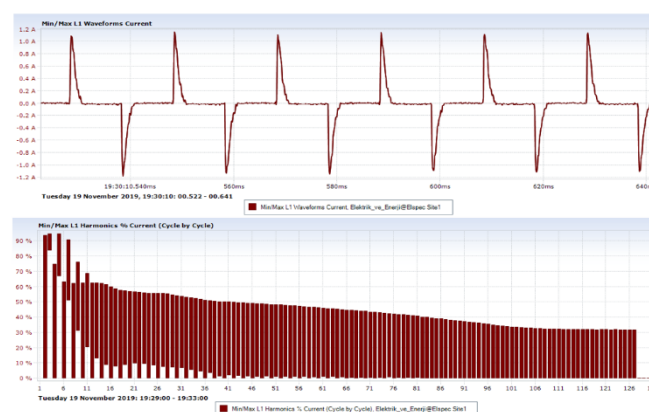


Figure 29. % THD and current waveform of a magnetic LED Slim Panel (6 W) Luminaire



Figure 30. % THD and current waveform of a LED Projector (50 W) Luminaire

LED systems are very sensitive due to their construct. Sudden fluctuations which may arise on the network are able to damage the functions of these systems. For this reason, during switching performed for 1 minute, inrush currents were measured on these loads. In Figure 32, this state for LED bulb, LED panel, and LED projector was summarized. In Figure 32, inrush current graphs of 3 different LED loads are indicated. These are LED loads consuming 4 W, 6 W, and 50 W power, respectively. In Figure 32, 4 W LED bulb at the top draws a current of 0.078 A from the network, but it forms an inrush current up to 5.9 A. In the same manner, the one in the middle is the graph of inrush current of a 6 W LED panel type

luminaire. Under normal conditions, this load demands 0.05 A current from the network, but it forms an inrush current of 26.24 A. And on the bottom graph in Figure 32, the LED projector load, which drawn a current of 0.29 A under normal conditions, forms an inrush current up to 75.52 A. Due to the analyses performed, when the middle and bottom graphs in Figure 32 are examined, the inrush currents of these two loads are very high, and when the graphs in Figure 31 are examined, the crest factor values of these loads are high. Moreover, the current waveforms and harmonic spectrums in Figures 29 and 30 exhibit that these two loads are very high in harmonic sense. Therefore, by the analyses performed, the % THD values of lighting sources, with high inrush current values and crest factor values, are being very high. Moreover, when the PF values of these loads were examined, it was observed that they had capacitive characteristics, and that they exceeded the value of PF=1, and that their $\cos\phi$ values were not equal to the value of PF.



Figure 31. Graphs of crest factors of different LED loads (LED bulb at the top, LED panel in the middle, and LED projector at the bottom)

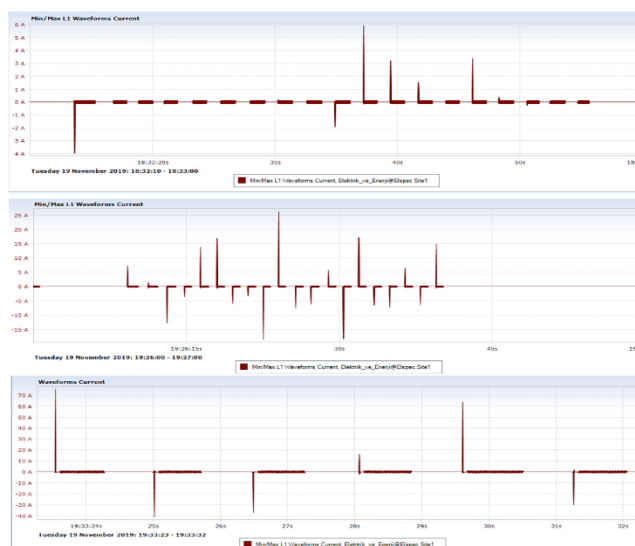


Figure 32. Graphs of temporal change of inrush currents obtained during switching for one minute of three different LED laps (LED bulb at the top, LED panel in the middle, and LED projector at the bottom)

In Table 4, as the result of the experimental measurements performed, the effects on the network of lighting sources used are indicated as not present (-), and present (+). As observed in Table 4, as the lighting devices don't form voltage fluctuations, voltage drops, overvoltage, imbalance and notch, some laps and LED lamps operating as per the principle of gas discharge are able to be affected from inrush currents arising by the instantaneous voltage fluctuations on the network itself. The main reason of this is the inferiority of the actuator and ballast sourced systems where they are used, and as a result difference of power factor values from the $\cos\phi$ values, and formation of excessive harmonics on the system.

TABLE 4
NEGATIVE EFFECTS ON THE NETWORK OF LIGHTING ELEMENTS USED IN EXPERIMENTAL ANALYSES

Lighting Elements Used	Voltage Drop	Voltage Fluctuations	Overvoltage	Harmonics	Imbalance	Inrush Current	Crest Factor $<\sqrt{2}$	Notch	Flicker Effect
LED Bulb	-	-	-	+	-	+	+	-	+
Halogen Glow Bulb	-	-	-	-	-	+	+	-	-
LED 15W Bulb	-	-	-	+	-	+	+	-	-
Compact_Key_30 W	-	-	-	+	-	+	+	-	-
Compact_wanlee_32 W	-	-	-	+	-	+	+	-	-
Compact_Osram_32 W	-	-	-	+	-	+	+	-	-
SlimLEDPanel_hliteDriver_6 W	-	-	-	+	-	+	+	-	+
LEDProjector_50 W	-	-	-	+	-	+	+	-	+
LED Downlight_AcUltraLight	-	-	-	+	-	+	-	-	-
Road Lighting_Mercury_E27_70 W	-	-	-	+	-	+	+	-	-
Road Lighting_Mercury_E40_Philips150 W	-	-	-	+	-	+	+	-	-
Road Lighting_Sodium_E40_HST150 W	-	-	-	+	-	+	+	-	-
Fluorescent_2x36 W	-	-	-	-	-	+	+	-	-

In Table 5, the results of measurements of all the loads used in the analyses performed are shown. Moreover, considering especially the operation characteristics of LED and gas discharge lamps by the use of external non-linear driver/ballast units on these light sources, the effects of lighting elements on quality of power are examined as sub-articles.

All the lighting devices used in the experiments form inrush currents during initial switching, and relevant instant switching power losses. But depending on the type and power of the lamp, and on the quality of actuator on which it is used, inrush currents' amplitude values and their ratios to nominal currents varied. Even if the inrush currents of mercury and sodium

vapor luminaires used for road lighting were high by being about 75.58 A, this rate is being about 75 times by drawing of about 1 A current, and it is low compared to other LED lamps. But especially in 6 W LED Slim, and 50 W Projector Luminaires with 100% THD level, the inrush currents were measured as 26.24 A and 75.52 A, respectively. These lamps normally drew 0.057 A and 0.291 A current from the network, respectively. Considering this circumstance, this type of LED systems are very sensitive loads in terms of their functions. For instance, as the ratios of inrush currents of these 2 types of LED lamps to their current drawn from the network were 460 times and 259 times respectively, it was found as very high compared

TABLE 5
RESULT OF EXPERIMENTAL MEASUREMENTS OF LIGHTING ELEMENTS USED IN THE ANALYSIS

Bulb Types	Experiment Voltage's Average (RMS) Value (Volt)	Average Current Drawn from the System (Ampere)	Max. Inrush Current (Ampere)	Total Harmonic Distortion of Load Current Drawn from the Network, average %THD	Crest Factor Current, average	Power Values Drawn from the System (average W, VAr, VA)	Fundamental Power Factor (Cosφ)		True Power Factor (PF) Fundamental + Harmonics
LED Bulb	7	0.078A	5.9A	22%	1.64A	2.6 W ; - 17.49VAr; 17.68VA	-0.14	cap	-0.14 cap
Halogen Bulb	227.83V AC	0.127A	0.8A	1.90%	1.46A	29W ; - 0.62VAr; 29.04VA	0.99	ind	0.99 ind
LED 15 W Bulb	228.49V AC	0.065A	0.09A	19.65%	1.58A	14.31W ; - 4.11VAr ; 14.89VA	-0.97	cap	-0.96 cap
Compact_key_30 W_bulb	229.33V AC	0.143A	12.22A	87.83%	3.1A	21.74W ; 24.72VAr ; 32.93VA	-0.88	cap	-0.66 cap
Compact_wanlee_32 W_bulb	228.76V AC	0.121A	12.74A	99.99%	3.08A	17.09W ; - 21.30VAr ; 27.31VA	-0.91	cap	-0.62 cap
Compact_osram_24 W_bulb	228.87V AC	0.112A	8.17A	99.24%	2.98A	16.91W ; - 19.98VAr ; 26.18VA	-0.91	cap	-0.64 cap
LEDSlimPanel_hliteDriver_6W_bulb	229.47V AC	0.057A	26.24A	100%	4.3A	6.6W ; - 11.26VAr ; 13.06VA	-0.95	cap	-0.5 cap
LED Projector_50 W_bulb	230.27V AC	0.291A	75.52A	100%	4.23A	34.19W ; - 57.99VAr ; 67.33VA	-0.94	cap	-0.5 cap
LED Downlight_AcUltralight_bulb	229.63A AC	0.150A	3.39A	20%	1.38A	33.05W ; - 9.98VAr ; 34.54VA	-0.97	cap	-0.95 cap
Road Lighting_Mercury_E27_70W	229.18V AC	0.394A	36.75A	24.24%	1.71A	71.35W ; 48.37VAr ; 90.52VA	0.85	ind	0.82 ind
Road Lighting_Mercury_E40_Philips150W	230.13V AC	0.984A	75.55A	29.84%	1.82A	125.40W ; 172.45VAr ; 220.75VA	0.94	ind	0.91 ind
Road Lighting_Sodium_E40_HST 150 W	229.63V AC	0.964A	75.58A	30.36%	1.85A	108.88W ; 170.08VAr ; 206.82VA	0.88	ind	0.88 ind
Fluorescent_2x36 W	230.52V AC	0.911A	4.253A	9.65%	1.53A	91.12W ; 182.077VAr; 203.75VA	-0.90	cap	-0.44 cap

to road lighting devices. Thus, when a decision is being made for the use of LED lighting devices especially at enterprises, the sources with low THD values should be selected. In the experiments performed, it was observed that both the inrush currents of the LED sources with low harmonic levels, and the ratio of their inrush currents to nominal current were low. Moreover, as they are highly used at enterprises or factories as these systems are capacitive, they have significant negative effects of electricity demand, and for this reason, it is required to use compensation units at enterprises where such lighting elements are being used. In these lighting devices, with high harmonic values, the values of crest factor are also much above the normal by being 3-4 times higher.

4. CONCLUSION

While selecting lighting lamps, it is important to consider the circumstances which may create negativities such as harmonics, power factor, crest factor, inrush current, and flicker effect in terms of quality of power. In our study, the quality of power of lighting elements with glow filament, of lighting elements of discharge group, and of lighting elements of LED group was examined in detail. The findings obtained indicated significant negativities in terms of quality of power in all the lamps except halogen glow lamps in terms of their effects on the network despite not observing any notches on all the lamps. When these negativities are addressed individually as PF, harmonics, inrush currents, and crest factor, the PF values are at low values especially in LED lamp and fluorescent lamp luminaires, and they are able to form significant harmonics on the network as capacitive loads. And especially the PF values of some 30 W and 32 W compact fluorescent lamps, lower power 6 W LED slim panels, and 50 W projectors have 0.5-0.6 capacitive values, and they are far from the value of $\cos\phi$, and it was observed that they form significant current harmonics at the range of 87-100% THD. In the direction of these analyses, while using devices which can reach to high lighting amounts along with low power consumption in terms energy efficiency, their quality of power should be additionally considered in terms of their effects on the network, their lifetime, and the safety of environment. Especially by the extension of the use of LED systems today, in the process of decision making for use of numerous lighting sources at outer lightings, at road lightings, and at large enterprises, the negative effects on the network and on the users shouldn't be ignored. For this reason, in all the lighting lamps, the lighting sources with a THD rate below 10% should be preferred, and it shouldn't be ignored that the PF values may be above 1 by the use of numerous such lighting sources, and advanced compensation units should be additionally used.

ACKNOWLEDGEMENT

Authors would like to thank late Assistant Professor Doctor Selçuk Atış from Vocational School of Technical Sciences of University of Marmara for his tremendous effort and valuable contribution.

REFERENCES

- [1] N. Luewarasirikula, "A Study of Electrical Energy Saving in Office," *Procedia - Social and Behavioral Sciences*, vol. 197, pp. 1203 – 1208,

- 2015.W.-K. Chen, *Linear Networks and Systems*. Belmont, CA, USA: Wadsworth, 1993, pp. 123–135.
- [2] P. O. Oluseyi, T. E. Somefun, O. M. Babatunde, T.O. Akinbulire, O. Oluleke, O. O. Babayomi, A. Samuel, S. A. Isaac, D. E. Babatunde, "Evaluation of Energy-efficiency in Lighting Systems for Public Buildings," *International Journal of Energy Economics and Policy*, vol. 10, pp. 435-439, 2020.
- [3] K. Khaled Bataineh, A. Alrabee, "Improving the Energy Efficiency of the Residential Buildings in Jordan," *Buildings* 2018, 8, 85; doi:10.3390/buildings8070085.
- [4] A. Balaras, Constantin., G. A. Gaigla, E. Georgopoulou, S. Mirasgedis, Y. Sarafidis, P. D. Lalas, "European Residential Buildings and Empirical Assessment of The Hellenic Building Stock, Energy, Building and Environment," vol. 42, Issue 3, pp. 1298-1314, 2007
- [5] B. Mills, J. Schleich, "Household transitions to energy efficient lighting," *Energy Economics*, vol. 46, pp. 151-160, 2014.
- [6] K. R. Wagiman, M.N. Abdullah, N. H. Mohammad Radzi, M. Y. Hassan, "Lighting system control techniques in commercial buildings: Current trends and future directions," *Journal of Building Engineering* 31:101342, 2020. doi:10.1016/j.jobte.2020.101342.
- [7] S. R. Barrold, B. K. Patel "A thyristor reactive power compensator for fast-Varying industrial loads," *International Journal of Electronics*, vol.51, no.6, pp.763-767,198.
- [8] P. Devanathan, "A survey of harmonic distortion and reduction techniques," *International Journal of Pharmacy and Technology*, , vol. 8, pp. 23581-23589, 2016.
- [9] B. A. Adegboye, "Power Quality Assessment in a Distribution Network," *Advanced Materials Research* Vol. 62/64, pp. 53-59, 2009.
- [10] A. Ozdemir, A. Ferikoglu, "Low cost mixed-signal microcontroller based power measurement technique," *IEEE Proceedings-Science Measurement And Technology*, vol.151, pp.253-258, 2004. doi: 10.1049/ip-smt:20040242 - JUL , WOS:000222969400004.
- [11] S. Atış, U. K. Terzi, M. Onat, "Comparative Investigation of Effects of Inrush Currents on Switching Components of Energy Efficient Lighting Elements," 2018, Istanbul, Turkey
- [12] "ABS Guidance Notes On Control Of Harmonics In Electrical Power Systems," American Bureau of Shipping Incorporated by Act of Legislature of the State of New York 1862, pp. 29-60, 2006.
- [13] C. Venkatesh, D. S. Kumar, D. V. S. Sima Sarma, M. Sydulu, "Modelling of Nonlinear Loads and Estimation of Harmonics in Industrial Distribution System," Fifteenth National Power Systems Conference (NPSC), IIT Bombay, December 2008.
- [14] W.M. Grady, S. Santosa, "Understanding power system harmonics," USA, pp. 37 – 44, 2001.
- [15] J. Kumru Arrillaga, N. R. Watson, "Power System Harmonics," *Lohn Wiley & Sons, USA* , 2003.
- [16] P. J. Nelson, "A Beter Understanding of Harmonic Distortion in the Petrochemical Industry," *IEEE Transactions on Industry Applications*, vol. 40, pp. 220-231, 2002.
- [17] R. D. Henderson, J. Patrick, P. J. Rose, "Harmonics: The Effects on Power Quality and Transformers," *IEEE Transactions on Industry on Industry App.*, vol. 30, pp. 528-532, 1994.
- [18] S. J. B. Ong, Y. J. Cheng, "An overview of international harmonics standards and guidelines (IEEE, IEC, EN, ER and STC) for low voltage system," *International Power Engineering Conference*, 2007. IPEC 2007.
- [19] IEC 61000-3-2, (2004), Electromagnetic compatibility (EMC) – Part 3-2: Limits – Limits for harmonic current emissions (equipment input current ≤ 16 A per phase.
- [20] D. C. Agrawal, H. Leff, "Efficiency and efficacy of incandescent lamps," *American Journal of Physics*, vol. 64, pp. 649-654, 1996, doi:10.1119/1.18260.
- [21] P. Verma., N. Patel, Nirmal-Kumar C. Nair, "CFL to LED Transition: An Analysis From Harmonics Perspective," *IEEE International Conference on Power System Technology (POWERCON'16)*, 28 Sept.- 1 Oct., Wollongong, NSW, Australia.
- [22] S. Singh, S. Bhullar, "Hardware implementation of auto switching and light intensity control of LED lamps", *Balkan Journal of Electrical & Computer Engineering*, September 2016 Vol.4 No.2, pp.67-71
- [23] B.Yuksel, I. Kiyak, "Thermal Circuit Calculation and Real-Time Analysis of Led Light Source Luminaires", *European Journal of Technique (EJT)*, Vol 10, Number 2, 2020, pp.252-263.

BIOGRAPHIES

Sait Dursun was born in Van in 1983. He graduated from Marmara University Electrical Teaching Department in 2008 and Sakarya University Electrical-

Electronics Engineering in 2017. Since 2015, he has been continuing his postgraduate education at Marmara University, Faculty of Technology, Department of Electrical and Electronics Engineering. He worked at TEDAŞ between 2014-2018 and at Eltek Electric between 2018-2020. His research interests include High Voltage, Lighting Systems and Renewable Energy Systems.

Umit K. Terzi was born at Zonguldak in 1968. He received his B.S. and MSc. degrees from Marmara University in 1989 and 1994, respectively. He received his PhD degree from Marmara University in 2000. Since 2013, he is working as Prof. Dr. for Electrical-Electronics Department of Technology Faculty of Marmara University, and Electrical Education Department of Technical Education Faculty where he is head of the department. His research interests include Electrical Machinery, Power Systems, Energy Transmission and Distribution, and Renewable Energy Systems.

Onur Akar was born at Giresun in 1981. He received his undergraduate, graduate and doctorate degrees from Marmara University in 2005, 2011 and 2020, respectively. He worked as lecturer at Istanbul Gedik University between 2010-2020. In the period of 2012-2015, he served as the Head of the Electrical Program at Istanbul Gedik University. He is working at same university as Assistant Professor Dr. in the Electricity and Energy Department, and as the Head of the Department of Electricity and Energy since 2021. His research interests include Control Systems, Renewable Energy Systems, Power Systems, and Lighting Systems.

Temel Sonmezocak was born in Edirne in 1978. He received his B.S. degree from Marmara University in 2001. In 2015, he completed his M.Sc. degree at Istanbul Aydin University, Department of Electrical and Electronics Engineering. In 2016, he started his Ph.D. program in Electronics Engineering at Yıldız Technical University, and he is still continuing the same program. Since 2018, he is working as lecturer in Electrical Department of Istanbul Halic University. His research interests include Lighting Systems, Power Electronics, Algorithms, and Renewable Sources.

A Novel Local Feature Generation Technique Based Sound Classification Method for Covid-19 Detection using Lung Breathing Sound

Türker Tuncer¹, Erhan Akbal², Emrah Aydemir^{3*}, Samir Brahim Belhaouari⁴ and Sengul Dogan⁵

¹ Firat University, Department of Digital Forensics Engineering, Elazig, Turkey. (e-mail: turkertuncer@firat.edu.tr).

² Firat University, Department of Digital Forensics Engineering, Elazig, Turkey. (e-mail: erhanakbal@firat.edu.tr).

³ Sakarya University, Department of management information systems, Sakarya, Turkey. (e-mail: emrahaydemir@sakarya.edu.tr).

⁴ Hamad Bin Khalifa University, College of Science and Engineering, Doha, Qatar. (e-mail: sbelhaouari@hbku.edu.qa).

⁵ Firat University, Department of Digital Forensics Engineering, Elazig, Turkey. (e-mail: sdogan@firat.edu.tr).

ARTICLE INFO

Received: Aug., 24. 2021

Revised: Nov., 01. 2021

Accepted: Nov, 19. 2021

Keywords:

Lung breathing sound
present SBox pattern
Covid-19
maximum tent pooling
2 levelled feature selector

Corresponding author: *Emrah Aydemir*

ISSN: 2536-5010 / e-ISSN: 2536-5134

DOI: <https://doi.org/10.36222/ejt.986599>

ABSTRACT

Lung breathing sounds have been used to diagnose many diseases, including Covid-19. Nowadays, Covid-19 has affected daily life worldwide, and it has caused a global pandemic. Generally, computer vision methods have been presented to classify healthy, pneumonia, and Covid-19. They achieved high classification rates on datasets with a limited number of classes without taking into consideration other lung diseases. Our main hypothesis is to detect Covid-19 automatically among other lung diseases by using lung breathing sounds. Therefore, a dataset of lung breathing sound with ten classes has been collected, and a novel lung sounds classification method has been proposed in this paper. This method presents a novel local feature generation technique, and Substitution Box (S-Box) of the present lightweight encryption method is utilized as a pattern. A novel nonlinear pattern is presented based on S-Box, named Present-SBox-Pat (present S-Box pattern). A new pooling-based transformation (maximum tent pooling (MaTP)) is proposed to generate high, middle, and low levels features. It is considered as a preprocessing method of this work. ReliefF and iterative neighbourhood component analysis (RFINCA) selector is used to select the most discriminative and informative features. Two shallow classifiers are used to obtain results. The proposed Present-SBox-Pat and MaTP feature generation network and RFINCA feature selector-based method achieved 95.43% classification accuracy using the SVM classifier. These results demonstrated the success of techniques in generating and selecting features that facilitate the task of classifiers.

1. INTRODUCTION

Many methods/techniques have been presented to detect and cure the Covid-19 in the literature. One of them is machine learning [1, 2]. Machine learning methods have employed to detect Covid-19 automatically. Covid-19 affects the lungs and causes respiratory diseases. Respiratory sounds can provide information about human health to detect these diseases. Doctors and medical professionals also use lung breathing sounds in the diagnosis of many diseases. These are Fine Crackles (Rales), Wheezing (expiratory), Rhonchi, Stridor, Coarse Crackles (Rales), Bronchovesicular, Bronchial, and Coronavirus (COVID-19) [3, 4]. Covid-19 has become a disease that affects unprecedented public health in the world. The main symptoms in patients are cough, difficulty breathing, headache, and fever [5]. The disease exhibits

behaviors similar to bronchitis and pneumonia. Therefore, lung breathing sounds of the patients have listened with a stethoscope, and then CT images are taken, and lung conditions are monitored. Lung and heart injuries are seen on CT images [5]. PCR test is performed to make a definitive diagnosis [6]. Diagnosing Covid-19 patients at an early stage increases the success of the treatment. The use of CT or RT-PCR kits extends diagnosis time [7]. The virus mostly affects the lung in infected patients, and therefore lung breathing sounds can be used to diagnose. Thus, rapid diagnosis and early diagnosis will be provided. Doctors use many different methods to identify and diagnose lung breathing sound features. The simplest and most common method used is the use of a stethoscope [8]. After auscultation of the sounds with a stethoscope, additional examinations are requested. Different factors may cause errors in diagnosing with a stethoscope. These are the

doctor's inability to distinguish between lung sounds, or the ear cannot hear low-frequency sounds. Thus, there are errors in diagnosis. Computer-aided techniques are patient-friendly and economical. It also minimizes errors caused by the human factor and helps the doctor to decide. An automated lung sounds classifier algorithm consists of pretreatment of signals, extraction of features and classification stages.

1.1. MOTIVATION

The widely known lung diseases are asthma, bronchitis, water collection in the chest, shortness of breath, hydatid cyst, pleurisy, tuberculosis, pneumonia, and Covid-19. The purpose of lung testing is to diagnose lung diseases, if possible, to determine their causes and evaluate the degree of severity. Many doctors want to scan lung or pulmonary function tests (PFTs), chest films or CT to examine the oxygen and carbon dioxide levels, to help diagnose and monitor lung function, and the anatomy of the lungs. Covid-19 is a very contagious disease, and many healthcare professionals have been infected. Also, early detection of the Covid-19 disease is crucial like other diseases. Therefore, automated Covid-19 detection systems should be developed to help healthcare professionals, and many X-ray and CT based Covid-19 disease detection methods have been proposed in the literature [9-11]. These methods are machine learning-based methods and used image processing/computer vision methods [12, 13]. However, these methods have been applied to the image datasets with two or three classes dataset. Since they cannot achieve high classification accuracies by using CT or X-ray image datasets with more classes, this paper motivates us to detect Covid-19 disease using lung breathing sounds gathered from stethoscopes. Therefore, we collected a novel lung breathing sound dataset with *ten* classes, and one of these classes is Covid-19. Our other motivations are to develop a novel intelligent lung disease detection method by using an intelligent stethoscope and show the effectiveness of the sound-based ML method to image-based methods.

1.2. LITERATURE REVIEW

Breathing, coughing, sneezing sounds have been used in automatic recognition systems and have a high accurate classification rate [10, 14-17]. In the literature, there are various studies conducted to diagnose artificial intelligence based on lung breathing sounds [18]. It is difficult to decide as a result of listening to the sounds of the lungs using a stethoscope. Analyzing sounds with artificial intelligence algorithms reduces the error rate of misdiagnosis. Therefore, various studies have been conducted in literature. Sankur et al. [19] used samples from 12 healthy 13 respiratory disease patients sound. These sounds are divided into two classes with the autoregression model as normal and abnormal. They obtained a 93.75% accuracy rate with the k-nearest neighbour method. Doyle [18] analyzed 35 patients' breathing sounds to train clinicians. These sounds include crackles, wheezes, pleural friction rub, and stridor. Histograms of sounds were extracted, and obtained signals were analyzed by artificial neural networks. An 83% classification rate was obtained. Lei,

Rahman, and Song [20] placed a microphone close to the mouth and nose of the patients, and breathing sounds were collected from 90 people. The number of healthy people in the dataset is 40, and the number of people with different respiratory disorders such as influenza, pneumonia, and bronchitis is 50. Breathing sounds were recorded for 1 minute in a comfortable position, and analyzes were performed with LSVM, SSVM, MLP, RBF, SOM, LVQ, KNN. The highest classification rate was achieved by 99% using LSVM and LVQ. Shokrollahi et al. [21] collected tracheal sounds of 9 patients. It is aimed to diagnose sleep apnea by segmenting snoring sounds. 95.9% accuracy rate was obtained. Aykanat et al. [3] collected 17930 lung sounds over 1630 people. The sounds were transferred to the computer using a specially developed electronic stethoscope. Rale, rhonchus, and normal sounds were analyzed using Mel frequency cepstral coefficient. CNN and SVM methods achieved an 86% successful classification rate. Huq and Moussavi [22] examined the breathing sounds of 93 individuals without any respiratory distress. They present a method using several breath sound parameters to differentiate between the two respiratory phases. 95.6% accuracy rate was obtained.

Scientists are working hard to facilitate the treatment and diagnosis phase of Covid-19. Therefore, many diagnostic methods based on artificial intelligence have been proposed. Han et al. analyzed the speech sounds of patients diagnosed with COVID-19. Disease severity, sleep quality, fatigue, and anxiety states were categorized with a 69% accuracy rate [23]. Jiang et al. [24] presented a deep learning-based method using thermal cameras and mobile phones. He proposed a device for analyzing respiratory sounds and determining the health of Covid-19. The device can detect with an accuracy of 83.7%. Maghdid et al. [25] proposed a method that uses sensors on the cell phone to diagnose low-cost Covid-19. [26] examined CT images of 108 patients diagnosed with Covid-19 and 86 patients with specific and viral pneumonia diseases. The results of AlexNet, VGG-16, VGG-19, SqueezeNet, GoogleNet, MobileNet-V2, ResNet-18, ResNet-50, ResNet-101 and Xception were compared using images with the diagnosis of Covid-19. As a result, successful classification procedures were performed between 86.27% and 99.51%. Li et al. F. Shi et al. [27] 78 patients who were positive for the Covid-19 test classified them in three groups as mild, normal, and critical. CT images were analyzed using the total severity score method and classified with 95% accuracy. Shi et al. [28] examined CT images of 1027 community-acquired pneumonia patients with 1658 Covid-19 cases. Random Forest method was applied to feature extraction images. 87.9% of successful classification results were obtained. Narin et al. [29] performed chest X-ray images of 50 Covid-19 patients in ResNet50, InceptionV3 and Inception-ResNetV2. As a result of the analysis, 98% accuracy for ResNet50, 97% for InceptionV3 and 87% for Inception-ResNetV2 were obtained.

1.3. OUR METHOD

In this work, we collected a novel lung breathing sound datasets to propose an intelligent hand-crafted feature-based multilevelled feature generation network is suggested to

extract high, middle, and low levels features. A pooling based decomposition method is considered to create levels for multilevel feature generation and improve routing ability of the pooling methods. This method is called as MaTP. The proposed feature generation network uses both textural features (local binary pattern (LBP) like extractor feature) [30] and statistical features [31] together. In the LBP like feature extractors, linear patterns have been used for feature generation. This work uses a nonlinear pattern as feature extractors. S-Box of the present encryption method is considered as a pattern to design this textural feature extractor, and it is named as Present-SBox-Pat. The proposed Present-SBox-Pat and MaTP methods are used together to create a new generation hand-crafted feature generation network. RFINCA feature selector selects the most valuable features automatically. The selected features are utilized as an input of the k nearest neighbours (kNN) [32] and support vector machine (SVM) [33] classifiers, which are the most preferred shallow/conventional classifiers. This method aims to propose a highly accurate and automated breathing sound classification method.

1.4. CONTRIBUTIONS AND NOVELTIES

Novelties and contributions of the proposed Present-SBox-Pat and MaTP stable feature generator and RFINCA feature selector-based lung breathing sound classification method are;

- A new breathing sound dataset was collected from YouTube [34] to create a testbed for the sound classification method. These sounds are publicly published for educational purposes on YouTube. This experimental dataset is created to demonstrate the success of the sound classification method to diagnose lung diseases. Nowadays, Covid-19 is a disease that affects daily life the most. Therefore, this dataset includes Covid-19 breathing sounds.
- S-Boxes are the widely preferred nonlinear components of the symmetric encryption methods, and they have been generally used for substitution. This study uses an S-Box as a feature extractor for the first time as far as we know in the literature.
- Maximum pooling [35] has been widely used in deep learning networks, especially the convolutional neural network. A new improved version of maximum pooling is presented (MaTP) to improve the success of the maximum pooling.
- There are an optimum automated number of features selection problem for ReliefF [36] and NCA [37]. RFINCA method solves this problem and uses the usefulness of both ReliefF and NCA.
- We obtained a highly accurate model for lung breathing sound classification.

2. THE PROPOSED LUNG BREATHING SOUNDS CLASSIFICATION METHOD

This work proposes a new generation ML method to attain a high accurate breathing sound classification method. This method has four fundamental phases, and these are MaTP based preprocessing, feature generation, feature selection, and classification. MaTP method is utilized as

decomposition and level creation method to generate features deeply, and five levelled networks (five levelled networks is the best resulted according to experiments. Therefore, we used five levelled networks). To obtain high, low, and medium levels features, a fused feature generation network is presented by using the created levels by MaTP decomposition. In this network, statistical features and textural features are generated together. *Nineteen* most preferred statistical moments are employed for statistical feature generation. A new extractor is presented to extract textural features, and this method benefits the nonlinear structure of the symmetric ciphers, which is S-Box. Therefore, the S-Box of the present lightweight encryption method [38, 39] is employed as a pattern to show the success of the nonlinear structures in the feature generation. RFINCA method selects the most distinctive/illuminating features for the used classifiers, and these features selected are forwarded to classifiers. Graphical summarization of the proposed Present-SBox-Pat and MaTP based feature generator and RFINCA feature selector-based sound classification method is shown in Fig. 1.



Figure 1. Graphical summarization of the proposed Present-SBox and RFINCA based breathing lung sounds classification method.

Details of the proposed Present-Sbox and RFINCA based methods are clarified in sub-sections.

2.1. PREPROCESSING

The preprocessing phase is the first phase of our method. Maximum pooling is one of the most preferred decomposition and preprocessing methods. Since it is

useful and has low computational complexity, however, it is not a good router because it routes the peaks value of a fixed-sized block. Therefore, we presented a novel maximum pooling, and it is named MaTP. Maximum Tent Pooling (MaTP) is utilized as preprocessing. MaTP is created by using variable pooling methods with variable sized non-overlapping blocks. This work uses *four* maximum pooling with 3,4,5, and 7 sized non-overlapping blocks. Mathematical explanations of the proposed MaTP method are defined in Eqs. 1-9.

$$T_1 = \text{maxpool}(\text{Sound}, 3) \quad (1)$$

$$L_1 = \text{maxpool}(\text{Sound}, 4) \quad (2)$$

$$F_1 = \text{maxpool}(\text{Sound}, 5) \quad (3)$$

$$S_1 = \text{maxpool}(\text{Sound}, 7) \quad (4)$$

$$L_{k+1} = \text{maxpool}(L_k, 4), k = \{1,2,3\} \quad (5)$$

$$T_{h+1} = \text{maxpool}(T_h, 3), h = \{1,2,3,4\} \quad (6)$$

$$F_{h+1} = \text{maxpool}(F_h, 5) \quad (7)$$

$$S_{h+1} = \text{maxpool}(S_h, 7) \quad (8)$$

$$\text{maxpool}(p_1, p_2) = \begin{cases} p_1, & p_1 \geq p_2 \\ p_2, & p_2 > p_1 \end{cases} \quad (9)$$

In Eqs. 1-9, the mathematical definition of the proposed MaTP based preprocessing method is shown. T_k, L_k, F_k and S_k are k^{th} levelled of the maximum pooled sounds with 3, 4, 5, and 7 sized non-overlapping windows respectively. $\text{maxpool}(\dots)$ expresses maximum pooling function, p_1 and p_2 define first and second parameters.

By applying Eqs. 1-9, these pooled (decomposed) signals are calculated, and these decomposed signals and raw sound signal are utilized for feature generation. Details of the proposed feature generation are explained in Section 3.2.

2.2. FEATURE EXTRACTION

We used two feature extraction functions in the proposed feature generation network. These are statistical feature generation and the proposed Present-SBox-Pat based textural feature extraction. The main aim of this feature generation network is to use fused features to use the effectiveness of these functions together.

2.2.1. STATISTICAL FEATURE EXTRACTION

Our first feature extraction function used is statistical features. Statistical feature generation is one of the most useful feature generation methods. Therefore, they have been used for feature generation by researchers. We used 19 statistical moments as feature generation. These moments are shown in 10-28.

$$s1 = \frac{\sum_{i=1}^L \text{sound}_i}{L} \quad (10)$$

$$s2 = \sqrt{\frac{\sum_{i=1}^L (\text{sound}_i - s1)^2}{L}} \quad (11)$$

$$s3 = \sqrt{\frac{\sum_{i=1}^L (\text{sound}_i)^2}{L}} \quad (12)$$

$$s4 = \frac{\sum_{i=1}^L \text{sound}_i}{s3} \log\left(\frac{\text{sound}_i}{s3}\right) \quad (13)$$

$$s5 = \sum_{i=1}^L \frac{i * \text{sound}_i - s1}{\sigma_i} \quad (14)$$

$$s6 = \frac{\sum_{i=1}^L |\text{sound}_{i+1} - \text{sound}_i|}{L} \quad (15)$$

$$s7 = \frac{\sqrt{L(L-1)}}{L-2} \left(\frac{\frac{1}{L} \sum_{i=1}^L (\text{sound}_i - s1)^3}{\frac{1}{L} \sum_{i=1}^L (\text{sound}_i - s1)^2} \right) \quad (16)$$

$$s8 = \frac{L-1}{(L-2)(L-3)} \left[(L \right. \quad (17)$$

$$\left. + 1) \left(\left(\frac{\frac{1}{L} \sum_{i=1}^L (\text{sound}_i - s1)^4}{\frac{1}{L} \sum_{i=1}^L (\text{sound}_i - s1)^2} \right) - 3 \right) + 6 \right]$$

$$s9 = \text{sound} \left(\frac{L}{2} \right) \quad (18)$$

$$s10 = \{\text{sound}\} \quad (19)$$

$$s11 = \max\{\text{sound}\} \quad (20)$$

$$s12 = \frac{s1}{s2} \quad (21)$$

$$s13 = \sqrt{\frac{\sum_{i=1}^L \text{sound}_i^2}{L}} \quad (22)$$

$$s13 = \frac{\sqrt{\frac{1}{L} \sum_{i=1}^L \text{sound}_i^2}}{\frac{1}{L} \sum_{i=1}^L |\text{sound}_i|} \quad (23)$$

$$s15 = \frac{\max |\text{sound}|}{\sqrt{\frac{1}{L} \sum_{i=1}^L \text{sound}_i^2}} \quad (24)$$

$$s16 = \frac{\max |\text{sound}|}{\frac{1}{L} \sum_{i=1}^L \sqrt{|\text{sound}_i|^2}} \quad (25)$$

$$s17 = \frac{\max |\text{sound}|}{\frac{1}{L} \sum_{i=1}^L |\text{sound}_i|} \quad (26)$$

$$s18 = (\max(\text{sound}) - \min(\text{sound})) \quad (27)$$

$$s19 = (\max(\text{sound}) - s1) \quad (28)$$

where sound is the sound signal, L represents the length of the signal.

The procedure of the used statistical feature generation function is shown in Fig. 2.

Procedure: Statistical feature generation: <i>statistical(sound)</i>
Input: Sound signal or decomposed version of it with length of L (<i>signal</i>).
Output: Statistical features (<i>sf</i>) with length of 19
00: Load signal.
01: Apply Eqs. 10-18 to signal and obtain <i>sf</i> .

Figure 2. Statistical feature generation procedure.

2.2.2. THE PROPOSED PRESENT S-BOX BASED FEATURE EXTRACTOR

In this section, a novel textural feature extraction method is presented. This method includes information on both symmetric encryption and feature generation. This method aims to show nonlinear structures on the feature generation.

Therefore, the S-Box of the present encryption method is utilized as a pattern, and the signum function is employed as a binary feature generation method. The used present S-Box is shown in Fig. 3.

x	0	1	2	3	4	5	6	7	8	9	A	B	C	D	E	F
$S[x]$	C	5	6	B	9	0	A	D	3	E	F	8	4	7	1	2

Figure 3. S-Box of the present encryption method.

As seen in Fig. 3, the size of this S-Box is 16, and it has two values. These are the input value (x) and the output value ($S[x]$). Here, we used values indicated by the input values and output values in S-Box for bit generation. The proposed Present-SBox-Pat generates 16 bits in total. These bits are divided into two groups, and each group has 8-bits. These categories are named left and right, respectively. Two map values are generated by using these two categories. Histograms of these maps are concatenated, and feature vector with a size of 512 is obtained. Steps of the proposed Present-SBox-Pat are;

Step 1: Divide the signal into 16 sized overlapping windows.

$$b^i = \text{signal}(i:i + 15), i = \{1, 2, \dots, L - 15\}$$

Step 2: Generate binary features from the block by using b^i and S-Box. The used bit generation function is signum.

$$\text{bit}(k) = \text{Sg} \left(b^i(k + 1), b^i(S(k) + 1) \right), k = \{1, 2, \dots, 16\} \quad (30)$$

$$\text{Sg}(p_1, p_2) = \begin{cases} 0, & p_1 - p_2 < 0 \\ 1, & p_1 - p_2 \geq 0 \end{cases} \quad (31)$$

where $\text{Sg}(\dots)$ expresses signum function.

Step 3: Calculate left and right map values.

$$\text{left}(i) = \sum_{k=1}^8 \text{bit}(k) * 2^{k-1} \quad (32)$$

$$\text{right}(i) = \sum_{k=1}^8 \text{bit}(k + 8) * 2^{k-1} \quad (33)$$

Step 4: Extract histograms of the right and left map values.

$$\text{histogram}^{\text{right}}(j) = 0; j = \{1, 2, \dots, 256\} \quad (34)$$

$$\text{histogram}^{\text{left}}(j) = 0; j = \{1, 2, \dots, 256\} \quad (35)$$

$$\text{histogram}^{\text{right}}(\text{right}(i) + 1) \quad (36)$$

$$= \text{histogram}^{\text{right}}(\text{right}(i) + 1) + 1$$

$$\text{histogram}^{\text{left}}(\text{left}(i) + 1) \quad (37)$$

$$= \text{histogram}^{\text{left}}(\text{left}(i) + 1) + 1$$

Eqs. 34-37 define histogram extraction. Eqs. 34-35 express initial value assignment and Eqs. 36-37 define the histogram generation.

Step 5: Concatenate these histograms to obtain the final feature vector.

$$\text{feat}(j) = \text{histogram}^{\text{right}}(j) \quad (38)$$

$$\text{feat}(j + 256) = \text{histogram}^{\text{left}}(j) \quad (39)$$

where feat is the final feature vector with the size of 512.

These steps (Step 1-5) define the Present-SBox-Pat feature generation procedure.

2.2.3. OVERVIEW OF THE PROPOSED FEATURE GENERATION NETWORK

This work presented a multilevelled and fused features-based feature generation network, as shown in Fig. 1. Our extracted features are divided into three types. These are textural features, statistical features, and statistical features of the textural features. The used statistical feature generation and textural feature generation functions extract 19 and 512 features, respectively. Fig. 4 summarized the feature generation process of this network.

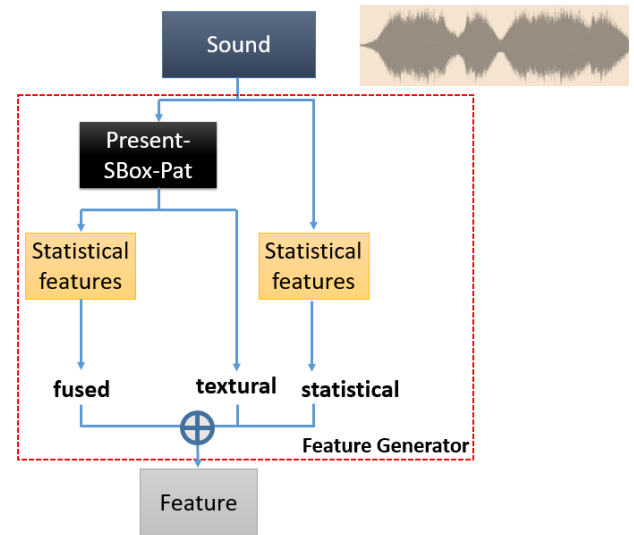


Figure 4. Our presented fused feature generation model.

Steps of our proposed feature generation network are;

Step 1: Extract statistical features of the raw sound signal and decomposed signals by using a statistical feature generation procedure, which is defined in Fig.4.

$$f s^1 = \text{statistical}(\text{Sound}) \quad (40)$$

$$f s^k = \text{statistical}(L_{k-1}), k = \{2, 3, \dots, 5\}, k = k + 4 \quad (41)$$

$$f s^k = \text{statistical}(T_{k-5}), k = \{6, 7, \dots, 10\}, k = k + 5 \quad (42)$$

$$f s^k = \text{statistical}(F_{k-10}), k = \{11, 12, \dots, 15\}, k = k + 5 \quad (43)$$

$$f s^k = \text{statistical}(S_{k-15}), k = \{16, 17, \dots, 20\} \quad (44)$$

Eqs. 40-45 define statistical feature extraction and $f s^k$ is k^{th} statistical feature vector with length of 19. 20

statistical feature vectors are obtained in this step. Therefore, 380 features are generated statistically in total.

Step 2: Extract textural features by using the proposed Present-SBox-Pat.

$$ft^1 = \text{Present} - \text{SBox} - \text{Pat}(\text{Sound}) \quad (45)$$

$$ft^k = \text{Present} - \text{SBox} - \text{Pat}(L_{k-1}), k = \{2,3, \dots, 5\}, k = k + 4 \quad (46)$$

$$ft^k = \text{Present} - \text{SBox} - \text{Pat}(T_{k-5}), k = \{6,7, \dots, 10\}, k = k + 5 \quad (47)$$

$$ft^k = \text{Present} - \text{SBox} - \text{Pat}(F_{k-10}), k = \{11,12, \dots, 15\}, k = k + 5 \quad (48)$$

$$ft^k = \text{Present} - \text{SBox} - \text{Pat}(S_{k-15}), k = \{16,17, \dots, 20\} \quad (49)$$

Eqs. 45-49 define textural feature extraction and ft^k is k^{th} textural feature vector with length of 512. Twenty textural feature vectors are obtained in this step. Therefore, 10240 features are generated texturally in total.

Step 3: Extract the statistical features of the textural features extracted.

$$ff^k = \text{statistical}(ft^k), k = \{1,2, \dots, 20\} \quad (50)$$

Eq. 50 expresses statistical feature extraction of the textural features and ff^k is k^{th} fused feature vector with length of 19. Twenty fused feature vectors are obtained in this step. Therefore, 380 features are generated in total.

Step 4: Concatenate these features and obtain the final feature vector (X) with a size of 11,000.

$$X = \text{concat}(fs^k, ft^k, ff^k), k = \{1,2, \dots, 20\} \quad (51)$$

In Eq. 51, $\text{concat}(\dots)$ expresses concatenation function

ReliefF and Iterative Neighbourhood Component Analysis feature selector: In this phase, a new generation 2-levelled feature selection method is presented, and this method is named as RFINCA. RFINCA uses the effectiveness of both ReliefF and NCA together [40]. ReliefF is used firstly. Since it generates both negative and positive weighted features, and negative weighted features express redundant features. Thus, to eliminate these redundant features, positive weighted feature selection is processed. In the second level of the RFINCA, the NCA feature selector is used. NCA is applied to selected positive weighted features. Then, the iterative NCA feature selection is processed. To calculated errors, each selected feature in this phase, the kNN classifier is chosen. The attributes of the used kNN classifiers are given as follows. k is selected one, and the distance metric is selected as Manhattan distance. The procedure of the RFINCA is shown in Fig. 5.

Procedure: RFINCA(X)	
Input:	Extracted features (X) with size of K .
Output:	Feature vector ($feature$) with size of 289.
00:	Load X
01:	for $i=1$ to K do
02:	$X(:, i) = \frac{X(:, i) - \min(X(:, i))}{\max(X(:, i)) - \min(X(:, i))}$; //Apply min-max normalization to each column
03:	end for i
04:	$ReliefF^{Weights} = ReliefF(X, target)$;
05:	counter = 0
06:	for $i=1$ to K do
07:	if $ReliefF^{Weights}(i) > 0$ then
08:	$f^{ReliefF}(:, counter) = X(:, i)$; // Positive weighted features selection.
09:	counter ++;
10:	end if
11:	end for i
12:	$endex = NCA(f^{ReliefF}, target)$; // Calculate indices of the features by using NCA.
	These indices are ordered indices.
13:	for $k=1$ to 980 do // Apply iterative NCA. Select number of features from 20 to 1000
14:	for $l=1$ to $19+k$ do
15:	$f^{NCA}(:, l) = f^{ReliefF}(:, endex(l))$; // Iterative NCA feature selection process.
16:	end for l
17:	$error(k) = kNN(f^{NCA})$; // Calculate error rates of each selected feature vector.
18:	end for k
19:	$[minimum, index] = \min(error)$;
20:	for $j=1$ to $index + 19$ do // Select optimal features.
21:	$f^{final}(:, i) = f^{ReliefF}(:, endex(j))$;
22:	end for i

Figure 5. The procedure of the RFINCA feature selector.

RFINCA selects 289 the most informative features in this work.

Step 5: Select the most informative features by using RFINCA.

$$f^{final} = RFINCA(X) \quad (52)$$

where f^{final} is final feature.

2.3. CLASSIFICATION

Two shallow classifiers are used to obviously denote high capabilities of the Present-SBox-Pat and MaTP based fused features generation network and RFINCA feature selector. Our fused feature generation network generates 11,000 features, and RFINCA selects 289 the most valuable features from these 11,000 features. kNN and SVM classifiers are chosen to perform the classification process. The kNN used is also considered as an error value calculator. Attributes of the SVM used are given as follows. The kernel function is 3rd-degree polynomial, box constraint value (C) is chosen as one and coding type is selected as one-vs-all [41]. The validation and test strategy is employed as a 10-fold CV. The last step of the proposed Present-SBox-Pat and MaTP based fused features generation network, and RFINCA feature selector is classification, and this step is shown as below.

Step 6: Classify the selected 289 features (f^{final}) by using kNN or SVM classifier.

3. EXPERIMENTAL RESULTS

3.1. COLLECTED DATASET

An experimental sound dataset is used in this work. This dataset uses YouTube breathing sounds videos, and these videos have been published for educational purposes. Therefore, there is no information about patients. This dataset was created by using 68 variable videos to prevent overfitting, and it includes 657 sounds with *ten* classes. The sampling rate of these sounds is 48 kHz. The characteristics of this experimental dataset are shown in Table 1. This dataset can be downloaded by using <https://websiteyonetimi.ahievran.edu.tr/Dosyalar/Genel/RespiratorySounds.rar> URL. It is a public dataset.

TABLE I

Characteristics of the used breathing sound experimental dataset.

ID	Lung breathing sound type	Number of observations	Number of recordings
1	Vesicular	83	7
2	Fine Crackles (Rales)	57	7
3	Wheezing (expiratory)	70	8
4	Rhonchi	72	8
5	Stridor	63	7
6	Coarse Crackles (Rales)	82	7
7	Broncho vesicular	61	8
8	Bronchial	65	5
9	Coronavirus (COVID-19)	29	1
10	Healthy	75	10
Total		657	68

3.2. EXPERIMENTAL SETUP

In Section 3, details of the proposed Present-SBox-Pat and MaTP based fused features generation network, and RFINCA feature selector-based sound classification method was given, and this method consists of preprocessing, feature generation, feature selection, and classification. To realize simulations of this method, MATLAB [42] programming environment was used on a system. This system has 32-GB main memory (RAM), Core i7-7700 (3.20 GHz) microprocessor (CPU). We did not use any graphics card components like GPU cores. MATLAB m files were utilized for coding MaTP preprocessing, feature generation, and feature reduction phases. MATLAB Classification Learner toolbox was considered to obtain results of the classifiers used, which are kNN and SVM. MATLAB source codes of kNN and SVM were generated to obtain more results, and these codes were related codes that were added to these m files.

3.3. RESULTS

Classification Accuracy (*CA*), Unweighted Average Recall (*UAR*), Unweighted Average Precision (*UAP*), F1-score (*F1*) and Geometrical Mean (*GM*) results were used to test the proposed Present-SBox-Pat and MaTP based fused features generation network and RFINCA feature selector based sound classification method comprehensively [43-45]. The number of true positives (*tp*), false positives (*fp*), true negatives (*tn*) and false negatives (*fn*) are employed to calculate these measurements as below.

$$CA = \frac{tp_j + tn_j}{tp_j + tn_j + fp_j + fn_j}, j = \{1, 2, \dots, H\} \quad (53)$$

$$UAR = \frac{1}{H} \sum_{j=1}^H \frac{tp_j}{tp_j + fn_j} \quad (54)$$

$$UAP = \frac{1}{H} \sum_{j=1}^H \frac{tp_j}{tp_j + fp_j} \quad (55)$$

$$F1 = \frac{2 * UAP * UAR}{UAP + UAR} \quad (56)$$

$$GM = \sqrt[H]{\prod_{j=1}^H \frac{tp_j}{tp_j + fp_j}} \quad (57)$$

In Eqs. 53-57, *H* is number of classes.

The results of the used kNN and SVM classifiers were listed in Table 2.

TABLE II

Performances (%) of the used kNN and SVM classifiers.

Performance metric	kNN	SVM
<i>CA</i>	94.98	95.43
<i>UAR</i>	95.04	95.39
<i>UAP</i>	95.08	96.37
<i>F1</i>	95.06	95.86
<i>GM</i>	95.01	95.35

4. DISCUSSIONS AND CONCLUSION

Lung breathing sounds classification is one of the crucial topics for biomedical engineering and machine learning. Covid-19 is a new version of flu, and it causes lung disease. Nowadays, we have lived quarantine days of Covid-19. Therefore, proposing of automated Covid-19 disease detection methods is very important. Our main aim is to detect Covid-19 by using breathing sounds. However, there is no public breathing sound dataset includes Covid-19. Therefore, we collected an experimental breathing sound dataset. This dataset contains 657 breathing sound with *ten* classes (9 lung diseases and one healthy). An innovative hand-crafted features-based lung breathing sounds classification method for automated diagnosing lung diseases is presented in this work. We motivated to solve three problems, and these problems are to propose appropriate and effective preprocessing, feature generation, and feature selection methods. Therefore, a novel MaTP decomposition method is presented as preprocessing to improve the capability of the pooling-based decomposition methods. In the second phase, we combined structures of textural feature generation and symmetric encryption methods. S-Box of the present ultra-lightweight encryption method is utilized as a pattern for textural feature generation. Statistical features and statistical features of the extracted textural features were also used to obtain a comprehensive feature set. By using these methods, a novel fused feature generation network has been presented. RFINCA feature selector is employed to the extracted features, and it selected 289 most informative features. Two shallow classifiers were used to denote the classification capability of the extracted and selected features. 94.98% and 95.43% classification accuracies were achieved by

using kNN and SVM classifiers, respectively. Confusion matrices of these classifiers were also shown in Fig. 6 for apparent evaluation.

True Class	1	78	1	1	2	0	0	0	1	0	0
	2	0	53	1	0	0	2	1	0	0	0
	3	0	4	64	0	0	1	0	0	0	1
	4	0	1	1	67	0	1	1	0	0	1
	5	0	0	0	1	61	0	1	0	0	0
	6	0	3	0	0	0	79	0	0	0	0
	7	0	0	0	0	0	0	59	1	1	0
	8	3	0	0	0	0	0	1	61	0	0
	9	0	0	0	1	0	0	0	0	28	0
	10	0	0	0	1	0	0	0	0	0	74
	1	2	3	4	5	6	7	8	9	10	
Predicted Class											

(a) kNN

True Class	1	80	1	1	0	0	0	0	1	0	0
	2	1	51	0	0	0	3	2	0	0	0
	3	4	1	65	0	0	0	0	0	0	0
	4	2	0	0	69	0	1	0	0	0	0
	5	1	0	0	0	62	0	0	0	0	0
	6	4	0	0	0	0	78	0	0	0	0
	7	1	1	0	0	0	0	59	0	0	0
	8	3	0	1	0	0	0	0	61	0	0
	9	1	0	0	0	0	0	0	0	28	0
	10	1	0	0	0	0	0	0	0	0	74
	1	2	3	4	5	6	7	8	9	10	
Predicted Class											

(b) SVM

Figure 6. The calculated confusion matrices (a) kNN (b) SVM.

Fig. 6 evidently denotes the success rates of each class. The 9th class is Covid-19, and both classifiers achieved 96.55% classification accuracy for Covid-19 detection. Sharma et al [46] also used breathing and cough sounds for the diagnosis of Covid-19 and achieved 66.74% accuracy rate. On the other hand, Mugili et al [47] obtained the highest 75.17% AUC value from the speech voice by using different methods. In another study, detection was made from the sound of breathing with an accuracy rate of 80% [48]. In another article that tried to detect the presence of Covid-19 from respiratory sounds in binary, 80% AUC was obtained [49]. A cumulative accuracy of 99.8% was obtained using cough sounds collected from patients in Pakistan [50]. In this study, it is thought that only binary classification has an effect on obtaining a high success rate. In this study, 10 different diseases are detected. In another study conducted by analyzing respiratory sounds obtained over the phone, it was tried to determine whether there was Covid-19 by binary classification and 94.96% specificity was obtained [51]. Although this study has obtained values close to our study, it is thought the fact that it has made a binary classification is an issue that increases the success.

Overall, significant benefits of the proposed Present-SBox-Pat and MaTP based fused features generation network and RFINCA feature selector based sound classification method are;

- A novel experimental lung disease dataset was collected and published publicly.
- This work denoted the success of Covid-19 detection by using breathing sounds.
- A novel S-Box based feature generator was presented, and the proposed feature generator is shown the effectiveness of the S-Box for textural feature generation.
- A new maximum pooling-based decomposition method (MaTP) was proposed to extract high, medium, and low levels features.
- The proposed feature generation network used the effectiveness of both textural features and statistical features.
- The optimal distinguished feature selection problem was solved by using RFINCA.
- This method achieved high classification accuracies by using two conventional classifiers (see Table 2).
- The proposed method is a general ML method for one-dimensional data. Other one-dimensional data classification problems can be solved by using this method.
- The proposed lung sound classification method can run on a basic system with straightforward configurations.
- An intelligent lung disease monitoring system or stethoscope can be designed by using this method. Overall, the disadvantages of this work are;
- The proposed Present-SBox-Pat and MaTP based fused features generation network and RFINCA feature selector-based sound classification method was tested on an experimental dataset. It can be tested on real, and more significant lung sounds datasets when they publicly published.
- The time complexity of RFINCA is high. Therefore, we used kNN (it is one of the fastest classifiers) as a loss calculator. Novel and more effective feature selectors can be used to select optimal number of features.

REFERENCES

- [1] C. B. Kaya and K. Ebubekir, "A Novel Approach Based to Neural Network and Flower Pollination Algorithm to Predict Number of COVID-19 Cases," *Balkan Journal of Electrical and Computer Engineering*, vol. 9, no. 4, pp. 327-336, 2021.
- [2] L. GÖKREM and M. ALTINDAŞ, "ENVIRONMENTAL NOISE TRACKING SYSTEM BASED ON WEB OF THINGS," *European Journal of Technique (EJT)*, vol. 9, no. 2, pp. 175-185, 2019.
- [3] M. Aykanat, Ö. Kılıç, B. Kurt, and S. Saryal, "Classification of lung sounds using convolutional neural networks," *EURASIP Journal on Image and Video Processing*, vol. 2017, no. 1, p. 65, 2017.
- [4] U. Ozkaya, S. Ozturk, and M. Barstugan, "Coronavirus (COVID-19) Classification using Deep Features Fusion and Ranking Technique," *arXiv preprint arXiv:2004.03698*, 2020.
- [5] C. Huang *et al.*, "Clinical features of patients infected with 2019 novel coronavirus in Wuhan, China," *The lancet*, vol. 395, no. 10223, pp. 497-506, 2020.
- [6] L. Lan *et al.*, "Positive RT-PCR test results in patients recovered from COVID-19," *Jama*, vol. 323, no. 15, pp. 1502-1503, 2020.
- [7] T. Ai *et al.*, "Correlation of chest CT and RT-PCR testing in coronavirus disease 2019 (COVID-19) in China: a report of 1014 cases," *Radiology*, p. 200642, 2020.
- [8] H. Pasterkamp, S. S. Kraman, and G. R. Wodicka, "Respiratory sounds: advances beyond the stethoscope," *American journal of respiratory and critical care medicine*, vol. 156, no. 3, pp. 974-987, 1997.

- [9] J. Zhang, Y. Xie, Y. Li, C. Shen, and Y. Xia, "Covid-19 screening on chest x-ray images using deep learning based anomaly detection," *arXiv preprint arXiv:2003.12338*, 2020.
- [10] S. Amiriparian *et al.*, "CAST a database: Rapid targeted large-scale big data acquisition via small-world modelling of social media platforms," in *2017 Seventh International Conference on Affective Computing and Intelligent Interaction (ACII)*, 2017: IEEE, pp. 340-345.
- [11] M. Li *et al.*, "Coronavirus disease (COVID-19): spectrum of CT findings and temporal progression of the disease," *Academic radiology*, 2020.
- [12] A. Alimadadi, S. Aryal, I. Manandhar, P. B. Munroe, B. Joe, and X. Cheng, "Artificial intelligence and machine learning to fight COVID-19," ed: American Physiological Society Bethesda, MD, 2020.
- [13] M. Barstugan, U. Ozkaya, and S. Ozturk, "Coronavirus (covid-19) classification using ct images by machine learning methods," *arXiv preprint arXiv:2003.09424*, 2020.
- [14] Z. Dokur, "Respiratory sound classification by using an incremental supervised neural network," *Pattern Analysis and Applications*, vol. 12, no. 4, p. 309, 2009.
- [15] R. X. A. Pramono, S. Bowyer, and E. Rodriguez-Villegas, "Automatic adventitious respiratory sound analysis: A systematic review," *PloS one*, vol. 12, no. 5, 2017.
- [16] J. Schröder, J. Anemillier, and S. Goetze, "Classification of human cough signals using spectro-temporal Gabor filterbank features," in *2016 IEEE International Conference on Acoustics, Speech and Signal Processing (ICASSP)*, 2016: IEEE, pp. 6455-6459.
- [17] Z. Moussavi, A. Yadollahi, and S. Camorlinga, "Breathing sound analysis for detection of sleep apnea/popnea events," ed: Google Patents, 2009.
- [18] M. S. Doyle, "Analysis of lung sounds using neural networks," Vanderbilt University, 1994.
- [19] B. Sankur, Y. P. Kahya, E. Ç. Güler, and T. Engin, "Comparison of AR-based algorithms for respiratory sounds classification," *Computers in Biology and Medicine*, vol. 24, no. 1, pp. 67-76, 1994.
- [20] B. Lei, S. A. Rahman, and I. Song, "Content-based classification of breath sound with enhanced features," *Neurocomputing*, vol. 141, pp. 139-147, 2014.
- [21] M. Shokrollahi, S. Saha, P. Hadi, F. Rudzicz, and A. Yadollahi, "Snoring sound classification from respiratory signal," in *2016 38th Annual International Conference of the IEEE Engineering in Medicine and Biology Society (EMBC)*, 2016: IEEE, pp. 3215-3218.
- [22] S. Huq and Z. Moussavi, "Acoustic breath-phase detection using tracheal breath sounds," *Medical & biological engineering & computing*, vol. 50, no. 3, pp. 297-308, 2012.
- [23] J. Han *et al.*, "An Early Study on Intelligent Analysis of Speech under COVID-19: Severity, Sleep Quality, Fatigue, and Anxiety," *arXiv preprint arXiv:2005.00096*, 2020.
- [24] Z. Jiang *et al.*, "Combining Visible Light and Infrared Imaging for Efficient Detection of Respiratory Infections such as COVID-19 on Portable Device," *arXiv preprint arXiv:2004.06912*, 2020.
- [25] H. S. Maghdid, K. Z. Ghafoor, A. S. Sadiq, K. Curran, and K. Rabie, "A novel AI-enabled framework to diagnose Coronavirus COVID 19 using smartphone embedded sensors: Design study," *arXiv preprint arXiv:2003.07434*, 2020.
- [26] A. A. Ardakani, A. R. Kanafi, U. R. Acharya, N. Khadem, and A. Mohammadi, "Application of deep learning technique to manage COVID-19 in routine clinical practice using CT images: Results of 10 convolutional neural networks," *Computers in Biology and Medicine*, p. 103795, 2020.
- [27] K. Li *et al.*, "CT image visual quantitative evaluation and clinical classification of coronavirus disease (COVID-19)," *European Radiology*, pp. 1-10, 2020.
- [28] F. Shi *et al.*, "Large-scale screening of covid-19 from community acquired pneumonia using infection size-aware classification," *arXiv preprint arXiv:2003.09860*, 2020.
- [29] A. Narin, C. Kaya, and Z. Pamuk, "Automatic detection of coronavirus disease (covid-19) using x-ray images and deep convolutional neural networks," *arXiv preprint arXiv:2003.10849*, 2020.
- [30] T. Ahonen, A. Hadid, and M. Pietikainen, "Face description with local binary patterns: Application to face recognition," *IEEE transactions on pattern analysis and machine intelligence*, vol. 28, no. 12, pp. 2037-2041, 2006.
- [31] M. Elangovan, N. Sakthivel, S. Saravanamurugan, B. B. Nair, and V. Sugumaran, "Machine learning approach to the prediction of surface roughness using statistical features of vibration signal acquired in turning," *Procedia Computer Science*, vol. 50, pp. 282-288, 2015.
- [32] S. A. Dudani, "The distance-weighted k-nearest-neighbor rule," *IEEE Transactions on Systems, Man, and Cybernetics*, no. 4, pp. 325-327, 1976.
- [33] J. A. Suykens and J. Vandewalle, "Least squares support vector machine classifiers," *Neural processing letters*, vol. 9, no. 3, pp. 293-300, 1999.
- [34] YouTube, 11.05.2020. [Online]. Available: www.youtube.com.
- [35] D. Scherer, A. Müller, and S. Behnke, "Evaluation of pooling operations in convolutional architectures for object recognition," in *International conference on artificial neural networks*, 2010: Springer, pp. 92-101.
- [36] I. Belakhdar, W. Kaaniche, R. Djemal, and B. Ouni, "Single-channel-based automatic drowsiness detection architecture with a reduced number of EEG features," *Microprocessors and Microsystems*, vol. 58, pp. 13-23, 2018.
- [37] C. Qin, S. Song, G. Huang, and L. Zhu, "Unsupervised neighborhood component analysis for clustering," *Neurocomputing*, vol. 168, pp. 609-617, 2015.
- [38] A. Bogdanov *et al.*, "PRESENT: An ultra-lightweight block cipher," in *International Workshop on Cryptographic Hardware and Embedded Systems*, 2007: Springer, pp. 450-466.
- [39] V. Nandan and R. G. S. Rao, "Minimization of digital logic gates and ultra-low power AES encryption core in 180CMOS technology," *Microprocessors and Microsystems*, vol. 74, p. 103000, 2020.
- [40] T. Tuncer and F. Ertam, "Neighborhood component analysis and reliefF based survival recognition methods for Hepatocellular carcinoma," *Physica A: Statistical Mechanics and its Applications*, vol. 540, p. 123143, 2020.
- [41] U. Jain, K. Nathani, N. Ruban, A. N. J. Raj, Z. Zhuang, and V. G. Mahesh, "Cubic SVM Classifier Based Feature Extraction and Emotion Detection from Speech Signals," in *2018 International Conference on Sensor Networks and Signal Processing (SNSP)*, 2018: IEEE, pp. 386-391.
- [42] D. J. Higham and N. J. Higham, *MATLAB guide*. SIAM, 2016.
- [43] A. Rosenberg, "Classifying skewed data: Importance weighting to optimize average recall," in *Thirteenth Annual Conference of the International Speech Communication Association*, 2012.
- [44] T. Tuncer, S. Dogan, P. Plawiak, and U. R. Acharya, "Automated arrhythmia detection using novel hexadecimal local pattern and multilevel wavelet transform with ECG signals," *Knowledge-Based Systems*, vol. 186, p. 104923, 2019.
- [45] S. D. Kumar, S. Esakkirajan, S. Bama, and B. Keerthiveena, "A Microcontroller based Machine Vision Approach for Tomato Grading and Sorting using SVM Classifier," *Microprocessors and Microsystems*, p. 103090, 2020.
- [46] N. Sharma *et al.*, "Coswara--A Database of Breathing, Cough, and Voice Sounds for COVID-19 Diagnosis," *arXiv preprint arXiv:2005.10548*, 2020.
- [47] A. Muguli *et al.*, "DiCOVA Challenge: Dataset, task, and baseline system for COVID-19 diagnosis using acoustics," *arXiv preprint arXiv:2103.09148*, 2021.
- [48] U. Sait *et al.*, "A deep-learning based multimodal system for Covid-19 diagnosis using breathing sounds and chest X-ray images," *Applied Soft Computing*, p. 107522, 2021.
- [49] C. Brown *et al.*, "Exploring automatic diagnosis of COVID-19 from crowdsourced respiratory sound data," *arXiv preprint arXiv:2006.05919*, 2020.
- [50] M. U. Khan, S. Ali, K. Habib, H. Khan, F. Tariq, and S. Bibi, "A Novel Intelligent Model For COVID-19 Detection Using Cough Auscultations and Hjorth Descriptors," in *ICAME21, International Conference on Advances in Mechanical Engineering, Pakistan*, 2021, pp. 1-10.
- [51] M. Alkhodari and A. Khandoker, "Detection of COVID-19 in smartphone-based breathing recordings using CNN-BiLSTM: a pre-screening deep learning tool," *medRxiv*, 2021.

BIOGRAPHIES

Turker Tuncer, was born in Elazig, Turkey in 1986. He received the B.S. degree from the Firat University, Technical Education Faculty, Department of Electronics and Computer Education in 2009, M.S. degree in telecommunication science from the Firat University in 2011 and Ph.D. degree department of software engineering at Firat University in 2016. He works as research assistant Digital Forensic Engineering, Firat University. His research interests include data hiding, image authentication,

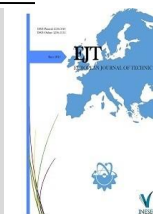
cryptanalysis, cryptography, feature extraction, machine learning and biomedical engineering.

Erhan AKBAL is currently working as an assistant professor at Digital Forensics Engineering Department of Firat University. He received his Ph.D. degree in electrical and electronics engineering in 2012, the M.S. degree in computer engineering in 2007, from Firat University, Turkey. His research interests include computer network security, wireless sensor network, intrusion detection and digital forensics.

Emrah Aydemir received the M.S. degrees in computer teaching from the University of Elazig Firat, in 2012 and the Ph.D. degree in informatics from Istanbul University, Turkey, TR, in 2017. From 2012 to 2015, he was an Expert with the Istanbul Commerce University. Since 2017, he has been an Associate Professor with the Sakarya University. He is the author of three books, more than 10 articles, and more than 40 conference presentation. His research interests include artificial intelligence, microcontroller, database and software.

Samir Brahim Belhaouari received the master's degree in telecommunications and network from the Institute National Polytechnique of Toulouse, France, in 2000, and the Ph.D. degree in mathematics from the Federal Polytechnic School of Lausanne-Switzerland, in 2006. He is currently an Associate Professor with the University of Hamad Bin Khalifa, Qatar foundation, in the Division of Information and Communication Technologies, College of Science and Engineering, HBKU. During last years, he also holds several Research and Teaching positions at Innopolis University-Russia, Alfaisal University-Saudi Arabia, the University of Sharjah-UAE, University Technology PETRONAS- Malaysia, and the EPFL Federal Swiss School-Switzerland. His research interests include vary areas from applied mathematics, statistics, and data analysis until artificial intelligence, image and signal processing (biomedical, bioinformatics, forecasting, etc.), due to both Mathematics and Computer Science backgrounds.

Sengul Dogan received the master's degree in bioengineering the Ph.D. degree in electrical and electronics engineering from the Firat University, Elazig, Turkey, in 2007 and 2011, respectively. She is currently an Associate Professor with the Digital Forensics Engineering, Technology Faculty, Firat University. Her main research interests include computer forensics, mobile forensics, image processing, and signal processing. She has been working actively on developing algorithms in machine learning for biomedical data.



Investigation of the Effects of Use of GNP and GNP Reinforced Nano-Fibers with Epoxy Adhesive on Tension Tests

Edip Çetkin^{1*}

^{1*} Batman University, Electricity and Energy Department, Batman, Turkey. (edip.cetkin@batman.edu.tr).

ARTICLE INFO

Received: Jun., 25. 2021

Revised: Oct., 04. 2021

Accepted: Oct, 13. 2021

Keywords:

Adhesive

GNP

Hybrid joining

Nano-Fiber

Corresponding author: *Edip Çetkin*

ISSN: 2536-5010 / e-ISSN: 2536-5134

DOI: <https://doi.org/10.36222/ejt.957654>

ABSTRACT

In this study, the effects of different ratios graphene nanoparticles (GNP) and Nanofibers were investigated on bonding joints. For this, AA5754 alloy samples were bonded by DP460 adhesive to different ratios of graphene nanoparticle (GNP) and Nanofibers. Reinforcement ratios were chosen as 0.1% wt., 0.2% wt., and 0.3% wt. Adherent samples of 75x30x3 mm and patches of 40x30 mm were used, which cut from AA5754 alloy plate. Tensile tests of samples were conducted to see the effects of each parameter on the bonding joints after the bonding process. After tension tests, macrostructure and SEM images of the rupture surfaces were taken. Tensile test results, the best tensile damage load has been obtained in bonding joints where Nanofiber has been used together with 0.2% wt GNP. In addition, it has been observed that CHZ + Fiber + CHZ and AHZ + CHZ structures seen in macrostructure images have positive effects on tensile test results.

1. INTRODUCTION

The method of joining by the adhesive is widely used because it offers significant advantages in many technological fields such as aviation, construction, automotive, and marine. However, there may be many problems due to some disadvantages as well as the advantages obtained in adhesive bonding methods. One of these problems is the occurrence of stress intensities at the edges of adhesive joints. There are different methods to reduce these stresses, such as thinned the bonding tip, created an adhesive radius, changing the overlap geometry, and hybrid double overlap [1-9]. Marannano et al. [5] were carried out a studying to experimentally and numerically test the mechanical behavior of hybrid bonded/riveted joints. As a result of the experiments, static and fatigue values were respectively obtained 20% and 45% higher in the hybrid joints type created using rivet in bonding joints. Various techniques have been tried to establish a hybrid joining type in adhesive bonded joints and obtain a more robust structure at the same time. One of them is the joining made by adding nano-particles into the epoxy adhesive. Gültekin et al. examined the impacts of nano-graphene powder reinforcement on epoxy bonding bonds. According to their results, nano-graphene reinforcement has a significant effect on adhesive joints [10]. Akpınar et al. investigated the effects of 0.25% wt., 0.5% wt., 1% wt., 2% wt., and 3% wt. Nano-graphene-COOH, Carbon Nanotube-COOH, and Fullerene C60 supplements on single lap bonded joints. They stated that the reinforcements used in different rates have different effects on the adhesive

bonded joints based on the mixing ratio and the type of reinforcement. In addition, they were indicated the best recuperation was obtained from 1% wt. of Fullerene C60 supplement [11]. Jia et al. tried to determine the effect of graphene nanoplatelets-reinforced adhesive on the Mode I fracture resistance in double cantilever beam joints. They stated that 0.25% wt. graphene nanoplatelets reinforcement has a strength of 5 times higher than the pure epoxy adhesive on the breaking resistance of the joints. They also have emphasized that as the graphene nanoplatelets ratio increased, the toughness of the joints decreased [12]. Moriche et al. endeavored to determine the impacts of GNP/epoxy nanocomposite adhesives on thermal conductivity and shear resistance. They stated that thermal conductivity increased by 206% and 306% respectively as a result of adding 8% and 10% graphene nanoplatelets into the epoxy adhesive. They also expressed that there was no clear effect on shear resistance [13]. Khoramishad et al. investigated the effect of temperature on graphene oxide nano-platelet reinforced nanocomposite adhesive joints. They stated at the end of the experiments performed on 1% wt. and 3% wt. graphene oxide nano-platelet supplements that the critical temperature of the 1% reinforcement ratio was 60 °C and the critical temperature of 3% wt. reinforcement ratio was 40°C [14]. Sadigh and Marami investigated the tensile and compressive stresses of the joints made at different extension ratios with reduced graphene oxide (RGO) reinforcement into the epoxy adhesive, experimentally and numerically. In the joints made with 0.5% reduced graphene oxide reinforcement, the tensile and compressive

stresses were 30% and 26% better, respectively, compared to the pure epoxy connections. They stated that successful results were obtained when the experimental and numerical results were compared. [15].

When the literature studies were examined, many studies have been conducted on the use of adhesive materials with various nanoparticles. However, it has not been seen that Nano-Fiber as an interlayer has been used in any study. In this study, Nano-Fibers produced with 1% wt. GNP reinforcement by Electro-spinning method were used as an intermediate layer in order to investigate this situation. In addition, adhesions were made with DP460 adhesive and an adhesive mixture prepared with 0.1% wt., 0.2% wt., and 0.3% wt. GNP reinforcement to this adhesive. After the bonding process, the samples were subjected to tensile tests in order to see the effects of each parameter on the bonding strength. Finally, after the tensile tests, the macrostructure and microstructure examinations of the separated surfaces were made.

2. EXPERIMENTAL PROCESSES

In this study, the adherent material was used the AA5754 aluminum alloy, which provides spectacular performance in extreme areas of use. It has a high resistance to seawater and industrial chemicals. AA5754 aluminum alloy has a high weldability and fatigue strength; it resists seawater corrosion and has good cold workability in soft temper form. Because of these properties, it is widely used in the shipbuilding industry, chemical devices, storage tanks, pressure vessels, folding bridges, welded truck bodies, military vehicle bodies, and armors [16]. In Figure 1, it was given the stress-strain graphic of AA5754 alloy [17]. DP460 was utilized as the adhesive material. This material has two components as epoxy and intensifier electrode (accelerator). The adhesive displays high resistance when the epoxy/accelerator ratio is 2/1. Special holozoic ends were used to provide this ratio. Figure 2 shows the stress-strain graphic of DP460 adhesive material. In this study, which used the adhesive bonding technique, Nano graphene particle reinforced nano-fibers produced by electro-spinning method and Nano Graphene particles (GNP) adding to DP460 adhesive were used to obtain a better bond strength in bonding joints. Nano graphene particle thickness is 5-8 nm; diameter was 5 μm ; the surface area is 120-150 m^2/g ; purity was 99% and density is 0.05 g/cm^3 . Figure 3 shows the macro and micro images of graphene used in the experimental study.

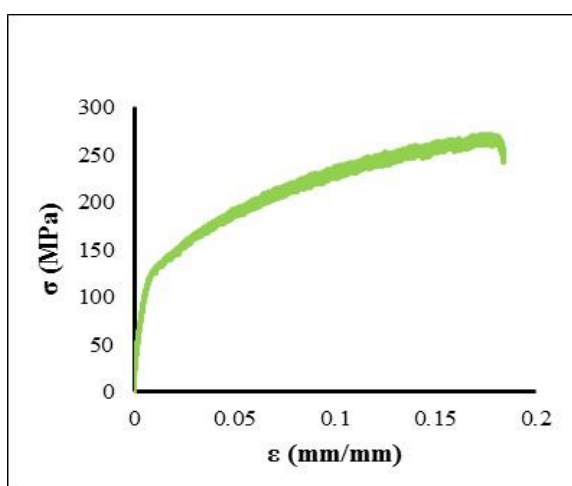


Figure 1. Stress-strain graphic of AA5754 material

TABLE 1
AA5754 MECHANIC PROPERTIES

Elastic Modulus	78.586GPa
Slip Modulus	25.9GPa
Poisson's Ratio	0.324
Yield Strength	140 MPa
Tensile Strength	272.0561MPa

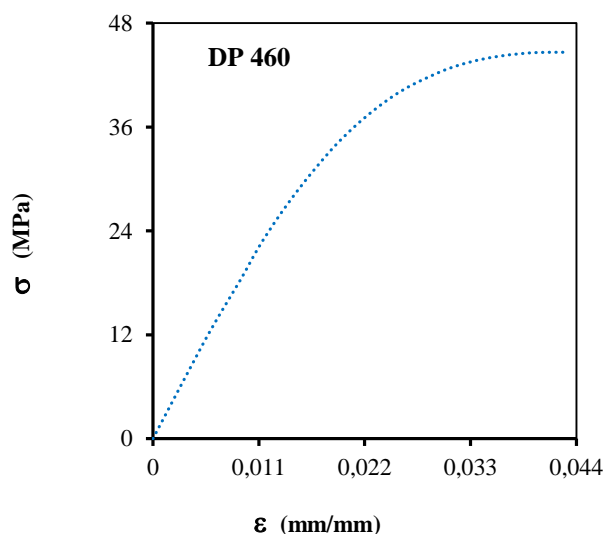


Figure 2. Stress-strain graphic of DP460 material

TABLE 2
DP460 MECHANIC PROPERTIES

Elastic Modulus	2077.1 MPa
Poisson's Ratio	0.38
Tensile Strength	44.616 MPa

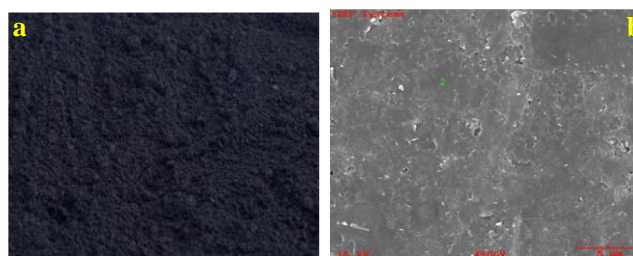


Figure 3. Macro and SEM images of the graphene particle used in the experimental study (a-Macro; b-Micro)

2.1. Preparing double patched test samples

First of all, in this study, the AA5754 aluminum plate of 3 mm thick, 2000 mm long, and 1000 mm wide was provided for the bonding process. The aluminum plate in 2000x1000x3 mm dimensions was cut into samples of 30 mm width and 75 mm length for experimental study. Similarly, the parts that were utilized as patches in the bonding process were cut from the AA5754 aluminum alloy plate in 40x30x3 mm dimensions. In the final processings of the experiment samples, the preparation of the region where the bonding process could be performed was. For this, the regions to be contacted with the adhesive were cleaned with 100-sized sandpaper. After the cleaning process, it was kept in acetone for 10 minutes. After acetone treatment, samples and patches were cleaned with water and left to dry. In Figure 4, an image of the sample and patches used in the bonding process is given.

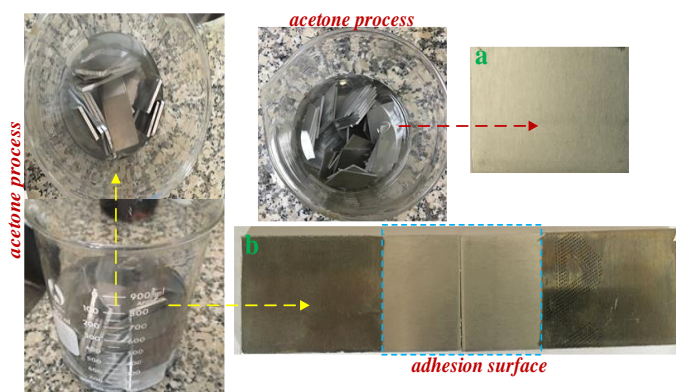


Figure 4. Preparation of sample and patch used in bonding (a- Patch sample b- Adherent sample)

2.2. Preparation of neat and graphene reinforced adhesives

The bonding process was started after the process of preparation of samples. Firstly, the bonding process was done using DP460 adhesive. Figure 5, shows DP460 adhesive and the equipment used in bonding with graphene reinforced. All these types of equipments were obtained from 3M Company. After the bonding process using DP460 adhesive, nano-sized graphene particles were added to the DP460 adhesive at the rates of 0.1% wt., 0.2% wt. and 0.3% wt., and bonding was carried out. A homogeneous mixture was obtained by using an ultrasonic mixer to obtain a good adhesion from graphene particles added in different proportions in DP460 adhesive. It was mixed DP460 adhesive and nano-sized graphene particles in an ultrasonic mixer for 15 minutes and 30 Hz at room temperature conditions for this process (Figure 6).



Figure 5. Equipment used in the bonding processing

2.3. Preparing nanofibers with graphene reinforced

1% Graphene reinforced nanofibers were used as an intermediate layer between DP460 adhesive and AA5754 aluminum sample and the same material-based patch piece in the experimental study. The electro-spinning method was used for the production of graphene reinforced nanofibers used in this study. The electro-spinning test device consists of three parts. Related parts are the polymer solution supply system, high voltage power supply, and cylindrical collector (Figure 7).

Commercially available Polyvinyl butyral (PVB) polymer, hardener Tetraethyl orthosilicate (TEOS), and ethanol were used to produce nanofibers in the electro-spinning method. Molecular weight and melting temperature vary between 165-185°C in PVB 40000-70000 g/mol. These properties are important. Because the solution, which significantly affects the structural and morphological properties of nanofibers, must be prepared based on these properties.

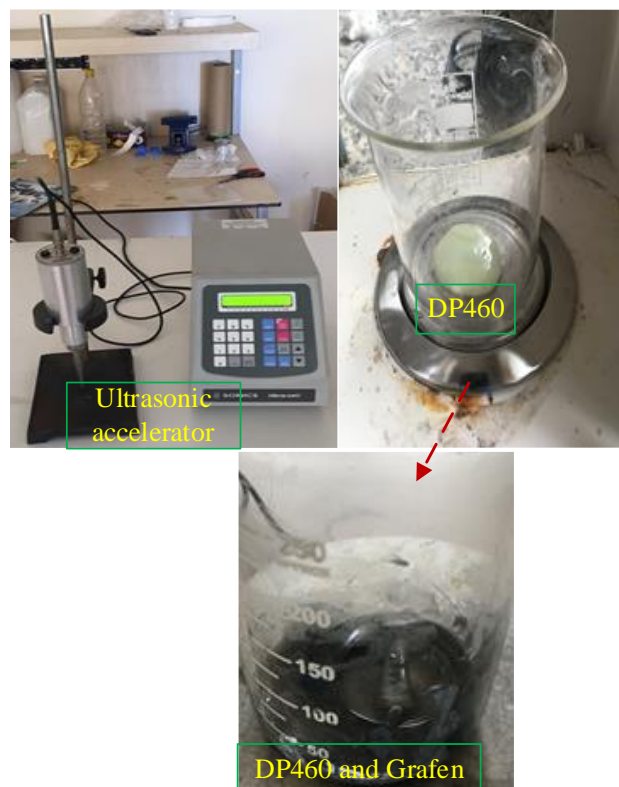


Figure 6. The ultrasonic mixing process of DP460 and Graphene

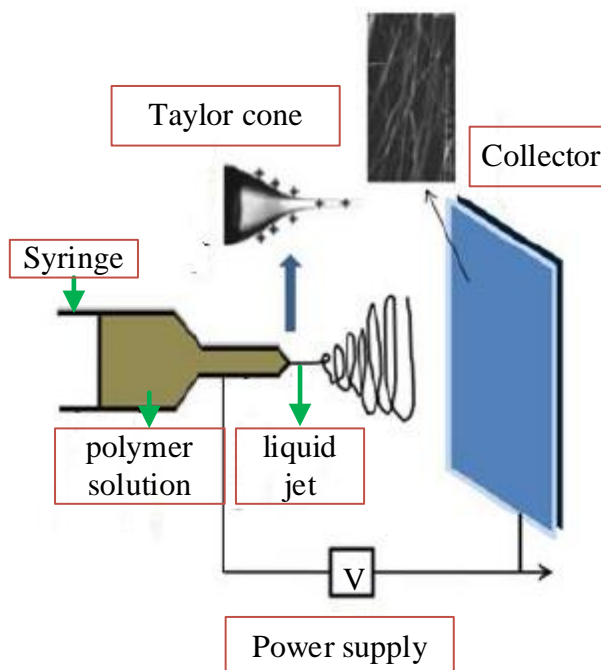


Figure 7. Electro-spin Device Schematic View [17]

PVB polymer was mixed with a magnetic stirrer for 4 hours at 50 °C in ethanol with a ratio of 10% by weight [18, 19] in the solution preparation process. In this mixing process, 50% TEOS was added according to the amount of polymer and the mixture was mixed until it became homogeneous and stable. Graphene nanoparticles were mixed in ethanol for 10 minutes at low frequencies (15 kHz) with the help of an ultrasonic probe to be homogeneous. Then, solutions were prepared by adding PVB polymer and TEOS so that the GNP ratio in the mixture was 1% wt. It was transferred into a sterile syringe and placed on the automatic syringe pump after the solution was prepared. The distance between the collector and the metallic needle tip was arranged so as to be 15 cm. It was chosen a cylindrical mandrel as a collector and aluminum foil was wrapped on it to collect nanofibers in terms of ensuring homogeneity. The speed of the cylindrical mandrel was 400 rpm while nanofibers were collected. The prepared nanofibers were left to dry in the drying oven at 40 °C for 30 minutes. Figure 8 shows the processes of nanofiber production; Figure 9 shows produced nanofiber.

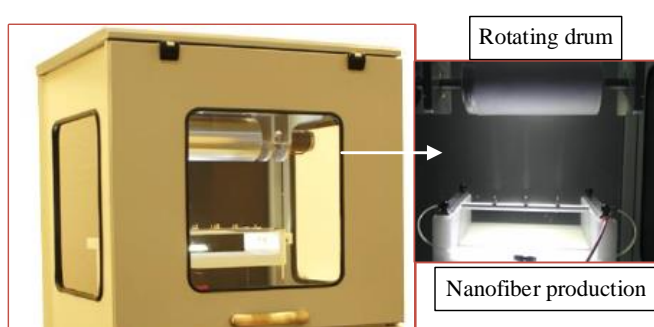


Figure 8. Schematic picture showing the electrospinning process; the image of Nano-Fibers produced with a multi-needle tip

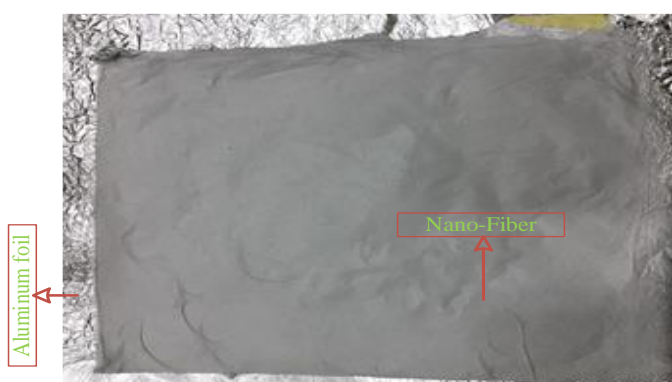


Figure 9. Nano-fiber, which particle reinforced

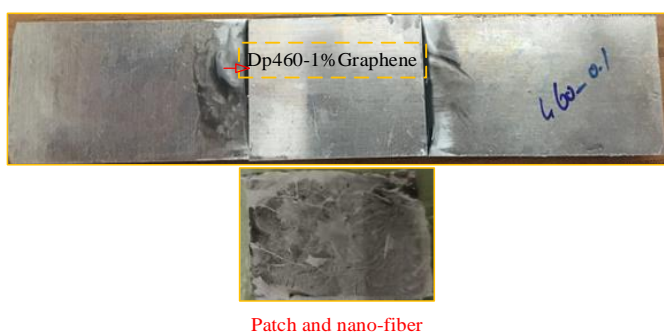


Figure 10. Nano-fiber and 1% wt. GNP reinforced bonding process

2.4 Bonding processing and tensile tests

It was performed tensile tests after the specimens were carried out bonding process (Figure 10). Tensile tests were carried out in SHIMADZU AG-IC brand tensile tester with 250 KN capacity at a constant feed rate of 1mm/min (Figure 11). In the tensile test repeated 3 times for each parameter, the average tensile force was determined and the margin of error was minimized. Then, force-elongation curves were obtained by using these values.

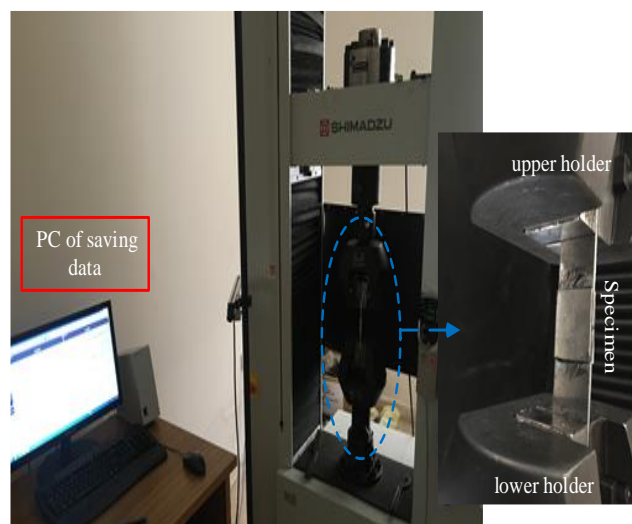


Figure 11. Tensile experiment processes

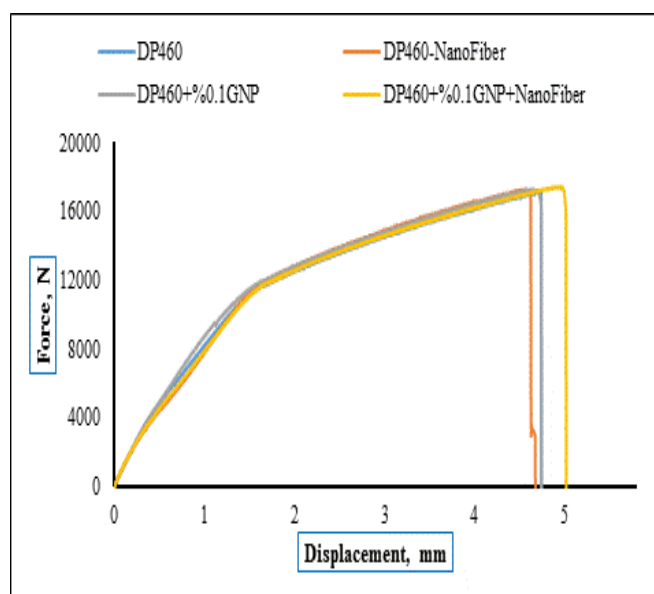


Figure 12. Force and elongation of the joints using 0.1% GNP and Nanofiber

3. RESULTS AND DISCUSSION

In this study, AA5754 aluminum alloys were bonded with double patches. For the bonding process, DP460 adhesive and together with this adhesive, 0.1% wt., 0.2% wt., 0.3% wt. Graphene nanoparticles and 1% Graphene nanoparticle reinforced Nano-Fibers were used. After the bonding processes, the effect of each parameter on the bonding tensile force was investigated. For this, the tensile tests of the samples bonding in each parameter were made. After the tensile tests were completed, their structures on the adhesion surface were examined. Therefore, macro and micro images of the adhesion region were taken after the tensile test of each sample. Figure

12, Figure 13, and Figure 14 were given force-elongation graphics of the samples using Graphene nanoparticles and Nanofibers produced with 1% wt. Graphene nanoparticle reinforcement.

3.1 Tensile Tests

Tensile test results of bonding joints using DP460 adhesive, GNP, and Nanofibers are given in Figure 12, Figure 13 and Figure 14.

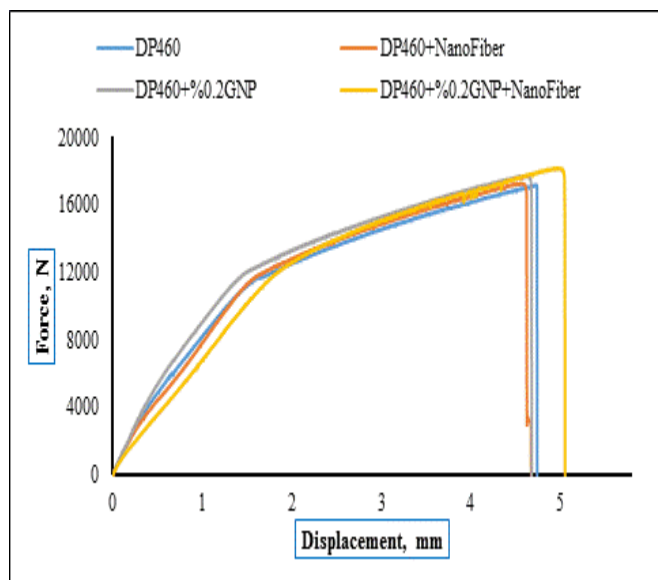


Figure 13. Force and elongation of the joints using 0.2% GNP and Nanofiber

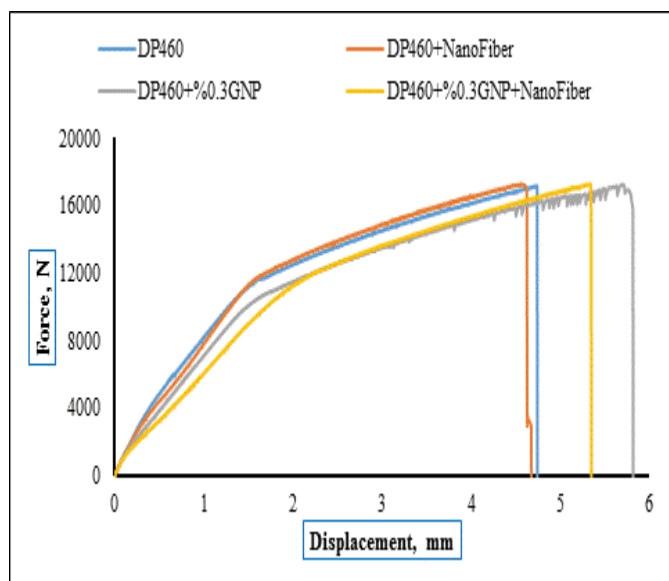


Figure 14. Force and elongation of joints using 0.3% GNP and Nanofiber

In Figure 12, the force-elongation graph of double-patch AA5754 aluminum alloy samples using DP460 adhesive and 0.1% wt. graphene nanoparticles added to this adhesive and nanofibers produced with 1% graphene nanoparticle addition is given. Considering the force-elongation values obtained by adding graphene nanoparticles and nanofiber to DP460 adhesive in Figure 12. It is seen that the using of 0.1% graphene nanoparticles and nanofibers did not make a significant change on the adhesive joints, but higher tensile damage force and elongation were obtained in the joints where 0.1% wt. graphene nanoparticles and nanofibers were used together. The best

adhesive-bonded joint was obtained from the joint using 0.2% GNP and Nano-Fiber together in bonding joints obtained with 0.2% GNP and Nano-Fiber reinforcement. Similarly, as is in Figure 12, a higher tensile damage load was obtained from adhesive bonded joints where 0.2% GNP and Nano-Fiber were separately used compared to joints using DP460 adhesive. We can see a partial improvement when looking at the force-elongation values in Figure 13. Also, it clearly, it can states that the reinforcement ratio has a significant effect here. Saraç et al. In their study stated that nanoparticle reinforcement ratios and types have a significant effect on adhesive joints [20].

The joints obtained with 0.3% wt. GNP reinforcement (Figure 14) showed a different behavior than the bonding joints using 0.1% wt. and 0.2% wt. GNP and nanofibers. Here, the highest tensile force and elongation were obtained from the joints obtained with the reinforcement of 0.3% wt. graphene nanoparticle. Similarly, Topkaya et al. stated that GNP reinforcement has a positive effect on the bonding tensile force of the joints. They also emphasized the importance of 0.2% wt. GNP supplementation in their study [21].

The better tensile damage force was obtained than the bonds obtained with DP460 adhesive in all bonding joints where 0.1% wt., 0.2% wt. and 0.3% wt. graphene nanoparticles and nanofibers produced with 1% graphene nanoparticle reinforcement were used. However, the best tensile damage force was obtained from adhesion joints where nanofiber and GNPs were used together. In addition, the best tensile damage force was obtained as 18183.8 N from the joints used nanofibers produced with 0.2% graphene nanoparticle and 1% graphene nanoparticle reinforcement. When the force-elongation graphs are examined, the elastic behavior of the bonded joints using 0.1% GNP and nanofiber is linear. However, there is a partial fluctuation in the elastic region in the connections where 0.2% GNP, 0.3% GNP and nanofiber are used. There was also an increase in yield force relative to 0.1% GNP and nanofiber. Table 3 gives values for all tensile damage forces.

TABLE 3
RESULTS OF TENSILE TESTS

Reinforcement (%)	Force (N)
DP460	17187.5
DP460 + Nanofiber	17312
DP460+0.1Graphane	17281.3
DP460+0.1Graphane+NanoFiber	17453
DP460+0.2Graphane	17730.5
DP460+0.2Graphane+NanoFiber	18183.8
DP460+0.3Graphane	17265.6
DP460+0.3Graphane+NanoFiber	17289.1

3.2. Macro and micro images of surfaces of adherence

Obtaining a good joining structure in the joints made with adhesive depends on a good surface of adherence between the samples bonded with the adhesive. Therefore, it is essential to clean the surface of adherence of the samples bonded in the joints made with the adhesive. It needs to review the surface morphological structure of the joints to observe the effects of the processes and adhesion technique on the adhesion quality. In this study, photographs of the ruptured surface regions of each sample were taken after the tensile tests to observe the structural effects of nanoparticles and nanofibers on tensile damage loads. It was tried to determine adhesion mechanisms

on the surface of the bonding of samples. Finally, the relation or effects of mechanisms between the adhesion damage loads were explained. In Figure 15, firstly was given the Nano-fiber SEM images.

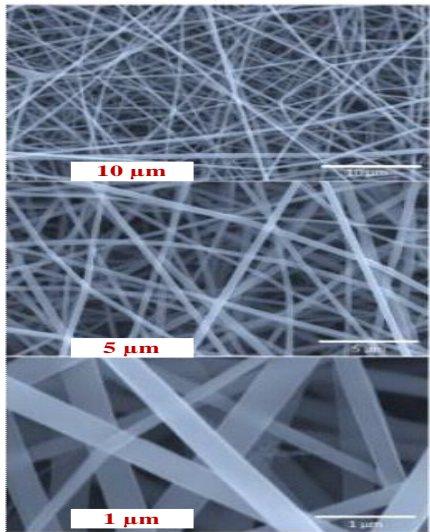


Figure 15. SEM images of Nanofiber

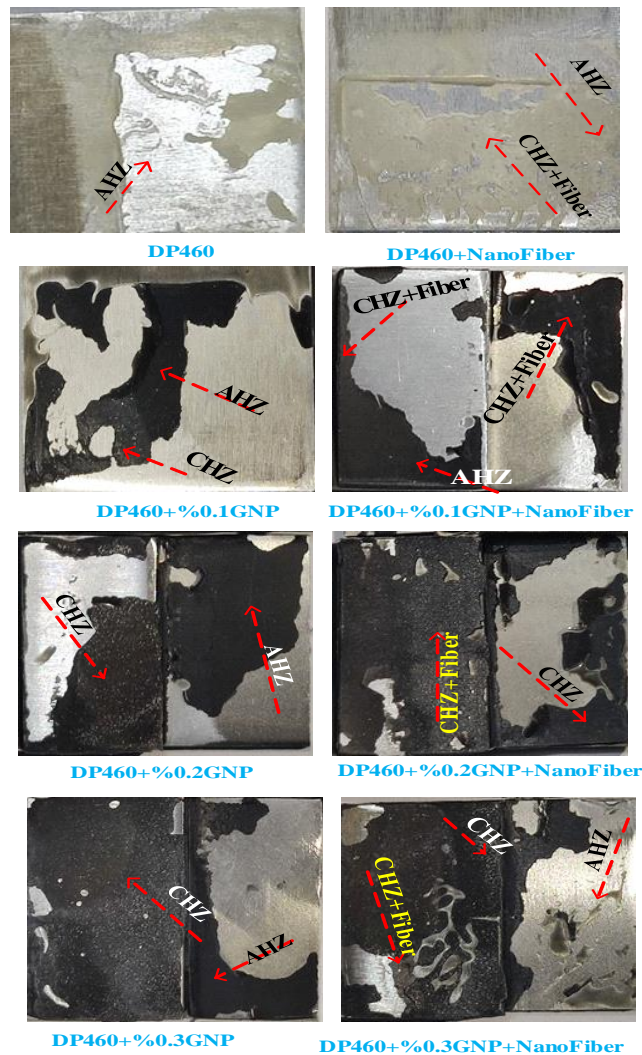


Figure 16. Surfaces of adherence of samples separated by tensile tests

In Figure 15, SEM images of the morphologies of different sizes of PVB / TEOS / 1GNP nanofibers produced by electro-

spinning are given. Examination of the SEM images, it is understood that the nanofibers have a homogeneous structure.

Macro and SEM photographs of the ruptured surface of adherence of each sample were given in Figure 16 and Figure 17 after the tensile tests.

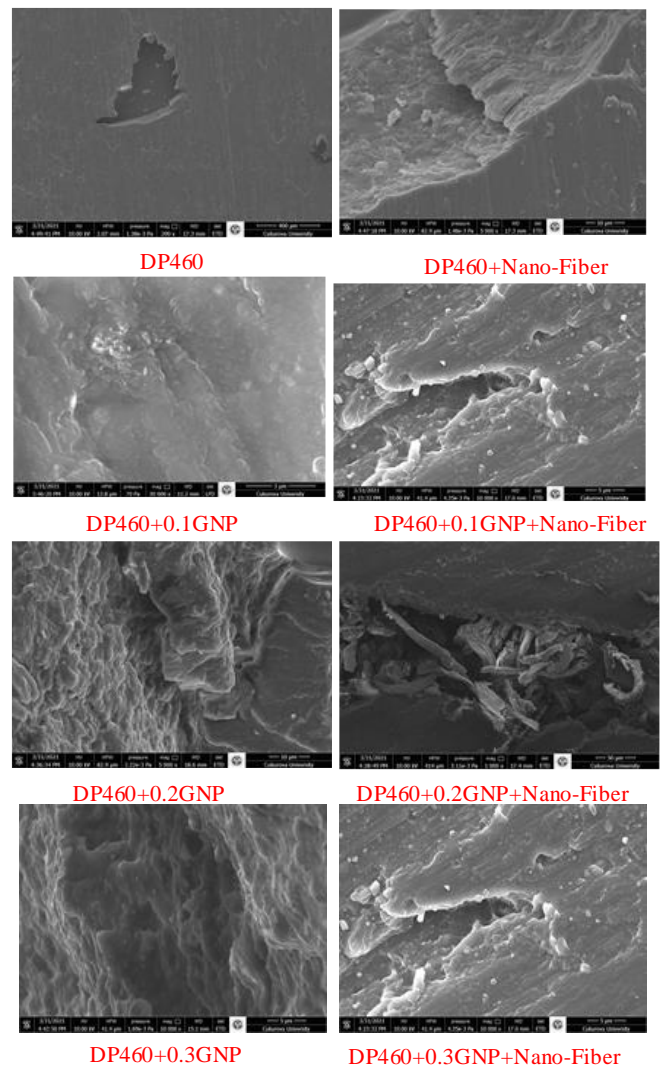


Figure 17. SEM images of the surfaces of samples separated by tensile tests (10000X-5μm)

Only adhesion (AHZ) was seen in joints DP460. Adhesion (AHZ) and cohesion (CHZ) were observed together in the joints where NanoFibers with Graphene nanoparticle and Graphene nanoparticle reinforcement were used. There was also made a definition as CHZ+Fiber in joints with nanofibers. It is seen when tensile test results were compared with surfaces of CHZ + Fiber, CHZ, and AHZ structures that there are better results in surfaces with CHZ+Fiber and CHZ. It is thought that there are enhancing effects on tensile forces on surfaces of CHZ+Fiber +CHZ and AHZ+CHZ structures (figure16). When SEM images were examined (figure17), it was seen that there was a thin and long microstructure on the rupture surface of the bonding made with DP460 + 0.2GNP + Nano-Fiber parameters. It is thought that this microstructure is formed by the effect of nanofibers used as reinforcement elements. In addition, the reason why the joint made with this parameter rupture at maximum load is attributed to the transport of the load on these homogeneous thin long fibers.

4. CONCLUSION

AA5754 aluminum alloys were bonded with double patches using DP460 adhesive and also used adhesive mixtures prepared with 0.1% wt., 0.2% wt., and 0.3% wt. GNP added to these adhesives. Nanofibers produced with 1% GNP reinforcement were also used with DP460 adhesive and the adhesive mixtures of GNP. Subsequently, samples bonded were subjected to the tensile test to determine the effect of Nano-fiber and GNP reinforcement ratios on bonding joints. Finally, the adhesion mechanisms of each sample were determined by taking macro images and SEM of the fracture surfaces after the tensile process was completed. All results obtained were provided below.

✓ Tensile forces of double patched joints made with a mixture of DP460 adhesive and Graphene nanoparticle (GNP) were obtained as higher than tensile forces of double-patch joints achieved using only DP460 adhesive.

✓ The tensile forces partially increased in double patched joints where nanofibers were used together with DP460 adhesive.

✓ The tensile forces of the joints including adhesive prepared with the reinforcement of nanofibers and graphene nanoparticle (GNP) to DP460 adhesive provided the highest values. The best tensile force was obtained as 18183.8 N from samples where 0.2% graphene nanoparticles and Nano-Fibers were utilized together.

✓ AHZ, CHZ + Fiber + CHZ, and AHZ + CHZ surface structures were formed on the surfaces of bonding. In addition to all these, good tensile damage loads were obtained in samples with CHZ + Fiber + CHZ and AHZ + CHZ surface structures.

REFERENCES

- [1] H. Adin, "The effect of angle on the strain of scarf lap joints subjected to tensile loads," *Appl Math Model* ;36:2858-67, 2012.
- [2] F. Ascione, "the influence of adhesion defects on the collapse of FRP adhesive joints." *Compos Part B Eng*; 87:291-8, 2016.
- [3] A. Avia, M. I. Yoshida, M. G. Carvalho, E. C. Dias, J. A. Junior, "An investigation on post fire behaviour of hybrid nanocomposites under bending loads," *Compos Part B Eng* 2010;41:380-7.
- [4] O. Sayman, "Elasto-plastic stress analysis in an adhesively bonded single-lap joint," *Compos Part B Eng* 2012;43:204-9.
- [5] G. Marannano, B. Zuccarello, "Numerical experimental analysis of hybrid double lap aluminium-CFRP Joints," *Compos Part B Eng* 2015;71:28-39.
- [6] M. Y. Solmaz, T. Topkaya, "Progressive failure analysis in adhesively, riveted, and hybrid bonded double-lap joints" *J Adhesion* 2013;89:822-6.
- [7] S. Akpınar, "the strength of the adhesively bonded step-lap joints for different step numbers," *Compos Part B Eng*; 67:170-8, 2014.
- [8] N. A. Siddiqui, S. U. Khan, P. C. Ma, C. Y. Li, J. K. K. Kim, "Manufacturing and characterization of carbon fibre/epoxy composite prepregs containing carbon nanotubes," *Compos Part A*; 42:1412-20, 2011.
- [9] G. Di Franco, B. Zuccarello, "Analysis and optimization of hybrid double lap aluminium-GFRP joints" *Compos Struct*; 116:682-93, 2014.
- [10] K. Gültekin, S. Akpınar, A. Gürses, Z. Eroglu, S. Cam, H. Akbulut, Z. Keskin, A. Ozel, "the effects of graphene nanostructure reinforcement on the adhesive method and the graphene reinforcement ratio on the failure load in adhesively bonded joints," *Composites Part B* 98 (2016) 362-369. <http://dx.doi.org/10.1016/j.compositesb.2016.05.039>.

- [11] İ. A. Akpınar, K. Gültekin, S. Akpınar, H. Akbulut, A. Ozel, "Experimental analysis on the single-lap joints bonded by a nanocomposite adhesives which obtained by adding nanostructures," *Composites Part B* 110 (2017) 420-428. <http://dx.doi.org/10.1016/j.compositesb.2016.11.046>.
- [12] Z. Jia, X. Feng, Y. Zou, "Graphene Reinforced Epoxy Adhesive for Fracture Resistance," *Composites Part B* 155 (2018) 457-462. <https://doi.org/10.1016/j.compositesb.2018.09.093>.
- [13] R. Moriche, S. G. Prolongo, M. Sánchez, A. Jiménez-Suárez, F.J. Chamizo, A. Ureña, "Thermal conductivity and lap shear strength of GNP/epoxy nanocomposites adhesives," *International Journal of Adhesion and Adhesives* 68(2016)407-410. <http://dx.doi.org/10.1016/j.ijadhadh.2015.12.012>.
- [14] H. Khoramshad, R. S. Ashofteh, H. Pourang, F. Berto, "Experimental investigation of the influence of temperature on the reinforcing effect of graphene oxide nano-platelet on nanocomposite adhesively bonded joints" *Theoretical and Applied Fracture Mechanics* 94, 95-100. <https://doi.org/10.1016/j.tafmec.2018.01.010>.
- [15] M. A. S. Sadigh and G. Marami, "Investigating the effects of reduced graphene oxide additive on the tensile strength of adhesively bonded joints at different extension rates," *Materials and Design* 92, 36-43. <http://dx.doi.org/10.1016/j.matdes.2015.12.006>.
- [16] E. Çetkin and S. Temiz, "Repair of aluminium plates which has different sizes notch with aluminium patch" *DUFED* 5 (2), 56-69.
- [17] M. Prabaharan, R. Jayakumar, S. V. Nair, "Electro spun Nano fibrous scaffolds-current status and prospects in drug delivery," *Advances in Polymer Sciences*, 246, 241-262.
- [18] S. Jahangiri, E. Ozden-Yenigun, "the stability and dispersion of carbon nanotube-polymer solutions: A molecular dynamics study," *J Ind Text.*, 47(7):1568-83.
- [19] B. C. Weng, F. H. Xu, G. Garza, M. Alcoutlabi, A. Salinas, K. Lozano, "The Production of Carbon Nanotube Reinforced Poly(vinyl) Butyral Nanofibers by the Force spinning (R) Method," *Polym Eng Sci.*, 55(1):81-7.
- [20] İ. Saraç, H. Adin, S. Temiz, "Experimental Determination of the Mechanical Properties of Adhesive Joints Bonded Epoxy Adhesive Included Al₂O₃ Nanoparticle," Vol 6, Number 2, 2016 *European Journal of Technic*.
- [21] T. Topkaya, Y. H. Çelik, E. Kilickap, "Mechanical properties of fiber/graphene epoxy hybrid composites" *Journal of Mechanical Science and Technology* v (34), P,4589-4595.

BIOGRAPHIES

Edip ÇETKİN obtained his BSc degree in mechanical engineering from Inonu University (IU) in 210. He received the BSc., and MSc. diploma in Mechanical Engineering from the Inonu University in 210 and 2013 respectively, a Ph.D. degree in Mechanical Engineering from the Batman University, Batman, Turkey, in 2018. His research interests are weldings, adhesive materials, composite materials. In 2011 he joined the Faculty of Engineering and Architecture, batman University as a research assistant, where he is presently assistant professor doctor. He is active in teaching and research on adhesive materials.



Investigation the Physical and Rheological Properties of Bitumen Modified with Warm Mix Asphalt Additive

İslam GÖKALP^{1*}

^{1*}Batman University, Faculty of Engineering and Architecture, Civil Engineering, . (e-mail: islamgokalp@gmail.com).

ARTICLE INFO

Received: Jul., 08. 2021

Revised: Sep., 13. 2021

Accepted: Sep., 15. 2021

Keywords:

Bitumen
Modification
Polymer
Sasobit
Warm Mix Asphalt

Corresponding author: *İslam GÖKALP*

ISSN: 2536-5010 / e-ISSN: 2536-5134

DOI: <https://doi.org/10.36222/ejt.966398>

ABSTRACT

Bituminous binders constitute 4-7% of the flexible pavements by weight play an important role on the structural and functional performance of pavements. Traditional hot mix asphalt (HMA) production is done at 150-190 °C that results high-energy usage, smoke and odor emission therefore significant cost loss and environmental damage. Increasing environmental awareness has questioned whether HMA can be produced at lower temperatures. Consequently, warm mix asphalt (WMA) and cold asphalt applications were developed as alternatives. WMA applications researched within the scope the current study can be done by using organic, chemical additives or foaming methods, which are based on the reduction of the viscosity of bitumen. The aim of this study was to modify the base bitumen by adding WMA additive called Sasobit, the most widely used chemical product in the world, within the rates between 1% and 5% and therefore to investigate the changes in physical and rheological properties of bitumen. In this research, penetration, softening and flash point, viscosity tests were applied under physical properties, thermal sensitivity was analysed, and rheological properties of base and short-term aging from, which required high-temperature grade of bitumen, were investigated using dynamic shear rheometer. Eventually, the effect of using Sasobit in modification were determined. A brief evaluation in the light of present studies were done on economic and environmental effect of using WMA technology. The results showed that significant changes occur in the studied properties of bitumen except of flash point.

1. INTRODUCTION

Bituminous binders are adhesive and water-resistant construction materials with volatile components. As a valuable and versatile product, bitumen can be obtained from crude oil with a series of industrial processes as well as from lake and rock-induced formation, naturally. There are numerous usage area of bitumen for different purposes including adhesive, infiltration, pie protector, water impermeable additive, pavement binder etc. Moreover, bitumen are visco-elastic, sensitive to heat material, and dissoluble by 99% within toluene based chemicals [1]. Although they have complex chemical components, four main component take significant role in the form of bitumen. These are (1) Saturated, (2) Asphaltene, (3) Resin, and (4) Aromatics [2, 3]. Due to their origin and production process, there are significant differences between their atomic structure, size and weight of molecular structure, and aromatic properties etc., which cause significant changes in physical and rheological properties [4-12].

Flexible pavement consists of large part (approximately 90-97%) of network of highway in our country, Turkey such as the other country including Germany, Australia, Unite States of America, and New Zealand [13]. Flexible pavement consists of aggregate and bitumen beside of some additives. Aggregate

forms 93-96% by weight of the pavement and the remaining part by bitumen and additive. The role of the aggregate is to provide a skeleton of pavement, while that of bitumen is to keep the aggregates together and prevent them to disintegrate under repeated traffic loads and harsh environmental conditions [14-17]. Although the rate of bitumen is quite lower than that of aggregates, it is important to provide superior functional and structural performance from constructed pavement.

Under increasing traffic loads and changeable climatic conditions, the expected performance from traditional bituminous binders cannot be provided, generally. For this reason, it is necessary to improve the bitumen characteristics to resist against such harsh conditions. This directs the researchers interests in modification of bitumen with different additive that may be chemical product for sale and/or industrial or household waste. The materials used to modify bitumen changes bitumen characteristics including physical and rheological properties, and chemical structure [17, 18]. All has significant effect on functional and structural performance of pavements. Beside of durability concerns, constructing economic and eco-friendly pavement construction are crucial for sustainability. In this respect, significant number of studies focused on the bitumen modification [19-24].

Bitumen is a sensitive material against temperature. The physical form of them is viscous as exposed to high temperature, while in the form of solid or semi-solid at low temperature conditions. According to hot mix asphalt (HMA) production processes, flexible pavement is constructed in ideal temperature ranges between 120 and 190 °C. To provide an efficient mixing process for HMA, standards identify certain limitations for viscosity values, and the HMA is prepared according to the requirements given to the contractor [25]. In this case, significant amount of energy are required to produce HMA at desired conditions, which causes of high costs and adverse effects on environment due to emission and odor [26]. Environmental and economic awareness direct the to whom it may concern to use the present energy resources, efficiently [27-29]. This encourage the researchers to improve innovative technological developments to provide ecologic, energy-efficient and labor friendly production. In this regard, numerous investigations have been done to make the bitumen structural and functional properties better and/or stable under high traffic loads and harsh environmental conditions. Novel additives and technological processes have been developed being used in bitumen modification and to production of HMA. Throughout the development process, new method in production of asphalt mixture including cold and warm mix asphalt (WMA) have been developed [30, 31]. The recent studies show that the temperatures for mixing and compaction can be reduced about 15 °C, which leads to significant reduction in the cost of investment and emerged amount of emission and odor that are hazardous for living creatures health [32]. Such advantages are the reasons that encourage the researcher and contractor to construct flexible pavements with WMA technology. There are numerous WMA additives including organic additives, chemical additives, and the technic consists of water injections and /or foamed with minerals [33]. Sasobit is one of common WMA polymer that used as an additive in the scope of this study.

Numerous researcher have investigated the effect of WMA additives on bitumen properties and/or performance of HMA produced with them. There are some of them at the following presented in brief.

Arshad et al. [34] modified the bitumen with Sasobit in certain rate ranging between 1 and 3% with 0.5 increments. The authors investigate the effect of WMA on bitumen samples with penetration and viscosity at different temperature ranging between 70 and 135 °C. They reported that the penetration and viscosity values above 115 °C are lower than the one found for base bitumen. Moreover, they indicated that the viscosity of WMA samples higher at 70 and 80 °C. Fazaeli et al. [35] used different WMA additive called Fischer Tropsch- Paraffin in certain rates from 1 to 4% for modification of bitumen with 58-22 graded according to SuperPAVE performance grade (PG) system. To investigate the changes in properties of bitumen, physical and rheological tests were performed on the WMA samples. The results reported by authors were that significant changes occur in both physical and rheological properties. For examples, the PG of WMA sample with 4% additive was determined as 70-22. However, the changes in properties at intermediate temperatures were not significant. Moreover, the test performed with rotational viscometer showed that there is increase in WMA additive rate causes decreasing in mixing and compaction temperatures about 15-25 °C. Yero and Hainin [36]

reported that significant increasing in temperature susceptibility of WMA samples produced with 1 and 5% additive is observed while examined with penetration index (PI) and penetration viscosity number (PVN). The changes in viscosity were evaluated with rotational viscometer under the temperature ranging from 60 and 150 °C. The viscosity was determined higher at low temperature, while lower at higher temperature, especially the one bigger than 100 °C while compared with base one. Similar to the summarized studies, higher rutting resistance in WMA samples was determined. Cao and Ji [37] investigated long-term performance of Sasobit modified bitumen produced in certain rates from 2 to 5% by conventional and rheological test methods. The reported results showed that significant changes occur in properties of produced WMA samples and the level of changes are depended on bitumen and additive type as well as additive rates. Dokandari and Topal [38] investigated the short and long-term aged properties of WMA produced with foamed and non-foamed additive up to 7% by weight of bitumen in rate. Conventional bitumen tests and the indirect tension tests were performed on WMA samples. Besides, temperature susceptibility of WMA was examine with PI analysis. The results implied by authors that the studied WMA produced with non-foamed exhibits better properties than that of produced with foamed additive. The influence of water on warm-modified asphalt in the views of adhesion, morphology and chemical characteristics were investigated in a study done by Liu et al. [39]. Highlighted results were that Sasobit can reduce the water-induced adhesion degradation and water-induced aging and Sasobit can delay polar enrichment of asphalt. Yue et al [40] investigated the fatigue characteristics and healing potential of asphalt binder modified with Sasobit and polymers under linear amplitude sweep test. They indicated that after Sasobit modification, the performance of polymer modified bitumen by means of fatigue life, healing capacities. Bhat and Mir [41] investigated the performance of Nano-modified asphalt binders incorporated with warm mix additives such as Fisher-Tropsch wax (FT wax) and organosilane. The results of this study revealed that incorporation of WMA additives decreased the viscosity of both the control and nanosilica-modified asphalt binders, while improved elevated temperature performance and the resistance against fatigue cracking and aging.

As can be seen from summarized studies, WMA addition are considerably effective on bitumen and asphalt concrete properties. This task is not new for the world, but it is quite new with a few of study for our country, Turkey. To fill the gap in the literature of the country and to support and improve the existing worldwide studies, the current study is established. Moreover, the level of effect may change due to both additive and bitumen type and origin, therefore to evaluate it for our country condition; it is valuable to analyze the characteristics of bitumen produced in Turkey modified with Sasobit. To achieve the aim, Sasobit was used in modification to produce WMA in different rates from 1 to 5% by weight of bitumen. Conventional or physical including penetration, softening point, viscosity and flashing point and DSR as well-known rheological test were implemented on WMA samples to determine the effect of Sasobit to bitumen properties. Additional analyses including for thermal susceptibility of bitumen considering Penetration index (PI), Penetration

Viscosity Number (PVN) methods, and mixing and compaction temperatures considering rotational viscometer test results were done. Consequently, all the test and analyses results were reported and discussed throughout the scope of the current study.

2. MATERIALS AND METHOD

2.1. Materials

A base bitumen with 50/70 penetration grade and WMA additive, Sasobit, were used. Bitumen was supplied from General Directorate of Highway, 5th Regional Directorate located in Mersin, while Sasobit additive from a commercial firm. The properties of bitumen and Sasobit are given in Table 1 and Table 2, respectively. The codes of the bitumen samples and modification components are shown in Table 3.

TABLE 1
PROPERTIES OF BITUMEN

Property	Standard	Unit	Result
Penetration	TS EN 1426	0.1 mm	66.9
Softening Point	TS EN 1427	°C	46.0
Flashing Point	TS EN ISO 2592	°C	268.0
Ductility (25 °C)	TS EN 13398-A1	cm	93.0
Viscosity (110 °C)			2263.0
Viscosity (135 °C)	ASTM 4402	cP	517.5
Viscosity (165 °C)			139.2
Penetration Index	TS EN 1427	-	-1.59
Specific Gravity	TS EN 15326	kg/m ³	1031.0
SuperPAVE Grading	TS EN 14770	°C	70-22

TABLE 2
PROPERTIES OF SASOBIT

Property	Standard	Unit	Result
Color	-	-	Off-White
Odor	-	-	Odorless
Flashing Point	TS EN ISO 2592	°C	285.0
Specific Gravity	TS EN 15326	g/cm ³	0.900
Average Molecular Mass	-	-	≈ 1000 g/mol
Ph Value	TS 132	-	Neutral
Physical Form	-	-	Solid
Thermal Decomposition Temperature	-	°C	250.0
Reaction Temperature	TS EN ISO 2207	°C	> 90
Water Solubility	-	-	Insoluble

TABLE 3
BITUMEN CODES AND MODIFICATION COMPONENTS

Code	Components
BB	Base bitumen
SAS-0.01	Base bitumen + 1% (by bitumen weight) Sasobit additive
SAS-0.02	Base bitumen + 2% (by bitumen weight) Sasobit additive
SAS-0.03	Base bitumen + 3% (by bitumen weight) Sasobit additive
SAS-0.04	Base bitumen + 4% (by bitumen weight) Sasobit additive
SAS-0.05	Base bitumen + 5% (by bitumen weight) Sasobit additive

2.2. WMA modification procedures

The modification procedures followed throughout the scope of the study to produce WMA were determined in the light of the earlier studies [42-46]. The steps of the procedures are as following.

(1) The base bitumen was heated at 150±5 °C for 60 minutes to make it fluid,

(2) 500 grams of the fluid bitumen was poured in a metal container,

(3) The bitumen-filled container was put on a heater worked at 140±5 °C and remained on it for 10 minutes to provide temperature stability,

(4) The Sasobit additive in determined rates were weighted and poured into the heat bitumen,

(5) The Sasobit-bitumen mixture was stirred for 45 minutes under 1500 revolution per minutes (rpm) with a propeller mixer. This process was done for bottom, middle and top section of the bitumen-filled container for 15 minutes, individually to provide homogeneity.

2.3. Conventional bitumen test methods

Throughout the scope of study, penetration, softening points, flashing points, rotational viscosity at different temperatures were performed on the WMA samples. The tests were applied at least two times according to the related EN and ASTM standard. Moreover, temperature susceptibility of produced WMA samples were evaluated with penetration index (PI) and penetration-viscosity number (PVN). Mentioned test methods are briefly described at this section.

Penetration test can be applied with a standard needle under certain load and temperatures. The test duration is 5 seconds and thereafter reading the penetration of the needle is taken. In the scope of the current study TS EN 1426 [47] was followed and the applied load was 100 grams, in total.

Softening point test is common test used all over the world to determine the bitumen flow behavior under elevated temperature. The test apparatus are two ring and ball that are in standard size and weight. Besides, a heater with magnet and grade temperature and the fluid with glass container. The principle of the test is based on the temperature values determined after flowing of the samples for a certain distance. Moreover, TS EN 1427 [48] was followed in this study.

Flashing point test is a kind of safety test that enable the operator to determine the flashing and firing point. Since the bitumen is one of construction material with volatile components. If there is not heated the bitumen at temperature in safe range, it may cause explosion due to gas jam or may cause fire while the bitumen contact with a source of fire. Cleveland open cup flash point apparatus was used in this study according to TS ISO EN 2592 [49].

Viscosity test is applied on bitumen to determine the viscous properties of the bitumen under different temperatures. The test is important, since bitumen is one of visco-elastic construction material that the characteristic changes with heating. At low temperature, the bitumen is stiffer while it is more viscous at high temperature. Besides, determining the viscoelastic characteristics of bitumen is essential to identify the temperature for mixing and compaction of asphalt concrete. In this study, Brookfield rotational viscometer method was performed on bitumen samples at different temperatures (110, 135, and 165 °C) according to ASTM 4402 [50].

Temperature susceptibility analysis is done to determine the sensitivity of the bitumen to temperature changes. The most common analyzing methods are PI and PVN and these two were taken into consideration to do the analysis in this study.

The following equalities were used to calculate the values refer to the susceptibility of bitumen to temperature.

$$PI = \frac{20 - 500 \times A}{1 + 50 \times A} \quad (1)$$

$$A = \frac{\text{Log}(800) - \text{Log}P_{25}}{T_{YN} - 25} \quad (2)$$

$$PVN = \frac{4,258 - 0,7967 \times \text{Log}P_{25} - \text{Log}V}{0,795 - 0,1858 \text{Log}P_{25}} \quad (3)$$

where,

Tsp: Softening point,

P₂₅: Penetration at 25 °C,

V: Kinematic viscosity at 135°C.

2.4. Rheological bitumen test methods

The rheological test methods identified in the scope of the SuperPAVE grading system including dynamic shear rheometer, bending beam rheometer and aging methods (rolling thin film oven test and pressure aging vessel) in case of short-term and long-term were used in assessment of bitumen properties. These test methods were described in brief at the following.

Dynamic shear rheometer test (DSR) is one of the major equipment used in Superior Performing Asphalt Pavements (SuperPAVE) system developed by Strategic Highway Research Program. DSR results gives deep-information about the viscous and/or elastic behavior of bituminous materials under different temperatures either at high or intermediate level and loading conditions [51]. SuperPAVE system requires testing base and aged bitumen samples in case of short-term aging and long-term aging. DSR test can be performed on base and aged bitumen samples within defined logical framework and the results formed throughout specific software program. The test results include complex shear modulus (G*) and phase angle (δ°) of bitumen sample at different temperatures. The available testing temperatures are between 7 and 88 °C, if a logical framework works with water bath system, while the testing temperature range can change while logical frame system integrated with hot/cold air. DSR with a water bath integrated logical frame is used in the scope of the current study.

SuperPAVE system identifies limit values for G* of base, short-term and long-term aged bitumen samples to evaluate their rutting and fatigue resistance characteristics, which are 1000 Pa (1 kPa), 2200 Pa (2.2 kPa), and 5x10⁶ Pa (5000 kPa), respectively. On the other hand, phase angle shows the viscous or elastic form of bitumen samples at each test temperature. If the angle approaches to 0°, it refers to elastic form of bitumen samples, while it approaches to 90°, then it means to viscous form of the samples. By determining G* and δ°, the DSR are able to provide more information about the behavior of asphalt at pavement service temperatures. Some of them are rutting and fatigue resistance of bitumen. Rutting factor is determined with

G*/Sinδ°, while fatigue factor is calculated with G*.Sinδ°. The test was implemented by following TS EN 14770 standard [52].

Aging methods are different for short and long-term cases that are required to determine rutting and fatigue resistance, and to prepare the samples for thermal cracking resistance evaluation. Short-term aging process refers to the aging of bitumen during production to construction of asphalt pavements, while long-term aging process covers the time of pavement construction to the end of pavement service life. It is possible to simulate both aging process of bitumen can be provided in laboratory condition. Rolling thin film oven (RTFO) and pressure aging vessel (PAV) are the most commonly used methods to provide short and long-term aged bitumen samples, respectively. The test temperature is 163 °C and the time duration is 75 minutes for RTFO method according to the TS EN 12607-1 standard [53]. On the other hand, PAV method can be conducted at different temperature including 90, 100, 110 °C. In the scope of the study, only short-term performance of bitumen samples were evaluated and therefore RTFO based experiment conducted on bitumen samples according to related standard.

3. RESULTS AND DISCUSSION

The results of the test and analyzing method conducted on bitumen samples are expressed and discussed in this section.

3.1. Conventional test results

The results of conventional tests, which are penetration, softening and flashing point, and viscosity with rotational viscometer, applied on bitumen samples are presented in Figure 1. Beside, mixing and compaction temperatures were determined based on the data obtained from viscosity test at 135 and 165 °C and the results are given in Table 4.

The Figure 1 showed that penetration values of Sasobit based WMA decreases with increases in rate of additive. The change in penetration values is significant up to the rate of 3%, but the changes in penetration rates decreases as contribution rates are 4 and 5% compared to the WMA prepared with the rate of 3% Sasobit. Contrary to the penetration values, there are significant decrease in softening point with increasing in the rate of Sasobit used in the bitumen modification. On the other hand, the figure indicates that decrease about 15 °C occur while the rate of Sasobit is 5% in produced WMA. Rotational viscometer based testing gives important data about the effect of Sasobit addition on viscoelastic characteristics of bitumen. There are considerable decrease in viscosity of bitumen samples with Sasobit modification. The changes are seen clearly at lower temperature than the ones at higher temperature.

TABLE 4
MIXING AND COMPACTION TEMPERATURE OF BITUMEN SAMPLES

Code	Mixing Temperature (°C)	Compaction Temperature (°C)
BB	164.1 – 161.0	156.2 – 151.5
SAS-0.01	161.3 – 157.2	151.0 – 144.8
SAS-0.02	160.0 – 155.4	148.5 – 141.5
SAS-0.03	159.5 – 154.6	147.3 – 139.9
SAS-0.04	157.9 – 152.6	144.8 – 137.0
SAS-0.05	156.4 – 150.7	142.2 – 133.6

Table 4 indicated that the mixing and compaction temperatures of base bitumen is higher than that of WMA produced with Sasobit additive. The difference between mixing temperatures determine for BB and SAS-0.05 occurs about 15 °C, while about 12 °C is determined for differences between compaction temperatures. The results also highlighted that considerable amount of energy conservation can be provided, and preservation of environment can be satisfied due to decrease in greenhouse gas production with WMA.

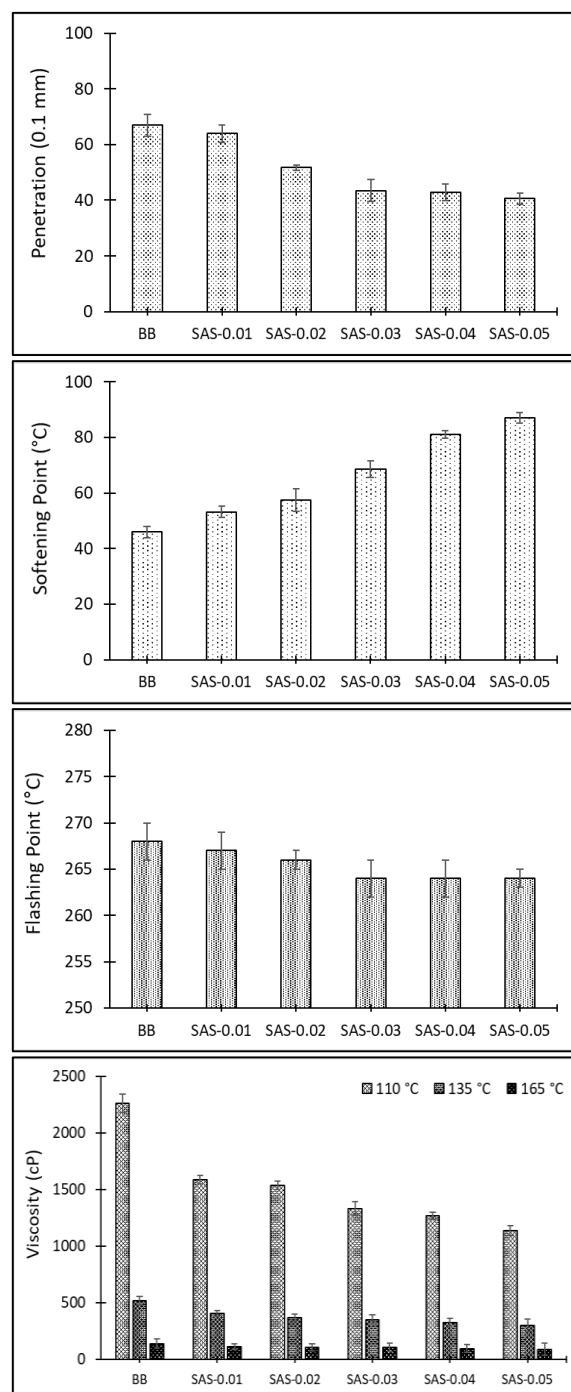


Figure 1. The results of conventional tests

Bitumen is viscoelastic construction material, and it is susceptible to temperature. It is possible to determine the temperature susceptibility characteristic of bitumen with numerous analyses. As mentioned before that the most common two methods are PI and PVN, which are utilized

within the scope of the current study. The PI is established on penetration and softening point test results, while PVN is constructed on penetration and viscosity test results. The results are presented in Figure 2 for the both cases.

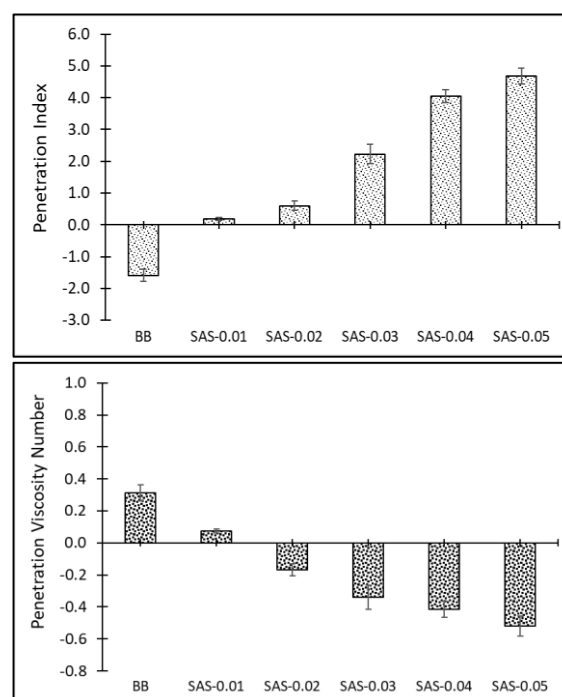


Figure 2. Thermal susceptibility of bitumen samples

The penetration index (PI) indicates temperature susceptibility of bitumen. An increase in the PI means that the bitumen is less sensitive to heat. Contrary to PI, bitumen with higher PVN shows less susceptible temperature property. For a conventional bituminous binder, the expectation for penetration index value are laid between -2 and +2. When the penetration index results given in Figure 2 are evaluated, it is seen that the penetration index value increases with the addition of Sasobit additive to the bitumen. Therefore, Sasobit additive makes the bitumen resistant against temperature changes. When the analysis of the PVN values given in Figure 2 that calculated based on the results of the penetration tests and the viscosity measured at 135 °C, is examined, it will be seen that it confirms the results obtained in the penetration index analysis.

3.2. Rheological test results

Because of the modification of PG 70-22 pure bitumen used in this study to be modified with the Sasobit additive at different rates, it has been observed that the traditional (basic) engineering properties have changed. It is obvious that the rheological properties of bitumen will change with the changing basic engineering properties. For this reason, the scope of the study was expanded by determining the rutting resistance of pure and modified bitumen based on the Superpave classification system with dynamic shear rheometer, which is one of the rheological test methods, as well as determining the classification high failure temperatures. In this context, numerous experiments with DSR were performed on each unaged sample and the short-term aged samples, the results of the test are given in Figure 3 and Figure 4, respectively.

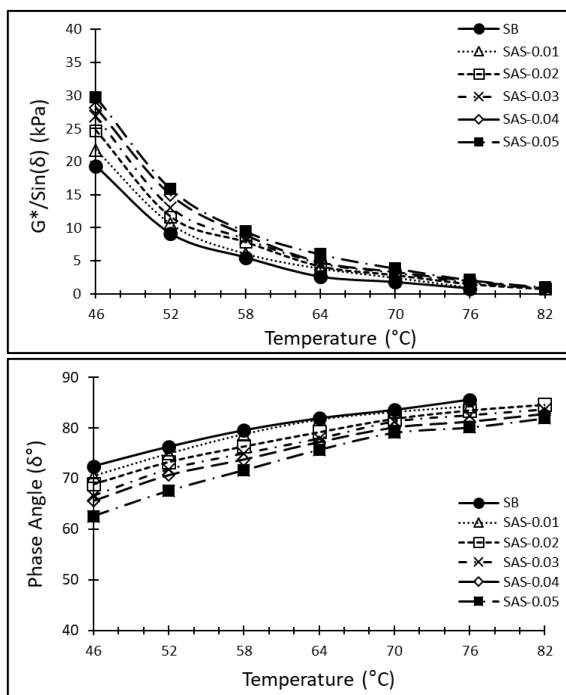


Figure 3. DSR test results of unaged samples

As can be seen in Figure 3, Sasobit additive increases the resistance of the bitumen binder against rutting. In addition, as the temperature increases, it is seen that the measured values, especially the test results obtained at 76 and 82°C, converge to each other.

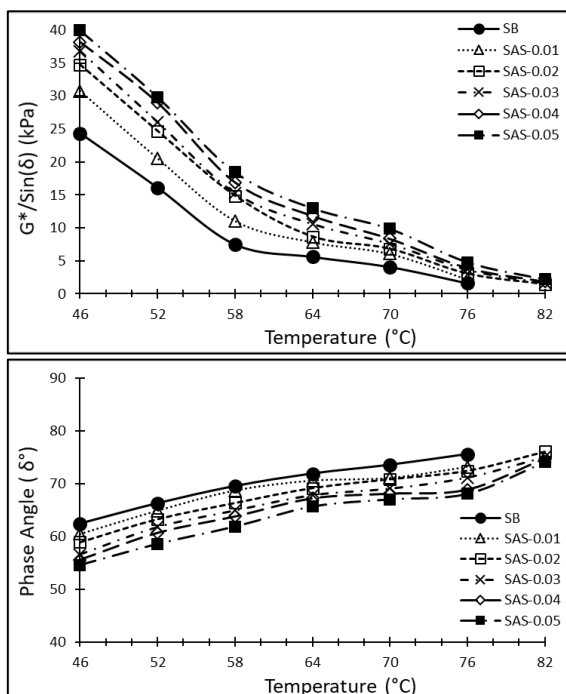


Figure 4. DSR test results of short-term aged samples

Test results on short-term aged specimens (Figure 4) confirm the test results of unaged specimens. On the other hand, the complex modulus values increased due to aging, and the phase angle values decreased due to its more elastic structure.

The failure and classification base temperatures and $G^*/\text{Sin}(\delta)$ for each unaged bitumen sample according to the Superpave system are as shown in Table 5. Likewise, the results of the short-term aged bitumen samples are given in Table 6.

TABLE 5

FAILURE AND CLASSIFICATION TEMPERATURES AND COMPLEX MODULUS VALUES OF UNAGED BITUMEN

Bitumen type	Failure (°C)	$G^*/\text{Sin}(\delta)$ (kPa)	Class (°C)	$G^*/\text{Sin}(\delta)$ (kPa)
BB	76	0,81	70	1,77
SAS-0.01	76	0,95	70	2,43
SAS-0.02	82	0,72	76	1,48
SAS-0.03	82	0,81	76	1,65
SAS-0.04	82	0,87	76	1,96
SAS-0.05	82	0,98	76	2,09

TABLE 6

FAILURE AND CLASSIFICATION TEMPERATURES AND COMPLEX MODULUS VALUES OF SHORT-TERM AGED BITUMEN

Bitumen type	Failure (°C)	$G^*/\text{Sin}(\delta)$ (kPa)	Class (°C)	$G^*/\text{Sin}(\delta)$ (kPa)
BB	76	1,61	70	4,07
SAS-0.01	76	2,21	70	6,07
SAS-0.02	82	1,42	76	3,03
SAS-0.03	82	1,61	76	3,65
SAS-0.04	82	1,87	76	3,96
SAS-0.05	82	2,18	76	4,79

When Tables 5 and 6 are examined, following can be said. The classification temperatures of base bitumen and bitumen modified with 1% Sasobit additive are the same in case of failure. The complex modulus values of both samples are different from each other. Both the failure and classification temperatures of the bitumen modified with 2% or more Sasobit additive were found to be higher. This showed that the Sasobit additive increases the resistance of the bitumen to rutting.

3.3. Economic and environmental effect evaluation

As can be considered from the current study and present literature that benefits such as significant energy and therefore environmental protection on basis of reduction in greenhouse gases can be provided with using WMA techniques in production of HMA. Since reduction in viscosity increases workability of bitumen, therefore asphalt mixture can be mixed at lower temperatures changing from 100°C-140°C dependign on the additive and bitumen type in rate and/or in origin compared to conventional HMA production done at 150°C-190 °C without sacrificing quality of it [54, 55]. Since, it has been proven that using WMA technology can reduce energy consumption during production of HMA up to 30% and gas emissions up to 30-50%, thanks to its ability to be produced at low temperatures [56].

4. CONCLUSION

Within the scope of this study, the changes in the modified bitumen obtained as a result of the addition of Sasobit, one of the warm mix asphalt additives, to the bitumen at rates between 1% and 5% determined with an increase of 1% were investigated. In the research, traditional bitumen test methods such as penetration, softening point, flash point, viscosity tests at different temperatures were used. the Mixing and compression temperatures were determined with using the viscosity test results of the bitumen. In addition, analyzes were

made with two different methods (penetration index, penetration-viscosity number), which are widely used for the evaluation of sensitivity to temperature. Finally, the dynamic shear rheometer test, which is one of the rheological test methods and used to determine the rutting and fatigue resistance of the bitumen binder, was also performed on unaged and short-term aged samples. The results obtained as a result of this study can be listed as follows. Sasobit modification

1. reduced the penetration value of bitumen,
2. increased the softening point value,
3. decreased the flash point value, but this decrease is negligible,
4. reduced the viscosity value, significantly, therefore, decreased mixing and compression temperatures by around 10-15 °C,
5. decreased bitumen thermal sensitivity,
6. increased the resistance against rutting, and
7. changed the class of bitumen according to the Superpave classification system.

The following topics, which are out of the scope of this study but there is a need to be investigated, are suggested to researchers.

- The performance of WMA added bitumen after long-term aging;
- Low temperature performance of WMA added bitumen;
- Properties of modified bitumen produced with different WMA additives;
- Analysis of modified bitumen under the microscope;
- Storage Stability between WMA and bitumen,
- Structural and functional performance of hot mix asphalt using modified bitumen with WMA additives.

ACKNOWLEDGEMENT

I would like to thank Adana Bitumen Chief of the General Directorate of Highways for supplying bitumen samples and providing laboratory facilities, and TEKNOMET Mühendislik Tem. ve Tic.t Ltd. Şti for providing Sasobit additive.

REFERENCES

- [1] D. Lesueur, "The colloidal structure of bitumen: Consequences on the rheology and on the mechanisms of bitumen modification," *Advances in colloid and interface science*, vol. 145, pp. 42-82, 2009.
- [2] H. Shi, T. Xu, P. Zhou, and R. Jiang, "Combustion properties of saturates, aromatics, resins, and asphaltene in asphalt binder," *Construction and Building Materials*, vol. 136, pp. 515-523, 2017/04/01/ 2017.
- [3] S. H. Firoozifar, S. Foroutan, and S. Foroutan, "The effect of asphaltene on thermal properties of bitumen," *Chemical Engineering Research and Design*, vol. 89, pp. 2044-2048, 2011.
- [4] J. Neves, A. Correia Diogo, and L. de Picado Santos, "Bituminous Binders and Mixtures," in *Materials for Construction and Civil Engineering: Science, Processing, and Design*, M. C. Gonçalves and F. Margarido, Eds., ed Cham: Springer International Publishing, 2015, pp. 237-271.
- [5] M. Yılmaz, B. V. Kök, N. Kuloğlu, and T. Alataş, "Elastomer türü polimerler ile modifiye edilmiş bitümlü bağlayıcıların depolama stabilitelerinin ve reolojik özelliklerinin," *Dokuz Eylül Üniversitesi Mühendislik Fakültesi Mühendislik Bilimleri Dergisi*, vol. 15, pp. 67-77, 2013.
- [6] L. Lewandowski, "Polymer modification of paving asphalt binders," *Rubber Chemistry and Technology*, vol. 67, pp. 447-480, 1994.
- [7] C. Giavarini, "Polymer-modified bitumen," *Developments in Petroleum Science*, vol. 40, pp. 381-400, 1994.
- [8] Y. Yildirim, "Polymer modified asphalt binders," *Construction and Building Materials*, vol. 21, pp. 66-72, 2007.
- [9] J. Oner, B. Sengoz, S. F. Rija, and A. Topal, "Investigation of the rheological properties of elastomeric polymer-modified bitumen using warm-mix asphalt additives," *Road Materials and Pavement Design*, vol. 18, pp. 1049-1066, 2017.
- [10] C. Plug, A. de Bondt, and H. Roos, "Performance of bitumen 70/100 obtained from different suppliers," presented at the 5th European Asphalt Technology Association Conference, Germany, 2013.
- [11] A. Sağlık and E. Öztürk, "Türkiye'de üretilen sathi kaplamalarda kullanılan bitümlerin performans sınıflarının belirlenmesi " *Gazi Üniversitesi Mühendislik-Mimarlık Fakültesi Dergisi*, vol. 29, 2014.
- [12] U. Isacsun and H. Zeng, "Relationships between bitumen chemistry and low temperature behaviour of asphalt," *Construction and Building Materials*, vol. 11, pp. 83-91, 1997.
- [13] ASMÜD. (2017, 14.08.2017). *Karayolu ağının kaplama tipine göre oranı*.
- [14] M. Yılmaz and B. V. Kök, "Stiren-Butadien-Stiren modifiyeli bitümlü bağlayıcıların superpave sistemine göre yüksek sıcaklık performans seviyesinin ve işlenebilirliğinin belirlenmesi," 2008.
- [15] M. Sienkiewicz, K. Borzędowska-Labuda, A. Wojtkiewicz, and H. Janik, "Development of methods improving storage stability of bitumen modified with ground tire rubber: A review," *Fuel Processing Technology*, vol. 159, pp. 272-279, 2017.
- [16] L. Liu, F. Xiao, H. Zhang, and S. Amirhanian, "Rheological characteristics of alternative modified binders," *Construction and Building Materials*, vol. 144, pp. 442-450, 2017
- [17] I. Gökalp, H. M. Çetin, Y. Özinal, H. Gündoğan, and V. E. Uz, "Polimer Modifiye Bitüm Modifikasyonuna Etki Eden Parametreler Üzerine Bir Literatür Araştırması," *Ömer Halisdemir Üniversitesi Mühendislik Bilimleri Dergisi*, vol. 8, pp. 954-964, 2018.
- [18] J. C. Munera and E. A. Ossa, "Polymer modified bitumen: Optimization and selection," *Materials & Design (1980-2015)*, vol. 62, pp. 91-97, 2014.
- [19] T. McNally, "1 - Introduction to polymer modified bitumen (PmB)," in *Polymer Modified Bitumen*, ed: Woodhead Publishing, 2011, pp. 1-21.
- [20] F. Navarro, P. Partal, F. Martinez-Boza, and C. Gallegos, "Thermo-rheological behaviour and storage stability of ground tire rubber-modified bitumens," *Fuel*, vol. 83, pp. 2041-2049, 2004.
- [21] R. Blanco, R. Rodriguez, M. Garcia-Garduño, and V. Castaño, "Rheological properties of styrene-butadiene copolymer-reinforced asphalt," *Journal of Applied Polymer Science*, vol. 61, pp. 1493-1501, 1996.
- [22] M. Iwanski and G. Mazurek, "Rheological characteristics of synthetic wax-modified asphalt binders," *Polimery*, vol. 57, pp. 661-664, 2012.
- [23] G. Polacco, S. Filippi, M. Paci, F. Giuliani, and F. Merusi, "Structural and rheological characterization of wax modified bitumens," *Fuel*, vol. 95, pp. 407-416, 2012
- [24] T. Yi-qiu, Z. Lei, G. Wei-qiang, and G. Meng, "Investigation of the effects of wax additive on the properties of asphalt binder," *Construction and Building Materials*, vol. 36, pp. 578-584, 2012
- [25] ISFALT, *Asfalt ve Uygulamaları*, 1 ed. İstanbul: İSFALT, 2001
- [26] EAPA, "İlk Karışım Asfalt," ASMÜD, Ankara, Türkiye, 2016
- [27] T. Litman and D. Burwell, "Issues in sustainable transportation," *International Journal of Global Environmental Issues*, vol. 6, pp. 331-347, 2006.
- [28] L. Steg and R. Gifford, "Sustainable transportation and quality of life," *Journal of transport geography*, vol. 13, pp. 59-69, 2005.
- [29] C. Mihyeon Jeon and A. Amekudzi, "Addressing sustainability in transportation systems: definitions, indicators, and metrics," *Journal of infrastructure systems*, vol. 11, pp. 31-50, 2005
- [30] I. Thanaya, S. Zoorob, and J. Forth, "A laboratory study on cold-mix, cold-lay emulsion mixtures," in *Proceedings of the Institution of Civil Engineers: Transport*, 2009, pp. 47-55, 2009
- [31] R. Pereira, A. Almeida-Costa, C. Duarte, and A. Benta, "Warm mix asphalt: Chemical additives' effects on bitumen properties and limestone aggregates mixture compactibility," *International Journal of Pavement Research and Technology*, vol. 11, pp. 285-299, 2018.
- [32] . A. Dokandari, J. Oner, A. Topal, and B. Sengoz, "A Laboratory Study of An Organic Warm Mix Asphalt Additive on Aging Characteristics of Bituminous Mixtures," *Pamukkale University Journal of Engineering Sciences*, vol. 20, pp. 332-337, 2014.
- [33] M. C. Rubio, G. Martínez, L. Baena, and F. Moreno, "Warm mix asphalt: an overview," *Journal of Cleaner Production*, vol. 24, pp. 76-84, 2012.

- [34] A. K. Arshad, F. A. M. Kridan, and M. Y. A. Rahman, "The effects of Sasobit® modifier on binder at high and intermediate temperatures," *International Journal of Engineering and Advanced Technology (IJEAT)*, vol. 2, pp. 81-84, 2013.
- [35] H. Fazaeli, H. Behbahani, A. A. Amini, J. Rahmani, and G. Yadollahi, "High and low temperature properties of FT-paraffin-modified bitumen," *Advances in Materials Science and Engineering*, vol. 2012, 2012.
- [36] S. A. Yero and M. R. Hainin, "Viscosity characteristics of modified bitumen," *ARPN Journal of Science and Technology*, vol. 2, pp. 500-503, 2012.
- [37] D. Cao and J. Ji, "Evaluation of the Long-term Properties of Sasobit Modified Asphalt," *International Journal of Pavement Research & Technology*, vol. 4, 2011
- [38] P. A. Dokandari and A. Topal, "Effects of warm mix asphalt additives on aging characteristics of bituminous mixtures," *Periodica Polytechnica Civil Engineering*, vol. 59, pp. 475-486, 2015
- [39] X. Liu, A. Sha, C. Li, Z. Zhang and H. Li, "Influence of water on warm-modified asphalt: Views from adhesion, morphology and chemical characteristics," *Construction and Building Materials*, 264, 120159, 2020.
- [40] M. Yue, J. Yue, R. Wang and Y. Xiong, "Evaluating the fatigue characteristics and healing potential of asphalt binder modified with Sasobit® and polymers using linear amplitude sweep test," *Construction and Building Materials*, 289, 123054, 2021.
- [41] F. S. Bhat and M. S. Mir, "Investigating the Performance of Nano-Modified Asphalt Binders Incorporated with Warm Mix Additives," *Journal of Materials in Civil Engineering*, 33(11), 04021319, 2021.
- [42] S. Carlina, B. S. Subagio, and A. Kusumawati, "The Performance of Warm Mix for the Asphalt Concrete-Wearing Course (AC-WC) Using the Asphalt Pen 60/70 and the Sasobit® Additives," *Journal of Civil Engineering*, vol. 26, pp. 11-16, 2019.
- [43] J. Raveesh, R. Dhumagond, and S. Bijjur, "Experimental Study of WMA by Using Sasobit Additive," *International Journal of Applied Engineering Research*, vol. 13, pp. 163-165, 2018
- [44] J. Zhang, F. Yang, J. Pei, S. Xu, and F. An, "Viscosity-temperature characteristics of warm mix asphalt binder with Sasobit®," *Construction and Building Materials*, vol. 78, pp. 34-39, 2015.
- [45] G.-j. Zhao and P. Guo, "Workability of Sasobit warm mixture asphalt," *Energy Procedia*, vol. 16, pp. 1230-1236, 2012.
- [46] G. C. Hurley and B. D. Prowell, "Evaluation of Sasobit for use in warm mix asphalt," *NCAT report*, vol. 5, pp. 1-27, 2005.
- [47] CEN, "Bitüm ve bitümlü bağlayıcılar-İğne batma derinliği tayini (Bitumen and bituminous binders - Determination of needle penetration), TS EN 1426," ed, 2015.
- [48] CEN, "Bitüm ve bitümlü bağlayıcılar-Yumuşama noktası tayini-Halka ve bilye yöntemi (Bitumen and bituminous binders - Determination of the softening point - Ring and Ball method), TS EN 1427," ed, 2015
- [49] CEN, "Petrol ürünleri-Parlama ve yanma noktası tayini-Cleveland açık kap metodu (Determination of flash and fire points - Cleveland open cup method), TS EN ISO 2592," ed, 2006.
- [50] ASTM, "Standard Test Method for Viscosity Determination of Asphalt at Elevated Temperatures Using a Rotational Viscometer, ASTM D4402," ed, 2015.
- [51] Y. Taşdemir, "Bitümlü kaplamaların termal davranışlarının performans testleri ile incelenmesi," Doktora PhD, İnşaat Mühendisliği, İstanbul Teknik Üniversitesi, 2003
- [52] CEN, "Bitümler ve bitümlü bağlayıcılar - Karmaşık kesme modülü ve faz açısının tayini - Dinamik kesme rheometresi (Bitumen and bituminous binders - Determination of complex shear modulus and phase angle - Dynamic Shear Rheometer (DSR), TS EN 14770," ed, 2012.
- [53] CEN, " Bitüm ve bitümlü bağlayıcılar - Isı ve hava etkisi altında sertleşme direncinin tayini - Bölüm 1: RTFOT yöntemi Başlık (Bitumen and bituminous binders - Determination of the resistance to hardening under influence of heat and air - Part 1: RTFOT method), TS EN 12607-1 " ed, 2015.
- [54] K. Karakuzu and H. Özen. "Türkiye Şartlarında İlık Karışım Asfalt Uygulamasının Ekonomik ve Çevresel Değerlendirmesi," *Erzincan Üniversitesi Fen Bilimleri Enstitüsü Dergisi*, 13(2), 429-443, 2020.
- [55] A. Topal, J. Oner, B. Sengoz, P. A. Dokandari, D. Kaya Evaluation of rutting performance of warm mix asphalt. *International Journal of Civil Engineering*, 15(4), 705-714, 2017.
- [56] Z. Arega, A. Bhasin "Interim Report: Binder Rheology and Performance in Warm Mix Asphalt", Texas Transportation Institute, Texas, USA, Report No. 0-6591, 2012.

BIOGRAPHIES

İslam GÖKALP obtained his BSc degree in civil engineering from Muğla Sıtkı Koçman University in 2012. He received MSc. diploma in Civil Engineering from the Graduate School Of Natural and Applied Science of Adana Science and Technology University in 2016 and PhD degrees in Graduate School Of Natural and Applied Science of Süleyman Demirel University in 2021. His research interests are transportation engineering. .

Model of Combined IPT and NNLVQ for Classification of Healthy and Sick Broilers In Terms of Avian Influenza

Ahmet Kayabasi^{1*} 

^{1*} Karamanoglu Mehmetbey University, Electrical and Electronics Engineering Department, 70100, Karaman, Turkey. (e-mail: ahmetkayabasi@kmu.edu.tr).

ARTICLE INFO

Received: Feb., 22. 2021

Revised: Jul., 26. 2021

Accepted: Aug., 03. 2021

Keywords:

Broiler chicken

Classification

Avian influenza

Neural network

Learning vector quantization

Corresponding author: *Ahmet Kayabasi*

ISSN: 2536-5010 / e-ISSN: 2536-5134

DOI: <https://doi.org/10.36222/ejt.884730>

ABSTRACT

Poultry meat is an important and economical protein source in providing the animal protein requirement for human nutrition. The poultry diseases such as avian influenza that are a feature of fast-spread in farms seriously threatens both the economy and human health. Avian influenza must be detected early because it spreads rapidly. Earlier detection of poultry diseases has become more possible with the development of systems combining image processing techniques (IPTs) and artificial intelligence techniques (AITs). In this study, the neural network (NN) based model using learning vector quantization (LVQ) structure is proposed for the classification of broiler chickens as healthy and sick. In the literature, seven main visual feature parameters that indicate the health status of broilers were acquired through the IPTs. The data set includes seven visual features is used for training, testing and validating process of the NNLVQ model. The classification performance of the neural network (NN) using learning vector quantization (NNLVQ) is compared with IPT concerning its efficiency and accuracy. In the training process, the NNLVQ model classifies the broilers in terms of avian influenza with an accuracy error (AE) of 0.384%. The results point out that, the IPT based application using NNLVQ is successfully classified the broilers in terms of their health conditions.

1. INTRODUCTION

The poultry meat is seen as an important and economical protein source in providing the animal protein needs required for human nutrition with its low fat and high protein content. Poultry meat consumption has been increased in recent years due to cheaper and shorter production times than red meat [1]. Therefore, poultry meat production increased to second place after pork in meat production. To meet this need, broiler chickens are grown which are fast-growing, better utilizing than feed and producing high-quality carcass. The most important factor in poultry farming is the health and regular control of poultry. The prevalence of poultry diseases has seriously affected poultry farming in recent years. This situation poses a threat not only for economic reasons but also for human health. Today, the diagnosis of poultry diseases is performed manually with the observation of the veterinarian and using various laboratory tests. However, manual processes are time-consuming, difficult, and yet fail to detect some of the diseases. Therefore, rapid detection of poultry diseases has become an important issue in broiler breeding. The automatic detection of broiler diseases with the help of image processing techniques (IPTs) has been an important topic in the point of fast diagnosis. For this issue, the neural network (NN) using

learning vector quantization (LVQ) can be combined with IPTs.

The several studies regarding the diagnosis of broiler diseases using NNs combined IPT have been proposed in the literature [2]–[8]. In [2], it was comparatively determined by different machine learning algorithms that the broiler chickens were healthy or sick for avian influenza disease and the most successful result was obtained with a support vector machine (SVM). The data set used in machine learning algorithms was created by computer vision. The body weights of live broilers were estimated by using IPT analysis by Mollah et al. [3]. The estimated weights and manual measurement results were shown to be very close to each other. In [4], different artificial intelligence techniques (AITs) were used to estimate intestinal broiler microflora. The results show that the Enterobacteriaceae population was predicted better than the lactic acid bacteria with the proposed models. A novel algorithm of image analysis was investigated for early detection of lameness for broilers by Aydın and some feature variables of broilers were detected by the proposed algorithm [5]. In [6], the welfare status in commercial broiler breeders was assessed by the data mining algorithms combined with IPT and results were obtained successfully. The NNs such as artificial neural network (ANN) and adaptive neuro-fuzzy

inference system (ANFIS) were proposed to predict chick body mass and more successful results were achieved with ANN by Ferraz et al. [7]. In [8], the weight prediction of broiler chickens five regression model integrated with 3D computer vision was used and the best result was obtained with the Bayesian ANN model.

In this study, the NN using LVQ (NNLVQ) is modeled to classify broiler chickens as healthy and sick in terms of avian influenza infection. In the literature, the data set includes 7 main visual feature parameters that indicate the health status of broilers were acquired through the IPTs [9]. These visual parameters are concavity, skeleton attitude angle, skeleton splicing angle and shape features (area-linear rate, elongation and circularity). About seven visual features, the 300 data sets were created, 150 of which were healthy and 150 of sick broilers [9]. The accuracy of the models is determined by selected 260 training, 20 testing and 20 validating broilers data set and their performances of classification are compared to each other. In the training process, the NNLVQ model successfully classifies the broilers as healthy and sick with an accuracy of 99.616%.

2. DATA SET

The automatic classification application based on NNs is carried out through a data set reported elsewhere [9], containing 7 main visual feature parameters of broiler chickens. In the literature, four to six weeks old broiler chickens were divided into two groups and placed in isolator cages [2]–[9]. Ten of the twenty R381 group broilers were vaccinated with 0.1 mL volume of 106 EID50 H5N2 avian influenza virus (R381 / 2008) and the other ten were intranasally injected with 0.1 mL phosphate-buffered saline (PBS). Clinical symptoms of avian influenza were observed in twenty broilers after 14 days [2]–[9]. As shown in Figure 1, the images of broilers were captured with a resolution of 640 by 480 pixels by using a Logitech C922 CCD camera and image processing was performed using an algorithm based on VS2013 and OpenCV 2.4.13 [2]. To calculate the skeletal structure of the broiler, the algorithm only extracts the image of the broiler from the complex background as shown in Figure 2. The eigenvectors are determined according to the features such as concavity, skeleton attitude angle, skeleton splicing angle and shape features [2]–[9]. Briefly, the process for obtaining data on the visual properties of the broiler is shown as topology in Figure 3.

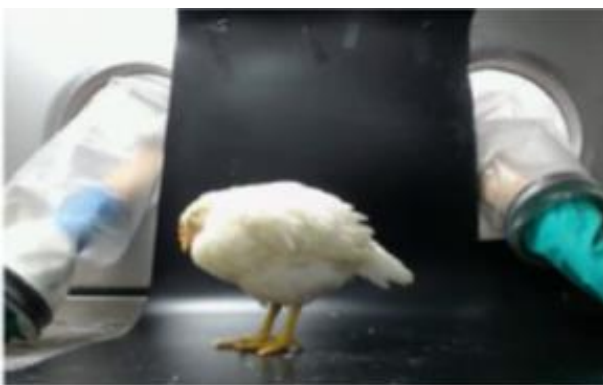


Figure 1. Image of broilers capture environment [2]



Figure 2. Image of extracted broiler from the background [2]

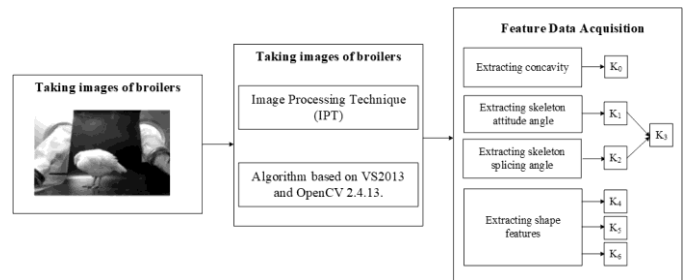


Figure 3. Image The topology of IPT

2.1. Broiler feature extraction

In this section, the extraction of the features of broilers will be briefly summarized according to what is described in Zhuang et al. [2]. Concavity, skeleton attitude angle, skeleton splicing angle, area-linear ratio, elongation and circularity were named K_0 , K_1 , K_2 , K_4 , K_5 and K_6 respectively [2]. K_3 was obtained by using the methods of skeleton simplification and skeleton splicing [2].

$$K_0 = \mathring{\mathbf{a}} \sum_{i=1}^n \frac{b(s_1, s_2)l(s_1)l(s_2)}{[l(s_1) + l(s_2)]r} \quad (1)$$

$$K_1 = \mathring{\mathbf{a}} \sum_{i=1}^n \frac{l_i}{L} b \quad (2)$$

$$K_2 = b = \arctan \frac{\mathring{\mathbf{a}} \sum_{i=1}^n |y_i^r - y_i^l|}{\mathring{\mathbf{a}} \sum_{i=1}^n |x_i^r - x_i^l|} \quad (3)$$

$$K_4 = \frac{S}{C} \quad (4)$$

$$K_5 = \frac{H}{W} \quad (5)$$

$$K_6 = \frac{4pS}{C^2} \quad (6)$$

In the Figure 4, 2D scattering of the broilers features is demonstrated to show how healthy and sick broilers

discriminate among each other by the feature parameters. In addition, the graphs of all feature parameters (K_0 , K_1 , K_2 , K_4 , K_5 and K_6) are plotted in Figure 5. It is observed that healthy and sick broilers distinctly cluster for the visual feature parameters.

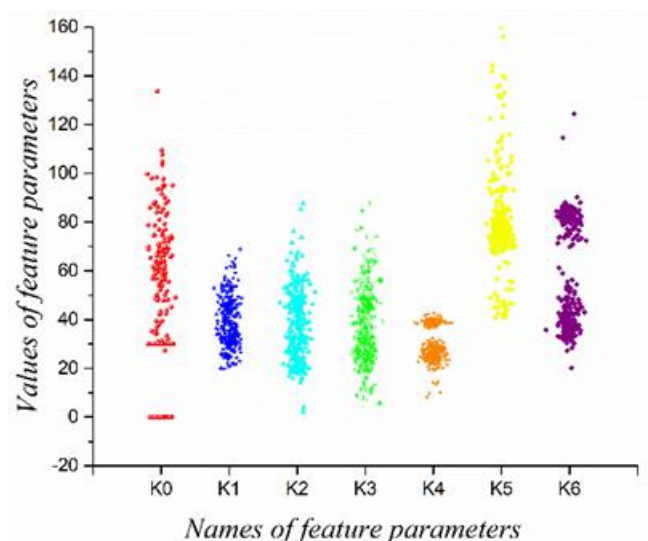


Figure 4. 2D scattering of 300 broilers according to feature parameters

3. NEURAL NETWORK

The NN currently provides the best solutions to many problems in image recognition. The NN interprets the raw input by labeling or clustering with a kind of machine perception. It helps to group unlabeled data according to similarities between sample inputs and classify data when they have a data set labeled for training [2], [3], [13], [4]–[8], [10]–[12]. The modeling and training of the NNLVQ for the classification of broilers in terms of avian influenza are described below.

3.1. Modelling and training of neural network

The NNLVQ is modeled and trained with appropriate set parameters according to the topology illustrated in Figure 6. The computer used in this study has property of Intel Core i7 CPU with 3.1 GHz and 8 GB DDR3 RAM. According to the result of the training, the model is updated and the training is repeated. Modeling and training processes are carried out one after the other to try to obtain the lowest classification accuracy error. The NNLVQ model numerically calculates the outputs according to accuracy error (AE) in given Eq. (7).

The NN consists of neurons that are organized into different layers. These neurons containing a non-linear type of functions are mutually connected by synaptic weights. These weights increase or decrease to output closer to target throughout the training process [11]–[13]. As shown in Figure 7, along with the set parameters given in Table 1, NNLVQ is designed to classify the broilers into “healthy” or “sick” according to the feature parameters. The NNLVQ model is constructed with an input layer having 7 neurons, one hidden layer having 5 neurons and one output layer have 2 neurons.

$$AE = \frac{Error \times 100}{Actual \ value} \quad (7)$$

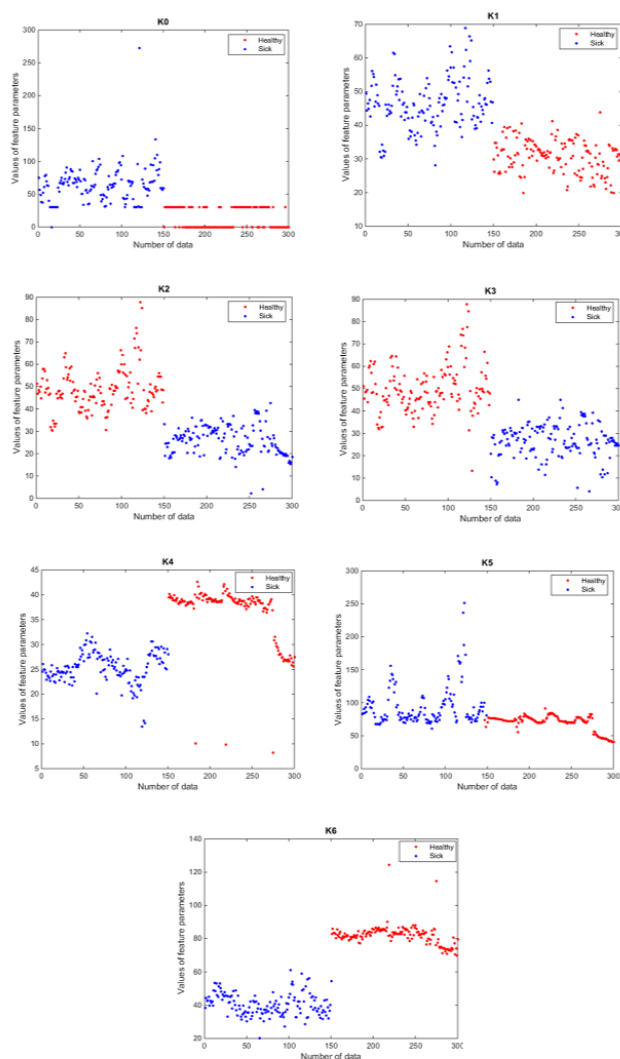


Figure 5. Separately graphs of feature parameters

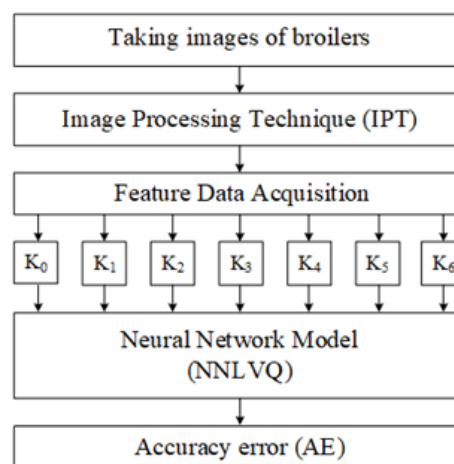


Figure 6. Topology of the NNLVQ model

TABLE I
THE SET PARAMETERS OF THE NNLVQ MODEL

Model	Parameters	Set type/value
ANN _{LVQ}	Epochs	200
	Minimum gradient descent	10 ⁻⁷
	Learning rate	0.02
	Validation checks	7
	Output class percentage	0.5, 05

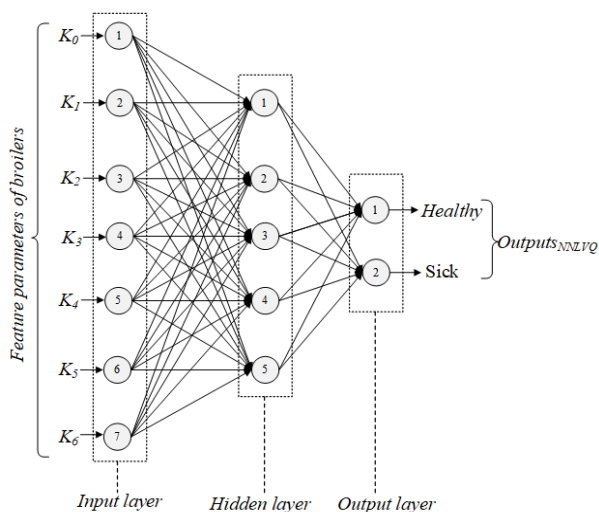


Figure 7. Structure of the NNLVQ model

The 260 visual data of broilers randomly selected from 300 data are used for the training of NNLVQ. The only one of 260 data sets used for the training process are incorrectly classified in the NNLVQ model.

3.2. Testing and validating of neural network

The data of 20 broilers' visual features is used to test the accuracy of the NNLVQ. The tabulated in Table 2, 20 test data are randomly selected among 300 broiler visual features and are not utilized during the training phase. The results of NNLVQ model are tabulated in Table 3 for testing process. Only one of the 20 data sets used for the testing process is misclassified in the NNLVQ model.

TABLE II
THE USED DATASET IN THE TESTING PROCESS

Sample #	Broiler visual feature parameters						
	K_0	K_1	K_2	K_3	K_4	K_5	K_6
1	63.107	45.511	47.432	48.280	24.506	92.983	49.032
2	77.059	56.150	57.923	60.245	23.494	104.790	41.570
3	94.870	52.251	53.972	53.208	27.032	106.771	39.533
4	48.201	40.805	44.882	52.308	21.656	102.395	44.597
5	88.663	38.896	40.130	13.331	27.826	74.370	45.486
6	30.000	30.537	30.441	32.421	25.180	67.822	53.184
7	42.109	40.774	41.463	43.884	22.894	74.899	31.859
8	57.653	43.820	45.626	45.525	28.944	76.513	38.068
9	56.507	44.460	46.838	45.537	26.090	83.886	44.182
10	71.938	46.576	48.617	48.596	26.984	84.884	34.354
11	0.000	33.062	27.811	27.422	40.251	79.293	84.501
12	0.000	25.632	27.911	27.911	39.089	68.627	86.474
13	30.000	30.170	31.432	31.776	37.738	71.717	80.250
14	0.000	38.272	28.407	32.292	38.397	72.330	80.937
15	30.000	30.656	31.446	31.735	38.659	74.510	81.526
16	0.000	37.426	25.710	27.892	40.695	71.698	81.854
17	0.000	27.892	26.842	11.737	29.655	52.381	74.457
18	0.000	35.241	28.457	28.457	39.116	80.000	82.462
19	0.000	30.149	32.986	32.986	38.708	83.505	82.744
20	0.000	37.808	27.126	29.947	38.190	72.195	80.570

The proposed NNLVQ model is validated with the remaining 20 broiler data given in Table 4. All 20 data sets used for the validating process are correctly classified in the NNLVQ model. As it is seen from the validating results given in the Table 5, the proposed model can be successfully implemented to such classification of broilers as healthy or sick.

TABLE III

THE RESULTS OF NNLVQ MODEL IN THE TEST PROCESS

#	Target	Numerical outputs				Classification
		NNLVQ				
		NNLVQ	NNLVQ	NNLVQ	NNLVQ	
1	0.000	1.000	0.000	1.000	Healthy	
2	0.000	1.000	0.000	1.000	Healthy	
3	0.000	1.000	0.000	1.000	Healthy	
4	0.000	1.000	0.000	1.000	Healthy	
5	0.000	1.000	0.000	1.000	Healthy	
6	0.000	1.000	1.000	0.000	Sick	
7	0.000	1.000	0.000	1.000	Healthy	
8	0.000	1.000	0.000	1.000	Healthy	
9	0.000	1.000	0.000	1.000	Healthy	
10	0.000	1.000	0.000	1.000	Healthy	
11	1.000	0.000	1.000	0.000	Sick	
12	1.000	0.000	1.000	0.000	Sick	
13	1.000	0.000	1.000	0.000	Sick	
14	1.000	0.000	1.000	0.000	Sick	
15	1.000	0.000	1.000	0.000	Sick	
16	1.000	0.000	1.000	0.000	Sick	
17	1.000	0.000	1.000	0.000	Sick	
18	1.000	0.000	1.000	0.000	Sick	
19	1.000	0.000	1.000	0.000	Sick	
20	1.000	0.000	1.000	0.000	Sick	

TABLE IV

THE USED DATASET IN THE VALIDATING PROCESS

Sample #	Broiler visual feature parameters						
	K_0	K_1	K_2	K_3	K_4	K_5	K_6
1	73.249	42.214	44.400	45.639	27.376	77.211	31.599
2	35.776	47.980	49.050	49.021	25.439	79.237	38.477
3	32.124	33.947	36.189	36.621	28.928	71.260	47.783
4	69.812	53.009	56.221	56.280	19.768	112.752	39.254
5	88.663	38.896	40.130	13.331	27.826	74.370	45.486
6	50.140	36.713	38.415	41.469	30.807	77.000	38.730
7	63.107	45.511	47.432	48.280	24.506	92.983	49.032
8	59.294	46.962	48.768	48.673	25.266	73.646	32.114
9	48.201	40.805	44.882	52.308	21.656	102.395	44.597
10	30.000	65.139	85.255	84.659	24.316	172.881	56.283
11	30.000	24.690	23.574	23.574	39.190	70.202	86.018
12	30.000	30.656	31.446	31.735	38.659	74.510	81.526
13	0.000	30.149	32.986	32.986	38.708	83.505	82.744
14	0.000	31.578	30.196	32.819	38.687	71.212	85.141
15	0.000	37.808	27.126	29.947	38.190	72.195	80.570
16	0.000	34.013	38.177	38.177	38.914	77.500	80.801
17	30.000	30.170	31.432	31.776	37.738	71.717	80.250
18	0.000	27.487	17.788	16.077	40.307	70.531	84.474
19	0.000	35.241	28.457	28.457	39.116	80.000	82.462
20	30.000	22.279	23.376	25.104	36.441	70.202	76.827

TABLE V

THE RESULTS OF NNLVQ MODEL IN THE VALIDATING PROCESS

#	Target	Numerical outputs				Classification
		NNLVQ				
		NNLVQ	NNLVQ	NNLVQ	NNLVQ	
1	0.000	1.000	0.000	1.000	Healthy	
2	0.000	1.000	0.000	1.000	Healthy	
3	0.000	1.000	0.000	1.000	Healthy	
4	0.000	1.000	0.000	1.000	Healthy	
5	0.000	1.000	0.000	1.000	Healthy	
6	0.000	1.000	1.000	0.000	Sick	
7	0.000	1.000	0.000	1.000	Healthy	
8	0.000	1.000	0.000	1.000	Healthy	
9	0.000	1.000	0.000	1.000	Healthy	
10	0.000	1.000	0.000	1.000	Healthy	
11	1.000	0.000	1.000	0.000	Sick	
12	1.000	0.000	1.000	0.000	Sick	
13	1.000	0.000	1.000	0.000	Sick	
14	1.000	0.000	1.000	0.000	Sick	
15	1.000	0.000	1.000	0.000	Sick	
16	1.000	0.000	1.000	0.000	Sick	
17	1.000	0.000	1.000	0.000	Sick	
18	1.000	0.000	1.000	0.000	Sick	
19	1.000	0.000	1.000	0.000	Sick	
20	1.000	0.000	1.000	0.000	Sick	

It is seen from these results that the proposed NNLVQ model based on IPT is successful. This model can be used to

automatically detect sick broilers in a farm as shown in Figure 8. In this regard, images taken at certain intervals with cameras on a farm can be analyzed using NNLVQ. After determining the coordinate of the sick broiler, it can be taken to another area by removing the broiler with a 3-dimensional movable mechanism. In this way, early screening can be done by making an instant scan and the spread can be prevented. Also, the presented models can be easily integrated into farm industry to automatically classify of different animal.

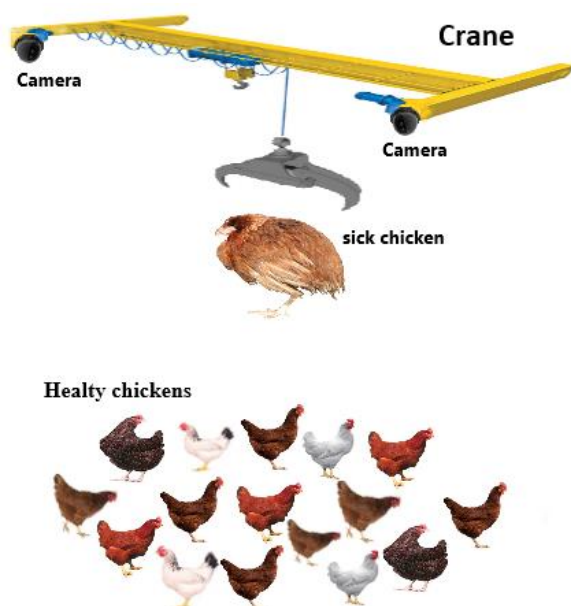


Figure 8. The system of automatically detect sick broilers

4. RESULT and CONCLUSION

The poultry diseases such as avian influenza that are a feature of fast-spread in farms seriously threatens both the economy and human health. Avian influenza must be detected early because it spreads rapidly. Earlier detection of poultry diseases has become more possible with the development of systems combining IPTs and AITs. In this paper, application of IPT based NNLVQ is successfully carried out for classification of broilers in terms of avian influenza. The model is conducted through 300 data of which visual features of broilers acquired using IPT. The training, testing and validating of the NNLVQ model is accomplished by using data of 260, 20 and 20 visual data, respectively. In the training process, the NNLVQ model successfully classifies the broilers as healthy and sick with an accuracy of 99.616%. The NNLVQ model classifies the outputs with accuracy of 100%, for validating process. The proposed NNLVQ model can be integrated to a hardware system so as to automatically classify sick broilers in a farm. In addition, automatic classification of broilers in terms of different health problems can be made after NNLVQ are updated.

REFERENCES

[1] A. C. Fanatico, P. B. Pillai, J. L. Emmert, and C. M. Owens, "Meat quality of slow- and fast-growing chicken genotypes fed low-nutrient or standard diets and raised indoors or with outdoor access," *Poult. Sci.*, vol. 86, no. 10, pp. 2245–2255, 2007, doi: 10.1093/ps/86.10.2245.

- [2] X. Zhuang, M. Bi, J. Guo, S. Wu, and T. Zhang, "Development of an early warning algorithm to detect sick broilers," *Comput. Electron. Agric.*, 2018, doi: 10.1016/j.compag.2017.11.032.
- [3] M. B. R. Mollah, M. A. Hasan, M. A. Salam, and M. A. Ali, "Digital image analysis to estimate the live weight of broiler," *Comput. Electron. Agric.*, 2010, doi: 10.1016/j.compag.2010.02.002.
- [4] H. R. Hemati Matin, A. A. Saki, M. Bayat Varkeshi, and H. Zare Abyaneh, "Comparison and validation of artificial intelligent techniques to estimate intestinal broiler microflora," *Neural Comput. Appl.*, 2013, doi: 10.1007/s00521-012-1059-2.
- [5] A. Aydin, "Development of an early detection system for lameness of broilers using computer vision," *Comput. Electron. Agric.*, 2017, doi: 10.1016/j.compag.2017.02.019.
- [6] D. F. Pereira, B. C. B. Miyamoto, G. D. N. Maia, G. Tatiana Sales, M. M. Magalhães, and R. S. Gates, "Machine vision to identify broiler breeder behavior," *Comput. Electron. Agric.*, 2013, doi: 10.1016/j.compag.2013.09.012.
- [7] P. F. P. Ferraz et al., "Predicting chick body mass by artificial intelligence-based models," *Pesqui. Agropecu. Bras.*, 2014, doi: 10.1590/S0100-204X2014000700009.
- [8] A. K. Mortensen, P. Lisouski, and P. Ahrendt, "Weight prediction of broiler chickens using 3D computer vision," *Comput. Electron. Agric.*, 2016, doi: 10.1016/j.compag.2016.03.011.
- [9] T. Zhang, M. Bi, J. Guo, and X. Zhuang, "Data for: Broiler chickens posture feature extraction and disease early-warning algorithm," *Mendeley Data*, V1, 2017, <https://data.mendeley.com/datasets/txjj8mwtz6/1>.
- [10] T. Temel, "A new classification algorithm: Optimally Generalized Learning Vector Quantization (OGLVQ)," *Neural Netw. World*, 2017, doi: 10.14311/NNW.2017.27.031.
- [11] S. Haykin, M. C. Publishing, J. Kacprzyk, and J. Wiley, "Neural Networks: A Comprehensive Foundation, Possibility Theory. An Approach to the Computerized Processing of Uncertainty (Plenum the Management of Uncertainty, edited by L. A. A.)," 1994.
- [12] Ö. Dursun, S. Toraman, and A. Türkoğlu, "Comparison Of The Classification Performances Of Criminal Tendencies Of Schizophrenic Patients By Artificial Neural Networks And Support Vector Machine," *Eur. J. Tech.*, vol. 7, no. 2, pp. 177–185, 2017.
- [13] B. Kilic, "Impedance Image Reconstruction with Artificial Neural Network in Electrical Impedance Tomography," *Eur. J. Tech.*, Dec. 2019, doi: 10.36222/ejt.650616.

BIOGRAPHIES

Ahmet Kayabasi received his B.S. and M.S. degrees in EEE from Selcuk University, Turkey, in 2001, 2005 respectively. In 2015, he received his Ph.D. degree in electrical and electronics engineering from Mersin University, Turkey. From 2001 to 2015, he was a lecturer in the Electronics and Automation Department of Selcuk University. He has been working as Associate Professor in the Department of Electrical and Electronics Engineering at Karamanoglu Mehmetbey University. His current research interests include image processing techniques, artificial intelligent, antennas, microstrip antennas, computational electromagnetic.

A New Joining Algorithm for Multi-hop Non-mobile Wireless Sensor Networks

M. Çibuk¹ , D. Arı² , F. Ağgün³ 

¹Bitlis Eren University, Department of Computer Engineering, Bitlis, Turkey, (mcibuk@beu.edu.tr)

²Bitlis Eren University, Department of Computer Engineering, Bitlis, Turkey, (dari@beu.edu.tr)

³Bitlis Eren University, Department of Computer Technologies, Bitlis, Turkey, (faggun@beu.edu.tr)

ARTICLE INFO

Received: Apr., 15. 2021

Revised: Sep., 24. 2021

Accepted: Sep., 29. 2021

Keywords:

Wireless Sensor Networks
Relay Mechanism
Channel Allocation
Joining Algorithm

Corresponding author: M. Çibuk

ISSN: 2536-5010 / e-ISSN: 2536-5134

DOI: <https://doi.org/10.36222/ejt.916717>

ABSTRACT

Wireless Sensor Networks (WSN) are divided into two categories as single-hop and multi-hop according to the connection states of the sensor nodes. In the single-hop WSNs, the sensor nodes communicate directly with the management unit (coordinator node). On the other hand, in multi-hop WSNs, the sensor nodes, which are out of the coverage area of the coordinator node communicate with the coordinator over other joined sensor nodes. Multi-hop WSNs preferred for complex applications where there are many sensor nodes. In such applications, connecting to the network and maintaining the continuity in the network is difficult and requires very complicated algorithms for sensor nodes.

In this study, a new network-joining algorithm for multi-hop WSNs has been proposed and designed. According to the algorithm, there is a management unit which is named as coordinator node (CN) for maintaining the network connectivity and the nodes which are the members of the network sends network joining requests over a common contention-based channel for joining the network. If there is a coordinator node in the coverage area, the sensor node joins directly to the network and coordinator allocates an appropriate channel to the new node. If the channel has multiple users, it is used as time-shared. If the sensor node is out of coverage area, directly joining to the network is impossible. In this case, the sensor node sends a relay request to the other joined sensor nodes. The available sensor node responds to this relay request via handshake. The sensor node uses the relay node's channels as shared by using time-sharing methods. Therefore, the new node joins the network from the relay node's channel. The main goal of this algorithm is to speed up joining of sensor nodes to the networks in multi-hop WSNs. Also, another goal is maximizing the continuity of the sensor nodes in the network. Thus, the algorithm improves performance and ensures data transfer continuity of WSNs.

1. INTRODUCTION

Wireless Sensor Networks (WSNs) consists of Sensor Nodes (SNs) connected wirelessly with each other. In the WSNs, there are sensor nodes and a coordinator node as basic network elements. The Coordinator Node (CN) organizes the other network elements. The most basic feature of sensor nodes is to sense environmental data, to process sensed data and to transmit processed data[1]–[3]. The required sensor node count changes from application to application. For example, in order to track environmental imaging and natural catastrophes, because of the land structure, requires a large number of sensor nodes. It is obvious that increasing the number of sensor nodes in the network makes more complicated the network. Complex structured WSNs use a multi-hop network structure as a connection method. In such networks, as shown in Figure 1, the sensor nodes extend coverage of the network by communicating with each other [4], [5]. In multi-hop networks, the sensor nodes perform not

only their own sensing tasks but also for its neighbor nodes the relay function. Multi-hop WSNs have advantages such as coverage, high data transmission rate, low cost[6]. Thanks to these networks, which spread over large areas, data can be collected by consuming less energy. Thus, the lifetime of the network extends[7].

On the contrary of the above mention advantages of the multi-hop WSN, there are some difficulties. Difficulties which foreseen in the multi-hop WSN design are negative factors such as congestion[1], end-to-end delay, hidden node, simultaneous communication, a disconnection of nodes from the network, topology changes[4], and fairness[6]. These difficulties have a negative impact on the performance of the network. When looking at the literature[8]–[11], the existence of studies can be observed on which contains the solution of these difficulties. While the studies, which do for the post-setup phase of the network are more frequent, the studies for network initialization phase seems to be less.

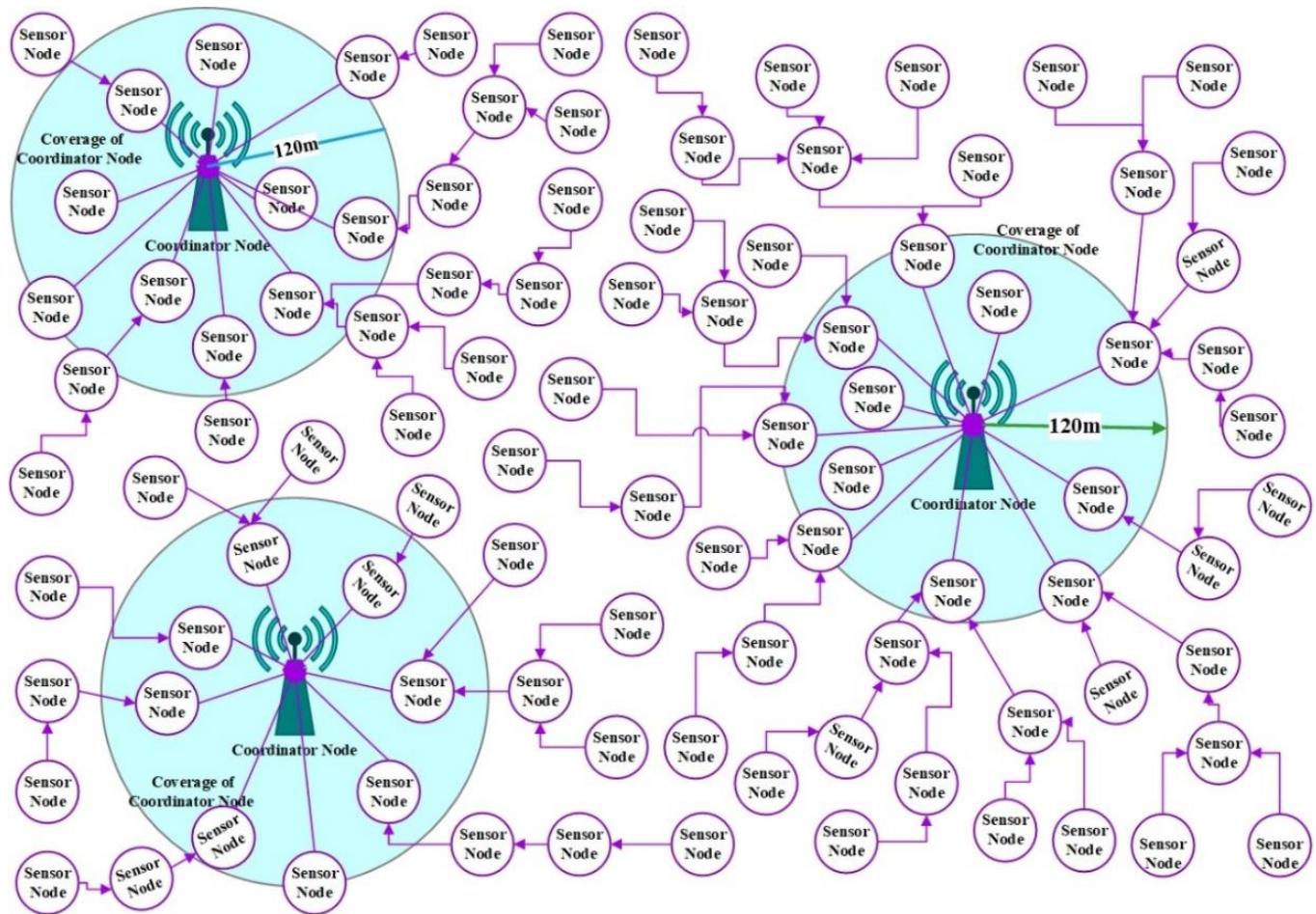


Figure 1. Connection state of Multi-hop Wireless Sensor Networks

In this study, a new joining network algorithm have been developed for the multi-hop non-mobile WSNs. According to the algorithm, the sensor nodes have sensing functions as well as a relay function that for other nodes can be used when needed. Furthermore, in this algorithm, a multi-channel (FDMA) structure has been used to minimize the collision. The nodes use a common contention-based (CSMA-CA) channel for their request to join the network, after which for the communication the nodes uses the channel which allocated by the CN. The sensor node directly joins the network if it is in the coverage area of the CN. If the sensor node is not in the coverage area of CN, the nodes send a request in order to join the network to the nearest sensor node, which has joined before. Neighbor sensor node, which received this network-joining request, sends a request to the CN. If CN accepts to request, the node sets the request-sender node as its relay node and use channels of the relay node. The nodes communicate with the CN as time-shared (TDMA) by using relay node channels. The performance of this algorithm has been tested based on node counts at random form of nodes in the Riverbed Modeler simulation environment.

2. A NEW JOINING ALGORITHM FOR MULTI-HOP NON-MOBILE WIRELESS SENSOR NETWORKS

According to the algorithm, firstly, the nodes listen to the *CH_REQUEST* channel and attempts to obtain the *CH_REQUEST* channel by using the CSMA-CA method, as

shown in Figure 2. *CH_REQUEST* is a common channel, which nodes use to send *CTRL_PKT* (control packet, network-join request) packets to the CN. When the node obtained the channel, it sends a *CTRL_PKT* to the CN. Later, the node starts to listen to the *CH_SCHEDULE* channel that CN uses to send the *SCH_PKT*s which tell conditions of nodes in the network to the SNs. After this stage, the node starts a counter to hold the *Count* for not scheduled and a *wait_time* counter for determining the time without getting any packet. If there is *SCH_PKT* on the channel and a channel allocation is present for itself, the node will be connected to the CN directly. Otherwise, if there is *SCH_PKT* on the channel but channel allocation is not for itself counter will be incremented and it will be returned to listen to *CH_SCHEDULE* channel state until the counter exceeds the *threshold_count* threshold. If there is not any packet on the *CH_SCHEDULE* channel within the *wait_time* the node sets *CTRL_PKT*s relay/request bit as 1 and starts to broadcast a this packet to the neighboring sensor nodes.

The neighboring node that received this packet will send a *RRQUEST_PKT* (relay request packets which supply to join as a relay to the network) to the CN. The relay node becomes the parent of the sensor node, which wants to join the network. After this stage, the relay node starts to send the *SCH_PKT*s which coming from CN to all child nodes by using the *CH_SCHEDULE* channel. The searching relay node or connecting CN directly period continues as described below. After this step, the node repeats the same phase as the phase of direct CN connection that mentions above, as shown in Figure 2.

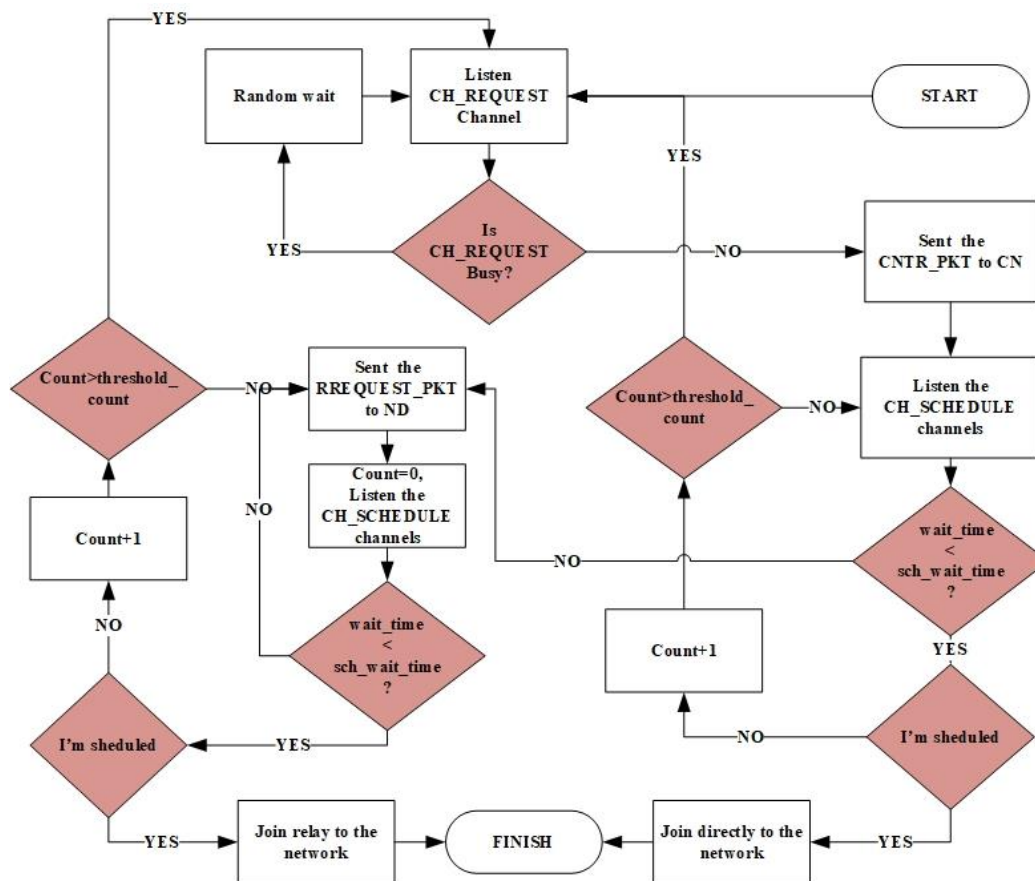


Figure 2. Flowchart of the algorithm

```

Start
Initial_Values_Set, Count=0, Time_out,
wait_time
RREQUEST_PKT, SCH_PKT, CTRL_PKT,
CH_SCHEDULE, CH_REQUEST, CN, ND;
Step:1 Listen CH_REQUEST channel
Step:2 If (Is CH_REQUEST channel busy?)
    Random_wait;
    GoTo Step1;
    Else
        Sent CTRL_PKT to CN
        GoTo Step4;
Step:3 While(Listen CH_SCHEDULE channel){
    If (Is there SCH_PKT)
        GoTo Step4;
    Else
        GoTo Step5
Step:4
    If(I'm scheduled)
        GoTo Step7;
    Else
        Count++;
        If(Count=> threshold_count)
            GoTo Step5;
        Else
            GoTo Step1;
Step:5 sets CTRL_PKT's relay/request bit TRUE
Send CTRL_PKT
Count=0;
While (Listen CH_SCHEDULE channel){
    If (Is there SCH_PKT)
        GoTo Step6;
    Else
        GoTo Step5
Step:6 If(I'm scheduled)
    GoTo Step7;
    Else
        Count++;
        If(Count=> threshold_count)
            GoTo Step1;
        Else
            GoTo Step5;
}
Step:7 I'm joining the network
Finish;

```

3. SIMULATION AND TEST

In this study, Riverbed (Opnet) [12] Modeler simulation environment has been preferred because it has many advantages such as an advanced graphical interface, hierarchical modeling, and simultaneously simulations with multiple inputs to test the algorithm. It also supports from very small networks to very large networks [13].



Figure 3. Scenario of 200 node in Riverbed Modeler network project environment (3200mX3200m)

In this study, the node counts have been defined as 25, 50, 100, 200, 400, 600, 800, 1000 to test the effect of node counts on network joining. The maximum coverage area of both CNs and SNs is set to 120m. Both CNs and nodes are randomly distributed in the simulation area. Thus, a multi-hop structure has been achieved. There are seven CNs in the network and each uses a different schedule channel. In order for the algorithm to have a flexible structure, the SNs configured to listen to all the CN channels. Network environments have been shown in Figure 3.

4. CONCLUSION

The proposed algorithm has shown that all nodes in all scenarios join to the network. As the number of nodes in the scenario increases, hop count increases, so the network joining latency have increased. In Figure 4, it has been shown that status of the node joining to the network for SN side in all scenarios. In Figure 5, it has been shown that status of the node joining to the network for CN side in all scenarios. As seen from the figures the differences between graphs are very small. As the number of nodes increases, the fluctuations in joining network have increased. Even if there is a delay as seen in the figures, all the nodes have joined the network.

Our main goal is not to join the nodes to the CN neither early nor late, but all nodes connect directly or indirectly (relay) to the CN.

Another goal of developed algorithm in this study is to ensure the continuity of connected nodes. It is obvious that the fast reconnection of nodes that are disconnected from the network is very important for the performance of the network. Looking at the results, it is seen that the proposed algorithm produces realistic results close to one hundred percent in network joining.

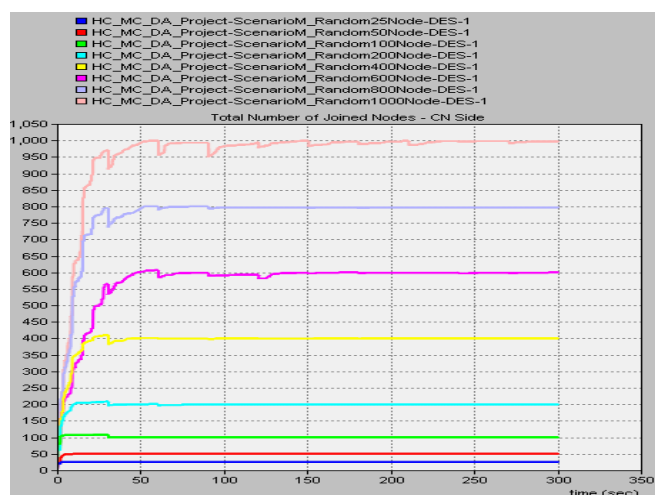


Figure 4. Total Number of Joined Nodes - ND Side

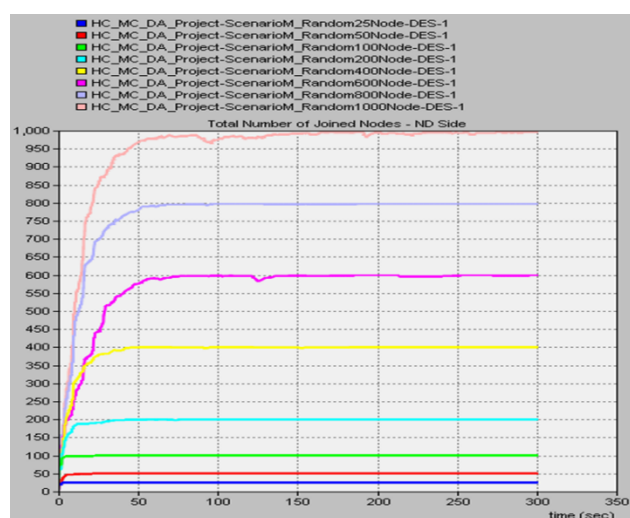


Figure 5. Total Number of Joined Nodes - CN Side

In this study, network joining algorithm considered for the non-mobile WSN networks and performance analysis has performed in the simulation environment. In the future, it is planned to adapt this algorithm for WSN networks consisting of mobile sensor nodes.

ACKNOWLEDGEMENT

The only abstract of this paper was presented in ICCESSEN'17 conference. This paper is an extended full text version of previously presented abstract in ICCESSEN'17.

REFERENCES

- [1] O. Chughtai, N. Badruddin, and A. Awang, 'A novel congestion alleviation procedure in multi-hop wireless sensor networks', 2016 6th International Conference on Intelligent and Advanced Systems (ICIAS), IEEE, pp. 1-6, 2016.
- [2] F. Alshahrany, M. Abbod, and I. Moualek, 'WSN and RFID Integration to Support Intelligent Monitoring in Smart Buildings Using Hybrid Intelligent Decision Support Systems', Acta Phys. Pol. A, vol. 128, no. 2B, p. B-152-B-160, 2015.
- [3] C. Z. Zulkifli, H. N. Hassan, W. Ismail, and S. N. Semunab, 'Embedded RFID and Wireless Mesh Sensor Network Materializing Automated Production Line Monitoring', Acta Phys. Pol. A, vol. 128, no. 2B, p. B-86-B-90, 2015.

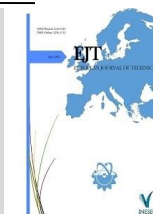
- [4] P. Murdiyati, K. S. Chung, and K. S. Chan, 'A multi-channel MAC for multi-hop wireless sensor networks minimizing hidden node collision', 2016 22nd Asia-Pacific Conference on Communications (APCC), IEEE, pp. 535–540, 2016.
- [5] P. Murdiyati, K. S. Chung, and K. S. Chan, 'Predicting the network throughput of wide area WSN in rural areas', The 20th Asia-Pacific Conference on Communication (APCC2014), IEEE, pp. 106–111, 2014.
- [6] D. D. Vergados, D. J. Vergados, A. Sgora, D. Vouyioukas, and I. Anagnostopoulos, 'Enhancing Fairness in Wireless Multi-Hop Networks', Proceedings of the 3rd International ICST Conference on Mobile Multimedia Communications, ICST, pp. 1–6, 2007.
- [7] C. Duan, F. Shi, X. Ding, X. Xiao, and P. Duan, 'A novel TDMA and multi-hop MAC protocol in cluster-based wireless sensor networks', 2011 6th IEEE Conference on Industrial Electronics and Applications, Bitlis, IEEE, pp. 805–808, 2011.
- [8] K. Nguyen and Y. Ji, 'Achieving Minimum Latency in Multi-Hop MAC Protocol for Wireless Sensor Networks', 2011 IEEE 73rd Vehicular Technology Conference (VTC Spring), IEEE, pp. 1–5, 2011.
- [9] Ji-Jun Zhao and Xiang Sun, 'MAC protocol based on T-MAC multi-hop reservation for short-latency wireless sensor network', 2008 11th IEEE International Conference on Communication Technology, Hangzhou, China, IEEE, pp. 114–117, 2008.
- [10] K. Nguyen and Y. Ji, 'AM-MAC: an energy efficient, Adaptive Multi-hop MAC protocol for sensor networks', Proceedings of the 6th International Wireless Communications and Mobile Computing Conference on ZZZ - IWCMC '10, New York, USA, ACM Press, p. 432, 2010.
- [11] J.-W. Lee and H.-S. Cho, 'Cascading Multi-Hop Reservation and Transmission in Underwater Acoustic Sensor Networks', Sensors, vol. 14, no. 10, pp. 18390–18409, 2014.
- [12] Riverbed Modeler, 'Riverbed Modeler', <https://www.riverbed.com/gb/products/steelcentral/steelcentral-riverbed-modeler.html>, accessed 9 April 2021.
- [13] X. Chang, 'Network simulations with OPNET', Proceedings of the 31st conference on Winter simulation Simulation-a bridge to the future - WSC '99, vol. 1, New York, USA, ACM Press, pp. 307–314, 1999.

BIOGRAPHIES

Musa Çıbuk obtained his bachelors' degree in the Electrical-Electronic Engineering Department at Firat University, Elazığ/Turkey in 1997, his master degree in the Electrical-Electronic Engineering Department at Firat University, Elazığ/Turkey in 2002 and PhD degree in the Electrical-Electronic Engineering Department at Firat University, Elazığ/Turkey in 2009. He is still an academic member of the Computer Engineering Department at Bitlis Eren University. His major areas of interests are: Wireless Communication, Internet, Server Systems, Sensor Networks and Image Processing.

Davut Arı obtained his BSc degree in computer engineering from Harran University (HRU) in 2014. He received the MSc diploma in Electric Engineering from the Bitlis Eren University in 2018. Her research interests are Computational Intelligence, Genetic Programming, Wireless Sensor Networks. In 2015 he joined the Computer Engineering, Faculty of Engineering And Architecture, Bitlis Eren University as a research assistant.

Fikri Ağgün obtained his bachelors' degree in the Computer Engineering Department at Selçuk University, Konya/Turkey in 2001, his master degree in the Biometry and Genetic Department at Yüzüncü Yıl University, Van/Turkey in 2011, Phd Study is resuming. He is still an academic member of the Informatics Department at Bitlis Eren University. His major areas of interests are: Computer Networks, Wireless Sensor Networks and Vehicular Adhoc Networks.



Investigation of Power Consumption Effect of Various Memristor Emulators on a Logic Gate

Sevgi Gürsul¹ , Serdar Ethem Hamamci² 

¹Inonu University, Electrical and Electronic Engineering Department, Malatya, Turkey. (e-mail: sevgi.gursul@inonu.edu.tr).

²Inonu University, Electrical and Electronic Engineering Department, Malatya, Turkey. (e-mail: serdar.hamamci@inonu.edu.tr).

ARTICLE INFO

Received: May., 02. 2021

Revised: Jun., 14. 2021

Accepted: Oct., 06. 2021

Keywords:

Memristor
Memristive systems
Memristor emulators
NAND gate
Power consumption

Corresponding author: *Sevgi Gürsul*

ISSN: 2536-5010 / e-ISSN: 2536-5134

DOI: <https://doi.org/10.36222/ejt.931338>

ABSTRACT

Memristor, also known as memory resistor, is considered as the fourth passive electronic element expressing the relationship between magnetic flux and electric charge. One of the most important features of the memristor is that it has low power consumption. Minimizing power consumption is an important issue in the electronic circuits. However, the fact that the memristor element was not yet fully manufactured has led researchers to design memristor-like emulator circuits. These circuits, which approximate the memristor properties, are realized by combining the other existing electronic elements. In this paper, a basic NAND logic gate is considered and the change in power consumption when using a memristor instead of the standard resistor in the gate circuit is examined. For this purpose, the NAND logic circuit was constituted for four different memristor emulators, and the power consumption values of these circuits were obtained by simulation and experiments. These values are compared with the power consumption values of NAND circuits obtained by using standard resistors equivalent to the memristor resistance. The results clearly show that the memristor gate circuits reduce power consumption compared to standard resistive gate circuits.

1. INTRODUCTION

The basic electrical variables of circuit theory are defined as voltage, current, electric charge and magnetic flux. Considering the relationships between these variables, Professor Leon O. Chua of Berkeley University in 1971 reported that the relationship between electric charge and magnetic flux was missing. Since it is not possible to overcome this deficiency with different combinations of existing elements such as resistor, capacitor and inductor, he introduced a new element called *memristor* and defined its electrical behavior as *memristance* [1]. With this discovery, all the interrelationships between four basic electrical variables were revealed, as shown in Fig. 1. However, Chua was not able to directly obtain the memristor element in those years due to the lack of possibilities and therefore he designed an emulator circuit that approached the role of memristor. In the following years, Chua continued his work on memristor such as the description of memristive systems [2], modeling of various circuits using memristor and other nonlinear circuit elements [3], etc. Other researchers have also made various contributions to the literature on memristor. Definition of the bond-graph model of the memristor [4], analysis of nonlinear circuits containing memristor [5], dynamical analysis of the memristive diode model [6], expression of memristor with

inverse Lagrangian equations [7], the design of an alternative memristive diode model [8], the definition of the resistance switching behavior that can be reproduced in thin oxide films whose hysteresis structure properties resemble the hysteresis of the memristor [9], and the use of memristive nano devices in pattern recognition [10] can be listed as the studies. All of them are theoretical studies on the memristor [11]. In 2008, a group of researchers from HP laboratories announced that they modeled the memristor using titanium dioxide doped with oxygen and physically obtained it [12,13]. With the modeling of the memristor, the interest on the subject has gained an increasing attention on the areas of electrical circuits [14,15], computer memory architectures [16], neuromorphic devices [17], chaotic systems [18,19], and so on.

Memristor element is not yet an element commercially available in the electronics market due to its high cost and stability problems. This has led researchers to design different emulator circuits that can serve as a memristor. One of these studies is a memristor emulator circuit formed using a differential amplifier, an integrator, an analog multiplier and some passive elements [20]. In the circuit, since the analog multiplier expresses the product of the current and the charge, the output of the emulator is nonlinear. Another is a memristor emulator presented by Muthuswamy and designed using an

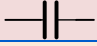


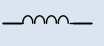
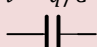
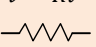
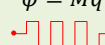
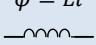
	Electrical charge (q)	Current (i)	Voltage (v)	Magnetic flux (φ)
Electrical Charge (q)	-	$q = \int i dt$	Capacitance $q = Cv$ 	Memristance $q = \varphi/M$ 
Current (i)	$i = dq/dt$	-	Resistance $i = v/R$ 	Inductance $i = \varphi/L$ 
Voltage (v)	Capacitance $v = q/C$ 	Resistance $v = Ri$ 	-	$v = d\varphi/dt$
Magnetic Flux (φ)	Memristance $\varphi = Mq$ 	Inductance $\varphi = Li$ 	$\varphi = \int v dt$	-

Figure 1. Basic linear electronic components and their relations.

analog multiplier, an integrator op-amp, a derivative op-amp and some passive elements [21]. In another study, Alharbi *et al.* designed a current controlled emulator with an exponential amplifier and an integrator using a second generation non-inverting current conveyor (CCII+). In the circuit, the exponential amplifier is used to provide the nonlinearity required for memristive behavior [22]. Another emulator circuit proposed by Alharbi *et al.* has voltage controlled feature and consists of AD844 operational amplifier and analog multiplier elements [23]. In addition to these emulator circuits mentioned, there are also many different emulator circuits in the literature (for more details, see [11] and [24]).

In this study, a NAND gate is considered in order to investigate the logic gate power consumption performances of some memristor emulators proposed in the literature. For comparison, four different emulator circuits are used as memristor. The power values consumed in each circuit built with memristor emulators are determined. Then, the power consumption of the gate circuits using standard resistance equivalent to the memristance value of the memristor emulator is examined. The power consumption values of the NAND gate using memristor emulators and also standard resistors selected as equivalent to the memristance of emulators are compared. As a result, it is clearly seen that using memristor instead of standard resistor in the NAND gate results in lower power consumption. To the best of the authors' knowledge, no previous attempt has been made to compare the performance of these emulators in logic applications in this way. Therefore, the main contribution of the study to the literature is to show that the memristor can be used in logic circuits in terms of lower power consumption. This gives an idea that the use of memristor in electronic circuits and computer systems will lead to more advantageous results in the future.

2. BASIC PROPERTIES OF MEMRISTOR ELEMENT

The memristance of a memristor is defined by

$$M(q(t)) = \frac{d\varphi(t)}{dq(t)} \quad (1)$$

where M represents the memristance, φ is the magnetic flux and q is the electrical charge. So, as can be understood from Eq. (1), the memristor is expressed by the ratio of magnetic flux to electrical charge. The differential expression can be arranged as

$$M(q(t)) = \frac{d\varphi/dt}{dq/dt} = \frac{v(t)}{i(t)}. \quad (2)$$

From Eq. (2), it is seen that the expression of memristance is similar to the ohm law in resistance, but its value changes depending on the amount of charge flowing through it. Therefore, memristor is a circuit element whose memristance decreases when the current is applied from one direction, and its memristance increases when applied in the opposite direction. If the current applied to the element is interrupted, the charge transfer on it stops. However, when the current is applied again, the charge flow continues where it left off. Because of this feature, memristor is also defined as a memory resistor. As mentioned above Chua proved that the new element will generate voltage from current like a resistor, but this voltage will show a more complex and dynamic change depending on the voltage build-up with the change of current and magnetic flux as a result of the movement of the charge (Fig. 2). As shown in Fig. 2, if the memristance of a memristor characterized by a differential load controlled φ - q curve has a non-negative value, that is $(q) \geq 0$, then the instantaneous power of the element has given as

$$P(t) = M(q(t))(i(t))^2. \quad (3)$$

The power will be positive from Eq. (3) and therefore the memristor will show the passive element characteristics [1].

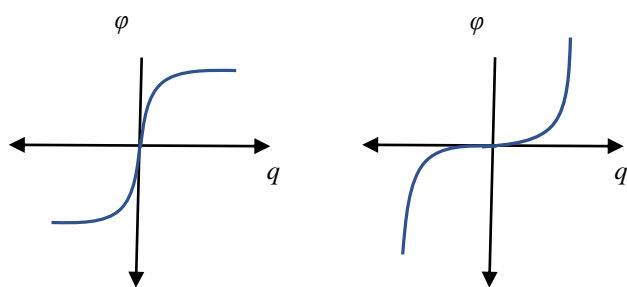


Figure 2. φ - q curves of a memristor [1].

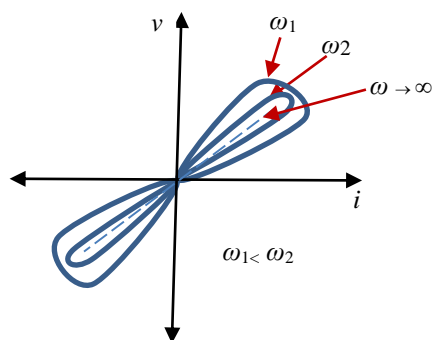


Figure 3. v - i characteristic of a memristor [2].

Continuing their memristor research, Chua and his team proved in their subsequent research that the current-voltage characteristic of a memristor, as seen in Figure 3, exhibits a hysteretic property in the form of a two-leaf clover that changes according to the frequency value applied to the element [2]. As the frequency increases, the hysteretic field narrows and when it approaches infinity, the characteristic resembles the linear resistance characteristic. According to the i - v characteristic, the memristor can have many memristance values varying within a limited range. When the current flowing through the memristor is zero, the voltage is also zero, i.e. there is no phase difference and thus no energy is stored on the memristor. This is a result of the pinched hysteretic feature. Including this feature of the memristor in his work in 1980, Chua summarized some characteristic properties of the memristor as follows [3]:

- Under very high frequency periodic large signal current excitation, the memristive element is equivalent to a linear resistor whose resistance depends on the initial state $x(0)$ which gives rise to the periodic voltage response.
- A passive memristive element can only dissipate energy; that is, it cannot store energy for later recovery.
- Any voltage-current signal pair of a single port memristive element must pass through the zero point in the same time period.
- The memristive element is passive for every $(x,i) \in R^{(n+1)}$ only if $R(x,i) > 0$.

3. MEMRISTOR EMULATOR CIRCUITS

The circuits that provide the characteristic features of the memristor and consist of different electronic elements are called *memristor emulator circuits*. In the literature, many memristor emulator circuits have been designed using different methodologies and topologies, and some of them are mentioned in Section 1. The first of these is an analog memristor emulator designed by Chua in 1971 [1].

In this section, four memristor emulators chosen from the literature will be simulated and installed in the laboratory, then the graphs of the hysteretic current-voltage characteristics will be presented. Thus, it will be checked whether each emulator generates the desired memristor characteristics or not.

3.1. Memristor emulator designed by Mutlu-Karakulak

The memristor emulator presented to the literature by Mutlu and Karakulak consists of a differential amplifier, an integrator, an analog multiplier, a diode and seven resistors [20]. The emulator circuit was established in the Multisim program and the desired current-voltage characteristic was obtained as a result of the simulation. The memristance value of the emulator is determined as 24.49 k Ω . It has been observed that when the frequency is reduced in the circuit, the leaves of the hysteresis curve expand, when the frequency is increased, the hysteresis curve becomes narrower and at very high frequencies the hysteresis curve turns into a standard resistance characteristic. In order to verify the simulation results, the circuit was also set up in the laboratory and it was verified that the desired hysteresis properties were achieved. Experimentally, the memristance value of Mutlu and Karakulak emulator was obtained as 23.405 k Ω . The experimental and simulation results of the Mutlu-Karakulak memristor emulator are given in Fig. 4, and the usability of this emulator in both experimental and simulation environments has been revealed.

3.2. Memristor emulator designed by Muthuswamy

The emulator circuit proposed by Muthuswamy, a student of Chua, is a circuit designed specifically to use in chaotic circuits and has more nonlinear properties [21]. The emulator consists of two analog multipliers, an integrator, a differential amplifier and some resistors. The multisim schema of this memristor emulator is shown in Fig. 5. According to the simulated results, the memristance value of the emulator is 25.23 k Ω , while the experimental memristance value is 20.5 k Ω . As can be seen from Fig. 5, it was observed that the memristor emulator designed by Muthuswamy provided the necessary characteristics.

3.3. Current controlled memristor emulator designed by Alharbi et al

Alharbi *et al.* presented a current controlled memristor emulator to the literature [22]. The simulation circuit of the emulator and the hysteresis curve are obtained in Fig. 6. According to the simulation results, the memristance value of the circuit was found to be approximately 2.5 k Ω . Increasing frequencies values are also applied to the circuit and it has been observed that the leaves gradually contract at high frequencies, which are a memristor feature. The hysteresis curve of the current-controlled emulator implemented in the laboratory is also given in the Fig. 6. The memristance value of the emulator is 2.3 k Ω . According to the experimental results obtained from the implemented circuit, the necessary memristive properties are provided.

3.4. Voltage controlled memristor emulator designed by Alharbi et al

Another memristor emulator is the voltage controlled circuit designed by Alharbi *et al.* [23]. Based on the operational amplifier, second generation current conveyors and analog multiplier, this circuit is advantageous in that it is a low-element memristor emulator. The simulation diagram of the circuit and the current-voltage characteristics obtained

from simulation and experimental results are given in Fig. 7. According to the simulation results, the memristance value of the emulator is approximately 1.38 kΩ. According to the data obtained in the laboratory, the memristance value of the

emulator is 1.33 kΩ. It has also been observed that when the frequency is increased more, the hysteresis curve becomes narrower.

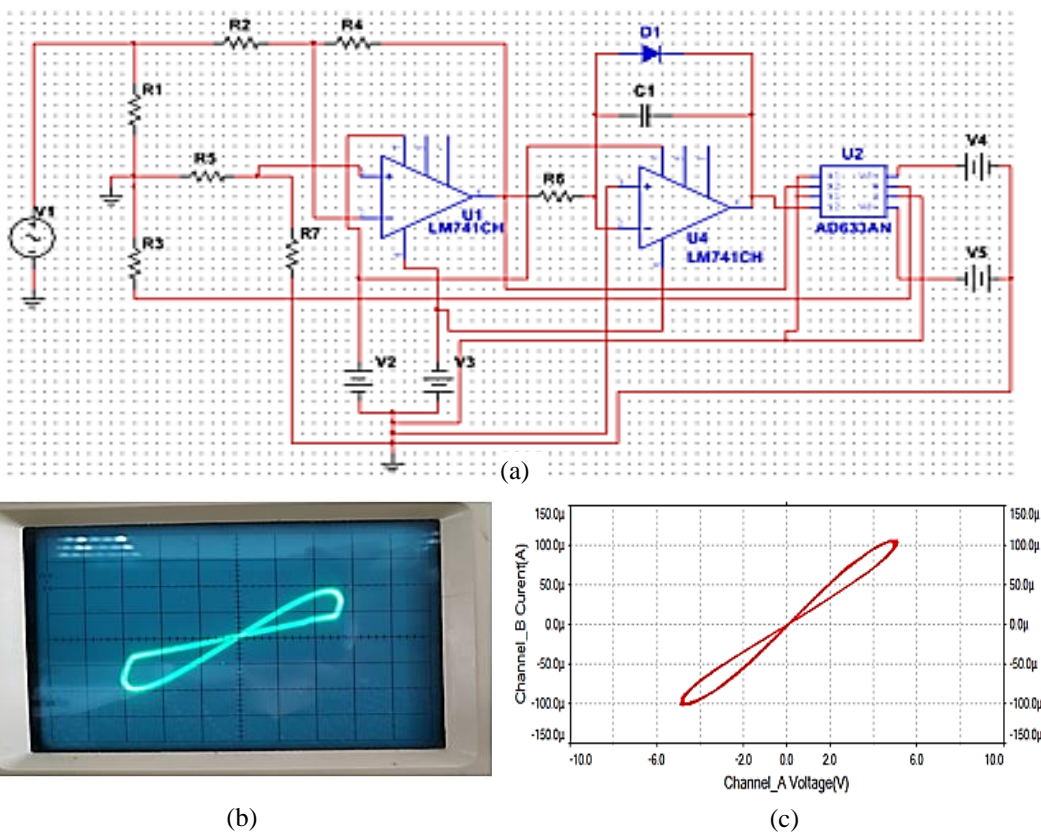


Figure 4. Mutlu-Karakulak's memristor emulator: Simulation circuit (a)- experimental *i-v* characteristic (b)-simulation *i-v* characteristic (c).

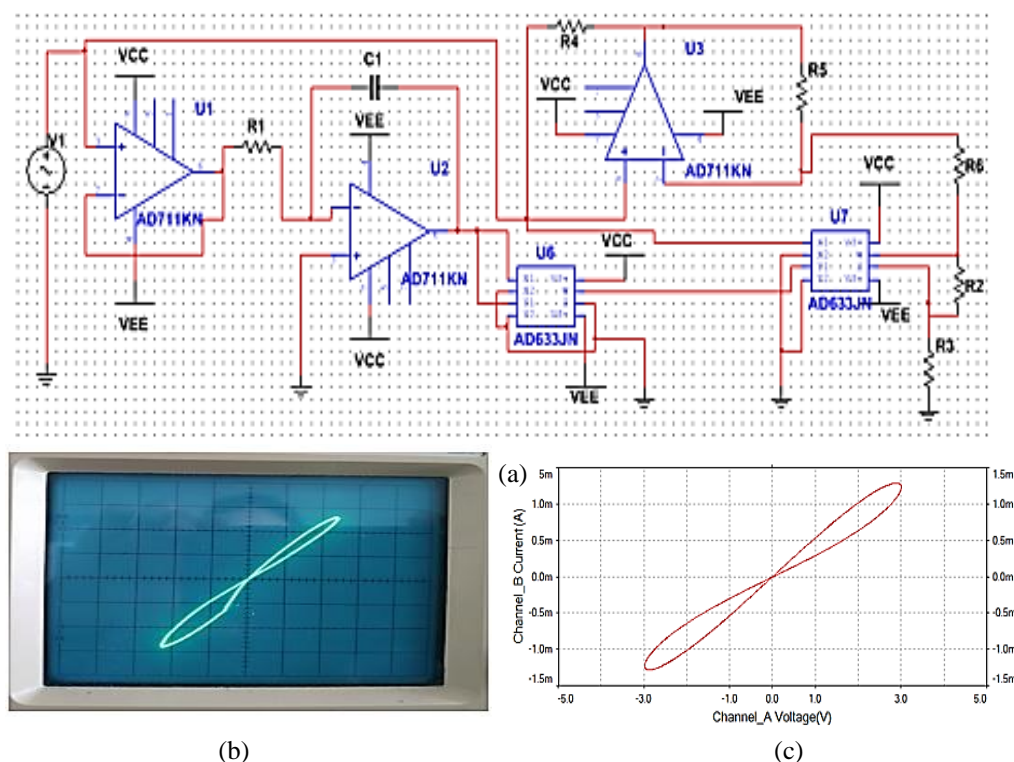


Figure 5. Muthuswamy's memristor emulator: Simulation circuit (a)- experimental *i-v* characteristic (b)-simulation *i-v* characteristic (c).

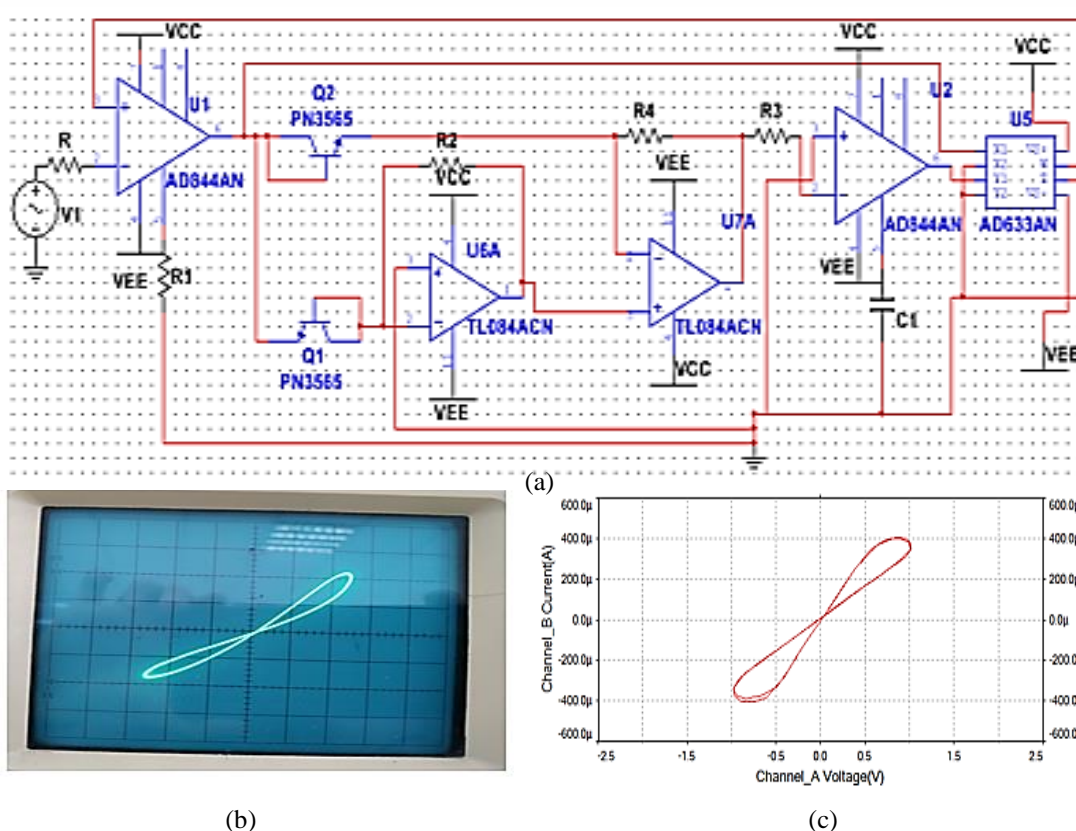


Figure 6. Alharbi *et al*'s current controlled memristor emulator: Simulation circuit (a) - experimental *i-v* characteristic (b)-simulation *i-v* characteristic (c).

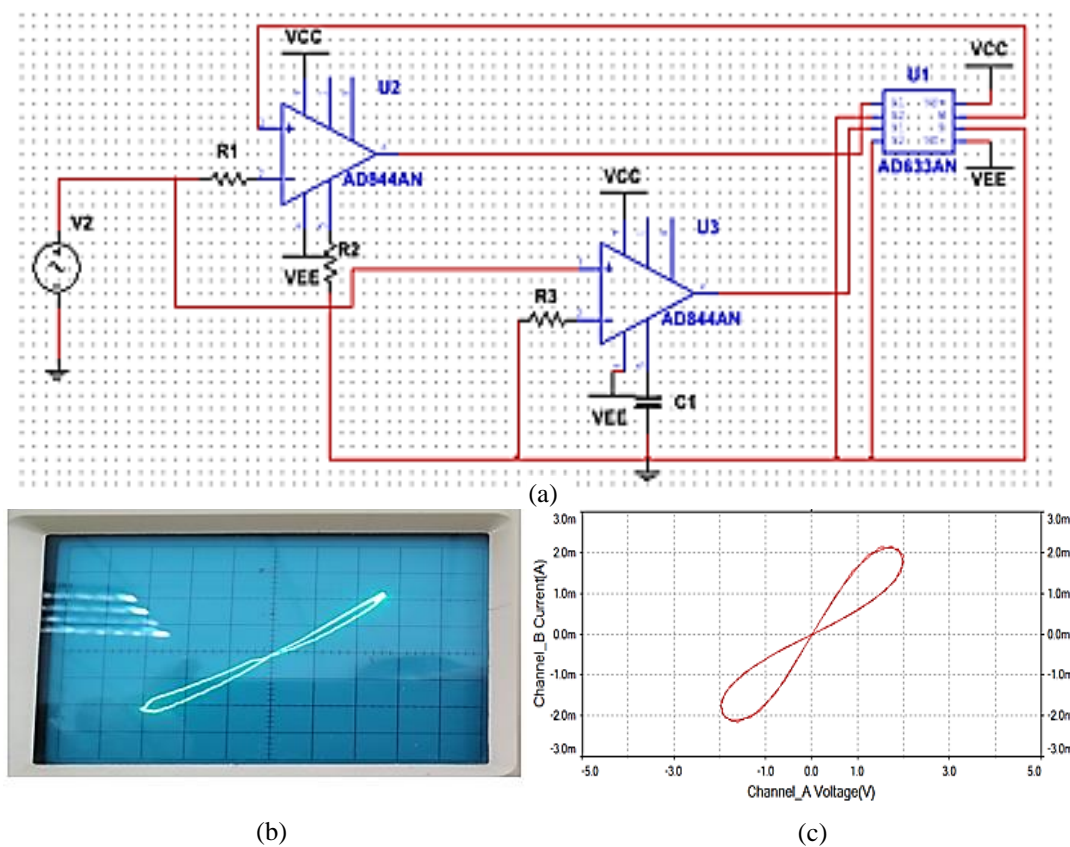


Figure 7. Alharbi *et al*'s voltage controlled memristor emulator: Simulation circuit (a) - experimental *i-v* characteristic (b)-simulation *i-v* characteristic (c).

4. NAND LOGIC GATE WITH MEMRISTOR EMULATOR

Logical gate circuits produce logical results that match the input data in a given Boolean Algebra framework. These logic gates have many features such as speed, noise immunity, power consumption, output capacity, input capacity, supply voltage, propagation delay, logic voltage levels and so on. A good logic integration should consume little power, work fast, be low cost and be less sensitive to environmental conditions [25]. Therefore, power consumption is an important consideration for a designer. The amount of power consumed in a logic gate is related to the average of the currents drawn by the gate output in the logic 0 and logic 1 states. The logic zero value has to be taken into account because in this logic case there is also power consumption. The current drawn from the supply of a logic gate is obtained in the form of

$$I_{logic} = 0.5(I_{logic\sim 0} + I_{logic\sim 1}). \quad (4)$$

where $I_{logic\sim 0}$ denotes the current drawn when the logic gate output is 0 while $I_{logic\sim 1}$ represents the current drawn when the logic gate output is 1. The power taken from the supply source (P) is obtained as the product of the supply voltage (V_{logic}) and the current drawn from the supply (I_{logic}) as follows

$$P = V_{logic} \times I_{logic}. \quad (5)$$

where V_{logic} given in Eq. (5) is the source feed of the gate.

In this study, a NAND gate is considered to examine the usability of memristor in terms of power consumption in logic gates. The NAND gate is preferred because it has an internal circuit structure that contains more elements than classical AND and OR gates. In Fig. 8, a traditional NAND circuit with MOSFETs and its new version obtained by using a memristor instead of R resistor in the circuit is given.

In the emulator circuits seen in Figs. 4-7, the terminals of the voltage sources are used as the terminals of the memristor to be connected instead of the resistance in the gate circuit.

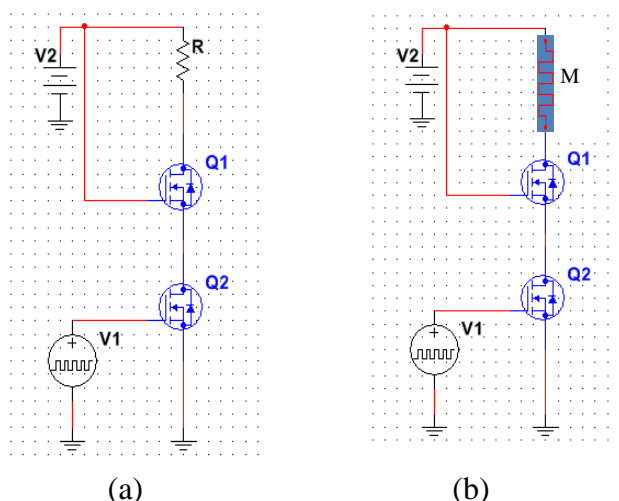


Figure 8. NAND logic gate with standard resistor (a) and with memristor (b).

The comparison of the power consumed by the NAND gates containing the emulator of Mutlu and Karakulak, and the containing the standard resistor equivalent to the memristor of the emulator is given in Fig. 9. Similarly, the power consumption data of NAND circuits obtained using the emulators of Muthuswamy and Alharbi *et al.* and using resistors equal to the memristances of these emulators are shown in Figs. 10-12, respectively. In these figures, the average values of the input voltage, the current drawn from the source and the power consumption values obtained according to Eq.(4) are shown. The simulated and experimental results of power consumption values for four different memristor emulators and their equivalent standard resistors are given in Tables 1 and 2. According to the simulation results given in Table 1, the logic gate using Mutlu-Karakulak memristor emulator consumed 41.67% less power than the logic gate using standard resistor. The logic gate in which Muthuswamy memristor emulator is used consumes 33.33% less power than the standard resistive logic gate. Similarly, the logic gate in which the Alharbi *et al* current-controlled memristor emulator is used consumes 41.04% less power than the standard resistive logic gate. Finally, the logic gate using the Alharbi *et al* voltage-controlled emulator, consumes 10.11% less power than the standard resistive logic gate. According to the experimental results given in Table 2, the logic gate using Mutlu-Karakulak memristor emulator consumed 25.00% less power than the logic gate using standard resistor. The logic gate in which Muthuswamy memristor emulator is used consumes 32.14% less power than the standard resistive logic gate. Similarly, the logic gate in which the Alharbi *et al* current-controlled memristor emulator is used consumes 32.33% less power than the standard resistive logic gate. Another comparison, the logic gate using the Alharbi *et al* voltage-controlled emulator, consumes 25.25% less power than the standard resistive logic gate. From these tables, it is clear that for each pair of memristor emulator-resistor, the memristive NAND gate consumes less power than the classical resistive NAND gate. This result shows that it is more advantageous to use memristor instead of classical resistor in logic circuits where low power consumption is important. Thus, it can be thought that the memristor element will be widely used in the industry when it is commercially available in the future.

5. CONCLUSIONS

In this study, the advantages of using memristor for low power consumption in logic circuits are investigated. In a NAND logic gate, the memristor emulator representing the memristor element is used instead of the standard resistor. Four different memristor emulators were considered, namely Mutlu-Karakulak, Muthuswamy, Alharbi *et al*'s current-controlled and voltage-controlled emulators. Firstly, memristive properties of emulators were obtained by experimental and simulation. Later, these emulators were connected instead of the standard resistor of the NAND gate and their power consumption was examined. Accordingly, all four emulators were found to have less power consumption than standard resistors. The results obtained by using memristor in this study can lead to new research areas by taking into account memory-based speed, power quality factor and similar features for future studies.

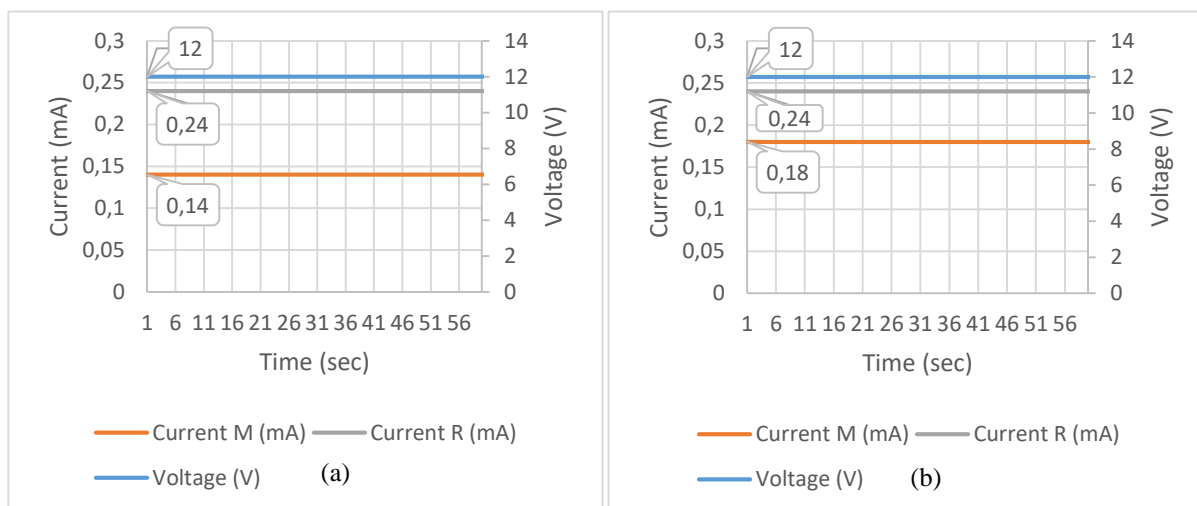


Figure 9. Simulation (a) and experimental (b) results of current-voltage values consumed by NAND logic gate with standard resistor and Mutlu-Karakulak emulator

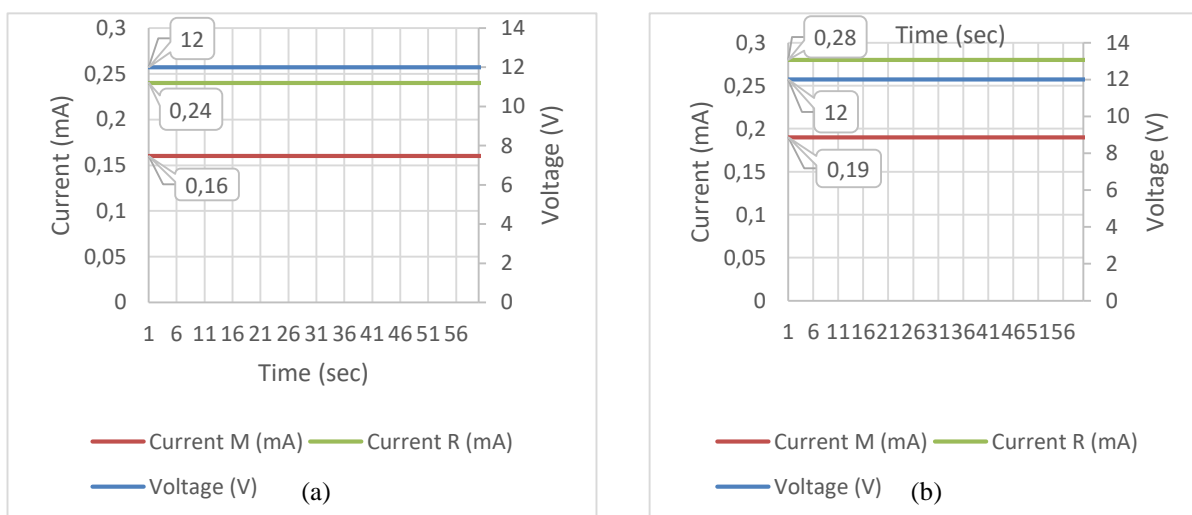


Figure 10. Simulation (a) and experimental (b) results of current-voltage values consumed by NAND logic gate with standard resistor and Muthuswamy emulator.

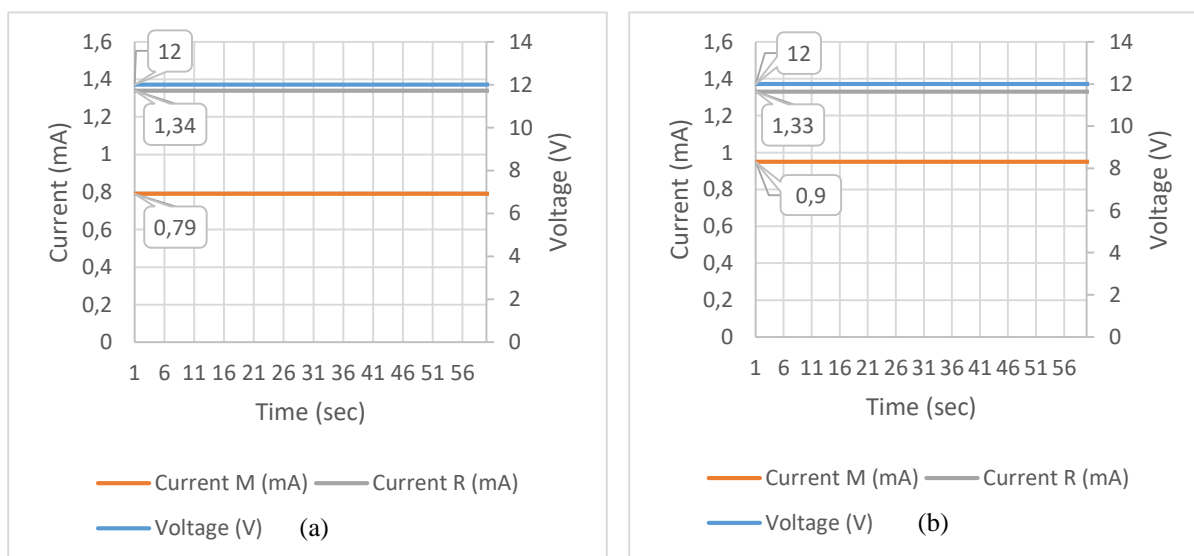


Figure 11. Simulation (a) and experimental (b) results of current-voltage values consumed by NAND logic gate with standard resistor and Alharbi *et al* current controlled emulator.

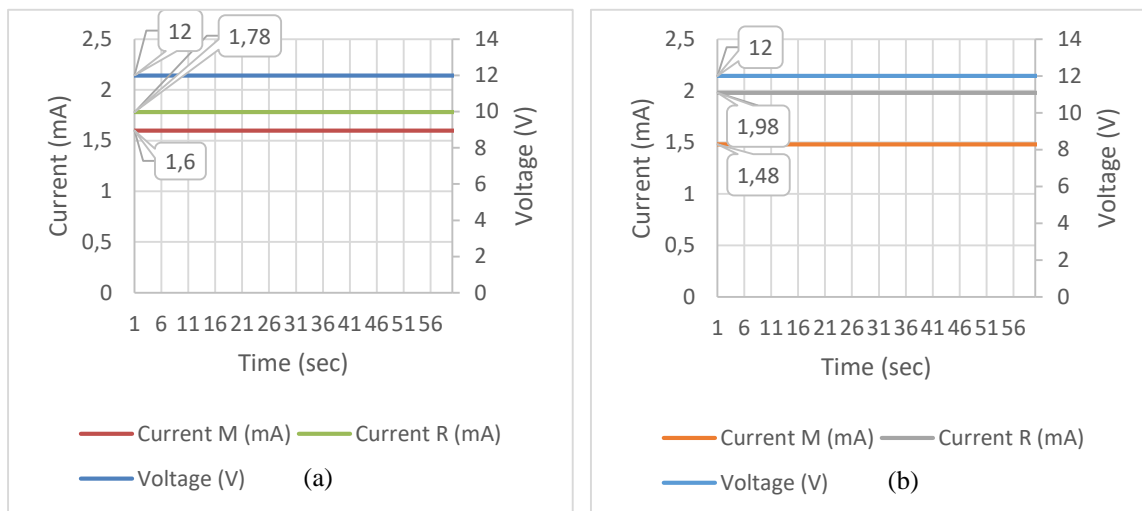


Figure 12. Simulation (a) and experimental (b) results of current-voltage values consumed by NAND logic gate with standard resistor and Alharbi *et al* voltage controlled emulator.

TABLE 1. SIMULATED LOGIC CIRCUITS; VOLTAGE, AVERAGE CURRENT AND POWER VALUES

Logic Circuits	Voltage (V)	Average Current (μ A)	Power (mW)	Memristor's Power Minimization
NAND gate with Mutlu <i>et al</i> emulator ($M=24.49$ k Ω)	12	140	1.68	%41.67
NAND gate with resistance equivalent to Mutlu <i>et al</i> emulator ($R=24.49$ k Ω)	12	240	2.88	
NAND gate with Muthuswamy emulator ($M=25.23$ k Ω)	12	160	1.92	%33.33
NAND gate with resistance equivalent to Muthuswamy emulator ($R=25.23$ k Ω)	12	240	2.88	
NAND gate with Alharbi <i>et al</i> current controlled emulator ($M=2.5$ k Ω)	12	790	9.48	%41.04
NAND gate with resistance equivalent to Alharbi <i>et al</i> current controlled emulator ($R=2.5$ k Ω)	12	1340	16.08	
NAND gate with Alharbi <i>et al</i> voltage controlled emulator ($M=1.38$ k Ω)	12	1600	19.2	%10.11
NAND gate with resistance equivalent to Alharbi <i>et al</i> voltage controlled emulator ($R=1.38$ k Ω)	12	1780	21.36	

TABLE 2. EXPERIMENTAL LOGIC CIRCUITS; VOLTAGE, AVERAGE CURRENT AND POWER VALUES

Logic Circuits	Voltage (V)	Average Current (μ A)	Power (mW)	Memristor's Power Minimization
NAND gate with Mutlu <i>et al</i> emulator ($M=23.4$ k Ω)	12	180	2.16	%25.00
NAND gate with resistance equivalent to Mutlu <i>et al</i> emulator ($R=23.4$ k Ω)	12	240	2.88	
NAND gate with Muthuswamy emulator ($M=20.5$ k Ω)	12	190	2.28	%32.14
NAND gate with resistance equivalent to Muthuswamy emulator ($R=20.5$ k Ω)	12	280	3.36	
NAND gate with Alharbi <i>et al</i> current controlled emulator ($M=2.3$ k Ω)	12	900	10.8	%32.33
NAND gate with resistance equivalent to Alharbi <i>et al</i> current controlled emulator ($R=2.3$ k Ω)	12	1330	15.96	
NAND gate with Alharbi <i>et al</i> voltage controlled emulator ($M=1.33$ k Ω)	12	1480	17.76	%25.25
NAND gate with resistance equivalent to Alharbi <i>et al</i> voltage controlled emulator ($R=1.33$ k Ω)	12	1980	23.76	

ACKNOWLEDGEMENT

The work of S. Gursul and S. E. Hamamci was supported by the Inonu University Project of Scientific Research Unit (BAP) under the project number FYL-2019-2012.

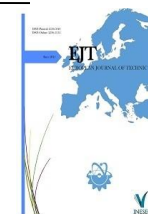
REFERENCES

- [1] L. O. Chua, "Memristor-the missing circuit element," IEEE Transactions on Circuit Theory, vol. 18, no.5, pp. 507-519,1971.
- [2] L. O. Chua and S. M. Kang, "Memristive devices and systems," Proceedings of the IEEE, vol. 64, no.2, pp. 209-223,1976.
- [3] L. O. Chua, "Device modeling via nonlinear circuit elements," IEEE Transactions on Circuits and Systems, vol. 27, no.11, pp. 1014-1044, 1980.
- [4] G. Oster and D. Auslander, "The Memristor: A New Bond Graph Element," Transactions of ASME, vol.72, pp.1-4, 1972.
- [5] Y. F. Lam, "Formulation of normal form equations of nonlinear networks containing memristors and coupled elements," IEEE Transactions on Circuit Theory, vol. 19, no.6, pp.585-594,1972.
- [6] K. C. Liu, "Dynamic behavior of a memristive circuit model for long-base P-N junction diodes," Northridge: California State University, Master of Science Engineering Project Report,1975.
- [7] M. Miliç and L. Novak, "The anti-Lagrangian equations: A missing network description," Journal of the Franklin Institute, vol.307, no. 3, pp.183-191,1979.
- [8] F. A. Buot and A. K. Rajagopal, "Binary information storage at zero bias in quantum-well diodes," Journal of Applied Physics, vol.76, no.9, pp.5552-5560,1994.
- [9] A. Beck *et al.*, "Reproducible switching effect in thin oxide films for memory applications," Journal of Applied Physics, vol. 77, no.1, pp.139-141, 2000.
- [10] G. Snider, "Self-organized computation with unreliable, memristive nanodevices," Nanotechnology, vol. 18, no.36, pp. 365202, 2007.
- [11] S. Gursul, "Investigation of the effects of different memristor emulators on electronic circuits," Msc Thesis, Inonu University, Malatya, Turkey, 2020.
- [12] R. S. Williams, "How we found the missing memristor," Spectrum, IEEE, 45, pp.28-35, 2008.
- [13] D. B. Strukov *et al.*, "The missing memristor found," Nature 453, pp. 80-83, 2008.
- [14] S. Gürsul and S.E. Hamamci, "Comparison of Different Memristor Emulators on Low-Pass Filter Circuit," presented at. ISMSIT 2019 3rd International Symposium on Multidisciplinary Studies and Innovative Technologies, Ankara, 1-4, 2019.
- [15] S. Gürsul and S.E. Hamamci, "Performance Comparison of Various Memristor Emulators on a Phase Shifting Oscillator Circuit," presented at 7th International Conference on Electrical and Electronics Engineering (ICEEE), Antalya, 23-27, 2020.
- [16] K. A. Faruque *et al.*, "Memristor-based low-power high-speed nonvolatile hybrid memory array design," Circuits Syst. Signal Process, vol.36, no.9, pp.3585-3597,2020.
- [17] S. H. Jo *et al.*, "Nanoscale memristor device as synapse in neuromorphic systems," Nano Lett, vol.10, no.4, pp.1297-1301, 2010.
- [18] M. E. Sahin *et al.*, "Design of a hyperchaotic memristive circuit based on wien bridge oscillator," Computers & Electrical Engineering, vol.88, no. 106826, 2020.
- [19] M. E. Sahin *et al.*, "Application and Modeling of a Novel 4D Memristive Chaotic System for Communication Systems," Circuits, Systems, and Signal Processing, vol.39, pp.3320-3349, 2020.
- [20] R. Mutlu and E. Karakulak, "Emulator circuit of TiO2 memristor with linear dopant drift made using analog multiplier", ELECO2010 Electrical, Electronics and Computer Engineering, pp.380-384, 2010.
- [21] B. Muthuswamy, "Implementing Memristor Based Chaotic Circuits," International Journal of Bifurcation and Chaos, vol.20, no.5, pp.1335-1350, 2010.
- [22] A. G. Alharbi *et al.*, "A new simple emulator circuit for current controlled memristor," 2015 IEEE International Conference on Electronics, Circuits, and Systems (ICECS), pp. 288 – 291, 2015.
- [23] A. G. Alharbi *et al.* "Simple generic memristor emulator for voltage-controlled models," In 2016 IEEE 59th International Midwest Symposium on, pp.1-4, 2016.
- [24] A. G. Alharbi and M. H. Chowdhury, Memristor Emulator Circuits, Springer International Publishing, 2021.
- [25] M. M. Mano and C. R. Kime, Logic and Computer Design Fundamentals, Prentice Hall, 2007.

BIOGRAPHIES

Sevgi Gürsul received the B.S. and MSc degrees from Inonu University, Malatya, Turkey. She is currently a research assistant in Department of Electrical-Electronics Engineering at Inonu University, Malatya, Turkey. Her research interests include memristor and memristive systems.

Serdar Ethem Hamamci received the B.S. degree from Erciyes University, Kayseri, Turkey, and the M.S. and Ph.D. degrees in circuits and control science from Firat University, Elazığ, Turkey. He is currently a Professor in Department of Electrical-Electronics Engineering at Inonu University, Malatya, Turkey. His research interests include control system design, memristive systems and chaotic phenomena.



Medium and Large Vector-Based SVPWM Technique for Five-Phase Two-Level Inverter

Erkan Deniz^{1*}

¹Firat University, Technology Faculty, Electrical-Electronics Engineering, 23119, Elazig, Turkey. (e-mail: edeniz@firat.edu.tr).

ARTICLE INFO

Received: Nov., 27. 2021

Revised: Dec., 07. 2021

Accepted: Dec., 08. 2021

Keywords:

Discontinuous Space Vector PWM
Five Phase Inverter
Large and Medium Vectors
THD Analysis

Corresponding author: *Erkan Deniz*

ISSN: 2536-5010 | e-ISSN: 2536-5134

DOI: <https://doi.org/10.36222/ejt.1029249>

ABSTRACT

In recent years, interest in the use of multi-phase (more than three-phase) dc/ac inverters in applications such as electric vehicles, electric traction, more electric aircraft, ship propulsion, aerospace applications, etc. has been increasing day by day. The paper presents the Discontinuous Space Vector Pulse Width Modulation (DSVPWM) technique for control of a five-phase two-level inverter. The five-phase DSVPWM algorithm uses zero, medium and large vectors combination. When calculating vectors dwell times, calculations are made by directing the V_{ref} to Sector-1 regardless of which sector it falls into. Thus, complex calculations are reduced. DSVPWM controlled five-phase two-level inverter that feeds an RL load is simulated using MATLAB/Simulink-Simscape blocks. To demonstrate the effectiveness of the used DSVPWM algorithm, five-phase inverter's output voltages, current waveforms and their FFT analysis are given for different modulation indexes and switching frequencies.

1. INTRODUCTION

Conventional variable speed electric drives, widely used in industry, consist of a three-phase power electronic converter and ac motor/motors. Since the power electronic converter is an intermediate device that separates the source and the machine, the number of phases of the machine in variable speed electric drives does not necessarily need to be limited to three [1]. The increase in the switching frequencies of power electronic switches and the decrease in their prices have made both the control of electric motors easy and flexible, and the number of phases of the machine has also become a design parameter [2]. Today, multi-phase motors larger than three-phase have become a promising technology, especially for medium and high power applications. There is a high possibility of the coincidence of the poles in motors with even phase numbers, which reduces the motor's performance. Therefore, motors with odd phase numbers are preferred in practice [3]. The lowest multi-phase motors most commonly used in this case are the five-phase ones. As the number of phases increases in electric motors, higher efficiency and torque density are obtained while the amplitude of the torque fluctuations decreases and its frequency increases [4]. In addition, the stator currents per phase and thus the stator copper losses decrease, while the fault tolerance of the motor also increases. An m -phase motor can operate with the $(m-3)$ phase in the event of a fault, provided that the non-faulted phases are designed to withstand transient currents. For example, in the event of a fault, a five-phase motor can continue to operate by

creating a rotating magnetic field with its solid two phases. This high fault tolerance has increased the interest in using multi-phase motors in sensitive applications that are very popular today, such as electric vehicles, electric locomotives, ships and space applications [5, 6]. On the other hand, three-phase machines have two stator winding types of triangle and star, while different winding configurations occur in multi-phase machines. For example, for a 5-phase motor, there are star, pentagonal and five-pointed star winding types. As a result, as the number of phases increases, the increase in the stator winding connection types allows obtaining motors with different speed-torque characteristics [6, 7].

Utilizing the potential of an m -phase motor is only possible if a power electronic converter with an m -phase feeds the motor. Because the conventional electrical grid does not have more than three phases [8]. As the number of phases increases, the power on one leg of the inverter decreases. In this case, large powered inverters for a multi-phase drive system can be realized with lower-rated semiconductor devices. It has also been observed that the overall performance and especially fault tolerance of multi-phase systems are better compared to conventional three-phase system drives [9]. In multi-phase inverters, the number of switching increases with the increasing number of switches. For example, 32 switching states and the associated voltage space vectors form in a five-phase inverter with ten switches. In this way, five-phase inverters allow better adjustment of flux and torque in the motor compared to three-phase inverters. In multi-phase drive systems, two types of pulse width modulation (PWM) strategies are commonly used

to obtain a voltage of variable amplitude and variable frequency from a voltage source inverter. These are carrier-based sinusoidal PWM (SPWM) and space vector PWM (SVPWM). Compared to SPWM, the SVPWM technique has advantages such as easy implementation for digital applications, more efficient use of dc-link voltage and lower THD in output waveforms [10].

There are two switching sequences for SVPWM. One of them is continuous and the other is discontinuous SVPWM (DSVPWM) [11]. In continuous SVPWM, half of a switching period starts with a zero vector (00000) and ends with another zero vector (11111) to obtain a symmetrical switching signal. There are also active vectors in the switching sequence. In DSVPWM, it is aimed to reduce switching losses and total harmonic distortion (THD) in output current by making less number of switching. This can be done by arranging the placement of the zero voltage vectors in a switching period. Reducing switching losses in multi-phase drive systems means increasing energy efficiency, as the application areas are high power range and the number of switches is more [12]. Six different DSVPWM techniques have been used in the literature. The method where $T_{31}(11111)$ is kept zero for a switching period is called DPWMMIN and the method where $T_0(00000)$ is kept zero is called DPWMMAX. Other methods called DPWM0, DPWM1, DPWM2 and DPWM3 organize zero space vectors in various ways in sectors. Especially at low modulation indices, the DPWMAX scheme offers the lowest THD value [12, 13].

In this study, the DSVPWM technique is used to control a five-phase two-level inverter. In this way, the switching status of one leg of the inverter is kept constant throughout the switching period. The DPWMMAX scheme of DSVPWM is proposed to obtain low THD output from the inverter output even at low modulation indices. This algorithm was developed as software using *S-Function blocks* in MATLAB/Simulink environment. In order to reduce the computational complexity, the reference vector is always directed to sector-1, regardless of sector number. The control of the five-phase inverter created with MATLAB/Simscape blocks was made using the developed DSVPWM algorithm. Inverter output phase and phase-to-phase voltages and phase currents are given for different modulation indexes and switching frequencies. The simulation results obtained show the accuracy of the algorithm. This article is organized as follows: The advantages of a five-phase source over a three-phase are given in section II. In Chapter III, the five-phase SVPWM algorithm is given in detail. A discontinuous DPWMMAX algorithm is proposed for the control of the inverter. The simulation results are given in Section-4.

2. COMPARISON OF THREE PHASE AND FIVE PHASE SOURCES

For a balanced Y-connected three-phase system shown in Figure 1(a), the phase voltages have the same amplitude ($V_a=V_b=V_c=V_L$) and have a phase difference of 120° between them. The phase-to-phase voltages are $V_{ab}=V_{bc}=V_{ca}=V_{LL}=\sqrt{3}V_L$ and the phase current is equal to the phase-to-phase current ($I_{LL}=I_L$). In this case, the three-phase power can be calculated using of Eqs. (1).

$$P_3 = 3V_L I_L \cos \varphi = \sqrt{3} V_{LL} I_{LL} \cos \varphi \quad (1)$$

For a balanced Y-connected five-phase system shown in Figure 1(b), the phase voltages have the same amplitude ($V_a=V_b=V_c=V_d=V_e=V_L$) and have a phase difference of 72° between them. For a five-phase system, there are five phase-to-phase voltages ($V_{ab}=V_{bc}=V_{cd}=V_{de}=V_{ea}=V_{LL1}$) with equal amplitude formed by adjacent phases, and also five phase-to-phase voltages ($V_{ac}=V_{bd}=V_{ce}=V_{da}=V_{eb}=V_{LL2}$) with equal amplitudes formed by non-adjacent phases. In addition, the phase current is equal to the phase-to-phase current ($I_{LL}=I_L$). The amplitudes of these phase-to-phase voltages can be calculated by Eqs. (2)-(3), respectively. As can be seen from the equations, the amplitudes of the phase-to-phase voltages formed by the adjacent phases are smaller than the three-phase system, while the amplitudes of the phase-to-phase voltages formed by the non-adjacent phases are larger. In this case, the five-phase power can be calculated by Eqs. (4) [14, 15].

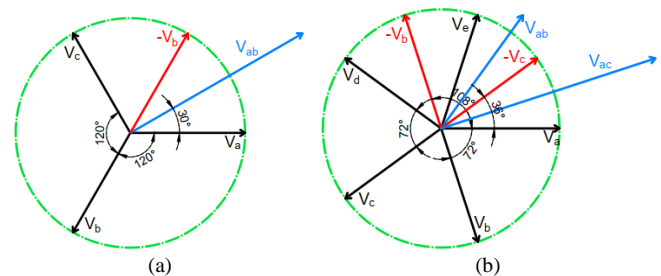


Figure 1. Phasor representation of voltages; (a) Three-phase, (b) Five-phase

$$|V_{LL1}| = |V_{ab}| = \sqrt{|V_a|^2 + |V_b|^2 + |V_a||V_b|\cos(3\pi/5)} = 1.1756 * V_L \quad (2)$$

$$|V_{LL2}| = |V_{ac}| = \sqrt{|V_a|^2 + |V_c|^2 + |V_a||V_c|\cos(\pi/5)} = 1.9025 * V_L \quad (3)$$

$$P_5 = 5V_L I_L \cos \varphi = (5/1.1756) V_{LL} I_{LL} \cos \varphi = 4.25 V_{LL} I_{LL} \cos \varphi \quad (4)$$

Considering Eqs. (1) and Eqs. (4) together, the currents drawn from a five-phase source for the same phase voltages and same output power will be approximately 40% less than a three-phase source. In this case, the reduction of current per phase for a five-phase inverter allows the use of smaller rated semiconductor switches, which reduces cost.

3. SVPWM TECHNIQUE FOR FIVE-PHASE VOLTAGE SOURCE INVERTER

The circuit of a five-phase two-level voltage source inverter is shown in Figure 2. This circuit consists of ten IGBTs and freewheeling diodes. There are $2^5 = 32$ possible switching states depending on whether the upper five switches on the circuit are turned on or turned off. These states determine the output voltage. In addition, the inverter generates 32 different voltage vectors for these 32 switching states. The 32 different switching states in a five-phase inverter circuit and their corresponding voltage vectors are given in Table 1. A switching state of "1" indicates that the upper switch is turned on, and "0" means that the lower switch of the same phase leg is turned off. Two of these vectors are called zero state vectors (V_0 and V_{31}) and the remaining thirty are called active state vectors (V_1 - V_{30}). When each switching state in Table 1 is substituted in Eqs. (5), the vector corresponding to the switching state is defined in space. Here, y is the number of the vector and $\underline{a} = e^{j\alpha}$, $\alpha = 2\pi/5$ [16].

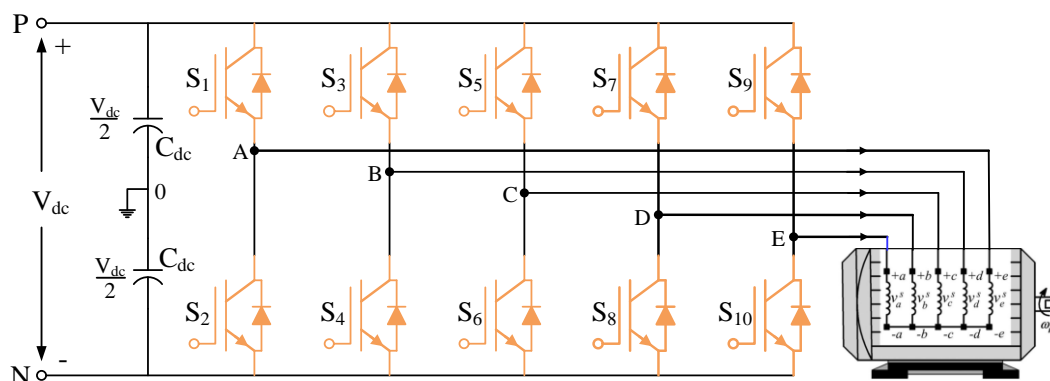


Figure 2. Five-phase two-level voltage source inverter circuit

TABLE I

ACTIVE VOLTAGE VECTORS AND CORRESPONDING SWITCHING STATES

Large Vectors 0.6472*V _{dc}		Medium Vectors 0.4*V _{dc}		Small Vectors 0.2472*V _{dc}	
\vec{V}_1 [11001]	\vec{V}_6 [00110]	\vec{V}_{11} [10000]	\vec{V}_{16} [01111]	\vec{V}_{21} [01001]	\vec{V}_{26} [10110]
\vec{V}_2 [11000]	\vec{V}_7 [00111]	\vec{V}_{12} [11101]	\vec{V}_{17} [00010]	\vec{V}_{22} [11010]	\vec{V}_{27} [00101]
\vec{V}_3 [11100]	\vec{V}_8 [00011]	\vec{V}_{13} [01000]	\vec{V}_{18} [10111]	\vec{V}_{23} [10100]	\vec{V}_{28} [01011]
\vec{V}_4 [01100]	\vec{V}_9 [10011]	\vec{V}_{14} [11110]	\vec{V}_{19} [00001]	\vec{V}_{24} [01101]	\vec{V}_{29} [10010]
\vec{V}_5 [01110]	\vec{V}_{10} [10001]	\vec{V}_{15} [00100]	\vec{V}_{20} [11011]	\vec{V}_{25} [01010]	\vec{V}_{30} [10101]

$$\vec{V}_y = \underline{V}_{\alpha\beta}^{inv} = \frac{2}{5} (V_a + \underline{a}V_b + \underline{a}^2V_c + \underline{a}^3V_d + \underline{a}^4V_e) \quad (5)$$

Considering a five-phase system, the inverter voltage vectors must be represented in a five-dimensional space. Such a space can be divided into two two-dimensional subspaces (α - β and x - y) and one one-dimensional subspace (zero sequences). For a star-connected system with an isolated neutral point, the zero sequence is not used. Therefore, it is sufficient to consider only two-dimensional subspaces (α - β and x - y). The x - y subspace is generally not used because it is a source of third-order harmonics. When 32 voltage vectors are placed on the α - β plane, a vector space containing three concentric decagons is formed as shown in Figure 3. There is three decagons with ten sectors of 36° each. Vectors in the innermost decagon are called small vectors, vectors in the middle decagon are called medium vectors, and vectors in the outermost decagon are called large vectors. The space vectors of the outermost and innermost decagon are formed when the upper three switches are on and the two switches are off in the inverter circuit. Thus, the innermost space vectors in the α - β plane are redundant and are usually ignored. Space vectors in the middle decagon are formed when the upper four switches are on and one switch is off in the inverter circuit [17]. The five-phase voltages desired to be obtained from the output of the inverter can be expressed with a reference voltage vector V_{ref} in the α - β subspace as seen in Figure 3. The amplitude and angle of the reference vector are obtained using Eqs. (6), (7) and (8). Where, $\underline{a} = e^{j\alpha}$, $\alpha = 2\pi/5$.

$$\begin{bmatrix} V_\alpha \\ V_\beta \end{bmatrix} = \begin{bmatrix} 1 & \cos \alpha & \cos 2\alpha & \cos 3\alpha & \cos 4\alpha \\ 0 & -\sin \alpha & -\sin 2\alpha & -\sin 3\alpha & -\sin 4\alpha \end{bmatrix} \begin{bmatrix} V_a \\ \vdots \\ V_e \end{bmatrix} \quad (6)$$

$$V_{ref} = \sqrt{(V_\alpha)^2 + (V_\beta)^2} \quad (7)$$

$$\theta = \tan^{-1}(V_\beta/V_\alpha) \quad (8)$$

The phase voltages in Eqs. (6) are defined as follows ;

$$\begin{aligned} V_a &= V_m \sin(\omega t) & V_b &= V_m \sin(\omega t - 2\pi/5) \\ V_c &= V_m \sin(\omega t - 4\pi/5) & V_d &= V_m \sin(\omega t - 6\pi/5) \\ V_e &= V_m \sin(\omega t - 8\pi/5) \end{aligned} \quad (9)$$

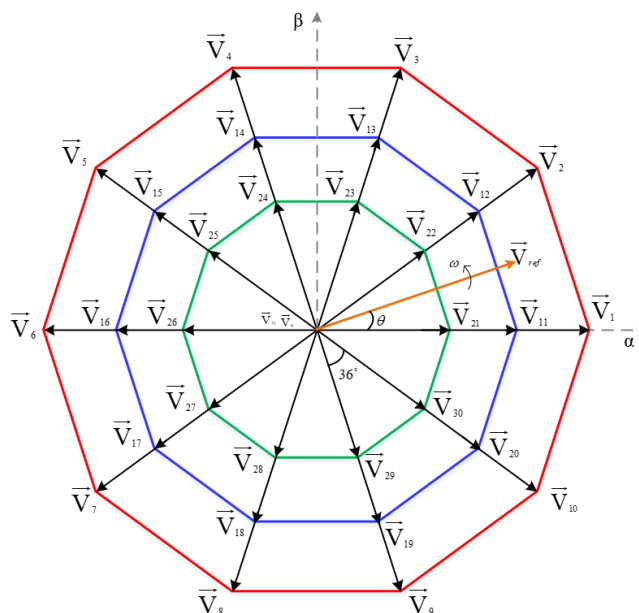


Figure 3. Vector space of five-phase two-level inverter in the α - β plane

The sequence followed when generating SVPWM switching signals for a five-phase inverter is similar to that of a three-phase. The angle used in determining the sector numbers is 36° and its multiples. Two different switching schemes are commonly used when calculating the dwell times of vectors according to the sector in which the reference vector is located. The first is to establish the volt-second balancing equation using only zero vectors and large vectors in the sector. The second is to establish the volt-second balancing equation by using two medium and two large vectors in the sector in addition to the zero vector [9,18]. The first scheme causes undesired low-order harmonics in the output phase voltage of the inverter. The number of space vectors used in a switching period should be kept equal to the inverter phase number to eliminate this disadvantage. This means that four active vectors

must be used in each switching period [19]. The use of two adjacent middle vectors together with two large vectors in each switching period makes it possible to maintain zero mean values in the second subspace (x - y) and obtain a sinusoidal output. The use of four active space vectors in a switching period requires the calculation of the four dwell-times of the large and medium vectors, represented by T_{al} , T_{bl} , T_{am} , T_{bm} in Figure 4. If V_{ref} is in Sector-1, the voltage-time balancing equation is as follows [16].

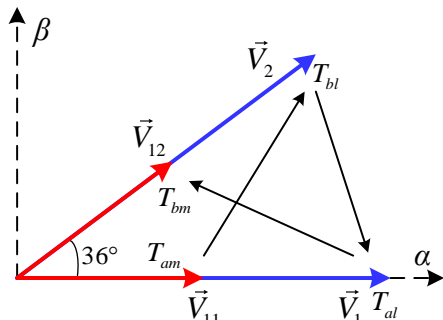


Figure 4. Principles of volt-second balancing for sector-1

$$\begin{aligned} \vec{V}_{ref} * T_s &= \vec{V}_{al} * T_{al} + \vec{V}_{am} * T_{am} + \vec{V}_{bl} * T_{bl} + \vec{V}_{bm} * T_{bm} + \vec{V}_0 * T_0 \\ T_s &= T_{al} + T_{am} + T_{bl} + T_{bm} + T_0 \end{aligned} \quad (10)$$

Here T_0 represents the switching times of the zero vectors. The lengths of the large, medium and zero vectors in Figure 4 are given in Eqs. (11).

$$\begin{aligned} |V_{am}| &= |V_{bm}| = |V_m| = (2/5) * V_{dc} \\ |V_{al}| &= |V_{bl}| = |V_l| = (2/5) * V_{dc} * 2 \cos(\pi/5) \\ |V_0| &= |V_{31}| = 0 \end{aligned} \quad (11)$$

In this SVPWM scheme, the ratio of the dwell times of the large and medium vectors is kept equal to the ratio of their lengths and expressed as follows.

$$\frac{T_l}{T_m} = \frac{|V_l|}{|V_m|} = \tau = 2 \cos(\pi/5) = 1.618 \quad (12)$$

After substituting the expressions in Eqs. (11) and Eqs. (12) in Equation 10, if the expressions are divided into real and imaginary parts, the general expression of the dwell times for all sectors is obtained as in Eqs. (13) and Eqs. (14) [17]. Here $k=1, 2, \dots, 10$ denotes the sector value. $|V_{ref}|$ symbolizes the amplitude of the reference space vector and θ its angle. The indices 'l' and 'm' are used to represent large and medium vectors, respectively.

$$\begin{aligned} T_{am} &= \frac{|V_{ref}| \sin\left(\frac{k\pi}{5} - \theta\right)}{|V_m| \sin\left(\frac{\pi}{5}\right)} \left[\frac{1}{1 + \tau^2} \right] T_s \\ T_{bm} &= \frac{|V_{ref}| \sin\left(\theta - \frac{(k-1)\pi}{5}\right)}{|V_m| \sin\left(\frac{\pi}{5}\right)} \left[\frac{1}{1 + \tau^2} \right] T_s \end{aligned} \quad (13)$$

$$\begin{aligned} T_{al} &= \frac{|V_{ref}| \sin\left(\frac{k\pi}{5} - \theta\right)}{|V_m| \sin\left(\frac{\pi}{5}\right)} \left[\frac{\tau}{1 + \tau^2} \right] T_s \\ T_{bl} &= \frac{|V_{ref}| \sin\left(\theta - \frac{(k-1)\pi}{5}\right)}{|V_m| \sin\left(\frac{\pi}{5}\right)} \left[\frac{\tau}{1 + \tau^2} \right] T_s \end{aligned} \quad (14)$$

The maximum value of the principal harmonic of the voltage that can be obtained using this SVPWM algorithm" is 85.41% of that obtained using only zero and large vectors. Therefore, it is about $0.5257 * V_{dc}$ which is as shown in Eqs. (15).

$$V_{max} = 0.8541 * V_l * \cos(\pi/10) = 0.5257 * V_{dc} \quad (15)$$

Regardless of the sector in which the reference vector is located, it is crucial to establish a correct switching sequence by determining the application order of the vectors. Switching sequence can be create in different ways for the best harmonic performance and low switching frequency for all inverters. When specifying the switching sequence, the transition from one switching state to the next should include only two switches on either leg of the inverter. At the same time, while one of the two switches on the same phase leg is on, the other must be off. In addition, to reduce the switching loss, the transition of the reference vector from one sector to the next should always be done with the least possible number of switching. Considering these situations, the switching sequence is very commonly used in which half of the switching period starts with one zero vector and ends with the other zero vector for a multi-phase inverter. This scheme is called Continuous SVPWM (CSVPWM). In Continuous SVPWM for a five-phase inverter, half of the switching period starts with zero vector V_0 and ends with other zero vector V_{31} .

In multi-phase inverters, switching losses are high at large powers due to the number of switches and therefore the number of switching. By connecting one or more inverter legs to the positive or negative DC-link in a switching period, the number of switching, i.e. switching losses, can be greatly reduced. This can be done by arranging the placement of the zero voltage vectors in a switching period. This kind of switching sequence is called discontinuous SVPWM (DSVPWM). There are six different discontinuous SVPWMs commonly used in the literature. The method where $T_{31}(11111)$ is kept zero for a switching period is called DPWMMIN, while the method where a $T_0(00000)$ is kept zero is called DPWMMAX. In the DPWM0 scheme, $T_0(00000)$ is kept zero in odd-numbered sectors and $T_{31}(11111)$ in even-numbered sectors. DPWM1 is the opposite of DPWM0. In the DPWM2 scheme, each sector is divided into two 18° segments. $T_0(00000)$ in the first segment and $T_{31}(11111)$ in the second segment are kept zero. DPWM3 is the opposite of DPWM2. Especially at low modulation indices, the DPWMMAX scheme offers the lowest Total Harmonic Distortion (THD) and Weighted Total Harmonic Distortion (WTHD) values [13]. Therefore, in this article, the DPWMMAX scheme is chosen for the control of a five-phase inverter. In this study, the switching sequences created for Sector-1 and Sector-2 using the DPWMMAX scheme are given in Figure 5.

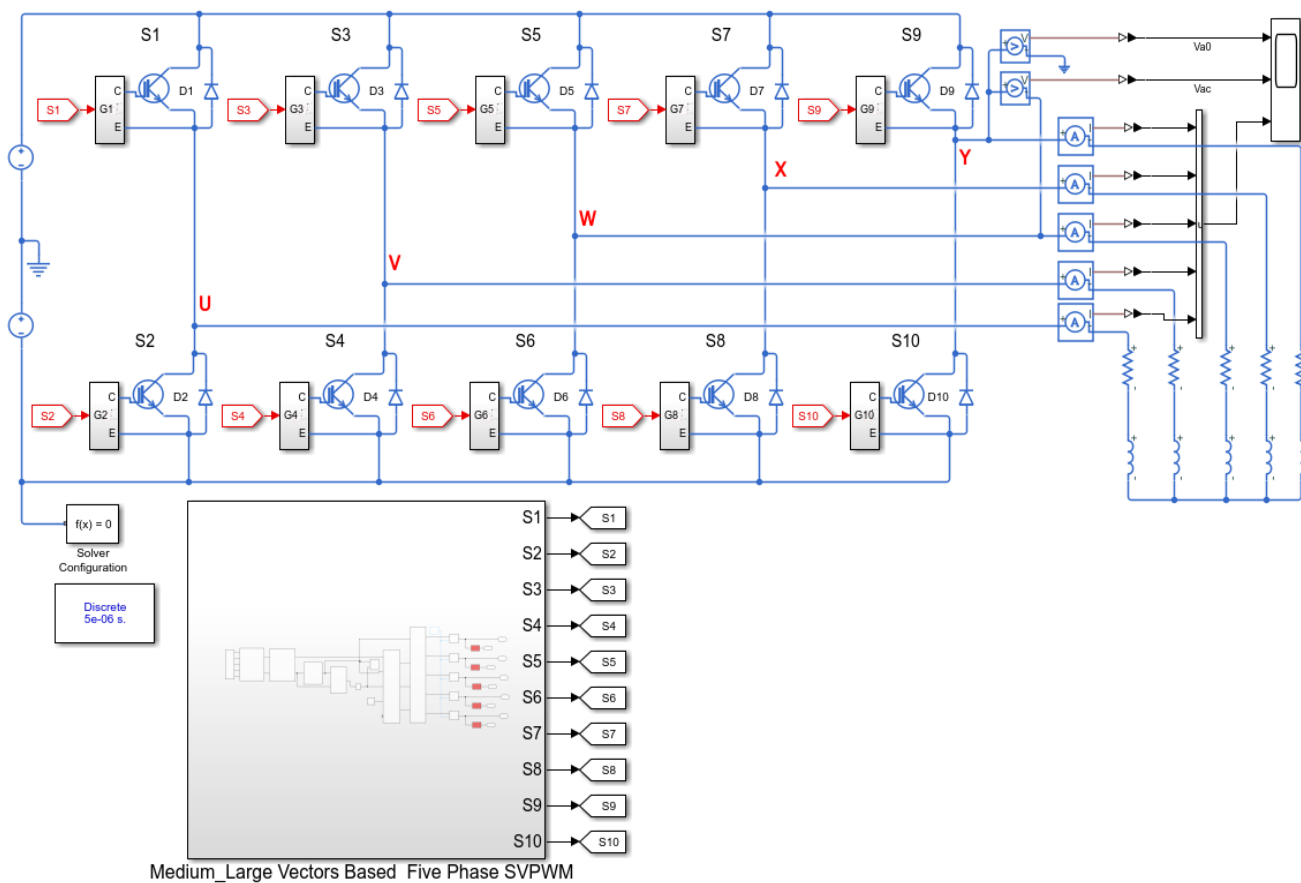


Figure 6. MATLAB simulation circuit of DSVPWM controlled five-phase inverter

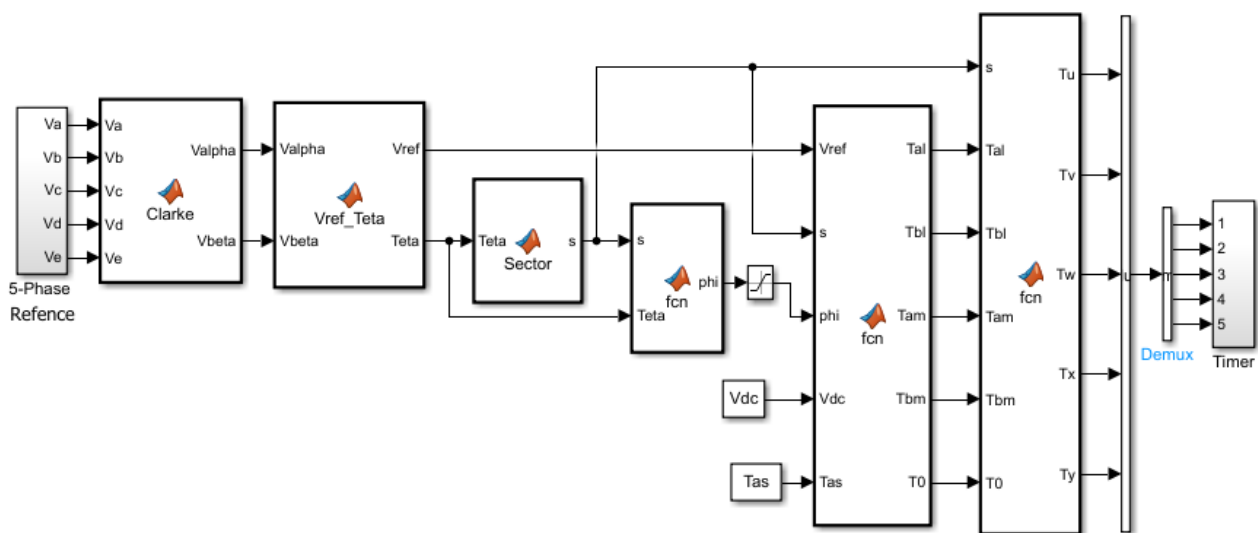


Figure 7. MATLAB algorithm of five-phase discontinuous SVPWM (DSVPWM)

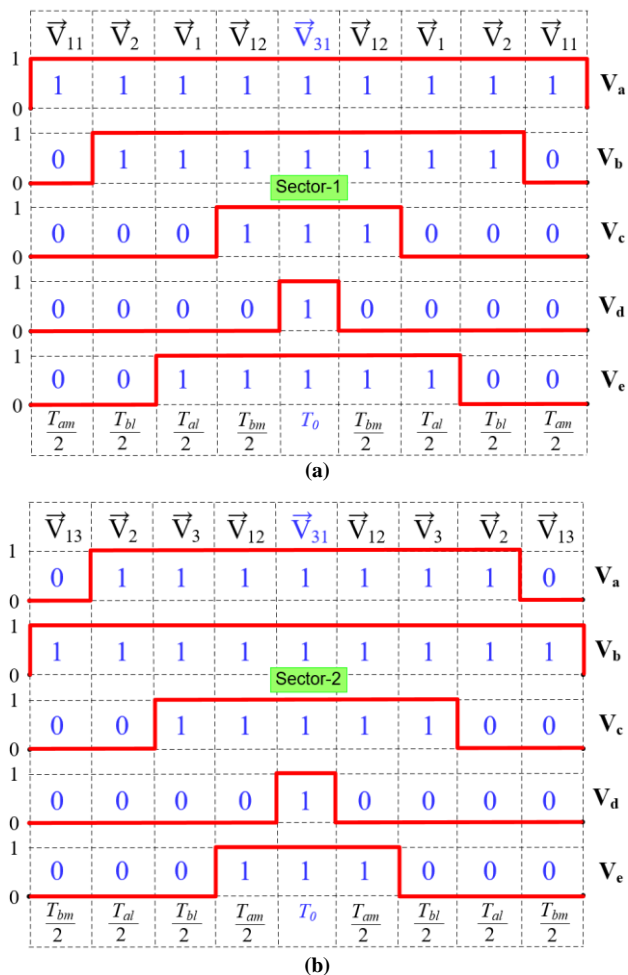


Figure 5. Switching sequence for (a) sector-1, (b) sector-2

4. MATLAB SIMULATION OF FIVE PHASE INVERTER

In this study, an SVPWM controlled five-phase two-level inverter feeding an RL load is simulated using MATLAB Simulink/Simscape blocks. The general view of the simulation circuit is given in Figure 6. The five-phase SVPWM algorithm developed for simulation is given in Figure 7. The SVPWM algorithm is created as software using MATLAB *S-Function blocks*, as seen in Figure 7. When calculating vectors dwell times, calculations are made by directing the V_{ref} to Sector-1 regardless of which sector it falls into. Thus, complex calculations are reduced. The five-phase SVPWM algorithm using zero, medium and large vectors is run for 9-segment Discontinuous mode. The sampling time was taken as $T_s=5\mu s$. The dc-line voltage of the inverter is $V_{dc}=400V$ and the output frequency is $f=50Hz$. The resistance and inductance value of the load is taken as $R=20\Omega$, $L=40mH$. Simulation results are obtained for different values of modulation index and switching frequency. The waveforms are given below for only one case where the modulation index is $M_a=0.98$, the output frequency is $f=50Hz$ and the switching frequency is $f_s=2250Hz$. Other simulation results for different M_a and f_s are presented in Table 2.

For $M_a=0.98$, the five-phase modulation signals obtained from the five-phase DSVPWM algorithm are given in Figure 8(a) and the turn-on time (T_u) of the S_1 switch on the U-phase leg is given in Figure 8(b).

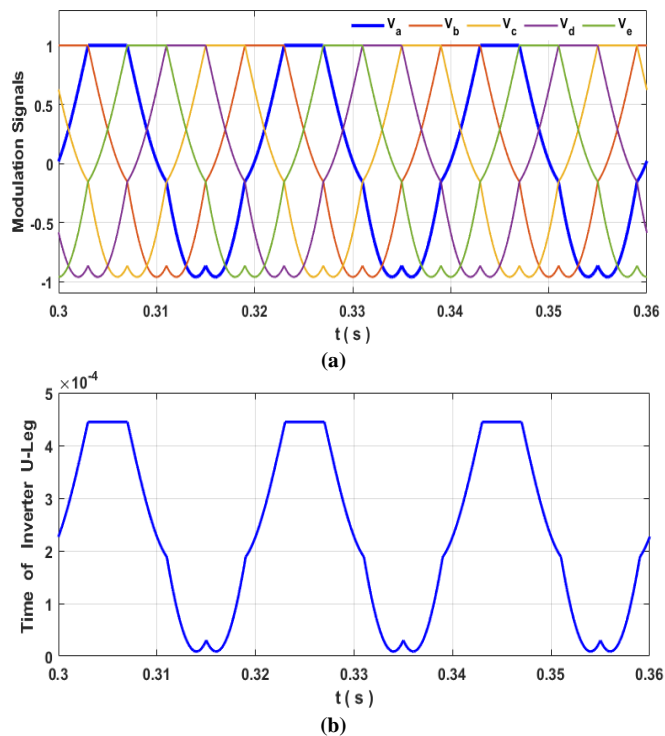


Figure 8. (a) 5-phase modulation signals, (b) the turn-on time (T_u) of the S_1

The V_{a0} output voltage waveform of the U-phase leg of the five-phase inverter with respect to the midpoint of the DC-link and its harmonic analysis are given in Figure 9. As can be seen from Figure 9, the output phase voltage is a two-level voltage with $\pm V_{dc}/2$ levels. For $M_a=0.98$, the amplitude of its fundamental harmonic is obtained as 206.10V. It is harmoniously with Equation 15. The %THD value was calculated as 93.86%.

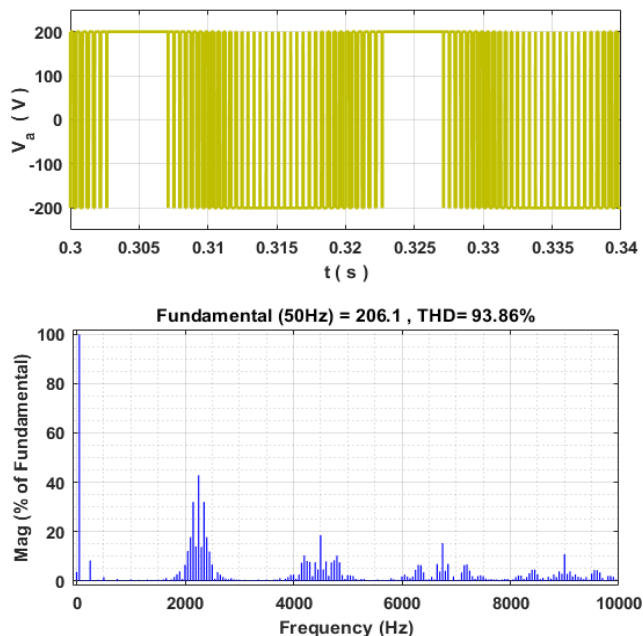


Figure 9. Output phase voltage and THD analysis of 5-phase inverter

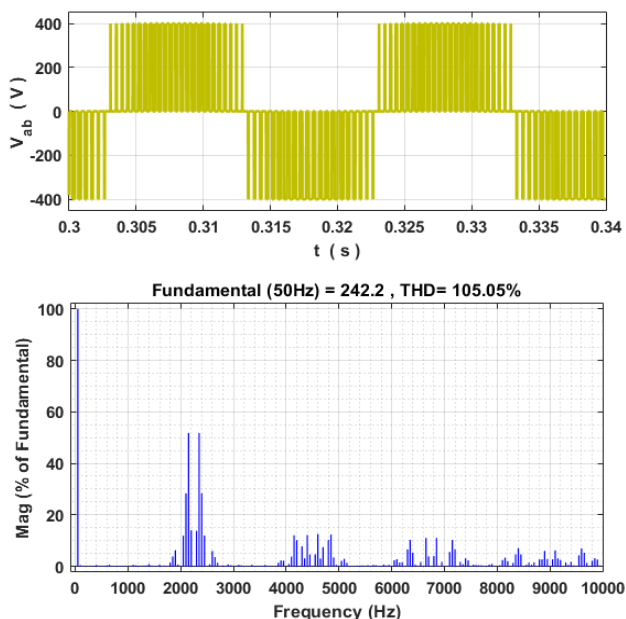


Figure 10. Output voltage and THD analysis between adjacent phase legs

The output voltage V_{ab} between two adjacent phase legs of the SVPWM controlled five-phase inverter and its harmonic analysis are given in Figure 10. The output voltage V_{ac} between two non-adjacent phase legs and its harmonic analysis are also given in Figure 11. As can be seen from Figure 10 and Figure 11, all output phase-to-phase voltages are three-level voltage with $-V_{dc}/2$, 0 , $+V_{dc}/2$ levels. For $M_a=0.98$, the amplitudes of the fundamental component were obtained as 242.30V ($V_a \cdot 1.1756$) for the V_{ab} voltage and 392.10V ($V_a \cdot 1.9025$) for the V_{ac} voltage. These values are compatible with Equation 2 and Equation 3. It is clearly seen from the harmonic analysis that the line voltage V_{ab} (105.02%) has a much higher harmonic content than the line voltage V_{ac} (54.75%).

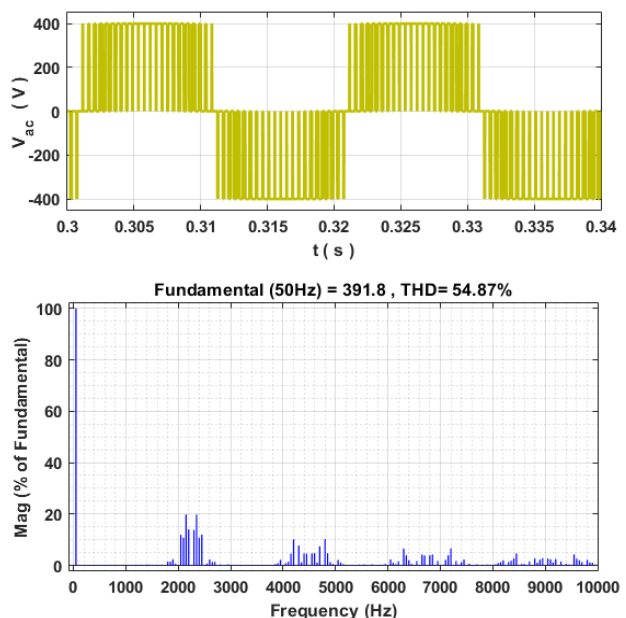


Figure 11. Output voltage and THD analysis between non-adjacent phase legs

The current waveform I_a of the U-phase leg of the five-phase inverter and its harmonic analysis are given in Figure 12, and the five-phase current waveforms are also given in Figure 13. The phase current of the inverter, which feeds an RL load

with $R=20\Omega$, $L=40mH$ ($Z=23.62\Omega$) and whose phase voltage is 206.10V, is obtained as 8.728A. As can be seen from the harmonic analysis, it is an advantage that the phase current has a low THD rate of 2.53%. This result is in accordance with the literature for the five-phase SVPWM technique using zero and four active vectors.

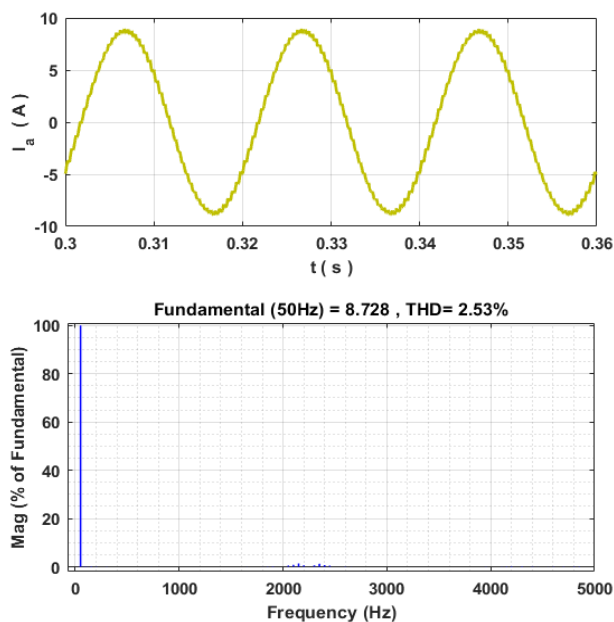


Figure 12. U-phase's current waveform and harmonic analysis

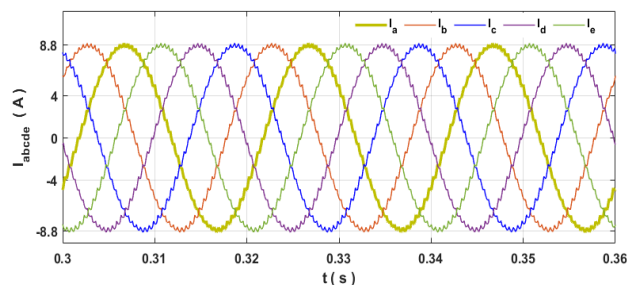


Figure 13. Current waveforms of the five-phase leg of the inverter

In addition to the results given above, the simulation is run for 0.7 and 0.4 values of the modulation index by keeping the switching frequency constant as 2250Hz. In addition, the simulation is run for the 5kHz and 10kHz values of the switching frequency by keeping the modulation index constant as 0.98. All obtained voltage, current and their THD values are given in Table-2. The values in Table-2 can be divided into two groups. The first is the case where f_s is constant and M_a is variable, and the second is the case where M_a is constant and f_s is variable. For constant f_s , as M_a increases, the amplitudes of the fundamental components of all output voltages increase and the %THD values decrease. In all cases, the amplitude of the voltage V_{ac} is greater than V_{ab} and the %THD of V_{ac} is smaller than V_{ab} . In general, the %THD values of the voltages are very close to the 3-phase inverter. In addition, as the M_a values increase, the %THD values decrease. The amplitude value of the phase current fundamental component increases as M_a increases. The %THD value of the current is around 5%, even at low M_a values. In the second case, as f_s increased for constant M_a , there is a slight decrease of 2-5V in the amplitudes of the fundamental component of the output voltages. This is because the switching losses of IGBTs increase due to high f_s . While the

TABLE II
SIMULATION RESULTS FOR DIFFERENT MODULATION INDEXES AND SWITCHING FREQUENCIES

Medium and Large Vectors– 9 Segment _DPWMMAX										
No	M_a	f_s (Hz)	V_{a0} (V)	V_{a_THD}	V_{ab} (V)	V_{ab_THD}	V_{ac} (V)	V_{ac_THD}	I_a (A)	I_a_THD
1	0.98	2250	206.10	%93.86	242.30	%105.02	392.1	%54.75	8.728	%2.53
2	0.70	2250	147.40	%152.46	173.50	%139.06	280.60	%90.31	6.246	%3.74
3	0.40	2250	84.29	%247.75	99.28	%203.21	160.60	%147.32	3.574	%5.35
4	0.98	5kHz	204.10	%95.65	240.00	%105.44	388.30	%56.03	8.642	%1.27
5	0.98	10kHz	202.10	%97.50	237.60	%106.08	384.50	%57.18	8.558	%1.15

amplitude values of the phase current fundamental component are approximately constant, its %THD values are much lower than 5%. It is about 1.5-2.5%, which is a good result.

5. CONCLUSION

There are two SVPWM methods for multi-phase VSI inverters. The first of these is the method in which only zero and large vectors are used. The second is the method in which zero, medium and large vectors are used. The method using zero and four active vectors provides output waveforms with lower THD from the inverter. Besides, there are two switching schemes in the SVPWM technique. These are called continuous and discontinuous SVPWM. The use of zero vectors for one switching period is reduced in the discontinuous SVPWM developed to reduce the switching losses in the inverter circuit. There are six different discontinuous SVPWM schemes in the literature. Of these, the DPWMMAX scheme provides lower THD even at low modulation indexes.

In this study, zero and four active vector-based SVPWM technique in discontinuous switching sequence (DPWMMAX) is proposed for a five-phase two-level VSI. The DSVPWM algorithm was created using MATLAB S-Function blocks. In addition, the complex calculations in the algorithm are reduced. To demonstrate the validity of the algorithm, a DSVPWM-controlled five-phase inverter feeding an RL load is simulated in MATLAB/Simulink environment. The simulation results show the accuracy of the DSVPWM algorithm used.

ACKNOWLEDGEMENT

This work is supported by Firat University Scientific Research Projects (FUBAP) with TEKF.21.15 numbered project, titled “Development of Space Vector PWM (SVPWM) Switching Techniques Using Digital Signal Processor (DSP) for Different Inverter Types”.

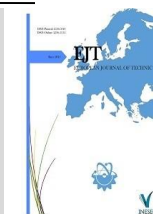
REFERENCES

- [1] A. A. Al-Abduallah, et al., “Five-phase induction motor drive system with inverter output LC filter,” presented at the 7th IEEE GCC Conf. Exhibition, Doha, Qatar, Nov. 17-20, 2013.
- [2] R. B. Shende, P. D. D. Dhawale, and P. K. B. Porate, “Modeling and simulation of five phase inverter fed im drive and three phase inverter fed im drive,” International Journal of Engineering Research and Applications, vol. 1, no. 1, pp. 33-40, Jan. 2014.
- [3] D. Raja and G. Ravi, “Design and implementation of five phase inverter with modified SVPWM switching technique for induction motor drive,” presented at the Fifth Inter. Conf. on Science Technology Engineering and Mathematics, Chennai, India, Mar. 14-15, 2019.
- [4] A. Pitrenas and A. Petrovas, “Six - phase VSI control using 8 - bit MCU,” Balkan Journal of Electrical & Computer Engineering, vol. 2, no. 3, pp. 104-107, Sept. 2014.

- [5] A. Gundogdu and R. Celikel, “Performance analysis of open loop v/f control technique for six-phase induction motor fed by A multiphase inverter,” Turkish J. Sci. Technol., vol. 15, no. 2, pp. 111-125, Sept. 2020.
- [6] A. Lega et al., “General theory of space vector modulation for five-phase inverters,” presented at the IEEE International Symposium on Industrial Electronics, Cambridge, UK, July 1-2, 2008.
- [7] A. Bıcaık, “Analysis of direct torque control method of five-phase permanent magnet synchronous motor in electric vehicles,” M.S. thesis, Dept. of Electrical and Electronics Engineering, Bursa Tech. Univ., Bursa, Turkey, 2018.
- [8] S. Sadeghi et al., “Wide operational speed range of five-phase permanent magnet machines by using different stator winding configurations,” IEEE Trans. Ind. Electron., vol. 59, no. 6, pp. 2621-2631, Apr. 2012.
- [9] M. Tariq, “Five-phase induction motor drive system driven by five-phase packed u cell inverter: its modeling and performance evaluation,” International Journal of Electrical and Computer Engineering, vol. 12, no. 9, pp. 664-669, May. 2018.
- [10] O. Aydogmus, E. Deniz, and K. Kayisli, “PMSM drive fed by sliding mode controlled pfc boost converter,” Arab. J. Sci. Eng., vol. 39, no. 6, pp. 4765-4773, June 2014.
- [11] E. Deniz, “ANN-based MPPT algorithm for solar PMSM drive system fed by direct-connected PV array,” Neural Comput & Applic, vol. 28, pp. 3061-3072, Oct. 2017.
- [12] M. A. Khan et al., “Analysis of discontinuous space vector PWM techniques for a seven-phase voltage source inverter,” Int. J. Power Electronics Drive Syst., vol. 2, no. 2, pp. 203-218, June 2012.
- [13] M. A. Khan, “Comprehensive analysis of discontinuous space vector pwm techniques for a five-phase voltage source inverter,” Int. J. Power Electronics Drive Syst., vol. 1, no. 2, pp. 1-17, Apr. 2015.
- [14] J. P. Corvalan, “Continuous and discontinuous modulation techniques for multiphase drives: analysis and contributions,” Ph.D. thesis, Dept. Electronica Eng., Seville Univ., Seville, Spain, 2016.
- [15] K. P. P. Rao, B. K. Veni, and D. Ravitjey, “Five-leg inverter for five-phase supply,” Int. J. Eng. Trends Technol, vol. 3, no. 2, pp. 144-152, Oct. 2012.
- [16] M. T. Tessema, “V/f control design and simulation for five-phase induction motor,” M.S. thesis, Dept. Electrical and Computer Eng., Addis Ababa Univ., Addis Ababa, Ethiopia, 2015.
- [17] J. G. Haitham, Abu-Rub, and Atif Iqbal, High performance control of ac drives with matlab simulink. West Sussex, UK: Wiley, 2021.
- [18] M. Narimani, and Bin Wu, High power converters and ac drivers. New Jersey, USA: Wiley, 2017.
- [19] J. W. Kelly, E. G. Strangas, and J. M. Miller, “Multiphase space vector pulse width modulation,” IEEE Trans. Energy Convers., vol. 18, no. 2, pp. 259-264, May 2013.

BIOGRAPHIES

Erkan Deniz was born in 1977. He received the B.S., M.S., and Ph.D. degrees from Firat University, Elazig, respectively in 2001, 2005, and 2011. From 2001 to 2012, he was a Research Assistant with the electrical teaching department. Since 2018, he has been an Associate Professor with the Electrical Electronics Engineering Department, Firat University. His research interests include power electronics, pulse width modulation techniques, power quality, STATCOM, energy storage systems, motor control.



An Investigation on Mechanical and Microstructural Properties of Porous Nickel-Based Alloy Fabricated by Investment Casting as an Implant Materials

Yusuf Er

*Firat University, Department of Airframes and Powerplants, 23119, Elazig, Turkey. (e-mail: yusufer@firat.edu.tr).

ARTICLE INFO

Received: Jul., 14. 2021
Revised: Sep., 22. 2021
Accepted: Sep., 25. 2021

Keywords:

Metal foams
Biomaterials
Mechanical properties
Investment casting
Nickel-Chrome-Molybdenum

Corresponding author: *Yusuf Er*

ISSN: 2536-5010 / e-ISSN: 2536-5134

DOI: <https://doi.org/10.36222/ejt.971029>

ABSTRACT

In this study, Nickel-Chrome-Molybdenum alloy is manufactured using investment casting method with centrifugal casting device from a polyurethane foam model in a regular and open-pore form, as a hard tissue implant. The samples produced have 10, 20, and 30 (± 3) pores per inch and 0.0008, 0.0017, and 0.0027 g/mm³ densities, respectively.

Young's modulus, hardness and mechanical behaviors of the samples were investigated by SEM, EDS and compressive test.

As a result, it is seen that the pore size and the pore wire diameter of the samples could be controlled thus compression strength and young modulus. In this way it was understood that an implant material could be produced with similar mechanical properties to the human bone.

1. INTRODUCTION

Lightweight cellular solids with stochastic cells can be manufactured from numerous metals and metal alloys by a wide variety of vapor, liquid and solid-state process [1]. The applications of metal foams are in a wide range of biomaterials, aircraft, impact energy absorbers, silencers, flame arresters, heaters, heat exchangers, constructional materials, etc. [2-7]. More than 20 years, fabrication methods for porous metals have been developed to imitate bone properties [8-16]. Many parameters on the porous implant should be taken into account to ensure biocompatibility, such as pore shape, pore size, porosity and high purity. Pore morphology, size and porosity are the determining factors. For this, a thorough understanding of fracture behavior is required for successful industrial application [17,18]. Furthermore, the hollow space created by these biomaterials' interconnected open-cellular microstructure enables for simple bodily fluid movement and, as a result, the formation of new bone tissues. The properties of these cellular materials depend upon the properties of base metal alloy, the relative density and the topology [19-21]. According to Curran, the material utilized for the manufacturing technique; the durability of the foams generated with metal powder and the powder metallurgy method was related to the smallest areas between the metal or granules. He observed that the specific

endurance of foams generated by powder metallurgy would be poor due to their manufacturing process [7]. Yamada et al. stated that an open pore casting was realized utilizing the infiltration technique using a polyurethane foam model, and that the materials utilized for production were of excellent quality and dependable, with a porosity rate of up to 98%. [22]. Yamada et al. further said that this process may be used to cast any alloy or metal. It is especially appealing because the strength and Young's modulus of the cellular materials may be changed by porosity modification to match the strength and Young's modulus of real bone. As a result, novel bone-substitute materials with high strength and suitable Young's modulus are required to assure the biomechanical characteristics of natural bones [22]. According to researches, the average pore size of the porous bone replacement material implanted must have pore size in order for the bone tissue ingrowth to progress. This size should be between 200 to 500 μ m. [20-24]. Nickel, Chromium and Molybdenum elements are in the class of metallic biomaterials [25, 26]. These elements are frequently used in biomaterials studies [26-34].

In this study, Ni-Cr-Mo alloy is manufactured using investment casting [21, 35, 36]. method from a polyurethane foam model in a regular and open-pore form, as a hard tissue implant. Young's modulus, hardness and mechanical behavior

of the samples were investigated by SEM, EDS, and compressive test

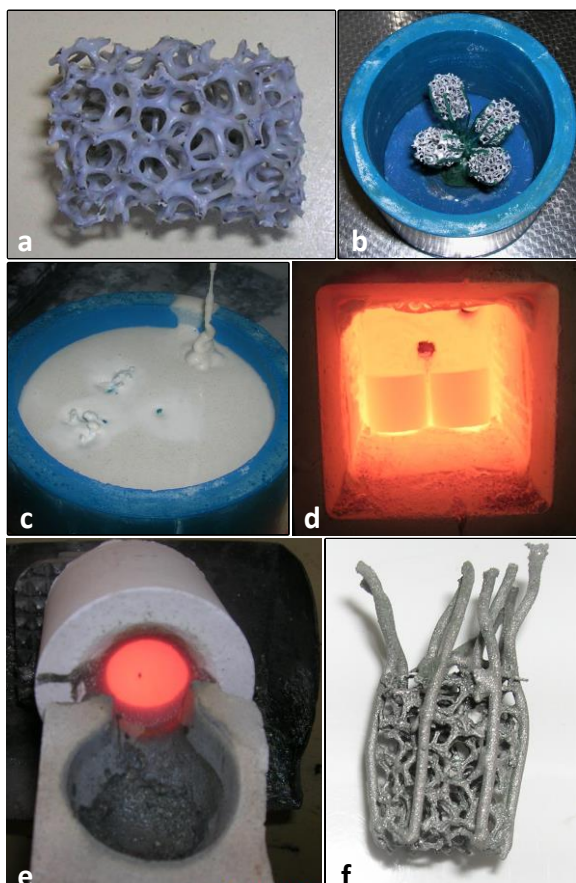
2. MATERIALS AND METHOD

2.1. Production of Samples

The alloy which was used in this study is commercially produced by the Böhler Company. The mechanical properties of alloy are given in Table 1. In the production of the samples, two-stage casting method was used. In this method, the open pore metal foams are produced by using polyurethane foams. Polyurethane foams with open pores in three different sizes were used as a sample model.

TABLE 1
THE MECHANICAL PROPERTIES OF ALLOY

Density	8.8 g/cm ³
Vickers hardness	195 HV
Young modulus	215 GPa
Melting temperature	1280 – 1350°C
Casting temperature	1410°C



Figures 1. a, b, c, d, e, f Production stages of samples

The sample models created had 10, 20, and 30 (± 3) pores per inch (ppi) and densities of 0.0008, 0.0017, and 0.0027 g/mm³, respectively (Fig. 1. a). Then the mold tree was created and placed in the mold chamber (Fig. 1. b). Precision casting plaster was poured into the mold cavities to create the molds (Fig. 1. c). For the preparation of precast, prepared molds were heated for 1 hour at 1000°C in a thermocouple equipped oven (Fig. 1. d). In this manner, the cast chamber in the mold was formed by burning away polyurethane foams. The alloy is then heated to

1410°C before being put into molds using a centrifugal casting process (Fig. 1. e). Molds were allowed to cool before being broken and cleaned to remove the casing. A sufficient number of samples were produced in this way (Fig. 1. f). Figures 1. shows the production stages.

2.2. Density Measurement

The mass and volume relationship was used to calculate the densities of the samples with different pore sizes. Formula (1) was used to determine the densities of solid metal (ρ_{Bulk}) and porous metal (ρ_{Porous}) samples. Then, using these density values obtained from each sample, the % porosity amounts (ε) were determined with the formula (2) [37].

$$\rho = \frac{m}{v} \quad (1)$$

ρ : Density, (g/mm³)

m : Mass, g

v : Volume, mm³

$$\varepsilon = \left(1 - \frac{\rho_{Porous}}{\rho_{Bulk}}\right) \times 100 \quad (2)$$

ε : % porosity amounts

2.3. Metallographic Examination

Porous samples which obtained from Ni-Mo-Cr alloys were prepared metallographically to examine the microstructure. The samples were abraded with 220, 400, 600, 800, 1200 mesh sandpaper, respectively. It was then polished with a 3 micron polycrystalline diamond paste using a broadcloth. As the etching process, firstly, 95 ml of water, 5 ml of HCl solution was kept in an electrolytic etching agent with 5-10 V and DC current for three minutes to release molybdenum. Then, the etching process was completed by immersing the sample in the chemical etching (5ml HNO₃, 200 ml HCl, 65g FeCl₂) for a few seconds. The microstructure characterization of the produced samples was examined under the LEO brand scanning electron microscope.

2.4. Mechanic Examination

Compression tests were performed on an Instron 8500 universal type tension-compression machine. For the compression experiments, a total of 9 compression samples, three from each of the three samples with different pore sizes were prepared. The dimensions of the samples prepared for the compression test were prepared according to the TS 6936 standard and at room temperature, different from the dimensions of the sample to be used as an implant.

3. RESULTS and DISCUSSION

3.1. Determination of Pore Ratio

The densities of the produced samples were calculated with the formulas specified in section 2.2. The densities of three samples for each sample group were calculated and the average values were found. Pore sizes were determined by the number of ppi. The exact density of the alloy material used in the casting and the pore ratio of the produced samples are given in

Table 2 by determining the relative densities as well as the % porosity amounts.

TABLE 2
DENSITIES AND POROSITIES VALUES

Sample Group	Bulk densities (g/mm ³) (ρ_{Bulk})	Pore sizes (ppi)	Porous densities (g/mm ³) (ρ_{Porous})	General porosities in percent (ϵ) (%)
A	0,0088	10 ± 3	0,0008	90,7
B	0,0088	20 ± 3	0,0017	81,0
C	0,0088	30 ± 3	0,0027	68,8

When the values in the table are examined; The fact that the percentage of porosity (%) of all three samples does not change regularly depending on the pore ratios may be related to the fact that the fiber sections are not the same. Yamada and his friends [22], used Al and Mg materials, for Al in the samples obtained by polyurethane foam model and infiltration method; For Mg between 0.0471 gr/mm³ and 0.0653 gr/mm³; Relative density values in the range of 0.028 gr/mm³ and 0.030 gr/mm³ were obtained. In this study; Unlike Yamada's study [22], centrifugal casting device was used instead of infiltration casting. For Ni-Cr-Mo (0.0088 gr/mm³) alloy, which is a denser metal; Relative density values were obtained in the range of 0.0008 gr/mm³ to 0.0027 gr/mm³.

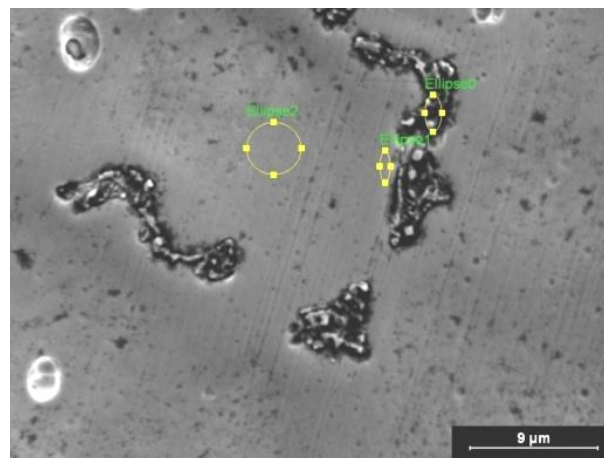
3.2. Metallographic Test Results

For SEM investigations, the produced samples were divided into three groups: group A, group B, and group C based on their pore diameters. SEM examinations and EDS analyzes of groups A, B and C are given, respectively.

EDS analyses were taken from three different regions shown with ellipses in the figure to determine the elemental amounts of group A samples. According to the EDS results received; When the results of the region marked as ellipse0 on the black islet in the matrix are examined, it is observed that the percentages of molybdenum and silicon elements increase, they become poorer in nickel, and there is no significant change in the chromium ratio (Figures 2). It is seen that the alloy content of the region shown as ellipse0 consists of 39.82% Ni, 23.52% Mo, 26.30% Cr and 10.35% Si elements. When the EDS analyses of the region marked with ellipse1 in the matrix adjacent to the islet on the same photograph were examined, it was observed that there was no enrichment in the nickel ratio, no depletion in the molybdenum and silicon ratios, and no significant change in the chromium ratio. When the alloy content of the region shown as Ellipse1 is examined, it is seen that it consists of 60.98% Ni, 28% Mo, 7.67% and 3.36% Si elements. When the EDS analysis of the point shown as ellipse2 in the SEM photograph taken on the matrix is examined, it is seen that the matrix consists of 64.39% Ni, 27.62% Cr, 5.87% Mo and 2.1% Si elements.

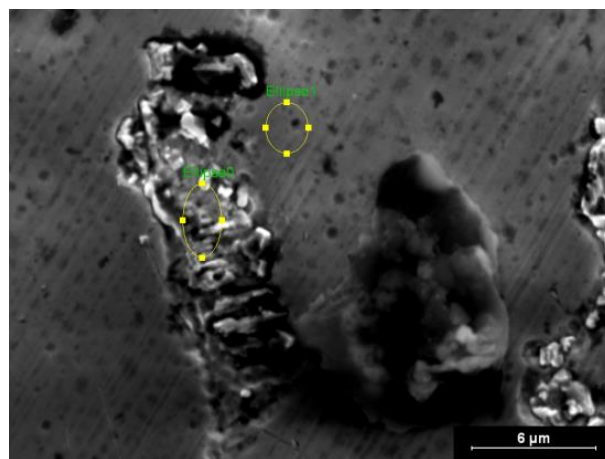
EDS analyses were taken from two different regions shown with ellipses in Figure 3 to determine the element ratios of the B group samples. According to the EDS results received; When the results of the region marked as ellipse0 on the black islet in the matrix are examined, it is observed that the percentages of molybdenum and silicon elements increase, they become poorer in nickel, and there is no significant change in the chromium ratio. It is seen that the alloy content of the region shown as ellipse0 consists of 46.18% Ni, 24.81% Cr, 19.93% Mo and 9.08% Si elements. When the EDS analyzes of the region marked with ellipse1 in the matrix adjacent to the islet

on the same photograph were examined, it was observed that there was no significant change in the nickel ratio, enrichment in the molybdenum and silicon ratios, and no significant change in the chromium ratio.



Figures 2. SEM image and EDS analysis regions of group A sample

When the alloy content of the region shown as Ellipse1 is examined, it is seen that it consists of 63.54% Ni, 27.39% Mo, 6.42% and 2.65% Si elements.

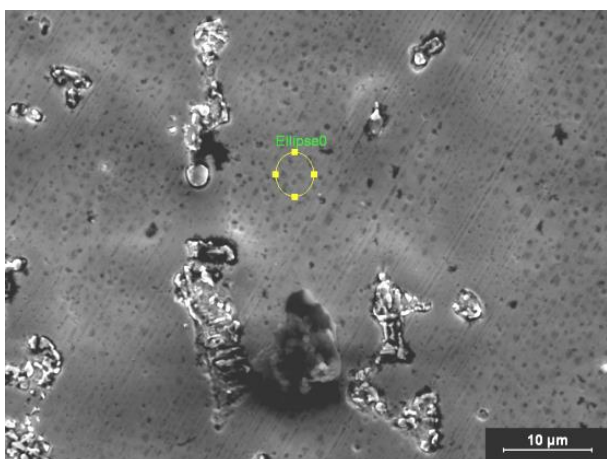


Figures 3. SEM image and EDS analysis regions of group B sample

In order to determine the element ratios of the C group samples, EDS analyses were taken from the region indicated by ellipse0 in Figure 4. When the EDS analysis of the point taken on the matrix and indicated by the ellipse0 is examined, it is seen that the matrix consists of 66.35% Ni, 26.34% Cr, 5.43% Mo and 1.89% Si elements. The results obtained in the examination and analysis were found to be very close to each other. According to the results obtained from the EDS analysis, it was concluded that the pore sizes did not affect the microstructure.

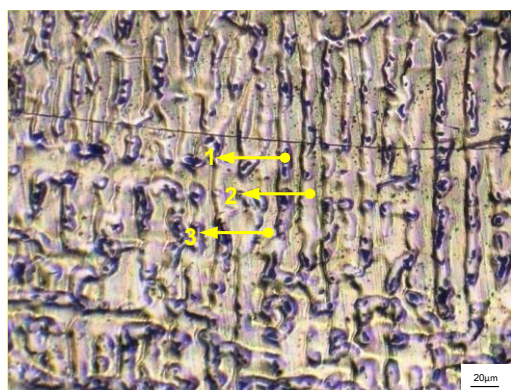
Figure 5 shows the microstructure photograph of the sample taken with an optical microscope. The photograph shows three separate solidification structures. The region numbered 1 is primary solidified, the region numbered 2 is secondary solidified and the region numbered 3 represents the interdendritic region. As can be seen from the microstructure photographs, the alloy exhibited a dendritic structure. When we look at the EDS values in general; While the matrix of the sample is predominantly Ni-Cr, it is understood that Mo and Si

precipitate in the matrix and form islets with a homogeneous distribution.



Figures 4. SEM image and EDS analysis regions of group C sample

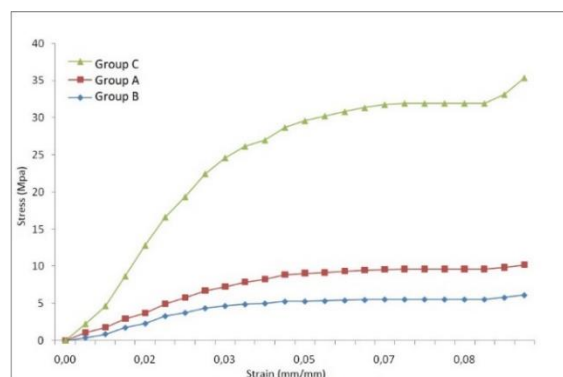
Christopher et al.; In their study, they produced a 62.2% Ni, 25% Cr, 9.5% Mo and 3.3% Si doped alloy named Matchmate as casting and defined the obtained microstructure as dendritic [38]. Study by Christopher et al. and the microstructure obtained in this study confirm each other.



Figures 5. Optical microscope image of sample

3.3. Compression Test Results

When the comparative stress-strain diagrams of the A, B and C group samples in Figure 6 are examined, it can be observed that pore ratios and filament diameters have an influence on modulus of elasticity. Stretching is found to grow in direct proportion to rising pore ratios. However, although the pore ratio of group B samples is higher than that of group A samples, the reason why the stress values of group A samples are higher can be attributed to the thicker cross-section of the filament diameters. When the diagram of the C group samples is examined, it is seen that the stress values rise based on both the pore ratio and the fiber section. This result is important in that it shows that the desired stress values can be controlled depending on the pore sizes and fiber cross sections. In their study Tuncer and Arslan determined that the plateau region becomes more ambiguous as the relative density increases in the stress diagram, they obtained from titanium foam with different levels of porosity, produced by space holder method [15]. Similarly, the smooth character of the curves in the diagram obtained in this study confirms that the ductile behavior of foams in the porosity range studied. (Figure 6)



Figures 6. Comparative stress-strain diagrams of A, B and C group samples

4. CONCLUSION

In this study, it was investigated Ni-based Ni-Cr-Mo alloy, which is widely used in orthopedics and dentistry, can be produced in an open pore structure by precision casting method and the controllability of pore size and filament thicknesses.

- It has been observed that a material with a Ni-Cr-Mo alloy can be successfully produced in its final shape in a centrifugal casting device with an open pore structure and a density range of 66.8% to 91.5%, without the need for a second process, by precision casting method.
- In the centrifugal casting device, the pore sizes and controllability of the fiber sections of the samples produced by the investment casting method are shown.
- As a result of the microstructure examinations on the sample as a result of the casting process, it was observed that the alloy exhibited a dendritic structure. While the matrix of the sample is predominantly Ni-Cr, it is understood that Mo and Si precipitate in the matrix and form islets with a homogeneous distribution.
- When the density values of the samples were examined, it was seen that the relative density was related to the increased pore size and filament cross section.
- As a result of the compression tests applied to the porous samples; It was seen that pore size and filament thicknesses play an important role in determining the modulus of elasticity. Accordingly, the sample with the smallest pore and relatively thick fiber section showed the highest modulus of elasticity, while the sample with the thinnest fiber section and relatively large pore size showed the lowest modulus of elasticity.

ACKNOWLEDGEMENT

The author acknowledges the Scientific Research Foundation, Firat University (FUBAP—Project no: 1018) for their financial support. I remember with respect Prof. Dr. Nuri Orhan who contributed technically to this study.

REFERENCES

- [1] Queheillalt, Douglas T., Yasushi Katsumura, Haydn NG Wadley, "Synthesis of stochastic open cell Ni-based foams", *Scripta Materialia* 50.3 (2004): 313-317.
- [2] Kılıç M., "Toz metalurjisi ile Üretilen NiTi Alaşımına Al'un Etkisi". *Bitlis Eren Üniversitesi Fen Bilimleri Dergisi*. 2021; 10(1): 256-267.

- [3] V. Koç, V. V. Çay, "Investigation of Wear Behavior of Ti6Al4V/B4C Composites Produced by Powder Metallurgy", *European Journal of Technique (EJT)* 10.2 (2020): 444-453.
- [4] M. F. Ashby, A. Evans, N. A. Fleck, L. J. Gibson, J. W. Hutchinson, H. N. G. Wadley: "Metal Foams: A Design Guide", *Butterworth Heinemann, Boston, USA* (2000)
- [5] J. Banhart: "Manufacture, characterization and application of cellular metals and metal foams", *Progress in Materials Science* 46 (2001), pp. 559-562
- [6] B. Jiang, N. Q. Zhao, C. S. Shi, J. J. Li: "Processing of open-cell aluminum foams with tailored porous morphology", *Scripta Materialia* 53 (2005), pp. 781-785
- [7] D. Curran, "Metal Foams", *Cambridge University Press, Cambridge, UK*, 2001
- [8] Mour M, Das D, Winkler T, Hoenig E, Mielke G, Morlock MM, Schilling AF., "Advances in Porous Biomaterials for Dental and Orthopedic Applications", *Materials*, 2010; 3(5):2947-2974.
- [9] D. C. Dunand, "Processing of Titanium Foams", *Advanced Engineering Materials*, 2004; 6(6), pp. 369-376.
- [10] V. Karageorgiou, D. Kaplan, "Porosity of 3D biomaterial scaffolds and osteogenesis", *Biomaterials*, Volume 26, Issue 27, 2005, pp 5474-5491,
- [11] M. A. Lopez-Heredia, J. Sohier, C. Gaillard, S. Quillard, M. Dorget, P. Layrolle, "Rapid prototyped porous titanium coated with calcium phosphate as a scaffold for bone tissue engineering", *Biomaterials*, Volume 29, Issue 17, 2008, pp 2608-2615,
- [12] G. E. Ryan, A. S. Pandit, D. P. Apatsidis, "Porous titanium scaffolds fabricated using a rapid prototyping and powder metallurgy technique", *Biomaterials*, Volume 29, Issue 27, 2008, pp 3625-3635,
- [13] V. K. Balla, S. Bodhak, S. Bose, A. Bandyopadhyay, "Porous tantalum structures for bone implants: Fabrication, mechanical and in vitro biological properties", *Acta Biomaterialia*, Volume 6, Issue 8, 2010, pp 3349-3359,
- [14] T.F. Hong, Z.X. Guo, R. Yang, "Fabrication of porous titanium scaffold materials by a fugitive filler method". *Journal of Materials Science: Materials in Medicine*, 19, 3489 (2008).
- [15] N. Tuncer, G. Arslan, "Designing compressive properties of titanium foams". *Journal of Materials Science*, 44, pp 1477-1484 (2009).
- [16] J. P. Li, S. H. Li, C. A. V. Blitterswijk, K. de Groot, "A novel porous Ti6Al4V: Characterization and cell attachment", *Journal of Biomedical Materials Research*, 73A(2), 2005, pp 223-233,
- [17] C.E Wen, M Mabuchi, Y Yamada, K Shimojima, Y Chino, T Asahina, "Processing of biocompatible porous Ti and Mg", *Scripta Materialia*, Volume 45, Issue 10, 2001, Pages 1147-1153,
- [18] M. S. Aly, "Effect of pore size on the tensile behavior of open-cell Ti foams: Experimental results", *Materials Letters*, Volume 64, Issue 8, 2010, Pages 935-937,
- [19] L. D. Zardiackas, D. E. Parsell, L. D. Dillon, D. W. Mitchell, L. A. Nunnery, R. Poggie, "Structure, metallurgy, and mechanical properties of a porous tantalum foam", *Journal of Biomedical Materials Research*, Volume 58, Issue 2, 2001, pp 180-187,
- [20] A. J. T. Clemow, A. M. Weinstein, J. J. Klawitter, J. Koeneman, J. Anderson, "Interface mechanics of porous titanium implants", *Journal of Biomedical Materials Research*, Volume 15, Issue 1, 1981, pp 73-82,
- [21] Y. Er, E. Ünsaldı, "The Production of Nickel-Chromium-Molybdenum Alloy with Open Pore Structure as an Implant and the Investigation of Its Biocompatibility in Vivo", *Advances in Materials Science and Engineering*, vol. 2013, Article ID 568479, 7 pages, 2013.
- [22] Y. Yamada, K. Shimojima, Y. Sakaguchi, "Effects of heat treatment on compressive properties of AZ91 Mg and SG91A Al foams with open-cell structure," *Materials Science and Engineering A*, vol. 280, no. 1, pp. 225-228, 2000.
- [23] C. E. Wen, M. Mabuchi, Y. Yamada, K. Shimojima, Y. Chino, and T. Asahina, "Processing of biocompatible porous Ti and Mg," *Scripta Materialia*, vol. 45, no. 10, pp. 1147-1153, 2001.
- [24] E. Tsuruga, H. Takita, H. Itoh, Y. Wakisaka, Y. Kuboki, "Pore size of porous hydroxyapatite as the cell-substratum controls BMP-induced osteogenesis", *Journal of Biochemistry*, vol. 121, no. 2, pp. 317-324, 1997.
- [25] Kilic, M., Kirik, I., Okumuş, M., "Microstructure examination of functionally graded NiTi/NiAl/Ni3Al intermetallic compound produced by self-propagating high-temperature synthesis", *Kovove Materialy*. 55. 97-106. 10.4149/km-2017-2-97.
- [26] H. Nishikawa, N. Maruyama, "Mechanical testing of metallic biomaterials", *Metals for Biomedical Devices (Second Edition)*, 2019, pp 189-211,
- [27] A. Glied, J. Mundiya, "Implant Material Sciences", *Dental Clinics of North America*, Volume 65, Issue 1, 2021, pp 81-88,
- [28] N. H. Mat-Baharin, M. Razali, S. Mohd-Said, J. Syarif, A. Mughtar, "Influence of alloying elements on cellular response and in-vitro corrosion behavior of titanium-molybdenum-chromium alloys for implant materials", *Journal of Prosthodontic Research*, Volume 64, Issue 4, 2020, pp 490-497,
- [29] S. Terpilowska, "Chapter 11 - Pro- and antioxidant activity of chromium(III), iron(III), molybdenum(III), or nickel(II)", *Toxicology*, Academic Press, 2021, pp 99-106,
- [30] D. Mehrotra, S. Kumar, P. Mehrotra, R. Khanna, V. Khanna, D. Eggbeer, P. Evans, "Patient specific total temporomandibular joint reconstruction: A review of biomaterial, designs, fabrication and outcomes", *Journal of Oral Biology and Craniofacial Research*, Volume 11, Issue 2, 2021, pp 334-343,
- [31] P. A. B. Kuroda, M. A. R. Buzalaf, C. R. Grandini, "Effect of molybdenum on structure, microstructure and mechanical properties of biomedical Ti-20Zr-Mo alloys", *Materials Science and Engineering: C*, Volume 67, 2016, pp 511-515,
- [32] N. Ranjan, "A Bibliometric Analysis and Visualisation of Research Trends in Health Issues of Nickel-Implants", *Turkish Journal of Computer and Mathematics Education*, Vol. 12 No. 2 (2021), pp 109-114,
- [33] G. Thind, "A Bibliometric Analysis and Visualisation of Research Trends in Toxicity of Nickel-implants", *Turkish Journal of Computer and Mathematics Education*, Vol.12 No.2 (2021), pp 75 -80,
- [34] V. V. Çay, S. Ozan, "Superalloys and Application Areas." *Doğu Anadolu Bölgesi Araştırmaları*, (2005).
- [35] S. Pattanaik, D. B. Karunakar, P.K. Jha, "Developments in investment casting process—A review", *Journal of Materials Processing Technology*, Volume 212, Issue 11, 2012, pp 2332-2348,
- [36] J. Banhart, J. Baumeister, "Production Methods for Metallic Foams", *MRS Proceedings*, (1998). 521, 121.
- [37] B. Y. Li, L. J. Rong, Y. Y. Li, and V. E. Gjunter, "Synthesis of porous Ni-Ti shape-memory alloys by self-propagating high temperature synthesis: reaction mechanism and anisotropy in pore structure", *Acta Biomaterialia*, vol. 48, no. 15, pp. 3895-3904, 2000.
- [38] M. W. Christopher, M. S. Richard, J. P. F. Garry, and J. D. Alison, "Dental materials," *Dental*, vol. 982, p. 10, 2006.

BIOGRAPHIE

Yusuf Er born in Batman in 1966, achieved his MSc and his PhD at the University of Firat, Elazig, Turkey, in 2002 and 2008, respectively, while working in the Ministry of Education, Gazi Vocational High School. At present, he is employed at the School of Aviation, University of Firat. His fields of interests include investment casting, porous materials, aircraft materials, composite materials, manufacturing techniques and wear.

Investigation of Failure Mechanism of a DCI Engine Connecting Rod

Mustafa Guven Gok^{1,2,*} , Omer Cihan^{3,4} 

^{1*} Department of Materials Science and Engineering, Hakkari University, Hakkari, Turkey. (m.guvengok@hakkari.edu.tr)

² Former Research Assistant at Department of Metallurgy and Materials Engineering, Istanbul Technical University, Istanbul, Turkey. (mngok@itu.edu.tr)

³ Department of Mechanical Engineering, Hakkari University, Hakkari, Turkey. (omercihan@hakkari.edu.tr)

⁴ Former Research Assistant at Department of Mechanical Engineering, Istanbul Technical University, Istanbul, Turkey. (ocihan@itu.edu.tr)

ARTICLE INFO

Received: Jun., 24. 2021

Revised: Sep., 03. 2021

Accepted: Sep., 06. 2021

Keywords:

Failure analysis

Connecting rod

Stress

Fatigue

Finite element analysis

Corresponding author: *Mustafa Guven*

Gok

ISSN: 2536-5010 / e-ISSN: 2536-5134

DOI: <https://doi.org/10.36222/ejt.957287>

ABSTRACT

In reciprocating engines, connecting rod cap and connecting bolts are critical as they are exposed to varying loads under different operating conditions. This paper focuses on the failure of the connecting rod of a 1.5 dci K9K diesel engine. As a result of the engine operating for approximately 378400 km, the connecting rod was broken, and the reasons for the failure of the connecting rod cap and connecting bolt were investigated. The connecting rod of the K9K engine was designed in accordance with the dimensions by using SolidWorks software, and then exported to ANSYS software for stress and fatigue analysis. Also, the macrostructure of the broken connecting rod cap and bolt was investigated. We knew that the mechanic who fixed the engine about two years ago tightened the connecting rod bolts without using a torque meter. Therefore, stress and fatigue analyses were performed to determine the effect of different tightening torques (ranging from 22.5 to 52.5 Nm) at 2000 rpm. According to the numerical analysis results, with increasing tightening torque, the maximum equivalent stress and alternating stress values increased significantly, while the fatigue safety factor and the cyclic life of the connecting rod decreased. First, a fatigue fracture occurred in the right hand bolt. Immediately after, the lower cup deformed and crashed to the cylinder liner. Therefore, a brittle fracture occurred on the left shoulder of the connecting rod shank. The chevron markings were clearly visible in the macrostructure as evidence of brittle fracture.

1. INTRODUCTION

Connecting rods are critical among reciprocating engine parts. It provides the connection between the piston and the crankshaft. The thrust force generated on the piston surface is transmitted to the crank shaft through the connecting rod, and then work is obtained by the rotation of the crankshaft [1]–[3]. Therefore, it is exposed to compression load as a result of combustion and tensile load due to inertia. A connecting rod must withstand these high cyclic loads for a long time (usually at least 10^8 cycles) [4], [5]. As a result, analyzes such as stress, fatigue and failure detection in the connecting rod have become important.

In researches made to date, the study of the connecting rod failure analysis was carried out in many ways. Many factors such as fatigue and improper material selection, poor design or fabrication defects, overload bending, incorrectly adjusted bolts, application of excessive load to critical stress areas, coupling and assembly deficiencies lead to failure in the connecting rod part [6]–[8]. Most of the failures occur in some parts of the connecting rod, such as the rounded fillet of the big connecting rod end [9], over the connecting rod body [10],

the small head of the connecting rod, the crank pin, the roller bearing and the connecting rod bolt [11]. Rakic et al. [12] conducted a failure analysis of the connecting rod in a 12-cylinder diesel engine. Structural steel marked 18H2N4MA was used as connecting rod material. Besides chemical and metallographic analysis, the stress distribution under maximum load has been evaluated. The location of the fracture in the analysis is consistent with the highest stress zone obtained in the experiment. The fracture occurred at the length of the connecting rod close to the piston pin. Juarez et al. [13] discussed the results of a failure analysis study in the connecting rod of a diesel engine used in electrical power generation. AISI / SAE 4140 low alloy steel material is used in the connecting rod. According to the experimental and microstructural analysis of the study, the connecting rod has fractured in the body in a section close to the crankshaft side. The source of the fracture was determined in the crankshaft lubrication channel. The lubrication channel has been found to have been embedded in the surface, possibly as a result of an incomplete manufacturing process of tungsten-based material from a machining tool. The purpose of use of this material is that it is more suitable for the application area in

terms of chemical composition and mechanical properties. [13]–[15]. Rezvani et al. [16] studied the catastrophic deformation of the 645E3B engine connecting rod due to unknown reasons. The used connecting rod has 42CrMo4 material. Critical loads and buckling forces on the connecting rod were calculated using ADAMS software. It turns out that the connecting rod failure is due to buckling with the hydrolock phenomenon. Rabb [17] analyzed the fatigue failure of a connecting rod in a medium speed diesel engine. 34CrNiMo6TQ + T was used as the connecting rod material. It had been found to be failure near the crankshaft side. The screw thread profile has been changed to prevent failure, and the connecting rod material has been changed to increase fatigue strength. Bari et al. [18] conducted a finite element analysis simulation to determine the cause of the failure connecting rod from a motorcycle engine. Simulation in the ANSYS software was used to verify the surface failure and strength studied. The connecting rod material is AISI 4140 steel, and it has broken at the big end and the bolt housing of the connecting rod. It was concluded that the connecting rod failed at the end of the exhaust stroke due to the fatigue loading.

The connecting rod must be able to withstand enormous loads and transfer large amounts of power smoothly. According to Lee et al. [19], failure usually occurs at the big end of the connecting rod. The stress distribution was estimated and the value of the corner radius was optimized by using ANSYS software. Andoko et al. [20] investigated the cause of the failure of a connecting rod in a car. AISI 4315 material was used. As a result, big near-edge cracks had greater stress and strain values than the far area. Mirehei et al. [21] investigated the problem of the connecting rod fatigue failure of the universal tractor (U650) by using ANSYS software. This research demonstrated the occurrence of fatigue failure in the connecting rod due to continuous cyclic loads and variable speeds. Thomas et al. [22] indicated that the probability of fatigue failure due to fluctuation of loads was very high. Dupare et al. [22] stated that 50-90% of the failure in the connecting rod was due to fatigue failure. For this reason, authors were emphasized that it was very important to consider fatigue failure in connecting rod design. Ranjbarkohan et al. [23] performed an analysis of a Samand engine connecting rod for fatigue failure using the ANSYS workbench. Maximum tensile and compression load was applied to assess critical failure points to improve the strength and life of the connecting rod. According to the analysis results, the maximum tension (297.361 MPa) was determined at the pin end.

Another issue that needs to be considered is the stress and failure analysis of the connecting rod in diesel engines. Witek and Zelek [24] conducted a study on the failure and stress analysis of the connecting rod of a turbocharged diesel engine. ANSYS software was used for analysis. In the nonlinear static analysis results, it was determined that the high stress regions were located at the crack centers during the operation of the engine with maximum power. The results showed that the bolt tightening torque has a significant effect on the maximum stress value at the center of the crack. When the results of the study are examined, the main cause of the failure of the connecting rod was the high pretension of the bolts and the high stresses in the areas near the bolt hole. Griza et al. [25] examined the fatigue of the engine connecting rod bolt due to the laps occurring. The torque disassembly of the connecting rod bolts was monitored, and the fractured parts were

examined in the laboratory. A finite element analysis based on an analytical fracture mechanics approach was carried out to evaluate the relationship between tightening force and fatigue crack propagation in connecting rod bolts. It has been suggested that engine collapse was caused by the forming laps in the grooves of the bolt shank. Zhu et al. [26] made a failure analysis of the connecting rod cap and connecting bolts for a reciprocating compressor. The reasons for the failure of the connecting rod cap and connecting bolts as a result of operation for approximately 175.200 hours were researched. In the study, microstructure (by using scanning electron microscope (SEM) and optical microscope) and chemical composition of the connecting rod material were examined, and tensile, hardness and impact tests were applied. Moreover, the general stress distributions in the connecting rod were evaluated based on the maximum stress criterion using the finite element method. Looking at the results of the research, it was determined that the cause of the failure was high cycle fatigue, and the initial crack location was consistent with the high stress concentration. Acri et al. [27] scrutinized the coating processes of bolts and their effects on fatigue life of the connecting rod. As a result, it was thought that the stress concentration factor was smaller than the first engaged thread and the failure to the head was caused by thread rolling in the connecting rod.

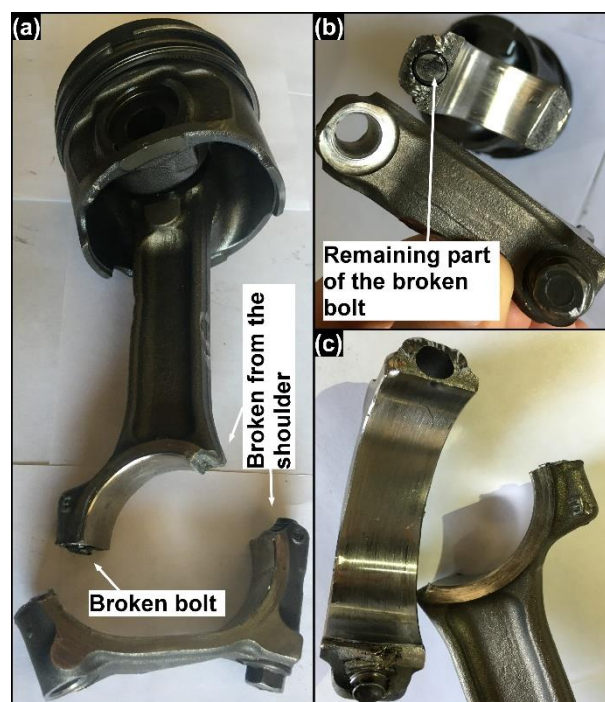


Figure 1. Macro view of the connecting rod after failure. (a) general view, (b) and (c) broken parts.

In this study, a broken connecting rod belonging to Renault Kangoo vehicle with 1.5 dci K9K (55kW) diesel engine was used. To simulate fatigue and stress distributions on the connecting rod, it was drawn according to its original dimensions by using SolidWorks software, and this drawn part was exported to ANSYS software. Different tightening torque values (22.5, 27.5, 32.5, 37.5, 42.5, 47.5 and 52.5 Nm),

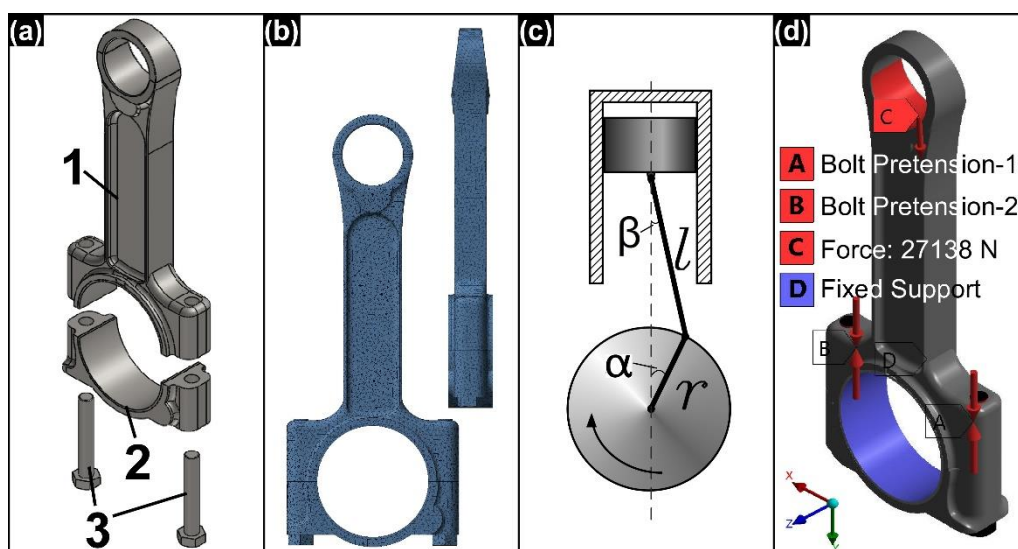


Figure 2. (a) Main parts of connecting rod, (b) finite element model showing meshes, (c) angles of crankshaft and connecting rod at the maximum in cylinder pressure, (d) loading conditions.

were evaluated at 2000 rpm. The fatigue behavior, maximum equivalent stress distributions, safety factor and alternating equivalent stress were analyzed to determine the effect of different tightening torques. Moreover, microstructural analysis was carried out to determine failure mechanism of the connecting rod.

2. MATERIALS AND METHOD (Helvetica 10p Bold)

2.1. Definition of failure and damaged connecting rod

The K9K type diesel engine used for power of a 2003 model Renault Kangoo type vehicle failed during operation. This engine had a turbocharger and a maximum power of 55 kW as can be seen from the detailed properties given in Table I.

TABLE I.
PROPERTIES OF K9K ENGINE [28].

Number of cylinders	4
Bore	76 mm
Stroke	81 mm
Compression ratio	18.3
Rated power	55 kW / 3900 rpm
Maximum torque	156 Nm / 2000 rpm
Admission type	Turbocharged

When the engine was disassembled, one of the connecting rods was found to be broken. The vehicle was known to be at 378400 km when the failure occurred. Also, about 2 years ago from the connecting rod failure, the crankshaft was changed for another reason, and therefore the connecting rods were removed and reassembled. However, it was learned that the mechanic did not use a torque meter during this removal and reassembly of the connecting rods. The connecting rod was removed, and as seen in Figure 1 (a), in the big end region, the left bolt connecting the lower cap and the upper cup of the connecting rod was broken in the middle. The remaining part of bolt on the connecting rod shank could be seen in Figure 1 (b). The bolt on the right was intact (Figure 1 (a and c)). However, the right side of the connecting rod was broken from the big end shoulder. Also the lower cap of the big end was deformed.

2.2. Numerical model, meshing, boundary and loading conditions of the connecting rod

To understand the mechanism of connecting rod failure, first, the geometric model of the connecting rod was created using SolidWorks software. As seen in Figure 2 (a), the connecting rod consisted of three basic components. Part 1, 2 and 3 were the connecting rod shank, lower cap and bolts, respectively. Then, the created model was exported to the ANSYS Workbench software for numerical analysis. AISI 4140 low alloy steel was defined as the material with linear-elastic properties [13]. The maximum young's modulus, yield strength, ultimate strength and poisson ratio of 4140 steel were 210 GPa, 1540 MPa, 2073 MPa and 0.29 %, respectively. In the next step the contact definitions between neighboring components were carried out. The friction coefficients of bolts and all other parts were defined as 0.15 and 0.1 μ , respectively [24]. Tetrahedron meshes were used to divide the connecting rod into finite elements (Figure 2 (b)). The average mesh quality value was tried to be 0.85 and above to obtain more accurate results. To achieve this, different operations such as patch independent, patch conforming and mesh sizing were applied. The model was occurred with 160994 nodes and 104508 elements.

In this study, as mentioned above, failure analysis of connecting rod of K9K diesel engine was made. In order to calculate the maximum load acting on the connecting rod in this engine, the maximum in-cylinder pressure must first be determined. Nutu et al [28] reported that maximum in cylinder pressure of K9K engine was about 58 bar at 2000 rpm and 70% load. This value was converted to the newton force by using Equation 1. The angle of α was 3.55 degrees, as the maximum pressure occurred when the crank angle was 10° after top dead center (ATDC) (see Figure 2 (c)) [29]. As seen in Figure 2(d), the load was applied according to this angular value. On the other hand, net force acting on connecting rod was calculated by using Equation 2. The force arising from inertia ($F_{inertia}$) of the connecting rod and reciprocating mass, and force arising from friction ($F_{friction}$) of the piston rings, and the piston were calculated according to Equations 3 and 4, respectively.

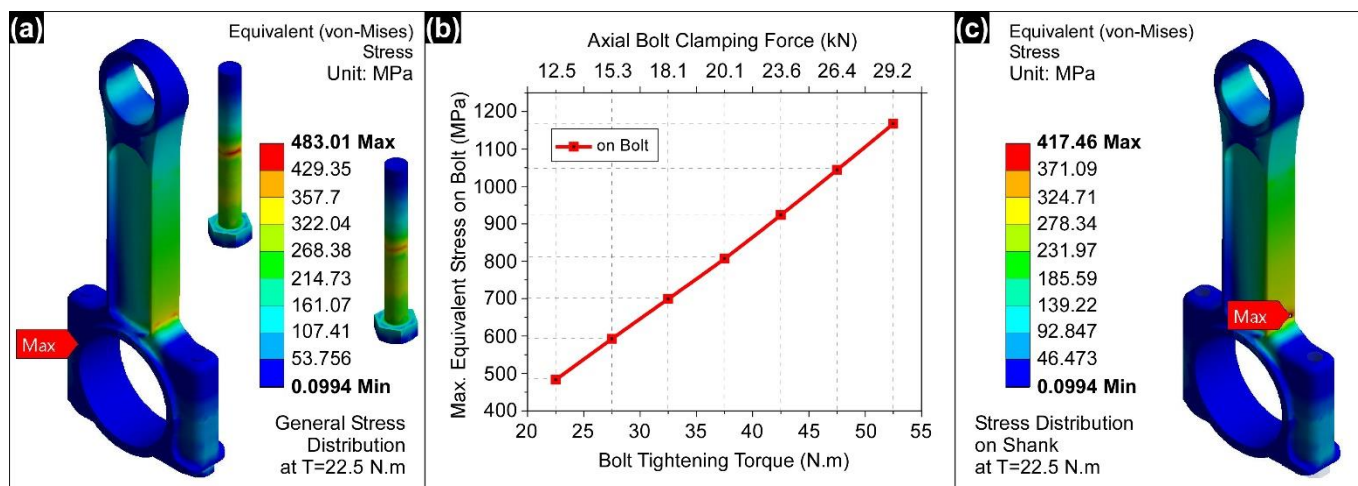


Figure 3. (a) equivalent (von-Mises) stress distributions on the all components of connecting rod, (b) graph of max. equivalent stress values on the bolt as a function of bolt tightening torque, (c) equivalent stress distributions on the connecting rod shank.

$$F_{gas} = \frac{\pi \cdot d^2}{4} * P_e \quad (1)$$

$$F = F_{gas} + F_{inertia} - F_{friction} \quad (2)$$

$$F_{inertia} = M * \omega^2 * r * (\cos\alpha + r * \frac{\cos\alpha}{l}) \quad (3)$$

$$F_{friction} = h * \pi * d * i * P_r * \mu \quad (4)$$

Here, M was mass of piston and rings + Piston pin + 1/3 rd of the connecting rod. ω , r and l were angular speed (rad/s), crank radius (mm) and length of the connecting rod (mm), respectively. α was crank angle ($^\circ$). Moreover, different bolt pressures were applied to the bolts as seen in Figure 2 (d). The required normal bolt tightening torque value was obtained from the K9K engine workshop repair manual (Renault Technical note) [30]. This value was $20 \pm 2 \text{ Nm} + 45^\circ \pm 6^\circ$, and it converted to the clamping force (N) value by using simply Equation 5.

$$T = K * F * d \quad (5)$$

Here, T , K and F were tightening torque (Nm), a constant factor and the clamping force (N), respectively. d was the diameter (m) of the bolt. According to this formula, the clamping force at the normal tightening torque was about 12500 N. Big end bearing surfaces of the connecting rod was fixed as fixed support.

2.3. Analyzes

Six different (abnormal) tightening torque values, which are above the given normal value, were used to perform the numerical analysis of the failure of the connecting rod.

Because as mentioned above, during the previous engine repair, the mechanic tightened the connecting rod bolts without using a torque meter. The maximum equivalent stresses (von Mises) were analyzed to determine the effect of different tightening torques. In addition, fatigue analyzes were made in each case according to Goodman stress theory. The minimum life (cycles) and safety factor values were determined. During the analyses, the ambient temperature was set to 95°C .

3. RESULTS AND DISCUSSION

3.1. Stress Analysis

As a result of nonlinear static analyzes performed with the application of different bolt pretensions, maximum equivalent stress values in the connecting rods were obtained (Table II). During the analyses, bolt pre-tensions caused by different tightening torques varying in between 22.5 - 52.5 Nm were applied to the connecting rod. As seen in Figure 3 (a), the zone of maximum equivalent stress (483.01 MPa) at normal bolt tightening torque (22.5 Nm) was observed at the left-side bolt. This zone corresponded to the junction of the lower and upper cup of the connecting rod. In fact, as seen in Figure 1, the bolt on the left-side was broken at this zone. This equivalent stress value was considerably lower than the yield strength value of the bolt (1540 MPa). Therefore, at normal tightening torque, the stress safety factor in this zone was about "3.2" and it did not pose any problem. However, as seen in Figure 3 (b), the maximum stress value in this region significantly increased with the increase of the tightening torque. Such that, at the 52.5 Nm tightening torque, the maximum equivalent stress value on the bolt was 1167.5 MPa. This meant that the stress safety factor was approximately "1.3".

TABLE II.
RESULTS OF STRESS AND FATIGUE ANALYSES.

Bolt tightening torque (Nm)	Axial bolt clamping force (N)	Force due to combustion (N)	Equivalent stress (N)	Equivalent alternating stress (N)	Safety factor for fatigue	Life (cycle) $\times 10^7$
22.5	12500	27138	483.01	284.72	1.9878	1×10^3
27.5	15278	27138	592.35	359.53	1.6208	1×10^3
32.5	18056	27138	699.23	437.05	1.3731	1×10^3
37.5	20883	27138	806.89	519.96	1.1899	1×10^3
42.5	23611	27138	923.52	615.78	1.0396	3.45×10^2
47.5	26389	27138	1044.1	722.13	0.91952	6.81
52.5	29167	27138	1167.5	839.37	0.8224	2.25×10^{-1}

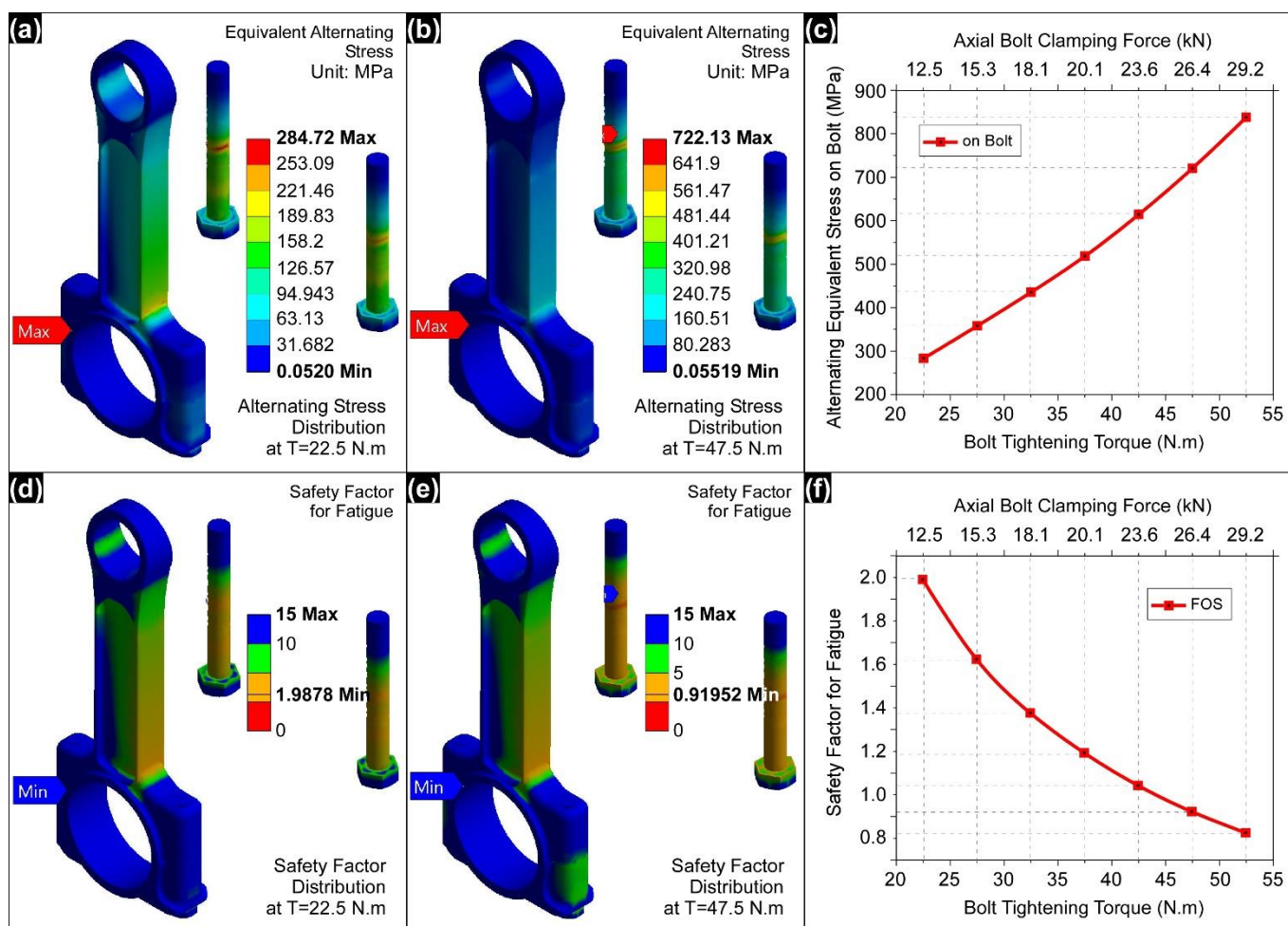


Figure 4. (a) Distribution of equivalent alternating stress at $T=22.5$ Nm, (b) distribution of equivalent alternating stress at $T=47.5$ Nm, (c) graph of alternating stress vs bolt tightening torque, (d) distribution of safety factor for fatigue at $T=22.5$ Nm, (e) distribution of safety factor for fatigue at $T=47.5$ Nm and (f) graph of safety factor for fatigue vs bolt tightening torque.

Witek et al. [24] stated that connecting rod bolts were subjected to complex loads acting as both tension and compression during engine operation. Therefore, the risk of breaking of the connecting rod bolts was high when the bolts were tightened above the normal tightening torque. On the other hand, as seen in Figure 3 (c), the maximum stresses on the connecting rod shank were concentrated in the right shoulder zone (417.46 MPa). This zone (right shoulder region of the connecting rod) was also the region where the break in the connecting rod shank occurred (see Figure 1). Because the maximum in cylinder pressure occurred when the crank angle was 10° after the piston top dead center, the load was applied to the piston pin of the connecting rod at an angle of 3.55 degrees. Therefore, the zones where the stresses concentrated on the components of connecting rod and the zones where the fractures occurred were completely matched.

3.2. Fatigue Analysis

Fatigue analyzes were performed on the model to determine the effect of non-normal bolt tightening torque on the life of connecting rod components. During engine operation, connecting rods are subjected to cycling compression due to combustion force and tensile load due to inertia of moving parts [31]. Therefore, these loads should be considered in order to obtain realistic results in numerical modeling. As mentioned above, the maximum compression force due to combustion was 27138 N, and the tensile force due to inertia of moving parts was 1243 N. Hence, the ratio of

-0.046 was used for the stress-life fatigue analysis. As expected, equivalent alternating stresses were concentrated on the bolt where equivalent stresses were maximum (see Figure 1 (a and b)). The maximum value of equivalent alternating stress considerably increased with increasing bolt tightening torque. While the maximum value of equivalent alternative stress was 284.72 MPa at normal bolt tightening torque (22.5 Nm), this value increased to 839.37 MPa at 52.5 Nm bolt tightening torque (Figure 1 (a-c)). Tabulated data including all the results of the fatigue analysis are given in Table II. Tabulated data including all the results of the fatigue analysis were given in Table II. On the other hand, as seen in Figure 4 (d-f), safety factor values for fatigue decreased with the increasing bolt tightening torque. At normal bolt tightening torque, safety factor for fatigue was about "1.99" (Figure 4 (d and f)). This value was quite satisfactory in terms of fatigue. However, this value was lower than "1", especially with the application of 47.5 Nm and higher bolt tightening torque (Figure 4 (e and f)). This greatly increases the likelihood of fatigue damage. As Consistent with this, as seen in Table II, at 42.5, 47.5 and 52.5 Nm bolt tightening torque values, the fatigue life of connecting rod decreased to 3.45×10^9 , 6.81×10^7 and 2.25×10^6 cycles, respectively. As explained in the previous section, the zones where alternating stresses and minimum safety factors

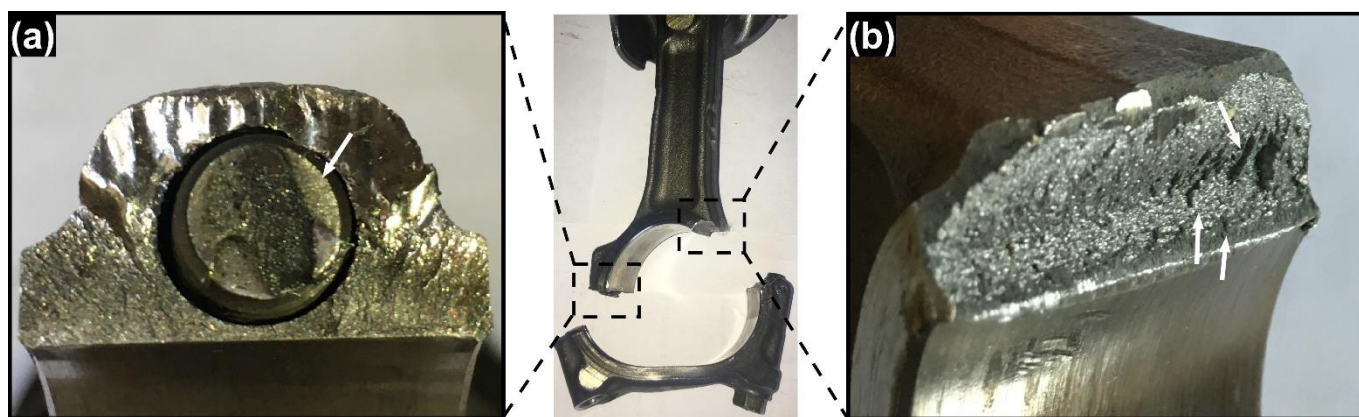


Figure 5. Macrostructure of damaged zones. (a) fracture surface of the remaining part of the broken left side bolt and (b) fracture surface of the broken right side shoulder.

concentrated were the points where breakage occurred in the connecting rod (left bolt and right shoulder).

3.3. Macrostructural investigation and failure mechanism

The macrostructural photograph of the damaged zones of the connecting rod was given in Figure 5 (a and b). In Figure 5 (a), the possible fatigue area in the remaining part of the broken bolt is indicated by the arrow. Due to the fact that the mechanic did not use a torque meter, fatigue occurred in the over-tightened bolt, and the remaining section of the bolt after the fatigue damage area was broken because it could not bear the axial clamping force. As proved in the previous sections, the stresses in the broken region of the bolt were maximum and the safety factors were minimum. Immediately after the bolt on the left broke, the right shoulder area of the connecting rod was overloaded (stresses were also concentrated in this area as the maximum cylinder pressure took place at the crank angle of 10° ATDC). The deformed lower cap hit the cylinder liner and broke on the right shoulder and completely separated from the connecting rod shank. As a result, a brittle fracture occurred in the right shoulder region (Figure 5 (b)). As evidence of this, chevron markings (indicated by arrows in Figure 5 (b)) were observed in the fracture zone. Because it was reported that chevron markings typically result from the brittle fracture of steel materials [32]. Then the rings and valves took damage due to the uncontrolled movement of the piston. Thus, the connecting rod bolt, which had fatigue fracture due to excessive tightening torque, caused the connecting rod to break completely and the engine to be seriously damaged.

4. CONCLUSIONS

The present work was aimed to determine failure mechanism of a K9K diesel engine connecting rod. Existing connecting rod was broken from right side bolt and left side shoulder (on shank). We knew that the mechanic who fixed the engine about two years ago tightened the connecting rod bolts without using a torque meter. Therefore, stress and fatigue analyzes were performed to determine the effect of different tightening torques (ranging from 22.5 to 52.5 Nm) at 2000 rpm. The maximum equivalent stress and alternating stress values increased from 483.01 to 1167.5 MPa and 284.72 to 839.37 MPa, respectively. After a tightening torque of 42.5 Nm, the fatigue safety factor was lower than "1", and cycling life decreased up to 2.25×10^6 cycles. The points where the failure in the connecting rod occurred and the zones where the stresses concentrated in the analyzes were compatible. Firstly, a fatigue

fracture occurred in the right hand bolt. Immediately after, the lower cup deformed and crashed to the cylinder liner. Therefore, a brittle fracture occurred on the left shoulder of the connecting rod shank. The chevron markings were clearly visible in the macrostructure as evidence of brittle fracture. As a result, the use of torque meters was very important in the assembly of engine post-repair parts.

ACKNOWLEDGEMENT

The authors would like to thank Istanbul Technical University Information Technologies Directorate for permission the use of the softwares.

REFERENCES

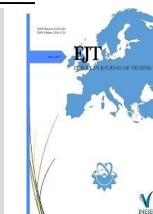
- [1] S. Fukuda and H. Eto, 'Development of fracture splitting connecting rod', *JSAE Rev.*, vol. 23, no. 1, pp. 101–104, 2002, doi: 10.1016/S0389-4304(01)00154-0.
- [2] Z. Pan and Y. Zhang, 'Numerical investigation into high cycle fatigue of aero kerosene piston engine connecting rod', *Eng. Fail. Anal.*, vol. 120, pp. 1–13, 2021, doi: 10.1016/j.engfailanal.2020.105028.
- [3] A. Gautam, 'Static Stress Analysis of Connecting Rod Using Finite Element Approach', *IOSR J. Mech. Civ. Eng.*, vol. 10, no. 1, pp. 47–51, 2013, doi: 10.9790/1684-1014751.
- [4] P. Singh, D. Pramanik, and R. V. Singh, 'Fatigue and Structural Analysis of Connecting Rod's Material Due to (C.I) Using FEA', *Int. J. Automot. Eng. Technol.*, vol. 4, no. 4, pp. 245–253, 2015.
- [5] A. Muhammad, M. A. H. Ali, and I. H. Shanono, 'Design optimization of a diesel connecting rod', *Mater. Today Proc.*, vol. 22, pp. 1600–1609, 2019, doi: 10.1016/j.matpr.2020.02.122.
- [6] B. yan He, G. da Shi, J. bing Sun, S. zhuan Chen, and R. Nie, 'Crack analysis on the toothed mating surfaces of a diesel engine connecting rod', *Eng. Fail. Anal.*, vol. 34, pp. 443–450, 2013, doi: 10.1016/j.engfailanal.2013.09.004.
- [7] X. L. Xu and Z. W. Yu, 'Failure analysis of a diesel engine connecting rod', *J. Fail. Anal. Prev.*, vol. 7, no. 5, pp. 316–320, 2007, doi: 10.1007/s11668-007-9058-9.
- [8] G. T. Reddy and C. Srinivas, 'Fatigue analysis and life predictions of Forged steel and Powder Metal connecting rods', *IOSR J. Mech. Civ. Eng.*, vol. 16, no. 053, pp. 15–19, 2016, doi: 10.9790/1684-16053031519.
- [9] M. N. Ilman and R. A. Barizy, 'Failure analysis and fatigue performance evaluation of a failed connecting rod of reciprocating air compressor', *Eng. Fail. Anal.*, vol. 56, pp. 142–149, 2015, doi: 10.1016/j.engfailanal.2015.03.010.
- [10] M. N. Mohammed, M. Z. Omar, S. Zainuddin, A. Salah, M. A. Abdelgnei, and M. S. Salleh, 'Failure analysis of a fractured connecting rod', *J. Asian Sci. Res.*, vol. 2, no. 11, pp. 737–741, 2009.
- [11] S. Khare, O. P. Singh, K. Bapanna Dora, and C. Sasun, 'Spalling investigation of connecting rod', *Eng. Fail. Anal.*, vol. 19, no. 1, pp. 77–86, 2012, doi: 10.1016/j.engfailanal.2011.09.007.
- [12] S. Rakic, U. Bugaric, I. Radisavljevic, and Z. Bulatovic, 'Failure analysis of a special vehicle engine connecting rod', *Eng. Fail. Anal.*, vol. 79, no. April, pp. 98–109, 2017, doi: 10.1016/j.engfailanal.2017.04.014.

- [13] C. Juarez, F. Rumiche, A. Rozas, J. Cuisano, and P. Lean, 'Failure analysis of a diesel generator connecting rod', *Case Stud. Eng. Fail. Anal.*, vol. 7, pp. 24–31, 2016, doi: 10.1016/j.csefa.2016.06.001.
- [14] A. Saravanan, P. Suresh, G. Sudharsan, and V. Suresh, 'Static analysis and weight reduction of aluminum casting alloy connecting rod using finite element method', *Int. J. Mech. Prod. Eng. Res. Dev.*, vol. 8, no. 3, pp. 507–518, 2018, doi: 10.24247/ijmperdjun201855.
- [15] P. Sarate, G. R. Kesheorey, and M. Shah, 'A Comparative Study on Forecasting and Analysis of 4140 Material Composition of Connecting Rod for Various Applications', no. November, 2017.
- [16] M. A. Rezvani, D. Javanmardi, and P. Mostaghim, 'Diagnosis of EMD645 diesel engine connection rod failure through modal testing and finite element modeling', *Eng. Fail. Anal.*, vol. 92, no. January, pp. 50–60, 2018, doi: 10.1016/j.engfailanal.2018.05.005.
- [17] R. Rabb, 'Fatigue failure of a connecting rod', *Eur. Struct. Integr. Soc.*, vol. 22, no. C, pp. 97–112, 1997, doi: 10.1016/S1566-1369(97)80011-8.
- [18] K. Bari, A. Rolfe, A. Christofi, C. Mazzuca, and K. V. Sudhakar, 'Forensic investigation of a failed connecting rod from a motorcycle engine', *Case Stud. Eng. Fail. Anal.*, vol. 9, no. May, pp. 9–16, 2017, doi: 10.1016/j.csefa.2017.05.002.
- [19] S. Y. Lee, S. B. Lee, H. S. Kim, T. G. Kim, M. G. Kam, and J. W. Yoon, 'Failure Analysis of Connecting Rod at Big End', *Key Eng. Mater.*, vol. 306–308, pp. 345–350, 2006, doi: 10.4028/www.scientific.net/kem.306-308.345.
- [20] A. Andoko *et al.*, 'Failure analysis on the connecting rod by finite element method', *AIP Conf. Proc.*, vol. 2262, no. September, 2020, doi: 10.1063/5.0015728.
- [21] A. Mirehei, M. Hedayati Zadeh, A. Jafari, and M. Omid, 'Fatigue analysis of connecting rod of universal tractor through finite element method (ANSYS)', *J. Agric. Technol.*, vol. 4, no. 2, pp. 21–27, 2008.
- [22] T. G. Thomas, S. Srikari, and M. L. Suman, 'Design of Connecting Rod For Heavy Duty Applications Produced By Different Processes For Enhanced Fatigue Life', *SasTech J.*, vol. 10, no. 1, pp. 1–7, 2011.
- [23] M. Ranjarkohan, M. R. Asadi, M. Mohammadi, and A. Heidar, 'Fatigue analysis of connecting rod of samand engine by Finite Element Method', *Aust. J. Basic Appl. Sci.*, vol. 5, no. 11, pp. 841–845, 2011.
- [24] L. Witek and P. Zelek, 'Stress and failure analysis of the connecting rod of diesel engine', *Eng. Fail. Anal.*, vol. 97, pp. 374–382, 2019, doi: 10.1016/j.engfailanal.2019.01.004.
- [25] S. Griza, F. Bertoni, G. Zanon, A. Reguly, and T. R. Strohaecker, 'Fatigue in engine connecting rod bolt due to forming laps', *Eng. Fail. Anal.*, vol. 16, no. 5, pp. 1542–1548, 2009, doi: 10.1016/j.engfailanal.2008.10.002.
- [26] X. Zhu, J. Xu, Y. Liu, B. Cen, X. Lu, and Z. Zeng, 'Failure analysis of a failed connecting rod cap and connecting bolts of a reciprocating compressor', *Eng. Fail. Anal.*, vol. 74, pp. 218–227, 2017, doi: 10.1016/j.engfailanal.2017.01.016.
- [27] A. Acri, S. Beretta, F. Bolzoni, C. Colombo, and L. M. Vergani, 'Influence of manufacturing process on fatigue resistance of high strength steel bolts for connecting rods', *Eng. Fail. Anal.*, vol. 109, no. May 2019, p. 104330, 2020, doi: 10.1016/j.engfailanal.2019.104330.
- [28] N. C. Nutu, C. Pana, N. Negurescu, A. Cernat, D. Fuioreescu, and L. Nemoianu, 'An experimental approach on fuelling a passenger car diesel engine with LPG', *IOP Conf. Ser. Mater. Sci. Eng.*, vol. 444, no. 7, 2018, doi: 10.1088/1757-899X/444/7/072001.
- [29] M. Tuti, Z. Şahin, and O. Durgun, 'Thermodynamic diesel engine cycle modeling and prediction of engine performance parameters', *Gmo-Shipmar*, vol. 207, no. March, pp. 14–26, 2017, [Online]. Available: https://www.journalagent.com/gmo/pdfs/GMO_23_207_14_26.pdf.
- [30] Renault, 'Technical Note6006A KXX, and K9K engine - Engine workshop repair manual', 2004.
- [31] M. T. Alam, A. Thakur, V. Kumar PS, and S. Ghadei, 'Fatigue Failure Analysis of Diesel Engine Connecting Rod', in *SAE Technical Papers*, Jul. 2018, vol. 2018-July, pp. 1–8, doi: 10.4271/2018-28-0067.
- [32] J. W. Sowards, C. N. McCowan, and E. S. Drexler, 'Interpretation and significance of reverse chevron-shaped markings on fracture surfaces of API X100 pipeline steels', *Mater. Sci. Eng. A*, vol. 551, pp. 140–148, 2012, doi: <https://doi.org/10.1016/j.msea.2012.04.108>.

BIOGRAPHIES

Mustafa Guven Gok graduated from Firat University department of Metallurgical Education with a bachelor and master of science degrees in 2008 and 2010, respectively. After, he graduated from Istanbul Technical University department of Metallurgical and Materials Engineering in 2015 with Ph.D. degree. Dr. Gok joined to the Materials Science and Engineering Department of Hakkari University in 2015 and he has been working in Hakkari University since 2016. His study fields include: Plasma Spray Coating and Spark Plasma Sintering (SPS) Processes, Thermal Barrier Coatings, Self-Healing Ceramics, Biomaterials, Finite Element Analysis and Materials of Internal Combustion Engine.

Omer Cihan born in 1986, studied Mechanical Training. He completed his MSc degrees in department of Mechanical Training from Firat University, Elazığ, Turkey, in 2011. Then, He completed his PhD degrees in Mechanical Engineering from Istanbul Technical University, Istanbul, Turkey, in 2017. He has been worked as a research assistant at University of Istanbul Technical, Mechanical Engineering Department, Turkey, from 2010 to 2017. He is currently working at Hakkari University, Turkey, as Assist. Professor. The primary topics of his scientific work are such as Engine materials, Friction, Wear, Engine testing, Engine performance and emissions, Engine construction, Rotary engine, Engine electronic control unit and Internal combustion engine.



Design and Development of a Helmholtz Pair System for Production of a Low-Magnetic Field of up to 7.5 mT

Yenal Gokpek^{1*}, Ozgun Boray Yurdakos², Ozkan Doganay³

¹Ege University, Fundamental Oncology Department, Institute of Health Sciences, 35100, Izmir, Turkey. (e-mail: yenalgokpek@gmail.com).

²Ege University, Fundamental Oncology Department, Institute of Health Sciences, 35100, Izmir, Turkey. (e-mail: obyurdakos@gmail.com).

³Ege University, Fundamental Oncology Department, Institute of Health Sciences, 35100, Izmir, Turkey. (e-mail: ozkan.doganay@ege.edu.tr).

ARTICLE INFO

Received: Oct., 06. 2021

Revised: Nov., 21. 2021

Accepted: Nov., 23. 2021

Keywords:

Helmholtz Coil

Magnetic Field

Spin Exchange Optical Pumping

Corresponding author: *O. Doganay*

ISSN: 2536-5010 / e-ISSN: 2536-5134

DOI: <https://doi.org/10.17694/ejt.991890>

ABSTRACT

In this study, the design, numerical modelling, and construction of various Helmholtz pair coil systems were investigated to produce a homogeneous magnetic field. The magnetic field was simulated using three different Helmholtz coil systems including 2-coil, 3-coil, and 4-coil combinations in order to optimize the field homogeneity and strength over a region of interest that consists of a cylindrical geometry with a height of 700 mm and a diameter of 90 mm. The simulated magnetic field created by the 4-coil system was found to be more homogenous than 3-coil and 2-coil systems over the region of interest. The 4-coil system was constructed and tested by using two commercially available low-power (P=600 W) DC power supplies. For further optimization, the number of turns and diameter of coil elements were simulated. The optimum number of turns and elements were determined to be 140 and 80 turns for the outer pair and inner pair of the 4-coil system, respectively. Finally, the produced magnetic field strength was measured using a hand-held gaussmeter and compared to the simulated magnetic field. We found that the system can produce a magnetic field of $B=7.5047 \pm 0.0562$ mT, and the correlation between simulated and measured magnetic fields were calculated to be $R=0.9824$ with ($p<0.001$) suggesting a statistically significant agreement.

1. INTRODUCTION

Recent improvements in the field of magnetic resonance imaging (MRI) have shown that relatively low-magnetic fields lower than 0.5 Tesla can be used to achieve reasonable image quality compared to the clinical MR scanners that employ magnetic field strength stronger than 1 Tesla [1, 2]. Compared to the conventional MR systems, low-field systems promise to provide more effective field homogeneity with the advantage of easy installation and cost-effective maintenance [3]. Additionally, the novel hyperpolarized MRI techniques including Xenon-129, Helium-3, and Carbon-13 renewed interest in the design and optimization of the low-magnetic field systems [4-10] with the advantage of reduced magnetic field strength in the order of 2-10 mT [6, 11-14]. One other relevant application of low-strength magnetic field is the spin-exchange optical pumping (SEOP) technique that is used to polarize Xenon-129 gas [15-18].

Recent studies have investigated the feasibility of low-field systems for imaging organs including the brain, lungs, heart, and musculoskeletal [19-22]. Additionally, custom-built magnet systems and detectors were widely used in nuclear magnetic resonance (NMR) systems for producing uniform

magnetic fields in medical, biological and chemical analysis applications [23-27]. While these systems generate relatively uniform magnetic fields in small volumes between 100-200mm, they are not capable of relatively larger volumes. Although Helmholtz coils were very effective for generating uniform magnetic fields over larger volumes, the classical two-coil systems require a distance between the coils that is equal to the coil radius making it difficult to implement into the low-field NMR and MRI systems. In this respect, Helmholtz systems that consist of multi-coil pairs would offer further improvements in the design and construction of the low-field systems.

In this study, a theoretical optimization and design of a low-field Helmholtz coil system have been investigated to produce a magnetic field that takes up less space than the classical Helmholtz coil systems for the use of SEOP and the low-field animal MR imaging systems.

2. MATERIALS AND METHODS

2.1. Numerical Simulations:

Three different Helmholtz coil systems were simulated for investigating the magnetic field homogeneity: (i) the first

designed Helmholtz coil system assembled of four coil elements (i.e. 4-coil as shown in Figure 1), (ii) the second system contained three coil elements (i.e. 3-coil), and (iii) the third system contained two elements (i.e. 2-coil). Then, for the best number of elements, the winding numbers were simulated to further optimize the uniformity of the magnetic field.

Magnetic fields generated by each coil system (2-coil, 3-coil, 4-coil) were calculated using MATLAB with a fixed mesh size of 2 mm and solving the general magnetic vector potential equations [28]. The magnetic field vector for a single winding was calculated by the superposition principle as well as the net magnetic field [29].

Since the DC power supplies could create 600W power, the magnetic field was simulated for an electric current of 19.5A. The cross-sections of the simulated magnetic fields were compared between three different coil systems for determining the most homogenous magnetic field.

To optimize winding numbers, magnetic field variations were calculated by the ratio of standard deviation to mean magnetic field strength within the ROI as shown in Figure 1 as the red cylinder. The ROI was chosen to be 700 mm long, 90 mm wide, and centered to the middle of the coil systems for investigating the feasibility of this system in the field of small animal imaging or a SEOP system.

The number of windings was varied from 1 to 200 turns in 1 turn increments for elements I-IV and elements I-III while keeping the positions and electric currents constant.

2.2. System Configurations:

Each coil element was numbered from top to bottom as shown in Figure 1a and powered by a DC power supply (TT-TECHNIC, KXN-3020D) in constant current mode. I-element and IV-element in Figure 1a were connected in series to a power supply, as well as II-element and III-element to an identical power supply for crude shimming as previously explained by Mair et al. [7]. Physical parameters of coil systems including electric current, windings, coil element positions, and diameters were given in Table 1. Coil elements were constructed by hand-winding an enamel-coated copper wire with a diameter of 3 mm and length of 900 m onto custom-made aluminum spools as shown in Figure 2. The frame that holds the coils in place was constructed with 45x45mm aluminum sigma profiles. The constructed 4-coil element Helmholtz system is shown in Figure 2.

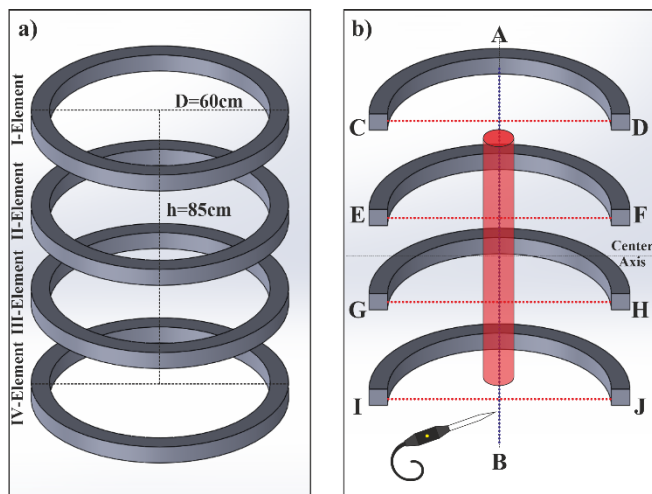


Figure 1. 3D representation (a) and measurement points (b) of the simulated and constructed system (ROI shown in red).

TABLE I
PARAMETERS OF COIL SYSTEMS

	COIL ELEMENTS	ELECTRIC CURRENTS (A)	TURNS (N)	DISTANCE	COIL DIAMETER (MM)
				FROM CENTER AXIS (MM)	
2-COIL SYSTEM	I AND II	18.3	140	260	600
3-COIL SYSTEM	I AND III	18.3	140	360	600
	II	23.6	80	0	600
4-COIL SYSTEM	I AND IV	18.3	140	425	600
	II AND III	19.5	80	127	600



Figure 2. Constructed system: (a) I-element, (b) II-element, (c) III-element, (d) IV-element, and (e) power supplies.

2.3. Magnetic Field Measurements

The generated magnetic field along the coil axis and radii were measured horizontally and vertically between points A-B, C-D, E-F, G-H, I-J using a gaussmeter probe with a step size of 10mm as shown in Figure 1b. The gaussmeter probe (PCE-MFM 3000) was capable of measuring magnetic field strength values up to 300mT with a resolution of 0.025mT. For validating the simulation results and model, the correlation between the measured magnetic field strength and simulation results were compared using Pearson's correlation, including the p-values.

To investigate the linearity between applied electric current and produced magnetic field, the 4-coil system was driven by varying electric current values from 1A to 19A while keeping the ratio of electric currents between the power sources constant.

3. RESULTS

For optimization of the number of windings, the simulated magnetic field homogeneity concerning coil elements I-IV and II-III are shown in Figure 3. The values of 140 turns for I- and IV-elements and 80 turns for II- and III-elements, which are shown in Figure 3 provided the most homogeneous magnetic field distribution. More turns would increase the resistance value of the coils, which in turn increases the value of the required voltage for supplying desired electric currents. The constructed I-IV-elements had approximately 1.39Ω resistance in series and II- III-elements had approximately 0.78Ω

resistance in series at room temperature. This resistance resulted in a temperature increase of 58.9°C in I- and IV-elements and 50.1°C in II and III elements which did not affect the constant current mode performance of the power supplies.

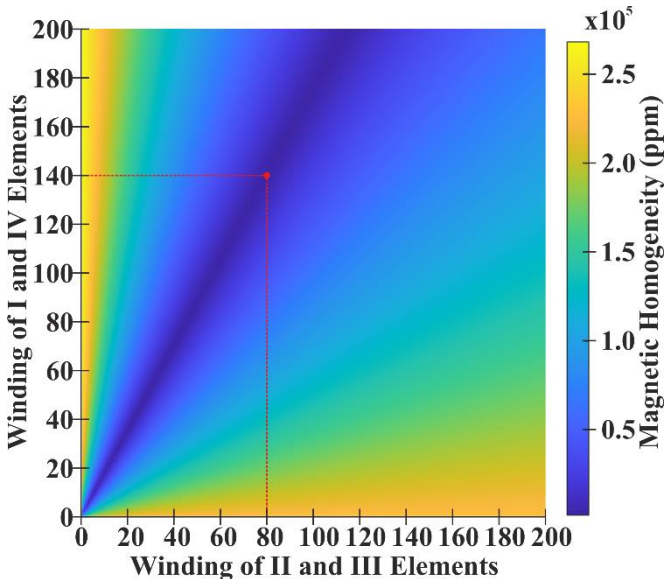


Figure 3. Magnetic field homogeneity values (in ppm) depending on winding numbers of elements are shown.

The linearity of the produced magnetic field strength with the applied current is shown in Figure 4.

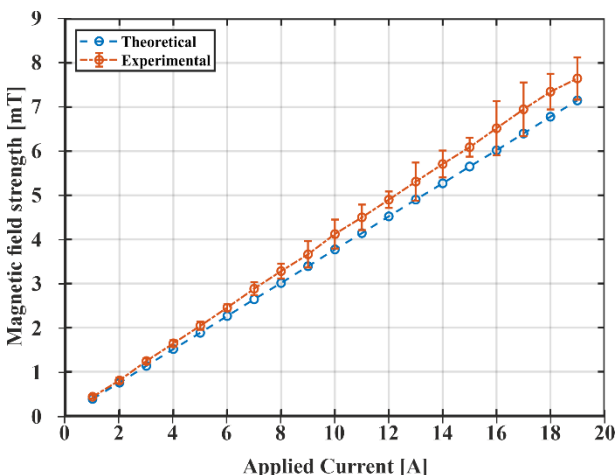


Figure 4. Simulated (blue) and measured (orange) magnetic field values at the center of the 4-coil system as a function of electric current.

The simulated magnetic field cross-sections are shown in Figure 5 for the 2-coil, 3-coil, and 4-coil Helmholtz systems with the simulation parameters that are given in Table 1. The simulated magnetic fields within the ROI were summarized in Table 2. The standard deviation was lowest for the 4-coil system, suggesting that the produced magnetic field was more homogeneous than other coil setups. In a closer inspection, the generated magnetic field was very homogenous over the ROI with the magnetic field variations of less than 1%.

Figure 6.a shows the simulated and measured magnetic field vertically from point A to B in Figure 2.b. Particularly, the magnetic field variations were less than 0.056mT at ROI between points -350mm and +350mm showing that the system produces a very uniform magnetic field. The simulated line profile of the magnetic field from A to B (Figure 6a) was also compared to the experimental measurements. The measured

magnetic field strength values were slightly greater than the simulated values of 5.6% suggesting a reasonable agreement between the simulated and measured magnetic fields.

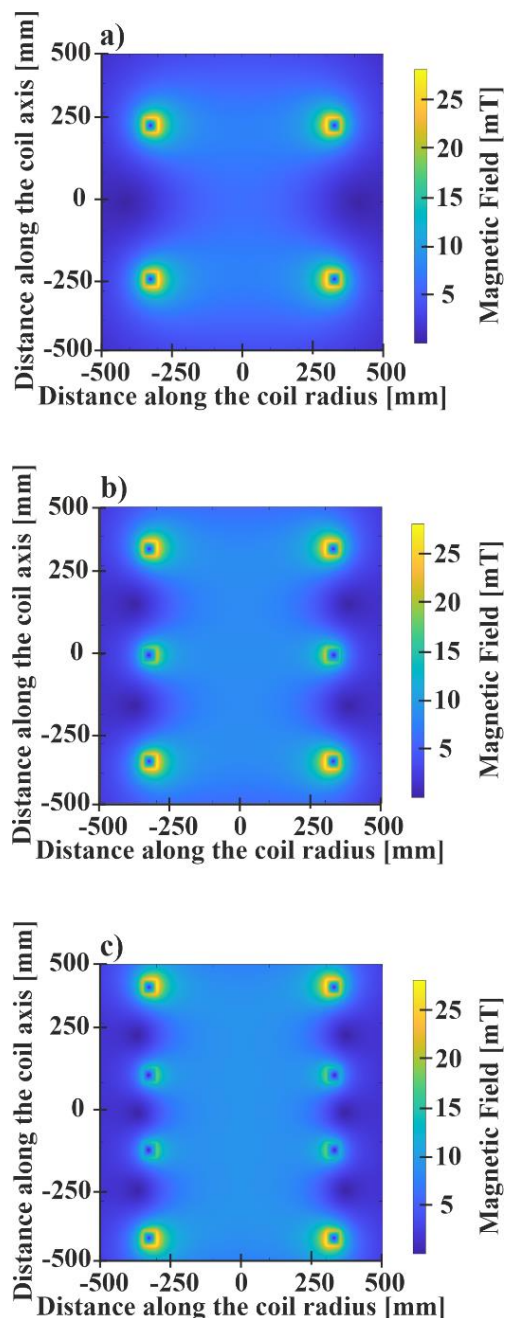


Figure 5. Theoretical calculation of magnetic field strength (in mT) for 2-coil (a), 3-coil (b), and 4-coil (c).

TABLE II
MAGNETIC FIELD STRENGTH VALUES GENERATED BY COIL SYSTEMS FROM A TO B WITHIN THE ROI

	HELMHOLTZ SYSTEMS	MEAN MAGNETIC FIELD STRENGTH (MT)	STANDARD DEVIATION (MT)	STANDARD DEVIATION (PPM)
SIMULATION	2-COIL	5.2818	0.3430	64932
	3-COIL	6.5218	0.0617	9465
	4-COIL	7.1045	0.0099	1395
EXPERIMENT	4-COIL	7.5047	0.0562	7485

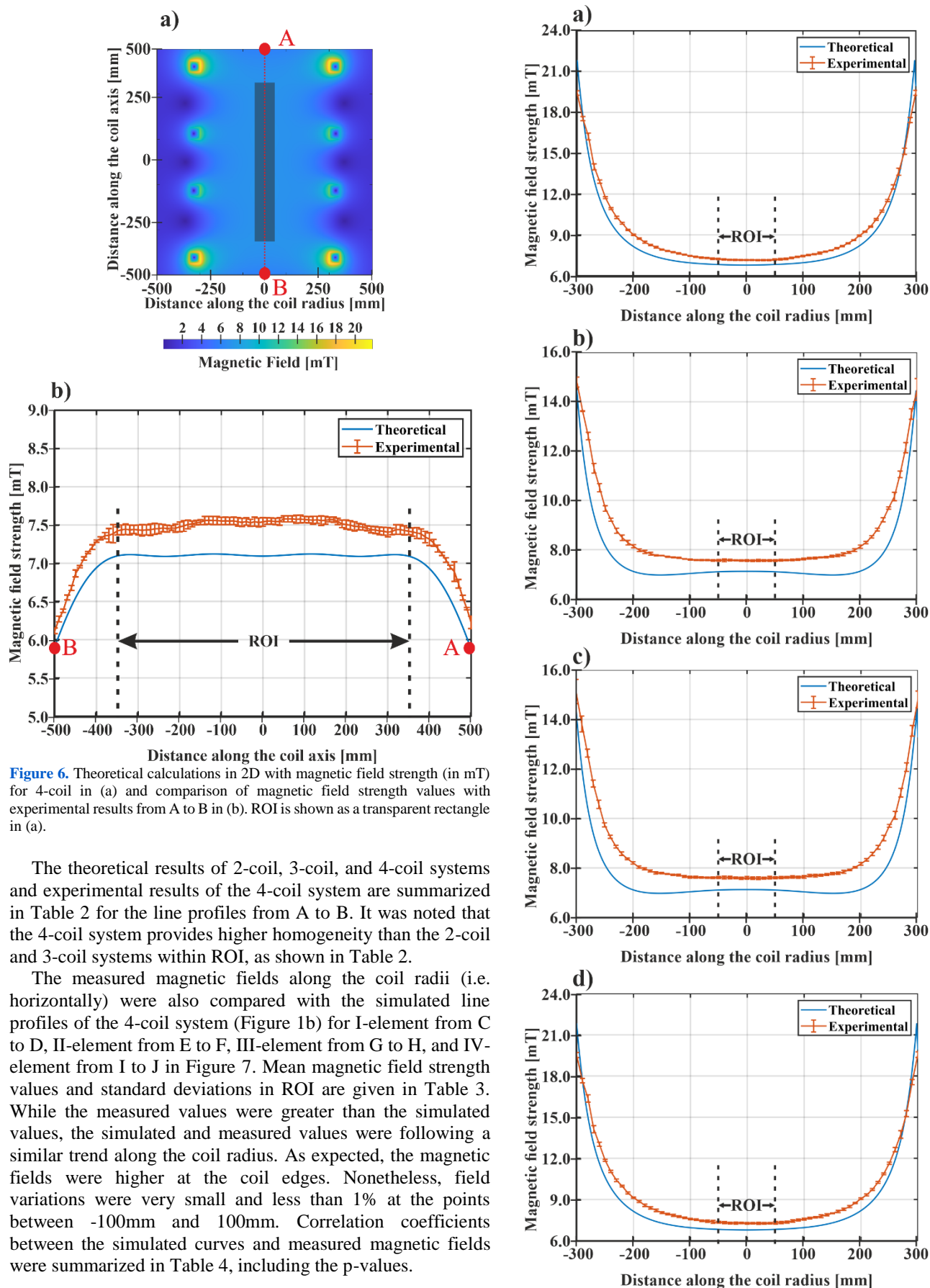


TABLE III

MAGNETIC FIELD STRENGTH VALUES OF RADII GENERATED BY COIL SYSTEMS WITHIN THE ROI

	MEAN MAGNETIC FIELD STRENGTH (MT)	STANDARD DEVIATION (MT)	STANDARD DEVIATION (PPM)
C-D (I-ELEMENT)	7.1722	0.3520	4907
E-F (II-ELEMENT)	7.5616	0.0592	783
G-H (III-ELEMENT)	7.5946	0.1214	1598
I-J (IV-ELEMENT)	7.2909	0.3802	5215

TABLE IV

CORRELATION COEFFICIENTS BETWEEN SIMULATED AND MEASURED VALUES

	CORRELATION	P-VALUE
A-B	0.9824	<0.001
C-D (I-ELEMENT)	0.9922	<0.001
E-F (II-ELEMENT)	0.9783	<0.001
G-H (III-ELEMENT)	0.9810	<0.001
I-J (IV-ELEMENT)	0.9923	<0.001

4. DISCUSSION

A Helmholtz coil pair system forming of 4 coil elements was designed and optimized for the production of a uniform magnetic field that is potentially suitable for a low-field MRI or SEOP system. The coil windings, number of elements, and electric current were simulated to optimize the design and construction. Using an inexpensive copper wire and power supplies, the designed system generated a magnetic field of 7.5mT with a field homogeneity less than 1% over a selected ROI that was covered 700mm vertically and 90mm horizontally. Although the horizontal homogeneity analysis was performed over a length of 90mm, it can be extended up to 200mm depending on the application.

The proposed system generated a magnetic field strength and uniformity that was comparable to the Helmholtz coil system reported by Mair et al. that could generate a field strength of 3.8mT and a field uniformity of 1000ppm. However, the proposed 4-coil setup benefits a smaller coil diameter (i.e. diameter of 600mm) compared to the system designed by Mair et al. (i.e. diameter of 2000mm) [7].

Although an electric current of 19.5A was used in this study due to the limiting power of the DC supply, the magnetic field strength greater than 7.5mT can be achieved with more powerful DC supplies. Using the aluminum frames with the proposed design would benefit from the heat dissipation for the use of larger electric currents. Considering the resistive heating, our system was stable at 58.9°C without using any additional chiller system. Potentially for doubling the produced magnetic field strength, the copper wire used in this system can handle an electric current of up to 40A using a chiller system.

The difference of ~5.6% in magnetic field strength between experimental and theoretical values may originate from the sensitivity of the gaussmeter or the amplifying effect of the coil spools/surrounding ferromagnetic materials, which are in

agreement with the similar results in the literature [30, 31], showing the experimental magnetic field strength measurements can be higher than the simulated magnetic field. Although the difference was 5.6% in the amplitude, the Pearson's correlation of line profiles was above 0.98 with $p < 0.001$ suggesting a statistically reasonable correlation. Despite the understanding of the variations in the amplitude requires more work, the proposed simulations were sufficient for the optimization of homogeneity and field strength.

As an alternative to high-field MRI, novel developed techniques have demonstrated the feasibility of low-field MRI with reasonable image quality. Particularly hyperpolarized ^{129}Xe gas renewed the interest in open-access low-field MRI systems with a magnetic field strength in the order of a few mT [7]. While the image artifacts originating from magnetic field inhomogeneity were still a problem, the development of more homogeneous magnetic field systems is expected to address image artifact-related problems [32]. The low cost of installation and maintenance of low-field MRI systems further validates the use of this imaging technique as an alternative to high-field MRI. The proposed 4-coil system would be suitable for the use of SEOP and/or small animal low-field MR imaging systems. In the future, we will discuss the use of the proposed systems for low-field MR imaging applications and polarization of ^{129}Xe gas for SEOP systems using a more powerful current supply including a power amplifier and a chiller system.

5. CONCLUSION

This study involved the simulation and optimization of 4-coil resistive electromagnet and construction to create a homogeneous magnetic field over a selected ROI. The system was constructed using a total copper wire length of 900m. The required electric current is supplied by a standard low-power DC supply.

The proposed system provided a homogeneous magnetic field strength of 7.5mT with experimental variations of approximately 0.75% within an ROI of 700mm to 90mm. The maximum resulting resistive heating was found to be 58.9°C for an electric current of 19.5A without using a chiller system.

ACKNOWLEDGEMENT

This work was supported by the Scientific and Technological Research Council of Turkey (TÜBİTAK), Grant No: 118C189.

REFERENCES

- [1] J. Hatta, M. Miyamoto, Y. Adachi, J. Kawai, G. Uehara, & H. Kado. "SQUID-Based Low Field MRI System for Small Animals". Ieee Transactions on Applied Superconductivity, 21(3), 526-529, 2011.
- [2] A.E. Campbell-Washburn, R. Ramasawmy, M.C. Restivo, I. Bhattacharya, B. Basar, D.A. Herzka, M.S. Hansen, T. Rogers, W.P. Bandettini, D.R. McGuirt, C. Mancini, D. Grodzki, R. Schneider, W. Majeed, H. Bhat, H. Xue, J. Moss, A.A. Malayeri, E.C. Jones, A.P. Koretsky, P. Kellman, M.Y. Chen, R.J. Lederman, & R.S. Balaban. "Opportunities in Interventional and Diagnostic Imaging by Using High-Performance Low-Field-Strength MRI". Radiology, 293(2), 384-393, 2019.
- [3] T. Tavernier, & A. Cotten. "High- versus low-field MR imaging". Radiol Clin North Am, 43(4), 673-81, viii, 2005.
- [4] W. Dominguez-Viqueira, J. Parra-Robles, M. Fox, W.B. Handler, B.A. Chronik, & G.E. Santyr. "A variable field strength system for

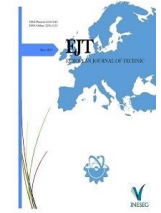
- hyperpolarized noble gas MR imaging of rodent lungs". Concepts in Magnetic Resonance Part B-Magnetic Resonance Engineering, 33b(2), 124-137, 2008.
- [5] G.P. Wong, C.H. Tseng, V.R. Pomeroy, R.W. Mair, D.P. Hinton, D. Hoffmann, R.E. Stoner, F.W. Hersman, D.G. Cory, & R.L. Walsworth. "A system for low field imaging of laser-polarized noble gas". Journal of Magnetic Resonance, 141(2), 217-227, 1999.
- [6] C.H. Tseng, G.P. Wong, V.R. Pomeroy, R.W. Mair, D.P. Hinton, D. Hoffmann, R.E. Stoner, F.W. Hersman, D.G. Cory, & R.L. Walsworth. "Low-field MRI of laser polarized noble gas". Physical Review Letters, 81(17), 3785-3788, 1998.
- [7] R.W. Mair, M.I. Hrovat, S. Patz, M.S. Rosen, I.C. Ruset, G.P. Topulos, L.L. Tsai, J.P. Butler, F.W. Hersman, & R.L. Walsworth. "He-3 lung imaging in an open access, very-low-field human magnetic resonance imaging system". Magnetic Resonance in Medicine, 53(4), 745-749, 2005.
- [8] A.M. Coffey, K.V. Kovtunov, D.A. Barskiy, I.V. Koptuyg, R.V. Shchepin, K.W. Waddell, P. He, K.A. Groome, Q.A. Best, F. Shi, B.M. Goodson, & E.Y. Chekmenev. "High-Resolution Low-Field Molecular Magnetic Resonance Imaging of Hyperpolarized Liquids". Analytical Chemistry, 86(18), 9042-9049, 2014.
- [9] O. Doganay, T.N. Matin, A. McIntyre, B. Burns, R.F. Schulte, F.V. Gleeson, & D. Bulte. "Fast dynamic ventilation MRI of hyperpolarized Xe-129 using spiral imaging". Magnetic Resonance in Medicine, 79(5), 2597-2606, 2018.
- [10] O. Doganay, T. Matin, M. Chen, M. Kim, A. McIntyre, D.R. McGowan, K.M. Bradley, T. Povey, & F.V. Gleeson. "Time-series hyperpolarized xenon-129 MRI of lobar lung ventilation of COPD in comparison to V/Q-SPECT/CT and CT". European Radiology, 29(8), 4058-4067, 2019.
- [11] Y. Zheng, G.D. Cates, W.A. Tobias, J.P. Mugler, & G.W. Miller. "Very-low-field MRI of laser polarized xenon-129". Journal of Magnetic Resonance, 249, 108-117, 2014.
- [12] S. Patz, I. Muradian, M.I. Hrovat, I.C. Ruset, G. Topulos, S.D. Covrig, E. Frederick, H. Hatabu, F.W. Hersman, & J.P. Butler. "Human pulmonary imaging and spectroscopy with hyperpolarized Xe-129 at 0.2T". Academic Radiology, 15(6), 713-727, 2008.
- [13] I.C. Ruset, L.L. Tsai, R.W. Mair, S. Patz, M.I. Hrovat, M.S. Rosen, I. Muradian, J. Ng, G.P. Topulos, J.P. Butler, R.L. Walsworth, & F.W. Hersman. "A system for open-access He-3 human lung imaging at very low field". Concepts in Magnetic Resonance Part B-Magnetic Resonance Engineering, 29b(4), 210-221, 2006.
- [14] A.M. Coffey, M.A. Feldman, R.V. Shchepin, D.A. Barskiy, M.L. Truong, W. Pham, & E.Y. Chekmenev. "High-resolution hyperpolarized in vivo metabolic C-13 spectroscopy at low magnetic field (48.7 mT) following murine tail-vein injection". Journal of Magnetic Resonance, 281, 246-252, 2017.
- [15] G. Norquay, G.J. Collier, M. Rao, N.J. Stewart, & J.M. Wild. "Xe-129-Rb Spin-Exchange Optical Pumping with High Photon Efficiency". Physical Review Letters, 121(15), 2018.
- [16] B. Driehuys, J. Pollaro, & G.P. Cofer. "In vivo MRI using real-time production of hyperpolarized Xe-129". Magnetic Resonance in Medicine, 60(1), 14-20, 2008.
- [17] P. Nikolaou, A.M. Coffey, L.L. Walkup, B.M. Gust, C.D. LaPierre, E. Koehnemann, M.J. Barlow, M.S. Rosen, B.M. Goodson, & E.Y. Chekmenev. "A 3D-Printed High Power Nuclear Spin Polarizer". Journal of the American Chemical Society, 136(4), 1636-1642, 2014.
- [18] F.W. Hersman, I.C. Ruset, S. Ketel, I. Muradian, S.D. Covrig, J. Distelbrink, W. Porter, D. Watt, J. Ketel, J. Brackett, A. Hope, & S. Patz. "Large production system for hyperpolarized Xe-129 for human lung imaging studies". Academic Radiology, 15(6), 683-692, 2008.
- [19] C.Z. Cooley, J.P. Stockmann, B.D. Armstrong, M. Sarracanie, M.H. Lev, M.S. Rosen, & L.L. Wald. "Two-Dimensional Imaging in a Lightweight Portable MRI Scanner without Gradient Coils". Magnetic Resonance in Medicine, 73(2), 872-883, 2015.
- [20] P.C. McDaniel, C.Z. Cooley, J.P. Stockmann, & L.L. Wald. "The MR Cap: A single-sided MRI system designed for potential point-of-care limited field-of-view brain imaging". Magn Reson Med, 82(5), 1946-1960, 2019.
- [21] T. O'Reilly, W.M. Teeuwisse, D. de Gans, K. Koolstra, & A.G. Webb. "In vivo 3D brain and extremity MRI at 50 mT using a permanent magnet Halbach array". Magn Reson Med, 85(1), 495-505, 2021.
- [22] O. Doganay, M. Chen, T. Matin, M. Rigolli, J.A. Phillips, A. McIntyre, & F.V. Gleeson. "Magnetic resonance imaging of the time course of hyperpolarized Xe-129 gas exchange in the human lungs and heart". European Radiology, 29(5), 2283-2292, 2019.
- [23] P. Judeinstein, F. Ferdeghini, R. Oliveira-Silva, J.M. Zanotti, & D. Sakellariou. "Low-field single-sided NMR for one-shot 1D-mapping: Application to membranes". J Magn Reson, 277, 25-29, 2017.
- [24] M.C. Tourell, T.S. Ali, H.J. Hugo, C. Pyke, S. Yang, T. Lloyd, E.W. Thompson, & K.I. Momot. "T(1)-based sensing of mammographic density using single-sided portable NMR". Magn Reson Med, 80(3), 1243-1251, 2018.
- [25] D. Izi. "Feasibility of Gold based Hall Devices for Biosensing Purposes". European Journal of Technique, 36-49, 2020.
- [26] M. Adil, & Z. Rakisheva. "Design and Simulation of Uniform Magnetic Field". Balkan Journal of Electrical and Computer Engineering, 6(4), 22-26, 2018.
- [27] D. İzi. "Constructing an Electronic Circuitry for Label-free Hall Biosensors". Balkan Journal of Electrical and Computer Engineering, 366-372, 2019.
- [28] R.A. Schill. "General relation for the vector magnetic field of a circular current loop: A closer look". Ieee Transactions on Magnetics, 39(2), 961-967, 2003.
- [29] J.E. García-Farieta, & A.H. Márquez. "Exploring the magnetic field of Helmholtz and Maxwell coils: a computer-based approach exploiting the superposition principle". Revista Brasileira de Ensino de Física, 42, 2020.
- [30] A.F. Restrepo, E. Franco, H. Cadavid, & C.R. Pinedo. "A comparative study of the magnetic field homogeneity for circular, square and equilateral triangular Helmholtz coils". 2017 International Conference on Electrical, Electronics, Communication, Computer, and Optimization Techniques (Iceccot), 13-20, 2017.
- [31] S.R. Gyawali, & N.E. Islam, "Design and construction of helmholtz coil for biomagnetic studies on soybean.", University of Missouri-Columbia, Columbia, Mo., 2008.
- [32] M. Mullen, & M. Garwood. "Contemporary approaches to high-field magnetic resonance imaging with large field inhomogeneity". Prog Nucl Magn Reson Spectrosc, 120-121, 95-108, 2020.

BIOGRAPHIES

Yenal Gökpek obtained his BSc. degree in the physics department from Ege University in 2014. He received his MSc in mathematical physics from the same university in 2017. He is currently enrolled in the Ph.D. program of Fundamental Oncology Department of the Institute of Health Sciences at Ege University. His research interests are hyperpolarized Xenon-129, finite element analysis, magnetic field coils, RF coils, NMR, MRI, and their medical applications.

Özgün Boray Yurdakoş obtained his BSc. degree in the electrical engineering department from Dumlupınar University in 2012. He received his MSc in nanotechnology in 2016 and his second MSc in electrical engineering in 2019 from Dokuz Eylül University. He is currently enrolled in the Ph.D. program of Fundamental Oncology Department of the Institute of Health Sciences at Ege University. His research interests are medical image analysis, MR sequence design, multi-dimensional signal processing, and segmentation methods for medical images.

Özkan Doğanay received his BSc. degree in Physics at Ege University in 2007. He completed his MSc in the Department of Biomedical Physics at Ryerson University in 2007 and his Ph.D. in the Department of Medical Biophysics from the University of Western Ontario in 2015, where he earned a national cancer-research-training award (CIHR in CaRTT). He went on to work as a post-doctoral researcher in the Department of Oncology at the University of Oxford in 2015. His research interests are developing functional imaging techniques for early detection and quantification of lung diseases, the development of specialized magnetic resonance imaging (MRI) methods for detection of functional (i.e. gas exchange) abnormalities in lungs associated with thoracic radiation treatment of cancer, and lung ventilation disorders including Chronic Obstructive Pulmonary Diseases (COPD) and asthma. He is currently an Assistant Prof at Ege University in the Institute of Health Sciences. He builds a new laboratory, named Functional Lung Imaging laboratories at Ege University Hospital Respiratory Diseases Center (EGE-SAM) and develops novel hyperpolarized Xenon-129 MR imaging techniques.



Comparative Analysis of Six Phase Induction Motor

Ismail Sarigül^{1*}, Mehmet Özdemir²

¹Inonu University, Electrical and Electronics Engineering Department, Malatya, Turkey. (e-mail: ismail.sarigul@inonu.edu.tr).

²Firat University, Electrical and Electronics Engineering Department, Elazığ, Turkey. (e-mail: mozdemir@firat.edu.tr).

ARTICLE INFO

Received: Oct., 15. 2020

Revised: May, 21. 2021

Accepted: Aug., 10. 2021

Keywords:

Induction motor

Six phase

d-q model

Simulation

Three phase

Corresponding author: *Ismail Sarigül*

ISSN: 2536-5010 / e-ISSN: 2536-5134

DOI: <https://doi.org/10.36222/ejt.811334>

ABSTRACT

In recent years, AC induction motors have replaced DC motor. The most important reason for this is that DC motors have a mechanical brush and commutator system that is subject to wear and tear over time. While DC motor drivers need a lot of maintenance due to this system, induction motors do not require almost any maintenance since this system is not available. In recent years, technological advances in the field of multiphase induction motors have led to a significant evolution. A lot of research has been done around the world and a lot of new and interesting developments have been reported to the literature.

This paper provides information about six-phase induction. In addition, what kind of advantages the concept of multiphase provides and how this structure is formed contains information about them. The six-phase induction motor will be simulated through the MATLAB/SIMULINK package program and compare with three-phase induction motor. Both motors were run in simulation using the same parameters. At the end of the simulation, current, moment and speed graphs of the six-phase induction motor and three-phase induction motor will be drawn according to time. The study also included equations used during modeling and equivalent circuits belonging to a six-phase induction motor. It has been graphically shown that a six-phase induction motor is more advantageous than a three-phase motor. For example, in six-phase induction motors, the transition time to a continuous state is shorter. In addition, while the frequency of torque vibration increases, its amplitude decreases, the current value of each phase decreases, the stator copper losses are less than the three-phase induction motor. In motors, usually the power needed is divided by the number of phases. So the more phases there are, the greater the power carrying capacity. Today, multi-phase induction motor drives are used in special applications such as electric vehicles, space technology, aerospace applications, as moving power on ships, electric trains, which require high reliability and power.

1. INTRODUCTION

Due to the benefits they offer, induction motors have become a form of motor that is commonly used in today's industry. The absence of mechanical brushes and collectors is one of these benefits. As is known, DC motors include in their structures a brush and collector device. Over time, this system is prone to wear and tear. DC motors need more frequent maintenance requirements for this reason. In comparison, induction motors require almost no maintenance.

Thanks to unnecessary maintenance standards, DC motors have been replaced by induction motors. In recent years, research on induction motors has increased around the world, and an attempt has been made to look for answers to the question of how induction motors can be used even more efficiently. In induction motors, which are divided into two types according to rotor structures, squirrel cage induction motors are a type of motor that we often

encounter in factories due to their cheap and robust structure. Slip ring induction motors, which are more expensive than squirrel cage induction motors, are preferred in applications requiring high starting torque.

The voltage levels of today's induction motors differ from a few watts to high power levels such as 35 MW, from 110 V to 27 kV [1].

Induction motors, which are also produced in single-phase in small power systems, are usually produced in three-phase. In the current situation, induction motors are more commonly used in a three-phase structure, so they are known in the literature as traditional three-phase induction motors. Apart from three phase and single phase induction motors, the concept of multi-phase induction motor has taken its place in the literature in recent years. The concept of multiphase induction motor is a general name given to induction motors with more than three phases. The first official records are known by the authors as dating back to 1969, and for the first time it is suggested that multiphase

motor drives are induction motors feed five-phase voltage source inverter [2]. Generally, compared to traditional three-phase induction machines, multi phase induction machines have many advantages.

Some of these advantages are as follows;

- As the number of phases increases, the required power is divided among multiple phases, thus providing higher power carrying capacity,
- Vibration of the torque decreases
- Better as reliability
- The start or operation of the induction machine is not prevented by phase loss in the stator,
- In comparison to a three-phase machine of the same scale, the moment produced per ampere increases.
- Copper losses occurring in the stator are reduced,
- The rotor's harmonic current decreases according to the angle of placement [3].

Ships, electric or hybrid cars, aircraft, electric trains, spacecraft and systems requiring high power are the major areas of operation for multi-phase induction motors [4].

2. MODELLING OF THREE PHASE AND SIX PHASE INDUCTION MOTOR

Induction motors basically have two main components; the stator, which is stationary, and the rotor, which makes a rotational movement [5]. From these components, the task of the stator is to create a magnetic field, while the task of the rotor is to produce the force that provides movement.

It was mentioned that the concept of multiphase is used for motors whose stator has more than three phase numbers. Here, six-phase induction motor will be examined as a multi-phase induction motor. Six-phase induction motors have a double three-phase winding structure. First, one three-phase winding group is placed in the stator, and the other three phase winding groups are placed in such a way that there is a 30° electrical phase difference between the first winding group. This structure (dual 3-phase) enables better torque generation compared to traditional three-phase motors. This function makes them ideal for applications. For example, ship propulsion, spacecraft and electric vehicles requiring high current and high power [6].

Initially, it was thought that the spatial displacement between two stator phases in sequence in an m-phase symmetric induction machine was determined by the formula $\alpha=2\pi/m$. The stator windings were treated as m-phases and the windings were assumed to be sinusoidal distributed, so the higher harmonics of the magnetic force in the whole space were negligible. The number of phases (m) can be single or double.

The problem of magnetic circulating currents arose when dual three-phase windings were designed with a 60° displacement angle according to the formula. Therefore, the double three-phase windings were placed asymmetrically at an angle of 30° so that some harmonics (6n + 1) were eliminated. (n=1,3,5...) [7].

2.1. Multi-Phase Induction Motor Model

In this study, d-q transformations are used when constructing the simulink model of a six-phase induction motor.

Some assumptions are made as follows, in order to construct the model.

- The air gap between the stator and the rotor is identical, the windings of stator are distributed evenly throughout the air gap.
- Friction and wind losses are neglected in the system.
- There has been neglect of magnetic saturation and core losses [8].

Parameters of motors shows Table I.

TABLE I
PARAMETERS OF MOTORS

Parameters	Value
r_s (Ω)	1.9
r_r (Ω)	2.1
L_{ls} (H)	0.0132
L_{lr} (H)	0.0132
L_m (H)	1
L_{jm} (H)	0.011
V_n (volt)	230
f (Hz)	50
P	2
Rated Power(KW)	3
Nominal speed (rad/sn)	299.46

The simplified six-phase induction motor diagram is shown in Figure.1

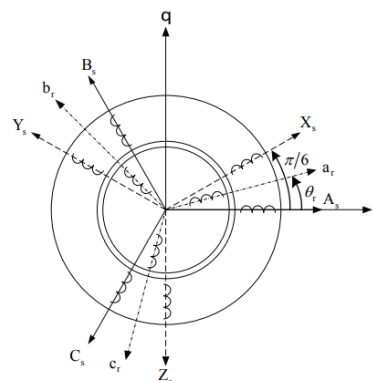


Figure 1. Simplified six-phase induction motor model

The voltage equations of six-phase induction motor are given below[9];

$$V_{qs1} = r_s \cdot i_{qs1} + \frac{d}{dt} \varphi_{qs1} + \omega \cdot \varphi_{ds1} \quad (1)$$

$$V_{ds1} = r_s \cdot i_{ds1} + \frac{d}{dt} \varphi_{ds1} - \omega \cdot \varphi_{qs1} \quad (2)$$

$$V_{qs2} = r_s \cdot i_{qs2} + \frac{d}{dt} \varphi_{qs2} + \omega \cdot \varphi_{ds2} \quad (3)$$

$$V_{ds2} = r_s \cdot i_{ds2} + \frac{d}{dt} \varphi_{ds2} - \omega \cdot \varphi_{qs2} \quad (4)$$

$$V'_{qr} = r'_r \cdot i'_{qr} + \frac{d}{dt} \varphi'_{qr} + (\omega - \omega_r) \cdot \varphi'_{dr} \quad (5)$$

$$= r'_r \cdot i'_{dr} + \frac{d}{dt} \varphi'_{dr} - (\omega - \omega_r) \cdot \varphi'_{qr} \quad (6)$$

The flux relation equations are;

$$\varphi_{qs1} = L_{ls} \cdot i_{qs1} + L_{lm}(i_{qs1} + i_{qs2}) + L_m \cdot (i_{qs1} + i_{qs2} + i'_{qr}) \quad (7)$$

$$\varphi_{ds1} = L_{ls} \cdot i_{ds1} + L_{lm}(i_{ds1} + i_{ds2}) + L_m \cdot (i_{ds1} + i_{ds2} + i'_{dr}) \quad (8)$$

$$\varphi_{qs2} = L_{ls} \cdot i_{qs2} + L_{lm}(i_{qs1} + i_{qs2}) + L_m \cdot (i_{qs1} + i_{qs2} + i'_{qr}) \quad (9)$$

$$\varphi_{ds2} = L_{ls} \cdot i_{ds2} + L_{lm}(i_{ds1} + i_{ds2}) + L_m \cdot (i_{ds1} + i_{ds2} + i'_{dr}) \quad (10)$$

$$\varphi'_{qr} = L'_{lr} \cdot i'_{qr} + L_m \cdot (i_{qs1} + i_{qs2} + i'_{qr}) \quad (11)$$

$$\varphi'_{dr} = L'_{lr} \cdot i'_{dr} + L_m \cdot (i_{ds1} + i_{ds2} + i'_{dr}) \quad (12)$$

The electromagnetic torque (Te) can be calculated from the equation below[9];

$$Te = \left(\frac{3}{2}\right) \left(\frac{P}{2}\right) \left(\frac{L_m}{L'_r}\right) [\varphi'_{dr} \cdot (i_{qs1} + i_{qs2}) - \varphi'_{qr} \cdot (i_{ds1} + i_{ds2})] \quad (13)$$

The rotor speed equation is;

$$\omega_r = \left(\frac{1}{J_r}\right) \cdot \int (T_e - T_l) dt \quad (14)$$

The six-phase induction motor model d-q was created on the reference frame. Figure.2 shows the d-axis single phase equivalent circuit and the Figure.3 shows q-axis single phase equivalent.

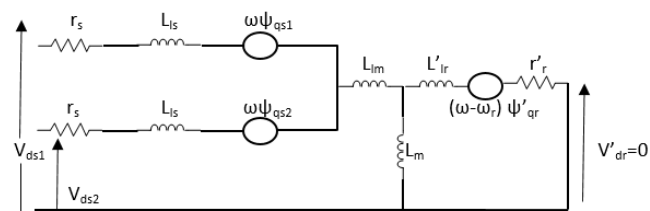


Figure 2. Single phase equivalent circuit of a dynamic d-axis six-phase induction motor

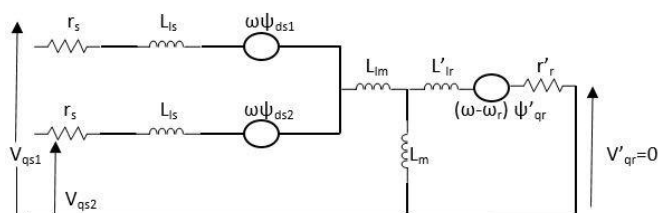


Figure 3. Single phase equivalent circuit of a dynamic q-axis six-phase induction motor

2.2. Three-Phase Induction Motor Model

In this study, d-q transformations are used when constructing the simulink model of a three-phase induction motor. The assumptions stated in the six-phase induction motor model also apply to the three-phase induction motor.

The voltage equation of the motor are mentioned below[9];

$$V_{qs} = r_s \cdot i_{qs} + \frac{d}{dt} \varphi_{qs} + \omega \cdot \varphi_{ds} \quad (15)$$

$$V_{ds} = r_s \cdot i_{ds} + \frac{d}{dt} \varphi_{ds} - \omega \cdot \varphi_{qs} \quad (16)$$

$$V'_{qr} = r'_r \cdot i'_{qr} + \frac{d}{dt} \varphi'_{qr} + (\omega - \omega_r) \cdot \varphi'_{dr} \quad (17)$$

$$V'_{dr} = r'_r \cdot i'_{dr} + \frac{d}{dt} \varphi'_{dr} - (\omega - \omega_r) \cdot \varphi'_{qr} \quad (18)$$

The flux linkage equations are as follows;

$$\varphi_{qs} = L_{ls} \cdot i_{qs} + L_m(i_{qs} + i'_{qr}) \quad (19)$$

$$\varphi_{ds} = L_{ls} \cdot i_{ds} + L_m \cdot (i_{ds} + i'_{dr}) \quad (20)$$

$$\varphi'_{qr} = L'_{lr} \cdot i'_{qr} + L_m \cdot (i_{qs} + i'_{qr}) \quad (21)$$

$$\varphi'_{dr} = L'_{lr} \cdot i'_{dr} + L_m \cdot (i_{ds} + i'_{dr}) \quad (22)$$

The electromagnetic torque (Te) can be calculated from the equation below:

$$Te = \left(\frac{3}{2}\right) \cdot \left(\frac{P}{2}\right) \cdot \left(\frac{L_m}{L'_r}\right) \cdot [\varphi'_{dr} \cdot (i_{qs}) - \varphi'_{qr} \cdot (i_{ds})] \quad (23)$$

The rotor speed equation is

$$\omega_r = \left(\frac{1}{J_r}\right) \cdot \int (T_e - T_l) dt \quad (24)$$

3. SIMULATION RESULTS

In this part of the study, the six-phase induction motor model was fed by six single-phase sources. The motor is loaded for certain periods of time and its results are graphically shown. Simulink model of six-phase induction motor is shown in Figure.4. After the first run, a three-phase induction motor with three-phase same parameters was started. Simulink model and graphics of three phase induction motor are also presented.

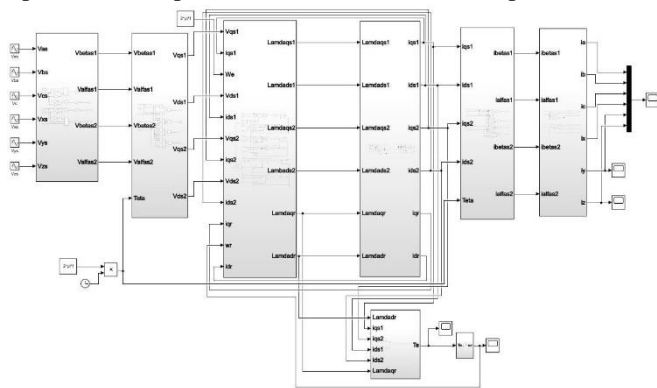


Figure 4. Simulink model of six-phase induction motor

The induction motor was operated without load for 0-2 seconds, with load moment of 5 N.m between 2-4 seconds and with load moment of 10 N.m between 4-6 seconds. Figure-5 shows six phase current graphs taken at the output of a six-phase induction motor.

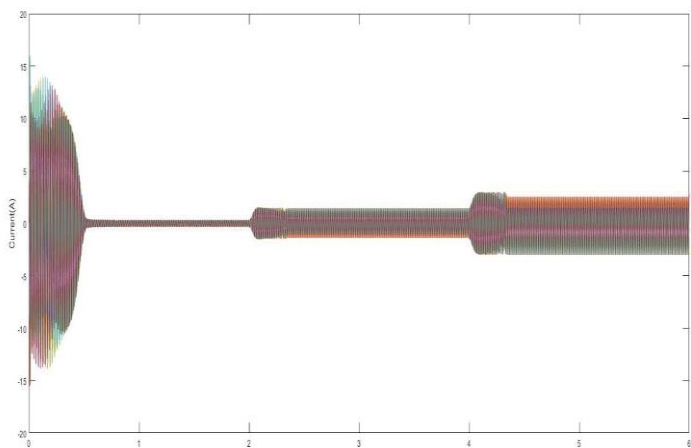


Figure 5. Currents of six-phase induction motor

Figure-6 shows speed response and Figure-7 shows electromagnetic torque response of six phase induction motor.

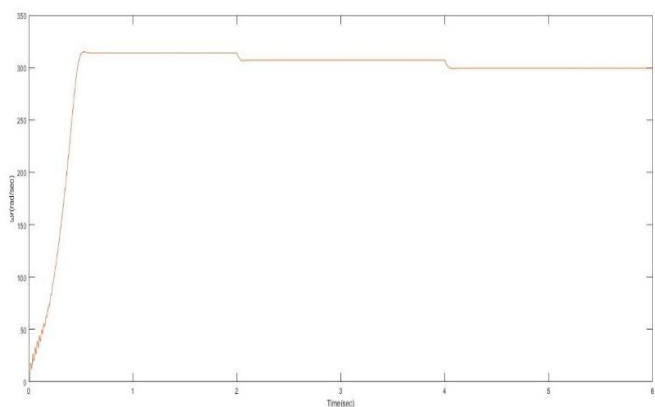


Figure 6. Speed response of six-phase induction motor

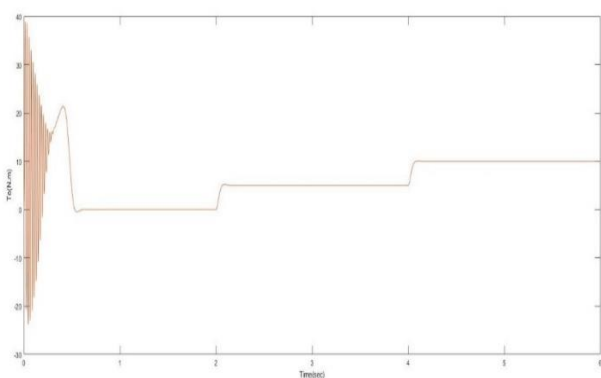


Figure 7. Electromagnetic torque response of six phase induction motor

Similarly, a three-phase induction motor with the same parameters was started and the following results were obtained. Simulink model of three-phase induction motor is shown in Figure.8.

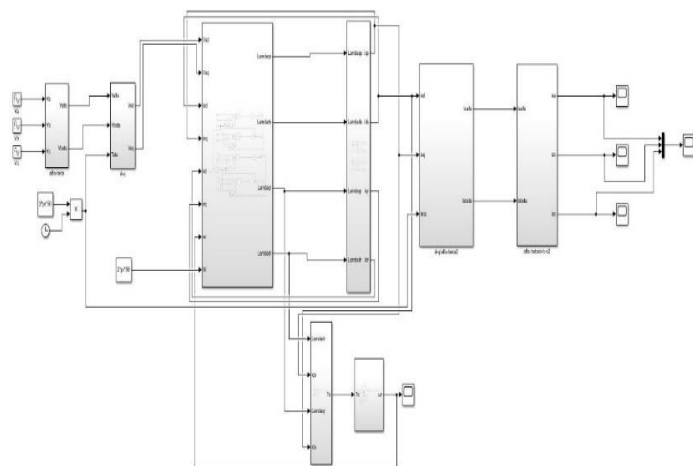


Figure 8. Simulink model of three-phase induction motor

Figure-9 shows three phase current graphs taken at the output of a three-phase induction motor.

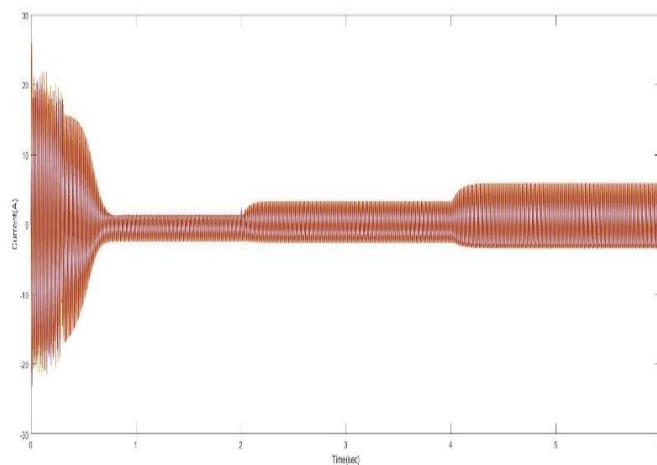


Figure 9. Currents of three-phase induction motor

Figure-10 shows speed response and Figure-11 shows electromagnetic torque response of three phase induction motor.

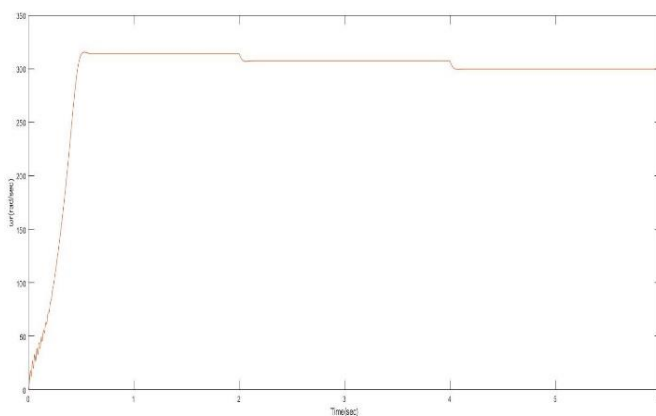


Figure 10. Speed response of three-phase induction motor

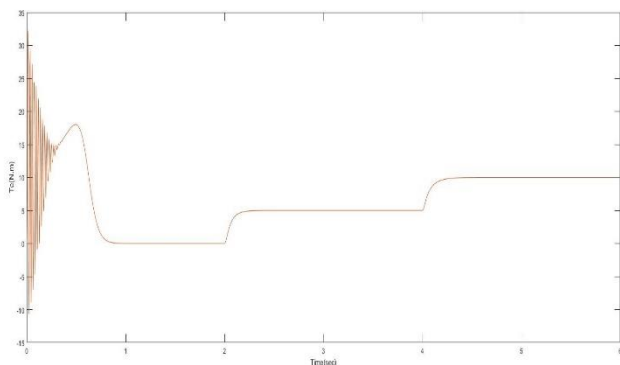


Figure 11. Electromagnetic torque response of three-phase induction motor

Some values for the results are given in Table II.

TABLE II
COMPARISON OF PERFORMANCE OF SPIM AND TPIM UNDER SAME CONDITIONS

Parameters	SPIM	TPIM
No-load current (A)	0.605	1.441
5-Nm load current(A)	1.515	3.468
10-Nm(nominal) load current(A)	3.03	6.375
Settling time (sec)	0.552	0.882
Stator copper loss for nominal-load (W)	104.66	231.65

4. CONCLUSION

As induction motors are commonly used, it is noted that studies of induction motor control are also widely used. The multi (six) phase induction motor structure, which is more advantageous than the traditional three-phase induction motor, has become a subject that is widely used in other countries and many studies have been made. With the development of power electronics, inverters have become more useful and this has facilitated the control of multi-phase induction motors.

In this study, the multi-phase induction motor model was operated using six single-phase sources in MATLAB/Simulink. Then the three-phase induction motor is modeled in the same package program. The same parameters are used for both induction motors during the simulation. In the literature, the same parameters were used for both motor in comparison studies. But even if they have the same parameters, it seems to be more advantageous because there are two groups of three-phase windings in a six-phase induction motor.

According to the simulation results, six-phase induction motor is more advantageous than the traditional three-phase induction motor.

From the result, the advantages of six phase induction motor over conventional three phase induction motor, which are given below, have been shown to deliver better performance;

- When the speed-time graph is examined, it has been observed that the speed decreases very slightly in loading situations,
- According to the moment-time graph, the six-phase induction motor has a higher starter moment than the three-phase induction motor.
- Settling time is less, which means that compared to the three-phase induction motor, its transient duration is rapidly dying-out,

- The six-phase induction motor draws a fairly low current at start time,
- The current of the six-phase induction motor is less than that of the three-phase induction motor in operating situations with a load of 5 and 10 Nm,
- Because the six-phase induction motor reaches a continuous state in less time, less copper loss occurs in the stator windings,
- Six-phase induction motors operate more efficiently because stator copper losses are less,
- Torque per ampere is increased, because its capacity for power handling is increased since the required power is split into several phases.

Multi-phase induction motors will be of great importance today, especially in electric / hybrid vehicle technology and space technology. Because in these areas, saving space (the area it occupies) and weight are among the priority issues.

With the same dimensions multi phase induction motors and three phase induction motors under the same conditions, compared to multi-phase induction motors produce more torque on them in a more advantageous position.

Some harmonics have been eliminated due to the placement of windings in the six-phase induction motor. Control of induction motors with inverters has become quite easy. In induction motor control with inverter, a much more efficient and reliable control can be realized by using modulation techniques. Especially with the space vector pulse width modulation technique, more efficient multi-phase induction motor control can be achieved by reducing harmonics.

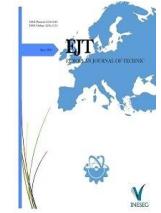
REFERENCES

- [1] Akman O. Ürkmez A., 2005, Asenkron Motor Tasarımının Bilgisayar Programı İle Gerçekleştirilmesi, Makina Tek Dergisi
- [2] Ward, E.E., and Ha'rer, H.: 'Preliminary investigation of an inverter-fed 5-phase induction motor', Proc. IEE., 1969, 116, (6), pp. 980-984
- [3] Y. Zhao, T.A. Lipo, "Space- vector PWM control of dual three phase induction machine using vector space decomposition", IEEE Trans. on Ind. Appin., Vol.31, No.5 Sept./Oct.1995,
- [4] G.K. Singh, "Multiphase induction machine drive research – a survey", Electric Power system Research, Vol.61, 2002, pp.139-147.
- [5] Saroğlu, M.K., Boğosyan, S. Ve Gökaşan, M. (2003), Asenkron Makinalar ve Kontrolü, Birsen Yayınevi, 392 s.
- [6] K. Gopalkumar, Mahopatra, "A novel scheme for six phase induction motor with open end windings." 28th Annual Conference of IEEE Industrial Electronics Society, Spain. 5th - 8 th November, 2002.
- [7] Emil Levi, "Recent Developments in High Performance VariableSpeed Multiphase Induction Motor Drives" Sixth International Symposium Nikola Tesla, Belgrade, Serbia. 18th - 20th October, 2006.
- [8] Gülez K., 1999, Asenkron Motorların DSP (Sayısal İşaret İşleyici) Tabanlı Bir Kontrol Sistemi Kullanarak YSA (Yapay Sinir Ağları) ile Performansının Artırılması, Doktora Tezi, Yıldız Teknik Üniversitesi.
- [9] Mandal Sumit, "Performance Analysis of Six-Phase Induction Motor" International Journal of Engineering Research & Technology (IJERT), Vol.4, No.02 Feb.2015.

BIOGRAPHIES

Ismail Sarigul born in 1995 in Elazig-Turkey. He received B.sc degree from Firat University. He is a M. Sc student at Firat University. He is currently Research Assistant in the Electrical and Electronic Dept. of Inonu University. His research interest areas are electrical machines, drive systems and power electronics.

Mehmet Ozdemir born in 1958 in Elazig-Turkey. Received B.Sc., M.Sc. and Ph.D degrees in Electrical Engineering from Firat University (Elazig-Turkey) in 1980, 1984 and 1993, respectively. He is currently Associate Professor in the Electrical and Electronic Dept. of Firat University. His area of interest is Electrical Machines and Drives.



Demand-Side Energy Management in Smart Buildings: A Case Study

Nazlı Hasanova^{1*} , Secil Varbak Nese² 

^{1*}Marmara University, Institute of Pure and Applied Sciences, M.Sc.Student, Istanbul, Turkey. (e-mail: nana.hesenova1998@gmail.com).

²Marmara University, Electrical Electronics Engineering Department, 34722, Kadikoy, Istanbul, Turkey (e-mail: secil.varbak@marmara.edu.tr).

ARTICLE INFO

Received: Jul., 12. 2021

Revised: Sep., 23. 2021

Accepted: Oct., 24. 2021

Keywords:

Smart buildings
Energy management system
Demand side management
Fuzzy logic controller

Corresponding author: *Nazlı Hasanova*

ISSN: 2536-5010 e-ISSN: 2536-5134

DOI: <https://doi.org/10.36222/ejt.969881>

ABSTRACT

Electrical energy is indispensable in our daily life with the developing technology. The most important feature is reliable and sustainable transmission of electrical energy to consumers is to provide the supply-demand balance in real-time. The ever-increasing demand for electrical energy, gradual depletion of traditional resources used to meet demand, and increasing dependence on foreign sources resulted in diverse electricity generation plants. As a result of this diversity, with the increase in the importance of electricity storage systems and awareness of energy-saving, Demand Side Management (DSM) gains great importance in ensuring supply-demand balance. DSM reduces costs by scheduling consumption instead of increasing generation to balance supply and demand. Residences constitute a large part of energy consumption worldwide, so DSM applications in buildings increase efficient usage of energy. Various management strategies can be used to save energy depending on the building type. In this article, an overview of Energy Management System (EMS) strategies to increase energy efficiency is presented. Then a case study is carried out in a residential model in Matlab/Simulink environment. The electrical devices were controlled with a Fuzzy Logic Controller (FLC), taking into account comfort, cost, and Demand Response (DR). In addition, Renewable Energy Resources (RES) to demonstrate their contribution were modelled and integrated into the system. Finally, case studies were conducted, and a comparative analysis of obtained results was carried out.

1. INTRODUCTION

With the increase in the world population, electrical energy consumption continues to increase continuously [1]. One of the main problems that may be encountered in the near future is increasing power demand. By 2028, electricity demand will increase by 19%, while existing infrastructure efficiencies could only increase by 6%, is estimated [2]. Effective and efficient energy usage becomes essential due to technological developments, population growth, and increasing concern about the depletion of fossil fuels [3]. With the growing urbanization in recent years, the rising number of buildings causes an increase in energy consumption [4]. In worldwide, energy used in buildings can be 45% -50% of total energy consumption in countries [5]. Especially in energy crises and environmental pollution, energy-saving and efficiency in buildings are essential [6]. These reasons encourage building and business owners to use new technologies to reduce energy consumption and environmental pollution [2]. The reason for emergence and interest in term Smart Building (SB) is that it includes systems that provide energy efficiency and consumer comfort [7].

The most important unit of SB systems is Building Energy Management System (BEMS), which is applied to manage energy effectively [8, 9]. This technology manages and controls energy flow in building through different types of information to ensure operational safety, reliability, and economy by automating DR approaches [4]. Research on comfort and energy management in buildings has gained considerable momentum in the last decade [10].

This study aims to examine the energy management strategies and techniques in buildings in the literature, model and control basic electrical appliances, and address the management of energy consumption in buildings. An FLC has been implemented to control the usage of loads with a demand-side strategy that considers both total building energy consumption and comfort conditions. With DSM, both cost and energy consumption were saved by shifting load demand during hours when consumption is intense, and unit price of electricity is high compared to the tariff, to lower and off-peak hours or the hours of RES generation.

In this study, firstly, SB concept was examined, and studies on BEMS to increase energy efficiency in buildings

were investigated in detail. Then, a residential model was created in Matlab/Simulink software, and case studies were carried out. Next, FLC has been designed to control electrical devices, taking into account comfort, cost, and DR. In addition, RES has been modeled and integrated into the model in case studies. Finally, a comparative analysis was carried out with all obtained results.

2. SMART BUILDING

Since the past, under the developments in all fields lies the effort of people to improve themselves and to bring their own lives to a more comfortable and comfortable level [11]. Especially after the 2nd World War, significant progress has been made in the building sector [12]. With machine power usage and Industrial Revolution, new styles and materials have emerged in construction and architecture. For the first time, these developments came together in “High-Tech” buildings in the 1970s. Also, many positive results, adverse effects such as a large amount of energy loss emerged. The first energy crisis in 1973 led people to re-examine used energy methods and created awareness about energy saving [13]. SBs, whose most important feature is to achieve high comfort with less energy, ensure sustainability by minimizing energy consumption, and prevent environmental pollution [7], first emerged in the USA in the early 1981's [13]. SBs can be defined as buildings that maximize energy efficiency without concession comfort of users, have communication systems, and contain an automatic control system developed for monitoring systems such as ventilation, heating, lighting, and security [14]. SB structure includes energy generation, storage, demand management, control, and communications controlled by BEMS [10].

Since the second half of the 21st century, developments in automation and computer fields have caused SBs to become widespread [15]. As a result, next-generation SBs must not only consider features such as weather conditions and predicted occupancy. Still, they must also be adaptable enough to maximize RES and energy storage usage, times that the unit price of electrical energy is low.

3. ENERGY MANAGEMENT STRATEGIES FOR BEMS

BEMSs are computer-based central systems that control and record all separate systems in a building, such as electrical systems, mechanical systems, elevators, air conditioning, lighting, security, monitoring, access, and emergency alarms [16, 17]. According to different advanced functions or control logic, these systems can monitor and control energy usage in industry and buildings [10]. There are two types of BEMS methods, active and passive. Passive methods are based on presenting future strategies and improving energy awareness of users to affect and reduce energy usage in buildings indirectly. Active methods are based on mix of actuators and sensors infrastructures in the building. They also aim to reduce energy waste through the control of SB actuators and devices [10]. This study examines active approaches under DSM, DR, Time of Use (TOU) tariffs according to BEMS management strategy, scheduling according to RES/battery systems, and optimization for generation uncertainties in RES.

3.1. Demand Side Management

DSM is a portfolio of measures to improve the energy system on the consumption side [18]. DSM, a function of EMS, refers to programs implemented by electrical utilities to control energy consumption in response to the changing operating conditions of the grid. The objectives of implementing a DMS plan range from reducing end-user operation costs to reducing transmission/distribution losses and carbon emissions [19]. DSM aims to educate electricity consumers to change their electricity usage patterns to reduce demand to provide continuous energy supply. DSM uses different strategies, as shown in Figure 1, especially peak demand reduction and load shifting [20].

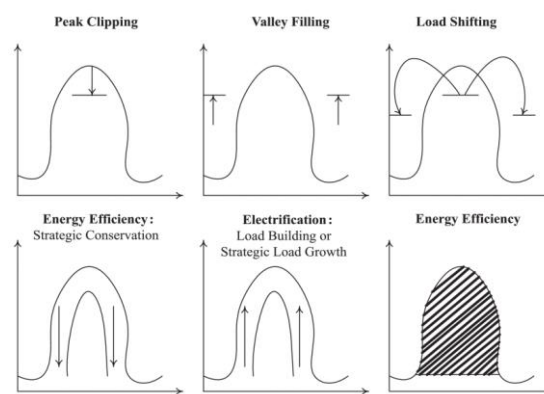


Figure 1. DSM strategies [21]

Fuzzy Logic (FL) based EMS have been developed to reduce cost, energy consumption, and Peak to Average Ratio (PAR) without sacrificing comfort and to improve further decision making regarding intelligent fault detection [22-24]. For example, an FLC has obtained savings of 15% and 18.5% in electricity costs, respectively, during peak periods by shifting loads from peak periods with high electricity prices to hours with low electricity prices, resulting in [22]. Intuitive optimization techniques with FL are used for planning controllable devices to reduce PAR in addition to cost and energy consumption [23]. Also, there are studies for the same aim [21, 25]. Based on DSM strategy, Genetic Algorithm (GA) is used to solve the scheduling and optimization problem [25], a constraint-based Multi-Objective Optimization (MOO) method is used in day-ahead scheduling, and a hybrid bacterial foraging algorithm and GA optimization technique are used to control the efficiency of the system. PAR and electricity costs reduced by 50% and 40% respectively [21], and by 22.63% and 22.77% [25].

A game theory-based strategy that takes DMS into account has also been developed [26, 27]. In another study, first household appliances modeled as controllable and uncontrollable loads then presented a scheduling framework to optimize consumption cost, user comfort, and PAR with an enhanced normalized normal constraint strategy. A significantly lower cost of 104.30 cents per day is achieved [26].

There are studies on combining supply-demand perspectives in one approach based on DSM strategy, on both time and event-based building automation, on EMS for smart homes that allow them to make changes when needed, used in smart meters or measuring devices [19, 28, 29]. An algorithmic simulation is applied to understand the power

demand in 1 hour per day [28]. Unlike other studies, an electricity meter with a data logger and logic interface is designed on the IzoT platform [29]. While [19] providing cost savings of more than 10% with their proposed strategy in experimental results, [29] stated that occupancy signals should be correlated with available power data to provide accurate information about the demand level.

3.2. Demand Side Response

DR is an electricity market mechanism where consumers can reduce consumption during energy price fluctuations or when the electricity grid reaches critical levels. Programs that allow demand change by responding to a control signal sent from network to users at times of high consumption are called DR [30]. DR-based EMSs developed to examine coordinated control of household appliances, limit the load demand at certain times of a day, schedule household appliances based on dynamic pricing signals, and learn air-conditioning weighted controllable loads [31-35]. Integrated automation of DR, Photovoltaic (PV), and ice storage are examined to achieve demand reduction targets. Experiments in office building have shown that, in addition to DR and ice storage, PV helps further to reduce demand at higher tariffs [31]. A new binary backtracking search algorithm was proposed and compared with Particle Swarm Optimization (PSO) method. The proposed controller provided energy savings of 4.87 kW on weekdays and 6.6 kW on weekend days, while energy savings of the PSO controller were 4.52 kW and 6.3 kW during DR periods, respectively [32]. An interdisciplinary approach is presented that combines machine learning, optimization, and data structure design to create a DR home EMS. In simulation results for actual weather conditions, learning-based DR and EMS were efficient among other tested DR algorithms [33].

Many studies have also been done on demand uncertainties and scheduling problems. For example, on-demand uncertainty and scheduling problems, Mixed-Integer Non-Linear Programming (MINLP) is used to solve the scheduling problem in their proposed models and [36-39]. The EMS is designed by taking into account TOU pricing together with DR [37]. In the simulation results, [37] a reduction of 29.5%-31.5%, [38] achieved reduction in energy costs as 19.5% and 25.6% (when demand elasticity exists) according to two different energy management strategies. [36] stated that proposed model not only eliminates demand-side uncertainty and reduces CO₂ emissions.

3.3. Time of Use (TOU)

General practices aim to minimize energy costs considering energy systems limitations and retail prices that change over time [40]. TOU is the abbreviation for time-of-use electricity rates. These rates are determined by local utilities and vary according to hours of the day. Electricity unit price is higher during peak demand periods and cheaper during low demand periods. There are studies on smart houses, including RES and battery systems, within the scope of different physical restrictions and TOU tariffs to minimize cost and power consumption from grid [4, 41-43]. An adaptive TOU-Model Predictive Control (MPC) management system is designed in a real-time electricity pricing environment. Energy cost optimization is realized as 49,059% of the total energy demand in low demand and 46,072% in high demand [41]. An EMS is developed based on estimations of output of PV

integrated to building, uncontrollable loads, and outdoor temperature. The operation of all components is optimized with synergistic distribution of source-load-storage area using MOO within scope of TOU price [4]. Home appliances based on the TOU pricing scheme have been efficiently planned. By using PSO, consumer's bill was reduced by more than 29%, and even in the case of only feeding on grid, the bill is reduced by 19.36% [42]. A real-time, rule-based control algorithm, taking into account TOU pricing, is proposed to avoid high peak demand. The algorithms following PV, battery, and grid reduced electricity cost significantly [43]. Also, deep neuro-fuzzy optimization by combining FL and neural networks is proposed to provide energy and cost savings using TOU tariffs [44]. The operation status of devices from total demand data of houses is determined with neuro-fuzzy and non-invasive load monitoring techniques [45].

3.4. Scheduling and Optimization

DSM also uses energy storage units to store energy during off-peak hours and discharge it during peak hours [46]. With the application of RES in modern buildings, the system becomes more complicated due to extraordinary uncertainties in electricity generation besides saving [4]. In this respect, relatively new applications for DSM help grid operators to balance intermittent generation of wind and solar units, especially with timing and sizing of energy demand [46]. In many studies, battery systems and active load control have been investigated to optimize load predictability against uncertainties in RES generation and to solve the scheduling problem [47-58]. A smart meter and smart DSM system using FL-based algorithms by addressing the uncertainties of RES is implemented and achieved 15% energy savings by providing digital communication [47]. An FL-based smart controller is developed to control charge and discharge status of the battery according to the power generation of PV and consumption status [48]. A new FL-based EMS is proposed to increase the use of RES power supply and reduce energy consumption via offload. In addition, tests are carried out using actual meteorological data from the Adrar region [49].

Studies have also been carried out on FL-based management strategies to operate power system control successfully due to the difficulty of load fluctuation [50-52]. [52] have shown in the study that FL not only provides the load, but diesel generator helps to keep battery charged only in the event of an unforeseen power outage. Intermittent and variable energy generation characteristics of RES negatively affect nominal voltage and frequency values of the system. FL-based intelligent control strategies are proposed to ensure continuity of power supply in case of grid failure for voltage and frequency regulation by [59] and improve the focusing properties of the system response to the uncertainties of RES parameters by [50]. In the simulation results, [50] reduced deviations in frequency, while [59] confirmed that they kept frequency and voltage at optimum limits and ensured their stability.

Among studies on RES generation uncertainty, estimations are modeled and solved as MILP in [54], as MINLP problems in [58]. In [55], while optimizing the cost of customer in the DR program, taking into account uncertainty in RES generation, the electricity bill is reduced up to 42% with proposed stochastic EMS model [55].

The Lyapunov optimization method depends on an online energy management algorithm based on event triggering and instant data to plan controllable loads for solving the energy scheduling problem in a house equipped with PV devices. The electricity bill is less with the proposed algorithm without compromising user's comfort [56]. On the other hand, a column and constraint generation algorithm are adopted to solve with MILP in optimization model for uncertainties and scheduling [57]. Furthermore, MILP technique is used to optimize integration of RES, storage systems, and switchable electric vehicles [60].

A risk-based decision-making framework is created for the SB EMS in case of supply and demand uncertainty in building integrated with wind power. The MILP problem is solved in modeled EMS. Using a proposed microgrid-based system, approximately 92%, 93%, and 85% savings are achieved in total cost, energy supply cost, and total emission costs, respectively, respectively [53].

The integration difficulties caused by stochastic structures of RES and battery systems are studied in [61]. The constrained optimization problem is formulated as a mathematically multiple knapsack problem and then solved using heuristic GA, binary PSO, wind-driven optimization, bacterial foraging optimization, and hybrid GA-PSO algorithms. The integration of RES and energy storage systems resulted in a 19.94% and 21.55% reduction in electricity bills and PAR. In addition, home EMS based on a hybrid algorithm outperformed other heuristic algorithms, reducing the bill by 25.12% and PAR by 24.88%.

Multi-agent systems are used for monitoring and optimal control of homes, buildings, and microgrid systems with controllable loads and RES. [62] stated that it is possible to guarantee safe and optimum system operation, especially through agent-based storage system control. Regarding scheduling, a simple estimation algorithm is presented for uncontrollable loads, using minimal data and calculations. The other motion detection or outdoor temperature sensors aren't used. The 24-hour prediction error of the algorithm is between 8.2% and 6.2% in summer months and between 11.4% and 15.9% in winter months [63]. In EMS developed in another study, PV panels, small wind turbines, batteries, and the scheduling of controllable loads were optimized with GA for minimum energy cost. With this algorithm, consumed power is reduced at discharge load from 496.5 kW to 191.5 kW while providing an average gain of 25.23% from the annual electricity bill and improving RES utilization by 61.43% [64].

Unlike other studies concept of SB cluster is proposed for operation of more than one SB in smart grid environment. The designed model has benefited more effectively from advantages of DS and RES, reducing the total electricity cost of SBs by 4.6% and providing the characteristic optimization of the load [65]. On the other hand, a two-level (local and general EMS) optimization algorithm focused on total electricity cost and thermal comfort level of multiple smart homes with distributed energy sources is proposed. The results showed that proposed distributed algorithm achieved almost the same performance as central electrical optimization algorithm [66].

An optimum switching control model is proposed under practical constraints such as electricity cost, balance of demand, and PV output under TOU program in one of the studies carried out to make adequate use of solar energy. In the results, that monthly electricity bill is decreased to about 50% [67]. In an EMS, the hybrid system within scope of TOU is modeled to minimize electricity cost while matching user demand and PV output. MPC is used which can learn environmental situations [68]. A model with FLC combined with cost-benefit analysis is created to assess the real economic benefits of load schedule. In cost-benefit analysis, economic comfort is associated with matching generation and consumption patterns for all PV system sizes [69-71]. A multi collector-based online fuzzy coordination algorithm is presented for charging electric vehicles. The results stated that such integration of transportation industry, proper use of clean energy, and reduction of load fluctuation resulted in an 87% improvement in load factor [72,73]. In [74], home EMS within the framework MILP for a joint evaluation of RES generation system, electric vehicles, and the dual use of the energy storage system and DR strategies [75]. With their proposed strategy achieved cost savings of up to 65%.

4. MODEL AND CASE STUDY

In this study, a housing model has been studied to increase energy efficiency in buildings.

In addition, electricity generation with wind and solar RES has been modeled and integrated into the system. Wind turbine and PV generations are modeled based on changes in data obtained from measurement station used for Göztepe, Istanbul, in a thesis study. The control procedure is set to improve current power profile, avoid interruption by managing device according to comfort preferences and prioritize user approval. The Simulink model of the study is shown in Figure 2 and includes five separate sections: the most commonly used devices in residences, power consumed by each device, total power cost, RES, and FLC. Output signals of devices are power consumptions and collected as input of FLC. The other inputs of FLC are time, output of clock, and generated power by RES that is output of RES model.

Typically, devices can be divided into two categories, controllable and uncontrollable devices. Controllable devices can be closed or partially used by controllers. Uncontrollable devices are passive loads that cannot be switched off or made partially. Table I shows the category and power consumption of each load.

TABLE I

LOAD CATEGORIES AND POWER CONSUMPTIONS			
Controllable loads		Uncontrollable loads	
HVAC	2500 W(winter), 1944(summer)	Washing machine	303 W
Water heater	1500 W	Dish washer	510 W
Lamp	15 W	Oven	2000 W
Refrigerator	120W	Iron	350 W
TV, PC	100 W		

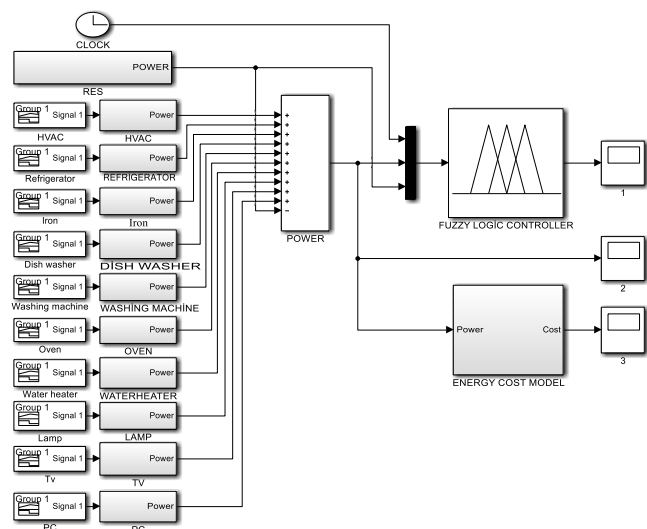


Figure 2. Simulink model of residential devices and control system [2].

4.1. Fuzzy Logic Controller

FLC is designed for scheduling power consumption. FL provides control overloads in line with priority given. Based on 3-time tariff in Turkey, FL based controller defines non-priority loads to be turned off when consumers increase their consumption during hours when there is no RES generation, and the unit price of electricity is high. In this case, the controller ensures that power supplied to high priority loads is used appropriately by suggesting that some loads are cut, encouraging them to be shifted to off-peak and RES generation hours. The controller also keeps energy consumption within a certain limit, which means that it cannot exceed limit during high consumption hours; consumer approval takes precedence.

Figure 3 shows block diagram of FLC with 75 rules, three input signals, and two output signals. The input and output signals of FLC are as follows.

“Electricity Price”: Sampled over 24 hours. It defines hours when the unit price of electricity is low or expensive.

“Power Demand”: It is the load consumption demand according to the operating times of the existing devices.

“Renewable Energy”: It is 24-hour generation of PV and wind turbine.

“Load Scheduling”: It is amount of load to be shifted in kW.

“Run Loads”: The total load in kW that controller will allow to operate in a given time.

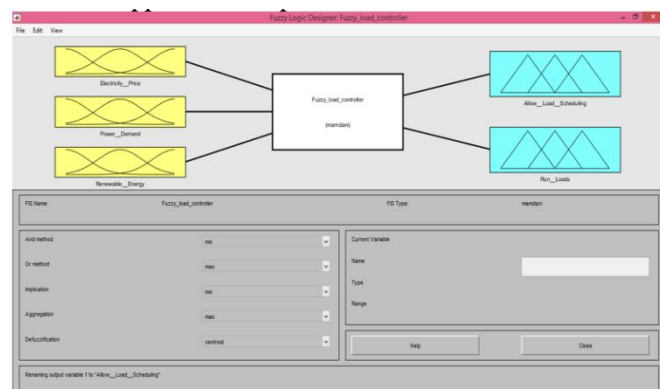


Figure 3. Block diagram of FLC.

4.2. Fuzzy Membership Functions

Among membership functions, input and output signals of FLC membership functions were selected by trial&error method. According to 3-time tariff, membership functions of “Electricity Price” input were set as “Night” when the unit price of electricity is low (22:00-06:00), “Day” when it is medium (06:00-17:00), and “Peak” when it is expensive (17:00-22:00). All input and output membership functions are shown in Figures 4, 5, 6, 7, 8.

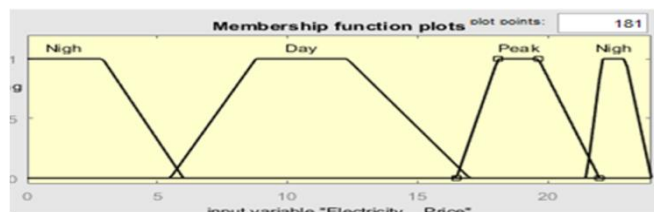


Figure 4. Fuzzy membership function of electricity price (Input 1).

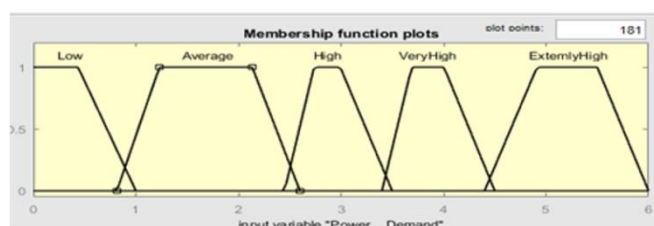


Figure 5. Fuzzy membership function of power demand (Input 2).

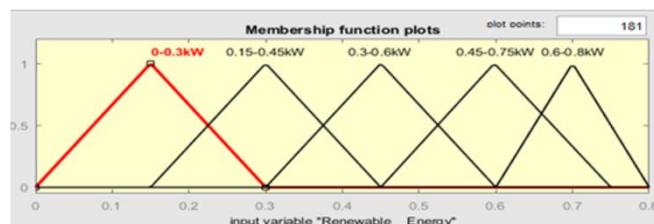


Figure 6. Fuzzy membership function of renewable energy (Input 3).

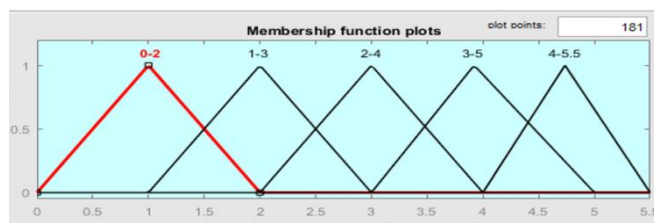


Figure 7. Fuzzy membership function of load scheduling (Output 1).

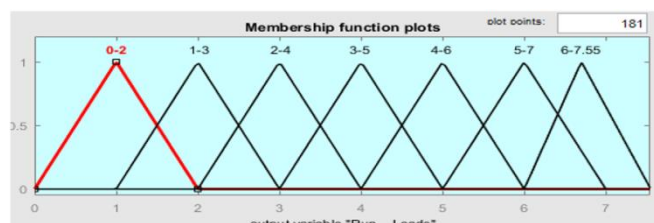


Figure 8. Fuzzy membership function of run loads (Output 2).

Depending on the number of membership functions considered in input and output blocks, 75 rules were created, considering the needs and constraints.

4.3. Case Study

In this study, energy management and efficiency in smart buildings were examined in four cases.

1. Energy consumption in uncontrolled SB,
2. Energy consumption in SB with FLC,

3. Energy consumption in uncontrolled SB with RES,

4. Energy consumption in SB with FLC and RES.

For all four cases, analyses made by considering summer and winter days and simulation results were compared.

First, the energy consumption and cost of uncontrolled building and building with FLC are compared and are shown in Figure 9 and Figure 10 for the winter and summer days, respectively

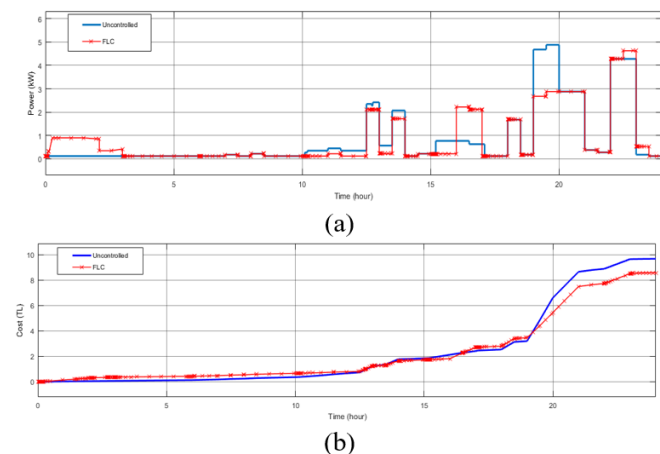


Figure 9. Comparison of power consumption (a) and cost (b) of uncontrolled building and building with FLC for a winter day.

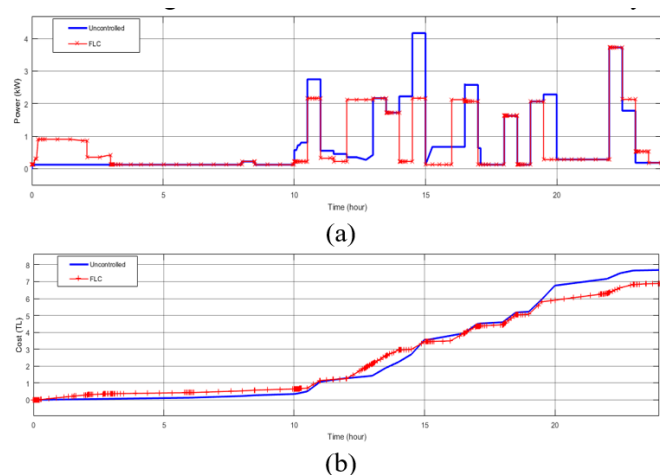


Figure 10. Comparison of power consumption (a) and cost (b) of uncontrolled building and building with FLC for a summer day.

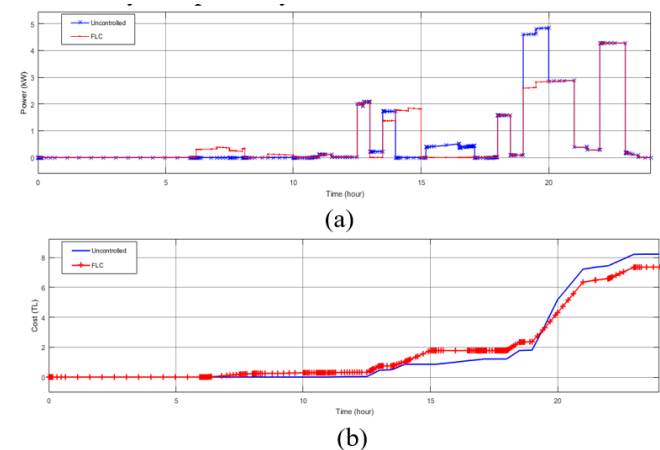


Figure 11. Comparison of power consumption (a) and cost (b) of uncontrolled buildings with RES and with RES and FLC for a winter day.

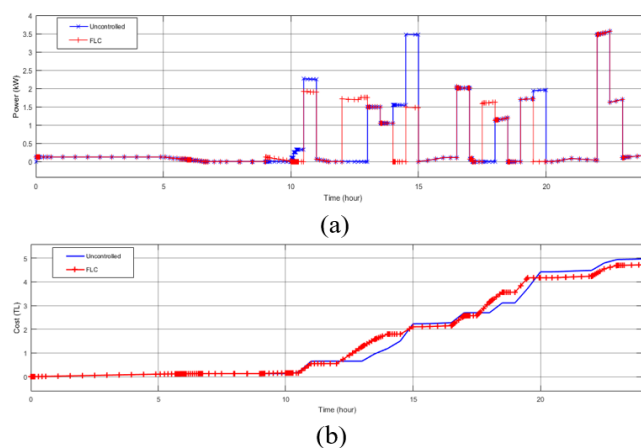


Figure 12. Comparison of power consumption (a) and cost (b) of uncontrolled buildings with RES and with RES and FLC for a summer day.

There was no change in total energy consumption for both seasons since operation of loads was shifted only in time. In addition, a daily provide saved of 1.10 TL (11.36%) in winter and 0.80 TL (10.41%) in summer in cost of building with FLC compared to cost of a building uncontrolled.

The energy consumption of uncontrolled buildings with RES and with RES and FLC are shown in Figure 11 and Figure 12 for winter and summer days, respectively.

The building with FLC and RES has been saved 0.62 kW (3.88%) and 0.86 TL (10.46%) in winter, 0.49 kW (4.05%), and 0.25 TL (5.03%) in summer, compared to an uncontrolled building with RES.

The highest total energy consumption and cost were obtained as 19.74 kW, 9.69 TL in winter, 17.88 kW, and 7.69 TL in summer, in the case that without a controller and so control is dependent on user. The lowest consumption price was 7.36 TL in winter, 4.72 TL in summer, and minimum energy consumption of 15.35 kW in winter and 11.62 kW in summer, for building with FLC and RES.

5. CONCLUSION

This study examines innovative energy management approaches based on modeling and optimization techniques, which have recently attracted attention due to increasing awareness of energy efficiency. While there is much experience in optimizing energy generation, distribution, and consumption, the demand-side has received increasing attention from academia and industry as a function of EMS.

In this study, a case study was carried out by considering need to increase energy efficiency on a residential model and taking into account comfort, cost, RES, and DR within the scope of DSM. Energy consumption and energy cost results are investigated of four SB conditions for summer and winter days. The four SB conditions are uncontrolled SB, FLC controlled SB, uncontrolled SB with RES, FLC controlled SB with RES. The building with FLC and RES has been saved 3.88% energy and 10.46% cost in winter, 4.05% energy, and 5.03% cost in summer, compared to an uncontrolled building with RES.

The best result in the case study is obtained by feeding system from RES if there is generation, limiting power consumption of some loads during peak hours if there is no renewable energy generation and shifting these loads to the RES

generation time or off-peak period. So, SB with FLC and RES makes the best use of RES and consumes the least energy from grid compared to other situations.

ACKNOWLEDGEMENT

The authors thank to Bilgin for contributing to this research by providing data collected for M. Bilgin, "Fotovoltaik Panellerin Verimine Panel Yüzey Sıcaklığı Etkisinin İncelenmesi," Master Thesis, Marmara University, Istanbul, Turkey, 2013.

REFERENCES

- [1] L. Hurtado, P. Nguyen, W. Kling, W. Zeiler, "Building energy management systems—Optimization of comfort and energy use," presented at the 48th International Universities' Power Engineering Conference, Dublin, Ireland, Sept. 2-5, 2013.
- [2] M. P. Fanti, A. M. Mangini, M. Roccotelli, "A simulation and control model for building energy management," *Control Engineering Practice*, vol. 72, pp. 192-205, 2018.
- [3] P. H. Shaikh, N. B. M. Nor, P. Nallagownden, I. Elamvazuthi, "Intelligent multi-objective optimization for building energy and comfort management," *Journal of King Saud University-Engineering Sciences*, vol. 30, no. 2, pp. 195-204, 2018.
- [4] F. Wang, L. Zhou, H. Ren, X. Liu, S. Talari, M. Shafie-khah, J. P. Catalao, "Multi-objective optimization model of source-load-storage synergetic dispatch for a building energy management system based on TOU price demand response," *IEEE Transactions on Industry Applications*, vol. 54, no. 2, pp. 1017-1028, 2017.
- [5] O. Akar, U. K.Terzi, T. Sonmezocak and B.K. Tuncalp. "Determination of the optimum Hybrid renewable power system: a case study of Istanbul Gedik University Gedik Vocational School", *Balkan journal of electrical&computer engineering*, Vol.7, No.4, pp.456-463, 2019.
- [6] U. Civan, "Akıllı binaların çevresel sürdürülebilirlik açısından değerlendirilmesi," Master Thesis, İstanbul Teknik University, İstanbul, Turkey, 2006.
- [7] F. M. Bhutta, "Application of smart energy technologies in building sector—future prospects," *IEEE International Conference on Energy Conservation and Efficiency*, Pakistan, Lahore, Nov. 22-23 2017.
- [8] A. Altayeva, B. Omarov, Y. Im Cho, "Multi-objective optimization for smart building energy and comfort management as a case study of smart city platform," presented at the 19th International Conference on High Performance Computing and Communications; IEEE 15th International Conference on Smart City; IEEE 3rd International Conference on Data Science and Systems, Bangkok, Thailand, Dec.18-20, 2017.
- [9] S. Smitha, J. Savier, F. M. Chacko, "Intelligent control system for efficient energy management in commercial buildings," *Annual International Conference on Emerging Research Areas and International Conference on Microelectronics, Communications and Renewable Energy*, Kanjirapally, India , June 4-6, 2013.
- [10] D. Mariano-Hernández, L. Hernández-Callejo, A. Zorita-Lamadrid, O. Duque-Pérez, F. S. García, "A review of strategies for building energy management system: model predictive control, demand side management, optimization, and fault detect & diagnosis," *Journal of Building Engineering*, p. 101692, 2020.
- [11] I. T. Erhan, "Akıllı binalarda aydınlatma otomasyonunun enerji verimliliğine katkısının incelenmesi," Master Thesis, İstanbul University, İstanbul, Turkey, 2018.
- [12] H. Kılıç, "Akıllı binalar, kurulumları ve işletilmeleri," Master Thesis, İstanbul Teknik University, İstanbul, Turkey, 2007.
- [13] H. M. Günaydın, and S. Zağpus. "Türkiye'de Bina Otomasyon Sistemlerinin Mimarlar Tarafından Algılanması, Akıllı Bina Tasarım Süreci ve Kalitesi". VI. Ulusal Tesisat Mühendisliği Kongresi ve Sergisi. https://www1.mmo.org.tr/resimler/dosya_ekler/28aa8ac200e659d_ek.pdf
- [14] Ö. Karadişoğulları, "Akıllı binalarda kullanılan sistemlerin sürdürülebilirlik bağlamında irdelenmesi," Master Thesis, Haliç University, İstanbul,Turkey, 2013.
- [15] Bilgi Teknolojileri ve İletişim Kurumu, "Elektronik Haberleşme Sektöründe Teknolojik Gelişmeler ve Eğilimler Raporu," Ankara, 2014.
- [16] J. Smiciklas, F. Spitzer, .A. Hay, R. Delgado, S. Kondepudi "Intelligent sustainable buildings for smart sustainable cities"," ITU-T Focus Group on Smart Sustainable Cities, Focus Group Technical Report, 2015.
- [17] D. Minoli, K. Sohrawy, B. Occhiogrosso, "IoT considerations, requirements, and architectures for smart buildings—Energy optimization and next-generation building management systems," *IEEE Internet of Things Journal*, vol. 4, no. 1, pp. 269-283, 2017.
- [18] P. Palensky, D. Dietrich, "Demand side management: Demand response, intelligent energy systems, and smart loads," *IEEE transactions on industrial informatics*, vol. 7, no. 3, pp. 381-388, 2011.
- [19] M. Batić, N. Tomašević, G. Beccuti, T. Demiray, S. Vraneš, "Combined energy hub optimisation and demand side management for buildings," *Energy and Buildings*, vol. 127, pp. 229-241, 2016.
- [20] M. Zehir, M. Bağrıyanık, "Akıllı Şebekelerde Gelişmiş Yerel Talep Yönetimi," V. Enerji verimliliği ve Kalitesi Sempozyumu, İstanbul, Turkey, pp. 14-18, 2013.
- [21] A. Khalid, N. Javaid, M. Guizani, M. Alhussein, K. Aurangzeb, and M. Ilahi, "Towards dynamic coordination among home appliances using multi-objective energy optimization for demand side management in smart buildings," *IEEE access*, vol. 6, pp. 19509-19529, 2018.
- [22] F. Alfaverh, M. Denai, Y. Sun. "Demand response strategy based on reinforcement learning and fuzzy reasoning for home energy management," *IEEE Access*, vol. 8, pp. 39310-39321, 2020.
- [23] R. Khalid, N. Javaid, M. H. Rahim, S. Aslam, A. Sher. "Fuzzy energy management controller and scheduler for smart homes," *Sustainable Computing: Informatics and Systems*, vol. 21, pp. 103-118, 2019.
- [24] V. Mpelogianni, K. Giannousakis, E. Kontouras, P. P. Groumpos, D. Tsipianitis. "Proactive Building Energy Management Methods Based On Fuzzy Logic And Expert Intelligence," *IFAC-PapersOnLine*, vol. 52, no. 25, pp. 519-522, 2019.
- [25] M. B. Rasheed, N. Javaid, M. Awais, Z. A. Khan, U. Qasim, N. Alrajeh, Q. Javaid. "Real time information based energy management using customer preferences and dynamic pricing in smart homes," *Energies*, vol. 9, no. 7, p. 542, 2016.
- [26] M. Waseem, Z. Lin, S. Liu, Z. Zhang, T. Aziz, D. Khan, "Fuzzy compromised solution-based novel home appliances scheduling and demand response with optimal dispatch of distributed energy resources," *Applied Energy*, vol. 290, p. 116761, 2021.
- [27] M. I. Ghiasi, A. Hajizadeh, M. A. Golkar, M. Marefati, "Demand and supply side management strategies for zero energy buildings," *IEEE 17th International Conference on Ubiquitous Wireless Broadband (ICUWB)*, Salamanca, Spain, Sept. 2-15, 2017.
- [28] W. Li, T. Logenthiran, W. L. Woo, V.-T. Phan, D. Srinivasan. "Implementation of demand side management of a smart home using multi-agent system," *IEEE Congress on Evolutionary Computation (CEC)*, Vancouver, BC, Canada, July 24-29, 2016.
- [29] A. Ożadowicz and J. Greła. "An event-driven building energy management system enabling active demand side management," *Second International Conference on Event-based Control, Communication, and Signal Processing*, Krakow, Poland, June 13-15, 2016.
- [30] M. M. Rahman, S. Hettiwatte, S. Gyamfi, "An intelligent approach of achieving demand response by fuzzy logic based domestic load management," *Australasian Universities Power Engineering Conference*, Perth, WA, Australia, Sept. 28, 2014.
- [31] F. Sehar, M. Pipattanasomporn, S. Rahman, "An energy management model to study energy and peak power savings from PV and storage in

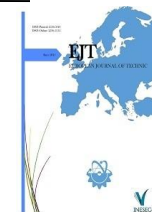
- demand responsive buildings," *Applied Energy*, vol. 173, pp. 406-417, 2016.
- [32] M. S. Ahmed, A. Mohamed, T. Khatib, H. Shareef, R. Z. Homod, J. Abd Ali, "Real time optimal schedule controller for home energy management system using new binary backtracking search algorithm," *Energy and Buildings*, vol. 138, pp. 215-227, 2017.
- [33] D. Zhang, S. Li, M. Sun, Z. O'Neill, "An optimal and learning-based demand response and home energy management system," *IEEE Transactions on Smart Grid*, vol. 7, no. 4, pp. 1790-1801, 2016.
- [34] Z. Nadeem, N. Javaid, A. W. Malik, S. Iqbal, "Scheduling appliances with GA, TLBO, FA, OSR and their hybrids using chance constrained optimization for smart homes," *Energies*, vol. 11, no. 4, p. 888, 2018.
- [35] V. Pradhan, V. M. Balijepalli, S. A. Khaparde, "An effective model for demand response management systems of residential electricity consumers," *IEEE Systems Journal*, vol. 10, no. 2, pp. 434-445, 2014.
- [36] A. Baldauf, "A smart home demand-side management system considering solar photovoltaic generation," present at the 5th International Youth Conference on Energy, Pisa ,Italy, May 27-30, 2015.
- [37] M. A. F. Ghazvini, J. Soares, O. Abrishambaf, R. Castro, Z. Vale, "Demand response implementation in smart households," *Energy and Buildings*, vol. 143, pp. 129-148, 2017.
- [38] J. K. Gruber, M. Prodanovic, "Two-stage optimization for building energy management," *Energy Procedia*, vol. 62, pp. 346-354, 2014.
- [39] Z. Xu, Q.-S. Jia, X. Guan, "Supply demand coordination for building energy saving: Explore the soft comfort," *IEEE Transactions on Automation Science and Engineering*, vol. 12, (2), pp. 656-665, 2014.
- [40] J. K. Gruber, F. Huerta, P. Matatagui, M. Prodanović, "Advanced building energy management based on a two-stage receding horizon optimization," *Applied Energy*, vol. 160, pp. 194-205, 2015.
- [41] M. Yilmaz, "Real measure of a transmission line data with load forecast model for the future", *Balkan Journal of Electrical and Computer Engineering* 6 (2), 141-145.
- [42] I. Ullah, N. Javaid, Z. A. Khan, U. Qasim, Z. A. Khan, S. A. Mehmood, "An incentive-based optimal energy consumption scheduling algorithm for residential users," *Procedia Computer Science*, vol. 52, pp. 851-857, 2015.
- [43] H. A. Özkan, "A new real time home power management system," *Energy and Buildings*, vol. 97, pp. 56-64, 2015.
- [44] S. Javaid, M. Abdullah, N. Javaid, T. Sultana, J. Ahmed, N. A. Sattar, "Towards Buildings Energy Management: Using Seasonal Schedules Under Time of Use Pricing Tariff via Deep Neuro-Fuzzy Optimizer," presented at the 15th International Wireless Communications & Mobile Computing Conference, Tangier, Morocco, June 24-28, 2019.
- [45] M. Z. Abbas, I. A. Sajjad, R. Liaqat, M. Abdullah, M. A. Shah, M. F. Nadeem, "Non-intrusive Load Monitoring for Residential Customers Using Adaptive-Neuro Fuzzy Interface System and Fine Tree Classifier," presented at the 23rd International Multitopic Conference, Bahawalpur, Pakistan, Nov. 5-7, 2020.
- [46] A. Pina, C. Silva, P. Ferrão, "The impact of demand side management strategies in the penetration of renewable electricity," *Energy*, vol. 41, no. 1, pp. 128-137, 2012.
- [47] D. Karna, A. Vikram, A. Kumar, M. Rizwan, "A Novel Fuzzy based Intelligent Demand Side Management for Automated Load Scheduling," presented at the 4th International Conference on Green Energy and Applications, Singapore, March 7-9, 2020.
- [48] K. P. Sharma, N. Baine, "Application of a Fuzzy Logic based Controller for Peak Load Shaving in a Typical Household," *IEEE International Conference on Fuzzy Systems (FUZZ-IEEE)*, New Orleans, LA, USA, June 23-26, 2019.
- [49] A. Saidi, A. Harrouz, I. Colak, K. Kayisli, R. Bayindir, "Performance Enhancement of Hybrid Solar PV-Wind System Based on Fuzzy Power Management Strategy: A Case Study," 7th International Conference on Smart Grid, Newcastle, NSW, Australia, Dec. 9-11, 2019.
- [50] M. Elsisy, N. Bazmohammadi, J. M. Guerrero, M. A. Ebrahim, "Energy management of controllable loads in multi-area power systems with wind power penetration based on new supervisor fuzzy nonlinear sliding mode control," *Energy*, vol. 221, p. 119867, 2021.
- [51] W. Dong, Q. Yang, X. Fang, W. Ruan, "Adaptive optimal fuzzy logic based energy management in multi-energy microgrid considering operational uncertainties," *Applied Soft Computing*, vol. 98, p. 106882, 2021.
- [52] K. Meje, L. Bokopane, K. Kusakana, M. Siti, "Optimal power dispatch in a multisource system using fuzzy logic control," *Energy Reports*, vol. 6, pp. 1443-1449, 2020.
- [53] H. Golpira, S. A. R. Khan, "A multi-objective risk-based robust optimization approach to energy management in smart residential buildings under combined demand and supply uncertainty," *Energy*, vol. 170, pp. 1113-1129, 2019.
- [54] R. Hemmati, H. Saboori, "Stochastic optimal battery storage sizing and scheduling in home energy management systems equipped with solar photovoltaic panels," *Energy and Buildings*, vol. 152, pp. 290-300, 2017.
- [55] M. Shafie-Khah, P. Siano, "A stochastic home energy management system considering satisfaction cost and response fatigue," *IEEE Transactions on Industrial Informatics*, vol. 14, no. 2, pp. 629-638, 2017.
- [56] W. Fan, N. Liu, J. Zhang, "An event-triggered online energy management algorithm of smart home: Lyapunov optimization approach," *Energies*, vol. 9, no. 5, p. 381, 2016.
- [57] C. Wang, B. Jiao, L. Guo, Z. Tian, J. Niu, S. Li, "Robust scheduling of building energy system under uncertainty," *Applied Energy*, vol. 167, pp. 366-376, 2016.
- [58] D. Setlhaolo X. Xia, "Combined residential demand side management strategies with coordination and economic analysis," *International Journal of Electrical Power & Energy Systems*, vol. 79, pp. 150-160, 2016.
- [59] Y. Krim, D. Abbes, S. Krim, and M. F. Mimouni, "Intelligent droop control and power management of active generator for ancillary services under grid instability using fuzzy logic technology," *Control Engineering Practice*, vol. 81, pp. 215-230, 2018.
- [60] F. Y. Melhem, O. Grunder, Z. Hammoudan, and N. Moubayed, "Optimization and energy management in smart home considering photovoltaic, wind, and battery storage system with integration of electric vehicles," *Canadian Journal of Electrical and Computer Engineering*, vol. 40, no. 2, pp. 128-138, 2017.
- [61] A. Ahmad et al., "An optimized home energy management system with integrated renewable energy and storage resources," *Energies*, vol. 10, (4), p. 549, 2017.
- [62] A. Anvari-Moghaddam, A. Rahimi-Kian, M. S. Mirian, J. M. Guerrero, "A multi-agent based energy management solution for integrated buildings and microgrid system," *Applied Energy*, vol. 203, pp. 41-56, 2017.
- [63] W. El-Baz, P. Tzschentschler, "Short-term smart learning electrical load prediction algorithm for home energy management systems," *Applied Energy*, vol. 147, pp. 10-19, 2015.
- [64] S. Arun, M. Selvan, "Intelligent residential energy management system for dynamic demand response in smart buildings," *IEEE Systems Journal*, vol. 12, (2), pp. 1329-1340, 2017.
- [65] L. Ma et al., "Multi-party energy management for smart building cluster with PV systems using automatic demand response," *Energy and Buildings*, vol. 121, pp. 11-21, 2016.
- [66] I.-Y. Joo D.-H. Choi, "Distributed optimization framework for energy management of multiple smart homes with distributed energy resources," *IEEE Access*, vol. 5, pp. 15551-15560, 2017.
- [67] Z. Wu, X. Xia, "Optimal switching renewable energy system for demand side management," *Solar Energy*, vol. 114, pp. 278-288, 2015.
- [68] Z. Wu, H. Tazvinga, X. Xia, "Demand side management of photovoltaic-battery hybrid system," *Applied Energy*, vol. 148, pp. 294-304, 2015.

- [69] L. Ciabattoni, F. Ferracuti, M. Grisostomi, G. Ippoliti, S. Longhi, "Fuzzy logic based economical analysis of photovoltaic energy management," *Neurocomputing*, vol. 170, pp. 296-305, 2015.
- [70] E. Aykut, UK. Terzi. Techno-economic and environmental analysis of grid connected hybrid wind/photovoltaic/biomass system for Marmara University Goztepe campus. *International Journal of Green Energy*. 2020 Dec 7;17(15):1036-43.
- [71] M Yilmaz, H Kilic "Smart grid road map and challenges for Turkey", IET Digital Library, *Microgrids for Rural Areas: Research and case studies*, 2020, pp. 389-420.
- [72] Ghorai, D. Majumdar, T. Jash, S. Ray, "PV assisted Fuzzy based EV charge scheduling for demand side energy management: a case study," *IEEE Calcutta Conference (CALCON)*, Kolkata, India, Febr. 28-29, 2020.
- [73] MS Can, M Sam "Imitation of Fuzzy Logic Controller Based Artificial Neural Network, And Application Of Inverted Pendulum System Control" *European Journal of Technique*, Volume 9, Issue 2, 121 - 136, 30.12.2019
- [74] O. Erdinc, N. G. Paterakis, T. D. Mendes, A. G. Bakirtzis, J. P. Catalão, "Smart household operation considering bi-directional EV and ESS utilization by real-time pricing-based DR," *IEEE Transactions on Smart Grid*, vol. 6 (3), pp. 1281-1291, 2014.
- [75] UK. Terzi , HE Ilhan, H Kaymaz, H Erdal, H. Çalik. A Review of Commercial Electric Vehicle Charging Methods. *Promet-Traffic&Transportation*. 2020 Mar 15;32(2):291-307.

BIOGRAPHIES

Nazli Hasanova received the B.S. degree in Electrical Engineering from Azerbaijan State Agricultural University in 2017. In 2017, she started her education in the Electrical Electronics Engineering Master's program at Marmara University, Institute of Science and Technology.

Secil Varbak Nese received the B.S. degree in Electrical Education from Kocaeli University, Kocaeli, Turkey, in 2004, the M.S. degree in Electrical Education from the Afyon Kocatepe University, Afyonkarahisar, Turkey, in 2008, and the Ph.D. degree in Electrical Education from the Marmara University, Istanbul, Turkey, in 2015. She is currently an Assistant Professor Dr. at Electrical-Electronics Engineering in Marmara University, Istanbul, Turkey. Her current research interests include power systems, renewable energy.



Detection of Covid-19 from X-ray Images via Ensemble of Features Extraction Methods Employing Randomized Neural Networks

Ömer Faruk Ertuğrul¹ , Emrullah Acar¹ , Abdulkemir Öztekin¹ , Erdoğan Aldemir^{1*} 

^{1*} Electrical and Electronics Engineering Dept., Archit. and Eng. Faculty , Batman University. (e-mail: erdogan.aldemir@batman.edu.tr).

ARTICLE INFO

Received: May, 19, 2021

Revised: Dec., 23, 2021

Accepted: Dec., 29, 2021

Keywords:

Covid-19
neural network
textural features,
automatic diagnosis

Corresponding author: *E. Aldemir*

ISSN: 2536-5010 / e-ISSN: 2536-5134

DOI: <https://doi.org/10.36222/ejt.1035007>

ABSTRACT

Artificial intelligence-based solutions have achieved significant successes in the field of health in recent years. These solutions have been started to be used for pre-diagnosis and decision support for a virus that spreads rapidly such as COVID-19 and thus creates fear and panic among the public. They also have augmented clinical expertise and thus have great potential to mitigate the virus outbreak burden of health experts. In this context, the load of healthcare workers can be significantly reduced through the help of an automatic diagnosis system of a high number of patients who apply to healthcare organizations with suspicion of disease. In this study, a machine-learning automatic diagnosis system exploiting x-ray images is proposed to detect diseases caused by COVID-19. The proposed system employs powerful texture features (Histogram of Oriented Gradients, Law's Texture Energy Measure, Gabor Wavelet Transform, Gray Level Co-Occurrence Matrix, and Local Binary Pattern) for the x-ray images to train a randomized neural network, a fast network, to establish a robust and fast diagnosis process for the virus. This study has raised the thesis that the mentioned image texture features extracted from the virus patients' images contain determinative indicators in two-dimensional space that make it possible to diagnose the disease. The proposed system contributes to the literature by using the tissue properties of x-ray images for the diagnosis of the virus. The disease is detected with an accuracy of %100 utilizing Law's Texture Energy Measure features and randomized neural network approach.

1. INTRODUCTION

Humanity faces a major disaster rarely seen in history due to coronavirus disease, nowadays. This highly pathogenic coronavirus 2019 (COVID-19) is the new type of the coronavirus family, which is also called SARS-CoV-2 standing for severe acute respiratory syndrome coronavirus 2 [1]. To date, the COVID-19 has infected over one hundred million humans worldwide, with over 2 million deaths, and still continues threatening our lives [2]. The clinical studies have shown that most of the COVID-19 patients suffer from fever, cough, and shortness of breath, and other symptoms may include abdominal pain, muscle pain, diarrhea, sore throat, chills, sputum production, and loss of taste and smell [3].

Even though the spread of the virus may be possible before the appearance of symptoms, in symptomatic cases it is most contagious and symptoms may appear between 2-14 days after exposure to the virus [4]. Older adults and people who have severe medical conditions seem to be at higher risk [5] and need to take extra precautions [6]. Unfortunately, there is currently no specific antiviral treatment method or vaccine therapy for COVID-19, however, there are many clinical trials evaluating potential therapies.

To combat the spread of COVID-19 disease, effective screening of patients and emergency medical response for

infected patients is vital. The standard screening method of diagnosis is by reverse transcription-polymerase chain reaction (RT-PCR) test using nasopharyngeal swabs [7], [8]. Although the transcription-polymerase chain reaction (RT-PCR) test is the most common and reliable method for COVID-19 detection, it is a time-consuming process, laborious and complex in means of application [9]. The epidemiological history of the disease, clinical symptom analysis, positive pathogenic tests, and chest radiography (i.e., CT and x-ray) can be used in the diagnosis of COVID-19. In most of the COVID-19 cases, radiographic images have similar features in the early stage and pulmonary consolidation in the late stage [10]. A comparison of chest CT to RT-PCR test in the diagnosis of COVID-19 has been given by the study of Fang et al., which reports up to 98% sensitivity chest CT [11].

Today, artificial intelligence (AI) based analyses are widely used in the diagnosis of a variety of types of tumor and cancer detection. A number of deep learning and machine learning-based methods have been employed for the detection and screening of COVID-19 on the CT dataset, which is given in [12], [13]. There are several studies in the literature using AI and/or deep learning-based detection techniques from chest CT scans for the analysis and pre-diagnosis of COVID-19 cases, prior to applying PCR or pathogenic tests and thus saving significant time for further treatments [14], [15]. The CT

images of chests is known to be a very effective imaging method in the diagnosis of lung-related illness; however, chest x-ray imaging is more common in terms of availability, cost, and processing time [16]. One of the best ways to combat this epidemic is to turn the time in our favor by making the fastest diagnosis. The x-ray imaging is almost available even in all rural regions and most ambulatory care facilities and plays a vital role in clinical treatments and epidemiological studies [17]. Thus, the pandemic has pushed the health system to develop a telemedicine-integrable solution [18]. It is frequently used in the diagnosis of pneumonia, lung irritation/inflammation, swellings, distended/enlarged lymph nodes, and abscesses. While a typical x-ray imaging is very helpful in the early screening of suspicious cases, it may sometimes cause confliction as images of positive COVID-19 cases are similar to images of other viral cases of pneumonia that cause difficulties in distinguishing it from other cases. It, therefore, requires a radiologist to be available to perform the task, and this may take a considerably valuable time when the epidemic rapidly spreads and healthcare professionals and other resources are scarce [19]. A misdiagnosis of a true positive COVID-19 case will cause a very crucial risk, as well as a misdiagnosis of the non-positive case, will cause unnecessary effort, cost, and congestion in the current situation where hospitals are overloaded. It is, therefore, necessary to develop and design an AI-based automatic diagnosis system to shorten the analysis time and significantly speed up the screening for medical professionals.

The rest of the paper has been organized as follows: the details of the image dataset and the employed methodology are expressed in Section 2. The results and discussion are given in Section 3 and Section 4, respectively. Finally, Section 5 concludes the paper.

2. Material and Methods

2.1. Data Collection and Image Pre-processing

The data used in this study is attained from the Kaggle's Chest X-ray Images (Pneumonia) dataset [20]. The data set consists of 50 total x-ray images (25 of patients are diagnosed as COVID-19 positive and 25 of patients are healthy). Sample images for normal and Covid-19 x-ray are indicated in Figure 1.



Figure 1. a) healthy patient b) Covid-19 patient c) low contrast x-ray d) high-contrast x-ray

Each of x-ray images is resized as 256×256 . Then, these images are converted to 8-bit (unsigned integer) resolution monochrome images. Then, the low-contrast of each gray scale image is adjusted into high-contrast image intensity values as shown in Figure 1. The multi-feature extraction methods, which consist of Histogram of Oriented Gradients (HOG), Law's Texture Energy Measurement (TEM), Gabor Wavelet Transform (GWT), Gray Level Co-Occurrence Matrix (GLCM), and Local Binary Pattern (LBP), are implemented to the attained pre-processed gray scale images and mentioned methods are elucidated in the following sub-section.

2.2. Feature Extraction

2.2.1. Histogram of Oriented Gradients

Histogram of Oriented Gradients (HOG) is a gradient-based feature extraction method that is firstly suggested in the research of [21]. It explains an image as a series of local histograms and each local histograms is the dispersion of the occurrences number of gradients in specified directions computed in a particular field described as a cell upon the image [22]. The stage of feature extraction with the HOG algorithm is accomplished in three steps, which are the computation of gradient, computation of histogram, and block normalization.

The Computation of Gradient

The gradient values in horizontal and vertical directions of each point on the image are computed with the following equations. Here, Sobel filters are mostly employed to measure these components.

$$f_x(i, j) = I(i + 1) - I(i - 1, j) \quad (1)$$

$$f_y(i, j) = I(i, j + 1) - I(i, j - 1) \quad (2)$$

Here, the expression $I(i, j)$ points out the brightness at the spatial coordinates (i, j) . The magnitude of the computed gradients $M(i, j)$ and the direction of the gradient $\phi(i, j)$ are indicated via the following equation (3) and equation (4).

$$M(i, j) = \sqrt{\{f_x(i, j)^2 + f_y(i, j)^2\}} \quad (3)$$

$$\phi(i, j) = \arctan\left(\frac{f_x(i, j)}{f_y(i, j)}\right) \quad (4)$$

The Computation of Histogram (Experimental Distribution)

While computing the histogram, $\phi(i, j)$ can be categorized into identical regions in the range of 0° to 180° or 0° to 360° angles, based on the implementation. In our study, nine gradient regions in different directions are picked up between $0^\circ - 180^\circ$ with angles of 20° . The gradient dimension of each pixel in the cell is deployed to histogram regions on the basis of the angle it has, as indicated in Figure 1. This deployment is commonly carried out by linear and trilinear interpolation approaches [21]. The linear interpolation is utilized in our study.

Block Normalization

The main histogram is acquired by merging the entire sub histograms formed in a block and it is normalized using the following equation (5):

$$v = \left(\frac{V_m}{\sqrt{\|V_m\|^2 + 1}}\right) \quad (5)$$

Here, v and V_m represent the normalized HOG feature vector and the main histogram vector of a block, respectively. In our study, histogram regions are constituted by computing the unsigned gradients on rectangular cells (R-HOG) [23] and L2-Norm is employed for normalization. Moreover, the whole image is 125 split up into 3×3 rectangular cells, and a local histogram is formed from each cell. After that, nine histogram regions per cell ($180^\circ / 20^\circ = 9$) are integrated with nine local histograms, and a feature vector with a length of ($9 \times 9 = 81$) is generated. Finally, these vectors are used as inputs of the classification stage.

2.2.2. Laws Texture Energy Measure

Laws Texture Energy Measure (TEM) method gathers preset one-dimensional kernels into diverse convolution filters. Then, one-dimensional filters with vector length $l = 5$: L5 (Level) = [1 4 6 4 1], E5 (Edge) = [-1 -2 0 2 1], S5 (Spot) = [-1 0 2 0 1], R5 (Ripple) = [1 -4 6 -4 1] are employed for feature extraction. There, L5 offers the center-weighted local average. E5 replies to step edges in columns and rows. S5 detects points and R5 identifies fluctuations. If a column vector is multiplied by a row vector of the same length, a filter of size 1×1 is attained. Thus, different size filters are attained employing diverse rows and columns. These filters are then convolved with the image in order to extract texture features from this image and hence the attained new image is called "energy image". In the end, feature vectors are constituted by taking the statistical values (e.g., entropy, mean, standard deviation) of the obtained energy images. The mathematical expression of the texture energy map E_m for filter m is stated in Equation 6.

$$\sum_m(a, b) = \sum_{j=b-7}^{b+7} \sum_{i=a-7}^{a+7} F_m(i, j) \quad (6)$$

Here, $F_m(i, j)$, (i, j) , and (a, b) represent the m th-filtered image at pixel (i, j) , the sizes of the filtered image, and the sizes of the energy map, respectively. Finally, first-order statistic (i.e., mean) is implemented to the energy map to form a feature vector and sixteen parameters are computed as inputs of the classification stage from each image.

2.2.3. Gabor Wavelet Transform

Gabor wavelets are immensely similar to the visual system of human-based on their frequency and orientation characteristics. These wavelets compose a perfect filter for both orientation and spatial localization. A complex Gabor wavelet filter can be described as the product of a complex sinusoidal and a Gaussian kernel. A two-dimensional GWT can be stated by the convolution of the image $I(a, b)$ as shown in Equation 7 [24]:

$$J(a, b) = \iint I(a', b') g(a - a', b - b') da' db' \quad (7)$$

Here, the $gf(a, b)$ function illustrates the Gabor filter as:

$$gf(a, b; \lambda, \phi, \sigma, \gamma) = \exp\left(\frac{a_1^2 + \gamma^2}{2\sigma^2}\right) \exp\left(j\left(2\pi\frac{a_1}{\lambda} + \psi\right)\right) \quad (8)$$

$$a_1 = a \cos\phi + b \sin\phi \quad \text{and} \quad a_2 = -a \sin\phi + b \cos\phi$$

Here, ϕ and λ correspond to the angular orientation of the Gabor function and the wavelength scale of the cosine parameter, respectively. And ψ and γ express the phase offset value and the spatial view angle, respectively. The statistical parameters are computed from the GWT that are standard deviation (σ), mean (μ), and entropy (ϵ). Assume that $I(i, j)$ represents the GWT matrix of each gray scale image with the size of $m \times n$, then these parameters are computed as shown in Equation 9.

$$\mu_{ij} = \frac{1}{mn} \sum_i^m \sum_j^n I_{ij} \quad (9a)$$

$$\sigma_{ij} = \frac{1}{mn} \sum_i^m \sum_j^n (I_{ij} - \mu_{ij}^2) \quad (9b)$$

$$\epsilon_{ij} = -\sum_{i,j} I(i, j) \log(I_{ij}) \quad (9c)$$

After calculating three statistical parameters for each wavelet, the statistical variables obtained from eight wavelets (two scales and four angular orientations) of each image are added sequentially and ($3 \times 8 = 24$) parameters are created to form the feature vector of each gray scale image.

2.2.4. Gray Level Co-Occurrence Matrix

Gray Level Co-Occurrence Matrix (GLCM) describes the relationship amid the reference pixel and adjacent pixel [25]. A co-occurrence matrix is clarified as being the distribution of co-occurring pixel values, at a predetermined offset $(\Delta a, \Delta b)$. The number of columns and rows of a GLCM matrix is equal to the 145 gray level numbers in the image. In which, the distribution is set on the basis of the distance between the angles and pixels [26]. An image with p distinct gray levels gives a $p \times p$ co-occurrence matrix for a predetermined offset. The GLCM matrix (G) of an image $I(k \times l)$ is indicated in Equation 10.

$$G_{\Delta a, \Delta b} = \sum_{a=1}^k \sum_{b=1}^l \begin{cases} 1 & I(a, b) = i \text{ and } I(a + \Delta a, b + \Delta b) = j \\ 0 & \text{otherwise} \end{cases} \quad (10)$$

Here, (a, b) , (i, j) , $(\Delta a, \Delta b)$ and $I(a, b)$ illustrate the spatial location in the image, the pixel values, the offset values, and the pixel value at pixel (a, b) , respectively. The G matrix can also be described in terms of an angle θ and distance d instead of the offset values $(\Delta a, \Delta b)$ and $I(a, b)$. Here, θ angles are used commonly as 0° , 45° , 90° , and 135° [27]. In this study, 22 GLCM parameters are employed which consist of auto-correlation, contrast, correlation, cluster prominence, cluster shade, difference entropy, difference variance, dissimilarity, energy, entropy, homogeneity, information measure of correlation 1&2, inverse difference normalization, inverse difference moment normalization, maximum probability, sum average, sum entropy, the sum of squares and sum variance. Mathematical statements of these parameters are given in detail in [28].

2.2.5. Local Binary Pattern

Micro-textons are sought for on the basis of the relation among the pixels and their neighbors by Local Binary Pattern (LBP) [29]. A binary number is then assigned by comparing a central pixel by its neighbors [30]. After all comparisons, a set of binary numbers is attained and these numbers are transformed to decimal numbers that will be employed instead of these pixels [30]. The decimal number corresponds to the textural information regarding the relationship among the central pixel and its neighbors. Thus, each of them indicates a distinct pattern. The statement of Local Binary Pattern (LBP) $[L(x)]$ for each pixel is indicated as [31].

$$t = I(x_i) - I(x) \quad (11)$$

$$L(x) = \sum_{i=0}^p R(t)^2 (i - 1) \quad (12)$$

$$R(t) = \begin{cases} 1 & t \geq 0 \\ 0 & t < 0 \end{cases} \quad (13)$$

Here, x , x_i , and $I(\cdot)$ represents the central pixel, neighboring pixel at i th, and the gray-scale image, respectively. Eventually, a histogram is composed of the attained decimal numbers that are between 0 and 255 [33]. Moreover, it is observed that uniform patterns might be used in place of an overall histogram that has 256 distinct values. The uniform patterns have at the best bitwise passage as (0 to 1 or 1 to 0).

2.2.6. Randomized Neural Network

Randomized Neural Network (RNN) is a robust machine learning method for feed-forward neural networks (FFNN),

which has a single hidden layer. It can be utilized for classification and regression purposes. Input weights and bias parameters are not required to be set in contrast to other usual feed-forward network implementations. Therefore, these parameters can be chosen as random, and the output weights can be analytically ascertained. This situation allows RNN to be easy and fast in data processing [32] and ensures a fine generalization achievement for a single FFNN [33]. Compared to the other known gradient-based learning algorithms, RNN has several advantages like the potential of reaching the minimum training error, operating with non-differentiable activation functions, and employing a single hidden layer [34]. Moreover, the number of observations is more than the number of neurons in the RNN hidden layer [35]. The RNN output y can be computed via Equation 14 [33].

$$y = \sum_{j=1}^m \rho_j G(\sum_{i=1}^n W_{ij} \cdot x_i + b_j) \quad (14)$$

Here, x , n , m , W_{ij} , ρ_j , b_j and $G(\cdot)$ express the input, neuron numbers of the input, neuron numbers of the hidden layer, the input weights, the output weights, the biases of the neurons, and the activation function, respectively.

2.3. The Proposed Approach

The block diagram of the recommended system is indicated in Figure 2. First, a dataset, which consists of 50 x-ray images (25 COVID-19 positives and 25 normal cases) are obtained

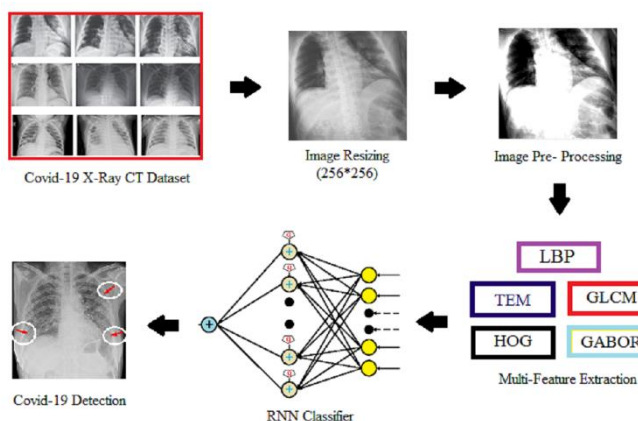


Figure 2. A block diagram, which summarizes all stages of the Covid-19 detection from x-ray images.

from the Kaggle. Second, whole x-ray images are resized as 256×256 and these images are transformed to 8-bit resolution gray scale images. After the transformation phase, the low-contrast of each gray scale image is set into high-contrast image intensity values. The multi-feature extraction methods, namely HOG, TEM, GWT, GLCM, and LBP, are then applied to the pre-processed images.

Finally, the attained feature vectors for each image are employed as inputs of the RNN classifier to determine whether the existence of the virus. In the training and testing stage of RNN, 10-fold cross-validation is implemented and 16 different activation functions (1-sigmoid, 2-sinusoidal, 3-radial-basis, 4-hard-limit, 5-symmetric hard-limit, 6-saturating linear, 7-tangent sigmoid, 8-triangular-basis, 9-positive linear, 10-pure linear, 11-cosinusoidal, 12-log sigmoid, 13-saturating linear, 14-hyperbolic tangent, 15-Gaussian, 16-multi quadratic) with the different number of hidden neurons (NHN) is chosen to determine optimal parameters. Moreover, the testing accuracies vs. NHN for all activation functions (AF) are given

in the Results and Discussion section. Here, the testing accuracy is computed as:

$$\text{Testing Accuracy (\%)} = \frac{TP+TN}{TP+TN+FP+FN} \times 100 \quad (15)$$

Here, TP, FN, FP, and TN illustrate the number of true positives, false negatives, false positives, and true negatives, respectively.

3. EXPERIMENTS

In this section, the total of 50 x-ray images (25 COVID-19 positives and 25 normal) with different resolutions are resized as 256×256 and they are converted to 8-bit resolution gray scale images. After that, the contrast of resized gray scale images is increased into high-intensity values. Then, multi-feature extraction methods, which are HOG, TEM, GWT, GLCM, and LBP, are implemented to the pre-processed monochrome images and feature vectors are attained from them. As a final step, the RNN classifier that utilized the feature vectors extracted from x-ray images detects COVID-19. The methodology performances are presented individually for all feature vectors are employed in the following subsections.

3.1. Detection of COVID-19 from X-ray Images Using HOG and RNN

In this section, 81 HOG features are employed as inputs of the RNN classifier, and testing accuracies vs. NHN for all activation functions (AF) are given in Table I. The performance of the system employed by the HOG feature differs according to the parameters of seven NHN and sixteen AF functions. There is not an evident linear relationship between the accuracy of diagnosis and the NHN and AF parameters. The maximum accuracy rate, which is 95%, is obtained by employing AF-2 with 20 NHN.

TABLE I

Testing Accuracy (%) for all AF with 5 different NHN using HOG features and RNN Classifier

NHN	AF														
	1	2	3	4	5	6	8	9	10	12	13	14	15		
1	30	34	34	33	36	38	33	35	35	34	36	33	36		
5	73	66	61	35	33	66	76	71	69	64	78	76	74		
10	83	88	80	41	40	86	88	81	88	74	80	79	79		
15	85	84	85	45	41	88	81	90	91	83	83	91	86		
20	86	95	83	43	44	88	81	89	86	91	85	93	83		
25	85	89	84	48	45	83	85	90	80	84	88	80	79		
50	84	83	80	53	44	75	78	78	76	73	85	71	71		

In general, the performances for NHN 1 and 5 remain under average performance compared to other NHN. However, considering the AF parameter, there does not exist a significant difference in the performance of the system between the AF parameters employed, except the functions 4 and 5 that provide the least accuracy rate regardless of the NHN parameters. In addition, the activation functions AF-7, AF-11, and AF-16 were also applied experimentally, and they are not presented in Table I because their performances are below the other functions given in the table.

3.2. Detection of COVID-19 from X-ray Images Using TEM and RNN

The proposed system employs 15 TEM features as inputs of the RNN classifier and testing accuracies vs. NHN for all activation functions (AF) are yielded in Table II. Similar to the HOG, except for functions 4 and 5, the use of other functions (AF parameters) does not make a significant difference to the performance of the system, and functions 4 and 5 provide the least accuracy rate regardless of the NHN parameters. The system achieves the highest accuracy rate, which is 100%, by employing AF-7 with 10 NHN. The TEM feature achieves better accuracy of diagnosis compared to the HOG feature, in general.

The performance of the system considerably decreases for NHN 1 and 50. The decrease reaches up to nearly 50% compared to the previous accuracy rate, e.g. 88% for NHN 25 and 54% for NHN 50 both for the AF 3. Accordingly, the determination of optimality for the parameters of the system is crucial to obtain better results for diagnosis. The system employing the TEM reaches remarkable performance for diagnosis of the COVID-19, overall.

TABLE II

Testing Accuracy (%) for all AF with 5 different NHN using TEM features and RNN Classifier

NHN	AF															
	1	2	3	4	5	6	7	8	9	10	11	12	13	14	15	16
1	36	40	34	36	32	32	36	34	42	36	36	40	36	36	32	30
5	82	92	82	36	38	92	94	82	84	88	92	88	90	90	88	96
10	92	88	86	38	38	88	100	94	96	92	92	92	90	92	94	94
15	94	96	88	40	38	90	92	94	88	86	96	94	82	90	88	92
20	90	94	86	58	46	92	88	90	88	88	92	92	88	88	92	92
25	86	88	88	42	54	94	88	86	94	88	86	88	88	82	86	94
50	66	54	72	44	66	88	64	86	88	94	60	66	90	58	60	66

3.3. Detection of COVID-19 from X-ray Images Using GWT and RNN

The system is implemented using 24 GWT features as inputs of the RNN classifier and testing accuracies vs. NHN for all activation functions (AF) are yielded in Table III. The GWT is the feature that provides knowledge about the orientation of the patterns existing in x-ray images that may uncover the indicators for diagnosis. The performance of the GWT reaches a 96% rate for diagnosis that is the second-highest performance. A recent deep-learning classifier announces a %95 accuracy rate of diagnosis using chest Xr-ray images [36].

TABLE III

Testing Accuracy (%) for all AF with 5 different NHN using GWT features and RNN Classifier

NHN	AF															
	1	2	3	4	5	6	7	8	9	10	11	12	13	14	15	16
1	26	22	24	32	26	32	32	26	24	24	26	22	30	32	26	30
5	64	68	64	28	28	64	78	64	70	76	74	72	62	60	66	70
10	82	82	84	34	32	84	76	86	88	84	72	84	86	80	78	80
15	82	76	82	28	26	88	86	82	88	86	78	84	88	84	82	74
20	92	84	84	26	28	92	90	90	88	92	92	92	86	94	86	80
25	82	80	90	36	30	88	86	96	92	90	88	86	90	86	86	88
50	60	58	48	28	32	86	66	82	92	88	58	68	94	60	62	68

The feature provides the least accuracy rate in the case of NHN 1, 5, and 50, similar to TEM and HOG. For the remaining NHN, the systems achieve a notable accuracy rate of diagnosis.

3.4. Detection of COVID-19 from X-ray Images Using GLCM and RNN

For detection of the virus, 22 GLCM features are employed as inputs of the RNN classifier, and testing accuracies vs. NHN for all activation functions (AF) are given in Table IV. Overall performance of the GLCM feature remains under the TEM, HOG, and GWT.

TABLE IV

Testing Accuracy (%) for all AF with 5 different NHN using GLCM features and RNN Classifier

NHN	AF															
	1	2	3	4	5	6	7	8	9	10	11	12	13	14	15	16
1	30	34	30	28	26	26	32	34	34	34	30	32	32	28	26	26
5	62	78	62	34	38	70	54	46	60	58	58	64	62	58	62	66
10	56	60	62	32	42	68	66	64	60	72	64	58	74	54	56	68
15	78	82	70	32	42	70	66	70	76	72	78	80	68	78	74	58
20	78	74	78	44	48	78	76	66	68	66	68	74	70	74	84	72
25	76	78	88	40	32	72	70	70	78	80	78	86	66	74	80	68
50	64	50	58	40	48	76	46	62	68	66	58	48	74	60	40	72

The system performed by the GLCM reaches an 88% rate that remains under the performance of the aforementioned features for diagnosis. Not surprisingly, functions 4 and 5 provide the least diagnosis performance while the performance of other activation functions does not show a notable fluctuation.

3.5. Detection of COVID-19 from X-ray Images Using LBP and RNN

The proposed system has been implemented with 6 LBP features that are employed as inputs of RNN classifier and testing accuracies vs. NHN for all activation functions (AF) are yielded in Table V.

TABLE V

Testing Accuracy (%) for all AF with 5 different NHN using LBP features and RNN Classifier

NHN	AF															
	1	2	3	4	5	6	7	8	9	10	11	12	13	14	15	16
1	28	26	30	38	28	30	36	32	28	24	28	26	32	38	28	32
5	72	64	70	30	30	60	54	64	64	62	72	70	68	64	64	62
10	64	74	66	44	36	56	60	68	60	64	62	72	70	66	68	58
15	70	62	74	28	40	66	62	66	68	50	68	68	62	68	68	76
20	70	74	68	32	34	70	74	62	60	66	78	76	64	62	72	68
25	78	76	74	44	42	66	74	52	60	68	78	72	64	80	74	74
50	74	68	68	38	50	62	80	72	72	64	80	58	54	84	86	66

The proposed methodology reaches an 86% accuracy rate with parameters of the activation function number of 15 and 50 NHN. The performance of LBP remains under the other features in general. Similar to the remaining features employed by the system, the least performance achievement is obtained in the case of using 4 and 5 AF.

4. DISCUSSION

The proposed automated COVID-19 diagnostic system has been implemented using 5 different feature extraction methods with 16 AF and 7 NHN parameters for a comprehensive evaluation. The best mean accuracy (%) results using multi-feature extraction methods and RNN classifiers with the aforementioned parameters are tabulated in Table VI.

TABLE VI

The best mean accuracy (%) results with computational time (s) for all features and RNN Classifier

Approach	Comp. Time (min.)	Feature Number	Testing Accuracy (%)
HOG+RNN	0.22	81	95
TEM+RNN	3.20	15	100
GABOR+RNN	0.83	24	96
GLCM+RNN	0.25	22	88
LBP+RNN	0.72	6	86

In addition, analyzes are made according to the computational time parameter, which will become even more important in the case of integration of the system into an active e-health network. In terms of overall performance, the ELM feature achieved an average of 100% performance in the automatic diagnosis of the data set, leaving all other features behind. It is seen that the ELM feature, which achieved the best diagnostic performance, classified the data set in a time of 3.2 seconds, which is a longer computational load than other methods. Although ELM is seen to have a relatively higher burden in terms of computational time compared to other methods, this does not prevent real-time use of the method thanks to modern workstations and advanced systems. Other remarkable features in terms of diagnostic success are GWT and HOG. These features both achieve over 95% performance (GWT 96% and HOG 95%) and provide the best results in terms of computing load. The accuracy announced between 87% and 98% for binary and multi-classes images [37], respectively. Deep-learning solutions announced in [38] and [39] give over a 90% diagnosis rate. Recent studies [40], [41] that utilize a deep learning-based framework as a support system achieves over %95 diagnosis rate. It is clear that the HOG feature has a significant advantage when considering both computational load and diagnosis performance. The system performs the least but still notable diagnosis accuracies rate for the GLCM (88%) and LBP (86%) features. Although these two features do not impose a high computational load, their performance remains under the performance of the ELM, HOG, and GWT features. The features utilized by the system can reveal different textural features of the image due to their algorithmic and mathematical structures. One example of this is GWT, which focuses on directional tissues in chest x-ray images, revealing some indicators that other methods cannot achieve. Since the mathematical structure and algorithmic designs of other features differ, a similar conclusion with GWT can be reached characteristics properties that aid to unveil diverse structures and indicators of the x-ray images. Therefore, an ensemble model established by utilizing diverse types of features has the potential to increase the performance of the system for COVID-19 diagnosis.

5. CONCLUSION

The COVID-19 pandemic, which has created great uneasiness all over the world, is a case that has not been encountered before by the modern health systems and as a result, it has brought a serious burden to the systems. In recent years, artificial intelligence-based systems have been widely used successfully in the field of health for decision support and making diagnoses. In this respect, it has the potential to significantly reduce the workload of healthcare workers by using AI-assisted systems in the preliminary diagnosis and decision-support phase of an easily transmitted virus such as COVID-19. Indeed, studies in this area have shown that artificial intelligence-based systems promise significant success.

The diagnosis and controlling of the large number of people applying to health institutions with the suspicion of a virus in a short time are serious burdens for health organizations due to the restricted time and cost of the tests. Therefore, it is clear that an artificial intelligence-based auxiliary system to be used for pre-diagnosis and decision support will make a great contribution to the health ecosystem. Motivated by this fact, an automated system based on AI that exploits multi-features extracted from x-ray images is proposed for the diagnosis of the virus, in this study. A set of two-dimensional image texture features having diverse characteristics have been used for unveiling the indicators for automatically diagnosing the cases. The TEM, GWT, LBP, GLCM, and HOG features are extracted from an x-ray image, and the RNN decision-maker is trained with these features. These features show diverse characteristics having the ability to uncover the indicators existing in x-ray images. These features show diagnosis performance ranging from 86% to 100%. It has been observed that the most dominant feature in automatic detection of the virus is TEM and, in the applications, performed on the dataset, it is diagnosed correctly with an average performance of 100%. Moreover, the various activation functions used are mathematical forms with different characteristics. Therefore, it directly affects the performance of the method in terms of physical and representation.

The fact that the system is performing a commonly used, fast, and easily accessible imaging system such as x-ray, is promising in terms of preliminary diagnosis for geographical regions where diagnostic kits are hard to access. Although the study has been carried out on a large data set, it has the potential to be further improved if the proposed system is integrated with an active health network that contains more diverse images and kinds of images such as CT or PET. Moreover, the features utilized by the proposed systems can be widened by using different textural features to improve the performance of the systems. Consequently, it has been shown that the proposed system based on AI for the diagnosis of COVID-19 using x-ray images achieved remarkable results. This proposed system, which has the potential to be developed in terms of data-set and image texture features, can be integrated into modern health systems and thus it can make significant contributions for the public health.

REFERENCES

- [1] S. B. Stoecklin *et al.*, "First cases of coronavirus disease 2019 (COVID-19) in France: surveillance, investigations and control measures, January 2020," *Eurosurveillance*, vol. 25, no. 6, p. 2000094, 2020.
- [2] T. T. Team, "TrackCorona," *TrackCorona*, 2021. .

- [3] Coronavirus Disease 2019, "Symptoms of Coronavirus," 2021. .
- [4] T. P. Velavan and C. G. Meyer, "The COVID-19 epidemic," *Trop. Med. & Int. Heal.*, vol. 25, no. 3, p. 278, 2020.
- [5] D. Flynn *et al.*, "COVID-19 pandemic in the United Kingdom," *Heal. Policy Technol.*, vol. 9, no. 4, pp. 673–691, 2020.
- [6] CDC, "People Who Are at Higher Risk for Severe Illness." .
- [7] M. E. H. Chowdhury *et al.*, "Can AI help in screening viral and COVID-19 pneumonia?," *IEEE Access*, vol. 8, pp. 132665–132676, 2020.
- [8] L. O. Hall, R. Paul, D. B. Goldgof, and G. M. Goldgof, "Finding covid-19 from chest x-rays using deep learning on a small dataset," *arXiv Prepr. arXiv2004.02060*, 2020.
- [9] W. Wang *et al.*, "Detection of SARS-CoV-2 in different types of clinical specimens," *Jama*, vol. 323, no. 18, pp. 1843–1844, 2020.
- [10] M. Chung *et al.*, "CT imaging features of 2019 novel coronavirus (2019-nCoV)," *Radiology*, vol. 295, no. 1, pp. 202–207, 2020.
- [11] Y. Fang *et al.*, "Sensitivity of chest CT for COVID-19: comparison to RT-PCR," *Radiology*, vol. 296, no. 2, pp. E115–E117, 2020.
- [12] O. Gozes *et al.*, "Rapid ai development cycle for the coronavirus (covid-19) pandemic: Initial results for automated detection & patient monitoring using deep learning ct image analysis," *arXiv Prepr. arXiv2003.05037*, 2020.
- [13] F. Shi *et al.*, "Large-scale screening of covid-19 from community acquired pneumonia using infection size-aware classification (2020)," *arXiv Prepr. arXiv2003.09860*, 2003.
- [14] S. Wang *et al.*, "A deep learning algorithm using CT images to screen for Corona Virus Disease (COVID-19)," *Eur. Radiol.*, pp. 1–9, 2021.
- [15] Y. Li and L. Xia, "Coronavirus disease 2019 (COVID-19): role of chest CT in diagnosis and management," *Am. J. Roentgenol.*, vol. 214, no. 6, pp. 1280–1286, 2020.
- [16] J. Zhang *et al.*, "Viral pneumonia screening on chest X-ray images using confidence-aware anomaly detection," *arXiv Prepr. arXiv2003.12338*, 2020.
- [17] T. Cherian *et al.*, "Standardized interpretation of paediatric chest radiographs for the diagnosis of pneumonia in epidemiological studies," *Bull. World Health Organ.*, vol. 83, pp. 353–359, 2005.
- [18] G. Ortega *et al.*, "Telemedicine, COVID-19, and disparities: policy implications," *Heal. Policy Technol.*, vol. 9, no. 3, pp. 368–371, 2020.
- [19] J. Portnoy, M. Waller, and T. Elliott, "Telemedicine in the era of COVID-19," *J. Allergy Clin. Immunol. Pract.*, vol. 8, no. 5, pp. 1489–1491, 2020.
- [20] Kaggle, "Chest X-ray Images (Pneumonia)," *Chest X-ray Images (Pneumonia)*, 2021.
- [21] N. Dalal and B. Triggs, "Histograms of oriented gradients for human detection," in *2005 IEEE computer society conference on computer vision and pattern recognition (CVPR '05)*, 2005, vol. 1, pp. 886–893.
- [22] E. Acar and M. S. Ozerdem, "The texture feature extraction of Mardin agricultural field images by HOG algorithms and soil moisture estimation based on the image textures," 2015, pp. 665–665, doi: 10.1109/siu.2015.7129912.
- [23] O. L. Junior, D. Delgado, V. Gonçalves, and U. Nunes, "Trainable classifier-fusion schemes: An application to pedestrian detection," in *IEEE Conference on Intelligent Transportation Systems, Proceedings, ITSC, 2009*, pp. 432–437, doi: 10.1109/ITSC.2009.5309700.
- [24] I. Buciu and A. Gacsadi, "Gabor wavelet based features for medical image analysis and classification," in *2009 2nd International Symposium on Applied Sciences in Biomedical and Communication Technologies*, 2009, pp. 1–4.
- [25] M.-H. Horng and J.-H. Zhuang, "Texture feature coding method for texture classification," *Opt. Eng.*, vol. 42, no. 1, pp. 228–238, 2003.
- [26] A. Emrullah, "Extraction of texture features from local iris areas by GLCM and Iris recognition system based on KNN," *Eur. J. Tech.*, vol. 6, no. 1, pp. 44–52, 2016.
- [27] D. K. Iakovidis, D. E. Maroulis, and D. G. Bariamis, "FPGA architecture for fast parallel computation of co-occurrence matrices," *Microprocess. Microsyst.*, vol. 31, no. 2, pp. 160–165, 2007, doi: 10.1016/j.micpro.2006.02.013.
- [28] R. W. Conners, M. M. Trivedi, and C. A. Harlow, "Segmentation of a high-resolution urban scene using texture operators," *Comput. vision, Graph. image Process.*, vol. 25, no. 3, pp. 273–310, 1984.
- [29] T. Ojala, M. Pietikäinen, and T. Mäenpää, "Multiresolution gray-scale and rotation invariant texture classification with local binary patterns," *IEEE Trans. Pattern Anal. Mach. Intell.*, vol. 24, no. 7, pp. 971–987, 2002, doi: 10.1109/TPAMI.2002.1017623.
- [30] R. Nosaka and K. Fukui, "HEP-2 cell classification using rotation invariant co-occurrence among local binary patterns," in *Pattern Recognition*, 2014, vol. 47, no. 7, pp. 2428–2436, doi: 10.1016/j.patcog.2013.09.018.
- [31] T. Chakraborti and A. Chatterjee, "A novel binary adaptive weight GSA based feature selection for face recognition using local gradient patterns, modified census transform, and local binary patterns," *Eng. Appl. Artif. Intell.*, vol. 33, pp. 80–90, 2014.
- [32] Ö. F. Ertugrul and M. E. Tagluk, "A fast feature selection approach based on extreme learning machine and coefficient of variation," *Turkish J. Electr. Eng. & Comput. Sci.*, vol. 25, no. 4, pp. 3409–3420, 2017.
- [33] G.-B. Huang, Q.-Y. Zhu, and C.-K. Siew, "Extreme learning machine: theory and applications," *Neurocomputing*, vol. 70, no. 1–3, pp. 489–501, 2006.
- [34] A. Öztekin and E. Erçelebi, "An efficient soft demapper for APSK signals using extreme learning machine," *Neural Comput. Appl.*, vol. 31, no. 10, pp. 5715–5727, 2019.
- [35] M. Li and D. Wang, "Insights into randomized algorithms for neural networks: Practical issues and common pitfalls," *Inf. Sci. (Ny)*, vol. 382, pp. 170–178, 2017.
- [36] I. Castiglioni *et al.*, "Machine learning applied on chest x-ray can aid in the diagnosis of COVID-19: a first experience from Lombardy, Italy," *Eur. Radiol. Exp.*, vol. 5, no. 1, pp. 1–10, 2021.
- [37] T. Ozturk, M. Talo, E. A. Yildirim, U. B. Baloglu, O. Yildirim, and U. R. Acharya, "Automated detection of COVID-19 cases using deep neural networks with X-ray images," *Comput. Biol. Med.*, vol. 121, p. 103792, 2020.
- [38] M. Tougaçar, B. Ergen, and Z. Cömert, "COVID-19 detection using deep learning models to exploit Social Mimic Optimization and structured chest X-ray images using fuzzy color and stacking approaches," *Comput. Biol. Med.*, vol. 121, p. 103805, 2020.
- [39] X. He *et al.*, "Sample-efficient deep learning for COVID-19 diagnosis based on CT scans," *medrxiv*, 2020.
- [40] M. Fontanellaz *et al.*, "A deep-learning diagnostic support system for the detection of COVID-19 using chest radiographs: a multireader validation study," *Invest. Radiol.*, vol. 56, no. 6, pp. 348–356, 2021.
- [41] Y. Wan, H. Zhou, and X. Zhang, "An interpretation architecture for deep learning models with the application of COVID-19 diagnosis," *Entropy*, vol. 23, no. 2, p. 204, 2021.

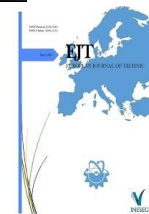
BIOGRAPHIES

Ömer Faruk Ertugrul received the B.S., M.S., and Ph.D. degrees in electrical and electronics engineering from Hacettepe University, Dicle University, and İnönü University, respectively. He is currently an Associate Professor of electrical-electronics engineering with Batman University. His research interests include machine learning, signal processing and Industry 4.0.

Emrullah Acar Emrullah Acar received the B.S. degree in electrical and electronics engineering from Çukurova University, Adana, Turkey, in 2009, the M.S. degree in biomedical engineering from Istanbul Technical University, Istanbul, Turkey, in 2010, and the M.S. and Ph.D. degrees in electrical-electronics engineering from Dicle University, Diyarbakır, Turkey, in 2012 and 2017, respectively. From 2008 to 2009, he was an Exchange Student in electrical engineering from Linköping University, Sweden. He is currently an Assistant Professor of electrical-electronics engineering with Batman University and also the Head of the Electronics Division. His research interests include digital image processing, machine learning, and remote sensing applications. Dr. Acar received awards and honors include The Scientific and Technological Research Council of Turkey (TUBITAK) Grant, Erasmus Mobility Grant, Sweden, and Erasmus Internship Grant, Germany.

Abdulkerim Öztekin, Berlin, Germany, in 1978. He received the B.S. degree in electrical and electronics engineering from Hacettepe University, Ankara, in 2001. He received the M.S. and the Ph.D. degrees in electrical and electronics engineering from Gaziantep University, Gaziantep, in 2018. From 2001 to 2011, he worked as a Senior Engineer in several companies in the industry, and from 2012 to 2018; he was a Lecturer with the Electronic Communication Department, Batman University. Since 2018, he has been an Assistant Professor with the Electrical and Electronics Engineering Department, Batman University. His research interests include signal processing, video coding, communication systems, and machine learning.

Erdoğan Aldemir received the B.Sc. degree from Uludağ University in 2010 and the M.Sc. degree from the Yıldız Technical University in 2013, all in electronics engineering. He received Ph.D. degree from Dokuz Eylül University in 2019. He is currently working on medical imaging, source coding, and image compression.



Evaluation of Machine Learning Hyperparameters Performance for Mice Protein Expression Data in Different Situations

Cafer Tayyar Bati^{1*} , Gazel Ser² 

^{1*} Van Yuzuncu Yil University, Institute of Science, Department of Animal Science, Van, Turkey. (e-mail: cafertayyarbati@gmail.com).

² Van Yuzuncu Yil University, Faculty of Agriculture, Department of Animal Science, Van, Turkey. (e-mail: gazelser@gmail.com).

ARTICLE INFO

Received: Jan., 27. 2021

Revised: Jul., 07. 2021

Accepted: Dec., 29. 2021

Keywords:

Artificial neural networks

Hyperparameter

Machine learning

Mice

Protein

Support vector machines

Corresponding author: *Cafer Tayyar Bati*

ISSN: 2536-5010 | e-ISSN: 2536-5134

DOI: <https://doi.org/10.36222/ejt.869094>

ABSTRACT

In this study, the aim was to assess the effect and significance of hyperparameters in four different datasets containing different values for observation numbers and variable counts with the machine-learning methods of support vector machines and artificial neural networks. With this aim, a dataset comprising 15 repeats of 77 protein levels from 38 healthy and 34 down syndrome mice was used. A total of 138 different models and model classification performance criteria were obtained from the datasets in the study comprising combinations of hyperparameters in machine-learning methods. Comparison of the models used criteria like accurate classification percentage, kappa statistic, mean absolute error and square root of mean error squares. According to performance criteria, the first dataset with 1080 observations x 77 variables had 71.30% accurate classification percentage for assumed parameters with the support vector machines polynomial kernel function, while changing the hyperparameter variables increased this rate to 99.44%. Similarly, the second dataset had 50.65% accurate classification percentage with the artificial neural network single hidden layer 2 neuron model, while changing the hyperparameter values increased this rate to 90.46%. In conclusion, in situations with low variable and observation numbers, the machine learning methods were determined to display lower performance. However, in datasets, it is very important for classification performance in artificial neural networks and support vector machines, especially polynomial and radial basis function kernel functions, to set hyperparameters according to the dataset. In situations with low variable numbers, especially, the effect of hyperparameters was determined to gain importance.

1. INTRODUCTION

With machine learning methods algorithms developed for complicated and large data can perform classifications with a high degree of accuracy [1]. In procedures for processing and assessing data at increasing scales, machine learning methods provide a transition from parametric methods to nonparametric methods. Due to machine learning, computers may be programmed to optimize a process based on previous experience or datasets. Thus, dataset classifications can be performed effectively in a short time, a model may be created at the end of this process and this model may be used for estimations about the future and auditing purposes [2].

Machine learning algorithms require adjustment before operation and include ‘hyperparameters’ with no clear defaults acceptable across a wide range of applications. Examples of these hyperparameters that require determination for these algorithms are the depth of a decision tree, number

of trees in the forest and number of neurons in each layer of an artificial neural network. These parameters have critical importance for machine learning because different hyperparameters generally result in performances with a significant degree of difference [3]. The ideal settings for hyperparameters do not just determine the performance in the training process, but more importantly, determines the quality of the prediction models which emerge [4,5]. Currently, though there are many studies about the importance of hyperparameters in the machine learning field [6-8], studies about the variability displayed in the effect of hyperparameters linked to factors like the structure and dimension of the dataset are limited [9]. In addition, it has been stated in many studies [10-13] on machine learning that artificial neural networks and support vector machines are very successful methods for classification and estimation, as well as the presence of more than one hyperparameter in methods has been effective in the preference of methods in the

study. In this context, this study aimed to assess the effect of hyperparameters in datasets in four different situations where observation numbers and variable numbers have different values.

2. MATERIAL AND METHOD

The ‘mice protein expression’ dataset used in the study was obtained from the UCI machine learning data repository [14]. This dataset created by Higuera *et al.* [15] contains 15 repeated measurements for 77 protein levels in 38 healthy and 34 Down syndrome mice. The dataset is divided into 8 classes according to the genotype of the mice (control (c), trisomy (t)), behavior (context-shock (CS), shock-context (SC)) and treatment (memantine (m), saline (s)). In total, there are 1080 observations for each protein. This dataset was chosen for the study due to its containing several features together like sufficient observations (1080), high numbers of variables (77), repeated measures (15) and sufficient class numbers (8).

2.1. Data analysis scenario

Four different datasets were created (Table 1), with different combinations of hyperparameters (Table 2) used (with grid search) and 138 different models were generated. Additionally, 10-fold cross-validation was used against overfitting situations that may occur in the models. In addition, the percentage of correct classification, kappa statistic, mean absolute error and root mean square error performance criteria were obtained (Table 3). Analyses were performed in the Weka (Waikato Environment for Knowledge Analysis, Version 3.8.1) program [16].

TABLE 1
DATA SETS USED IN THE STUDY

Data set	Number of Observations	Variable Number	Explanation
Data set I	1080	77	Original data set
Data set II	1080	9	By applying principal component analysis to the first data set,
Data set III	72	77	Deleting 14 repeated measurements of each individual in the first data set,
Data set IV	72	9	By applying principal component analysis to the third data set,

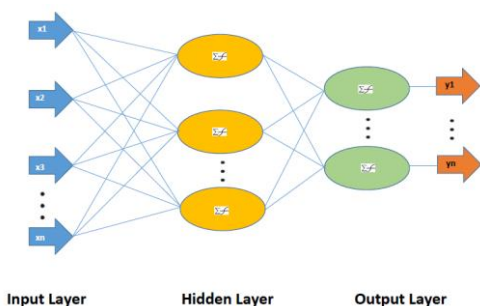


Figure 1. Multilayer perceptron

HYPERPARAMETERS USED IN THE STUDY		
Algorithm	Hyper Parameters*	
Support Vector Machines	Linear Kernel	C
	Polynomial Kernel	C and D
	Radial Basis Function Kernel	C and γ
Artificial Neural Networks	Hidden layers	
	The number of neurons in each layer	

* C: Editing parameter (1, 10, 100), d: Polynomial degree (2, 3, 5), γ : Kernel size (0.01, 0.1, 1, 10).

TABLE 3
PERFORMANCE METRICS [17]

Performance Metrics	Notation *
Correct classification percentage	$Accuracy = \frac{(T_p + T_n)}{(T_p + F_p + F_n + T_n)}$
Kappa statistics	$\mathcal{K} = \frac{(P_o - P_e)}{(1 - P_e)}$
Average absolute error	$MAE = \frac{1}{n} \sum_{t=1}^n x_t - \hat{x}_t $
Square root mean square error	$RMSE = \sqrt{\frac{\sum_{i=1}^n (x_t - \hat{x}_t)^2}{n}}$

* $T_p + T_n$: Number of correctly classified data, $F_p + F_n$: Number of incorrectly classified data, P_o : Accepted rate, P_e : Expected rate

2.2. Methods used in the study

Machine learning is an artificial intelligence application completing learning and development operations from available data without openly programming the computer. Machine learning searches for patterns in data based on data provided for training and applies these patterns to test data in order to make better decisions in the future. The purpose of these methods is to ensure computers learn automatically without human intervention. Artificial neural networks consider calculation units in a learning model as resembling human neural cells, mimicking human neural systems for machine learning tasks [18]. The greatest task of artificial neural networks is to create machines with artificial intelligence mimicking the architecture of the human neural system for calculations. The currently-used multilayer perceptron (Figure 1) comprises an input, hidden layers and output layer, different from a single-layer perceptron. Linked to the complexity of the problem to be solved, the number of hidden layers and the number of neurons in these layers may vary [19]. In a multilayer perceptron, information in the dataset is sent to the input layer, here some analyses are performed and then data is transferred to the next layer and here the number of layers changes according to the complexity (data dimensions, number of variables, relationships between variables, etc.) and dimensions of the dataset to be studied, with the condition that the number of layers is at least one. As the layers are interconnected, the output value obtained from one layer is organized as the input for another layer. The neurons in the layer act in connection with each other. The number of neurons is determined linked to the complex structure of the dataset. The final layer comprises an output layer where information or data from the input and hidden layers are operated. Figure 1 shows a multilayer perceptron model. The oval shapes in Figure 1 represent neurons, organized into output layers and hidden layers. Signals

TABLE 2

(values) from the input are subjected to a weighted total activation function (transfer function). In the figure, the curve shows the activation function (sigmoid) for each neuron. Support vector machines (SVM) are controlled machine learning algorithms that can be used for both classification and regression problems [20]. The basic function of this algorithm is to draw margins between two or more groups found on a plane and separate the groups from each other. This algorithm works with the logic that the drawn margin should be at the most distant point from the group members [21]. Currently, SVMs are used successfully for many real-world problems like classification of text and images, bioinformatic classification and detecting characters in handwriting [22]. SVM finds the data points in different classes and attempts to draw lines between them. The chosen data points are called support vectors, while the boundaries are called hyperplanes. The algorithm pays attention to each data pair until the closest pair in each class is found and a straight line (or plane) is drawn between them. In situations where input data can be linearly separated creating a hyperplane is simpler. However, generally, the classification regions overlap and it appears that no single hyperplane can complete the boundary function. In this situation, support vector machines create kernel functions to reflect the data at higher dimensions and complete the classification process [22].

The decision function for a two-class problem that can be linearly separated can be written by Equation 1 [21].

$$f(x) = \text{sign}(\sum_{i=1}^n \alpha_i y_i(x \cdot x_i) + b) \quad (1)$$

In situations where two classes cannot be clearly divided along a broad margin, the ξ_i parameter symbolizing crossed margins enters the target function and the aim is to minimize this parameter. In this situation when classes cannot be divided in a linear way, Equation 2 minimizes this. This equation is called the soft margin. Additionally, the C parameter in the equation is an equilibrium parameter balancing margin and misclassification rates. The larger the C value, the larger the importance given to the error; in other words, the method is more sensitive to variations in data compared to the available data [23].

$$P = \frac{1}{2} \|w\|^2 + C \sum_{i=1}^n \xi_i, \quad (y_i(w x_i + b) \geq 1 - \xi_i \text{ ve } \xi_i \geq 0) \quad (2)$$

In nonlinear support vector machines, in situations where it is not possible to perform linear classification, data is converted to a higher dimension based on the principle of dividing two classes with a hyperplane. The conversion to higher dimensions uses functions with various features. These functions are called kernel functions [23, 24].

The inner product is used for linear classifiers ($K(x_i, x_j) = x_i^T x_j$). If each data point is mapped to the higher-dimensional

attribute space by some transformations ($\Phi: x \rightarrow \varphi(x)$), then the inner product can be shown by Equation 3.

$$K(x_i, x_j) = \varphi(x_i)^T \varphi(x_j) \quad (3)$$

In Equation 3, $K(x_i, x_j)$ is the kernel function and in low-dimensional input space, it is sufficient to calculate this function instead of the high dimensional inner product [25].

The kernel functions used in the study are given in Table 4.

TABLE 4
KERNEL FUNCTIONS USED IN THE STUDY

Kernel	Notation
Linear	$k(x_i, x_j) = x_i^T x_j$
Polynomial	$k(x_i, x_j) = (1 + x_i^T x_j)^d$
Radial Basis Function	$k(x_i, x_j) = e^{-\gamma \ x_i - x_j\ ^2}, \quad \gamma > 0, \quad \gamma = 1/(2\sigma^2)$

3. RESULT AND DISCUSSION

The study examined 138 different models created from four different datasets with combinations of hyperparameters in machine learning methods. The results for the most successful, least successful and default models for the datasets and algorithms related to these models are given in Tables 5, 6, 7, and 8.

According to Table 5, the model obtained by changing the parameters of the default parameter model for the linear kernel function was not observed to cause a large change. Additionally, in terms of the use of the C parameter in the linear kernel, increasing the value of this parameter did not contribute to improving the model performance; in fact, it lowered model performance in some datasets (II and IV). This situation may be expected considering the low number of variables in these datasets. The C parameter is an equilibrium parameter balancing margin and misclassification rates, so considering large C values are more sensitive to variation in data [23], the use of small C values is required for lower variations. Additionally, more complicated decision curves may be obtained attempting to comply with all points in the data with large C values, so it should be considered that generalizing these decision curves to test data may be difficult [26]. Additionally, when the confusion matrix for model 1.1 is investigated, it appears 1045 mice were accurately classified (97% accuracy rate). However, it was determined that this model classified 8 mice in the memantine treatment group (c-CS-m) as the saline treatment group (c-CS-s) and 7 mice inversely as memantine group in spite of being in the saline treatment group.

TABLE 5
LINEAR KERNEL FUNCTION RESULTS FOR SUPPORT VECTOR MACHINES

Data Set	C ¹	Model No	Correctly Classified Instances	Accuracy (%)	Kappa Statistic	Mean Absolute Error	Root Mean Squared Error	Confusion Matrix ²
I	1	1.1*	1045	96.76	0.963	0.008	0.09	<pre> a b c d e f g h <-- 139 0 8 0 3 0 0 0 a 0 150 0 0 0 0 0 0 b 7 0 122 0 3 1 2 0 c 1 0 0 134 0 0 0 0 d 2 0 2 0 129 0 1 1 e 0 1 0 0 1 133 0 0 f 0 0 0 0 2 0 103 0 g 0 0 0 0 0 0 0 135 h </pre>
	10	1.2	1056	97.78	0.975	0.006	0.07	
II	1	2.1*	730	67.59	0.629	0.081	0.285	<pre> a b c d e f g h <-- 60 1 37 8 29 0 11 4 a 0 134 0 0 1 13 0 2 b 23 2 57 0 39 0 14 0 c 0 3 0 104 0 14 0 14 d 0 0 16 0 100 0 13 6 e 0 36 0 25 0 74 0 0 f 9 0 6 0 14 0 74 2 g 0 2 0 0 0 1 5 127 h </pre>
	100	2.3	691	63.98	0.588	0.09	0.300	
III	1	3.1*	42	58.33	0.523	0.104	0.323	<pre> a b c d e f g h <-- classified as 5 0 3 0 0 0 1 1 a = c-CS-m 0 9 0 0 0 1 0 0 b = c-SC-m 4 0 1 0 3 0 1 0 c = c-CS-s 0 0 0 7 0 1 0 1 d = c-SC-s 0 0 4 0 3 0 2 0 e = t-CS-m 0 3 0 2 0 4 0 0 f = t-SC-m 1 0 1 0 1 0 4 0 g = t-CS-s 0 0 0 0 0 0 0 9 h = t-SC-s </pre>
	10	3.2	43	59.72	0.539	0.100	0.317	
IV	1	4.1*	39	54.17	0.475	0.115	0.339	<pre> a b c d e f g h <-- classified as 3 0 5 0 0 0 1 1 a = c-CS-m 0 9 0 0 0 1 0 0 b = c-SC-m 4 0 1 0 2 0 2 0 c = c-CS-s 0 1 0 6 0 1 0 1 d = c-SC-s 0 1 4 0 4 0 0 0 e = t-CS-m 0 3 0 1 0 5 0 0 f = t-SC-m 2 0 0 0 1 0 3 1 g = t-CS-s 0 1 0 0 0 0 0 8 h = t-SC-s </pre>
	10	4.2	38	52.78	0.460	0.118	0.344	

¹C: Editing parameter, ²a=c-CS-m, b=c-SC-m, c=c-CS-s, d=c-SC-s, e=t-CS-m, f=t-SC-m, g=t-CS-s, h=t-SC-s, *: Default model.

According to Table 6, the model appeared to provide 71% success for classification with the default settings for dataset I, but changing the parameters increased the model performance to 99%. Additionally, changing the hyperparameter values for all datasets, especially dataset II, obtained very successful models, showing the effect of the hyperparameters is very significant. Additionally, when the confusion matrix for model 2.5 which accurately classified 616 mice is investigated, several of the most pronounced

errors in the model were classifying 85 mice from the saline treatment group (c-CS-s) as in the memantine treatment group (c-CS-m) and classifying 16 mice with context-shock behavior features as shock-context. Additionally, considering the use of the C parameter in the polynomial kernel in all datasets, the best performance was obtained when the C value was 100; additionally, the best performance was generally obtained when the polynomial degree was 3 (2nd degree in dataset III).

TABLE 6
POLYNOMIAL KERNEL FUNCTION RESULTS FOR SUPPORT VECTOR MACHINES

Data Set	C ¹	D ²	Model No	Correctly Classified Instances	Accuracy (%)	Kappa Statistic	Mean Absolute Error	Root Mean Squared Error	Confusion Matrix ³
I	1	2	1.4	745	68.98	0.64	0.08	0.28	
		3	1.5*	770	71.30	0.67	0.07	0.27	
I	100	3	1.11	1074	99.44	0.99	0.001	0.04	<pre> a b c d e f g h <-- 150 0 0 0 0 0 0 0 0 a 0 150 0 0 0 0 0 0 0 b 3 0 130 0 1 0 1 0 0 c 0 0 0 135 0 0 0 0 0 d 0 0 0 0 135 0 0 0 0 e 0 0 0 0 0 135 0 0 0 f 0 0 0 0 0 0 105 0 0 g 0 0 0 0 0 0 1 134 0 h </pre>
II	1	3	2.5*	616	57.04	0.506	0.107	0.328	<pre> a b c d e f g h <-- 121 0 0 25 0 0 1 3 1 a 0 95 0 33 0 22 0 0 0 b 85 0 31 16 1 0 2 0 0 c 0 0 0 134 0 1 0 0 0 d 35 0 4 0 93 0 3 0 0 e 0 15 0 82 0 38 0 0 0 f 55 0 7 3 14 0 26 0 0 g 3 6 0 46 0 2 0 78 0 h </pre>
		5	2.6	487	45.09	0.365	0.137	0.370	
III	1	2	3.10	43	59.72	0.538	0.107	0.317	<pre> a b c d e f g h <-- classified as 5 0 2 0 1 0 1 1 a = c-CS-m 0 9 0 0 0 1 0 0 b = c-SC-m 4 0 1 0 3 0 1 0 c = c-CS-s 0 1 0 6 0 1 0 1 d = c-SC-s 2 0 1 0 5 0 0 1 e = t-CS-m 0 3 0 1 0 5 0 0 f = t-SC-m 1 0 1 0 1 0 3 1 g = t-CS-s 0 0 0 0 0 0 0 9 h = t-SC-s </pre>
									3
III	1	3	3.5*	30	41.67	0.328	0.146	0.382	
		5	4.6	10	13.89	0.011	0.215	0.464	
IV	100	3	4.11	38	52.78	0.458	0.118	0.344	<pre> a b c d e f g h <-- classified as 7 0 3 0 0 0 0 0 a = c-CS-m 0 6 0 2 0 2 0 0 b = c-SC-m 3 0 3 0 2 0 1 0 c = c-CS-s 0 0 0 7 0 2 0 0 d = c-SC-s 2 0 1 0 3 2 1 0 e = t-CS-m 0 2 0 4 0 3 0 0 f = t-SC-m 3 0 1 0 1 0 2 0 g = t-CS-s 1 0 0 0 0 1 0 7 h = t-SC-s </pre>

¹C: Editing parameter, ²D: Polynomial degree, *: Default model, ³a=c-CS-m, b=c-SC-m, c=c-CS-s, d=c-SC-s, e=t-CS-m, f=t-SC-m, g=t-CS-s, h=t-SC-s

When the confusion matrix data for model number 3.21 given in Table 7 is investigated, it was determined that this dataset comprised 77 protein level measurements from 72 mice after removing repeated measures from the original dataset and that the model accurately classified 44 mice. However, it was

determined that this model classified 3 mice with trisomy genotype (t-SC-m) as control genotype (c-SC-m). Additionally, the model classified 2 mice in the trisomy genotype and memantine treatment group (t-SC-m) as control genotype and saline treatment group (c-SC-s).

TABLE 7
RBF KERNEL FUNCTION RESULTS FOR SUPPORT VECTOR MACHINES

Data Set	C ¹	Gamma ²	Model No	Correctly Classified Instances	Accuracy (%)	Kappa Statistic	Mean Absolute Error	Root Mean Squared Error	Confusion Matrix ³
I	1	0.01	1.13*	713	66.02	0.61	0.085	0.292	
	10	0.1	1.18	1080	100.0	1.0	0.0	0.0	<pre> a b c d e f g h <-- 150 0 0 0 0 0 0 0 a 0 150 0 0 0 0 0 0 b 0 0 135 0 0 0 0 0 c 0 0 0 135 0 0 0 0 d 0 0 0 0 135 0 0 0 e 0 0 0 0 0 135 0 0 f 0 0 0 0 0 0 105 0 g 0 0 0 0 0 0 0 135 h </pre>
II	1	0.01	2.13*	638	59.07	0.53	0.102	0.319	
	100	0.1	2.22	1064	98.52	0.983	0.003	0.061	<pre> a b c d e f g h <-- 149 0 0 0 0 0 0 1 a 0 146 0 0 0 4 0 0 b 2 0 131 0 0 0 2 0 c 0 0 0 134 0 1 0 0 d 0 0 0 0 135 0 0 0 e 0 4 0 0 0 131 0 0 f 1 0 0 0 1 0 103 0 g 0 0 0 0 0 0 0 135 h </pre>
III	1	0.01	3.13*	18	25	0.131	0.188	0.433	
	100	0.01	3.21	44	61.11	0.555	0.097	0.312	<pre> a b c d e f g h <-- classified as 6 0 2 0 0 0 1 1 a = c-CS-m 0 8 0 0 0 2 0 0 b = c-SC-m 4 0 2 0 2 0 1 0 c = c-CS-s 0 0 0 7 0 1 0 1 d = c-SC-s 2 0 0 0 4 0 2 1 e = t-CS-m 0 3 0 2 0 4 0 0 f = t-SC-m 2 0 0 0 1 0 4 0 g = t-CS-s 0 0 0 0 0 0 0 9 h = t-SC-s </pre>
IV	1	0.01	4.13*	18	25	0.131	0.188	0.433	
	100	0.1	4.22	43	59.72	0.539	0.101	0.317	<pre> a b c d e f g h <-- classified as 5 0 2 0 2 0 0 1 a = c-CS-m 0 8 0 0 0 1 0 1 b = c-SC-m 2 0 2 0 3 0 2 0 c = c-CS-s 0 2 0 5 0 1 0 1 d = c-SC-s 1 0 1 0 4 0 1 2 e = t-CS-m 0 1 0 1 0 7 0 0 f = t-SC-m 3 0 0 0 1 0 3 0 g = t-CS-s 0 0 0 0 0 0 0 9 h = t-SC-s </pre>
	10	4.24	9	12.5	-0.013	0.219	0.468		

¹C: Editing parameter, ²Gamma (γ): Kernel size, *: Default model. ³a=c-CS-m, b=c-SC-m, c=c-CS-s, d=c-SC-s, e=t-CS-m, f=t-SC-m, g=t-CS-s, h=t-SC-s

According to Table 7, the success rate for the default model for dataset I was 66%, and changing the parameters increased this rate to 100%. Additionally, all kernel functions used for dataset I displayed good performance, with the most successful model determined to be RBF (Tables 5, 6, 7). When the results for the support vector machines for the first dataset are assessed, especially adjusting the polynomial and RBF kernel parameter values according to the dataset was determined to significantly increase model performance. Additionally, changing the hyperparameter values in the RBF kernel function obtained very successful models among kernel functions used for dataset II; in this context, the most successful kernel was determined to be RBF (Model no: 2.22, accurate classification rate 99%, Table 7). When the results for the C parameter in the RBF kernel are investigated, the C value was 100 in the most successful models; additionally,

when the gamma value was 0.1 (gamma 0.1, dataset III) the most successful models were obtained in general. Based on these results, it was determined that the hyperparameter dataset was very important especially for polynomial and RBF kernel functions in support vector machines. Parallel to our study results, Van Rijn and Hutter [27] compared the performance of a variety of algorithms on several datasets and stated that the same hyperparameters were typically important for several datasets in these studies and that gamma and C parameters were very important for SVM. Additionally, when results for other datasets apart from the original dataset are investigated, it appears that the classification performance for models created with these datasets were lower compared to the default models. Machine learning algorithms require many data in order to learn the basic structure of data during the training process. The low dimensions of the dataset affect the

model performance and lower the chance of performing good generalization of the model. For this reason, higher amounts of training data in machine learning ensure higher performance [28, 29]. Therefore, this issue may be shown as the cause of the low default model performance in these data sets. Additionally, it was determined that the most successful models created with support vector machines were created with the RBF kernel. Additionally, the results obtained from the linear kernel for dataset I and II were determined to be very close to the RBF kernel results. This situation may be assessed as due to the excess number of variables in these two models

because the study by Hsu et al. [9] reported that in situations with high variable (feature) numbers, it is necessary to use the linear kernel. In their study, they stated that a large number of features also may not require data to be matched to a higher dimensional space and may improve non-linear mapping performance. They stated that RBF was as good as the linear kernel in this dataset; however, this function contains two parameters (C, gamma) and this increases operation load, while the use of the linear kernel containing only the C parameter is appropriate.

TABLE 8
RESULTS OBTAINED FROM ARTIFICIAL NEURAL NETWORKS

Data Set	Hidden Layer	Neuron Number	Model No	Correctly Classified Instances	Accuracy (%)	Kappa Statistic	Mean Absolute Error	Root Mean Squared Error	Confusion Matrix ¹
I	1	42	1.30*	1074	99.44	0.99	0.005	0.033	<pre> a b c d e f g h <-- 149 0 0 0 1 0 0 0 a 0 150 0 0 0 0 0 0 b 1 0 132 0 2 0 0 0 c 0 0 0 134 0 0 0 1 d 0 0 1 0 134 0 0 0 e 0 0 0 0 0 135 0 0 f 0 0 0 0 0 0 105 0 g 0 0 0 0 0 0 0 135 h </pre>
	2	2	1.31	567	52.5	0.45	0.139	0.266	
II	1	8	2.28*	918	85	0.828	0.049	0.179	<pre> a b c d e f g h <-- 103 0 16 1 20 0 10 0 a 1 133 0 0 0 15 0 1 b 12 0 114 0 1 1 7 0 c 0 0 0 112 0 9 0 14 d 0 0 7 0 121 0 5 2 e 0 19 0 4 0 112 0 0 f 3 0 4 0 4 2 90 2 g 0 2 0 0 0 0 0 133 h </pre>
	2	10	2.34	977	90.46	0.891	0.031	0.139	
III	1	10	3.29	50	69.44	0.650	0.102	0.242	<pre> a b c d e f g h <-- classified as 6 0 3 0 1 0 0 0 a = c-CS-m 0 8 0 2 0 0 0 0 b = c-SC-m 3 0 3 0 2 0 1 0 c = c-CS-s 0 0 0 9 0 0 0 0 d = c-CS-s 2 0 1 0 5 0 1 0 e = t-CS-m 0 1 0 1 0 7 0 0 f = t-SC-m 1 0 0 0 0 0 5 1 g = t-CS-s 0 1 0 0 0 1 0 7 h = t-SC-s </pre>
	2	42	3.30*	48	66.67	0.618	0.095	0.244	
IV	1	4	4.26	35	48.61	0.411	0.151	0.309	<pre> a b c d e f g h <-- classified as 5 0 2 1 0 0 2 0 a = c-CS-m 0 4 0 1 0 5 0 0 b = c-SC-m 2 0 3 0 4 0 0 0 c = c-CS-s 0 2 0 5 0 1 0 1 d = c-SC-s 2 0 0 0 6 0 0 1 e = t-CS-m 0 2 0 2 0 5 0 0 f = t-SC-m 3 0 0 1 2 0 1 0 g = t-CS-s 0 1 0 0 0 2 0 6 h = t-SC-s </pre>
	2	8	4.28*	31	43.06	0.347	0.150	0.322	
	2	2	4.30	10	13.89	0.001	0.219	0.331	

¹a=c-CS-m, b=c-SC-m, c=c-CS-s, d=c-SC-s, e=t-CS-m, f=t-SC-m, g=t-CS-s, h=t-SC-s, *: Default model.

Table 8 presents the results obtained from the artificial neural network. Accordingly, the classification performance for dataset IV was low, which again is assessed as linked to the low observation numbers and variable numbers in the dataset [28,29]. Additionally, the most successful model in this dataset was a single hidden layer and 4 neuron model number 4.26 (49% accuracy). When the confusion matrix for this model is investigated, 35 mice were accurately classified in the model; however, 5 mice with control genotype (c-SC-m) were classified as trisomy genotype (t-SC-m). Additionally, the most successful model for dataset I was model number 1.30 with 99% accurate classification rate. This model comprises a single hidden layer and there were 42 neurons in the hidden layer. This model is also the default model and the total number of neurons in the hidden layer is equal to the mean of the sum of the number of independent variables and the number of classes. This situation shows the importance of the appropriate setting of hyperparameters to the dataset in terms of model performance. An advantage of the Weka program used in the study is that the number of neurons in the hidden layer is automatically adjusted according to the dataset by taking as the default value [16]. The adjustment process generally causes better hyperparameter settings compared to the default values. Studies by Koch *et al.* [4] reported that even in situations where default settings provide good results, the hyperparameter adjustment process performs intuitive verification of these settings and has significant value in ensuring the construction of a model with higher accuracy.

4. CONCLUSION

According to the results obtained in our study;

- For all datasets, especially in polynomial and RBF kernel function support vector machines and artificial neural networks, the arrangement of hyperparameters according to the dataset is very important for classification performance,
- In situations with low numbers of variables and observations, machine learning methods displayed lower performance,
- In situations with a low number of variables, the effect of hyperparameters can be said to gain greater importance.

Generally, we recommend the following strategies for training of new networks due to these results;

Observation number > variable number

- Performance of all kernels used in support vector machines are close to each other,
- The effect of hyperparameters in polynomial and RBF kernels are more important,
- Support vector machines are more successful than artificial neural networks.

Observation number >> variable number

- RBF and polynomial kernels are more successful than the linear kernel,
- The effect of hyperparameters in all kernels is much more important,
- Support vector machines are more successful than artificial neural networks.

Observation number < variable number

- All kernel performances used in support vector machines are close to each other,

- The effect of hyperparameters in polynomial and RBF kernels are much more important,
- Artificial neural networks are more successful than support vector machines.

When researchers apply machine learning methods, they need to focus on the most important hyperparameters for the dataset in different situations, determine situations where hyperparameters are more important and significant, and decide on methods accordingly.

ACKNOWLEDGEMENT

This study was presented as a presentation at the Karadeniz 3rd International Applied Sciences Congress (25-26 April 2020, Ordu, Turkey) and printed as an abstract in the congress booklet.

REFERENCES

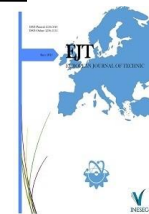
- [1] A. Gandomi, M. Haider, "Beyond the hype: Big data concepts, methods, and analytics", *International Journal of Information Management*, vol. 35, pp. 137-144, 2015.
- [2] A. Oussous, F.Z. Benjelloun, A.A. Lahcen, and S. Belfkih, "Big data technologies: A survey", *Journal of King Saud University Computer and Information Sciences*, vol. 30, pp. 431-448, 2018.
- [3] B. Wang, N.Z. Gong, "Stealing hyperparameters in machine learning", *IEEE Symposium on Security and Privacy*. DOI 10.1109/SP.2018.00038
- [4] P. Koch, B. Wujek, O. Golovidov, and S. Gardner, "Automated Hyperparameter tuning for effective machine learning", SAS514-2017. SAS Institute Inc. USA. 2017.
- [5] G. Ser, C. T. Bati, "Determining the best model with deep neural networks: Keras application on mushroom data", *YYU J. AGR. SCI.* vol. 29, no.3, pp. 406-417, 2019.
- [6] M. Claesen, B.D. Moor, "Hyperparameter search in machine learning" *The XI Metaheuristics International Conference*. arXiv:1502.02127v2 [cs.LG] 6 Apr 2015.
- [7] L.C. Padierna, M. Carpio, A. Rojas, H. Puga, R. Baltazar, and H. Fraire, "Hyper-parameter tuning for support vector machines by estimation of distribution algorithms." In *Nature-Inspired Design of Hybrid Intelligent Systems*. pp.787-800, 2017.
- [8] P. Probst, A.L. Boulesteix, and B. Bischl, "Tunability: Importance of Hyperparameters of Machine Learning Algorithms", *J. Mach. Learn. Res.*, vol. 20, no. 53, pp.1-32, 2019.
- [9] C.W. Hsu, C.C. Chang, C.J. Lin, "A practical guide to support vector classification", <http://www.csie.ntu.edu.tw/~cjlin/papers/guide/guide.pdf>. Date of access: 12.10.2020
- [10] M. Prevolnik, D. Škorjanc, M. Čandek-Potokar, and M. Novič, "Application of artificial neural networks in meat production and technology", *Computer and Information Science*, vol. 11, pp. 223-240, 2011.
- [11] S. Pour Hamidi, M.R. Mohammadabadi, M. Asadi Foozi, and H. Nezamabadi-pour, "Prediction of breeding values for the milk production trait in Iranian Holstein cows applying artificial neural networks", *Journal of Livestock Science and Technologies*, vol. 5, no.2, pp. 53-61, 2017.
- [12] K. Liakos, S.P. Moustakidis, G. Tsiotra, T. Bartzanas, D. Bochtis, and C. Parisses, "Machine Learning Based Computational Analysis Method for Cattle Lameness Prediction", *HAICTA* pp. 128-139, 2017.
- [13] H. Bisgin, T. Bera, H. Ding, H. G. Semey, L. Wu, Z. Liu, and W. Tong, "Comparing SVM and ANN based machine learning methods for species identification of food contaminating beetles", *Scientific reports*, vol. 8, no.1, pp.1-12, 2018.
- [14] UCI Database, 2020. <https://archive.ics.uci.edu/ml/datasets/Mice+Protein+Expression#>
- [15] C. Higuera, K.J. Gardiner and K.J. Cios, "Self-Organizing Feature Maps Identify Proteins Critical to Learning in a Mouse Model of Down Syndrome", *PLoS ONE* vol. 10, no:6, e0129126. [Web Link] [journal.pone.0129126](https://doi.org/10.1371/journal.pone.0129126), 2015.
- [16] E. Frank, A.H. Mark, H.W. Ian, "The WEKA Workbench. Online Appendix for Data Mining: Practical Machine Learning Tools and Techniques", Morgan Kaufmann, Fourth Edition, 2016.

- [17] C. Aydin, "Classification of Fire Station Needs Using Machine Learning Algorithms", *European Journal of Science and Technology*, no.14, pp. 169-175, 2018.
- [18] C.C. Aggarwal, "Neural networks and deep learning", Springer, 2018.
- [19] S. Haykin, "Neural networks and learning machines", Pearson Education Canada, 2008.
- [20] J. Rasmi, <https://www.hackerearth.com/blog/developers/simple-tutorial-svm-parameter-tuning-python-r/>. Date of access: 13.09.2020
- [21] T. Kavzaoglu, I. Colkesen, "Investigation of the effects of kernel functions on the classification of support vector machines and application images", *Journal of Map*, vol. 44, pp. 73-82, 2010.
- [22] C. Dawson, <https://towardsdatascience.com/a-guide-to-svm-parameter-tuning-8bfe6b8a452c>. Date of access: 04.08.2020
- [23] L. Igual, S. Seguí, "In Introduction to Data Science" pp. 1-4. Springer, Cham, 2017.
- [24] A. Moore, "Support vector machines", <https://www.autonlab.org/media/tutorials/svm15.pdf>. Date of access: 04.01.2020.
- [25] A. Guran, M. Uysal, and O. Dogrusoz, "Effects of support vector machine parameter optimization on sentiment analysis", *DEU Faculty of Engineering Journal of Engineering Sciences*, vol. 16, no. 48, pp. 86-93, 2014.
- [26] R. Pupale, <https://towardsdatascience.com/https-medium-com-pupalerushikesh-svm-f4b42800e989>. Date of access: 11.11.2020
- [27] J. N. Van Rijn, F. Hutter, "Hyperparameter importance across datasets", In *Proceedings of the 24th ACM SIGKDD International Conference on Knowledge Discovery & Data Mining*, pp. 2367-2376, 2018.
- [28] T. Shaikhina, D. Lowe, S. Daga, D. Briggs, R. Higgins, and N. Khovanova, "Machine learning for predictive modelling based on small data in biomedical engineering", *IFAC-PapersOnLine*, vol. 48, no. 20, pp. 469-474, 2015.
- [29] B. Xu, W. Wang, G. Falzon, P. Kwan, L. Guo, Z. Sun, and C. Li, "Livestock classification and counting in quadcopter aerial images using Mask R-CNN", *International Journal of Remote Sensing*, pp. 1-22, 2020.

BIOGRAPHIES

Cafer Tayyar Bati obtained his BSc degree from Van Yüzüncü Yıl University, Department of Mathematics in 2007, and his master's degree from Van Yüzüncü Yıl University, Faculty of Agriculture, Department of Animal Science/Biometry and Genetics in 2017. He started his Ph.D. studies in the same department in 2017. He is still continuing his Ph.D. education and working as a Mathematics teacher at Ipekyolu Anatolian High School. He carries out machine learning studies in the field of animal husbandry.

Gazel Ser graduated from Van Yüzüncü Yıl University, Faculty of Agriculture, Department of Food Engineering in 2001. She completed his master's degree in 2004 and his Ph.D. in 2011 at Van Yüzüncü Yıl University, Institute of Science, Department of Animal Science, Biometrics and Genetics. She was appointed as an assistant professor to Van Yüzüncü Yıl University, Faculty of Agriculture, Department of Animal Science in 2013, where she worked as an expert. She received the title of Associate Professor as of 2017 and still works as an Associate Professor in the same department.



Investigation of Mechanical And Tribological Properties of Boric Acid Reinforced Composite Plates

Taner Aydın¹ , Kadir Turan^{2*} , Nejat Yıldırım Sari³ 

¹Dicle University, Mechanical Engineering Department, Diyarbakır, Turkey.(e-mail: taner.aydin@dicle.edu.tr).

²Dicle University, Mechanical Engineering Department, Diyarbakır, Turkey.(e-mail: kturan@dicle.edu.tr).

³Kocaeli University, Mechanical Engineering Department, Kocaeli, Turkey. (e-mail: nsari@kocaeli.edu.tr).

ARTICLE INFO

Received: Apr., 21. 2021

Revised: Feb., 05. 2021

Accepted: Dec., 27. 2021

Keywords:

Composite materials

Boric acid

Wear resistance

Tensile test

Hybrid composite material

Corresponding author: *Kadir Turan*

ISSN:2536-5010 | e-ISSN: 2536-5134

DOI: <https://doi.org/10.36222/ejt.923954>

ABSTRACT

In this study, the mechanical and tribological properties of unidirectional glass fiber/polyester resin and unidirectional carbon fiber / polyester resin composite materials reinforced with boron particles have been investigated by experimental methods. Composite plates were produced by hand lay-up method using polyester resin mixed with boric acid particles (H_3BO_3) with a specific gravity of 1.51 g/cm³ and a molecular weight of 61.83 g/mol, which were utilized as boron particles. As particle reinforcement, 1%, 5% and 10% boron oxide polyester resin mixture was obtained. The effects of particle reinforcement on mechanical and tribological properties were investigated. As a result of the experimental studies, it was determined that, due to the increase in the particle ratio, the wear resistance increased by between the ratios 5% and 50% in some samples compared to the samples not reinforced with boric acid particles and the tensile strength improved up to 32% in some samples.

1. INTRODUCTION

Due to the decreasing resources and increasing needs, the discovery and development of new materials in harmony with the developing technology have emerged in order to meet those needs. As responses to the aforementioned needs, composite materials have emerged as materials with new properties, those that are different from the materials combined to form them. One of the most important features of composites is that they can respond to unlimited demands with unlimited production options. They are produced by wrapping strong, stiff fibers in relatively weaker and less solid matrix materials [1]. The materials which have gained more and more usage in industrial market, that have high technical performance and knowhow requirement an in addition to those have high added value can be called high-tech materials.[2]

Composite materials are widely used in areas such as automotive, aerospace, textile industry, sports equipment, food and construction industry. Usage areas of composite materials continues to grow day by day in the world and in our country. The composite material industry has come to a very important point thanks to various innovations and advanced technology applied on the materials that make them chemically, physically

and mechanically different, forming the composite material, matrix materials and reinforcing fibers. Polymer matrix composite materials are the most widely used composite materials. Fibers such as carbon, aramid and glass are especially used to increase the strength values of polymer matrix composite materials. In addition to the fibers used, it is also possible to use various particles by adding them to polymer matrix composite materials because their properties such as wear resistance, rigidity and bending strength are not good enough. The addition of the mentioned particles highly affects the physical and mechanical properties of the composite material [3-4]. There are many studies on particle reinforced composite materials in the literature. Navaneethakrishnana et al. [5] prepared boron nitride (BN) / epoxy nano composites containing different percentages of BN particles by liquid casting process. They analyzed the mechanical properties of composites such as hardness, tensile, bending and impact strength. Venkatesh Vijayaraghavan et al. [6] presented a comprehensive study with the help of molecular dynamic analysis of tensile loading mechanics of polyethylene (PE) nano composites reinforced with BN-C nano layers. They observed that the geometry and lattice arrangement of BN - C nano layers affect the tensile load properties of nano

composites. MeysamRahmat et al. [7] examined the quasi-static and dynamic performances of epoxy in two different classes which are with and without Boron nitride nanotubes (BNNTs). In addition to pure epoxy material, they also tested samples with concentrations of 1% and 2% BNNT by weight. In addition, they noted that the BNNT-modified tensile specimens showed up to 7% increase in tensile strength, up to 16% increase in modulus, and a 9% decrease in strain rate. Xiao Zhang et al. [8] produced a BN/PVDF composite by hot press method in their study. They stated that the distribution of BN is homogeneous, dense and directed towards PVDF (Polyvinylidene fluoride). They also stated that the thermal conductivity and tensile performance of the composite were greatly improved. Also, the thermal conductivity was measured as 0.57 W / (mK), which is an increase of 307% compared to pure PVDF. Burroughs et al. [9] investigated the utility of boric acid particles in PTFE and epoxy composite materials that are in slip contact with stainless steel. They stated that when boric acid is used as a filler, it reaches the level of 10⁻⁵ mm³ / N-m by providing a twenty-year decrease in the rate of wear. They reported that with sufficient ambient moisture, a reduced wear rate can be achieved without causing counter-surface wear and the friction of PTFE will be further reduced. They stated that boric oxide fillers in such environments can reduce the friction coefficient of epoxy from $\mu > 0.7$ to $\mu = 0.07$. Cavdar et al. [10] investigated the effect of boron-based flame retardants (BbFRs) and fiber loading on the mechanical, fire and thermal performances of impregnated spruce wood (WF), which is a filled high density polyethylene composite. For this purpose, they impregnated WF with boric acid solution, borax and their mixtures and dried before composite production. The effect of the separation on the limiting oxygen index (LOI) levels of the BbFR samples were also investigated. According to the test results, samples with borax provided better mechanical properties compared to samples containing boric acid and showed a 19% improvement in tensile modulus in those with 40% fiber loading compared to control samples. Hou et al. [11] investigated the effects of modified BN content on thermal and insulating properties by using hexagonal boron nitride micro particles modified with 3-aminopropyl triethoxysilane (APTES) to fabricate thermally conductive epoxy / BN composites. They found that the using h-BN particles as reinforcement to the epoxy matrix significantly increased the thermal conductivity of composites. They found the thermal conductivity of composites with a modified BN loading of 30% by weight is 6.14 times higher than that of pure epoxy, at 1.178 W m⁻¹ K⁻¹. Myshkin et al. [12] stated in their study that the tribological behavior of polymers was reviewed from the middle of the 20th century to the present. They said that with the new contact tack gauge, the surface energy of different coatings can be determined. They discussed friction with adhesion and deformation components. They demonstrated how load, sliding speed and temperature affect friction. Li et al. [13] have stated as their article's main purpose, using solid lubricants such as polytetrafluoroethylene (PTFE), ultra-high molecular weight polyethylene (UHMWPE) and a combination of the two, is to further optimize the tribological properties of glass fiber reinforced PA6 (GF / PA6,15 / 85 by weight) for high performance friction materials. They investigated the synergies of the tribological properties of these materials resulting from the inclusion of PTFE and UHMWPE. They stated that the results showed that at a load of 40 N and a speed of 200 rpm, PTFE was effective in improving the tribological abilities of the matrix material. They found that the combination of PTFE and UHMWPE further reduced the

friction coefficient of composites mixed with only PTFE or UHMWPE. They also discussed the effects of load and speed on tribological behavior. In order to better understand the mechanism of wear, they examined the eroded surfaces with a scanning electron microscope. Karatas et al. [14] stated that polyamide 6,6 (PA6,6) is one of the widely used engineering polymers and is being used for various applications. Moreover, they stated that the tribological and mechanical performance of PA6,6 could be improved by adding fibers or particles. However, they stated that the properties of reinforced PA6,6 matrix composites would be affected by many factors. They explained that the interfacial adhesion between the reinforcement and the matrix material is one of these factors and that good interfacial adhesion is required to obtain good final properties. They aimed to improve the tribological and mechanical properties of carbon fiber reinforced PA6,6 composites by improving fiber-matrix interaction by using graphen nanoplatelet (GNP) and 1,4-phenylene-bis-oxazoline (PBO). They performed adhesive wear test, tensile test, dynamic mechanics, differential scanning calorimetry and scanning electron microscopy analyses. As a result, all test results showed that composites coded CF_0.5GNP_PBO exhibit improved tribological and mechanical properties among all composites.

In this study, it is aimed to determine the wear behavior and mechanical properties of composite plates reinforced with boron particles. For this purpose, boric acid particles with a specific gravity of 1.51 g / cm³ (20 °C) and a molecular weight: 61.83 g / mol were mixed with polyester resin in the ratio of 1%, 5% and 10% by weight. Glass fiber / polyester and carbon fiber / polyester composite plates were produced by absorbing the obtained boric acid-added polyester resin on unidirectional glass fiber and unidirectional carbon fibers by hand lay-up and cold press method. Glass fiber / polyester and carbon fiber / polyester composite plates were produced with neutral resin as the control group. Wear tests and tensile tests of the composite plates obtained were applied. The obtained results are presented in tables and graphics.

2. EXPERIMENTAL STUDY

In this study, unidirectional glass fiber with a density of 250 g/m², turquoise brand polyester resin which is a non-thixotropic, non-accelerated, low reactive, low viscosity, orthophthalic based unsaturated suitable for hand lay-up and spray applications. It has the ability to quickly wet the fiber, coded as TP 220 and boric acid particles (H₃BO₃) with a specific weight of 1.51 g/cm³ (20 °C) and a molecular weight: 61.83 g/mol which were supplied from Etimaden plants have been used. Composite materials containing unidirectional glass fiber and carbon fiber are prepared by reinforcing with 1%, 5% and 10% boric acid by weight and also without reinforcement as pure. 1%, 5% and 10% by weight of boric acid was mixed into the polyester resin and mixed with the help of a mixer. The obtained boric acid reinforced polyester resin was impregnated on each fiber layer by hand lay-up method and at the end, it was left to cure for 12 hours under 5 MPa pressure in cold press. Figure 1 shows the production method.

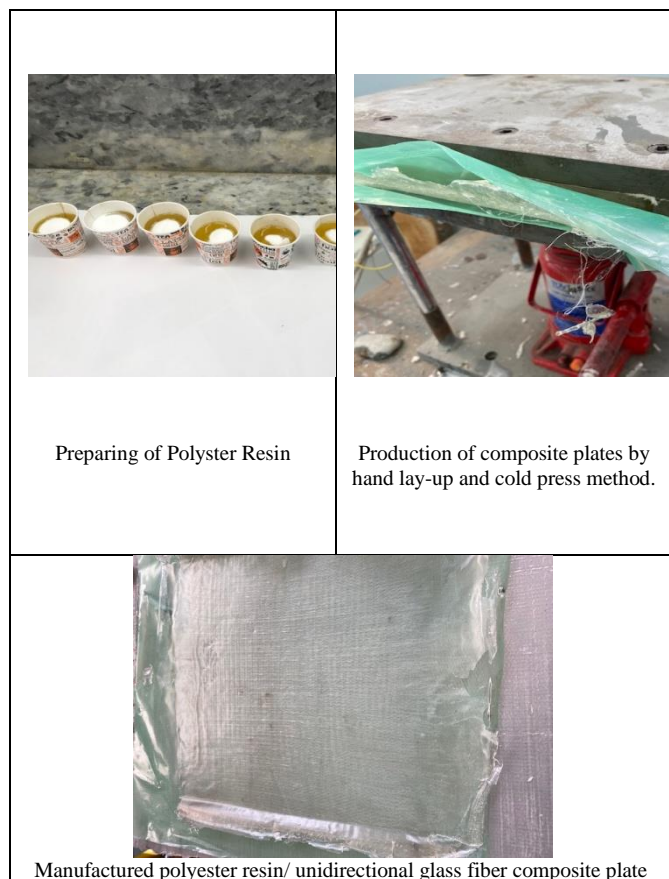


Figure 1 Production Method

Boric acid composition ratios and codes of the samples produced within the scope of the study are given in Table 1.

TABLE I

BORIC ACID COMPOSITION RATIOS AND CODES OF SAMPLES		
Sample Name	Boric Acid Reinforcement Percentage	Symbolic Notation
Unidirectional Glass Fiber	Pure	N-0-TYCF
	1%	1-0-TYCF
	5%	5-0-TYCF
	10%	10-0-TYCF
Unidirectional Carbon Fiber	Pure	N-90-TYCF
	1%	1-90-TYCF
	5%	5-90-TYCF
	10%	10-90-TYCF

2.1 Wear Test

Wear test was applied in order to determine the tribological properties of unidirectional glass fiber and carbon fiber reinforced composite materials containing neutral, 1%, 5% and 10% boric acid by weight, by cutting the plates obtained in 300 mmx215mm dimensions and 1.2 mm thickness in 30x30 mm dimensions. The relevant test was carried out using a

"Nanovea" brand "pin-on-disc" type tribometer device in Kocaeli University, Mechanical Engineering Department, Construction Laboratory. The wear test device is shown in Figure 2.

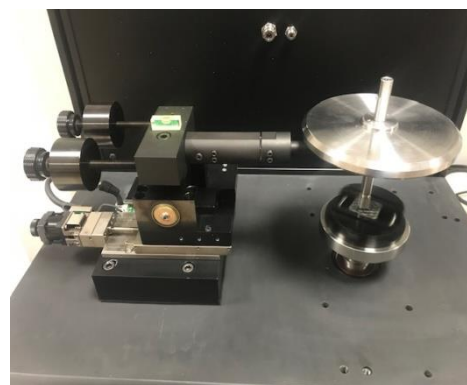


Figure 2. Nanovea Brand Wear Test Device

During the test, a 3 mm radius AISI 52100 steel metal ball was fixed to the load arm. The sample was placed on a rotating disk with a friction radius of 5 mm. All wear tests were carried out with 150 RPM rotation speed, 20 N contact load and sliding distance set to 50 m. During the test, the deformation on the samples was observed and recorded. The results of the wear test were automatically recorded by the computer, and the graphics and tables below were created based on these data.

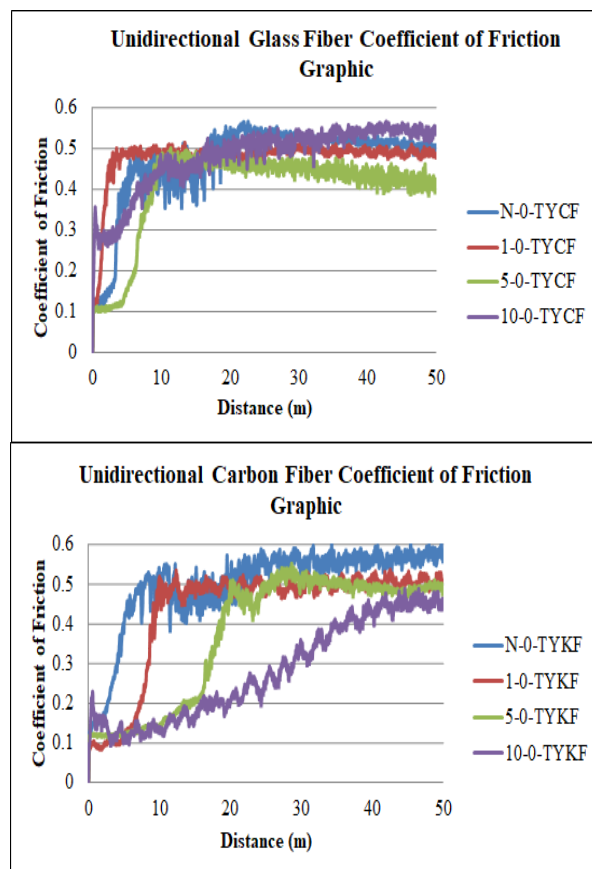


Figure 3. Coefficient of Friction Graphics Obtained As a Result of The Wear Test

The effect of boric acid reinforcement on the friction coefficient according to the sliding distance is shown in Figure 3. Due to the weak Van der Waals bonds of the solid lubricants,

the bonds between the two-dimensional layers cause easy sliding properties between the layers during the wear test period. In this case, it causes the lubrication effect of boric acid to appear and thus to reduce the friction coefficient.

2.2 Static Tensile Test

Static tensile tests were carried out at the Dicle University Mechanics laboratory and Dicle University Central laboratories. Tests were carried out in 3 samples from each prepared sample. During the tests, an Instron BS 8801 servo hydraulic tensile test device with a capacity of 100 kN was used. Tests were carried out in accordance with ASTM standards at room temperature. (ASTM - D, 1982). Tests have been carried out with the assumption that ambient humidity has no effect. The device is set so that the drawing speed is 1mm/min. The lower jaw of the test device is movable and the upper jaw is fixed. When the samples are being positioned in the device, attention has been paid to ensure that there is no angular displacement between the lower jaw and the upper jaw so that equal distribution of the force applied to both sides is ensured. During the test, the ways in which the samples were damaged were observed and the necessary information notes were taken. The damage loads and displacements obtained after the relevant test was applied were automatically recorded on the computer and graphics and tables were created using this data. Figure 4 shows the test setup.



Figure 4. Instron Brand Tensile Test Device

In the static tensile tests applied to the produced composite plates, $[0^\circ]_4$ unidirectional glass fiber and $[0^\circ]_4$ carbon fiber plates were used. While the plates were being produced; into the polyester resin, 1%, 5% and 10% by weight of boric acid was added and non-reinforced polyester resin was used. In static tensile tests, three samples were produced for each parameter and the experiments were repeated. The obtained load-displacement ratios are presented in Figure 5.

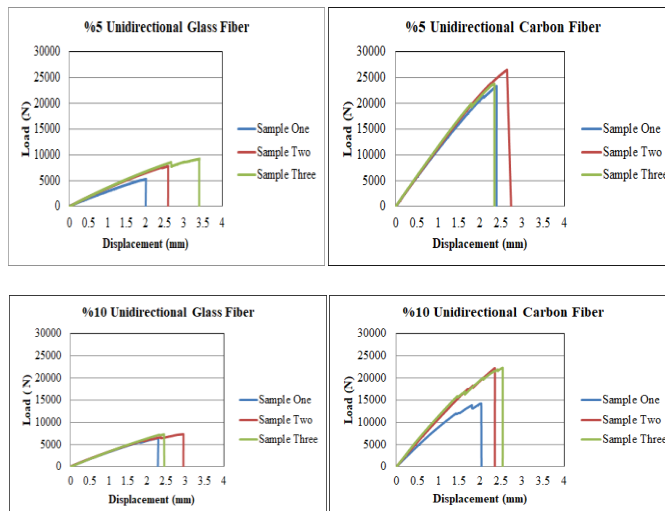
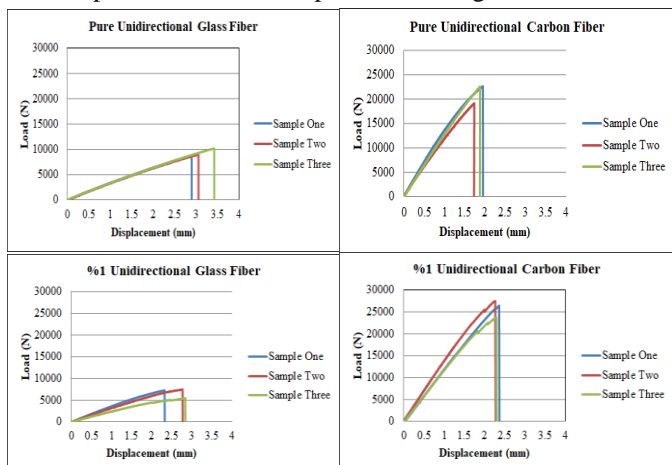


Figure 5. Graphics of Load (N) And Displacement (mm) Obtained As a Result of Tensile Test

In Figure 5, the load/displacement results of unidirectional glass and carbon fiber reinforced composite materials prepared by neutral and adding 1%, 5% and 10% boric acid by weight are shown graphically.

As can be seen from the figure, the load/displacement graphs of unidirectional glass fiber and unidirectional carbon fiber hybrid composite materials increase linearly. It is seen that damage occurs by instant breakage. The numbers of the samples are shown as 1, 2 and 3 in the graphics.

3. RESULTS AND DISCUSSION

In this study, the tribological and mechanical properties of the composite materials was experimentally investigated as the effect of the addition of boric acid in various additive ratios to the matrix material. The results were evaluated by applying the wear test and tensile test to the samples prepared by adding 1%, 5% and 10% boric acid by weight.

3.1. Effects of using boric acid as reinforcement for wear resistance

As a result of the wear tests, the average friction coefficient values obtained as a result of the wear test of polyester/unidirectional glass fiber and polyester/unidirectional carbon fiber composite plates, which were not reinforced and reinforced with 1%, 5% and 10% by weight of boric acid, are presented in Figure 6.

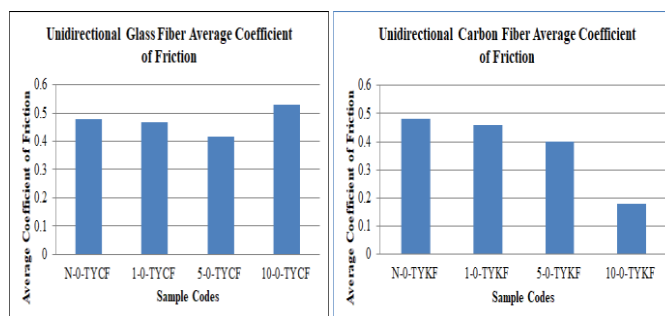


Figure 6. Wear Average Coefficient Variation Graph of Boric Acid Reinforced $[0^\circ]_4$ Polyester/Unidirectional Glass Fiber And $[0^\circ]_4$ Polyester/Unidirectional Carbon Fiber Composites.

It is seen from the literature that boric acid is used as a solid lubricant. Tribological contacts (friction and wear) typically

result in the transfer of a thin layer of material from the surface of the solid lubricant coating to the opposite surface, commonly known as a transfer film or tribofilm. A good transfer film formed by matrix material and solid lubricant increases the wear resistance by decreasing the friction coefficient. Boric acid also has a lubricating effect due to its good sliding property between its layers. Thanks to this effect, the friction coefficient of the polymer composite material decreases during the wear process. [9-16] Under the light of these evaluations, it can be seen in Figure 3 that as the boric acid ratio increases, the wear resistance of the unidirectional glass fiber composite material increases.

The reason why the friction coefficient of 10% boric acid - added polymer composite material is higher than other composite materials with unidirectional glass fiber samples may be that boric acid has agglomeration in this composite sample. [17-19]

3.2. Effects of using boric acid as reinforcement for tensile strength

The average tensile strength values obtained as a result of static tensile tests and the wear test of polyester/unidirectional glass fiber and polyester/unidirectional carbon fiber composite plates, which are not reinforced and reinforced with 1%, 5% and 10% boric acid by weight, are presented in Figure 7.

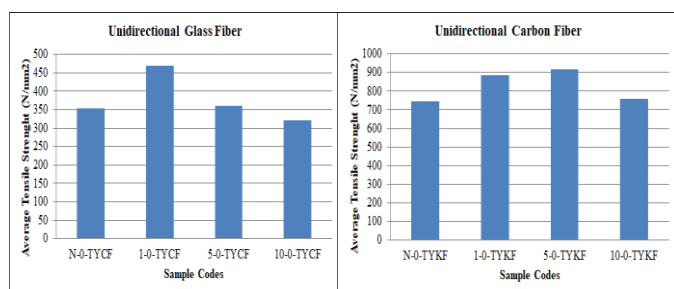


Figure 7. Average Tensile Strength Values of Unidirectional Glass Fiber and Unidirectional Carbon Fiber Composite Materials

When Figure 7 is examined, the average tensile strength value of unidirectional glass fiber hybrid composite materials, especially of the samples with 1% boric acid by weight, has increased. Again, in unidirectional carbon fiber hybrid composite materials, the average tensile strength values of the samples with 1% and 5% additives were increased. It is seen that the highest average tensile strength value in unidirectional glass fiber specimens is in the sample with 1% reinforced value with 469 N/mm², and the highest average tensile strength value in unidirectional carbon fiber specimens is in the sample that is 5% reinforced with a value of 915 N / mm². The results obtained have been shown in Table 2 in order to allow better understanding of the experimental study results.

When Table 2 is examined, it is seen that 1% by weight boric acid reinforcement can increase the average tensile strength by approximately 32% for unidirectional glass fiber composite samples. For unidirectional carbon fiber composite samples, it was observed that 5% by weight boric acid reinforcement can increase the average tensile strength by about 23%. For unidirectional glass fiber composite samples %10 by weight boric acid reinforcement decrease the average tensile strength by approximately 9,03% .And for unidirectional carbon fiber composite samples , %10 by weight boric acid reinforcement has little effect as %1.97 . After a certain amount of boron component reinforcement, it has been also shown in the literature that this components has a negative effect on average

tensile strength or does not affect it at all. Boztoprak and Kartal [20] showed in their study that the tensile strength value decreased due to the increase in the boron nitride ratio. Navaneethkrishnan et al. [5] showed in their study that %1 by weight boron nitride reinforcement increased tensile strength value on the other hand %2 by weight boron nitride reinforcement decreased. Taşgin, [21] reported that %10 by weight boric acid reinforcement decrease the average tensile strength compared to %5 by weight boric acid reinforcement.

TABLE II
AVERAGE TENSILE STRENGTH CHANGE RATE BASED ON BORIC ACID ADDITIVE RATIO

Sample Name	Boric acid Reinforcement Percentage	Symbolic Notation	Average Tensile Strength Value (N/mm ²)	Rate of Change (%)
Unidirectional Glass Fiber	Neutral	N-0-TYCF	354	
	1%	1-0-TYCF	469	(+) 32,4
	5%	5-0-TYCF	360	(+) 1,69
	10%	10-0-TYCF	322,33	(-) 9,03
Unidirectional Carbon Fiber	Neutral	N-90-TYCF	743	
	1%	1-90-TYCF	884,66	(+) 19,06
	5%	5-90-TYCF	915,66	(+) 23,24
	10%	10-90-TYKF	757,66	(+) 1,97

* (+ indicates that the rate of change is positive, - is negative)

4. CONCLUSIONS

The main purpose of this study is to investigate the effect of boric acid reinforcement on the mechanical and tribological properties of glass fiber/polyester and carbon fiber/polyester composite materials. Adhesion wear is defined as the wear of surfaces that are in contact with each other under the influence of normal force. Due to the fact that the surface areas of the surfaces in contact are very small, even if the force is constant, the applied pressure value is quite high. The surfaces in this situation are subject to plastic deformation. As a result of the relative movements of the contact surfaces, gaps are formed on the surface of the object, which is produced from soft material, due to the rupture of the aforementioned bonds, and particles begin to fall off between the two surfaces. During polymer transfer, it is seen that the wear volume and friction coefficient increase and the wear resistance decreases in parallel with the increase in the transfer amount.

It is evaluated that various additives that can be made to the matrix material in composite materials can reduce the surface to surface transfer amount and thus increase the wear resistance [20-23] In the study, it was determined that due to the lubricating effect of boric acid, its wear resistance increased with the addition of the matrix material. In addition, by adding boric acid to the matrix material to obtain hybrid composite material, the average tensile strength values have increased significantly depending on certain ratios by weight. The data obtained from this study will make a significant contribution to the determination of the mechanical and tribological properties of different fiber reinforcement angles and bi-directional fiber reinforced composite materials. The evaluations of the general results are presented below.

- The addition of boric acid increases the average tensile strength up to a certain rate,
- Addition of boric acid in increasing rates brings improvements in the tribological properties of the composite material, and the wear resistance increases,
- If boric acid is used as reinforcement at more than a certain amount, results have been obtained suggesting that it does not change or reduce the average tensile strength value.

REFERENCES

- [1] P. Mallick, "Fiber reinforced composites", Department of Mechanical Engineering University of Michigan Dearborn, Michigan, 1993.
- [2] E. Karacay, E. Alp, H.C. Cabbar, "Boron carbide production by sol-gel method and its characterization", *Journal of the Faculty of Engineering and Architecture of Gazi University*, 27(2), pp. 417-428, 2012
- [3] S. K. Mazumdar, "Composites manufacturing materials, product, and process engineering", *CRC Press*, London., 2002, pp.20-39
- [4] A.B. Strong, "Fundamentals of composites manufacturing: materials, methods, and applications", 2nd ed., SME, Michigan, 2008, pp.1-18.
- [5] G. Navaneethakrishnan, T. Karthikeyan, S. Saravanan, V. Selvam, "Influence of boron nitride on morphological, mechanical, thermal and wear characteristics of epoxy nano composites", *Mater. Res. Innov.*, 24:5, pp. 257-262, 2020.
- [6] V. Vijayaraghavan, L. Zhang, "Tensile and interfacial loading characteristics of boron nitride-carbon nanosheet reinforced polymer nanocomposites". *Polymers*. 11(6), pp. 1075, 2019.
- [7] M. Rahmat, A. Naftel, B. Ashrafi, M.B. Jakubinek, Y. Martinez-Rubi, B. Simard, "Dynamic mechanical characterization of boron nitride nanotube-epoxy nano composites", *Polym. Compos.*, 40, pp. 2119-2131, 2019.
- [8] X. Zhang and J. Zheng, "Polymer composites with enhanced mechanical and thermal properties by orientating boron nitride flakes", *IOP Conf. Ser.: Mater. Sci. Eng.* 493, 012137, 2019.
- [9] B. R Burroughs, J. H. Kim, T. A. Blanchet, B"oric acid self-lubrication of B2O3-filled polymer composites", *Tribol. Tran.*, 42(3), pp.592-600, 1999.
- [10] A. D. Cavdar, F. Mengeloğlu, K. Karakus. "Effect of boric acid and borax on mechanical, fire and thermal properties of wood flour filled high density polyethylene composites", *Measurement*, 60, pp. 6-12, 2015.
- [11] J. Hou, G. Li, N. Yang, L. Qin, M. E. Grami, Q. Zhang., N. Wang, X. Qu, "Preparation and characterization of surface modified boron nitride epoxy composites with enhanced thermal conductivity", *Chem.Sci.*, 4, pp. 44282-44290, 2014.
- [12] N. K. Myshkin, M. I. Petrokovets, A. V. Kovalev, (2005). Tribology of polymers: adhesion, friction, wear and mass-transfer, *Tribol. Int.*, 38, pp. 910-921, 2005.
- [13] D. X. Li, Y. L. You, X. Deng, W. J. Li, Y. Xie, "Tribological properties of solid lubricants filled glass fiber reinforced polyamide 6 composites", *Mater. Des.*, 46, pp. 809-815, 2013.
- [14] E. Karatas, O. Gul, N. G. Karšli, T. Yılmaz, "Synergetic effect of graphene nanoplatelet, carbon fiber and coupling agent addition on the tribological, mechanical and thermal properties of polyamide 6,6 composites", *Com. B. Eng.*, 163, pp. 730-739, 2019.
- [15] T. W. Scharf, S. V. Prasad, "Solid lubricants: a review", *J. Mater. Sci.*, 48, pp. 511-531, 2013.
- [16] M. Demir, Y. Çelik, E. Kılıçkap, "Cam ve karbon elyaf takviyeli kompozitlerde elyaf cinsinin, yükün, kayma hızı ve mesafesinin abrazyon aşınmaya etkisi", *Politeknik Dergisi*, 22, pp. 811-817, 2019.
- [17] D. Pedrazzoli, A. Pegoretti, K. Kalaitzidou, "Synergistic effect of exfoliated graphitenano platelets and short glass fiber on the mechanical and interfacial properties of epoxy composites", *Compos. Sci. Technol.*, 98, pp. 15-21, 2014.
- [18] S.Y. Yang, W.N. Lin, Y.L. Huang, H.W. Tien, J.Y. Wang, C.C.M. Ma, S.M. Li, Y.S. Wang, "Synergetic effects of graphene platelets and carbon nano tubes on the mechanical and thermal properties of epoxy composites", *Carbon*, 49, pp. 793-803, 2011.
- [19] X. Yang, Z. Wang, M. Xu, R. Zhao, X. Liu, "Dramatic mechanical and thermal increments of thermo plastic composites by multi-scale synergetic reinforcement: carbon fiber and graphene nano platelet", *Mater. Des.*, 44, pp. 74-80, 2013.

- [20] Y. Boztoprak, İ. Kartal, "Bor nitrür partikülleriyle takviyelendirilmiş vinil ester matrisli kompozitlerin mekanik özelliklerinin incelenmesi", *ECJSE*, 6(1), pp. 45-50, 2019.
- [21] Y. Taşgın, "Katalizör olarak katılan bor oksit ve borik asidin polyester üzerindeki etkilerinin mekanik ve mikro yapı açısından incelenmesi", *Fırat Üniversitesi Mühendislik Bilimleri Dergisi*, 30, pp. 303-311, 2018.
- [22] W. Brostow, V. Kovačević, D. Vrsaljko, J. Whitworth, "Tribology of polymers and polymer-based composites", *J. Mater. Educ.*, 32, (5-6), pp. 273-290, 2010.
- [23] H. Dong, T. Bell, "State-of-the-art overview: Ion beam surface modification of polymers towards improving tribological properties", *Surf. Coat. Technol.*, 111, pp. 29-40, 1999.
- [24] S. K. Sinha, B. J. Briscoe, "PolymerTribology", 1st ed., Imperial College Press, London, 2009.
- [25] N. G. Karšli, S. Demirkol, T. Yılmaz, "Thermal aging and reinforcement type effects on the tribological, thermal, thermomechanical, physical and morphological properties of poly(etheretherketone) composites", *Com. B. Eng.*, 88, pp. 253-263, 2016.

BIOGRAPHIES

Taner Aydin received his bachelor's degree in mechanical engineering from Kocaeli University, Turkey in 2012. He began studying for a master's degree at Kocaeli University in 2018. He has been working as a research assistant at Dicle University since 2020. He works on boron reinforced composite materials.

Kadir Turan received the B.S. degree from the Mechanical Engineering Department, Firat University, Elazığ, Turkey, in 2000, and the M.S. degrees from the Firat University in 2003 and PhD degrees from the Firat University in 2009. He was appointed as an Assistant Professor in 2011, Associate Professor in 2014, and Professor in 2020 to the same department. His research interests include mechanics of composite materials, finite element method, wreckage analysis. He has 12 articles in SCI-indexed journals and 15 articles in national journals.

Nejat Yıldırım Sarı received the B.S. degree from the Mechanical Engineering Department, Yıldız Technical University (YTU), Istanbul, Turkey, in 1987, and the M.S. degrees from the Yıldız Technical University in 1992 and PhD degrees from the Istanbul Technical University in 1999. He is currently an associate professor at the Kocaeli University. His research interests include Mechanical Engineering, Tribology, Engineering and Technology.